K. S. Vijay Sekar · Manoj Gupta
A. Arockiarajan   *Editors*

Advances in Manufacturing Processes

Select Proceedings of ICEMMM 2018

Springer

Lecture Notes in Mechanical Engineering

Lecture Notes in Mechanical Engineering (LNME) publishes the latest developments in Mechanical Engineering—quickly, informally and with high quality. Original research reported in proceedings and post-proceedings represents the core of LNME. Volumes published in LNME embrace all aspects, subfields and new challenges of mechanical engineering. Topics in the series include:

- Engineering Design
- Machinery and Machine Elements
- Mechanical Structures and Stress Analysis
- Automotive Engineering
- Engine Technology
- Aerospace Technology and Astronautics
- Nanotechnology and Microengineering
- Control, Robotics, Mechatronics
- MEMS
- Theoretical and Applied Mechanics
- Dynamical Systems, Control
- Fluid Mechanics
- Engineering Thermodynamics, Heat and Mass Transfer
- Manufacturing
- Precision Engineering, Instrumentation, Measurement
- Materials Engineering
- Tribology and Surface Technology

To submit a proposal or request further information, please contact: Dr. Leontina Di Cecco Leontina.dicecco@springer.com or Li Shen Li.shen@springer.com.

Please check the Springer Tracts in Mechanical Engineering at http://www.springer.com/series/11693 if you are interested in monographs, textbooks or edited books. To submit a proposal, please contact Leontina.dicecco@springer.com and Li.shen@springer.com.

More information about this series at http://www.springer.com/series/11236

K. S. Vijay Sekar · Manoj Gupta
A. Arockiarajan

Editors

Advances in Manufacturing Processes

Select Proceedings of ICEMMM 2018

Springer

Editors
K. S. Vijay Sekar
SSN College of Engineering
Chennai, India

A. Arockiarajan
Department of Applied Mechanics
Indian Institute of Technology Madras
Chennai, India

Manoj Gupta
Department of Mechanical Engineering
National University of Singapore
Singapore, Singapore

Preface

The Two-day International Conference on "Engineering Materials, Metallurgy and Manufacturing" (ICEMMM 2018) is organized by the Department of Mechanical Engineering, SSN College of Engineering, Kalavakkam, Chennai. The advent of the digital age is seeing a robust growth of research in smart materials and technologies, while the manufacturing processes ensure in making these new age products and prototypes. The need for energy savings, environment protection, and green-rated processes are further accelerators in the right direction. We are therefore happy to organize the International Conference on Engineering Materials, Metallurgy and Manufacturing (ICEMMM 2018) on February 15–16, 2018, in our esteemed institution. The aim and scope of the conference is to provide a robust platform for academicians, researchers, scientists, and students to present their ongoing research work in cutting-edge areas of materials, metallurgy, and manufacturing. It is also the endeavor of this conference to bring to the forefront the seminal research works in these key areas by eminent scholars worldwide and provide them with an opportunity to share their success stories with an earnest audience. This conference hopes to provide enough food for thought on challenges faced by the industry and eagerly awaits the amalgamation of ideas and solutions to address the current and future requirements. We sincerely hope all the delegates will cherish the exchange of new ideas and reap considerable benefits from the face-to-face interaction and potential future networking.

Chennai, India   K. S. Vijay Sekar
Singapore   Manoj Gupta
Chennai, India   A. Arockiarajan

Acknowledgements

About the Institution

SSN Institutions, founded by Padma Bhushan Dr. Shiv Nadar, Chairman, HCL Technologies, stand out as a premier center for higher learning with a mission of pursuing excellence in education and research. These institutions, with their diverse and dynamic community of students, offer a distinctive combination of some of the finest graduate, undergraduate, and research programs, accomplished faculty, world-class facilities, and a residential campus set on a sprawling 250 acres of sylvan surroundings. SSN Institutions provide a variety of stimulating environments for intellectual development, freethinking, and personal growth, challenging its students with dynamic learning opportunity and equipping them with the skills, insights, attitudes, and practical experiences that are necessary to take up responsibilities in the society. While students at SSN immerse themselves in academics, the college has a lot in store for them outside the classroom. Student life includes participation in sports, recreational and cocurricular activities, and culturals. In short, at SSN, students will find an academic and social environment where everyone—from faculty members to students—help shape their future. SSN is a home to aesthetically designed buildings with the state-of-the-art computer and Internet facilities, modern workshops, seminar halls, auditoriums, well-stocked libraries, and sports and games fields in addition to an indoor stadium with gymnasium. As an exemplary institution for learning, SSN follows an admission policy that strongly favors merit, even as it enables access to education for students from all strata of society through appropriate scholarships. The institution boasts of a strong alumni network with alumni events held every year serving as a platform for the past students to get back to SSN and share their experiences with its present fellow students. With so much to offer, it is only natural that the students of SSN get a unique opportunity to carve a niche for themselves in their chosen field of study that enables them to become well-rounded and discerning citizens, fully qualified for their chosen professions in the workplace.

Smart India Hackathon 2017: SSN was selected as one of the 26 nodal centers in India for conducting the grand finale of the Smart India Hackathon 2017, world's largest hackathon event organized by the Ministry of HRD, India. Two teams from

SSN won the first prize and the third prize under the Ministry of Skill Development and Postal Services, respectively.

NIRF rankings: SSN secured the all India 27th rank in the engineering category in the NIRF ranking system constituted by the Ministry of HRD. SSN College of Engineering was also accredited by NAAC with an A+ Grade in 2017.

About the Department

The Department of Mechanical Engineering was established in the year 2007. It offers a UG program in mechanical engineering and PG programs in manufacturing engineering and energy engineering.

The department is also recognized as a nodal research center for pursuing M.S. (By Research) and Ph.D. under Anna University, Chennai, for pursuing doctoral research works. The department has got 34 well-qualified and experienced faculty members, out of which 29 are Ph.D. degree holders and the remaining 5 are on the verge of completing their Ph.D. degrees. The department has 29 recognized Ph.D. supervisors and 103 Ph.D. research scholars registered under Anna University, Chennai, out of which 19 are full-time scholars and 84 are part-time scholars.

The faculty members and students actively engage in research and constantly publish papers in reputed international journals. The department regularly organizes national and international conferences and workshops in emerging areas. The department also has Industry Institute Partnership Cell (IIPC) for enhancing the relationship between the institute and industry.

The department has well-equipped laboratories with research facilities like friction stir welding, material processing, composite machining, cryogenic machining, and vibration analysis. Faculty members are actively involved in executing a number of R&D projects for government agencies like Department of Science and Technology (DST), All India Council for Technical Education (AICTE), and Naval Research Board (NRB) to the tune of more than 2.5 crores.

The major research areas are friction stir welding, metal cutting, composites, FEA, CFD, vibration analysis, nanotechnology, robotics, heat transfer, alternate fuels, thermal energy storage, and vapor absorption refrigeration systems.

About the Conference—ICEMMM 2018

The Two-day International Conference on "Engineering Materials, Metallurgy and Manufacturing" (ICEMMM 2018) is organized by the Department of Mechanical Engineering, SSN College of Engineering, Kalavakkam, Chennai. The principal objective of ICEMMM 2018 is to provide a neutral platform for researchers, engineers, academicians, and industrial professionals from all over the world to present their research results and development activities in materials, metallurgy, and manufacturing technology. This conference provides opportunity for the delegates to exchange new ideas and application experiences face to face, to establish business or research relations, and to find global partners for future collaboration. It is proposed to have several parallel sessions with invited keynote lectures by eminent academicians and experts from various fields. The selected papers will be published in the Lecture Notes in Mechanical Engineering (Springer publications). The papers have been selected from diverse fields like composite materials, welding metallurgy, powder metallurgy, tribology, conventional and advanced machining, metal forming processes, additive manufacturing, coating, and surface engineering. The conference hopes to bring out the multi-disciplinary fields of materials, metallurgy, and manufacturing under a single roof.

President's Message

One of the perennial problems being faced by the industry today is the spiraling manufacturing costs led by higher material cost and extraction costs. It has been the endeavor of the academia to find lasting solutions to these problems.

With this background, I am happy that the Department of Mechanical Engineering is conducting an International Conference on Engineering Materials, Metallurgy and Manufacturing—ICEMMM2018, on 15 and 16 February 2018. This conference will not only encourage knowledge sharing but also prove to be a platform for brainstorming ideas that will shape the Metallurgy and Material Science industry in future.

Research is an important facet of life at SSN and SSN researchers are working on finding practical solutions to a wide range of research problems. This conference aims at promoting exchange of ideas, building mutually rewarding collaborations and providing exposure and motivation to the budding researchers. I am sure this conference will be an enriching and inspiring experience for everyone involved.

I wish the organizers of the conference the very best and also warmly welcome all the participants. I am sure all the delegates will have a comfortable stay at the SSN campus and will take back lasting memories to cherish in future.

Ms. Kala Vijayakumar
President, SSN Institutions

Principal's Message

In today's world, it has become preeminent to constantly be networked and connected to stay abreast of the technical field and in this connection, academic conferences help in promoting and sharing of research findings and provide new avenues for all stakeholders.

SSN College of Engineering values its academic as well as research knowledge as its greatest wealth. A number of national and international conferences in various domains are conducted on a regular basis to feed the changing technological environment around us. These meetings encourage new ideas to be exchanged in a multitude of engineering domains amongst contemporary researchers. The magnitude of these efforts have increased over time and resulted in a higher level of thinking and execution which helps today's engineers navigate their lives and careers.

I take immense pleasure in welcoming the delegates of the International Conference on Engineering Materials, Metallurgy and Manufacturing—ICEMMM2018, organized by the Department of Mechanical Engineering on 15 and 16 February 2018. The conference aims to promote cutting edge research in futuristic areas of material, metallurgy and manufacturing. I am sure that, this platform will be an enriching experience for the delegates and the confluence of ideas will develop solutions to the problems faced by the industry.

I express my gratitude to the advisory committee, organizing committee, keynote speakers, session chairs, review committee, contributing authors and conference participants for their efforts in making this conference a grand success. I wish all the delegates an eventful two days at the conference as well as at their stay on campus.

<div align="right">

Dr. S. Salivahanan
Principal, SSNCE

</div>

HOD's Message

Any Engineer is associated with the task of developing solutions. Solutions come through appropriate selection of materials and processing technology. With the entire world being invited to "Make in India", manufacturing technologies play a major role. Newer applications demand newer materials. The advent of new materials necessitate corresponding developments in material processing technology. Advances in metallurgy enable better and efficient processing of materials.

Thus materials, metallurgy and manufacturing are three major aspects of importance to any mechanical engineer. I am happy to note that these are being covered by ICEMMM2018. Wishing the Conveners Dr. K. S. Vijay Sekar and Dr. A. K. Lakshminarayanan, and the Co-conveners Dr. L. Poovazhagan, Dr. M. Dhananchezian and Dr. K. Jayakumar, for a successful event.

Dr. V. E. Annamalai
Professor and Head, Mechanical Engineering, SSNCE

Conveners' Message

Dr. K. S. Vijay Sekar
Convener

Dr. A. K. Lakshminarayanan
Convener

Dr. L. Poovazhagan
Co-Convener

Dr. M. Dhananchezian
Co-Convener

Dr. K. Jayakumar
Co-Convener

The advent of the digital age is seeing a robust growth of research in smart materials and technologies while the manufacturing processes ensure in making these new age products and prototypes. The need for energy savings, environment protection, green rated processes are further accelerators in the right direction. We are therefore happy to organize the International Conference on Engineering Materials, Metallurgy and Manufacturing—ICEMMM2018, on February 15–16, 2018 in our esteemed institution.

The aim and scope of the conference is to provide a robust platform for academicians, researchers, scientists and students to present their ongoing research work in cutting edge areas of materials, metallurgy and manufacturing. It is also the endeavor of this conference to bring to the forefront, the seminal research works in these key areas by eminent scholars worldwide and provide them an opportunity to share their success stories with an earnest audience.

This conference hopes to provide enough food for thought on challenges faced by the industry and eagerly awaits the amalgamation of ideas and solutions to address the current and future requirement. We sincerely hope all the delegates will cherish the exchange of new ideas and reap considerable benefits from the face to face interaction and potential future networking. We express our gratitude to the management of SSN Institutions for giving us the opportunity to organize this important conference and also thank all the delegates for making this event a grand success. We also thank the Keynote speakers, Conference chairs, Advisory,

Program and Technical committees, Reviewers, Colleagues, the College administration, our friends, students and well-wishers for making this event a memorable one.

We thank one and all.

Keynote: I

The Promise of Magnesium (Composite) Technology for Sustainable Planet Earth

Dr. Manoj Gupta

Department of Mechanical Engineering, National University of Singapore, Singapore

Email: mpegm@nus.edu.sg

The development of technology for producing sustainable energy sources replacing fossil fuels is the vital subject imposed on researchers. A recent analysis has confirmed that the conversion of solar energy into electricity by solar cells is one of the most promising renewable energy technologies. Among the solar cells, nanoporous semiconductor based dye-sensitized solar cells (DSSCs) have gained much interest in recent years because of their low production costs and ease of fabrication. The performance of this type of solar cells depends on the semicon-ductor material, morphology, structure of the sensitizing molecules and redox mediator used. The interfacial recombination of the electrons injected by the sen-sitizer with the cations of the dye molecule or redox couple limits the efficiency of the DSSCs. It has been found that the coating of insulating layer on nanoporous semiconductor oxide material greatly suppresses the recombination in DSSCs and thereby increases the overall cell efficiency. The coating of insulating shell layer on

the core semiconductor oxide material may be an interesting approach to reduce the interfacial recombination in DSSCs. Therefore, our recent research has been focused on the development of core/shell structured nanomaterials by various solution growth techniques. In this study, we report a widely applicable and relatively simple approach for the successful preparation of core/shell structured semiconductor oxide thin films. Further, the promising applications of this core/shell structured nanomaterials will also be discussed.

Keynote: II

Design and Analysis of Structures Made of Long Fiber Reinforced Polymer Composites

Dr. Idapalapati Sridhar

School of Mechanical and Aerospace Engineering, Nanyang Technological University, Singapore

Email: MSridhar@ntu.edu.sg

Wood based natural composite materials are exploited by humans since ancient times for several load-bearing structures. Material intensive modern day aeroplanes, ships and wind-turbine blades are designed and fabricated with long glass or carbon fiber reinforced polymer composites leading to high specific strength and stiff designs. In this presentation, after a brief introduction to composite materials, design and analysis of sandwich structures comprising composite laminates as facesheets and polymeric foams as cores under static and impact loading conditions will be discussed. The competing failure modes of facesheet failure, core shear and localised core indentation failures through upper-bound analytical solutions, finite element based numerical solutions and their comparison with experimental measurements will be presented. A case study on the design and analysis of composite adhesive bonded joints under static and fatigue loading will be discussed for primary structures and as a tool for composites repair will be discussed.

Keynote: III

A-TIG Welding and Its Effect on Performance of the Stainless Steel Weld Joints

Dr. M. Vasudevan

Head, Advanced Welding Processes and Modeling Section,
Materials Development and Technology Division Professor, Homi Bhabha National Institute
Indira Gandhi Centre for Atomic Research, Kalpakkam

Email: dev@igcar.gov.in

Activated Tungsten Inert Gas (A-TIG) welding process has been developed for stainless steels which overcome the major limitations of TIG welding. Significant improvement in penetration performance over 300% has been achieved by A-TIG welding and variable weld penetration during autogenous TIG welding has been overcome. The mechanism causing the improvement in penetration in stainless steels has been identified as the reversal of marangoni flow in the weld pool caused by dissolved oxygen (surface active element) from the activated flux. The weld bead width is reduced and the weld bead profile is improved due to arc constriction caused by the activated flux. A-TIG welding process has been successfully employed for fabricating type 304 LN stainless steel, 316 LN stainless steel, Duplex stainless steel and 409 ferritic stainless steel weld joints. Significant improvement in

mechanical properties, corrosion resistance, large reductions in residual stresses and distortion and cost of fabrication have been demonstrated for the above stainless steel weld joints. A-TIG welding is already found applications in the nuclear industry for improving the performance of weld joints and reduce the cost of fabrication. A-TIG welding has greater potential for welding of structural components made of stainless steels.

Committee Members

Chief Patron
Dr. Shiv Nadar, Founder, HCL and SSN Institutions

Patrons
Ms. Kala Vijayakumar, President, SSN Institutions
Dr. S. Salivahanan, Principal, SSNCE

General Co-chairs
Dr. P. Ramasamy, Dean (Research)

Conference Chair
Dr. V. E. Annamalai, Professor and Head, Mechanical Engineering

Conveners
Dr. K. S. Vijay Sekar, Associate Professor
Dr. A. K. Lakshminarayanan, Associate Professor

Co-conveners
Dr. L. Poovazhagan, Associate Professor
Dr. M. Dhananchezian, Associate Professor
Dr. K. Jayakumar, Associate Professor

Technical Committee
Dr. S. R. Koteswara Rao, Professor
Dr. S. Vijayan, Associate Professor
Dr. B. Anand Ronald, Associate Professor
Dr. K. Babu, Associate Professor
Dr. K. Rajkumar, Associate Professor
Dr. D. Ananthapadmanaban, Associate Professor
Dr. K. L. Hari Krishna, Associate Professor
Dr. R. Damodaram, Associate Professor
Mrs. R. Rajeswari, Assistant Professor
Mr. R. Vimal Samsingh, Assistant Professor

Program Committee

Dr. N. Nallusamy, Professor
Dr. K. Subbaiah, Professor
Dr. N. Lakshmi Narasimhan, Associate Professor
Dr. M. Selvaraj, Associate Professor
Dr. K. S. Jayakumar, Associate Professor
Dr. M. Suresh, Associate Professor
Dr. M. S. Alphin, Associate Professor
Dr. S. Suresh Kumar, Associate Professor
Dr. S. Rajkumar, Associate Professor
Dr. R. Prakash, Associate Professor
Dr. A. S. Ramana, Associate Professor
Dr. M. Nalla Mohamed, Associate Professor
Dr. G. Satheesh Kumar, Associate Professor
Dr. G. Selvakumar, Associate Professor
Dr. S. Soma Sundaram, Associate Professor
Mr. D. Ebenezer, Assistant Professor
Mr. B. Jayakishan, Assistant Professor
Mr. C. Arun Prakash, Assistant Professor

International Advisory Committee

Dr. K. Prasad Rao, Research Professor, University of Utah, USA
Dr. J. Paulo Davim, Professor, University of Aveiro, Portugal
Dr. N. Krishnan, Professor, Charles Darwin University, Australia
Dr. Ramana V. Grandhi, Distinguished Professor, Wright State University, USA
Dr. Sinin Hamdan, Professor, University of Malaysia
Dr. R. Ganesan, Professor, Concordia University, Montreal, Canada
Dr. Dulce M. Rodrigue, Professor, University of Coimbra, Portugal
Dr. K. Elangovan, Professor, Ibri College of Technology, Oman
Dr. R. Mohd Amri B. Lajis, Universiti Tun Hussein Onn Malaysia (UTHM)
Dr. S. Parasuraman, Professor, Monash University, Malaysia
Dr. Mustafizur Rahman, Professor, NUS, Singapore
Dr. M. V. Venkatashamy Ready, Professor, NUS, Singapore
Dr. George Totten, Research Professor, Portland State University, Portland, Oregon
Dr. Esther Akinlabi, Professor, University of Johannesburg, South Africa
Dr. Hakeem Amuda, Associate Professor, University of Lagos, Nigeria
Dr. Sathish Jothi, Lecturer, Swansea University, UK
Dr. B. Prabhu, Coherent, Inc., Santa Clara, USA
Dr. Ramkumar Kandasamy, Volvo Construction Equipment, Sweden
Dr. Khalid Rafi, UL International Singapore Pte Ltd., Singapore
Dr. Kumar Kandasamy, R&D Manager, Oerlikon, USA

National Advisory Committee

Dr. G. Madhusudhan Reddy, Outstanding Scientist, DMRL
Dr. B.Venkataraman, Outstanding Scientist, IGCAR

Contents

About the Editors

Dr. K. S. Vijay Sekar obtained his Ph.D. in mechanical engineering from Anna University, Chennai, India, specializing in finite element analysis in machining. He has 22 years of teaching experience, 12 years of research experience, and successfully guided more than 25 postgraduate projects and 35 undergraduate projects in his long career. He received the Cognizant award for the Best Faculty of SSN College of Engineering for the year 2014–2015. He has published 25 research papers in international and national journals, and his research work has been presented at 20 international and national conferences. He has published a patent, and his areas of interest include studies on the machinability of composite materials and superalloys and the use of finite element tools to understand machining characteristics and optimize the manufacturing process.

Dr. Manoj Gupta is a former Head of Materials Division of the Mechanical Engineering Department and Director designate of Materials Science and Engineering Initiative at NUS, Singapore. He completed his Ph.D. at the University of California, Irvine, USA, and postdoctoral research at the University of Alberta, Canada. In August 2017, he was named among the top 1% scientist of the world by the Universal Scientific Education and Research Network. He pioneered the disintegrated melt deposition technique and the hybrid microwave sintering technique, an energy-efficient solid-state processing method of synthesizing alloys/micro-/nanocomposites. He has published over 490 articles in peer-reviewed journals and owns two US patents. He is a multiple award winner and has also co-authored six books.

Dr. A. Arockiarajan obtained his Ph.D. from the University of Kaiserslautern, Germany, with specialization in finite element modeling of ferroelectrics. He has industrial experience with Tata Motors, India, and Infineon, Germany. He is currently an associate professor in the Department of Applied Mechanics, Indian Institute of Technology Madras. His research interests include smart materials, ferroelectrics, electro-active polymers, piezo-composites, constitutive modeling, and numerical techniques. He serves as a consultant for various industries such as

BHEL, Rane NSK, Concord Electroceramics. He has published over 70 articles in international peer-reviewed journals in the areas of smart materials and composites. He is an associate fellow of the Indian National Academy of Engineering. He has also received the Young Engineer Award from INAE and ISSS Young Scientist Award from the Institute for Smart Structures and Systems (ISSS).

Development of Finite Element Model to Predict Temperature and Residual Stress Distribution in Gas Tungsten Arc Welded AA 5059 Aluminium Alloy Joints

Babu Narayanasamy, Karunakaran Narayan and Balasubramanian Viswalingam

Abstract High-strength armour grade AA 5059 aluminium alloy finds wide application in the fabrication of lightweight structures, which require a high strength-to-weight ratio. They include transportable bridge girders and military vehicles. In gas tungsten arc welding (GTAW), fusion zones are characterized by coarse columnar grains due to the thermal condition that prevails during solidification of weld metal. This accounts for inferior weld mechanical properties and poor resistance to hot cracking. The higher temperature and higher thermal gradients in welds make it difficult to exercise control on solidification structure in welds. The modelling procedure was developed in this research work using the software code of COMSOL. The boundary conditions, heat source model and the governing equations were incorporated into the finite element model. It is found that the predicted values of temperature while using three-dimensional finite element model are in good agreement with the experimental values.

Keywords Gas tungsten arc welding · Temperature distribution
Residual stress distribution · Finite element analysis

Babu Narayanasamy (✉)
Department of Mechanical Engineering, Alagappa Chettiar
Government College of Engineering and Technology, Karaikudi, India
e-mail: babu.manu11@gmail.com

Karunakaran Narayan
Department of Mechanical Engineering, Annamalai University, Chidambaram, India

Balasubramanian Viswalingam
Department of Manufacturing Engineering, Annamalai University, Chidambaram, India

1   Introduction

AA 5059 aluminium alloy exhibits good corrosion resistance, high strength-to-weight ratio and excellent formability. It is mainly recommended for the ship hull and superstructure. Also, this alloy is extensively used in the fabrication of cryogenic tanks and pressure vessels due to its strength, superior resistance to cracking and corrosion resistance [1]. This alloy is a newly developed magnesium (Mg)-based non-heat-treatable alloy and is mainly recommended for armour applications due to its high strength attained by mechanical strain hardening. For joining of aluminium alloy, gas tungsten arc (GTA) welding has been commonly used since it is easier availability and cost-effective. An electric arc triggered between the consumable tungsten electrode and the workpiece in the GTA welding process provides the thermal energy to melt the workpiece and the filler. The evolution of microstructure, especially on the hardening of precipitates is induced by elevated process temperatures. High thermal conductivity, high oxygen solubility makes welding of aluminium all the more difficult and challenging at elevated temperature. All these factors lead to defects in the weld bead [2, 3]. Joy Varghese et al. [4] reviewed the heat transfer analysis prevalent in GTAW process and concluded that there is a gap in the availability of procedure to address the multiphysics involved in the welding. De and Debroy [5] exhaustively studied the challenges attributed by the welding residual stress using 3D finite element model and real-time experiments. Tsai and Eagar [6] developed an analytical model for predicting temperature fields arising out of the moving heat source and concluded further that the weld process parameters and material properties play a significant role in weld pool shape prediction. The heat source modelling poses a challenge in the simulation of thermal field in the welding process and to make the choice of material properties that could be used for simulation [7, 8]. The precision of thermocouples and the calibration of the heat source are other challenges which need to be addressed; several studies have been carried out in the literature [9]. The finite element method (FEM) is now proven method deemed fit to product development. The weld strength is influenced by thermal cycle of the welding process as it plays a crucial role in grain growth and phase formation of the microstructure [10]. It is understood from the literature that research works carried out focusing on thermal analysis on AA 5000 series aluminium alloy welded joints are very scant. Hence, the present research work focuses on estimating the temperature and residual stress distribution in the welded joints experimentally as well as numerically.

2   Experimental Work

The parent material is used in this AA 5059 rolled plates of 4-mm-thick aluminium alloy. The chemical composition of the parent metal is presented in Table 1 [1]. The parent metal mechanical properties are shown in Table 2. The rolled plates were

Table 1 Chemical composition of parent metal

Si	Cu	Mn	Mg	Cr	Zn	Ti	Al
0.041	0.003	0.933	5.21	0.5–0.6	<0.001	0.489	Balance

Table 2 Mechanical properties of parent metal

Ultimate tensile strength (MPa)	0.2% yield strength (MPa)	Elongation in 50-mm gauge length (%)	Hardness (HV 0.5 N)
385	290	16	123

Table 3 Welding parameters used to fabricate the joint

Welding parameter	Parameter value
Current (A)	110
Voltage (V)	14
Welding speed (mm/s)	1.3
Weld efficiency	0.5 [20]

machined to the required size (300 × 150 mm), and the welding was carried out in butt square joint configuration using GTAW machine, Lincolin, USA. The GTAW process parameters used to make defect-free joints are shown in Table 3. After a number of trials, the joint which was free of volumetric defects and other defects such as porosity and inclusions was considered as the optimized condition for GTAW. K-type thermocouples made of chromel and alumel with a sensitivity of 41 μV K^{-1} were used for temperature prediction [11]. In order to fix the thermocouples, holes were drilled to a depth of 2 mm at three different locations 7, 12 and 17 mm away from the weld centre-line and along the mid-length at both sides of the plate.

3   Finite Element Modelling of GTAW

COMSOL is FEA software that allows for the simulation of theoretical and engineering applications [12]. Geometries can also be modelled within COMSOL itself, along with defining mesh type and element size. For the modelling of residual stress in welds, COMSOL offers the advantage to couple physics of solid mechanics and heat transfer relationships. The governing equation [13, 14] for heat transfer is derived from the Helmholtz equation

$$\frac{\partial}{\partial x}\left(kx\frac{\partial T}{\partial x}\right) + \frac{\partial}{\partial y}\left(ky\frac{\partial T}{\partial y}\right) + \frac{\partial}{\partial z}\left(kz\frac{\partial T}{\partial z}\right) + Q = 0, \tag{1}$$

where kx, ky and kz are the thermal conductivities in the x, y and z directions and Q is the internal heat generation.

3.1 Mesh

Different elements were used for finite element analysis. Figure 1 depicts the mesh pattern of the present study. The meshed model is composed of 13,100 tetrahedral elements, 915 triangular elements, 415 edge elements and 20 vertex elements. Mesh size varied from 0.225 to 5.25. The typical thermo-mechanical properties of AA 5059 are tabulated in Table 4.
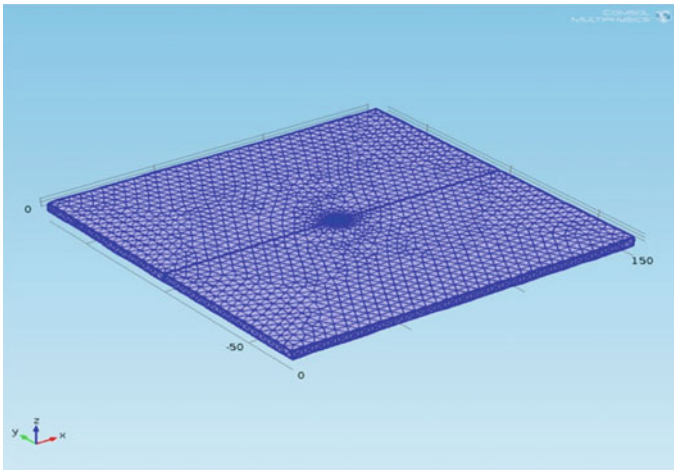
Fig. 1 Finite element mesh of the model

Table 4 Typical thermo-mechanical properties of AA 5059 [22, 23]

Name	Value
Heat capacity at constant pressure (J(kg^{-1})K^{-1})	904
Thermal conductivity (W (m^{-1} K^{-1}))	117
Density (kg m^{-3})	2640
Coefficient of thermal expansion [1/K]	23×10^{-6}
Young's modulus (Pa)	70×10^{-9}
Poisson's ratio	0.33

3.2   Thermal Efficiency of Welding Arc

For GTAW, the arc thermal efficiency is approximated as 0.71 by most of the researches, but actually it varies from 0.41 to 0.816 [15]. This large variation in the arc thermal efficiency can reduce the accuracy of thermal models.

3.3   Heat Source Model

The front and rear half of the heat source forms the two quadrants of the ellipsoidal model. The estimation of the heat input was made based on Eqs. (2) and (3) [16, 17]

$$q_f = \frac{6\sqrt{3}Qf_f}{\pi\sqrt{a_f}bc}\exp\left(-3\left[\frac{x^2}{a_f^w} + \frac{y^2}{b^2} + \frac{z^2}{c^2}\right]\right),$$ (2)

$$q_r = \frac{6\sqrt{3}Qf_r}{\pi\sqrt{a_r}bc}\exp\left(-3\left[\frac{x^2}{a_r} + \frac{y^2}{b^2} + \frac{z^2}{c^2}\right]\right),$$ (3)

where f_f and f_r are the frontal and rear fraction of the heat flux, and b and c are the parametric values obtained from the metallographic data. Based on the literature [21], a_f is 5 mm and a_r is 20 mm. Values of $f_f = 0.6$ mm and $f_r = 1.4$ mm were found to provide the best correspondence between the measured and calculated thermal history results. a_f is the forward portion of the area of heat application. a_r is the rear portion of the area of heat application. Q is the calculated heat input. Figure 2 shows the solid model of the welded specimen with heat source. An empirical relation for the combined convection and radiation heat transfer coefficient during welding can be represented by equation [21].

$$h = 24.1 \times 10^{-4}\varepsilon\, T^{1.169} \ \text{W/m}^2\,\text{K}.$$ (4)

3.4   Heat Input Calculation

For the estimation of the heat input (Q), the relationship used for constant current gas tungsten arc welding process is $Q = [(V \times I)/S]\,\eta$, where V is the voltage, I is the current, S is the welding speed, and η is the efficiency of utilization of the heat generated [15, 18]. The amount of heat input was found as the product of arc efficiency, voltage and current which were taken equal to 0.5, 14 V and 110 A, respectively, in this analysis. In this analysis, the amount of heat input was calculated as 592.32 J/mm.
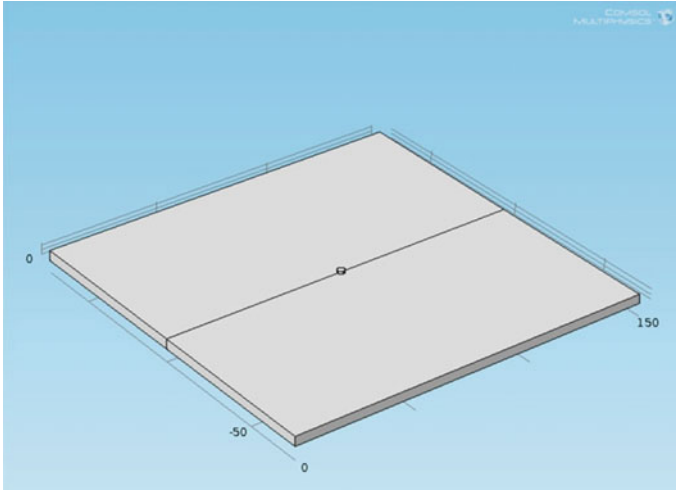
Fig. 2 Solid model of the welded specimen with heat source

3.5 Residual Stress Analysis

During the welding process, the total strain rate can be decomposed into three components as follows:

$$\epsilon_{\text{total}} = \epsilon_e + \epsilon_P + \epsilon_{\text{th}} \tag{5}$$

ϵ_{total} is the total strain produced, ϵ_e is the elastic strain, ϵ_p is the plastic strain, and ϵ_{th} is the thermal strain.

For elastic range, the stress–strain relations for thermo-elastic analysis are

$$\{\sigma\} = [D]\{\varepsilon^e\}, \tag{6}$$

$$\{\sigma\} = [D](\{\varepsilon\} - \{\alpha\}(T - T_0)). \tag{7}$$

The residual stresses mainly depend on the thermal histories experienced by the workpiece [19].

4 Results and Discussion

4.1 Temperature Profiles

Figure 3 shows time–temperature profiles recorded at a distances of 7, 12 and 17 mm from the weld centre-line normal to the welding direction. These profiles
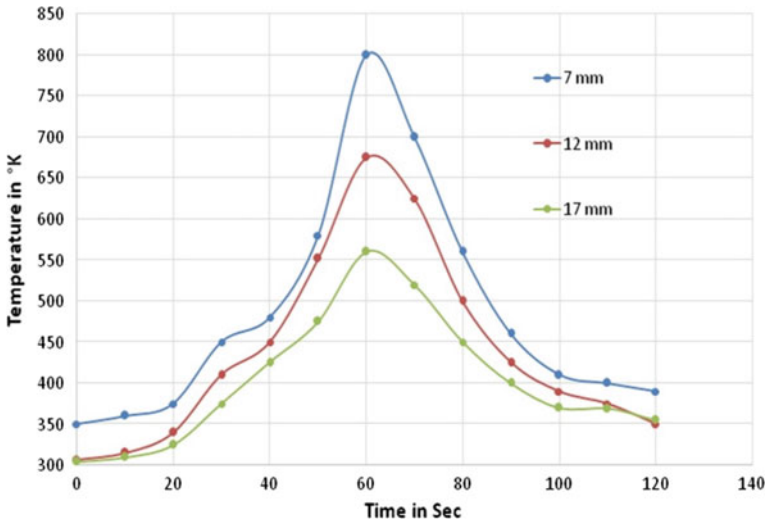
Fig. 3 Time–temperature profiles

were constructed from the experimental study by converting distance travelled by a welding torch to time using welding speed [20]. The highest temperature was recorded at the locations close to weld centre. The highest temperature 801 K was recorded at 7 mm from the centre of the weld. At 12 mm from the centre of the weld, 659 K temperature was recorded. At 17 mm from the centre of the weld, 560 K temperature was recorded. From this figure, it is understood that temperature decreases as it moves away from the weld zone, because of high thermal conductivity of base material.

4.2 Residual Stress Profiles

At weld bead, maximum tensile stress 200 MPa which is below the yield strength of the base material was recorded. At 7 mm from the centre of the weld bead, maximum tensile stress 109 MPa was recorded. A compressive stress of 15 MPa was recorded at a point 12 mm from the centre of the weld bead. Expansion of the heat-affected zone is restrained by the surrounding metal at lower temperature, and hence compressive stress is experienced by HAZ. The magnitude of the compressive stress increases with increasing distance from the weld or with decrease in weld temperature. Figure 4 shows the measured residual stress profile for the GTA welded of AA 5059 aluminium alloy joint.
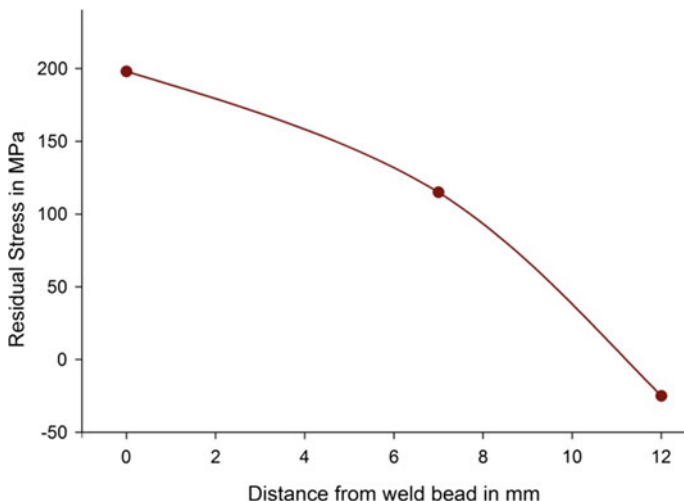
Fig. 4 Measured residual stress profile

4.3 Temperature Analysis (Numerical)

Figure 5 shows the predicted temperature distribution at transient condition. Maximum peak temperature, 2042.1 K, which is below the vaporization temperature that was observed at the weld centre, due to high heat input. The temperature remains at a maximum only as long as the source remains on that spot. Figure 6 shows the temperature distribution along the weld direction. From the figure, it is understood that the maximum temperature of 2042.1 K. is observed at the weld zone where the heat flux is applied, where the electrode initially comes in contact with the work piece. Peak temperature in the workpiece is attained at the top centre of the weld bead because of heat source. Even though the width of the plate is small, compared to the length of the weld specimen, the distribution of the temperature generated during the welding process is asymmetric. At 7 mm away from the centre of the weld, maximum temperature 795 K was predicted. At 12 mm from the centre of the weld, maximum temperature 655 K was predicted. At 17 mm from the centre of the weld, maximum temperature 565 K was predicted. It is concluded that when the distance increases away from the centre of the weld, the temperature decreases. Rapid temperature drops at aforementioned locations compared to weld centre because radiation is the dominant heat loss mechanism at higher temperature and later on convection comes into action at somewhat lower temperature. Both simulation and experimental results are in good agreement with each other.
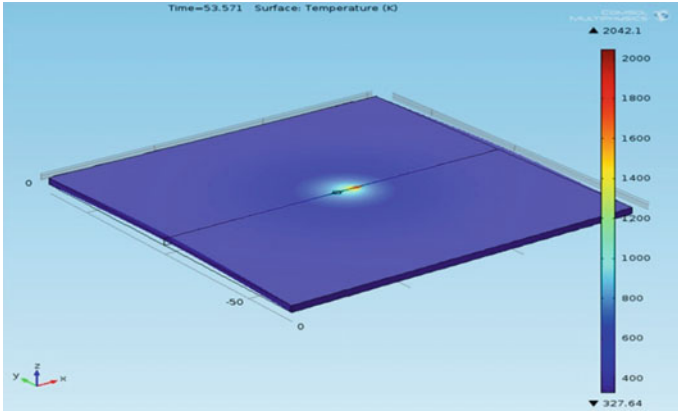
Fig. 5 Predicted temperature field (in K) for transient state
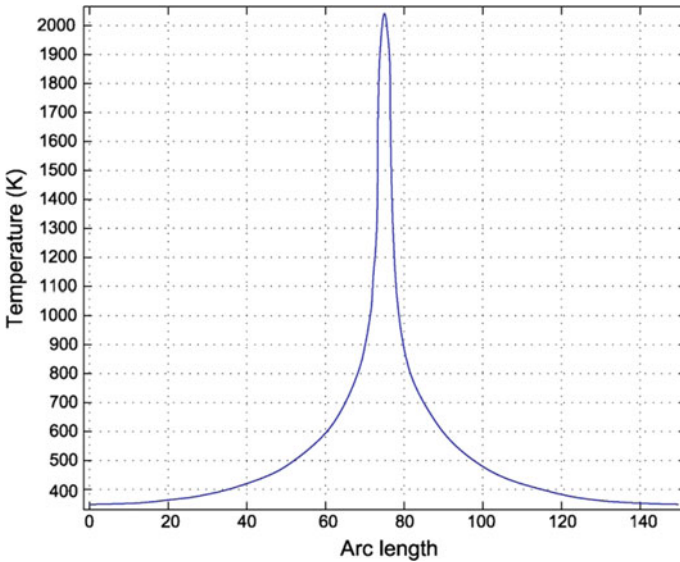
Fig. 6 Predicted temperature distribution along the weld direction

4.4 Residual Stress Analysis (Numerical)

The residual stress distribution in the transverse direction was measured. The residual stress was measured for one specimen at the weld centre, at 7 and 12 mm away from the weld centre. Figure 7 shows the numerically predicted residual stress distribution in the transverse direction. The weld metal region is in tensile region
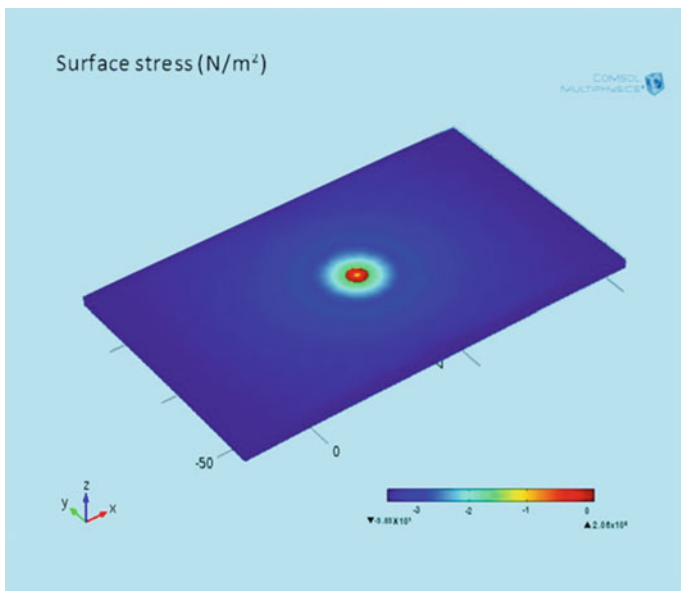
Fig. 7 Residual stress distribution of GTAW (numerical)

Table 5 Experimental and FEA values of residual stress distribution

Process	Weld centre		7 mm away from weld centre		12 mm away from weld centre	
	Experimental	FEA	Experimental	FEA	Experimental	FEA
GTAW	202 MPa	206 MPa	109 MPa	105 MPa	−15 MPa	−10 MPa

with a peak value of 206 MPa, which is below the yield strength of AA 5059 aluminium alloy.

Relatively, the weld area gets rapidly heated up when compared to the surrounding area and the connecting elements get fused locally. The colder material surrounding the weld area restricts the thermal expansion of material caused by the heat input. The compressive plastic flow is exhibited by the weld area as the local thermal stress exceeds the yield stress upon cooling; in the weld area, there develops tensile residual which self equilibriates compressive residual of the surrounding area. Numerical and calculated residual stress values which were obtained with optimized process parameters are presented in Table 5. The obtained results are in good agreement with each other. Figure 8 shows the comparison of numerical and experimental values of residual stress distribution of AA 5059 aluminium alloy joint.
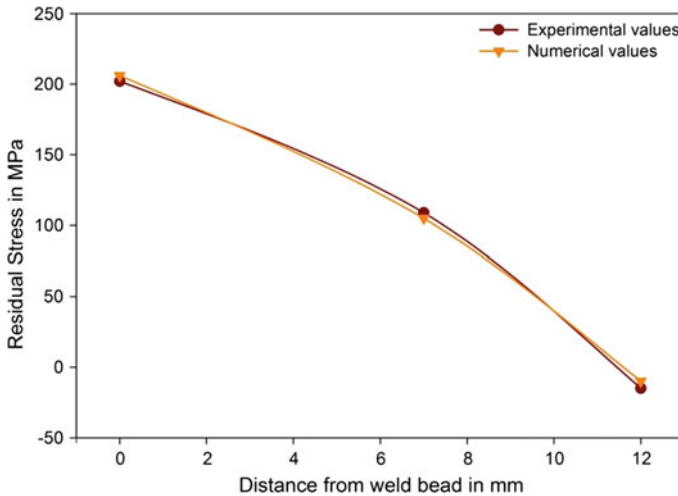
Fig. 8 Residual stress experimental versus numerical

5 Conclusions

- The predicted temperature profiles using the transient three-dimensional FEA model are in good agreement with the experimental temperature profiles. Maximum temperature of 2042.1 K was predicted at the weld centre. When the distance increases from the centre of the weld, the temperature decreases due to high thermal conductivity of the material.

- The residual stress estimated by the developed model is in good agreement with those obtained by the X-ray diffraction experiments. Since the high heat input is involved in this process, the magnitude of residual stress is also higher. Hence, the developed 3D finite element model can be effectively used to predict temperature and residual stress values at any location in the gas tungsten arc welded butt joints of AA 5059 grade aluminium alloy.

References

1. Babu, N., Karunakaran, N., Balasubramanian, V.: A study to estimate the tensile strength of friction stir welded AA 5059 aluminium alloy joints. Int. J. Adv. Manuf. Technol. **79**, 1–4 (2015)
2. Arunkumar, S., Rangarajan, P., Devakumaran, K., Sathiya, P.: Comparative study on transverse shrinkage, mechanical and metallurgical properties of AA 2219 aluminium weld joints prepared by gas tungsten arc and gas metal arc welding processes. Def. Technol. **11**, 262–268 (2015)

3. Nezamdost, M.R., NekouieEsfahani, M.R., Hashemi, S.H., Mirbozorgi, S.A.: Investigation of temperature and residual stresses field of submerged arc welding by finite element method and experiments. Int. J. Adv. Manuf. Technol. **87**, 615–624 (2016)

4. Joy Varghesh, V.M., Suresh, M.R., Sivakumar, D.: Recent developments in modeling of heat transfer during TIG welding—a review. Int. J. Adv. Manuf. Technol. **64**, 749–754 (2013)

5. De, A., Debroy, T.: Reliable calculations of heat and fluid flow during conduction mode laser welding through optimization of uncertain parameters. Weld J. **84**, 101–112 (2006)

6. Tsai, N.S., Eager, T.W.: Distribution of the heat and current fluxes in gas tungsten arcs. Metall. Trans. B **16**, 841–846 (1985)

7. Fan, T.W., Shi, Y.W.: Numerical simulation of the arc pressure in gas tungsten arc welding. J. Mater. Process. Technol. **16** (1996)

8. Aarbogh, H.M., Hamide, M., Fjær, H.G., Mo, A., Bellet, M.: Experimental validation of finite element codes for welding deformations. J. Mater. Process. Technol. **210**, 1681–1689 (2010)

9. Barsoumir, Z., Bhatti, A., Murakawas, H., Barsoumi, I.: Influence of thermo-mechanical material properties of different steel grades on welding residual stresses and angular distortion. Mater. Des. **65**, 878–889 (2015)

10. Karunakaran, N., Balasubramanian, V.: Effect of pulsed current on temperature distribution, weld bead profiles and characteristics of gas tungsten arc welding aluminium alloy joints. Trans. Nonferrous Met. Soc. China **21**, 278–286 (2011)

11. Sreesabari, S., Malarvizhi, S., Balasubramanian, V., Madusudhan Reddy, G.: Experimental and numerical investigation on under-water friction stir welding of armor grade AA 2519–T87 aluminium alloy. Def. Technol. **12**, 324–333 (2016)

12. http://www.comsol.com

13. Little, G.H., Kamtekar, A.G.: The effect of thermal properties and weld efficiency on transient temperatures during welding. Comput. Struct. **68**, 157–165 (1998)

14. Komanduri, R., Hou, Z.B.: On the role of axial load and the effects of interface position on the tensile strength of a friction stir welded aluminium alloy. Metall. Mater. Trans. A **31**, 1353–1370 (2000)

15. Bate, S.K., Charles, R., Warren, A.: Finite element analysis of a single bead on plate specimen using SYSWELD. Int. J. Press. Vessels Pip. **86**, 73–78 (2009)

16. Goldak, J., Chakravarti, A.: A new finite element model for welding heat sources. Metall. Trans. B. **15,** 299–305 (1984)

17. Goldak, J., Bibby, M., Moore, J., House, R., Patel, B.: Computer modeling of heat flow in welds. Metall. Trans. B. **17B**, 587–600 (1986)

18. Malik, A., Qureshi, E., Dar, N.U., Khan, I.: Analysis of circumferentially arc welded thin walled cylinders to investigate the residual stress fields. Thin-walled Struct. **46**, 1391–1401 (2008)

19. Shan, X., Davies, C.M., Wangsdan, N.P., O'Dowd., Nikbi, K.M.: Thermo-mechanical modeling of a single bead on plate welds using the finite element method. Int. J. Press. Vessel. Pip. **86**, 110–121 (2009)

20. Lindgren, L.E.: Numerical modeling of welding. Comput. Methods Appl. Mech. Eng. **195**, 6710–6736 (2006)

21. Kim, I.S., Basu, A.: A mathematical model of heat transfer and fluid flow in the arc gas metal arc welding process. J. Mater. Process. Technol. **77**, 17–24 (1998)

22. Grujicic, M., Arakere, G., Pandurangan, B., Ochterbeck, J.M., Yen, C.F., Cheeseman, B.A., Reynolds, A.P., Sutton, M.A.: Computational analysis of material flow during friction stir welding of AA 5059 aluminium alloys. J. Mater. Eng. Perform. **21**, 1824–1840 (2012)

23. Babu, N., Karunakaran, N., Balasubramanian, V.: Numerical predictions and experimental investigation of the temperature distribution of friction stir welded AA 5059 aluminium joints. Int. J. Mater. Res. **108**, 68–75 (2017)

Strain Analysis of AA6063 Aluminum Alloy by Tube Hydroforming Process

A. S. Selvakumar, B. Surya Rajan, M. A. Sai Balaji and B. Selvaraj

Abstract Tube hydroforming process is used to create parts from aluminum extrusions which reduce structural weight. Different approaches for the formability improvement in the hydroforming process are summarized. In this work, extruded aluminum (annealed) tubular specimen made up of AA 6063 alloy bulged from the diameter of 38–54 mm using hydroforming technique. The objective of this work is to analyze thickness distribution at bulging region along lateral (x) and longitudinal (y) directions. The parameters considered are axial feed (12 mm/min), tube thickness (1.5 mm), fluid pressure (9.6 N/mm^2) and die semi-cone angle (20°). The forming characteristics such as thickness distribution (along x and y) and bulged diameter were studied using toolmakers microscope and coordinate measuring machine. Maximum shear thinning is observed in the largest diameter of the bulged portion of the tube.

Keywords Hydroforming · Annealing · Thickness distribution
Forming pressure · Tube bulging · Formability

A. S. Selvakumar · B. Surya Rajan (✉) · M. A. Sai Balaji
Department of Mechanical Engineering, B.S. Abdur Rahman
Crescent Institute of Science and Technology, Vandalur, Chennai 600048, India
e-mail: suryarajan@bsauniv.ac.in

A. S. Selvakumar
e-mail: selvakumar@bsauniv.ac.in

M. A. Sai Balaji
e-mail: saibalaji@bsauniv.ac.in

B. Selvaraj
Department of Mechanical Engineering, College of Engineering Guindy,
Anna University, Chennai 600025, India
e-mail: selvaraj.mechpsna@gmail.com

1   Introduction

Hydroforming technique for making components with sheet metal and tubular materials is gaining popularity nowadays. One of the major advantages is being the reduction in the friction and wear at the contact region between the component and die [1]. Various parts manufactured using hydroforming process have been commonly used in automotive and aerospace applications [2]. Tubular components of the exhaust system of automobile vehicles and tubular pieces of the chassis parts are among many components produced by the hydroforming process [3].

In tube hydroforming, the fluid (incompressible) is used as forming medium. Pressurized fluid is used to plastically deform the sheet metal and tubular components in closed dies. In tube hydroforming, the tube was bulged into the desired size by the combination of axial feed of punch inside the tube and internal pressure developed through the axial feed and applied load [4]. The right combination of process parameters will fetch the best quality tubular part in minimum time period [5]. Hence, to achieve an economical delivery of product with adequate performance, it is very much essential to select the proper material and manufacturing process [6]. One of the main critical parameters in the forming of tubes is the coordination between the axial feeding along with the internal pressure [7].

Three different types of failures occur in the tube hydroforming process, which include buckling, wrinkling and bursting. These failures limit the expansion process in hydroforming [8]. Wrinkling type of failure occurs in the tube hydroforming process due to the mismatch in the relation between the punch feed rate and the internal pressure of the fluid medium [9]. Bursting type of tube failure occurs when the internal pressure on fluid forming medium is very high [10]. Hence, the optimal internal pressure of a fluid is vital. Better formability can be achieved by identifying the optimum process parameters of hydroforming. In this present work, AA 6063 tubular specimen is taken for hydroforming operation. The tubular specimen was placed in the split-type die and filled with oil as the forming medium. This die and punch set is mounted on a hydraulic press. The punch wrapped with Teflon (acts as sealing member) tape was moved into the tube to increase fluid pressure at the particular feed rate. By doing various experimental trials, the optimal expansion zone geometry was identified to achieve a flaw-free component. Improved stiffness, lesser tooling parts and weight reduction through more efficient section design are achieved by hydroforming process [11]. The formability of tubular material can be evaluated by biaxial loading conditions [12]. The forming pressure for deforming in sheet metal hydroforming can be determined by the theoretical model, and the finite element method helps to validate the results [13]. The dies shall be specially designed for the tube hydroforming process [14]. The process parameters such as material properties, lubricants and loading conditions are essential to design for forming of components [15]. In the authors' previous work, the effect of heat treatment process on different materials was evaluated using the hydroforming process. It was observed that annealing has a tremendous effect and improved formability [16].

In the present work, the formability characteristics of AA 6063 alloy were evaluated by considering the various important parameters, namely axial feed, thickness, fluid pressure and die semi-cone angle of 20°. Two tubular components were taken for the experiment. One with annealed and another without annealed condition. Since the un-annealed specimen has not shown any encouraging results, the results related to it are not shown in this work. After hydroforming, strain analysis was also carried out in both the longitudinal and lateral directions for checking the uniform thickness distribution.

2   Experimental Work

The experimental work was conducted to study the effect of the forming characteristics of the tube specimen made up of AA 6063 alloy after annealing treatment using hydroforming process. Initially, the test was conducted on the tube without annealing. The partial deformation was obtained, and the required bulging diameter was not achieved. To improve formability, the aluminum tubular specimen was annealed (annealing temperature: 413 °C; the soaking time: 2 h) and punch displacement of 30 mm was applied. The initial size of the aluminum tube is 38 mm in diameter, 1.5 mm thickness and 106 mm length. The required bulging diameter of tubes at 20° semi-cone angle is 54 mm. Optimum parameters are achieved by rectifying the process defects experienced during the hydroforming. Some defects occurred during the process are buckling of tube, pressure drop due to leakage of oil through sidewalls and wrinkling, etc.

A 100 ton hydraulic press is used to conduct the experimental trial. The split up die (top and bottom) and punch were fabricated using low carbon steel. The assembled die setup was mounted on the table of the hydraulic press, and punch was fitted with ram of the press. The annealed aluminum tubular specimen was inserted into the die and fluid medium of oil-filled completely inside the tube.

A Teflon sealing was provided on the front face of the punch and tube to avoid leakage of fluid through the sidewall of the tube and joints. A pressure gauge mounted with the bottom portion of the die was used to record the pressure developed during the forming process after punch traveling into the tube. The axial movement of the punch increases fluid pressure. The internal pressure of the tube can further build up by pressing the fluid through the punch forces on the fluid in a downward direction. The high internal pressure expands the tube in the radial direction and forms the required shape of the tube. Figure 1 shows the schematic diagram of tube hydroforming. The assembled view of the die is also shown in Fig. 1. The punch of displacement of 30 mm was applied to increase pressure. The observations obtained in the test are given in Table 1.
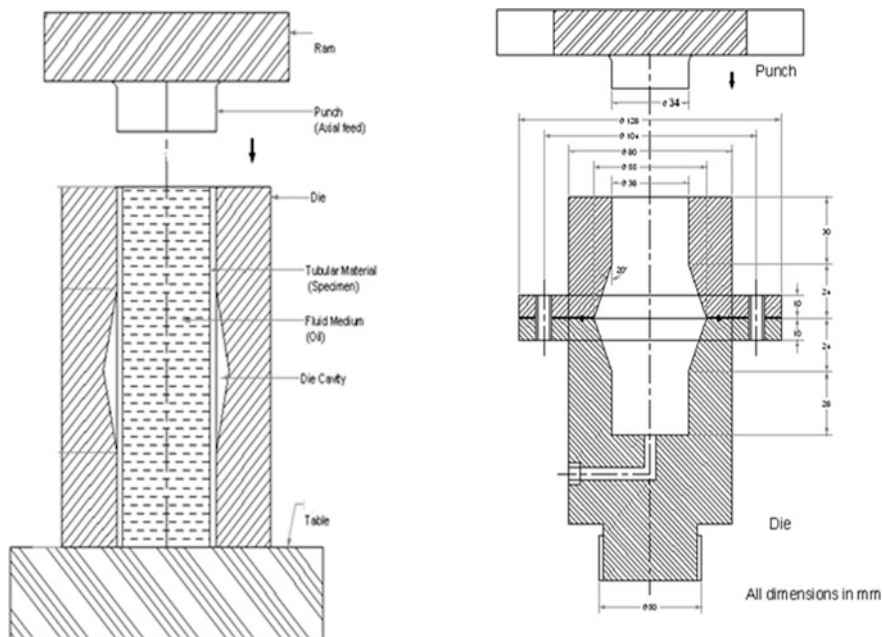
Fig. 1 Schematic representation of tube hydroforming and assembled view of punch and die

Table 1 Observation by the effect of axial feed and pressure

S. No.	Developed pressure (N/mm^2)	Axial feed (mm)	Remarks
1	9.6	30	Bulge diameter of 53.73 mm obtained

2.1 Forming Limit Diagram

Forming limit diagram (FLD) for AA6063 alloy is drawn by major and minor strain values. FLD involves etching a pattern of fine circles on the sheet metal before forming. After forming, the circles will deform into ellipses, which can be measured to find the major and minor strains of the material through Eqs. (1) and (2). Failure can be predicted using a plot (ref. Fig. 2) of the major and minor strains over a wide range of conditions.

$$\text{Major Strain} = \frac{(\text{major axis length} - \text{Original Circle diameter}) \times 100}{\text{Original Circle diameter}} \quad (1)$$

$$\text{Minor Strain} = \frac{(\text{minor axis length} - \text{Original Circle diameter}) \times 100}{\text{Original Circle diameter}} \quad (2)$$
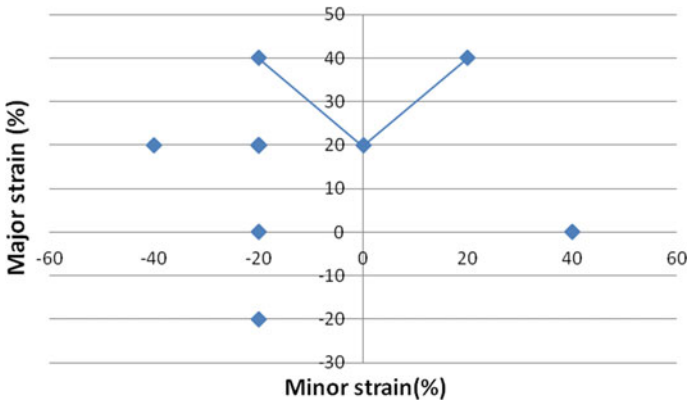
Fig. 2 Forming limit diagram for AA6063 alloy

2.2 Thickness Measurement Along Y Direction

The deformed components were separated into two halves by a wire cut electric discharge machine. The separated tubular pieces are shown in Fig. 3b. From the bottom end of one of the sliced tube, the distances of 10–100 mm were marked along y-direction as shown in Fig. 3c. At each uniformly marked distance, the final thickness was measured by a duly calibrated toolmakers microscope, which has a least count of 0.005 mm. The thickness strain was calculated by the ratio of change of thickness and original thickness. The final thickness is measured, and thickness
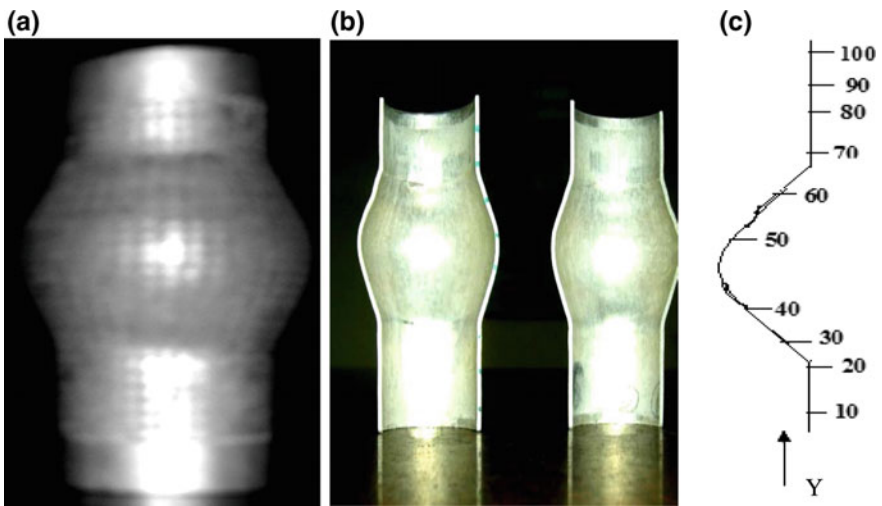
Fig. 3 **a** Hydroformed tube, **b** sliced pieces along *Y* direction, **c** distances marked in cut portion along *Y* direction
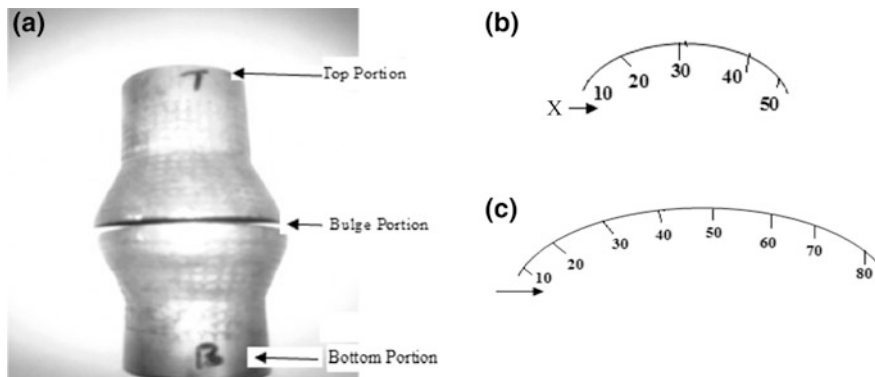
Fig. 4 **a** Sliced pieces along X direction, **b** distance marked in top and bottom ends, **c** distance marked for bulged portion

strain values are calculated using Eq. (3). The distance versus thickness strain (in the longitudinal direction) was plotted for the aluminum specimen as shown in Fig. 5.

$$\text{Thickness Strain} = \frac{\text{Change in thickness}}{\text{Original thickness}} \qquad (3)$$

2.3 Thickness Measurement Along X Direction

From the sliced piece of the formed component, it is separated into two portions along X direction as shown in Fig. 4a. The distances were marked along X direction for top bulged, and the bottom portion as 10–80 mm is shown in Fig. 4b, c. The final thickness is measured, and thickness strain (in the lateral direction) is calculated based on Eq. (3).

3 Results and Discussion

The ratio of the change in thickness (difference in thickness of tube before and after forming) and the original thickness is termed as the thickness strain of the tube. The thickness strain is plotted in Figs. 5 and 6.

The hardness of the specimen before annealing is 88 Hv and after annealing is 42 Hv. As expected, the hardness reduced on annealing process. The atoms in the metal lattice rearrange through solid-state diffusion, and the formability characteristics improved the alloy.
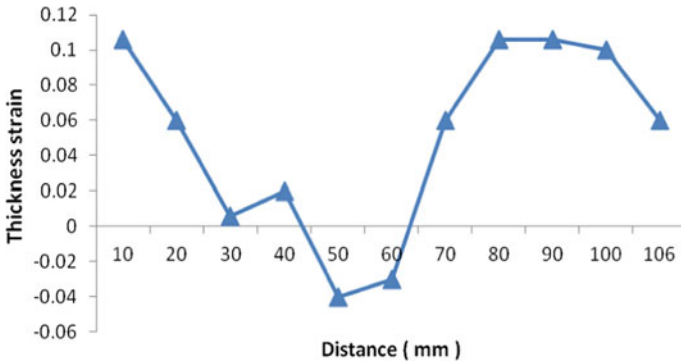
Fig. 5 Distance versus thickness strain for aluminum specimen
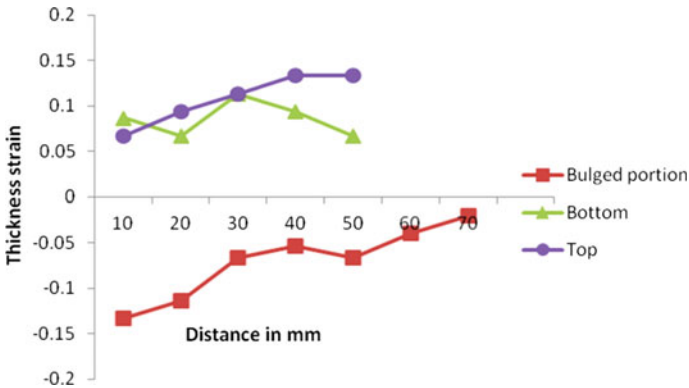
Fig. 6 Thickness strain results of aluminum specimen

The pressure developed during forming process is recorded as 9.6 MPa. Then the formed component was taken out from the die and bulge diameter measured using coordinate measuring machine and found to be 53.736 mm without defect. The formed tube was cut along X (lateral) and Y (longitudinal) directions using wire cut EDM. The negative thickness strain in both lateral and longitudinal directions (ref. Figs. 5 and 6) indicates shear thinning. The thickness at various locations which are at equidistance along X and Y was marked and measured by toolmakers microscope. It is observed that the thinning occurred in the formed (bulged) portion compared to top and bottom ends of the tube. Hence, it can be decided as optimum values for AA6063 tube with 1.5 mm thickness.

4 Conclusion

In this study, formability of tubular materials was evaluated by experimental analysis using hydroforming technique. The formability characteristics such as bulge diameter and thickness distribution were taken into consideration in the evaluation of formability. The process parameters considered were semi-cone angle of the die, axial feed through punch displacement and pressure using an annealed tubular specimen of aluminum.

Initially using die with semi-cone angle of 20°, without annealing of material, experimental trials were conducted in order to get a defect-free bulged geometry. The results showed that only partial deformation of the bulge was obtained and also the pressure drop happens due to the leakage of oil. In order to improve formability of tubular of materials, the materials were annealed and hydroforming trial conducted. Now in annealed aluminum for a die semi-cone angle of 20°, tube thickness of 1.5 mm, a punch displacement of 30 mm and a developed pressure of 9.6 MPa were resulted in a bulge diameter of 53.74 mm without any defect.

The thickness distribution analysis along Y direction and along X direction of formed components of an annealed aluminum was studied. The results showed that thinning is more at the bulged portion than at the top and bottom ends. Due to bulging, top and bottom portion of tubular component will have a lateral strain effect and hence resulted in thickness increases. The thickness distribution of hydroformed tube is improved with the following optimal process parameters

From the above experimental studies, the optimum process parameters arrived for the thickness of 1.5 mm AA6063 tube are as given below.

Annealed aluminum materials
Die semi-cone angle: 20°
Punch displacement: 30 mm
Pressure developed: 9.6 MPa
Bulge diameter: 53.74 mm

References

1. Hwang, Y.M., Chen, W.C.: Analysis of tube hydroforming in a square cross-sectional die. Int. J. Plast. **21**(9), 1815–1833 (2005)
2. Lang, L.H., Wang, Z.R., Kang, D.C., Yuan, S.J., Zhang, S.H., Danckert, J., Nielsen, K.B.: Hydroforming highlights: sheet hydroforming and tube hydroforming. J. Mater. Process. Technol. **151**(1), 165–177 (2004)
3. Koc, M., Altan, T.: An overall review of the tube hydroforming (THF) technology. J. Mater. Process. Technol. **108**(3), 384–393 (2001)
4. Fllice, L., Fratini, L., Micari, F.: A simple experiment to characterize material formability in tube hydroforming. CIRP Ann. Manuf. Technol. **50**(1), 181–184 (2001)

5. Johnson, K.I., Nguyen, B.N., Davies, R.W., Grant, G.J., Khaleel, M.A.: A numerical process control method for circular-tube hydroforming prediction. Int. J. Plast. **20**(6), 1111–1137 (2004)
6. Carleer, B., Van Der Kevie, G., De Winter, L., Van Veldhuizen, B.: Analysis of the effect of material properties on the hydroforming process of tubes. J. Mater. Process. Technol. **104**(1), 158–166 (2000)
7. Ahmetoglu, M., Altan, T.: Tube hydroforming: state-of-the-art and future trends. J. Mater. Process. Technol. **98**(1), 25–33 (2000)
8. Dohmann, F., Hartl, C.: Hydroforming-a method to manufacture light-weight parts. J. Mater. Process. Technol. **60**(1–4), 669–676 (1996)
9. Yuan, S., Yuan, W., Wang, X.: Effect of wrinkling behavior on formability and thickness distribution in tube hydroforming. J. Mater. Process. Technol. **177**(1), 668–671 (2006)
10. Dohmann, F., Hartl, C.: Tube hydroforming—research and practical application. J. Mater. Process. Technol. **71**(1), 174–186 (1997)
11. Manabe, K.I., Amino, M.: Effects of process parameters and material properties on deformation process in tube hydroforming. J. Mater. Process. Technol. **123**(2), 285–291 (2002)
12. Sokolowski, T., Gerke, K., Ahmetoglu, M., Altan, T.: Evaluation of tube formability and material characteristics: hydraulic bulge testing of tubes. J. Mater. Process. Technol. **98**(1), 34–40 (2000)
13. Chen, F.K., Wang, S.J., Lin, R.H.: A study of forming pressure in the tube-hydroforming process. J. Mater. Process. Technol. **192**, 404–409 (2007)
14. Siegert, K., Häussermann, M., Lösch, B., Rieger, R.: Recent developments in hydroforming technology. J. Mater. Process. Technol. **98**(2), 251–258 (2000)
15. Ahmetoglu, M., Sutter, K., Li, X.J., Altan, T.: Tube hydroforming: current research, applications and need for training. J. Mater. Process. Technol. **98**(2), 224–231 (2000)
16. Selvakumar, A.S., Kalaichelvan, K., Venkataswamy, S.: Effect of heat treatment process on hydroforming of tubular materials. Eur. J. Sci. Res. **68**(3), 377–388 (2012)

Performance Indices of Hot Liquid Sodium-Exposed Sacrificial Surface Layers in Fast Breeder Reactors

K. Mohammed Haneefa, Manu Santhanam and F. C. Parida

Abstract Leakage accidents in sodium cooled fast breeder reactors trigger various thermo-chemical degradations of structural materials used for their construction. The interactions of hot liquid sodium with concrete at around 550 °C and above are investigated in this paper. Potential materials were designed and tested. Degradation mechanisms and extend of damages were identified, and subsequently, performance indices were developed. Four types of cement, eight different *w/c* ratios and geopolymer composites were investigated in this study. Comprehensive mechanical, physical, chemical and microstructural characterizations were performed before and after exposure. Microanalytical tools such as SEM (SE and BSE), TG/DTA, XRF, XRD and thin-section petrography were used for characterizing the degradation behavior. Study revealed that the performance rankings were influenced by composition of concrete and water to cement ratios used for the conventional cement-based systems. Performance indices for geopolymer composites were superior to the conventional cement-based systems in hot liquid sodium hostile environment.

Keywords Fast breeder reactors · Hot liquid sodium interactions
Sacrificial layer · Limestone mortars · Geopolymers

K. Mohammed Haneefa (✉) · M. Santhanam
Department of Civil Engineering, IIT Madras, Chennai, India
e-mail: mhkolakkadan@gmail.com

M. Santhanam
e-mail: manusanthanam@gmail.com

F. C. Parida
Radiological Safety & Environment Group, Indira Gandhi Centre
for Atomic Research, Kalpakkam, Tamil Nadu, India
e-mail: parida@igcar.gov.in

1   Introduction

Fast breeder reactors (FBRs) employ sodium as a coolant. Sodium leakage accidents in FBRs results in formation of a pool of hot liquid sodium or sodium spray on Structural Concrete (SC). These interactions (at around 550 °C and above) elicit various thermo-chemical degradations of concrete structures employed in inert atmosphere (equipment cells or reactor cavity) or in air (containment and steam generator building). To prevent the SC from deterioration in FBRs, a sacrificial surface layer is employed over it. Even though various researchers have studied the hot liquid sodium and concrete interactions, there are not much studies exist in estimating the fundamental degradation mechanisms [1–9]. The present study summarizes the investigations of Haneefa et al. [10–20] and reports performance indices for 24 different mixes for hot liquid sodium-exposed sacrificial surface layers in FBRs.

2   Experimental Designs

Four types of cements were used in the study, namely Ordinary Portland Cement (OPC), Portland Pozzolana Cement (PPC), Portland Slag Cement (PSC) and High Alumina Cement (HAC). Studies were conducted with a range of water to cement ratios (*w/c*) 0.4 to 0.6 for OPC. At a *w/c* of 0.55, performances of different types of cements were studied. River sand and limestone aggregates were used in the study to evaluate their suitability for hot sodium hostile environment. Different geopolymer composites with varying molarities of NaOH (8, 12, 16 and 18 M), fixed solid sodium silicate to NaOH ratio (*s/n*) of 1.5 and varying activator fly ash ratios (0.45 and 0.50) were tested to check their suitability for sacrificial surface layer. Class F fly ash was used for making geopolymers. The experimental program was divided into three phases. In the first phase, the constituent materials used were tested for physical properties. Apart from that, mineralogical and microstructural characterizations were performed using microanalytical techniques. In the second phase, all the constituent materials and mixes were tested for thermal performance. The specimens were exposed to 550 °C (ideal operation conditions of FBRs) for duration of 30 min. The duration was a deemed one based on a maximum time required to flow away the accidently spilled hot liquid sodium and reach the collection pits in FBRs [13–15]. Thermal performance test was conducted in a muffle furnace with an average rise in temperature of 0.60 °C/s (Fig. 1). Hot liquid sodium exposure studies were conducted at Indira Gandhi Centre for Atomic Research (IGCAR), Kalpakkam, India. Specially designed carbon steel vessels equipped with dismountable thermal insulations of aluminum cladding (Fig. 2) were used with 1200 W electric surface heater. The temperatures were monitored and controlled by the help of long and flexible thermocouples. After the required sodium fire exposures, the samples hung from the top were removed and allowed to cool in ambient temperatures (Figs. 3 and 4). Post-test specimens were stored in an electronic desiccator after cleaning with ethyl alcohol and drying.

Fig. 1 Thermal exposure at
550 °C in a muffle furnace

Fig. 2 Sodium fire setup
used at IGCAR

Fig. 3 Sodium fire in
progress—Lifting of lid after
sodium fire

Fig. 4 Shifting of sodium
fired samples

Compressive strength, flexural strength as per ASTM C 348 [21], mass loss behavior and abrasion resistance conforming to IS 1237-1980 [22] were assessed to understand the thermal effects. Scanning electron microscopy (SEM) with back scattered imaging on polished specimens and secondary electron images on fractured surfaces, thin-section petrography on 30 µm slides using plane and crossed polarized light, X-Ray Fluorescence (XRF), X-Ray Diffraction and thermogravimetric differential thermal analysis (TG/DTA) were used to perform a comprehensive forensic analysis of different mixes after exposure to 550 °C with and without sodium.

3 Results and Discussions

3.1 Thermal Performance Indices

Table 1 provides the mixes and their compositions used in the study. Performance indices were developed based on performances in compressive strength, flexural strength, mass loss and abrasion resistance after exposure to 550 °C for 30 min [10–20]. Mixes are then ranked on a scale 1–8, for 1 being the best and 8 being the worst for limestone and river sand mortars. For the geopolymer mixes, the ranking was from 1 to 4 for pastes and mortars separately. For both the types of aggregate, the cement mortars with lower w/c ratios performed well in thermal in ranking. Similarly, among the different types of cement, the performance of Portland pozzolana cement was better in most of the cases. However, the relative performance of river sand mortar was inferior to limestone mortars. The reductions in compressive strengths after thermal exposure were 8.4, 9.1, 11.5, 16.1, 17.4, 12.9, 15.9 and 13.2% for limestone mortars LS1 to LS8. The corresponding values for river sand mortars were 12.3, 15.3, 18.1, 23.4, 22.4, 19.0, 19.1 and 17.6%, respectively, for the mixes RS1 to RS8. Similar trends were observed for flexural strength and mass loss. However, abrasion resistance of river sand mortars was better compared to limestone. This effect was resulted from the mineralogy of river sand and limestone (calcite has a Mohs hardness scale number of 3, whereas quartz is 7). Geopolymer pastes exhibited increase in compressive strengths upon heating at 550°C for 30 min. Hence, for the geopolymer pastes, strength indices were based on absolute values. Among the different pastes, the mix GM3 with 16 M ranked first. Increment in strength of geopolymers may be due to the attainment of high-level polymerization upon heat treatment. Similar trends were observed for other indices, except for abrasion. Further, geopolymer mortars with limestone aggregate were tested. The mixes with lower molarities ranked higher indicating mixes becoming more brittle with high molarities of NaOH. Moreover, the mix 18 M was severely cracked and broken upon thermal exposure.

Table 1 Mixes used in the study and performance indices based on 30-min exposure to 550 °C [10–20]

Mix	Composition	PIBCS[1]	RBCS[2]	PIBFS[3]	RBFS[4]	PIBML[5]	RBML[6]	PIBA[7]	RBA[8]
River sand mortars (Cement: Aggregate = 1:2.75)									
RS1	OPC, 0.40 w/c	1.00	1	1.06	2	1.00	1	1.00	1
RS2	OPC, 0.45 w/c	1.24	2	1.00	1	1.24	2	1.04	2
RS3	OPC, 0.50 w/c	1.47	4	1.32	3	1.33	3	1.11	4
RS4	OPC, 0.55 w/c	1.90	8	1.70	6	1.86	5	1.19	6
RS5	OPC, 0.60 w/c	1.82	7	2.19	8	2.6	8	1.28	7
RS6	PPC, 0.55 w/c	1.54	5	1.47	4	1.65	4	1.04	3
RS7	PSC, 0.55 w/c	1.55	6	1.57	5	1.9	6	1.15	5
RS8	HAC, 0.55 w/c	1.43	3	1.88	7	2.21	7	1.81	8
Limestone mortars (Cement: Aggregate = 1:2.75) [13]									
LS1	OPC, 0.40 w/c	1.00	1	1.00	1	1.00	1	1.00	1
LS2	OPC, 0.45 w/c	1.08	2	1.05	2	1.26	2	1.02	2
LS3	OPC, 0.50 w/c	1.37	3	1.29	3	1.42	3	1.04	4
LS4	OPC, 0.55 w/c	1.92	7	1.62	6	2.07	6	1.15	5
LS5	OPC, 0.60 w/c	2.07	8	2.18	8	2.76	8	1.21	6
LS6	PPC, 0.55 w/c	1.53	4	1.43	4	1.62	4	1.03	3
LS7	PSC, 0.55 w/c	1.80	6	1.54	5	2.03	5	1.22	7
LS8	HAC, 0.55 w/c	1.57	5	1.96	7	2.29	7	1.52	8
Geopolymer paste, s/n = 1.5									
GP1	8 M, a/f = 0.45	(+)07.90[a]	3	(+)0.58[a]	3	1.00	1	1.24	4
GP2	12 M, a/f = 0.45	(+)16.50[a]	2	(+)1.40[a]	2	1.06	2	1.41	3
GP3	16 M, a/f = 0.50	(+)15.40[a]	1	(+)4.14[a]	1	1.16	3	1.53	2
GP4	18 M, a/f = 0.50	(−)10.90[a]	4	(−)10.90[a]	4	1.33	4	1	1

(continued)

Table 1 (continued)

Mix	Composition	PIBCS[1]	RBCS[2]	PIBFS[3]	RBFS[4]	PIBML[5]	RBML[6]	PIBA[7]	RBA[8]
Geopolymer mortar, (fly ash: limestone aggregates = 1:2), s/n = 1.5									
GM1	8 M, a/f = 0.45	1.00	1	1.00	1	1.00	1	1.41	4
GM2	12 M, a/f = 0.45	1.46	2	1.07	2	1.43	2	1.35	3
GM3	16 M, a/f = 0.50,	2.74	3	1.21	3	1.66	3	1.32	2
GM4	18 M, a/f = 0.50	5.29	4	1.27	4	1.69	4	1	1

PIBCS[1]: Performance index based on compressive strength after 30-min exposure = (Strength Loss or Gain)i/(Strength Loss)min

RBCS[2]: Ranking based on compressive strength after 30-min exposure

PIBFS[3]: Performance index based on flexural strength after 30-min exposure = (Strength Loss or Gain)i/(Strength Loss)min

RBFS[4]: Ranking based on flexural strength after 30-min exposure

PIBML[5]: Performance index based on mass loss after 30-min exposure = (Mass Loss)i/(Mass Loss)min

RBML[6]: Ranking based on mass loss after 30-min exposure

PIBA[7]: Performance index based on abrasion after 30-min exposure = (Abrasion)i/(Abrasion)min

RBA[8]: Ranking based on abrasion after 30-min exposure

[a]Absolute values are used since there were reduction and increment in strengths of geopolymer paste mixes upon 30-min heating at 550 °C

3.2 Indices Based on Sodium Fire Performance

Based on performance indices from thermal study, limestone mortars with different cement types and *w/c*, geopolymer pastes and geopolymer mortars were considered for sodium fire tests. For cement-based mortars, calcium depletion and sodium enrichment indices were developed based on XRF data. Apart from these indices, aluminum depletion index was developed for geopolymer composites. These indices were calculated as (Reduction/increment in elemental composition after sodium fire) *i*/(Average elemental composition before exposure). Calcium depletion index and sodium enrichment index for limestone aggregate (LS) were found to be 0.436 and 802.5, respectively. Figure 5 depicts calcium depletion indices for cement-based limestone and limestone mortars after sodium fire. The indices after sodium fire corroborate the observations from the thermal performance indices. As the *w/c* ratio increases, the calcium depletion indices showed an increasing trend. Similar trends were observed in sodium enrichment indices (Fig. 6). The mixes with higher *w/c* might have resulted in more release of free water and subsequent formation of NaOH and hydrogen gas. These consequences intensify the reaction kinetics during the sodium fire associated with more calcium depletion and sodium enrichment by possible cationic exchanges. Since the present study simulates the worst case of sodium accidents, the maximum *w/c* ratio for FBRs sacrificial surface layer should be equal or less than 0.4 to extend the reinstatement period of sacrificial surface layers.

Figure 7 represents calcium depletion, sodium enrichment and aluminum depletion indices for geopolymer composites. Unlike the cement-based systems, geopolymer system contains more sodium content. As illustrated in Fig. 7, geopolymer pastes were less affected by sodium fire. However, the mortars exhibited significant changes upon sodium fire compared to geopolymer pastes. The developed indices pronounced that the performance of higher molarity geopolymers

Fig. 5 Calcium depletion indices for cement-based limestone mortars
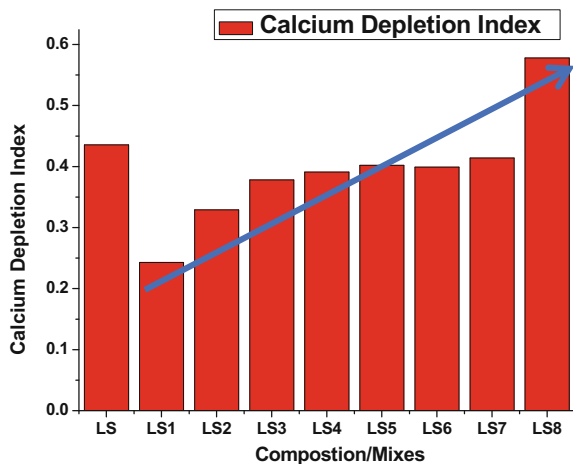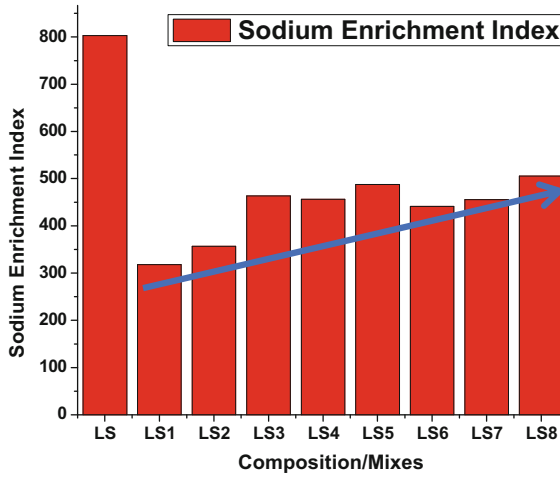
Fig. 6 Sodium enrichment indices for cement-based limestone mortars
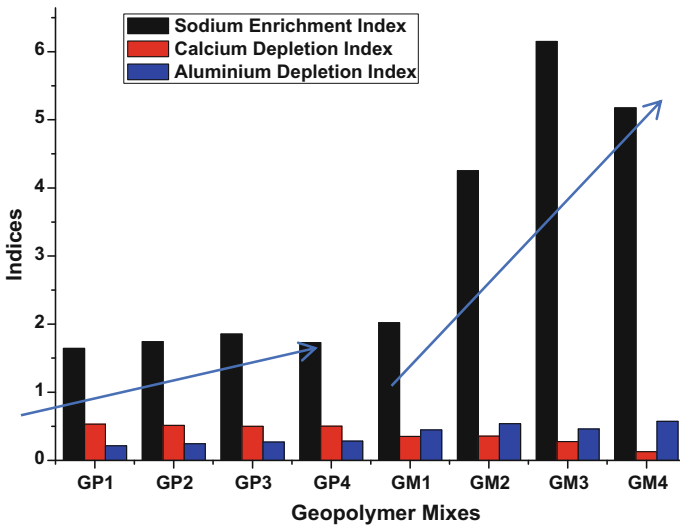
Fig. 7 Major elemental depletion indices for geopolymer composites

was deficient to the ones with lower concentrations. The elemental depletion indices after sodium fire of geopolymers revealed that the reaction kinetics of hot liquid sodium with geopolymer composites were less and eventually the degradation was minimal compared to conventional cement-based systems. Additionally, from the XRD study; Na_4SiO_4, Na_3SiO_3, Na_2CaSiO_4, NaOH, Na_2CO_3, $NaAlO_2$, $Ca(OH)_2$, Na (Hexagonal) and Na (Cubic) were found as reaction products.

Table 2 provides glimpses of TG/DTA analysis (a typical pattern is presented in Fig. 8 [16]) for all sodium fired specimens along with shape retaining indices ({[mass of unaffected inner core after sodium fire] *i*/[mass of the specimen before any exposure]} × 100)) and residual strength indices (absolute values of residual strength after sodium fire in MPa). Among the cement-based systems, only the mixes with 0.40 and 0.45 *w/c* ratios exhibited enthalpy changes corresponding to the decomposition of calcite ($CaCO_3$), which indirectly portrays that most of the calcite was decomposed in the mortars with higher *w/c* upon sodium fire. These results resembled that the degradation of mortars was worst at higher water cement ratios due to transport of hot liquid sodium into the inner core. Similarly, the formation of Ca $(OH)_2$ was high at higher *w/c*. Corroborating trends were observed in shape retaining indices calculated based on absolute values of mass retained after sodium fire. There were no inner cores present in the mixes with 0.50, 0.55 and 0.60 *w/c*. Due to high level of disintegration, residual strength calculation was not possible for cement-based system. The mix with fly ash blended PPC showed a sign of minor DTA peak 751.7 °C related to calcite decomposition which implies presents of unaffected limestone in the mortar after sodium fire.

Geopolymers displayed superior indices based on $CaCO_3$ and $Ca(OH)_2$ enthalpy changes, shape retaining indices and residual strength indices. Among the TG/DTA performed (the geopolymer mortars with 8 M and 12 M NaOH), both the mixes

Table 2 Indices based on hot liquid sodium fire

Mix	Enthalpy change of calcite ($CaCO_3$) decomposition	Enthalpy change of Ca $(OH)_2$ decomposition	Shape retaining index	Residual strength index
LS1	51.75 J/g	23.90 J/g	91.5	Disintegrated
LS2	12.75 J/g	39.44 J/g	43.2	Disintegrated
LS3	No complex peak	34.33 J/g	No inner core	Disintegrated
LS4	No complex peak	42.36 J/g	No inner core	Disintegrated
LS5	No complex peak	55.93 J/g	No inner core	Disintegrated
LS6	Minor peak at 751.7°C	35.55 J/g	83.7	Disintegrated
LS7	No complex peak	45.91 J/g	49.7	Disintegrated
LS8	No complex peak	5.88 J/g	41.4	Disintegrated
GP1	Not performed	Not performed	92.3	10.7
GP2	Not performed	Not performed	91.8	17.7
GP3	Not performed	Not performed	90.7	18.8
GP4	Not performed	Not performed	89.1	23.5
GM1	81.53 J/g	No complex peak	57.4	22.3
GM2	98.76 J/g	Minor peak at 451.3 °C	61.0	23.8
GM3	Not performed	Not performed	46.6	Disintegrated
GM4	Not performed	Not performed	Cracked	Disintegrated
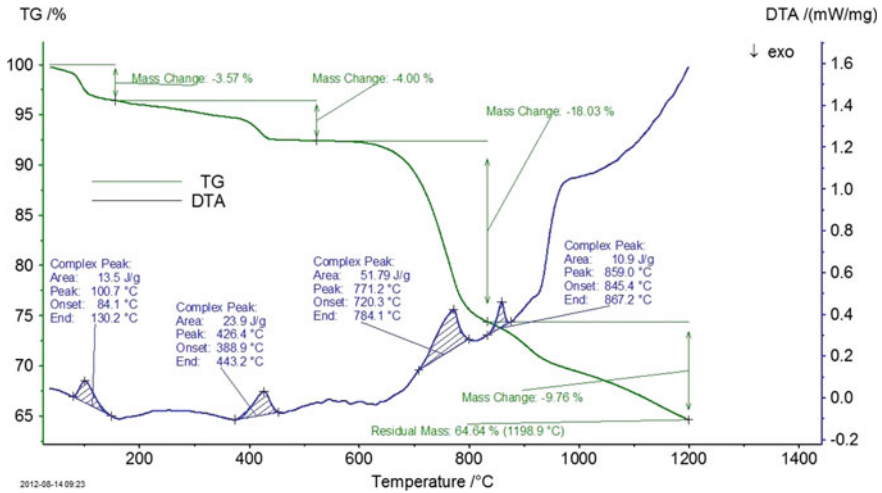
Fig. 8 Typical TG/DTA curve for OPC 0.4 *w/c* [16]

exhibited distinct complex peaks of 81.53 and 98.76 J/g, respectively. The result proved that the hot liquid sodium had not intruded into the geopolymer mortars and decomposes the limestone aggregates. Moreover, there were no any sign of enthalpy changes in TG/DTA corresponding to $Ca(OH)_2$ decomposition. Corroborating inferences were drawn from the shape retaining indices and residual strength indices of geopolymer composites. The minimum residual mass was 89.1% for paste phase and 46.6% for mortars. The mix 18 M was completely disintegrated. Meanwhile, the maximum changes in strengths were 23.5 and 22.3% for paste mortars, respectively. Due to the high level of damage, residual strengths were not able assess for the mortars mixes with 16 and 18 M of NaOH.

3.3 General Discussions on Influence of Microstructure Changes on Performance Indices

This section describes how the microstructural alterations influence the performance indices. Figure 9 represents a thin-section image of fire damaged river sand mortar [13]. Indian river sands are generally composed of weathered granite. The hypidiomorphic and interlocked texture of granite microstructure was cracked due to differential thermal expansion and contraction. Ferric oxidation and subsequent cleavage staining disrupts the mineral assemblage in river sand as seen in Fig. 9. These mechanisms result in more reduction in compressive strength of river sand mortars compared to the limestone aggregate mortars. Limestone is a mono-mineral rock with very less accessory impurity minerals in it. Its thermal stability at 550 °C is intact. Figures 10, 11, 12 and 13 provide SEM-back scatter electron images of

Fig. 9 Typical
microstructure of fire
damaged rivers sand mortars
[13]
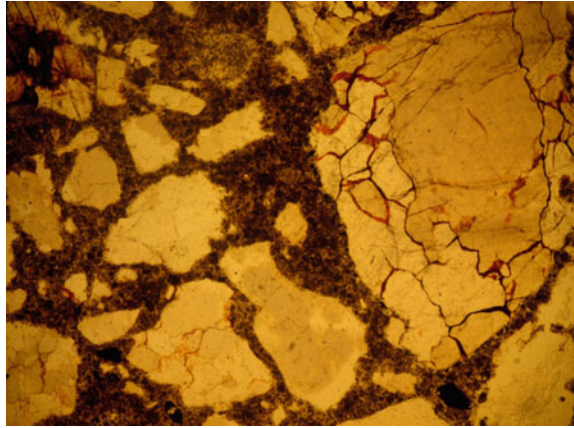
Fig. 10 SEM of sodium fired
OPC-0.40 mortar
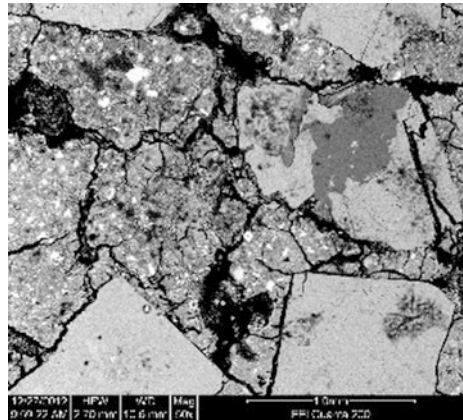
polished sodium fired specimens. The geopolymer microstructure (Fig. 10) was less affected upon sodium fire compared to the conventional cement-based systems (Fig. 11). Moreover, the formation of cracks in paste phases was more intensive in cement-based systems (Fig. 12 [15]) compared to the geopolymers (Fig. 13 [15]). These observations were directly reflected on performance indices of sodium fired specimens.

Fig. 11 SEM of sodium fired geopolymer mortar (8 M)
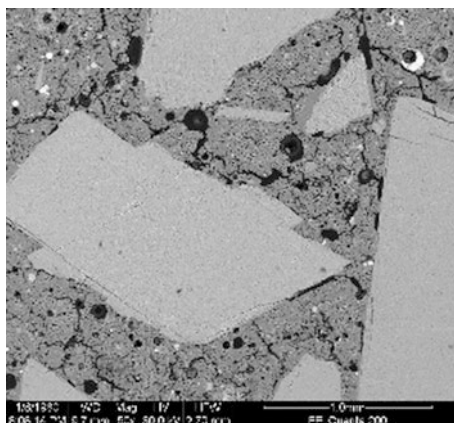
Fig. 12 SEM of sodium fired PPC-0.55 [15]
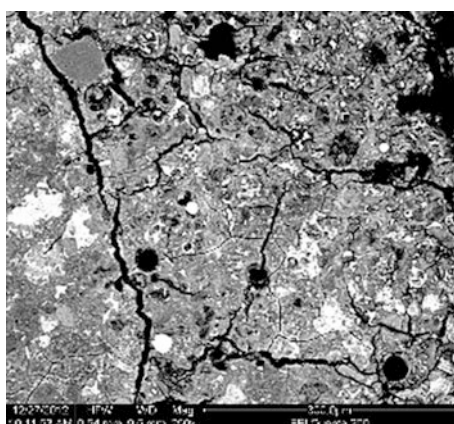
Fig. 13 SEM of sodium fired geopolymer mortar (12 M) [15]
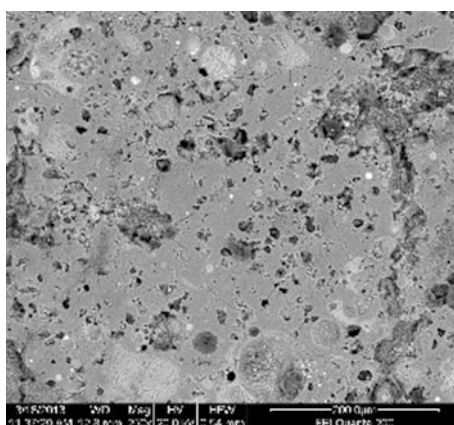
4   Conclusions

The current study considered 24 different mixes for sacrificial surface layer to protect structural concrete from hot liquid sodium fire in FBRs and performance indices were developed based degradation behavior. The study recommends the following;

(a) Use of limestone over river sand or granite for the sacrificial surface layer in FBRs
(b) Use of low *w/c* ratio concretes for sacrificial surface layer preferably less than or equal to 0.4
(c) Effective deployment of geopolymer technology for sacrificial layers in FBRs

References

1. Chasanov, M.G., Staahl, G.E.: High temperature sodium–concrete interactions. J. Nucl. Mater. **66**, 217–220 (1977)
2. Barker, M.G., Gadd, P.G.: A chemical study of the sodium–concrete reactions. In: Proceedings of the LMFBR Safety Topical Meeting, Lyon-Ecully, France, Part III, p. 91 (1982)
3. Fritzke, H.W., Schultheiss, G.F: An experimental study on sodium concrete interaction and mitigating protective layers. In: 7th International Conference on Structural Mechanics in Reactor Technology, pp. 135–142 (1983)
4. Muhlestien, L.D., Postma, A.K.: Application of sodium–concrete reaction data on breeder reactor safety analysis. Nucl. Safety **25**(2), 212–222 (1984)
5. Chawla, T.C., Pederesen, D.R.: A review of modeling concepts for sodium–concrete reactions and a model for liquid sodium transport to the un reacted concrete surface. Nucl. Eng. Des. **88**, 85–91 (1985)
6. Schultheiss, G.F., Minden, C.V., Fritzke, H.W.: Method for avoiding or reducing the interactions and their consequences from contact of hot liquid metallic sodium with concrete, United States Patent No. 4642300 (1987)
7. Bae, J.H., Shin, M.S., Min, B.H., Kim, S.M.: Experimental study on sodium–concrete reactions. J. Korean Nucl. Soc. **30**, 568–580 (1998)
8. Premila, M., Sivasubramanian, K., Amarendra, G., Sundar, C.S.: Thermo chemical degradation of limestone aggregate concrete on exposure to sodium fire. J. Nucl. Mater. **375**, 263–269 (2008)
9. Das, S.K., Sharma, A.K., Parida, F.C., Kashinathan, N.: Experimental study on thermo-chemical phenomena during interaction of limestone concrete with liquid sodium under inert atmosphere. Constr. Build. Mater. **23**, 3375–3381 (2009)
10. Haneefa, K.M., Santhanam, M., Parida, F.C.: Performance evaluation of sodium resistant mortars as sacrificial layer in fast breeder reactors. In: 9th Fib International PhD Symposium in Civil Engineering, Karlsruhe Institute of Technology (KIT)-University, Karlsruhe, Germany, July 22–24, 2012, pp. 715–721(2012)
11. Haneefa, K.M., Santhanam, M., Parida, F.C.: Performance evaluation of limestone mortars for elevated temperature application in nuclear industry. In: 3rd International Conference on

Repair, Rehabilitation and Retrofitting, ICCRRR-2012, University of Cape Town, South Africa, 12–15 Sept 2012, pp. 111–116 (2012)

12. Haneefa, K.M., Santhanam, M., Parida, F.C.: Review of concrete performance at elevated temperature and hot sodium exposure applications in nuclear industry. Nucl. Eng. Des. **258**, 76–88 (2013)
13. Haneefa, K.M., Santhanam, M., Parida, F.C.: Thermal performance of limestone mortars for use in sodium cooled fast breeder reactors. Indian Concr. J. **87**(12), 25–41 (2013)
14. Haneefa, K.M., Santhanam, M., Ramaswamy, R., Parida, F.C.: Hot sodium triggered thermo-chemical degradation of concrete aggregates in the sodium-resistant sacrificial layers of fast breeder reactors. Nucl. Eng. Des. **265**, 654–667 (2013)
15. Haneefa, K.M., Santhanam, M., Parida, F.C.: Performance characterization of geopolymer composites for hot sodium exposed sacrificial layer in fast breeder reactors. Nucl. Eng. Des. **2013**(265), 542–553 (2013)
16. Haneefa, K.M., Santhanam, M., Parida, F.C.: Deterioration of limestone aggregate mortars by liquid sodium in fast breeder reactor environment. Nucl. Eng. Des. **2014**(275), 287–299 (2014)
17. Haneefa, K.M., Santhanam, M., Parida, F.C.: Studies on hot liquid sodium and concrete interactions in fast breeder reactors. In: 2nd International Congress on Durability of Concrete, Norwegian Concrete Association, 4–6 Dec 2014, Paper 29 (2014)
18. Haneefa, K.M., Santhanam, M., Parida, F.C.: Performance characterization of hot sodium exposed sacrificial concrete layer for fast breeder reactors. In: Proceedings of the International Conference on Advances in Civil Engineering and Chemistry of Innovative Materials, ACECIM'14, Department of Civil Engineering and Department of Chemistry, SRM University, Chennai, India, 13–14 Mar 2014, pp. 842–847 (2014)
19. Haneefa, K.M., Santhanam, M., Parida, F.C.: A study on potential materials for hot sodium exposed sacrificial layer in Fast Breeder Reactors. In: Proceedings of the National Conference on Advances in Civil Engineering, ACE2K15, 23rd Mar 2015, SSN College of Engineering, Kalavakkam, Tamilnadu, India, pp. 173–181 (2015)
20. Haneefa, K.M., Santhanam, M., Parida, F.C.: Development of a forensic methodology for investigation of concrete structures affected by sodium fires in fast breeder reactors, National Conference on Forensic Structural Engineering, Vellore Institute of Technology, Chennai, Volume: Session 1, Paper No. 1, pp. 1–18 (2016)
21. ASTM C 348: Standard test method for flexural strength of hydraulic-cement mortars, ASTM International, U.S.A. (2014)
22. IS 1237: Cement Concrete Flooring Tiles—Specification. Bureau of Indian Standards, New Delhi (1980)

Turning Studies on A356-TiB$_2$/TiC In Situ Reinforced Composites

Ismail Kakaravada, A. Mahamani and V. Pandurangadu

Abstract In the past one decade, in situ composites have received the widespread attention from many researchers due to improved mechanical properties through reinforcing with a lower volume fraction of ceramic particulates. The present study deals with the synthesis of A356-TiB$_2$/TiC composites by reacting with the K$_2$TiF$_6$-KBF$_4$-graphite, characterization and machinability behaviour of the synthesized composites. Cutting speed, cutting depth and tool feed rate are selected as turning parameters to conduct an experimental investigation. Cutting force, surface waviness and flank wear are considered to appraise the machinability behaviour. Multi-coated tungsten carbide tool is used for machining study, and Taguchi L$_{16}$ orthogonal layout is followed to conduct the experimentation. This study is aimed to optimize the turning parameters to minimize the cutting force, surface waviness and flank wear by means of composite desirability grade approach. The analysis of variance (ANOVA) is conducted for composite desirability grade to recognize the influence of each turning parameter upon the responses.

Keywords In situ composites · Characterization · Turning · Cutting force
Flank wear · Surface waviness · Multi-response optimization

I. Kakaravada (✉) · V. Pandurangadu
Department of Mechanical Engineering, Jawaharlal Nehru
Technological University, Anantapuramu, India
e-mail: ismailmtech23@gmail.com

V. Pandurangadu
e-mail: pandurangaduv@yahoo.com

A. Mahamani
Department of Mechanical Engineering, Sri Venkateswara College
of Engineering and Technology (Autonomus), Chittoor 517127, Andhra Pradesh, India
e-mail: mahamanisudhan@gmail.com

1   Introduction

Ceramic particulate-reinforced aluminium matrix composites are highly potential materials to replace the heavyweight ferrous materials for the automobile field to reduce vehicle weight for an increase in fuel efficiency and to control emissions. Apart from this, these materials are used in countless engineering applications due to their advanced properties such as the high modulus of elasticity, chemical stability, improved resistance to wear, admirable castability, tremendous corrosion resistance and fabulous strength-to-weight ratio. This is a reason that Al–7Si–Mg (A356) alloy is extensively utilized in cylinder head and engine block [1]. Aluminium matrix composites are synthesized in a couple of ways, namely ex situ and in situ system. In ex situ method, the composites are fabricated by adding reinforcement externally to the matrix material. Cluster formation of reinforcement and poor adhesion between particle and matrix interface are considered as major limitations of the ex situ composites [2]. Tjong and Ma [3] discussed the processing of in situ composites and reported the several advantages over the conventional composites. This process has distinctive benefits such as fine, thermodynamically stable dust and oxide-free particle reinforcement and their uniform distribution in the matrix. During synthesis, an exothermic reaction initiated by the aluminium melt and halide salts offers the boiling effect. This effect facilitates the homogeneous spreading of reinforcement particles throughout the matrix material which improves mechanical and tribological properties of a composite material. Pradeep Kumar et al. [4] deliberated the consequence of TiC reinforcement, which is generated through the mixed salt reaction system in an aluminium matrix. They observed the embellished mechanical properties due to the uniform spreading of TiC ceramic phase, superior grain refinement and dislocation strengthening. Senthil et al. [5] conducted an experimental investigation to access the machinability behaviour of in situ Al–Cu/TiB$_2$ composites. The effect of machine tool parameters including the speed of cutting, cutting depth and feed rate on cutting force in addition to quality of machined surface was investigated during turning operations. At higher cutting speeds, build-up edge formation is restricted and thereby the superiority of the machined exterior is improved. Anandakrishnan and Mahamani [6] investigated the machinability behaviour of AA6061-TiB$_2$ in situ composites based on wear rate in a tool, surface roughness and forces generated by the tool during turning. From the experimental results, it is observed that with a raise in tool feed and cutting depth maximizes the cutting force along with tool wear rate, which results in a generation of poor surface finish. The multi-response optimization of machine tool operating parameters is well documented. Naveen Sait et al. [7] studied the multi-characteristic optimization of turning parameters during machining of glass fibre-embedded plastic composite using composite desirability grade approach. The most favourable level of machining parameters was identified to optimize the responses. The most momentous parameters on output responses are also estimated by the analysis of variance. Palani Kumar et al. [8] have developed a mathematical model to prefigure surface quality in turning of A356/SiC/20p

composites by means of response surface methodology and desirability function analysis. From the result, it is observed that speed at a higher level; lower level of feed rate and a moderate level of cutting depth are most favourable parameters to attain good surface roughness. The insufficient literature is available on a synthesis of A356-TiB$_2$/TiC composites, as well no author is addressed the machinability studies on A356-TiB$_2$/TiC composites. This paper discloses the machinability studies on A356-TiB$_2$/TiC composites with multi-response optimization using desirability grade approach. For a further contribution, the current exertion deals the optimization of parameters to minimize the cutting force, surface waviness and flank wear in turning of A356-TiB$_2$/TiC composites. Taguchi L$_{16}$ orthogonal array is followed to conduct experimentation. The desirability functional analysis was performed to integrate the multiple responses into single required value that is a composite desirability grade. Therefore, from the L$_{16}$ orthogonal array, an experimental run which is having higher composite desirability grade value is identified as an optimal machining parameter. Analysis of variance (ANOVA) is performed for composite desirability grade to identify the considerable parameter which affects the combine multiple responses.

2 Experimental Work

2.1 Work Materials and Method

In the current exertion, the Al–Si7–Mg alloy is selected for turning study, and the chemical composition of Al–Si7–Mg alloy is Si-6.5%, Fe-0.15%, Cu-0.03%, Mn-0.10%, Mg-0.4%, Zn-0.07%, Ni-0.05 and Ti-0.1%. A356-TiB$_2$/TiC composites fabricated with an increase as a volume fraction of reinforcement through a mixed salt reaction system. A premeasured quantity of halide salts, namely potassium hexa-fluoro-titanate (K$_2$TiF$_6$), potassium hexa-fluoro-borate (KBF$_4$) and graphite (C), is used to synthesize the composites. TiB$_2$ and TiC reinforcements are created through an exothermic reaction. The cast-out composites from the metallic mould are shown in Fig. 1. The EDAX (Model: Hitachi S-300 H) spectra of the A356-TiB$_2$/TiC composites are recorded by lithium drift silicon analyser with working voltage 20 kV and displayed in Fig. 2. This spectrum validates the presence of various elements in composites like titanium, carbon, copper and aluminium. The microstructure was investigated by means of SEM (Model: JEOL 6360 LV) and presented in Fig. 3. Figure 3 depicts the existence of uniformly distributed and cluster-free TiB$_2$/TiC reinforcements in the fabricated composites. The Vickers's micro-hardness number (VHN) of composites was evaluated by using micro-Vickers's hardness tester (Model: FMV-1-AD-AT) at one kg load with 8 s operated to dwell time. Hardness was measured at three different places, and average values are tabulated in Table 1. Taguchi's L$_{16}$ array was adopted to conduct the experiments. Cutting speed, feed rate, and cutting depth and % of

Fig. 1 A356-TiB$_2$/TiC composites
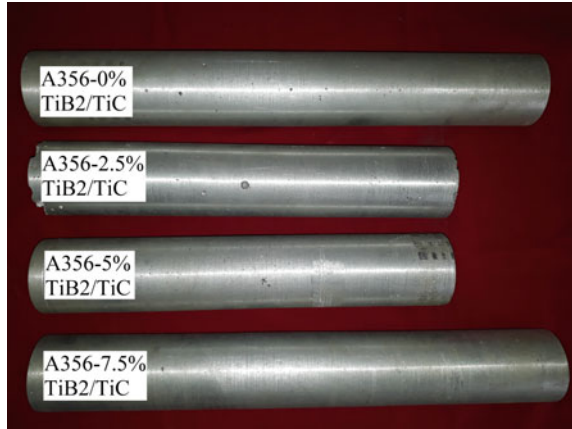
Fig. 2 EDAX spectra of A356-TiB$_2$/TiC
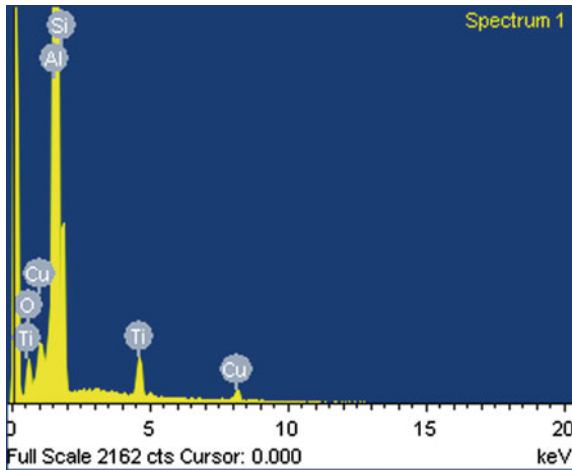
Fig. 3 SEM image for A356-7.5% TiB$_2$/TiC composite
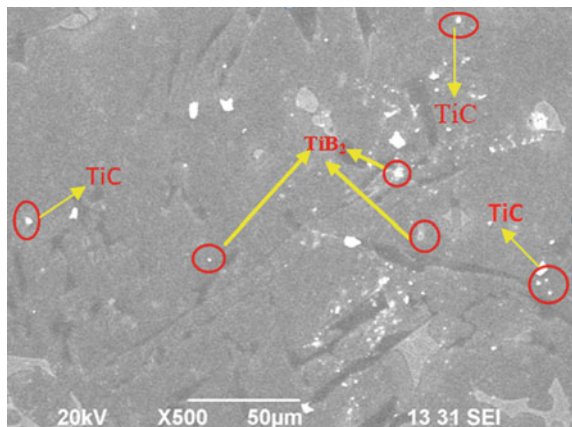
Table 1 Hardness values of A356-TiB$_2$/TiC composites

Composites	Trail 1	Trail 2	Trail 3	Avg. hardness
A356-0%	82	89	92	87.6
A356-2.5%	96.8	108.2	110.3	105.1
A356-5%	116	119.2	120.3	118.4
A356-7.5%	125	132.5	136.5	131.43

Fig. 4 Lathe with Kistler dynamometer set-up
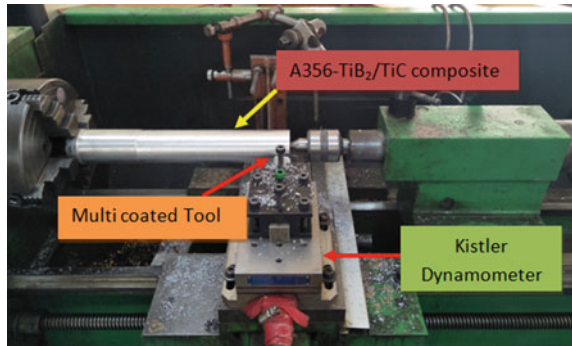
reinforcement are considered as turning parameters. Further, to optimize the multi-response characteristic in machining of composites desirability grade approach is adopted.

2.2 Turning Process

A conventional medium-duty lathe turn master-35 was used to carry out the experimental work. Higher spindle speed causes chatter in a tool and spoils machined surface finish. Heat generation at a machining interface also increases at higher spindle speed, which results in more tool wear. Hence, moderate cutting speeds (47, 55, 63, 71 m/min) are selected for experimentation. The selected level of four parameters is tabulated in Table 2. Experiments were conducted on A356-TiB$_2$/TiC composites cylindrical shafts having a diameter of 50 and 300 mm length as presented in Fig. 1. The multi-layered (TiN–TiCN–Al$_2$O$_3$–ZrCN) chemically vapour-deposited tungsten carbide insert was used to carry out the work

Table 2 Turning parameters and their levels

Factor	Process parameters	Units	Level 1	Level 2	Level 3	Level 4
A	Cutting speed	m/min	47	55	63	71
B	Feed rate	mm/rev	0.2	0.25	0.3	0.35
C	Cutting depth	mm	0.25	0.5	0.75	1
D	% of reinforcement	%	0	2.5	5	7.5

under dry environment. The machining length of each trail is considered as 110 mm during experimentation. The carbide insert (Model WP25CT) has a nomenclature with a negative rake angle of −7°. Tool clearance angle is 7°, 80° as a major cutting angle at an edge, 0° inclination with the cutting edge and 0.8 mm as a nose radius. The cutting insert was fastened to a tool holder (Model PSBNR-2525M12) which is used during experimentation. Piezo-electric-type three-component Kistler dynamometer (Model 9257B) coupled with amplifier (Type 5070) is used to account the cutting force during turning as shown in the Fig. 4. The data acquisition was carried out through the dynaware software. The microscope (Model Mitutoyo) with 30× magnification is used to evaluate flank wear during the investigation. The surface quality of machined surface was recorded by using a stylus-type (SJ210) surface roughness tester (Mitutoyo, 0.001 μm) with measuring a length of 5 mm.

2.2.1   Desirability Functional Analysis

In the year 1980, a functional approach was developed for multi-characteristic optimization by Dutch scientist Derringer and Such. According to their practice, they introduce a methodology to appraise the composite desirability. This method follows an objective function $D(X)$ is called composite desirability grade function, and it renovates an estimated response to a normalized value called desirability (d_i). The desirability (d_i) values range always lies in between zero and one

2.2.2   Target Is Best

The individual output response values $\hat{y}$ is required to achieve a desired expected value (T). When the $\hat{y}$ value is equalled to expected valve (T), the expected values must be equalled to one. If the individual $\hat{y}$ goes beyond an expected range than the expected value, then the desirability value is equalled to zero. This situation is a symbol of the worst case in experimentation. In the composite desirable function (d_i), y_{max} and y_{min} represented the greater and lower value limits of y and s, and t represents Eq. (1).

$$d_i = \begin{cases} \left(\frac{\hat{y}-y_{min}}{T-y_{min}}\right)^s, & y_{min} \leq \hat{y} \leq T, \ \ s \geq 0 \\ \left(\frac{\hat{y}-y_{max}}{T-y_{min}}\right)^t, & T \leq \hat{y} \leq y_{max}, \ \ t \geq 0 \quad [10] \\ 0, & \hat{y} \geq y_{min} \end{cases} \tag{1}$$

$$d_i = \begin{cases} 0, & \hat{y} \leq y_{min} \\ \left(\frac{\hat{y}-y_{max}}{T-y_{min}}\right)^t, & y_{min} \leq \hat{y} \leq y_{max}, \ \ r \geq 0 \quad [10]. \\ 1, & \hat{y} \geq y_{min} \end{cases} \tag{2}$$

2.2.3 Maximum Is Best

The individual response value of $\hat{y}$ is likely to be the maximum is best. The $\hat{y}$ values must be higher than the targeted value, and then the composite desirable value equals to one. Also, the $\hat{y}$ is lower than a targeted value, which is not acceptable, and it is always equal to zero. The maximum is better desirability function which is presented in Eq. (2), where the y_{min} stands for least values of tolerance limit of $\hat{y}$. The y_{max} stands for the higher tolerance limit of $\hat{y}$. 'r' represents an index. s, t and r in Eqs. (1–3) represent the weights, and it will be used as the necessity of the user. If the output response is projected to be nearer to the expected value, the characteristic weight values can be set to a maximum value; otherwise, the characteristic weight can be set to minimal value.

2.2.4 Minimum Is Best

The response value of $\hat{y}$ is accepted to be the minimum is best. The $\hat{y}$ value is lower than a targeted value, and then the composite desirable value equals to one. If the $\hat{y}$ value is greater than the expected target value which is not acceptable, then this value is equalled to zero. The minimum is best desirability function which is presented in Eq. (3). In the present work, the minimum is the best characteristic which is applicable to conclude the independent desirability values for flank wear, cutting force in addition to the surface roughness. Now, all responses have to be minimized with Eq. (3). The individual desirability of all responses has been accumulated to appraise the composite desirability grade and rank by using Eq. (4). Here, D is the final composite desirability value, (d_i) is the desirability value of each individual response value of each with ith quality characteristic, and 'n' is a number of experiments. Determination of the optimal machining parameters and their levels is achieved by choosing the greatest value of a composite desirability experiments. The desirability values of everyone's response and composite desirability grade values are recorded in Table 3. Finally, the persuade of each parameter on composite desirability grade is evaluated, and optimal level of each parameter is estimated.

$$d_i = \begin{cases} 1, \hat{y} \leq y_{min} \\ \left(\frac{\hat{y}-y_{max}}{y_{min}-y_{max}}\right)^r, & y_{min} \leq \hat{y} \leq y_{max}, \quad r \geq 0 \quad [10] \\ 0, \hat{y} \geq y_{min} \end{cases} \quad (3)$$

Composite desirability $\left(D_g\right) = \sqrt[n]{d_1 * d_2 * d_3 * d_4 \ldots d_n} \quad [10].$ (4)

Table 3 Taguchi's L$_{16}$ layout with results, individual desirability (d_i) and composite desirability (D_g) grade values

Process parameters					Response(s)			Individual desirability (d_i)			Composite desirability (Dg)	Rank
Exp. run	Cutting speed (A)	Feed rate (B)	Depth of cut (C)	% of reinforcement (D)	Cutting force (N)	Flank wear (mm)	Surface roughness (μm)	Cutting force (D1)	Flank wear (D2)	Surface roughness (D3)		
1	50	0.2	0.25	0	128.4	0.06	2.82	0.3242	1.0000	0.2613	0.4392	7
2	50	0.25	0.5	2.5	142.8	0.1	3.1	0.1901	0.9344	0.1206	0.2777	12
3	50	0.3	0.75	5	135.4	0.14	3.15	0.2590	0.8688	0.0954	0.2780	11
4	50	0.35	1	7.5	152.4	0.18	3.34	0.1006	0.8032	0.0000	0.0000	16
5	75	0.2	0.5	5	130.2	0.22	2.72	0.3075	0.7377	0.3115	0.4134	9
6	75	0.25	0.25	7.5	112.3	0.18	2.86	0.4743	0.8032	0.2412	0.4512	6
7	75	0.3	1	0	163.2	0.12	2.43	0.0000	0.9016	0.4572	0.0000	15
8	75	0.35	0.75	2.5	160.2	0.14	2.48	0.0279	0.8688	0.4321	0.2189	13
9	100	0.2	0.75	7.5	61.2	0.59	2.14	0.9505	0.1311	0.6030	0.4220	8
10	100	0.25	1	5	76.8	0.27	2.72	0.8051	0.6557	0.3115	0.5479	4
11	100	0.3	0.25	2.5	85.6	0.41	2.42	0.7231	0.42623	0.4623	0.5223	5
12	100	0.35	0.5	0	98.4	0.45	1.8	0.6038	0.3606	0.7738	0.5523	3
13	125	0.2	1	2.5	55.89	0.46	1.42	1.0000	0.3442	0.9648	0.6925	1
14	125	0.25	0.75	0	96.28	0.43	1.37	0.6236	0.3934	0.9899	0.6239	2
15	125	0.3	0.5	7.5	72.36	0.67	1.45	0.8465	0.0000	0.9497	0.0000	14
16	125	0.35	0.25	5	82.89	0.63	1.35	0.7483	0.0655	1.0000	0.3814	10

3   Results and Discussion

Generally, higher value of composite desirability grade is preferred for setting of most favourable parameters in turning operation. Table 3 depicts that the experiment number 13 has utmost value of composite desirability, which produces minimal values of surface roughness, wear in flank and cutting force during turning experimentation. The variance of analysis is carried out for composite desirability grade to find significant parameters, which influence on the multi-performance characteristics and exemplified in Table 4. From Table 4, it is observed that the rate of feed has the strongest weight on multi-performance characteristics as compared to other parameters. Table 3 illustrates that the experiment number 13 which has cutting speed at fourth level, feed rate at second level, depth of cut at fourth level and % of reinforcement at second level has maximum desirability grade value. Therefore, the most favourable levels of parameter during turning of A356-TiB2/TiC composite can be given as *A*4, *B*2, *C*4 and *D*2.

Figure 5 demonstrates the micro-graphs of multi-coated carbide insert cutting edge during trail number 15, which has maximum flank wear and moderate roughness of the surface, and cutting force is the reason for minimized composite

Table 4 ANOVA results for composite desirability grade

Process parameters	Degree of freedom	Sum of square	Mean square	*F*-value	*P*-value	%
Cutting speed	3	0.18904	0.06301	1.57	0.360	26.15
Feed rate	3	0.34528	0.08176	2.03	0.287	47.78
Depth of cut	3	0.05340	0.01780	0.44	0.740	7.38
% of reinforcement	3	0.11436	0.03812	0.95	0.517	15.82
Error	3	0.02055	0.04018			2.87
Total	15	0.72263				100

Fig. 5 SEM of multi-coated carbide insert cutting edge
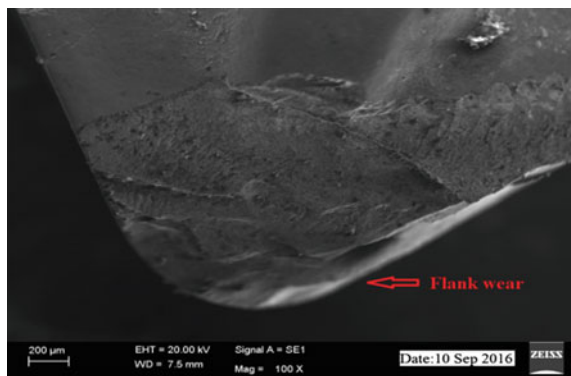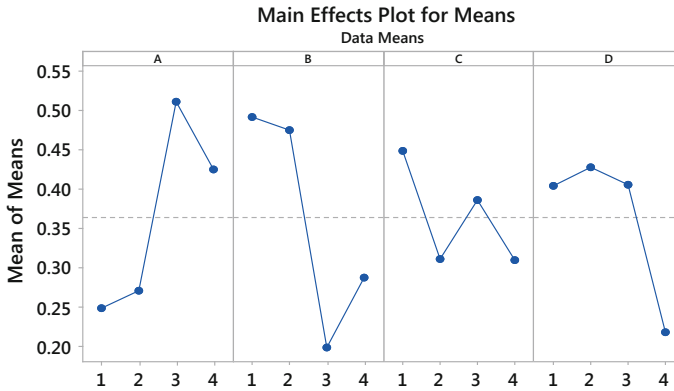
Fig. 6 Main effect plot for means of desirability grade

desirability value. Figure 6 explains that the moderate cutting speed has larger desirability value; this may be attributed to excessive flank wear at higher cutting speed.

Also, the deprived surface finish in addition to the excesses tool wear has observed at lesser cutting speed, and higher feed rate is a reason for the lesser desirability value compared with other parameters within the selected ranges. The moderate depth of cut yields more desirability value. At higher cutting speeds, the temperature of the cutting zone is enhanced, which in turn raises the plastic deformation of materials. Extreme temperature of an interface decreases the hardness of cutting tool and prone to flank wear [9]. The heat generation at the machining interface reduces the hardness of the workpiece, which minimizes the cutting force. The interaction between the chip and cutting tool is lower at higher cutting speed, which results in minimized surface roughness values during turning. A raise in rate of feed causes hike in cutting force due to improvement in friction heat between the cutting edge and workpiece [10]. Increase in feed rate hikes the feed marks across the surface due to additional friction in machining, because this surface roughness gets spoiled. The force acting about the axis during turning is more with increases in feed rate. A hike in cutting depth increases the shear angle which increases the cutting force. An increase in cutting depth results in more friction between the cutting edge and work piece, which causes an increase in the tool wear. At higher cutting depths, the formation of build-up edge on the rack face tool is more and spreading of this deposition over the machined surface spoils the surface finish [11]. An increase in the reinforcement ratio enhances the surface roughness values due to flank wear of a tool during turning, because of excess ceramic content presence in the composites. The extreme hardness has been observed at a higher reinforcement ratio which causes an increase in the tool wear and allows segmental type of chip formation during machining. Finally, the regression equation was developed for the composite desirability grade for mathematical evaluation to predict the optimal value.

Table 5 Conformation and validation results of the optimal experiment

	Initial parameter setting	Optimal machining parameter	
		Predicted	Experiment
Setting level	$A_1B_1C_1D_1$	$A_4B_2C_4D_2$	$A_4B_2C_4D_2$
Cutting force	128.4		55.89
Flank wear	0.06		0.46
Surface roughness	2.82		1.42
% of reinforcement	7.5		2.5
Desirability	0.43923	0.64324	0.69254
Improvement in desirability values = 0.25331			

$$D_g = 0.3638 - 0.1151\,A1 - 0.0929\,A2 + 0.1473\,A3 + 0.0607\,A4 + 0.1280\,B1$$
$$+ 0.1114\,B2 - 0.1637\,B3 - 0.0756\,B4 + 0.0847\,C1 - 0.0529\,C2 + 0.0219\,C3$$
$$- 0.0537\,C4 + 0.0401\,D1 + 0.0641\,D2 + 0.0414\,D3 - 0.1455\,D4.$$

$$(5)$$

Once the best possible level of machining parameter is selected, the final step is to predict and validate the enhancement of characteristic using best possible level of the machining parameters. The approximate composite desirability value is predicted by means of regression equation. Table 5 demonstrates the result of justification experiments using the best possible level turning parameter. As listed in Table 5, predicted desirable value attained from the regression equation is 0.64324. The desirability value recorded from the conformation experiment is 0.69254 with tool wear, flank wear is 0.46, surface roughness is 1.42, cutting force is 55.89, and % of reinforcement is 2.5%. There is 2.53% enhancement in the composite desirability over the expected mean value. Similarity of the composite desirability assessment between initial and optimal parameters is given in Table 5. The enhancement in desirability is recorded as 0.25331 and clearly shows the significant improve in response

4 Conclusion

In this study, the machinability of A356-TiB$_2$/TiC composites produced by K$_2$TiF$_6$-KBF$_4$-graphite reaction was examined and the subsequent conclusions are drawn.

- A356-TiB$_2$/TiC composites are successfully produced by K$_2$TiF$_6$-KBF$_4$-graphite reaction with different reinforcement ratios and characterization report from scanning electronic microscopy, and EDAX analysis confirms the presence of TiB$_2$ and TiC reinforcements and their distribution.
- The analysis exhibits that the rate of feed was most influential machining parameter followed by speed of cutting and cutting depth.

- The desirability function analysis of the cutting force, flank wear and surface roughness can convert the multi-characteristics performance optimization into the single performance characteristic which is called composite desirability value. As a result, the optimization of the intricate diversified performance characteristic can be greatly simplified.

References

1. Seeman, M., Ganesan, G., Karthikeyan, R.: Study on tool wear and surface roughness in machining of particulate aluminium metal matrix composite—response surface methodology approach. Int. J. Adv. Manuf. Technol. **48**(5), 613–624 (2010)
2. Tham, L.M., Gupta, M., Cheng, L.: Effect of limited matrix-reinforcement interfacial reaction on enhancing the mechanical properties of aluminium–silicon carbide composites. Acta Mater. **49**, 3243–3253 (2001)
3. Tjong, S.C., Ma, Z.Y.: Microstructural and mechanical characteristics of in-situ metal matrix composites. Mater. Sci. Eng. **29**, 49–113 (2000)
4. Pradeep Kumar, G.S., Praveennath, G.K., Keshavamurthy, R., Alipour, M.: Microstructure and mechanical behaviour of in-situ fabricated AA6061-TiC metal matrix composite. Arch. Civ. Mech. Eng. **17**, 535–544 (2017)
5. Senthil, P., Selvarj, T., Sivaprasad, K.: Influence of turning parameter on the machinability of homogenized Al-Cu/TiB2 in-situ metal matrix composites. Int. J. Adv. Manuf. Technol. **67**, 1589–1596 (2013)
6. Anandakrishnan, V., Mahamani, A.: Investigations of flank wear, cutting force, and surface roughness in the machining of Al-6061–TiB$_2$ in-situ metal matrix composites produced by flux-assisted synthesis. Int. J. Adv. Manuf. Technol. **55**, 65–73 (2011)
7. Naveen Sait, A., Aravindan, S., Noorul Haq, A.: Optimisation of machining parameters of glass fibre reinforced plastic (GFRP) pipes by desirability function analysis using Taguchi technique. Int. J. Adv. Manuf. Technol. **43**(5-6), 581–588 (2009)
8. Palanikumar, K., Muthukrishnan, N., Hariprasad, K.S.: Surface roughness parameters optimization in machining A356/SiC/20$_P$ metal matrix composites by pcd tool using response surface methodology and desirability function. Mach. Sci. Technol. **12**, 529–545 (2008)
9. Anil, K.C., Vikas, M.G., Shanmukha Teja, K.V., Sreenivas Rao, K.V.: Effect of cutting parameters on surface finish and machinability of graphite reinforced Al-8011 matrix composite. In: 2nd International Conference on Mining, Material and Metallurgical Engineering and IOP Conference Series: Materials Science and Engineering (2017). https://doi.org/10.1088/1757-899x/191/1/012025
10. Shoba, C.H., Ramanaiah, N., Nageswara Rao, D.: Effect of reinforcement on the cutting forces while machining metal matrix composites—An experimental approach. J. Engg. Sci. Technol. **67**, 1589–1596 (2015)
11. Sahoo, A.K., Sahoo, B.: Experimental investigations on machinability aspects in finish hard turning of AISI 4340 steel using uncoated and multilayer coated carbide inserts. Meas. J. Int. Measur. Confed. **45**, 2153–2165 (2012)

Optimization of Dissimilar Friction Stir Welding Process Parameters of AA5083-H111 and AA6082-T6 by CCD-RSM Technique

H. M. Anil Kumar, V. Venkata Raman, S. P. Shanmughanathan, Jacob John and U. Mohammed Iqbal

Abstract The non-heat-treatable aluminium alloy AA5083 is used widely for marine applications because of its high resistance to sea water and industrial chemical environments. The heat-treatable AA6082 is regarded as structural material exhibiting medium strength and good resistance to corrosion and occupies incredible applications in construction industry. The joining of these alloys is bit challenging in the fusion welding process because of inevitable welding defects like porosity, cracks, distortion. The friction stir welding (FSW) is a potential solid-state joining process which is found more appropriate for such alloys. In this study, dissimilar materials such as AA5083-H111 and AA6082-T6 are selected for the FSW and based on design of experiments 31 trials were chosen with four varying input factors (tool pin profile, tool rotational speed, welding speed and axial force) at five levels to optimize the output responses, namely ultimate tensile strength (UTS) and percentage of elongation (POE). The central composite design (CCD) technique with response surface methodology (RSM) is applied using Design of Expert Version 11 software to develop second-order linear regression quadratic mathematical models using analysis of variance (ANOVA) in order to establish the relationship between input parameters and output responses. Further

H. M. Anil Kumar (✉) · V. Venkata Raman
Department of Mechanical Engineering, BITM, Ballari, Karnataka, India
e-mail: hmanilkumar@yahoo.com

V. Venkata Raman
e-mail: vaddivvr@gmail.com

S. P. Shanmughanathan · J. John
Department of Mechanical Engineering, DSCE, Bengaluru, Karnataka, India
e-mail: nathansps@gamil.com

J. John
e-mail: j2js@hotmail.com

U. Mohammed Iqbal
Department of Mechanical Engineering, SRM Institute of Science and Technology,
Kattankulathur Campus, Chennai, India
e-mail: mohammediqbal.u@ktr.srmuniv.ac.in

the confirmation tests revealed that the joints fabricated using tapered square pin profile yield better tensile strength and elongation when compared to other profiles.

1   Introduction

The invention of friction stir welding (FSW) technology is unveiled in the year 1991, by Wayne Thomas at The Welding Institute (TWI), Cambridge, England. It is an effective and economical joining technique for different non-ferrous materials having low melting temperatures like aluminium, magnesium, copper. The research works are also going on ferrous materials at the cost of expensive tool materials. Many of the investigations proved that irrespective of the materials, the joints made out of FSW have better tensile strength and free from welding defects like cracks, porosity, distortion in contrast to the fusion welding process [1]. The technique makes use of a non-consumable tool made of steel materials to weld non-ferrous alloy. The plates to be friction stir welded are rigidly clamped to the backing plates to avoid jerking during the process. The location of work material is also to be given utmost importance along with other process parameters like tool rotational speed, welding speed, to yield better mechanical properties of the welded joint [2]. The material location refers to placement of the work material in the case of dissimilar materials joining. The base material having high tensile strength is to be placed in the retreating side and the one which has less tensile strength is to be placed in the advancing side [3].

Reza-E-Rabby et al. [4] did the work on effects of pin thread and thread interruptions (flats) on weld quality and process response parameters during FSW of 6061 aluminium alloy. Results showed that threads with flats significantly improved weld quality and reduced in-plane forces. Jagathesh et al. [5] analysed the factors influencing tensile strength in dissimilar welds of AA2024 and AA6061 produced by FSW using three-factor three-level Box–Behnken matrix using RSM. The optimum tensile strength was obtained from the moderate rotation speed of 500 rpm and traverse speed of 40 mm/min. Rajakumar et al. [6] established relationships between mechanical properties of six different aluminium alloys (AA1100, AA2219, AA2024, AA6061, AA7039, and AA7075) and optimized process parameters. Ahmed et al. [7] investigated the mechanical properties on similar and dissimilar joints using AA7075-T6 and AA5083-H111 at constant tool rotational speed of 300 rpm at varying welding speeds (50,100, 150, and 200 mm/min). The results indicated that the dissimilar joints exhibited UTS ranged between 245 and 267 MPa and fracture strain ranged between 3 and 5.6%. Suresha et al. [8] studied the effect of tool pin profiles on tensile strength of friction-stir-welded joints on AA 7075-T6 aluminium alloy using Taguchi orthogonal array. The results showed that in both the tool profiles, the tool rotational speed has more influence on

tensile strength than weld traversing speed. Jesus et al. [9] studied the effect of three different tool geometries and two joint geometries on quality of AA 5083-H111 T-welds. The results indicated that tunnel- and kissing bond-type defects are formed in joints produced with a pyramidal pin tool but welds produced with the tapered pin tool show only the presence of oxide lines.

Based on the literature survey, it is understood that the most of the works are carried out on similar materials and a less number of studies on dissimilar materials are found. In the recent past, research works in dissimilar FSW are burgeoning in the field of manufacturing industries, even for the automobiles it has become more imperative to achieve the fuel efficiency, good resistance to corrosion, creep and fatigue. Though there are some investigations on mechanical properties of dissimilar aluminium welds are made, however, optimization of the aluminium alloys AA5083-H111 and AA6082-T6 using central composite design (CCD) technique in conjunction with response surface methodology (RSM) through FSW process so far has not been reported to the authors best of knowledge.

Therefore in this paper, the main interest of the authors is to emphasize on optimization of FSW process parameters and develop a mathematical model on dissimilar friction-stir-welded aluminium alloys AA5083-H111 and AA6082-T6 which are widely used in marine application for the manufacture of ship hulls, construction and transportation industries.

2 Experimental Work

Aluminium alloy of 5083-H111 and 6082-T6 material is machined to the rectangular shape of dimension (140 × 70 × 4 mm) using milling machine. The abutting faces of the plates are well ground to minimize the joint gap between plates and cleaned to remove the dust, dirt, etc., with acetone. The chemical composition and mechanical properties of the alloys are shown in Table 1. Based on the previous research works. the several trial runs were conducted under different combinations of process parameters and average range of values are considered from minimum value to maximum value as shown in Table 2. The experimental work is carried out under four input factors (AL—axial load, TRS—tool rotational speed, TPP—tool pin profile and WS—welding speed) at five limits as shown in Table 2. Five

Table 1 Chemical composition and mechanical properties of alloys

Chemical composition of alloys in %wt										Mechanical properties	
Alloy	Si	Fe	Cu	Mn	Mg	Cr	Zn	Ti	Al	UTS YS (MPa)	POE
AA5083-H111	0.28	0.37	0.07	0.59	4.7	0.09	0.09	0.04	Balance	299,164	22
AA6082-T6	1.01	0.21	0.02	0.56	0.98	0.12	0.03	0.03	Balance	333,285	12

Table 2 FSW process parameters with levels

S. No.	Input factors	Designation	Limits				
			−2	−1	0	1	2
1	TPP	α	TC	TP	TS	TH	TO
2	TRS (RPM)	β	600	800	1000	1200	1400
3	WS (mm/min)	γ	50	70	90	110	130
4	AL (kN)	δ	3.9	5.8	7.8	9.8	11.7

Fig. 1 Photographic view of FSW tools

different tool profiles are used: tapered square (TS), triangular profile (TP), threaded cylindrical (TC), tapered hexagon (TH) and tapered octagon (TO) which are manufactured from High Speed Steels. The tools have 18 mm shoulder diameter, 3.6 mm pin length and 5 mm pin diameter. The photographic view of the five tools is shown in Fig. 1. The CCD involving 31 experimental trials is obtained from design of matrix as shown in Table 3. Out of 31 conditions, the first 16 ($2^4 = 16$) experiments is referred as full factorial design and remaining 8 is star points and 7 is the centre points of cube. Hence these 31 experimental runs with different process parameters at five different levels or limits are assigned to estimate and develop the mathematical quadratic model for UTS and POE. In each friction-stir-welded joint, three samples in each condition were cut at a 90° angle to the direction of welding using wire-EDM to prepare the tensile specimens as per the universal standards (ASTM E8M-04) which are shown in Fig. 2 to assess the UTS and POE of the joints. The yield strength in all the joints for various process parameters is observed and it is found to be higher (165 MPa) when welds are performed by tapered square tool pin profile at tool rotation of 1000 rpm, welding speed of 90 mm/min and axial load of 7.8 kN.

Table 3 Design matrix with input and output responses

EXP order	Input actual factors				Ultimate tensile strength (MPa)			Percentage of elongation		
	α	β	γ	δ	EV	PV	ER	EV	PV	ER
1	TP	800	70	5.8	227	225.38	0.72	12.2	12.05	1.24
2	TC	800	70	5.8	208	205.79	1.07	11.1	11.18	−0.63
3	TP	1200	800	5.8	214	211.96	0.96	9.2	9.35	−1.60
4	TH	1000	70	5.8	220	217.88	0.97	8.9	8.73	1.95
5	TP	800	90	5.8	229	227.29	0.75	14.1	14.08	0.14
6	TH	800	110	5.8	211	208.71	1.10	13.9	13.76	1.02
7	TP	1200	110	5.8	214	213.88	0.06	12.4	12.28	0.98
8	TH	1200	70	5.8	225	220.79	1.91	12.2	12.21	−0.08
9	TP	800	70	9.8	213	212.96	0.02	11.2	11.26	−0.53
10	TH	800	70	9.8	199	196.38	1.33	10.5	10.40	0.96
11	TP	1200	70	9.8	203	202.54	0.22	9.3	9.21	0.98
12	TH	1200	70	9.8	214	211.46	1.20	8.5	8.6	−1.05
13	TP	800	110	9.8	219	218.38	0.28	11.5	11.45	0.44
14	TH	800	110	9.8	205	202.79	1.09	11.2	11.13	0.63
15	TP	1200	110	9.8	210	207.96	0.98	10.3	10.30	0.00
16	TH	1200	110	9.8	219	217.88	0.51	10.3	10.23	0.68
17	TC	1000	90	7.8	215	215.83	−0.38	10.7	10.74	−0.37
18	TO	1000	90	7.8	200	206.17	−2.99	9.7	9.81	−1.12
19	TS	600	90	7.8	203	206.17	−1.54	13	13.12	−0.91
20	TS	1400	90	7.8	204	207.83	−1.84	9.5	9.52	−0.21
21	TS	1000	50	7.8	208	211.33	−1.58	9.7	9.69	0.10
22	TS	1000	130	7.8	216	219.67	−1.67	13.2	13.36	−1.20
23	TS	1000	90	3.9	220	224.67	−2.08	12.2	12.31	−0.89
24	TS	1000	90	3.9	207	209.33	−1.11	9.5	9.54	−0.42
25	TS	1000	90	7.8	252	252.43	−0.17	11.3	11.5	−1.74
26	TS	1000	90	7.8	256	252.43	1.41	11.4	11.5	−0.87
27	TS	1000	90	7.8	247	252.43	−2.15	11.7	11.5	1.74
28	TS	1000	90	7.8	255	252.43	1.02	11.6	11.5	0.87
29	TS	1000	90	7.8	253	252.43	0.23	11.5	11.5	0.00
30	TS	1000	90	7.8	252	252.43	−0.17	11.8	11.5	2.61
31	TS	1000	90	7.8	252	252.43	−0.17	11.2	11.5	−2.61

EXP experimental, *EV* experimental value, *PV* predicted value, *ER* error

Fig. 2 Tensile specimens prepared by wire-EDM

2.1 Developing the Mathematical Model

The present experimental work is to develop the mathematical model [3] for output response functions. Therefore, in this case UTS and POE is the response to the given input factors such as TPP (α), TRS (β), WS (γ) and AL (δ).

$$\text{Ultimate Tensile Strength} \quad \text{UTS} = f(\alpha, \beta, \gamma, \delta) \tag{1}$$

$$\text{Tensile Elongation} \quad \text{POE} = f(\alpha, \beta, \gamma, \delta) \tag{2}$$

The mathematical regression equations are given in Eqs. (3) and (4). The statistical calculations and ANOVA results are obtained by Design of Expert Version 11 software as depicted in Table 4.

$$\begin{aligned} \text{UTS} = {} & 252.43 - 2.42(\alpha) + 0.4167(\beta) + 2.08(\gamma) - 3.83(\delta) + 6.38(\alpha\beta) \\ & + 0.25(\alpha\gamma) + 0.75(\alpha\delta) + 0.75(\beta\delta) \\ & + 0.875(\gamma\delta) - 10.36(\alpha^2) - 11.36(\beta^2) - 9.23(\gamma^2) - 8.86(\delta^2) \end{aligned} \tag{3}$$

$$\begin{aligned} \text{POE} = {} & 11.5 - 0.23(\alpha) - 0.90(\beta) + 0916(\gamma) - 0.691(\delta) + 0.0625(\alpha\beta) + 0.137(\alpha\gamma) \\ & + 0.225(\beta\gamma) + 0.162(\beta\delta) - 0.462(\gamma\delta) - 0.306(\alpha^2) - 0.043(\beta^2) \\ & + 0.006(\gamma^2) - 0.143(\delta^2) \end{aligned} \tag{4}$$

Table 4 Statistical and ANOVA results

Response	Correlation total	Standard deviation	Mean	Coefficient of variation (%)	R-squared	Adjusted R-squared	Predicted R-squared	Adequate precision
UTS	10,223.35	3.8	221.61	1.72	0.9777	0.9576	0.8911	21.194
POE	61.03	0.18	11.12	1.69	0.9917	0.9844	0.9723	44.261

3 Results and Discussion

The relation between normal percentage probability and residual plots for ultimate strength and percentage elongation is shown in Fig. 3. Both the plots reveal that the residues are closer to straight line which indicates that errors are distributed in the normal population levels [10].

The regression equations, experimental (actual) versus predicted value for the responses, are shown in Fig. 4. From both the plots, it is observed that there is good
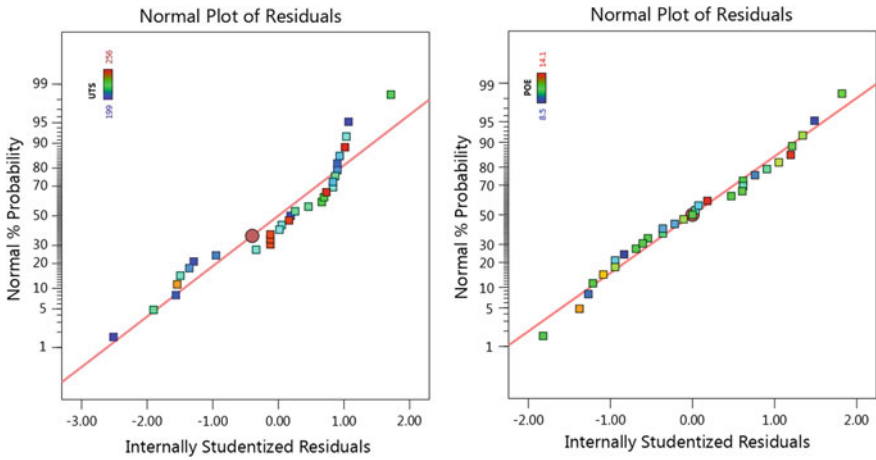
Fig. 3 Residuals versus normal % probability
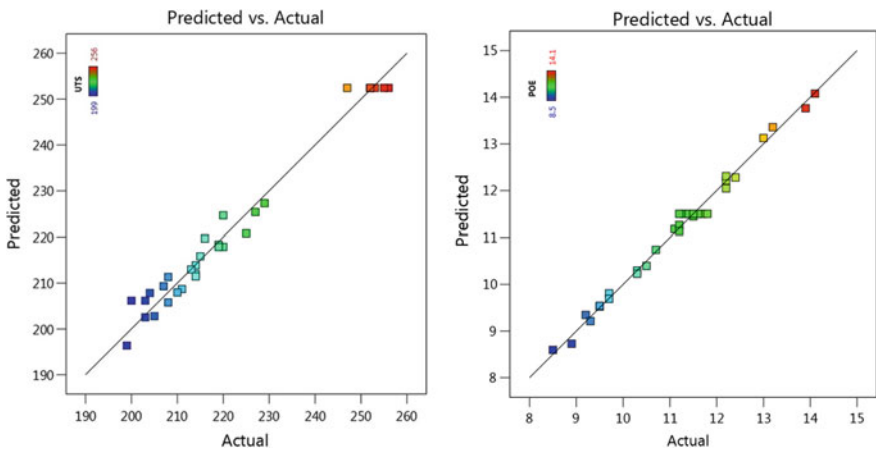
Fig. 4 Correlation between actual versus predicted

agreement among actual experimental results and predicted results of UTS and POE, as the errors between them lie within ±10 which is shown in Table 3.

3.1 Behaviour of UTS with Input Factors

From the quadratic model equation, the major input process parameters and combinations of process parameters associated with UTS identified are TPP, TRS, WS and AL, and when the tool speed raises with welding speed, improvement in ultimate tensile strength (UTS) property is evidenced. The behavioural responses of UTS against the varied input factors are analysed using surface plots. The 3D response surface plots for the UTS of the FSW region are illustrated in Fig. 5a–d. This plot helps to analyse the response during FSW process and shows the change of UTS when each FSW parameters moves from the lay down reference point.
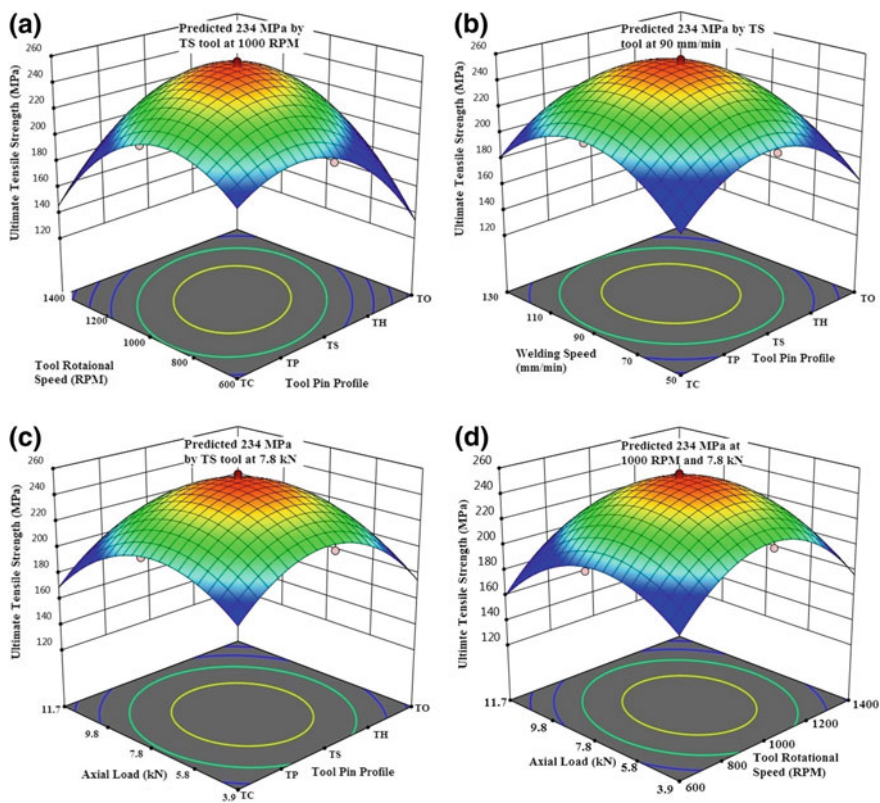
Fig. 5 Behaviour of UTS with input factors: **a** UTS versus TPP & TRS, **b** UTS versus TPP & WS, **c** UTS versus TPP & AL, **d** UTS versus TRS & AL

Figure 5a shows the classical relation between the response UTS versus TRS and TPP. It is observed that when the TRS approaches to 1000–1100 rpm, the value of UTS is found to be increased and at the same increased trend can be seen for the tapered square tool. This could be because the polygonal teeth of the tool allows smooth shearing of the metal during the stirring which causes more strengthening of the precipitates [11]. When the WS along the plate increases, the UTS also increases and is represented in Fig. 5b.

But in higher speed and feed, the tensile value is found to be reducing. The reason to happen is, when the combination of process parameters creates low or high heat due to friction and material flow, resulted lowers the tensile strength and for high speed and feed, more friction and flow of material towards the boundary leads to lower tensile property at that region [12]. Therefore, the maximum tensile strength can be seen at the mid of lower and higher values. All corresponding variations in the other responses with respect to the process parameters can be seen in the rest of the graphs. The performance of axial force with other input parameters for FSW process is shown in Fig. 5c, d. The coefficients of axial load in the quadratic model equation show the less impact on axial load in the FSW process, whereas the material processing done with tapered square tool shows a elevated tensile strength when compared with other TPP because of the multi-face and wider cutting edges of the tool which causes proper mixing and better consolidation during the stir welding [13].

3.2 Behaviour of POE with Input Factors

The effect of various process parameters and their combinations of comparisons on percentage elongation is shown in Fig. 6a–d. From the regression model equation of percentage elongation, it is seen that the coefficient terms such as WS, TPP, TRS and AL show a quality relation when multiplied with the respective process parameters and therefore it can be concluded that majority of the process parameters and their combinations on percentage elongations have challenging significance during the FSW process. The FSW conducted using tapered square pin shows the highest elongation, whereas threaded cylindrical pin profile showed the least percentage elongation. This could be due to the nature of non-circular (tapered square) tool profiles that yielded worked metal structure which gives high ductile property [14]. It is also evident from the microstructure shown in Fig. 7 that the joints fabricated by tapered square tool pin profile at tool rotational speed 1000 rpm, welding speed of 90 mm/min and axial load of 7.8 kN show equiaxed grains with the fine eutectic precipitates along the direction of welding without any defects.
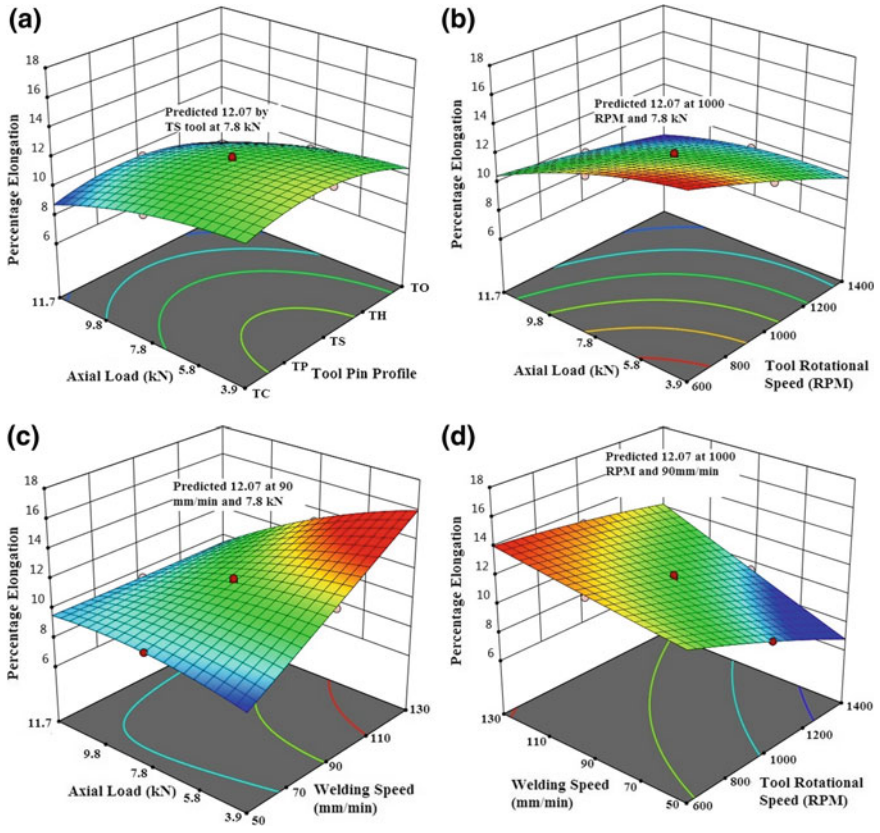
Fig. 6 Behaviour of POE on input factors: **a** POE versus TPP & AL, **b** POE versus TRS & AL, **c** POE versus WS & AL, **d** POE versus TRS & WS
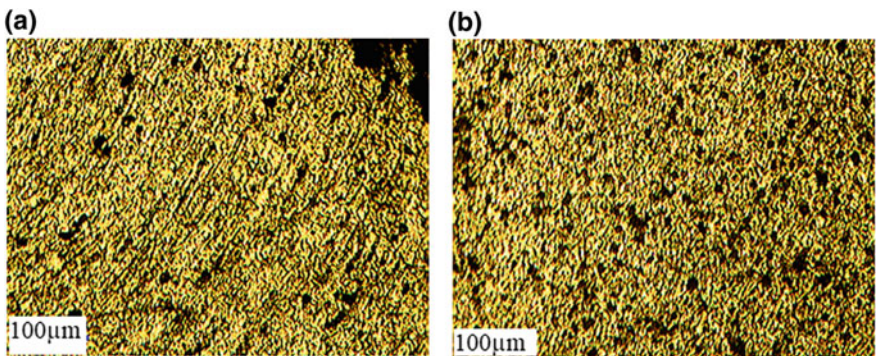
Fig. 7 Microstrucure of the dissimilar joint. **a** Thermomechanical affected zone, **b** weld nugget zone

3.3　Optimization of Input Parameters on FSW Process

The importance of optimization is to enhance the output responses (UTS and POE) through experimental investigation by considering various input factors which are said to be FSW process parameters by mathematical model. The predicted optimal results from the CCD-RSM technique for the responses UTS and percentage elongation are 234 MPa and 12.07%, respectively. The above values are located based on the following optimized conditions such as tool rotational speed as 1000 rpm, welding speed as 90 mm/min, axial force as 7.8 kN and tool pin profile as tapered square.

4　Conclusions

Aluminium alloys AA5083-H111 and AA6082-T6 successfully joined by FSW process by CCD technique and RSM as per DOE. The developed mathematical model through regression equations has predicted UTS and POE values considering TPP, TRS, WS, and AL as FSW process parameters. The behaviour of UTS and percentage of elongation (POE) are studied and optimized through response surface graphs. The model is tested for sufficiency through ANOVA. Further confirmation tests are conducted, which has proved that joints fabricated from tapered square tool pin profile at tool rotational speed of 1000 RPM, welding speed of 90 mm/min and axial load of 7.8 kN produced high tensile strength of 234 MPa and POE of 12.07.

References

1. Hassan, A.M., Qasim, T., Ghaithan, A.: Effect of pin profile on friction stir welded aluminum matrix composites. Mater. Manuf. Process. **27**(12), 1397–1401 (2012)
2. Daniolos, N.M., Pantelis, D.I.: Microstructural and mechanical properties of dissimilar friction stir welds between AA6082-T6 and AA7075-T651. Int. J. Adv. Manuf. Technol. **88**, 2497–2505 (2017)
3. Shanmuga Sundaram, N., Murugan, N.: Tensile behavior of dissimilar friction stir welded joints of aluminium alloys. Mater. Des. **31**, 4184–4193 (2010)
4. Reza-E-Rabby, Md., Tang, W., Reynolds, A.P.: Effects of thread interruptions on tool pins in friction stir welding of AA6061. Sci. Technol. Weld. Join. (2017)
5. Jagathesh, K., Jenarthanan, M.P., Dinesh Babu, P., Chanakyan, C.: Analysis of factors influencing tensile strength in dissimilar welds of AA2024 and AA6061 produced by Friction Stir Welding (FSW). Aust. J. Mech. Eng. **15**(1), 19–26 (2017)
6. Rajakumar, S., Balasubramanian, V.: Establishing relationships between mechanical properties of aluminium alloys and optimised friction stir welding process parameters. Mater. Des. **40**, 17–35 (2012)

7. Ahmeda, M.M.Z., Atayaa, S., El-Sayed Seleman, M.M., Ammara, H.R., Ahmeda, E.: Friction stir welding of similar and dissimilar AA7075 and AA5083. J. Mater. Process. Technol. **242**, 77–91 (2017)
8. Suresha, C.N., Rajaprakash, B.M., Upadhya, S.: A study of the effect of tool pin profiles on tensile strength of welded joints produced using friction stir welding process. Mater. Manuf. Process. **26**(9), 1111–1116 (2011)
9. Jesus, J.S., Gruppelaar, M., Costa, J.M., Loureiro, A., Ferreire, J.A.M.: Effect of geometrical parameters on Friction Stir Welding of AA 5083-H111 T-joints. Proc. Struct. Integr. **1**, 242–248 (2016)
10. Colligan, J., Paul, J., Konkol, Fisher, J.J., Pickens, J.R.: Friction stir welding demonstrated for combat vehicle construction. Weld. J. **82**(3), 34–40 (2003)
11. Benavides, S., Li, Y., Murr, L.E., Brown, D., McClure, J.C.: Low-temperature friction-stir welding of 2024 aluminium. Scr. Mater. **41**(8), 809–815(1999)
12. Kadaganchi, R., Gankidi, M.R., Gokhale, H.: Optimization of process parameters of aluminum alloy AA 2014-T6 friction stir welds by response surface methodology. Def. Technol. **11**, 209–219 (2015)
13. Ramanjaneyulu, K., Madhusudhan Reddy, G., Venugopal Rao, A., Markandeya, R.: Structure-property correlation of AA2014 friction stir welds: role of tool pin profile. J. Mater. Eng. Perform. **22**(8), 2224–2240 (2013)
14. Derringer, G., Suich, R.: Simultaneous optimization of several response variables. J. Qual. Technol. **12**(4), 214–219 (1980)

Effect of Flushing on Electrochemical Micromachining of Copper and Inconel 718 Alloy

K. Pooranachandran, J. Deepak, P. Hariharan and B. Mouliprasanth

Abstract Electrochemical micromachining (ECMM) is used on conductive materials to make complex features on the workpiece. The application of ECMM process has been limited due to factors such as overcut and taper formation during the machining of microholes. Passivation layer formation is an important issue in ECMM. During electrochemical micromachining process, metal hydroxides are formed at the workpiece–tool interface and get accumulated between the tool and the workpiece which forms a passivation layer. This passivation layer widens the flow of current and affects the accuracy of the machined hole. In this research work, an attempt has been made to improve the circularity of the machined hole by effectively removing the passivation layer formed at the workpiece tool interface using electrolyte flushing technique (EFT). Using EFT, copper and Inconel 718 alloy were machined with brass and copper tool electrodes, respectively. Material removal rate (MRR), circularity and taper angle were considered as primary output response parameters. Various flushing flow rates of electrolyte were taken as input parameters to study the effect of oxide layers formed in and around the tool–workpiece interface. Single-factor experiment optimization techniques were used for the fabrication of microholes. The result clearly shows that the usage of EFT on micromachining removes the passivation layer under different flow rates.

Keywords Electrochemical micromachining · Passivation layer
EFT

K. Pooranachandran (✉) · J. Deepak · P. Hariharan · B. Mouliprasanth
Department of Manufacturing Engineering, College of Engineering Guindy,
Anna University, Chennai, India
e-mail: kpchandran0604@gmail.com

1 Introduction

Electrochemical micromachining (ECMM) is an unconventional manufacturing process in which the shape of the tool is duplicated into the workpiece [1]. In ECMM, the tool electrode and the workpiece are submerged in an electrically conductive electrolyte, normally an aqueous salt solution such as sodium chloride (NaCl) or sodium nitrate ($NaNO_3$) [2, 3]. ECMM is an electrolytic process which works on the basis of anodic dissolution of the workpiece. Electrolysis is the passing of the current between two electrodes in an electrically conductive solution which is called an electrolyte, which completes the circuit [4, 5]. Nickel-based super-alloys have found many applications in aircraft engines, due to its superior strength and good temperature resistance [6]. Nickel-based super-alloys were used in the material for the wind turbines blades, and these super-alloys have effectively improved the operability and efficiency of wind turbines [7]. Nickel-based super-alloys are also difficult to machine, and the fabrication of complex shapes and structures from these materials using the conventional machining process can be problematic [1]. Film-cooling holes machined using ECMM are typical structures in turbine blades and are commonly tiny, numerous and irregularly divergent. The fabrication of microholes has been a significant challenge in the aerospace manufacturing industry [8, 9]. In hybrid machining process (ECDM process), the greatest obstacle in this method is the removal of machining by-products. It includes not only the melted and vaporized particles generated by EDM but also the hydroxide precipitates and the bubbles produced by ECM. The volume of the hydroxide is several hundred times larger than that of the EDM particles [10]. The debris (hydroxide layer) accumulated near workpiece–tool interface is also removed using different types of dielectric in EDM [11]. This study focuses on the removal of the passivation layer by the effect of flushing technique, and also the effect of material removal rate, circularity and taper angle is analysed in detail.

2 Experimental Set-up and Planning

An external flushing unit has been developed to study the effect of flushing on ECMM by varying flow rate of the electrolyte as shown in Fig. 1. For flushing 2- and 4-mm-diameter tubes have been used and the electrolyte flow has been regulated by control valve. The electrolyte flow rate was varied from 0.176 to 0.500 mm^3/min for 2-mm flushing tube, and for 4-mm flushing tube the electrolyte flow rate was varied from 0.381 to 1.112 mm^3/min. The plates of copper and Inconel 718 alloy have been used as workpiece material in this study. Brass tool electrode of 0.4 mm diameter has been used as tool material for machining copper workpiece and for machining Inconel 718 alloy; copper tool electrode of 0.4 mm diameter was used. Aqueous sodium chloride (NaCl) has been utilized as electrolyte medium for copper material, and for Inconel 718 alloy, aqueous sodium bromide (NaBr) has been used as

(a)Experimental setup   (b) Passive film
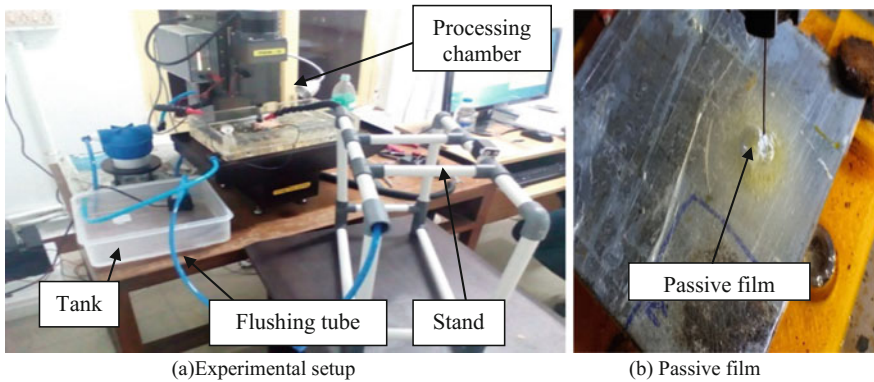
Fig. 1 Photographic view of ECM set-up

electrolyte medium. Applied voltage (V), electrolyte concentration (EC), microtool feed rate (MF) and duty cycle (DC) have been selected as constant input parameters for this study. Single-factor experiment was carried out based on the response factors, and results achieved during machining of copper. Since the major research is towards the more influential parameter, so flushing flow rates were calculated on Inconel 718 alloy. Based on those results, ANOVA were carried out for finding the percentage of influential factors in the experiments.

In single-factor experiment only one factor is investigated. The factor may be either qualitative or quantitative. The qualitative factors are copper and brass tool, and copper and Inconel 718 alloy as workpiece material, and the quantitative factors are flushing flow rate and flushing velocity. The optimization design chosen is completely randomized design. To investigate the effect of flushing on material removal rate (MRR), six different flushing flow rates have been selected and decided to obtain three observations at each flow rate. Thus, this study consists of 18 experiments (6 levels $\times$ 3 observations). The average diameter of the microhole was calculated by ($D_{\text{entrance}} + D_{\text{exit}}$)/2, and the taper angle θ is explained in Fig. 2.

Taper/unit of length = large end dimension − small end dimension/overall length

3 Effect of Passivation Layer While Machining

During ECMM process, metal hydroxides are formed at the workpiece–tool interface and get accumulated between the tool and the workpiece, which forms a passivation layer. Schematic view of electrolyte flushing technique is shown in Fig. 3. In Inconel 718 alloy, with higher Fe composition, electrolyte sodium bromide reacts with it to form ferrous hydroxide. The detailed chemical reaction is shown in Eqs. (1) to (6). When current is flown through a solution of sodium
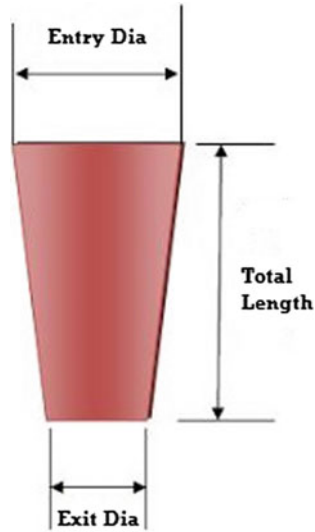
Fig. 2 Taper angle measurement
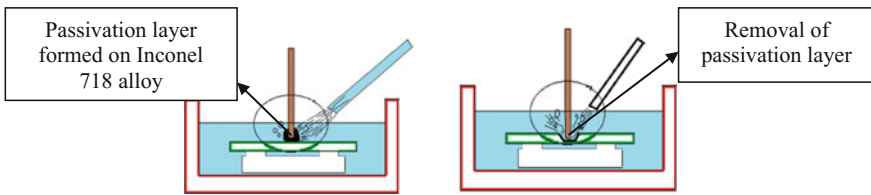
Fig. 3 Schematic view of electrolyte flushing technique (EFT)

bromide (NaBr) in water, ions are formed and will proceed to produce the desired effects. Positive ions move towards the cathode (tool material), and negative ions move towards the anode (workpiece material).

$$NaBr \leftrightarrow Na^+ + Br^- \tag{1}$$

$$H_2O \leftrightarrow H^+ + (OH)^- \tag{2}$$

Cathodic reactions: evolution of gas bubbles (hydrogen) and neutralization of positively charged metal ions

$$2H^+ + 2e^- \leftrightarrow H_2 \tag{3}$$

$$Na^+ + e^- \leftrightarrow Na \tag{4}$$

(a) Flow rate vs MRR   (b) Flow rate vs Circularity   (c) Flow rate vs Taper angle
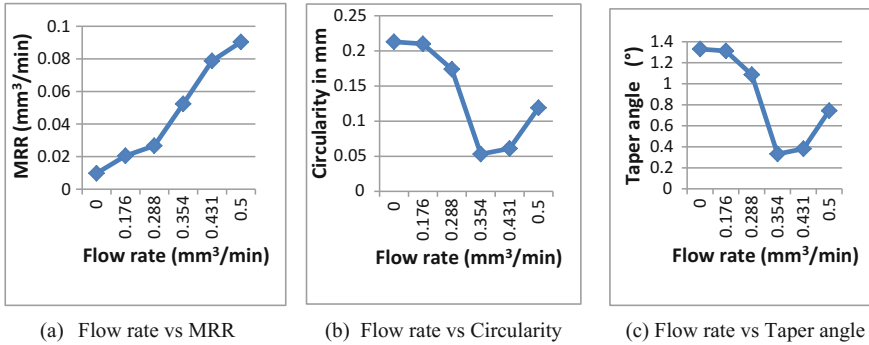
Fig. 4   Effect of flushing on MRR, circularity and taper angle for copper (2 mm)

Anodic reactions: the reaction leading to the dissolution of metal forms metal hydroxides which results in passive layer formation.

$$\text{Fe} \leftrightarrow \text{Fe}^{++} + 2\text{e}^- \tag{5}$$

$$\text{Fe}^{++} + 2(\text{OH})^- \leftrightarrow \text{Fe(OH)}_2 \tag{6}$$
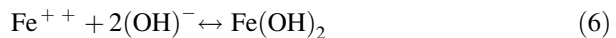
This ferrous hydroxide accumulates and forms a strong passive film around the machined hole, which affects the circularity.

4   Results and Discussion
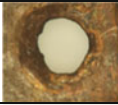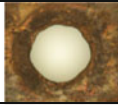
4.1   Influence of Flushing of Copper Using Flushing Tube of Diameter 2 mm

Copper has been tried as a base metal to know how it removes the passive layer on the surface, which formed while machining. In this section, the influence of the flushing flow rate of the electrolyte process parameters on performance measures such as MRR, circularity, passivating layer for copper material has been analysed. Initially, an experiment has been conducted with the above-said input process parameters without flushing and its performance measures are compared with the flushing experiments. Then, the intermittent flushing experiment was conducted with time interval of 5, 10 and 15 s; only few amounts of metal hydroxides have been removed in the tool–workpiece interface. The analysis of variance for copper is tabulated in Table 1.

Then the experiments were conducted by continuous flushing. The flow of these electrolytes does not allow the formation of stable passive layer. Passive layer formed is unstable; with EFT the layer becomes transpassive. The optical

Table 1 Analysis of variance for copper

Source of variation	Degrees of freedom	Sum of squares	Mean square	F ratio
Between samples	2	2.4089	1.2044	$F = 1.2044/0.0687$
Within samples (error)	15	1.0305	0.0687	$F = 17.53$
Total	17			

Flushing flow rate (mm^3/min)	0	0.500
Top diameter of hole(mm)	2.569	0.633
Top view (5X)		
Bottom diameter of hole(mm)	2.356	0.514
Bottom view		

Fig. 5 Optical microscope images of machined holes

microscope images of the hole without flushing and with flushing are shown in Fig. 5. The diameter of the hole without flushing is 2.569 mm, and the diameter of the hole with flushing is 0.633 mm. From the experimental results, it is clear that removal of passivation layer not only improves material removal rate and also results in good circularity. The effect of flushing on MRR, circularity and taper angle is shown in Fig. 4. As the flushing flow rate is higher in 4-mm flushing tube, the tool electrode bends during the machining process and elliptical shape hole has been machined. So, 4 mm flushing experiment was avoided for copper workpiece material.

4.2 Influence of Flushing on ECMM of Inconel 718 Alloy

In this section, the influence of the input flow rate and velocity of the electrolyte process parameters on performance measures such as MRR, circularity, passive layer for Inconel 718 alloy has been analysed. Initially, an experiment has been conducted without flushing and its performance measures are compared with the flushing experiments. Then, the intermittent flushing experiment was conducted with time interval of 5, 10 and 15 s; only few amounts of metal hydroxides have

Table 2 Analysis of variance for Inconel 718 alloy (2-mm flushing tube)

Source of variation	Degrees of freedom	Sum of squares	Mean square	F ratio
Between samples	2	0.0732	0.0366	F = 0.0366/0.0083
Within samples (error)	15	0.1253	0.0083	F = 4.4096
Total	17			

been removed in the tool–workpiece interface. The analysis of variance for Inconel 718 alloy for 2-mm tube is tabulated in Table 2.

Then the experiments were conducted by continuous flushing, and the combinations of input factors with their material removal rate have been analysed. The flow of these aqueous electrolytes does not allow the formation of stable passive layer. Passive layer formed is unstable; with EFT the layer becomes transpassive. The effect of flushing on MRR and taper angle for 2- and 4-mm tubes is shown in Figs. 6 and 7, respectively. The optical microscope images of the hole without flushing and with flushing for 2- and 4-mm flushing tube are shown in Fig. 8. The diameter of the hole without flushing is 3.128 mm, and the diameter of the hole with flushing is 0.481 mm. ANOVA table for 4-mm tube is tabulated in Table 3.

$F_{5\%, 2,15} = 3.68$. Since $F_0 = 4.4096 > 3.68$, H_0 is rejected.

The inference is that the treatment means are significantly different at 5% level of significance. That is, the treatment (flushing flow rate) has significant effect on the material removal rate.

(a) Flow rate vs MRR   (b) Flow rate vs Taper angle   (c) Flow rate vs Circularity
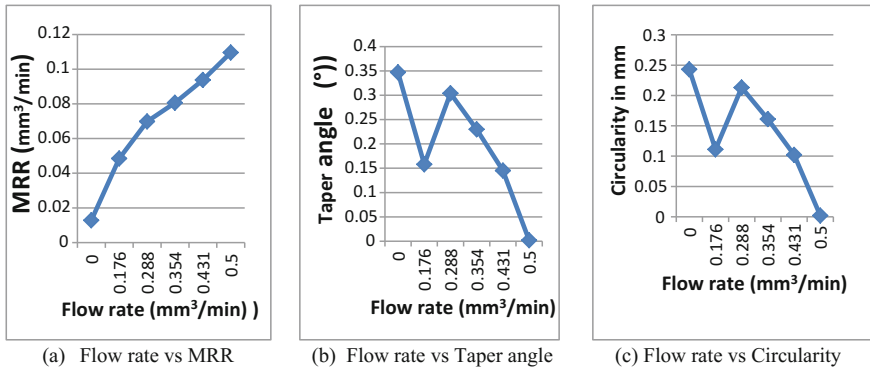
Fig. 6 Effect of flushing on MRR, taper angle and circularity for Inconel 718 alloy (2-mm tube)

(a) Flow rate vs MRR   (b) Flow rate vs Taper angle   (c) Flow rate vs Circularity
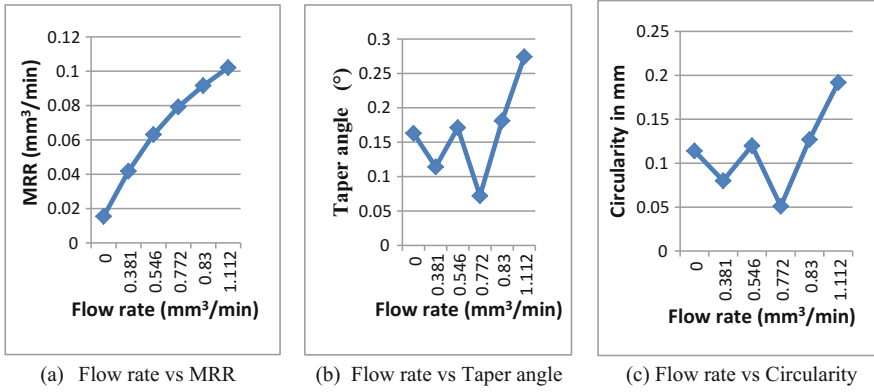
Fig. 7 Effect of flushing on MRR, taper angle and circularity for Inconel 718 alloy (4-mm tube)

Flushing tube diameter	2mm	2mm	4mm	4mm
Flushing flow rate (mm^3/min)	0	0.500	0	0.112
Top diameter of hole(mm)	3.371	0.481	3.128	0.812
Top view				
Bottom diameter of hole(mm)	2.854	0.479	2.968	0.633
Bottom view				

Fig. 8 Optical microscope images of machined holes

Table 3 Analysis of variance for Inconel 718 alloy (4-mm flushing tube)

Source of variation	Degrees of freedom	Sum of squares	Mean square	F ratio
Between samples	2	0.0281	0.0140	$F = 0.0140/0.0026$
Within samples (error)	15	0.0401	0.0026	$F = 5.38$
Total	17			

5 Conclusions

It is evident from the experimental work that continuous flushing is preferred for passivation layer removal which enhances the material removal rate and improves the accuracy of microhole. In this study, flushing was applied to ECMM by varying the flow rate and velocity of the electrolyte in the narrow machining gap. The following conclusions are drawn from the results of the study.

- Passivation layer formed will increase the corrosion resistance on the surface which reduces the material removal rate (MRR).
- As a base material, in copper, EFT gave better results. It increases material removal rate and reduces taper angle at higher flow rate.
- In Inconel 718 alloy, EFT has been compared with 2- and 4-mm flushing tube. Here 2 mm flushing process has improved material removal rate and reduced taper angle than 4-mm flushing tube. Successive machining results in decrease in diameter of hole from 3.371 to 0.481 mm.
- Overall, for effective removal of passivation layer, EFT should be used under different flow rates.

References

1. Bhattacharyya, B., Munda, J., Malapati, M.: Advancement in electrochemical micro-machining. Int. J. Mach. Tools Manuf. **44**, 1577–1589 (2004)
2. Loutrel, S.P.: Electrochemial Machining: Prediction of Operating Parameters Including Extreme Operating Conditions. Massachusetts Institute of Technology, Cambridge, MA (1971)
3. Bannard, J.: Electrochemical machining. J. Appl. Electrochem. **7**, 1–29 (1977)
4. Rajurkar, K.P., Zhu, D., Wei, B.: Minimization of machining allowance in electrochemical machining. CIRP Ann. Manuf. Technol. **47**, 165–168 (1998)
5. Zhang, Z., Wang, Y., Chen, F., et al.: A micro-machining system based on electrochemical dissolution of material. Russ. J. Electrochem. **47**, 819–824 (2011)
6. Munda, J., Malapati, M., Bhattacharya, B.: Control of micro-spark and stray-current effect during EMM process. J. Mater. Process. Technol. **194**, 151–158 (2007)
7. Rajurkar, K.P., Zhu, D., McGeough, J.A., Kozak, J., Silva, A.D.: New developments in electro-chemical machining. CIRP Ann. Manuf. Technol. **48**, 567–579 (1999)
8. Ghosal, B., Bhattarcharya, B.: Influence of vibration on micro-tool fabrication by electrochemical machining. Int. J. Mach. Tools Manuf. **64**, 49–59 (2013)
9. Zhang, Y.J., Tang, Y.J., Liu, X.K., et al.: Development of ultra-short pulse power supply applicable to micro-ECM. Mater. Sci. Forum **626–627**, 369–374 (2009)
10. Zhang, Y., Xu, Z., Zhu, D., Xing, J.: Tube electrode high-speed electrochemical discharge drilling using low-conductivity salt solution. Int. J. Mach. Tools Manuf. **92**, 10–18 (2015)
11. Sadagopan, P., Mouliprasanth, B.: Investigation on the influence of different types of dielectrics in EDM. Int. J. Adv. Manuf. (2015)

Comparative Study of Cutting Fluid Application Methods to Improve Machining Conditions During Surface Grinding on AISI 1040 Steel

I. Kantharaj, M. Sekar, X. Ajay Vasanth and S. Mohanasundaram

Abstract Finishing operations play a very important role in machining as they help to achieve the desired high-quality surface. Surface grinding, a widely employed finishing process uses wheels made of abrasive grains mixed with a bonding material. At the initial stages of the grinding process, the structure of the grain in the wheel will be in upright condition as the abrasive grains are sharp. As the process proceeds, abrasive grains become blunt due to the cutting force and the heat generated at the interface, thereby reducing the surface quality of the workpiece. Application of the coolant at the primary cutting zone reduces the temperature and also improves the grinding but at the cost of the environmental and health hazards which is prominent in the grinding process. In this research article, comparative experimental investigations between the different methods of application of coolant namely flood and minimal quantity lubricant (MQL) with the dry grinding process are carried out. It is the MQL method of coolant application that offers a desirable grinding operation, with reduced environmental impact and health hazards.

Keywords Surface grinding · Minimum quantity lubrication (MQL)
Dry grinding · Surface roughness

I. Kantharaj · X. A. Vasanth · S. Mohanasundaram
Department of Mechanical Engineering, Karunya Institute of Technology and Science,
Coimbatore, India
e-mail: kantharaj@karunya.edu

X. A. Vasanth
e-mail: vasantajay@gmail.com

S. Mohanasundaram
e-mail: johnmohana@yahoo.com

M. Sekar (✉)
Department of Mechanical Engineering, AAA College of Engineering and Technology,
Sivakasi 626005, Tamil Nadu, India
e-mail: sekar.m@gmrit.edu.in

1   Introduction

One of the major requirements of the machining industry of the modern era is to achieve better efficiency and to perform machining with better effectiveness. Out of the several machining processes, grinding operations carry extra importance as it is performed at the final stages of the component. The closer dimensional tolerances and surface finish achieved in this process are of paramount importance for the proper assembly of parts. It was observed from the literature that the major concern and drawback in grinding process are the thermal damage due to sharp thermal gradient [1]. The workpiece burn viewed by naked eye remains the most catastrophic damage. The heat energy created during grinding process causes such discoloration and blemishes [2, 3] which affects the value of the product. The workpiece burn influences the hardness of the workpiece to increase because of microstructural change leading to the formation of detrimental stress in the ground component [3]. These detrimental stresses can sometimes cause the machined component to crack in the case of sensitive materials [4]. Further these stresses seriously affect the fatigue life of the components.

Grinding zone is the area where the workpiece and the grinding wheel come into contact with each other for the purpose of metal removal by the abrasive grains. The friction produced during the dynamic grinding process releases a spurt of heat energy which is detrimental to the burn condition of the workpiece. It is apparent that the application of the coolants in the grinding zone reduces friction. The cutting fluid dissipates the heat and flushes away the chips and swarf formed during the grinding process [5–7]. The collection of grinding swarf near the cutting zone reduces the dissipation of heat [8, 9].

In the early stages, flood type of lubrication was employed in the grinding process, where a large quantity of coolant will be continuously fed into the grinding wheel and the workpiece interface. This forms an oil film on the interface and reduces friction which in turn reduces the grinding force. Though application of coolant proves to be critical for performing an effective grinding process, it is also a severe constraint as it is toxic and its disposal impacts the environment. The inclusion of cutting fluids during grinding process leads to the production of airborne mist, smoke, and other particles apart from the fact they also increase the cost of production [10]. Evaporation and volatilization of coolant is hazardous to the environment and the human body. The permissible exposure level (PEL) for metalworking fluid aerosol is 0.5 mg/m^3 as per the U.S. Occupational Safety and Health Administration (OSHA), and U.S. National Institute for Occupational Safety and Health (NIOSH). These regulatory requirements suggest that the quantity of the cooling fluid used during the grinding process has to be minimal. In contrast, the conventional cutting fluid application followed by many industries consumes a large quantity of cutting fluid and seems to be least effective economically and environmentally. Apart from the above-mentioned points, wet grinding had a major impact such as thermal softening and quench crack. The minimal quantity lubricant (MQL) uses very minimal quantity of lubricants and effective in the removal of the

heat generated by the cutting tool [11, 12]. The MQL arrangement can be immensely useful in high-speed micromachining applications where the coolant can only be applied in a limited quantity [13]. In addition, MQL is best suitable for nanomaterial-blended coolants from the view point of machining economics [14]. Zhang optimized the blend of nanomaterials for MQL grinding of abrasive mixed nanofluids and concluded a large mix of AL_2O_3 is required for better surface finish [15]. Though alternate methods for cooling are available, this MQL is the most feasible economic and environment friendly solution to grinding operations [16]. In recent years, study of MQL in grinding has gained interest among researchers. Hadad successfully modelled the MQL process using a finite element model (FEM). The authors stressed the importance of applying coolant in the critical zone of grinding [17] for better heat transfer. Li studied MQL grinding performances of various vegetable oils based on grinding force, grinding temperature, and energy ratio coefficient and concluded that palm oils are best suited for MQL applications [18]. Lucasz compared MQL with wet cooling and showed favourable reduced forces and temperatures in MQL regime [19]. It is apparent from the above a collective investigation of dry, wet and MQL yet to be explored. In this research work, a better understanding of the influence of machining parameters on dry, wet and MQL is aimed through a comparative performance analysis based on the experimental results of surface quality, temperate and cutting forces investigated under the various surface grinding conditions. The study is conducted with a ductile material AISI 1040 steel which is subjected to wheel loading compared to hardened steel counterparts.

2   Materials and Methods

2.1   *Investigation Parameters*

Surface grinding is a finishing process where a moving work piece is ground by a high-speed rotating abrasive wheel. Surface grinding improves the precision of the components by controlling the dimensional tolerance, surface finish and flatness. Typically surface grinding is carried out on hardened components with grinding wheels made of aluminium oxide and silicon carbide. A large amount of heat is generated in this metal removal process as the number of cutting edges on the grinding wheel slides over the component. Application of coolant is necessary to remove heat and hence most grinding operations are carried out under wet conditions though dry grinding is used for certain applications. In case of dry machining, frequent dressing with diamond tool is required to ensure proper grinding as the swarf generated is not flushed. A feasible solution can be achieved between wet and dry grinding which is known as near dry grinding.

The primary objective of this research work is to compare the performance of dry, flood and MQL coolant techniques in surface grinding with respect to the

Table 1 Grinding parameters used for investigation

Grinding parameters	Operating range
Depth of cut	0.005, 0.01, 0.015
Cross transverse speed	1.1 m/min (constant)
Wheel speed	1450 rpm

Table 2 MQL parameters used for investigation

Grinding parameters	Operating range
Flow rate of coolant	2.2 ml/min
Direction of application	Tool–work interface
Pressure at nozzle	2×10^5 Pa

Table 3 Flood cooling fluid parameters

Grinding parameters	Operating range
Flow rate of coolant	19.21 l/min
Direction of application	Tool–work interface
Cutting fluid	Soluble cutting oil with 90% water

machining parameters, namely depth of cut, wheel speed and traverse speed of the table (Table 1). In this study, the depth of cut was varied and other machining conditions were kept constant in the experiments for the sake of simplicity. The values of experimental parameters set for MQL and flood types of coolant application for grinding are stated in Tables 2 and 3, respectively.

2.2 Experimental Set-up

The grinding investigations were carried out on a precision hydraulic surface grinding machine (Model SG3060). AISI 1040 steel workpiece was employed for experimenting the grinding process with different types of coolant applications. The output parameters measured at different grinding conditions include main grinding force, surface roughness *Ra*, and grinding temperature. The main grinding force was measured using a Kistler type 9257B dynamometer. Surface roughness was measured using Mahr TR100 surface roughness tester of type Mahr Surf GD 25. Among the various surface roughness amplitude parameters such as roughness average (*Ra*), root-mean-square roughness (*Rq*), maximum peak-to-valley roughness (*Ry* or *R*max), *Ra* was selected to express the surface roughness in this study. *Ra* averages all peaks and valleys of the roughness profile and then neutralizes the few outlying points so that the extreme points have no significant impact on the final results. Also, it is considered as a simple and an effective method for monitoring surface texture and ensuring consistency in measurement of multiple surfaces.

The grinding temperature was measured with the help of a T-type thermocouples as they have a better stability and best suited for oxidizing atmospheres. A specially formulated cutting fluid was employed in this investigation. The formulation consisted of petroleum sulphonate (15% by weight), ethylene glycol (1% by weight), oleic acid (3% by weight), triethanolamine (3% by weight), alcohol ethoxylate (3% by weight) and paraffinic wax mineral oil (rest). The stand of distance between the nozzle and the workpiece was kept constant at 80 mm during the experiments.

The MQL set-up shown in Fig. 1 is custom built for the investigations carried out in this work. The MQL system consists of mixing chamber through which compressed air is passed. A minimum quantity of coolant is passed into it with the help of fluid regulator. The coolant fluid from the coolant tank is fed by gravity into the mixing chamber. Due to the mixing of compressed air stream with the coolant in the mixing chamber, the mixture becomes finely atomized (Fig. 2). The presence of large quantity of air flowing at high pressure makes the atomized coolant mixture sprayed in the form of mist on the tool–work interface. As the spray is directed towards the interface with pressure, a maximum cooling effect with a minimum coolant supply during the grinding process is achieved. The experimental set-up consists of a balanced grinding wheel of 50 cm diameter mounted on the spindle of the surface grinding machine. The dynamometer is fixed on the bed of the machine for grinding force measurement, and the workpiece is clamped on it by using machine vice. The flow of coolant is controlled using a coolant regulator so that precise metering of the coolant of about 2.2 ml/min is achieved. The compressed air along with the coolant becomes an excellent combination for the cooling and lubrication at the tool–work interface. In dry and flood cooling applications, all the parameters were set similar to the MQL. Wheel dressing was carried out after the completion of every experiment. Aluminium oxide wheels are used since the material used in the experiments was not hardened.

Fig. 1 MQL set-up

Fig. 2 A closer view of the MQL set-up in operation
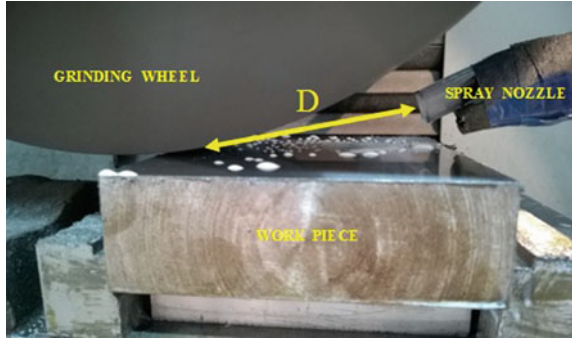
3 Results and Discussion

The performance of the aluminium oxide grinding wheel was studied using AISI 1040 steel under different lubrication conditions namely (i) dry, (ii) flood cooling and (iii) MQL. The performance of the different coolant applications in surface grinding is analysed by the comparison of experimental observations of surface roughness, grinding temperature and grinding force measured for three levels of depth of cut. The results are tabulated and compared for surface roughness Ra, grinding temperature and grinding force in Figs. 3, 4 and 5, respectively.

It can be observed from the results that irrespective of the depth of cut, the cutting temperature (Fig. 3), surface roughness Ra (Fig. 4), and grinding force (Fig. 5) show the improved characteristics with the MQL enabled grinding process. It is clearly evident that dry grinding has the highest cutting temperature compared with the other two coolant conditions as there are no external sources to remove the heat produced. As a result of the increased temperature, the grinding wheel starts to lose the binding material and thus the grinding force increases to result in a product in poor surface finish of the component. The inclusion of the cutting fluid as flood lubricant type removes the heat by reducing the friction and removes the chips. It is obvious that the quantity of the lubricant used for grinding is high compared to MQL (Table 2). Using MQL during grinding brings forth better grinding conditions and also required very minimum cutting fluid (Table 3). The reason behind better grinding condition with MQL can be attributed to the special arrangement of a nozzle positioned to supply the pressurized lubricant exactly at the critical zone.

Fig. 3 Surface roughness, Ra versus depth of cut for different lubricant condition
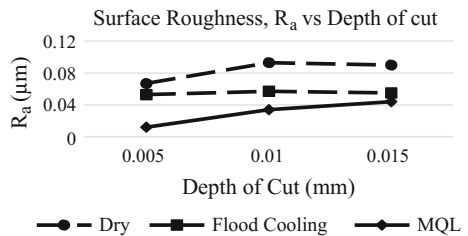
Fig. 4 Temperature versus depth of cut for different lubricant condition
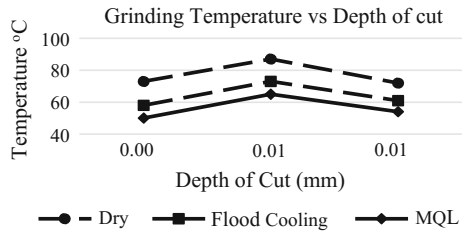
Fig. 5 Grinding force versus depth of cut for different lubricant conditions
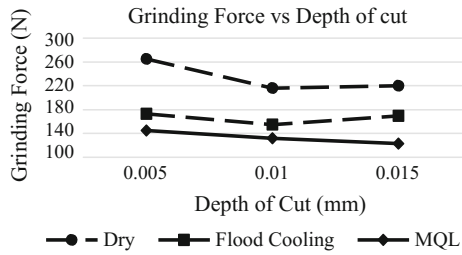
The minimal quantity of coolant applied in the critical zone successfully removes the heat created by the continuous engagement of rotating grinding wheel with the translating workpiece. The supply of pressurized lubricant at the critical zone not only removes heat effectively but also effectively flushes away the swarf produced during the surface grinding process.

The lack of supply of lubricant in the critical grinding zone in dry machining results in increased temperature and causes sharp thermal gradients on the workpiece resulting in workpiece burn. If the temperature at the critical zones is not removed at the right time, then the temperature will further increase and the initial nucleate boiling will aggravate to film boiling. At this point, a vapour film developed between workpiece and cutting fluid starts to act as an insulator preventing heat removal by the cutting fluid. This sudden rise in workpiece temperature causes workpiece burn even in flood cooling if coolant does not reach the critical zone. This problem can be completely eliminated in the case of MQL as the cutting fluid is supplied exactly to the critical zone in pressurized condition. MQL lubrication ensures the removal of tiny chips from the critical zone, produced by the sharp cutting edges of the grinding wheel. As the lubricant is supplied at high pressure, removal of the chip at the critical zone becomes effective and reduces the probability for the formation of build-up edges. The reduction of friction at the tool–workpiece interface with minimal quantity of cutting fluid ensures a corresponding reduction in grinding force. The reduction in grinding forces improves the stability of the operation and is extremely useful while machining thin-walled components. The improved characteristics summarized in Table 4 show MQL can be employed in conventional job shop and mass production environments.

The most important advantage of employing MQL in these production environments comes from the amount of coolant used. As the amount of coolant used is

Table 4 MQL parameters used for investigation

Depth of cut (mm)	Grinding temperature (°C)			Surface roughness (μm)			Grinding force (N)		
	Dry grinding	Wet grinding	MQL	Dry grinding	Wet grinding	MQL	Dry grinding	Wet grinding	MQL
0.005	73	58	50	0.067	0.053	0.012	265	172.9	145
0.01	87	73	65	0.093	0.057	0.034	216	154.7	132
0.015	72	61	54	0.009	0.055	0.044	220	169.6	123

comparatively very less than the flood cooling, the problems associated with disposal are reduced. The machining economics also gets improved due to the reduced use of coolants and benefits in quality of the components produced. Health hazards to workers can be further reduced though special arrangements to suck the mist sprayed while grinding. The MQL way of applying coolant can be further extended to other types of grinding process such as internal and external cylindrical grinding. The minimal application of coolant also helps the operator to better observe and monitor the grinding process which is critical in case of internal grinding of small objects. MQL combines the functionality of cooling lubrication with an extremely low consumption of lubricant, and therefore it has the potential to close the gap between overflow lubrication and dry cutting. There is a potential scope for further research on the study of influence of pressure on the surface grinding with MQL.

4   Conclusion

In surface grinding, parameters like surface roughness, grinding force, temperature were compared for different grinding conditions and it was found that the MQL is superior to other techniques such as dry, wet conditions. It is observed that the temperature during MQL grinding lies in between the dry condition and wet condition. Surface Roughness, grinding force and grinding temperature values clearly indicate that MQL is superior to wet and dry grinding. The application of atomized spray of coolants at the critical zone enables MQL to perform better than the other types. Though ductile materials are prone to wheel loading and frequent dressing, the MQL study shows favourable reduced cutting forces. The reduced cutting forces during the surface grinding operations play an important role while grinding thin-walled components. As the amount of fluid used for cooling is vastly reduced, it can be stated that MQL process is economically best suited in mass production environments. In addition, MQL promotes green manufacturing environment as it effectively reduces the hazards associated with the disposal of coolants.

References

1. Irani, R.A., Bauer, R.J., Warkentin, A.: A review of cutting fluid application in the grinding process. Int. J. Mach. Tools Manuf. **45**, 1696–1705 (2005)
2. Liu, C., Abe, S., Noda, M.: The influence of grinding oil viscosity on grinding heat and burn damage in creep-feed grinding. Lubr. Eng. **51**, 8 (1995)
3. Chen, X., Rowe, W.B., McCormack, D.F.: Analysis of the transitional temperature for tensile residual stress in grinding. J. Mater. Process. Technol. **107**, 216–221 (2000)
4. Desai, O., Bahadur, S.: Material removal and subsurface damage studies in dry and lubricated single-point scratch tests on alumina and silicon nitride. Wear **225**, 1264–1275 (1999)
5. Ebbrell, S., Woolley, N.H., Tridimas, Y.D., Allanson, D.R., Rowe, W.B.: The effects of cutting fluid application methods on the grinding process. Int. J. Mach. Tools Manuf. **40**, 209–223 (2000)
6. Wang, C.Y., Wei, X., Pan, X.C., Song, Y.X.: Effects of surfactant in stone machining. Key Eng. Mater. **250**, 194–199 (2003)
7. Ge, P.Q., Li, J.F., Lu, C.H., Liu, Z.C.: Performance evaluation & action mechanism analysis of extreme pressure additives used for oil-based cutting fluids. Key Eng. Mater. **250**, 281–286 (2003)
8. Rowe, W.B., Jin, T.: Temperatures in high efficiency deep grinding (HEDG). CIRP Ann. **50** (1), 205–208 (2001)
9. Webster, J., Brinksmeier, E., Heinzel, C., Wittmann, M., Thoens, K.: Assessment of grinding fluid effectiveness in continuous-dress creep feed grinding. CIRP Ann. **51**, 235–240 (2002)
10. Tawakoli, T., Hadad, M., Sadeghi, M.H., Daneshi, A., Sadeghi, B.: Minimum quantity lubrication in grinding: effects of abrasive and coolant-lubricant types. J. Cleaner Prod. **19**, 2088–2099 (2011)
11. Morgan, M.N., Barczak, L., Batako, A.: Temperatures in fine grinding with minimum quantity lubrication (MQL). Int. J. Adv. Manuf. Technol. **60**, 951–958 (2012)
12. Dureja, J.S., Singh, R., Singh, T., Singh, P., Dogra, M., Bhatti, M.S.: Performance evaluation of coated carbide tool in machining of stainless steel (AISI 202) under minimum quantity lubrication (MQL). Int. J. Precis. Eng. Manuf. Technol. **2**, 123–129 (2015)
13. Sekar, M., Yang, S.H.: Design and implementation of high-performance real-time free-form NURBS interpolator in micro CNC machine tool. Mech. Based Des. Struct. Mach. **42**, 296–311 (2014)
14. Mao, C., Tang, X., Zou, H., Huang, X., Zhou, Z.: Investigation of grinding characteristic using nanofluid minimum quantity lubrication. Int. J. Precis. Eng. Manuf. **13**, 1745–1752 (2012)
15. Zhang, X., Li, C., Zhang, Y., Wang, Y., Li, B., Yang, M., Guo, S., Liu, G., Zhang, N: Lubricating property of MQL grinding of Al2O3/SiC mixed nanofluid with different particle sizes and microtopography analysis by cross-correlation. Precis. Eng. **47**, 532–545 (2017)
16. Brusly, A., Sekar, M., Yang, S.H.: Analytical expression for thermal conductivity of heat pipe. Appl. Therm. Eng. **100**, 462–467 (2016)
17. Hadad, M., Sharbati, A.: Thermal aspects of environmentally friendly-MQL grinding process. Proc. CIRP **40**, 509–515 (2016)
18. Li, B., Li, C., Zhang, Y., Wang, Y., Jia, D., Yang, M.: Grinding temperature and energy ratio coefficient in MQL grinding of high-temperature nickel-base alloy by using different vegetable oils as base oil. Chin. J. Aeronaut. **29**(4), 1084–1095 (2016)
19. Lukasz, M.B., Batako, A.D.: Application of minimum quantity lubrication in grinding. Mater. Manuf. Processes **27**, 406–411 (2012)

Influence of Friction Coefficient and Failure Model in 3D FEA Simulation of Drilling of Glass Fiber Reinforced Polymer Composites

C. Prakash and K. S. Vijay Sekar

Abstract The applications of the glass fiber-reinforced polymers (GFRP) composites are increasing every day because of its superior properties when compared with conventional materials. The modern industries in the field of aviation, aerospace, construction, marine and automobiles are using the composites very effectively to reduce the weight and to increase the performance of the vehicle. While machining the components, drilling is an important machining process, which plays an important role in assembly operation. The selection of suitable machining parameter setting and adequate knowledge on chip formation and material removal is very much essential in drilling the GFRP laminate. In this paper, using ABAQUS/Explicit 3D finite element model (FEM) has been developed to simulate and to understand the drilling operation of the laminate. The selected friction coefficient and failure criteria play a significant role in the quality and accuracy of the FE model. Hence, it is essential to investigate the influence and effects of friction coefficient and failure model in a 3D FE drilling simulation. Friction coefficients and failure criteria were applied to the FE model in a wider range, and analysis was carried out. The thrust forces obtained from FE results were compared with the experimental results to evaluate the influence of the above-mentioned FE model parameters.

Keywords GFRP · Drilling experiment · Thrust force · Failure criteria
Friction coefficient · 3D FE model

C. Prakash (✉)
Anna University, Chennai 600 025, Tamil Nadu, India
e-mail: prakashc@suryagroup.edu.in

K. S. Vijay Sekar
SSN College of Engineering, Kalavakkam,
Kancheepuram District, Tamil Nadu, India
e-mail: vijaysekarks@ssn.edu.in

81

1   Introduction

Composite materials are widely used in the field of automobile, aerospace, marine and construction engineering because of its superior properties like low density, high tensile strength, corrosion resistance [1]. However, the different types of laminate failures occur during machining, such as delamination, matrix cracking, fiber failure, fiber pullout and debonding of fiber and matrix. Hence investigation of the drilling process in the GFRP laminate was carried out by many researchers to understand the machining process and to get defect-free holes, good surface finish, and efficient machining process, reduced tool wear and optimized machining time [2]. Conducting the experimental studies on drilling of GFRP composites is time consuming and very expensive, and the accuracy of the experimental result mainly depends on the instruments and data acquisition systems used for investigation. This practical limitation of doing experimental studies and the availability of good computational facilities in the current era lead to the development of 3D FE models. Using these FE models, investigation and simulating the machining process is easy and moreover, the FE simulation results reveal the machining process very effectively to visualize the chip formation and failure modes of the laminate. FE simulation results can also be obtained for a wider machinability matrix [2] (i.e., for a wider range of machining parameters).

The developed and validated 3D finite element model (FEM) is a boon to the industries and researchers to simulate and to understand the complex process of drilling the GFRP laminates [3]. Arrazola et al. [4] carried out the research on the influence of friction modeling in FE simulation of machining AISI4340 steel. The shear stress values obtained from FE results are correlated with the experimental results and found to be good. However, the quality and reliability of this FE model mainly depend upon the FE Model parameters such as friction coefficient, damage evolution, damage initiation criteria (failure criteria) and element size [4]. Hence it is mandatory to investigate the influence of the friction coefficient and the failure criteria to improve the quality of the FE model and to get better correlation with the experimental values [5].

This research work aims in investigating the influence of the friction coefficient and the damage evolution criteria (failure criteria) in the 3D FE model. A 3D FE model is developed in Abaqus 6.14-2 to simulate the drilling process in GFRP laminate. The FE model is then validated by comparing with the experimental results. The validated FE model is used in this investigation, to know the influence and effects of the friction coefficient and the damage evolution criteria on cutting force prediction.

2 Finite Element Model for Drilling Process

2.1 Methodology

A 3D finite element model in the drilling process of GFRP laminate has been developed using commercially available finite element analysis software ABAQUS 6.14-2. The Lagrangian finite element model is developed to simulate the drilling process [6]. The material model for the GFRP laminate is created using Autodesk Composite Material Manager 2016 software [7]. The 3D failure criteria are incorporated into this FE model using ABAQUS—AUTODESK HELIUS PFA plug-in [7]. A range of friction coefficients (between 0 and 1) and four different failure criteria were applied to the FE model, and analysis was carried out. The thrust forces obtained from FE results were compared with the experimental results to evaluate the influence of the above-mentioned FE model parameters.

2.2 3D Geometric Model and Meshing

The solid carbide twist drill (SANDVIK H10F Grade with 115° point angle and 30° helix angle) of diameter 10 mm and with two flute was modeled in CATIA V5R14 [8]. This 3D twist drill model is then imported to ABAQUS in STEP file format as a rigid body. A UD-GFRP laminate was modeled, using part module in ABAQUS 6.14-2 with dimensions of 15 mm × 15 mm × 10 mm. The FE model of the GFRP laminate was created for this analysis with the element size of 0.25 mm, and the model consists of 36,000 elements, meshed with C3D8R (linear 8-node linear brick, reduced integration, hourglass control). The 3D twist drill model is considered as a rigid body in order to reduce the computing difficulty [2, 3, 9, 10]. This twist drill model is meshed with ten thousand C3D10 M (10—node modified quadratic tetrahedron) elements, and the average element size is around one mm.

2.3 Material Model and Constitutive Damage Criteria

The material model is incorporated to the FE model with the Autodesk Helius PFA 2016 plug-in, because ABAQUS/Explicit does not have built in 3D damage criteria for composites [6, 7]. The damage criteria such as Hashin, Cristensen, LaRc02 and Puck were used for this research to test the reliability and accuracy of the 3D FE model. The thrust force results obtained from FE simulations were compared with the experimental values to evaluate and suggest the appropriate damage model. The damage initiation is controlled by the specified 3D damage criteria, and damage evolution is based on the stiffness degradation factors of 0.1 and 1E-6 for matrix and fiber, respectively [7].

Table 1 Machining parameters used in the drilling of GFRP laminate

Drilling parameter	Magnitude
Spindle speeds (rpm)	1800, 1152, 720, 515, 275, 164, 103, 73
Cutting speed (m/min)	56.52, 36.17, 22.60, 16.17, 8.63, 5.15, 3.23 2.29
Feed rate, f (mm/min)	10.00
Drill diameter (mm)	10.00

2.4 Tool—Workpiece Interaction, Boundary Conditions and Loading

The interaction between the tool and the laminate is created, to model the surface erosion of drilling operation using the general contact algorithm available in ABAQUS/Explicit [2, 10]. In order to account on the frictional effects between the mating surfaces of the cutting tool and the workpiece, the Coulomb friction concept is used in the model. The coefficient of friction between GFRP material and TiAlN-coated twist drill is considered as 0.45 by the other researchers [2]. The boundary conditions were applied considering the actual machining process; the two sides of the workpiece were fixed (clamped) and arrested for all six degrees of freedom (Encastre: $U1 = U2 = U3 = UR1 = UR2 = UR3 = 0$). The twist drill was constrained in X and Y directions and allowed to move and rotate along its feed axis only ($U1 = U2 = UR1 = UR2 = 0$). Then a translation (feed rate) and rotational velocity (Spindle speed) were applied to the tool tip (on a created rigid body reference point) of the twist drill [2, 3]. The cutting parameters are applied as per the experimental details (refer with: Table 1).

3 Drilling Experiment and Results

The drilling experiments were conducted on a radial arm drilling machine with 1.5 HP spindle power and a maximum speed of 2070 rpm. A solid carbide TiAlN-coated twist drill bit with the diameter 10 mm was mounted in its three-jaw universal chuck. A dynamometer was placed on the work table. The four-channel IEICOS drill tool dynamometer (Model number 651) was used to acquire thrust force and torque data. The obtained signal was converted and transmitted to the computer via an analogue–digital converter (digital oscilloscope Picoscope™). The IEICOS multi-component digital force indicator software (model 652 S) is used to capture the thrust force data during the drilling operation. The drilling experiments were conducted for eight different spindle speeds at a constant feed rate as given in Table 1, and the material properties of the UD-GFRP laminate is given in Table 2.

Table 2 Mechanical properties of GFRP laminate

Specifications	Value (s)	Specifications	Value(s)
Longitudinal modulus, $E1$ (GPA)	40	Longitudinal tensile strength, Xt (MPA)	1000
Transverse modulus, $E2$ (GPA)	8	Longitudinal comp. strength, Xc (MPA)	600
Transverse modulus, $E3$ (GPA)	8	Transverse tensile strength, Yt (MPA)	30
Shear modulus in 1–2 plane, $G12$ (GPA)	4	Transverse comp. strength, Yc (MPA)	110
Shear modulus in 2–3 plane, $G23$ (GPA)	3	Shear strength in 1–2 plane, $S12$ (MPA)	40
Shear modulus in 1–3 plane, $G13$ (GPA)	4	Shear strength in 2–3 plane, $S23$ (MPA)	40
Poisson's ratio, υ	0.25	Shear strength in 1–3 plane, $S13$ (MPA)	40
Density (kg/m^3)	1992	Resin/fiber ratio	35:65 [±5]
Specific gravity	1.99	Fiber orientation	0

4 FE Results and Discussion

Figures 1 and 3 show the thrust force pattern obtained while drilling the GFRP laminate. The thrust force varies with respect to angle of rotation of the tool. This is due to the inhomogeneous nature of the UD-GFRP laminate (Fiber orientation as shown in Fig. 2). During the drill bit rotation, the thrust force peaks, when the cutting tip is engaged perpendicularly (at 90° and 270°) with the Glass fiber, whereas at parallel positions (at 0° and 180°) cutting force is near zero [11].

Fig. 1 Changes in thrust force with cutting edge position when drilling GFRP Laminate. Thrust forces versus tool rotation angle in degrees
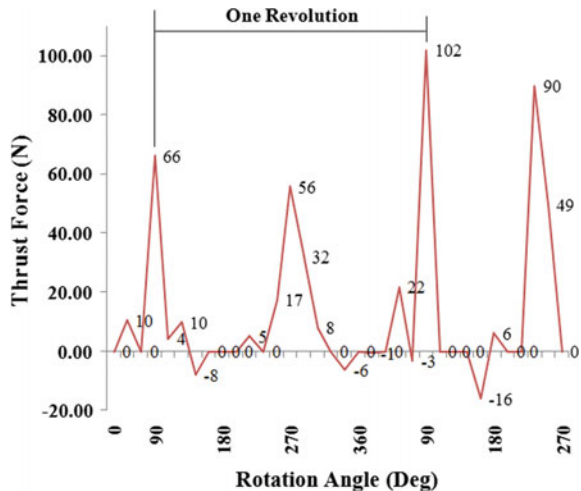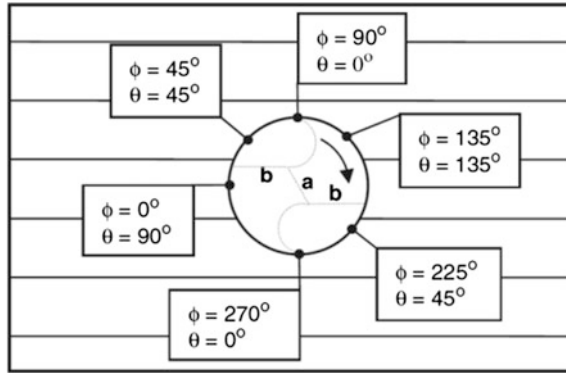
Fig. 2 Fiber orientation in drilling unidirectional GFRP laminate. **a** Chisel edge, **b** major cutting edge [11]
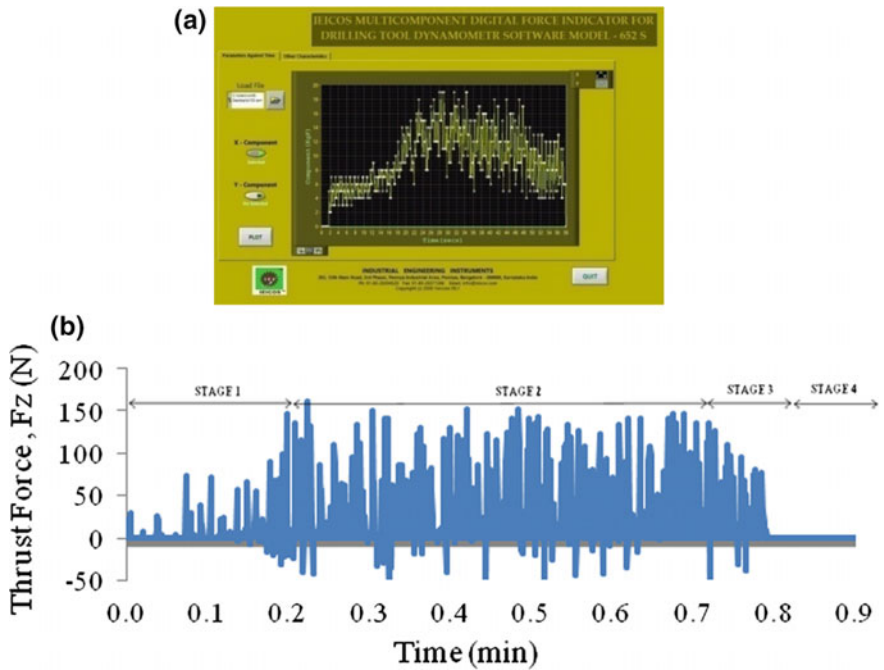
Fig. 3 Predicted thrust force profile from FE model in drilling GFRP laminate at $Vc = 3.23$ m/min, $N = 103$ rpm, Feed = 10 mm/min. **a** Experimental **b**. FE simulation

Table 3 Predicted thrust force data from FE simulation for different friction coefficients

Time (min)	Coefficient of friction (μ)									
	0.1	0.2	0.3	0.4	0.5	0.6	0.7	0.8	0.9	1.0
	Thrust force, Fz (N)									
0.1	−2.26	−21	−33.5	−28	−59	−38	−8.5	−32	−36	−8
0.2	−67	−79	−2.5	−18	−48	−9	−12	−88	−9.9	−46
0.3	73	−30	**−20**	**−20**	**−22**	**−20**	−40	−23	−33	−30
0.4	148	210	−64	**−40**	**−44**	−57	59	−98	31	−16
0.5	107	56	29	**−17.5**	**−15.5**	**−16.5**	−17.5	−13	−25	−20
0.6	117	15.5	10.5	0	−65	−38	7.5	7.5	−26	−2
0.7	84	34	−23	−111	−63	−7	−16	−26	−80	−87
0.8	97	1.0	138	−77	26	4	3	29	−15	−2

The thrust force (bold) values are in similar range when the coefficientof friction is 0.4 to 0.5.

4.1 Comparison of Thrust Force Data for Different Friction Coefficients

Table 3 describes the thrust forces obtained during drilling the GFRP laminate at Vc = 3.23 m/min, N = 103 rpm, Feed = 10 mm/min, Hashin failure criteria. The thrust force data are obtained from 10 No. of FE simulations with different friction coefficients ranging from 0 to 1 with respect to time (min). The effect and influence of friction coefficient over the 3D FE model are investigated and understood from the data given in Table 3. Analyzing these data it is found that coefficient of friction value within 0.4–0.5 range gives optimum thrust force results (highlighted in the Table 3). Hence, it is desirable to consider a value within this range (μ = 0.4–0.5) which also matches with the literature [2, 3] and experimental results within a deviation of 10–15% (Refer Table 4).

Table 4 Comparison of thrust force data obtained in drilling GFRP laminate at Vc = 3.23 m/min, N = 103 rpm, Feed = 10 mm/min

Time (min)	Output steps in FEA	Avg thrust force, Fz (N)		Stages in drilling
		Expt.	FEA	
0–0.1	0–100	32	46	I Penetration of drill tip
0.1–0.2	100–200	57	63	
0.2–0.3	200–300	79	86	II Complete engagement of the cutting lip
0.3–0.4	300–400	102	98	
0.4–0.5	400–500	112	122	
0.5–0.6	500–600	151	143	
0.6–0.7	600–700	123	128	
0.7–0.8	700–800	87	85	III Exit of the drill tip
0.8–0.9	800–900	56	42	
0.9–1.0	900–1000	10	0	IV Complete exit of the cutting lip

4.2   Comparison of Thrust Force Data for Different Failure Models

The damage criteria such as Hashin, Cristensen, LaRc02 and Puck were used for this research to test the influence of the failure criteria on the developed 3D FE model. Moreover, the reliability and accuracy of the finite element model was also studied. FE drilling simulation is carried out with all the four failure models, and the results were compared. From the FE results, it is found that the failure models don't influence much in the thrust force prediction. The thrust force values and profile are mostly unique, and moreover the predicted thrust force data match exactly with the experimental data also.

From the literature, it is understood that Hashin criterion identifies four modes of failure such as tensile fiber failure, compressive fiber failure, tensile matrix failure and compressive matrix failure [12]. The Christensen criterion identifies the following failure modes such as matrix failure and fiber failure. Puck criterion identifies fiber failure and inter-fiber failure only for unidirectional composite. The LaRc02 criterion identifies fiber failure and matrix cracking only in a unidirectional composite.

Figures 4, 5, 6 and 7 show the predicted thrust force data obtained from the 3D FE Drilling simulation studies for four different failure models. Hashin, Christensen and Puck models show similar thrust force profile and the average thrust forces of 90–100 N, during the time period 0.35–0.4 min.

Figure 7 shows the thrust force profile obtained from LaRc02 criterion which is very much different when compared with other failure model data and so, suitable failure model can be suggested from the remaining three criterions (Hashin, Christensen & puck). However, selection of failure model is very important in 3D FE machining simulation studies. Hence, the failure criterion may be selected by considering all the FE model outputs data such as thrust force profile, thrust force data, predicted shear stress, working stress, deformation, chip formation, chip morphology, delamination, predicting capability of failure modes etc.

The 3D FE simulation and the literature studies [2, 11] suggest the Hashin failure criterion as a suitable failure model for composites because it is excellent in predicting the major requisites (thrust force, damage modes, chip formation) very effectively.
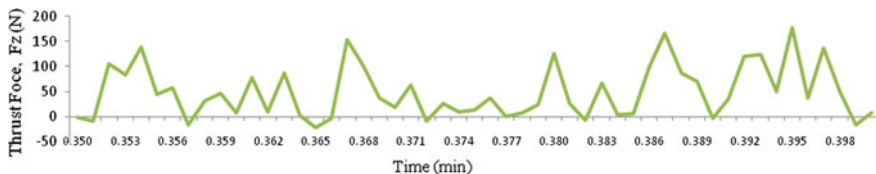
Fig. 4 Predicted thrust force profile from FE model in drilling GFRP laminate at Vc = 5.15 m/min, N = 164 rpm, Feed = 10 mm/min, Hashin Criterion
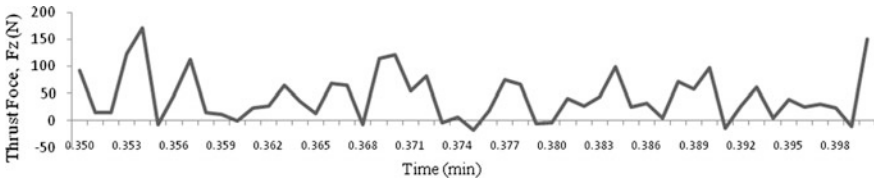
Fig. 5 Predicted thrust force profile from FE model in drilling GFRP laminate at $Vc = 5.15$ m/min, $N = 164$ rpm, Feed = 10 mm/min, Christensen Criterion
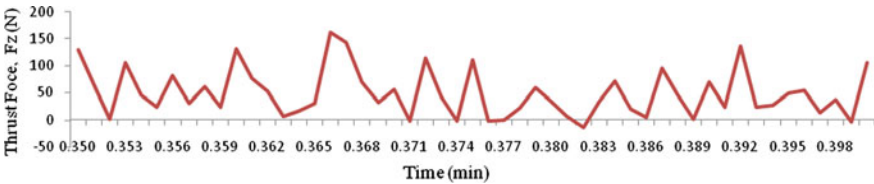
Fig. 6 Predicted thrust force profile from FE model in drilling GFRP laminate at $Vc = 5.15$ m/min, $N = 164$ rpm, Feed = 10 mm/min, Puck Criterion
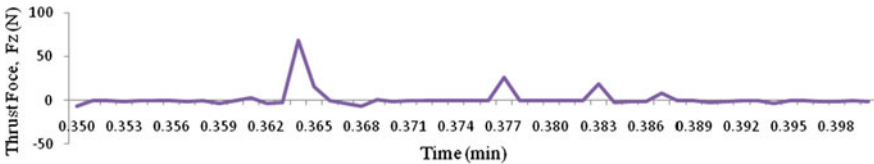
Fig. 7 Predicted thrust force profile from FE model in drilling GFRP laminate at $Vc = 5.15$ m/min, $N = 164$ rpm, Feed = 10 mm/min, LaRc02 Criterion

5 Conclusions

The 3D FE model developed in this research work for simulating the drilling of GFRP laminate is reliable and efficient in predicting the thrust force data.

- The friction coefficient ranged from 0 to 1.0 is incorporated, and simulation studies are carried out. From the simulation results, it is evident, when using friction coefficient of 0.4–0.5 provides outstanding thrust force results, and moreover it also matches exactly with the experimental results.
- Out of the four different failure criteria used in this research, Hashin failure criterion is suggested for further FE studies. Since, the thrust force profile obtained from Hashin damage criteria is good enough in predicting the force data accurately and it also matches with the literature and experimental results.

References

1. Alaiji, R., Lasri, L., Bouayad, A.: 3D finite element modelling of chip formation and induced damage in machining of fiber reinforced composites. Am. J. Eng. Res. **4**(7), 123–132 (2015)
2. Giasin, K., Ayyar-Soberanis, S., French, T., Padnis, V.: 3D finite Element Modelling of cutting forces in drilling fibre Metal laminates and experimental hole quality analysis. Appl. Compos. Mater. Open access journal (2016)
3. Phadnis, V.A., Makhdum, F., Roy, A., Silberschmidt, V.V.: Drilling in carbon/epoxy composites: experimental investigations and finite element implementation. Composites. Part A. **47**, 41–51 (2013)
4. Arrazola, P.J., Ozel, T.: Investigations on the effects of friction modeling in finite element simulation of machining. Int. J. Mech. Sci. **52**, 31–42 (2010)
5. Ozel, T.: The influence of friction models on finite element simulations of machining. Int. J. Mach. Tools Manuf. **46**, 518–530 (2006)
6. Simulia, D.: Abaqus 6.14 User's manual. Dassault systems, Providence, RI (2014)
7. Autodesk, AUTODESK HELIUS PFA 2016/HELP, Autodesk Knowledge Network
8. CATIA V5R14, User Manual, Dassault systems, Providence, RI (2014)
9. Chakladar, N.D., Pal, S.K., Mandal, P.: Drilling of woven glass fiber-reinforced plastic—an experimental and finite element study. Int. J. Adv. Manuf. Technol. **58**, 267–278 (2012)
10. Debnath, K., Singh, I.: Drilling of metal matrix composites: experimental and finite element analysis. J. Eng. Manuf. **229**(5), 886–890 (2015)
11. Sheikh-Ahmad, J.Y.: Machining of Polymer Composites. Springer (2009). e-ISBN 978-0-387-68619-6
12. Hashin, Z.: Failure criteria for unidirectional fiber composites. J. Appl. Mech. **47**, 329–334 (1980)

Surface Characteristics of Drilled Holes in Al–TiB$_2$ Metal Matrix Composites Using Electric Discharge Machine

N. Sathiya Narayanan, J. Hari Vignesh, R. I. Navin, S. Ramesh Kumar, P. Dinesh Babu and N. Pradeesh

Abstract This research work is focused on finding the variation of surface roughness and root-mean-square roughness of aluminium metal matrix composite which is reinforced with TiB$_2$ material for drilling holes using copper electrode in electric discharge machine (EDM). The friction stir casting process is carried out to prepare the specimens of 93% of Al6061 reinforced with 6% TiB$_2$. Full factorial design of experiments is conducted by considering the four input parameters namely current (A), gap voltage (V), depth of cut (d) and pulse duration (T) at five different levels. The 3-dimensional surface texture and roughness are measured using white layer interferometer for all the drilled holes, and the values are obtained using Gwyddion software. The results indicate if the current value and depth of cut increase, the value of the average surface roughness and the root-mean-square roughness also increases, whereas the surface roughness is inversely proportional to the discharge gap between the tool and work piece.

Keywords Stir casting · Metal matrix composite · Electric discharge machine (EDM) · White layer interferometer · Surface roughness

1 Introduction

Al–TiB$_2$ is a metal matrix composite consisting of 94% aluminium 6061 alloy and 6% titanium boride. Titanium boride is combined with aluminium in order to strengthen and improve its properties. Due to aluminium 6061 alloy's high corrosive resistance and low electrical resistance, it is extensively used in aerospace and naval applications. Adding TiB$_2$ further improves the properties of aluminium and also enhances the strength and wear resistance. The Al–TiB$_2$ metal matrix

N. Sathiya Narayanan · J. Hari Vignesh (✉) · R. I. Navin
S. Ramesh Kumar · P. Dinesh Babu · N. Pradeesh
School of Mechanical Engineering, SASTRA Deemed University,
Thanjavur 613 401, India
e-mail: harivignesh@mech.sastra.edu

composite (MMC) is prepared using the stir casting process. Christy et al. [1] manufactured Al–TiB$_2$ composite, and it was found to exhibit higher hardness, tensile strength and Young's modulus when compared to that of base Al 6061 alloy. Metal matrix composite (MMC) materials have two constituent materials. One is a metal and the other can be a metal or a ceramic or an organic compound. The matrix is the base metal which needs to be improved, and the reinforcement is the material that is added to improve the properties of the base metal. The reinforcement not only performs a structural task but also varies the physical properties such wear resistance, friction coefficient and thermal conductivity. The reinforcement can be either continuous or discontinuous. Continuous reinforcement leads to MMC being anisotropic, and discontinuous reinforcement leads to MMC being isotropic. The MMC can be manufactured by several methods such as solid-state method, liquid-state method, semi-solid-state method, vapour deposition method and in situ fabrication technique. MMC is more expensive than the conventional material. Stir casting process is a liquid-state reinforcement method. In this process, the discontinuous reinforcement particles are distributed in the molten metal which is continuously stirred and immediately poured into a cool sand mould and allowed to solidify. Lawrance et al. [2] manufactured Al–TiB$_2$ by stir casting process and found that the TiB$_2$ reinforcement was made to achieve a uniform distribution in the Al 6061 matrix through stir casting. And it was also found that increase in reaction hold time, there was an increase in tensile strength and hardness for up to 30 min. Suresh et al. [3] stated that Al–TiB$_2$, when machined with non-conventional methods like EDM, will show better machinability due to its higher electrical conductivity. Gopalakannan et al. [4] experimented optimizing process parameters of EDM on MMC of aluminium and found that the surface roughness increases with increase in pulse current and pulse-on time. Hung et al. [5] experimented on aluminium MMC reinforced with SiC$_p$ on EDM process and concluded that the input power determines the MRR, but the surface finish depends on the pulse current. Hocheng et al. [6] conducted a similar experiment on aluminium metal matrix reinforced with SiC, and their results show the predicted proportionality based on heat conduction model when compared to that of common steels in material removal rate. Singh et al. [7] investigated the EDM of aluminium MMC with 10% SiC and their MRR, TWR, SR and radial overcut were recorded. Dvivedi et al. [8] investigated on EDM of Al6063/SiC$_p$ composite to see the influence of process parameters on the MRR of the material. Nanimina et al. [9] experimented on 30% Al$_2$O$_3$ MMC with EDM process parameters and found that at high current and pulse-on time the MRR of Al6061 is more than that of the MMC and at lower current and off time the MRR is low, but the TWR is high. Singh [10] investigated the aluminium metal matrix composite Al6061/Al2O3 of 20% wt on EDM and the results indicated that the aspect ratio and the pulse current were the most significant parameters affecting the performance measures. Prabu et al. [11] studied Al/TiB$_2$ on EDM and stated the increase in reinforcement ratio decreases the MRR and surface cracks. Senthil et al. [12] proposed to optimize the process parameters of EDM on Al/Cu/TiB$_2$, and the result showed that the optimized results are in good agreement with the confirmation run.

2 Experimental Works

2.1 Metal Matrix Composite (MMC) Preparation

The Al–TiB$_2$ metal matrix composite is formed through stir casting. Stir casting is a liquid-state method of manufacturing metal matrix composites. This AMMC consists of 94 wt% Al 6061 alloy and 4 wt% TiB$_2$. Aluminium 6061 alloy is placed in the graphite crucible and preheated. After that, it is heated until it reaches its molten state. Simultaneously titanium diboride (TiB$_2$) powder is poured into the pre-heater furnace, later it is heated up to 650 °C. Then both the molten Al 6061 alloy and the heated TiB$_2$ particles are mixed into the stir cast furnace and stirred continuously at a proper temperature compensation (raise temperature by 50 °C to compensate the stirrer time cooling). Finally, 1 wt% magnesium is added to the mixture through an aluminium foil. This mixture is mixed for 10–15 min and then its poured into the cold sand mould to solidify. Through this process, the Al–TiB$_2$ composite is manufactured. The casted metal matrix composite is of the dimension 100 mm × 100 mm. Figure 1a shows the casted composite after being machined.

2.2 EDM Experiments

The experimental setup was made and conducted with the electrical discharge machine (EDM) using the copper rod as the electrode. Current, discharge gap, pulse-on and pulse-off time were varied as process parameters for the experiment (*The experiment was conducted in EDM at Shanmugha Precision Forging (SPF, Thirumalisamudram, Thanjavur-613 402, Tamil Nadu, India*). Figure 1b shows the EDM used for the experiments. The Al–TiB$_2$ composite is clamped, and the copper electrode is attached above the workpiece. The tool is moved into the right position with the help of apron hand wheel, and the electrode is adjusted to the required gap
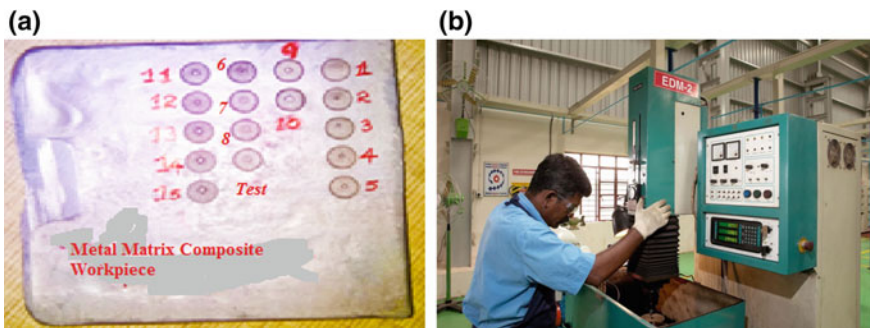
Fig. 1 **a** Machined composite material. **b** EDM setup at Shanmuga Precision Forging (SPF), Thanjavur

Table 1 Investigation of average surface roughness and root-mean-square roughness value

Set	Hole no	Current (I_o) A	Gap (δ) μm	D.O.C (d) mm	Pulse duration μs		Average surface roughness (R_a) μm	Root-mean-square roughness (R_q) μm
					T_{on}	T_{off}		
I	1	10	4	1	15	2	8.7	10.8
	2	12	4	1	15	2	9.1	11.4
	3	14	4	1	15	2	9.4	11.7
	4	16	4	1	15	2	9.7	12.2
	5	18	4	1	15	2	10.1	12.7
II	6	14	4	2	15	2	10.7	13.4
	7	14	4	3	15	2	11.1	13.9
	8	14	4	4	15	2	11.5	14.4
	9	14	4	5	15	2	12.1	15.2
	10	14	4	6	15	2	12.9	15.8
III	11	14	5	1	15	2	7.0	9.1
	12	14	6	1	15	2	6.9	8.9
	13	14	7	1	15	2	6.7	8.6
	14	14	8	1	15	2	6.6	8.4
	15	14	9	1	15	2	6.3	8.1

from the workpiece. The tank where the workpiece and tool are present is filled with dielectric fluid. Then for each experiment, the current, gap, pulse-on and pulse-off time are varied as shown in Table 1. After the machining is complete, the holes are examined under the white light interferometer to obtain the 3D surface roughness. From the image obtained surface roughness graph can be generated using the Gwyddion software.

2.3 Design of Experiments

Full factorial design of the experiments is constructed by varying three sets of parameters over five levels. Hence, the design consists of fifteen experiments. The current, discharge gap and depth of cut are the varying parameters, and the pulse-On/off time remains constant throughout the experiments. Table 1 shows the full factorial design of experiments. Each set in the design consists of one varying parameter where all other parameters are constant and also represents the resultant average surface roughness and root-mean-square roughness for each experiment.

3 Results and Discussion

From each experiment conducted, the average surface roughness value was determined from the 3D surface roughness image in the Gwyddion software. From the obtained results, the effect of current, discharge gap and depth of cut on surface roughness is studied.

3.1 Effect of Current on SR

Set I from Table 1 focuses on the variation of current value and its effect on surface roughness. In this set, the current alone is varied from 10 to 18 A, while the gap, depth of cut and pulse time remain constant. The 3D roughness image and the graph of holes 2 and 5 are shown in Figs. 2 and 3. As the current value increases, the value of the average surface roughness and the root-mean-square roughness also increases.

From the above two surface roughness images, it can be understood that with an increase in current there is an increase in the surface roughness. The graph in Fig. 4
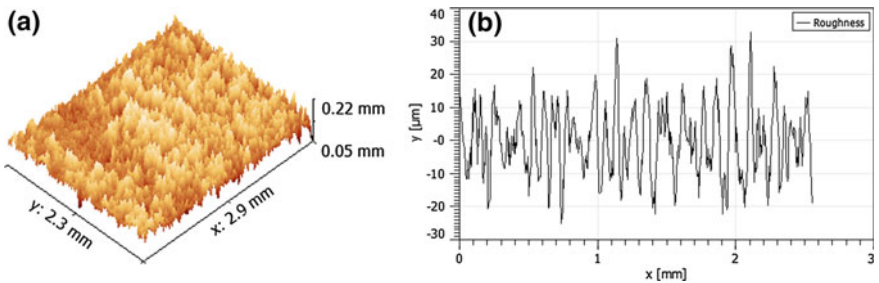
Fig. 2 **a** 3D Roughness image of hole 2. **b** Roughness graph hole 2
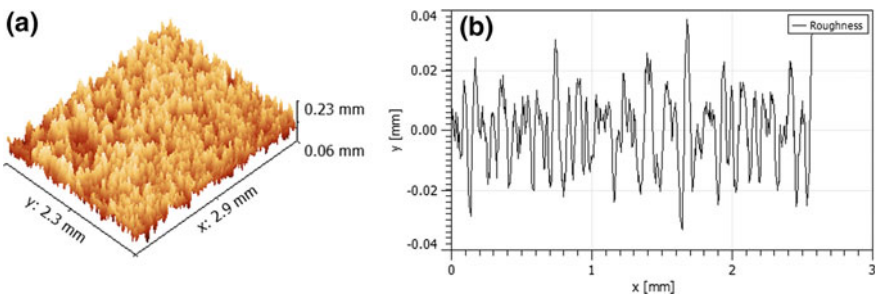
Fig. 3 **a** 3D Roughness image of hole 5. **b** Roughness graph of hole 5
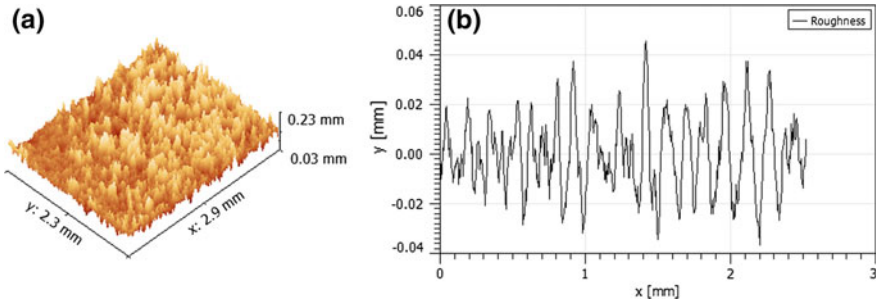
Fig. 4 **a** 3D Roughness image of hole 9. **b** 3D Roughness graph of hole 9

shows the variation average surface roughness (R_a) with respect to current (I_o). From this graph, it can be seen that surface roughness is directly proportional to the current used.

3.2 Effect of Depth of Cut on SR

Set II from Table 1 focuses on the variation of depth of cut and its effect on surface roughness. In this set, the depth of cut alone is varied from 2 to 6 mm, while the gap, current and pulse time remain constant. The 3D roughness image and the graph of holes 9 and 10 are shown in Figs. 4 and 5. As the depth of cut increases, the value of the average surface roughness and the root-mean-square roughness also increases.

From the above two surface roughness images, it can be understood that with an increase in depth of cut there is an increase in the surface roughness. The graph in Fig. 7 shows the variation average surface roughness (R_a) with respect to the depth of cut (d). From the results, it can be seen that surface roughness is directly proportional to the depth of cut of the hole.
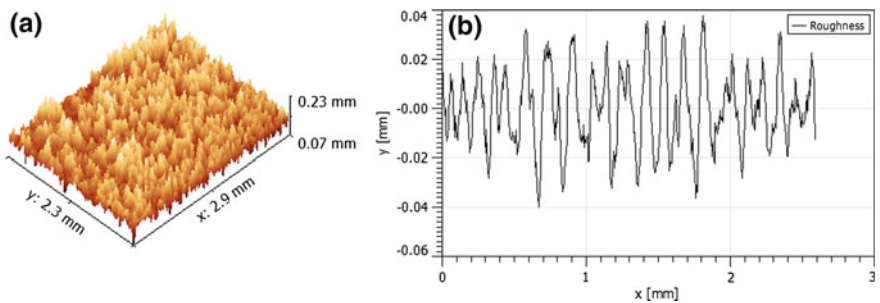
Fig. 5 **a** 3D Roughness image of hole 10. **b** Roughness graph of hole 10

3.3   Effect of Discharge Gap on SR

Set III from Table 1 focuses on the variation of discharge gap and its effect on surface roughness. In this set, the discharge gap alone is varied from 5 to 9 µm, while the depth of cut, current and pulse time remain constant. The 3D roughness image and the graph of holes 11 and 15 are shown in Figs. 6 and 7. As the discharge gap increases, the value of the average surface roughness and the root-mean-square roughness also increases.

   The graphs of holes 11 and 15 are compared with each other and from the above two surface roughness images; it can be understood that with an increase in discharge gap there is a decrease in the surface roughness. The graph in Fig. 8 shows the variation average surface roughness (R_a) with respect to discharge gap. From the results, it can be seen that surface roughness is inversely proportional to the discharge gap between the tool and workpiece.
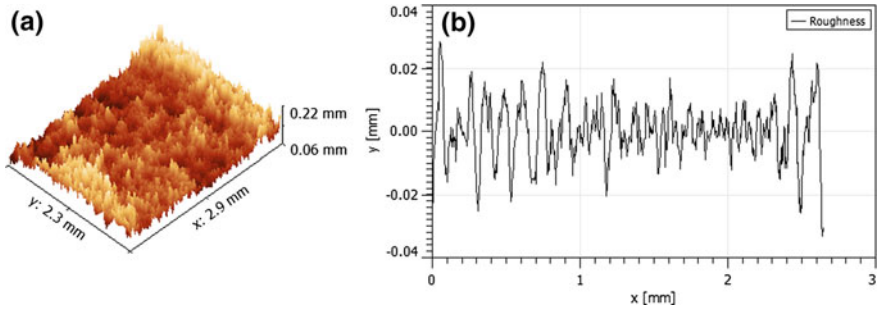
Fig. 6 a 3D Roughness image of hole 11. b Roughness graph of hole 11
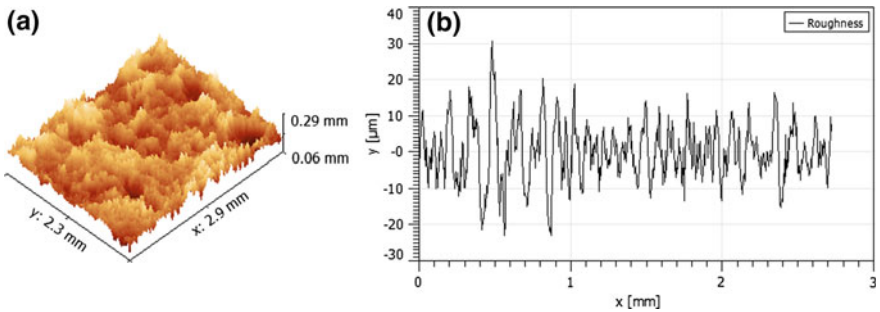
Fig. 7 a 3D Roughness image of hole 15. b Roughness graph of hole 15

Fig. 8 a Current versus average roughness. **b** Depth versus average roughness. **c** Discharge gap versus average roughness
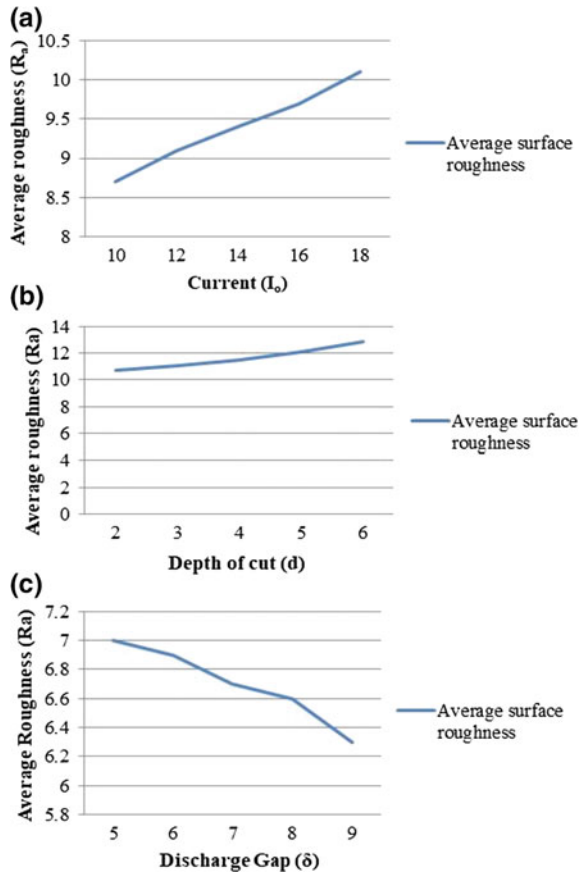
4 Conclusion

The Al–TiB$_2$ metal matrix composite was prepared from Al 6061 alloy and TiB$_2$ particles through stir casting process. On this composite material, holes were drilled using the EDM machine and copper as the electrode. A full factorial design of experiment was made taking the current, discharge gap and depth of cut as varying parameters. Each of these parameters was varied over five levels. Each of these holes was examined under white light interferometer to obtain the surface roughness image. This image can be used to generate the average roughness value and root-mean-square roughness value using the software. From studying the results following observations were made.

- As the current increases, the surface roughness of the machined hole also increases. Hence, the surface roughness is directly proportional to the maximum current applied.

- When the depth of cut is increased, the surface roughness of the machined hole also increases. Hence, the surface roughness is directly proportional to the depth of cut.
- When the electrode tip is close to the workpiece, the surface has higher roughness and less when the tip is farther away from the workpiece. Hence, the surface roughness is inversely proportional to the discharge gap. It is important to note that the gap should not be beyond the optimum distance or the sparking would not take place.
- The pulse duration of Ton and Toff has been kept constant due to the constraints of the EDM machine worked with, so the effect of pulse duration towards the surface roughness is not evaluated. Many authors also quoted that the pulse duration parameters played a major role in the surface roughness of the drilled holes.

References

1. Christy, T.V., Murugan, N., Kumar, S.: A comparative study on the microstructures and mechanical properties of Al 6061 alloy and the MMC Al 6061/TiB$_2$/12p. J. Minerals Mater. Charact. Eng. **9**(01), 57 (2010)
2. Lawrance, C.A., Prabhu, P.S.: Al 6061-TiB$_2$ metal matrix composite synthesized with different reaction holding times by in-situ method. Int. J. Compos. Mater. **5**(5), 97–101 (2015)
3. Suresh, S., Shenbag, N., Moorthi, V.: Aluminium-titanium diboride (Al–TiB$_2$) metal matrix composites: challenges and opportunities. Proc. Eng. **38**, 89–97 (2012)
4. Gopalakannan, S., Senthilvelan, T., Ranganathan, S.: Modeling and optimization of EDM process parameters on machining of Al 7075-B4C MMC using RSM. Proc. Eng. **38**, 685–690 (2012)
5. Hung, N.P., Yang, L.J., Leong, K.W.: Electrical discharge machining of cast metal matrix composites. J. Mater. Process. Technol. **44**(3–4), 229–236 (1994)
6. Hocheng, H., Lei, W.T., Hsu, H.S.: Preliminary study of material removal in electrical-discharge machining of SiC/Al. J. Mater. Process. Technol. **63**(1–3), 813–818 (1997)
7. Singh, P.N., Raghukandan, K., Rathinasabapathi, M., Pai, B.C.: Electric discharge machining of Al–10% SiC p as-cast metal matrix composites. J. Mater. Process. Technol. **155**, 1653–1657 (2004)
8. Dvivedi, A., Kumar, P., Singh, I.: Experimental investigation and optimisation in EDM of Al 6063 SiCp metal matrix composite. Int. J. Mach. Mach. Mater. **3**(3–4), 293–308 (2008)
9. Nanimina, A.M., Abdul-Rani, A.M., Ahmad, F., Zainuddin, A., Lo, S.J.: Effects of electro-discharge machining on aluminium metal matrix composite. J. Appl. Sci. **11**(11), 1668–1672 (2011)

10. Singh, S.: Optimization of machining characteristics in electric discharge machining of 6061Al/Al 2 O$_3$ p/20P composites by grey relational analysis. Int. J. Adv. Manuf. Technol. **63** (9), 1191–1202 (2012)
11. Prabu, M., Ramadoss, G., Narendersingh, P., Christy, T.V., Eswaran, V.V.: Electrical discharge machining of Al–TiB$_2$ with a low-frequency vibrating tool. Sci. Eng. Compos. Mater. **21**(3), 445–452 (2014)
12. Senthil, P., Vinodh, S., Singh, A.K.: Parametric optimisation of EDM on Al-Cu/TiB$_2$ in-situ metal matrix composites using TOPSIS method. Int. J. Mach. Mach. Mater. **16**(1), 80–94 (2014)

Development of an Expert System to Monitor Casting Defects in Foundries

D. Ananthapadmanaban and Amartya Karthik

Abstract Green sand molding is a commonly used casting technique for manufacturing steel castings. However, defects prevention and monitoring is an issue on which research is advancing continuously. The aim of this research work is to develop an expert system using C++. This system identifies the optimum input parameters, namely permeability, pouring temperature and green strength of the sand in order to give lower probability of defects. The defects used in this work are scabbing, sand fusion and blowholes. Experimental data from a foundry were collected for a period of 1 month with variations in the input parameters and analyzed for ranges of parameters in which defects are low. A rule-based expert system was written using CLIPS 2004, an expert system tool, wherein programming can be done using C++. The expert system so developed was used to predict the probability of occurrence of defects. Validation has to be done with more experimental work to fine-tune the expert system.

Keywords Expert systems · Casting defects · CLIPS 2004 software

1 Introduction

Expert systems have been used for the last 30–40 years to solve and diagnose complicated engineering problems. A common expert system is a knowledge-based system (KBS). In this system, intelligent inputs are provided by human beings to compute programs, thereby building a knowledge base. A KBS basically consists of three major components: the *knowledge base,* the *inference engine* and the *user interface.*

D. Ananthapadmanaban (✉) · A. Karthik
Department of Mechanical Engineering, SSN College of Engineering,
Kalavakkam 603110, India
e-mail: ananthapadmanaband@ssn.edu.in

A. Karthik
e-mail: amartyakartic@ssn.edu.in

The knowledge base contains the knowledge needed for the solution of a particular problem. Generally, some rules may be included in the program, heuristics may be included or problem-solving know-how may be incorporated. The knowledge, input in the knowledge base, is systematized in a form that can be understood by computer. Various techniques such as *production* or *IF-THEN* rules, *semantic nets* and *frames may be used.* The inference engine is the mechanism used by the KBS to use the knowledge and make inferences. It contains strategies and controls to apply the knowledge, which is input from the knowledge base. The user interface part enables interaction of the system with the user. It consists of screen displays, a consultation strategy and a module for explanation

Green sand molding has been used to manufacture castings, ranging from a few grams to a few tonnes. Defects like blowholes, shrinkage, scabbing and sand fusion occur in castings manufactured by green sand molding, if proper molding parameters are not selected and followed.

2 Literature Review

One of the first researchers to work on expert systems for defect prediction was Sudeesh Kannan et al. [1]. This team developed a knowledge-based expert system for defect identification in foundries in 1988. Clear-cut research on the types of defects occurring in castings and their remedies has been performed by Ian Kay et al. [2]. Casting defects have been analyzed by using computer simulations by Tapan Roy [3]. More recently, most of the available knowledge in experts systems and computer applications for defect identification have been compiled and integrated by Kluska Nawareka et al. [4]. Neural networks have been used for close to 30 years to solve complicated engineering problems. They have also been used to study casting defects and identify the conditions under which defects occur [5].

3 Development of an Expert System

One of the first attempts to explain the underlying principles of expert systems was done by Kaisler [6]. This was followed some years later by research on how to manage expert systems [7].

The following requirements in the development of knowledge-based expert systems (KBES) include:

- At least one human should provide expertise to develop the expert system. It is preferable to have a team of experts.
- The expert should be well experienced in his domain. He should have sound judgment.

- The expert must be able to articulate his problem-solving skills and apply it to the situation at hand.
- The domain should be clearly defined.
- An understanding of these systems must not involve much of conventional computer knowledge as the technology of software development to allow non-experts in informatics to apply the expert program.

3.1 Rule-Based Expert System

The most simple form of expert systems are the rule-based ones. Here, the rules are coded into the expert system. The definitions of rule-based system depend almost entirely on the expert or group of experts. Importance should be given to the fact that the system should mimic human reasoning as closely as possible knowledge is not set in a declarative, static way as a set of facts which are true, but are represented in terms of a set of rules that tells what action is to be taken or what conclusions can be drawn in a given situation.

A typical rule-based system has four basic components:

A list of rules or rule base: which is a specific type of knowledge base. The knowledge base stores all relevant information, data, rules, cases, and relationships used by the expert system.

Fuzzy logic can also be incorporated in rule-based systems as researched upon by Rai [8]. A software named ESWOLD has been created by Elbel et al. consisting of three modules. This software has been used for defect identification and prediction [9]. Another recent model where algorithms have been developed for modeling of castings has been published by Gaverieva [10].

An inference engine or semantic reason: infers information or takes action based on the interaction of input and the rule base. The interpreter executes a production system program by performing the following match-resolve-act cycle: The inference engine must find the right facts, interpretations and rules and assemble them correctly.

Match: This is the first phase. Here, the left-hand sides of all productions are matched against the contents of working memory. As a result a conflict set is obtained, which consists of subsets of all satisfied productions.

Conflict-resolution: During the second phase, a suitable production instantiation in the conflict set is chosen for execution.

Act: In this third phase, the actions of the production selected in the conflict-resolution phase are executed. Working memory may be affected by these actions. Now, it is returned to the first phase.

Temporary working memory: It is a temporary user interface, in other words, connection to the outside world through which input and output signals are received and sent.

3.2   Steps in Development

- Actual requirements are determined, knowledge is acquired, components of the system are constructed, and results are implemented.
- Knowledge acquisition is the most important element in the development of expert system. Domain experts are normally interviewed. There exist several methods to extract human knowledge. Cognitive work analysis (CWA) and the cognitive task analysis (CTA) provide frameworks to extract knowledge. Knowledge acquisition in our work was done by collecting data over a period of 1 month. Typical data collected is shown in Table 1.

The table mentioned above gives a sample of the data collected in the normal range of moisture, permeability and green strength for one particular day. Similar data has been collected over a period of one month, some of them showing the input values outside this range. All these values have been used to plot graphs shown in Figs. 1, 2, 3, 4 and 5, plotting defect probability versus moisture content and green compression strength. This has been discussed in the Results and Discussion section.

Table 1   Showing sample data collected at Hinduja Foundries correlating sand parameters with properties

Date	Time	Boxnumber	Jobnumber	Moisture	Permeability	Gstrength
Specification				3.0–3.3	110–140	18–22
31-Aug-16	7.40	5	105	3.20	126	18.7
31-Aug-16	8.25	36	105	3.15	128	19.1
31-Aug-16	9.10	82	105	3.26	134	18.3
31-Aug-16	9.50	14	113	3.17	126	19.2
31-Aug-16	10.35	6	150	3.23	128	18.7
31-Aug-16	11.25	32	150	3.27	134	18.1
31-Aug-16	12.10	19	1101	3.19	128	19.3
31-Aug-16	12.55	62	1101	3.24	128	18.5
31-Aug-16	13.30	18	131	3.20	126	19.2
31-Aug-16	14.15	20	105	3.16	134	18.4
31-Aug-16	15.00	100	105	3.23	128	18.7
31-Aug-16	16.10	16	160	3.15	126	18.8
31-Aug-16	16.50	31	105	3.20	128	18.6
31-Aug-16	17.35	66	105	3.26	126	18.4
01-Sep-16	0.20	39	105	3.24	128	18.4
01-Sep-16	1.05	6	115	3.19	126	18.8
01-Sep-16	1.40	38	115	3.27	134	18.5
01-Sep-16	2.15	68	115	3.22	128	18.9
01-Sep-16	3.45	107	115	3.24	126	18.7

Fig. 1 Shows probability of
blowholes with % increase in
moisture
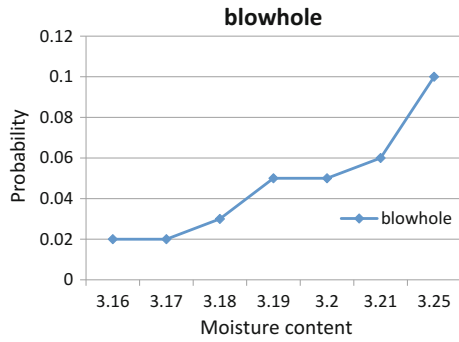
Fig. 2 Probabilty of defect
versus green compact strength
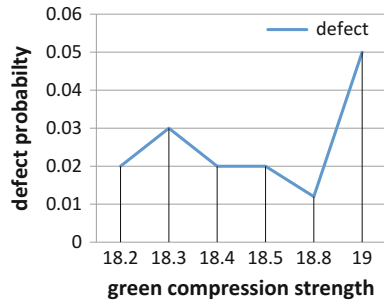
Fig. 3 Probability of sand
fusion versus compactness
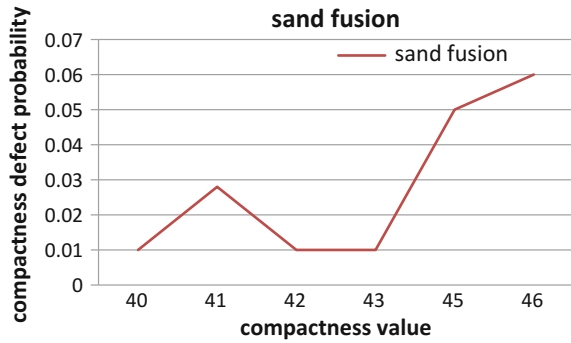
Fig. 4 Probability of fracture versus sand fusion compression strength
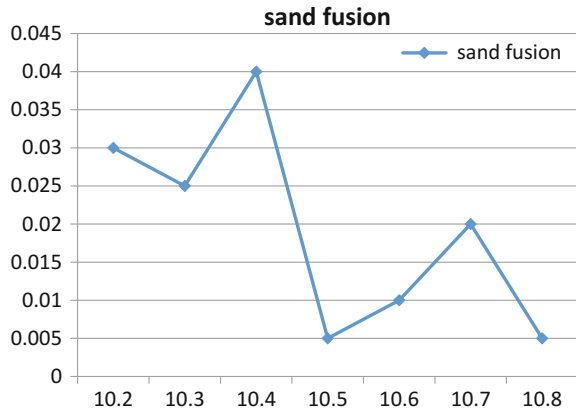
Fig. 5 Probability of scabbing versus green
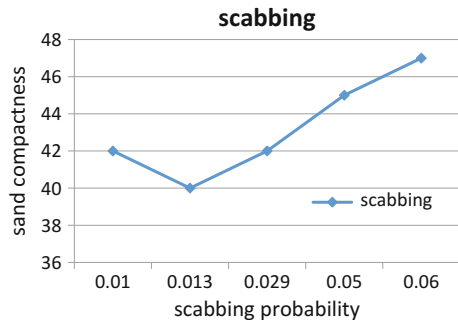
- CWA analyzes, designs and evaluates human computer interfaces. It identifies cognitive skills and mental demands.
- Shells are specialized software used in expert systems. These shells are equipped with an inference mechanism (backward chaining, forward chaining or both). They need knowledge to be entered according to a specified format.

3.3 Popular Expert System Shells

One of the most popular shells widely used throughout the government, industry, and academia is the CLIPS (CLIPS 2004). CLIPS is an expert system tool that provides a unique and full environment for the construction of rule- and/or object-based expert systems. CLIPS is a cohesive tool for handling rule-based, object-oriented and procedural type expert systems. CLIPS has been written in the C language. This provides for portability and speed.

4 Experimental Work

The data on various casting defects was collected from Hinduja foundries. Number, type of defect and the total number of defects per batch were also obtained. The various physical properties of the sand such as shear, friability, temperature moisture content were also obtained; all collected data was compiled into an excel sheet. Based on the literature survey as well as the data collected from the industry experts, the defects whose primary causes could be isolated were selected and the primary causes for the occurrence of these defects were determined. From the data collected on the number of defects of each type as well as the sand properties per each batch, graphs were plotted in order to determine how the sand properties change the occurrence of defects. Graphs were plotted to analyze how the various sand parameters affect the occurrence of the various defects. After the graphs were plotted, we determined the actual causes for each defect and how the variation in these sand properties actually affects the castings.

The next step is choosing of the expert system shell. The basic C++ shell was chosen due to its flexibility as well as its provision for object oriented programming as well as its simplicity. The next stage involves the setting up of the rules for the expert system to function. The knowledge base represents important information about the world. A knowledge base is similar to a public library, a database of related information about a particular subject. This knowledge system is constant and obtained from experts. The inference engine is an automated reasoning system that evaluates the current knowledge level, applies a set of rules. It then adds new knowledge into the knowledge base. The inference engine may also include abilities for explanation. This can explain the chain of reasoning to a user.

5 Results and Discussion

5.1 Variation of Defect Probability with Sand Properties

The above-mentioned graph shows the probability of defect occurring for different values of moisture content in the sand. From the graph, we observe that aside from sand with a very low moisture content the probability of blowholes occurring increases as the moisture keeps on increasing. However, at too high moisture level the probability of defect increases too; in this case, due to lack of shear strength of sand the probability of bad surface increases. At a range of values, between 3.19 and 3.22, the graph shows a steady state when there is no increase in the probability of the defect. There should be some moisture for proper defect-free castings, and this range could be the optimum moisture range where defects probability is stable and there is proper bonding of the sand; from this graph, we infer that the ideal range for the moisture values to ensure low probability of defects it must lie lower or equal to 3.17.

Figure 2 shows that defect probability is least when green compression strength is 18.8 N/m². At higher green compact strengths, the mold may be too rigid and may not have enough pores for the gases to escape. This may again lead to more defects. At too low green compact strengths, the sand may be too loosely packed and this may lead to defects. Hence, there is an optimum value of green compression strength which has been shown in Fig. 2.

Similarly, there is a range of compactness values between 42 and 43 units when defect probability is low. Again, it may be inferred that too compact sand may lead to more defects. Some amount of permeability in the sand is desirable to reduce defects.

Figure 4 shows that probability of fracture is lowest when sand fusion value is around 10.5. This seems to be the optimum value for lower defects. Similarly, when green compression strength is around 40 N/m², scabbing probability is lowest. Too high green compression strength increases scabbing probability. This may be because too high compression strength may make the surface of the sand very rough leading to scabbing at the surface of the castings. Too low sand compaction strength is obviously not desirable as some of the sand may crumble and get into the castings leading to defects.

5.2 Coding Defect Identification and Defect Prediction

The code consists of the option for the user to use the program for either defect identification or defect prediction. A switch case is used to determine user input. In this work, we have given data pertaining to defect identification only. In this work, only defect identification has been done. The initial part of the code is concerned with obtaining the input from the user inputs sand properties such as permeability, moisture content, compactness green compression strength as well as the pouring temperature, while there are several other chemical properties affecting the outcome of sand casting; this project focuses mainly on the physical properties. The input values are then stored, and various comparison operations are conducted on them.

The first stage of comparison involves the blowhole, or in hole defect, an if statement is used to compare the user input values to the optimum values for low probability of defect formation. If the input values are within the optimum value scale, then the statement low probability is returned but if the user inputs stray from the optimum values then the output high defect probability is returned and possible causes as well as any preventive methods are also provided. The 'goto' statement is then used to proceed to the next part of the code to check for the next defect.

If the input values are within the optimum value scale, then the statement low probability is returned, but if the user inputs stray from the optimum values then the output high defect probability is returned and possible causes as well as any preventive methods are also provided. The optimum conditions are also outputted to inform the user of them. The 'goto' statement is then used to then proceed to the next part of the code to check for the next defect.

6   Conclusions

Data collected over a period of one month from experimental work in a foundry were compiled. A rule-based expert system was written using CLIPS 2004 Software. This expert system gave the parameters under which defect-free castings could be obtained. The expert system was also able to identify under what conditions defects like blowholes, scab, etc., are obtained.

References

1. Sudesh, K., Prakash, G.R., Roshan, H.M.: Knowledge-based expert system for analysis of casting defects. AFS Trans. **96**, 178–192 (1998)
2. Kay, I., Nagel, M.: Its time to play-name that green sand casting defect. Mod. Cast. 29–32 (2001)
3. Roy, T.: Analysis of casting defects in foundry by computerised simulations (CAE)—a new approach along with some industrial case studies. In: Transactions of 61st Indian Foundry Congress, pp. 1–9 (2013)
4. Kluska-Nawarecka, S., et al.: Computer assisted integration of knowledge in the context of identification of the causes of defects in castings. Arch. Metall. Mater. **59**(2), 753–756 (2014)
5. Jančíková, Z.: Utilization of artificial intelligence elements for prediction of forge ingots defects. InActa Mechanica Slovaca, 13–15 1–A(2007)
6. Kaisler, S.: Expert systems: an overview. IEEE J. Oceanic Eng. **11**(4), 442–448 (1986)
7. Candlin, D.B., Wright, S.: Managing the introduction of expert systems. Int. J. Oper. Prod. Manag. **12**(1), 46–59 (1992)
8. Rai1, A., Ganguly, S.K.: Web-based expert system for some defect in sand castings. Int. J. Adv. Eng. Res. Stud. Jan–March (2015)
9. Elbel, T., Kralova, Y., Hampl, J.: Expert system for analysis of casting defects—ESVOD. Arch. Foundry Eng. **15**(1), 17–20 (2015)
10. Gavarieva, K.N., Simonova, L.A., Pankratov, D.L., Gavariev, R.V.: Development of expert systems for modeling of technological process of pressure casting on the basis of artificial intelligence. In: IOP Conference Series: Materials Science and Engineering, 240 (2017)

Influence of Design Parameters on Composite and Noncomposite Space Truss Structure Analysed Using ANSYS

P. Sangeetha, R. Senthil and P. Naveen Kumar

Abstract A space frame is a skeleton structural system assembled using linear elements so arranged that forces are transferred in a three-dimensional manner. Architects and engineers aim for new structural forms to accommodate large unobstructed areas. Space frames satisfy the objectives, and it provides lightness, economy, and speedy construction. Previous research investigation in the composite space truss, proved that using concrete slab acting compositely with the top chord member is to reduce the buckling of the compression chord members and also improve the overall behaviour of the space truss sturctures. The advantages of the composite space truss, gives confidence to use as floor system in the multistorey buildings. The composite space truss is influenced by various design parameters like cross-sectional area of the tubular member, support condition, module size and their depth, concrete strength and concrete slab thickness. The analysis of composite and noncomposite space truss as roof as well as floor for the building of size 30 m × 30 m was carried out using ANSYS software for varying design parameters. The overall maximum central deflection for the models was observed and compared with the codal provision. The load–deflection behaviour of the models was plotted, and the optimal solution for the noncomposite and composite space truss was arrived.

Keywords Composite space truss · Finite element analysis · Support condition Optimization

P. Sangeetha (✉)
Department of Civil Engineering, SSN College of Engineering, Chennai, India
e-mail: sangeethap@ssn.edu.in

R. Senthil
Division of Structural Engineering, CEG, Anna University, Chennai, India
e-mail: senthilr68@gmail.com

P. Naveen Kumar
Department of Structural Engineering, Anna University, Chennai, India
e-mail: navi.india93@gmail.com

1 Introduction

Space truss structures are used to cover assembly hall, toll plaza, airport, etc., as roof, and the major problem of the space truss structure is the buckling of the top chord compression members. To overcome this failure the concrete slab over the top chord member will act as area to take compressive load. Thus, the composite space truss can be used as floor slab in multistorey buildings as fast-track construction. The study on composite space truss with continuous top chord member with simple jointing method improves the composite action between the concrete slab and steel member and also concluded that composite space truss has higher strength and stiffness [1]. The experimental analysis to study the stability and ductility behaviour of the space roof system under eccentric and concentrate load was carried until collapse [2]. Nonlinear finite element programme for steel concrete composite structures has been developed, and comparison between the experimental and analytical results was made for RC slab and steel concrete composite structure [3]. A full-scale experiment for evaluating the ultimate load-carrying capacity of the hypar space truss was performed and compared with analytical behaviour [4]. The parametric study on the composite space structure was carried out using ANSYS and concluded that concrete slab enhanced the strength and stiffness of the top chord member [5]. The experimental and analytical study on the pin-jointed and rigid-jointed double-layer grid structures was done and concluded that in pin-jointed truss, outer bottom chord members were critical [6]. The dynamic behaviour of the long-span composite deck floor structure was investigated on a prototype composite space floor and concluded the use of passive control device to reduce the amplitude of the vibration [7]. The composite space truss without profile decking sheet was studied upto failure. The composite action between the space truss and concrete slab was achieved by using proposed steel bolt and flat plate as shear connector and compared with the analytical model developed using ANSYS [8]. The parametric study was carried out on the composite space truss against published experimental results. The study concentrated to know the stiffness and energy absorption capacity of the composite space truss by varying the parameters like slab thickness of the concrete slab, strength of concrete and module size of the space truss [9]. This paper describes the analytical behaviour of the space truss as roof and floor system for varying support condition, concrete slab thickness, cross-sectional area of the tubular member in order to arrive the optimal solution.

2 Analytical Study

2.1 Space Truss: Roof Structure

The space truss of size 30 m × 30 m × 2.121 m for varying support conditions was modelled using ANSYS workbench with single concentrated load at centre.
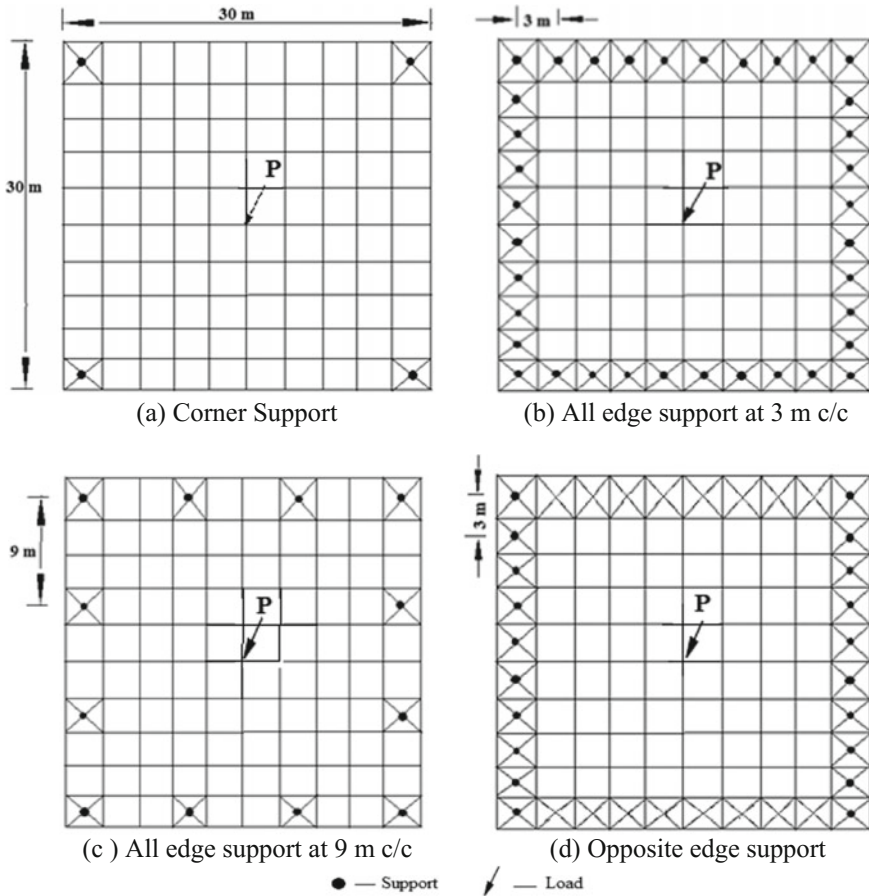
Fig. 1 Plan of the space truss with support condition

The double-layer grid configuration with the module of 3 m × 3 m was taken for both roof (noncomposite) and floor slab (composite). The boundary conditions of the space truss varied in the study are corner support (4-corner nodes), all-edge support at 3 m (all the nodes on four sides), all-edge support at 9 m (the nodes having centre to centre distance 9 m on all four sides) and opposite edge support (all nodes of opposite side). The floor slab was further analysed by varying the thickness of the slab and cross-sectional area of the tubular member. Figure 1a–d shows the plan of the 30 m × 30 m space truss with support condition. In the figure dark dots show the support at the nodes in the bottom chord members. The steel tubular structural sections for the members were considered as per IS 1161:1988. The cross-sectional area of the tubular member varied is 556, 641, 732, 788, 1070, 1110, 1230, 1550, 1730 and 1840 mm^2 to know the optimal thickness and cross-sectional area to meet the serviceability criteria.

2.2 Space Truss: Floor Slab

The space truss is normally used to cover large area as roof without the intermediate column. The space truss with concrete slab at the top acts as a floor slab, so the composite space truss can be used in the multistorey building as fast-track construction. The composite action in the space truss can be achieved with proper shear transfer mechanics. The study has been carried out analytically using ANSYS 16.0 for different support conditions and varying concrete slab thickness of the composite space truss. The nonlinear analysis of space truss model was carried out with single concentrated load at centre. The same four support conditions adopted in the roof system as per Fig. 1a–d were also used as boundary condition for modelling the composite space truss. The analysis of the composite space truss of size 30 m × 30 m was carried out for varying the thickness of the concrete slab from 40 to 120 mm (40, 50, 60, 70, 80, 90, 100, 110 and 120 mm). The compressive strength of concrete used in the study was 25 N/mm^2.

3 Results and Discussion

3.1 Effect of Support Condition

Figures 2a–d and 3a–d show the deformed shape of the composite and noncomposite space truss for varying support condition. The deflection at the centre of the space truss with corner supports is more, compared to other types of support condition irrespective of the truss-type composite or noncomposite. Though the space truss structures are used for column-free structures, all the support condition holds good for maximum deflection of 77.39 mm and this value is within the safe permissible limit as per code IS 11384 [10] (L/360 = 83.33 mm). Table 1 gives the maximum deflection of the composite space truss for varying support condition. The red zone throughout the images accounts for the deformation of the specimen. The variation of the deformation is having similar pattern for first three types of support condition. The maximum deflection of 77.39 mm was observed which is maximum for the space truss with corner support condition when compared to all other types of support condition. Figures 2d and 3d show different patterns of the deformed shape since it has been supported in the opposite edge. The deflection moves towards the unsupported edges of noncomposite and noncomposite space truss. Figures 4a–d and 5a–d show the load–deflection behaviour of the noncomposite and composite space for varying cross-sectional area of the tubular member and support condition. The linear behaviour of the specimens was studied from the analysis using ANSYS. From load–deflection curve, it was found the behaviour is the same and it is also observed that the increase in the cross-sectional area of the tubular members of the space truss makes the model stiffer. The space truss with all-edge support condition was stiffer than other support conditions irrespective of the cross-sectional area of tubular member.

(a) Corner Support

(b) All edge support at 3 m c/c

(c) All edge support at 9 m c/c

(d) Opposite edge support
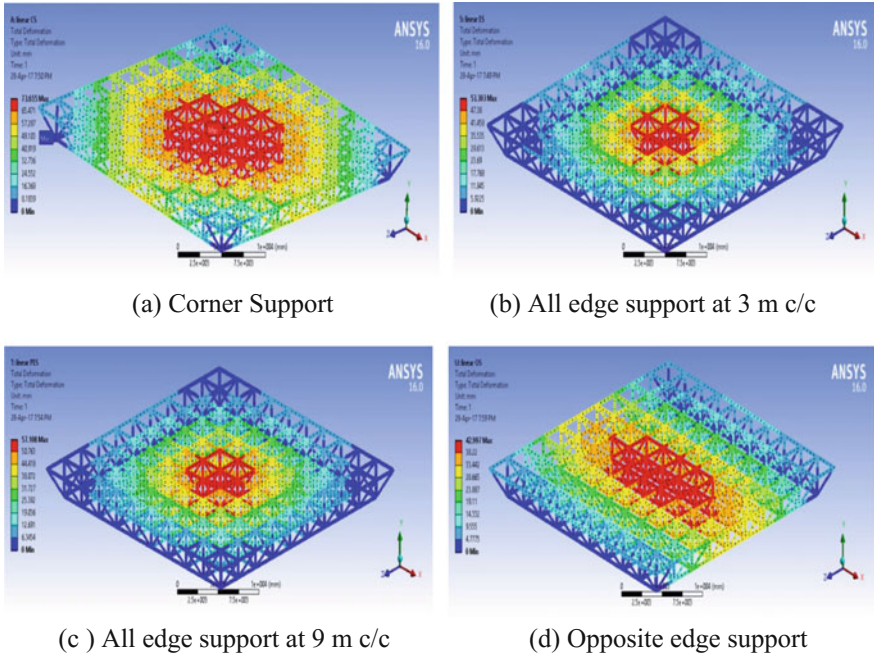
Fig. 2 Deformed shape of the noncomposite space truss (roof frame) for different support conditions

3.2 Effect of Slab Thickness

Figure 6 shows the plot between the maximum central deflection and thickness of the concrete slab for different support conditions. The deflection observed by the composite space truss with four-corner support, deflects more when compared to other support conditions. The percentage increase in the deflection of corner-supported composite space truss is 58, 36 and 35% when compared with all-edge support at 3 m c/c, all-edge support at 9 m c/c and opposite edge-supported space truss, respectively. The composite space truss with edge support 3 m c/c and 9 m c/c behaves similar irrespective of the concrete slab thickness. The opposite edge-supported composite space truss is stiffer than the other types of support condition. Table 2 gives the maximum deflection observed for varying concrete slab thickness and support condition.

(a) Corner Support

(b) All edge support at 3 m c/c

(c) All edge support at 9 m c/c

(d) Opposite edge support
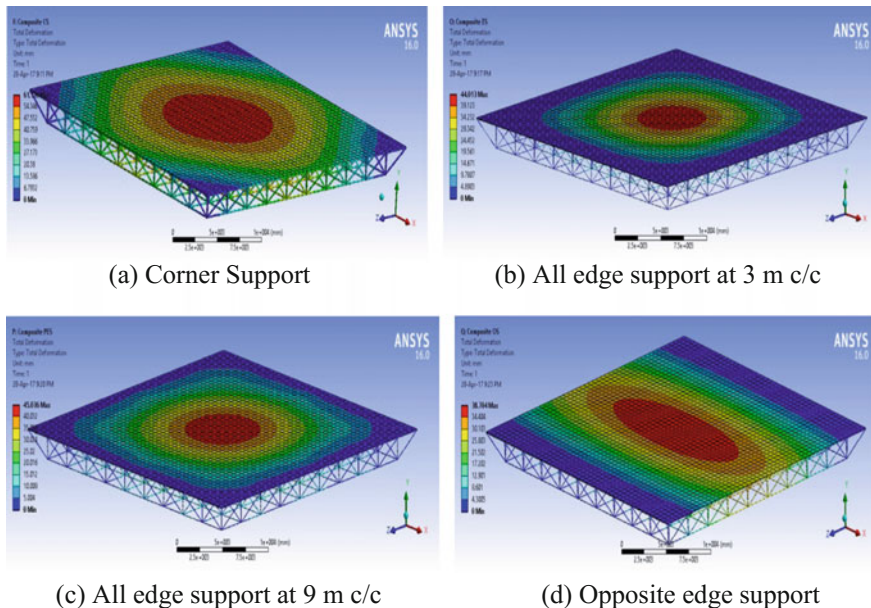
Fig. 3 Deformed shape of the composite space truss (floor frame) for different support conditions

Table 1 Maximum deflection of composite space truss for varying support condition and cross-sectional area of the tubular member

Support condition	Cross-sectional area of the tubular member (mm^2)	Maximum central deflection (mm)
Corner support condition	1550	**77.39**
	1730	73.65
	1840	67.54
All-edge support at 3 m c/c	556	**67.13**
	641	52.30
	732	45.79
All-edge support at 9 m c/c	641	**64.14**
	732	62.98
	788	62.01
Opposite edge support	1070	**66.55**
	1110	51.59
	1230	43.00

Bold values gives the Maximum deflection

(a) Corner Support

(b) All edge support at 3 m c/c

(c) All edge support at 9 m c/c

(d) Opposite edge support
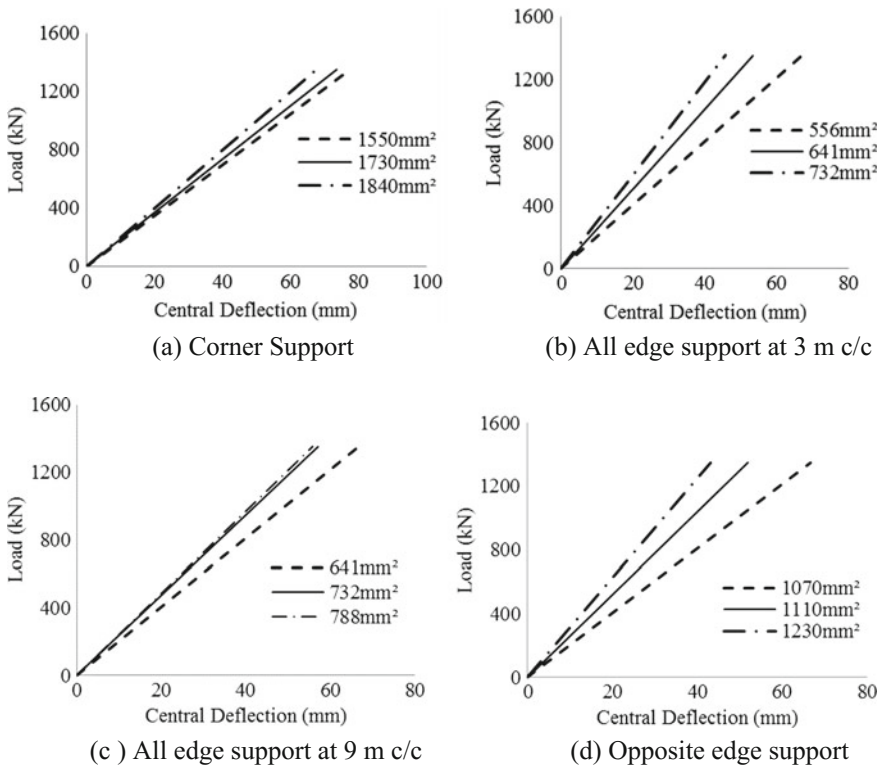
Fig. 4 Load–deflection curve of the noncomposite space truss (roof frame) for varying cross-sectional area of the tubular member

3.3 Effect of Type of Truss

The nonlinear analysis of the composite and noncomposite space of size 30 m 30 m was carried out using finite element software ANSYS. Figure 7a–d shows the load—central deflection of the composite and noncomposite space truss for varying support condition. The behaviour observed from the space truss with corner support and all-edge support at 3 m c/c was uniform. The percentage decrease in the deflection is 60% for converting space truss into composite space truss. Normally, space truss is used as roof for covering large area without intermediate columns, and the same space truss with concrete slab over it can be used as floor for large area. By providing concrete slab over the space truss, the buckling problem of the top chord members of the space truss can be overcome.

(a) Corner Support

(b) All edge support at 3 m c/c

(c) All edge support at 9 m c/c

(d) Opposite edge support
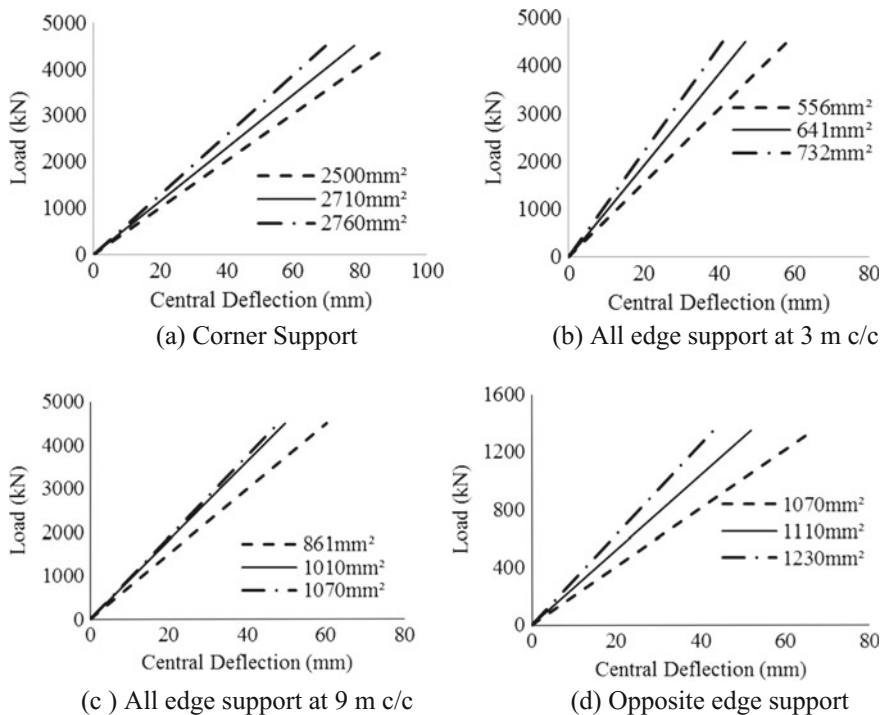
Fig. 5 Load–deflection curve of the composite space truss (floor frame) for varying cross-sectional area of the tubular member

Fig. 6 Maximum deflection versus concrete slab thickness for varying support condition of the composite space truss
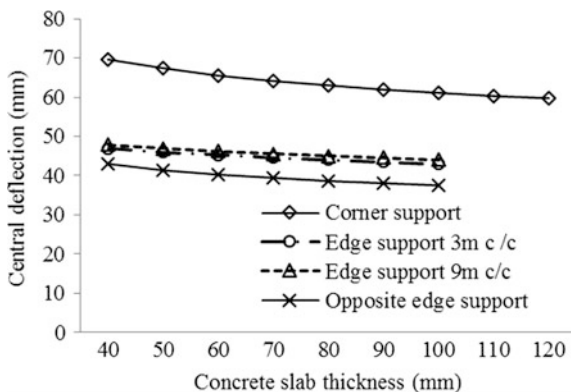
Table 2 Maximum central deflection of composite space frame (floor frame) for varying concrete slab thickness

Concrete slab thickness (mm)	Maximum central deflection (mm)			
	Corner support condition	All-edge support at 3 m c/c	All-edge support at 9 m c/c	Opposite edge support
40	69.694	46.922	47.911	42.996
50	67.304	45.993	46.959	41.451
60	65.533	**45.253**	46.218	40.324
70	64.138	44.609	**45.594**	39.439
80	62.988	44.013	45.036	**38.704**
90	62.005	43.435	44.514	38.066
100	**61.139**	42.859	44.014	37.491
110	60.357	–	–	–
120	59.637	–	–	–

(a) Corner Support

(b) All edge support at 3 m c/c

(c) All edge support at 9 m c/c

(d) Opposite edge support
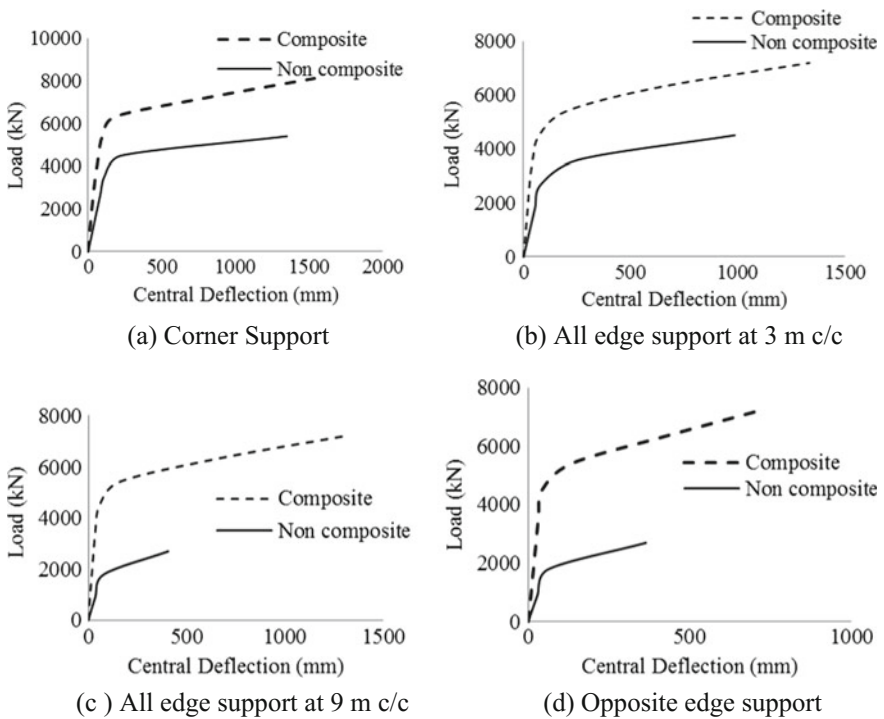
Fig. 7 Load–deflection curve of the composite and noncomposite space frame for different support conditions
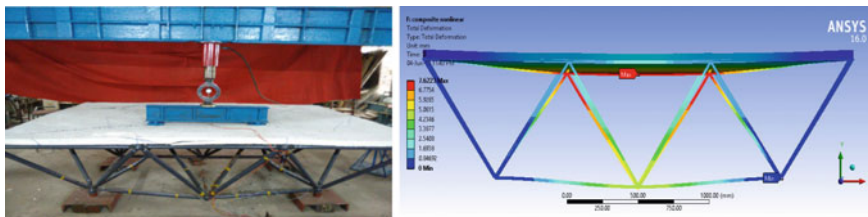
Fig. 8 Deformed shape of the composite space truss

3.4 Validation of Study

The published experimental behaviour of the composite space truss [8] was taken to validate the analytical results. The composite space truss of 3 m × 2 m × 0.71 m with 50-mm concrete slab thickness was tested to find the ultimate load-carrying capacity. The composite action was achieved using steel flat and bolts as shear connector. From the experimental investigation, it was observed that the specimen fails with the maximum central deflection of 7.2 mm for the ultimate load of 420 kN and also failed by the formation of clear yield line pattern on the slab. The same composite space truss was modelled and analysed using ANSYS 16.0 and observed the maximum deflection as 7.6 mm. The percentage difference in the experimental and analytical results in terms of deflection is 4%. The deformed shape of the experimental and analytical model of the composite space truss is shown in Fig. 8.

4 Conclusions

(1) The load-carrying capacity of the composite space truss was improved by 60% compared to noncomposite space truss.
(2) The all-edge and partially edge support conditions are proved to be economical since the 60% reduction in the weight of tubular member when compared to corner-supported space truss system. In this support condition, a number of columns on the periphery of the structure get increased.
(3) The members of the space truss are heavier in the corner-supported space truss and can be used for short span. It can also be overcome by providing members above the four-corner support with increased diameter and thickness.
(4) The increase in the slab thickness of the composite space truss increases the strength and stiffness of the space truss structure.
(5) Opposite edge-supported space truss is provided only when openings on two opposite edges are required for architectural purposes.
(6) The maximum deflection of the composite space truss obtained from the analytical study using ANSYS was compared with the published experimental deflection and percentage difference between them is 4%.

References

1. El-sheikh, A., McConnel, R.E.: Experimental study on behaviour of composite space trusses. J. Struct. Eng. **119**, 747–766 (1993)
2. Fulop, A., Ivanyi, M.: Experimentally analysed stability and ductility behaviour of a space-truss roof system. Thin Walled Struct. **42**, 309–320 (2004)
3. Sebastian, W.M., McConnel, R.E.: Nonlinear FE analysis of steel concrete composite structures. J. Struct. Eng. **126**, 662–674 (2000)
4. Kim, J.W., Kim, J.J., Rhew, H.J.: Analysis and experiment for the formation and ultimate load testing of a Hypar space truss. J. Constr. Steel Res. **62**, 189–193 (2006)
5. Lakshmikandhan, K.N., Senthil, R., Arul Jayachandran, S., Sivakumar, P., Ravichandran, R.: Parametric studies on the behaviour of steel and composite space structures. Int. J. Space Struct. **25**, 169–183 (2010)
6. Gupta, L.M., Harde, P.R.: Nonlinear analysis of double layer grid structures. J. Struct. Eng. **38**, 230–237 (2011)
7. Wendell, W.D., Battista, R.C.: Control of vibrations induced by people walking on large span composite floor decks. Eng. Struct. **33**, 2485–2494 (2011)
8. Sangeetha, P., Senthil, R.: A study on ultimate behaviour of composite space trusses. KSCE J. Civil Eng. **21**, 950–954 (2017)
9. Sangeetha, P.: Parametric study on the stiffness and energy absorption capacity of composite space truss. Int. J. Adv. Appl. Sci. **4**, 1–5 (2017)
10. IS 11384—1985.: Code of practice for composite construction in structural steel and concrete

Improve the Wear Property of En19 Steel by Boronizing Process

D. Kumaravel and K. Arunkumar

Abstract This project deals with improving the wear property of En19 steel by boronizing process. En19 steel is used in industrial applications such as gear and shaft manufacturing. It is often selected for high-strength application. Due to its less wear resistance property, En19 steel is not preferred for certain applications. In this project, boronizing by paste method was selected to increase the wear property of En19 steel. Boronizing is a surface modification technique used to enhance the hardness of a metal. Wear studies of the coated specimen were conducted as per the standards. The pin-on-disc tribometer with its combined computer control and Tribo-X software was used to rank the wear property of material.

Keywords Wear · Boronizing · En19 steel · Pin-on-disc · Muffle furnace

1 Introduction

Steel has high strength which is used for industrial applications such as automobile parts and oil pipelines. Steel materials are often affected by wear due to shear stress acting on the surface, and hence, the special treatment is needed to decrease the wear. If the metal is hardened using normal process, then it becomes brittle. Hence, the surface hardening process was preferred to improve the hardness of the surface. In surface hardening process, metal is packed along with substance having rich content of carbon and applies heat for required time period. This heat treatment causes the penetration of carbon into metal surface. Due to this process, metal surface gets hardened. Boronizing is a surface hardening process which helps to enhance the wear resistance using boron atom. In this method, metal is placed inside the boriding mixture at the temperature of 900 °C [1–3]. Penetration of boron

D. Kumaravel (✉) · K. Arunkumar
Department of Mechanical Engineering, Academy of Maritime Education
and Training, Chennai, India
e-mail: kevinkumaravel@gmail.com

atom into metal depends on temperature. In this experiment, En19 steel was taken as a base metal since the application is more. Though it is used for many industrial process, due to low wear resistance property En19 is not preferred for certain component [4–7]. In order to improve the surface hardness of En19 steel, it is subjected to boronizing process.

2 Material (En19 Steel)

Steel is a ferrous metal having combination of iron, carbon and various elements. Steel has a carbon content ranging from 0.002 to 2.14%. Strength and ductility property of steel is more when compared with other metals. It is recyclable, and the property can be modified by the addition of other elements. The ductility of steel can be enhanced by reducing the sulphur, and toughness of steel can be enhanced by the addition of nickel. Heat treatment is also utilized to modify the property of steel [8]. Various steels are produced according to the required property and application. Hardness of pure steel is lesser than copper, and its hardness is improved by adding carbon. En19 is an alloy steel having 0.45% of carbon with good resistance to shock and ductility property. En19 steel is generally used for the production of gears and pinions. It has a yield stress of 700 N/mm^2 and hardness of 302 HB. Table 1 gives the mechanical property of En19 steel.

3 Experimentation

3.1 Boronizing Process on En19 Steel

Boronizing is the method of enhancing the hardness of metal in which the boron atom gets diffused into the metal to prevent the surface from wear. Borides can enhance the wear resistance and hardness of material [9]. As compared with other hardening process, it shows better improvement in wear property. In this experiment the boride in powder form was taken and it was made as paste by adding required quantity of water. After applying the paste over the material, it was subjected to heat treatment process [10–15]. Figure 1 shows the En19 material after

Table 1 Mechanical properties of En19 steel		
Max stress	850–1000 N/mm^2
Yield stress	700 N/mm^2
Proof stress	680 N/mm^2
Elongation	9%
Impact value	55 J
Hardness	248–302 HB

Fig. 1 Boronized En19 steel

Fig. 2 SEM image of boronized En19 steel
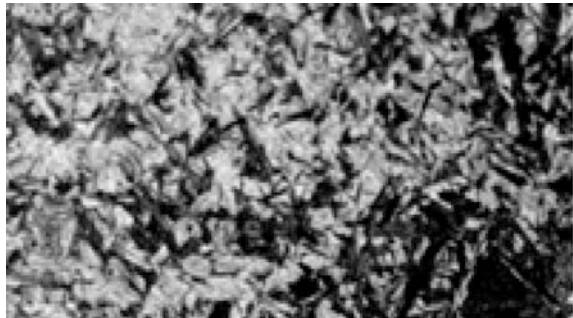
applying the boride paste. Boronizing process was done at the temperature around 1100 ° C. Figure 2 shows the SEM image of boronized steel which shows the penetration of boron particle into the steel material.

3.2 Heat Treatment Process

Muffle furnace is one type of oven for high-temperature heat treatment process used to modify the property of material. It is often used to do the research activities on various materials. In aerospace industries flame retardancy test is performed by muffle furnace at high temperature. In this equipment, heat is produced by coil and it is prevented by insulating material. Thermocouple sensor is used to monitor the temperature of furnace. If the temperature exceeds the required level, sensor will control the current passing to the coil and maintain the constant temperature. Compared with other furnace, it is safe and no combustion will occur during heat treatment process. The muffle furnace used for En19 heat treatment is shown in Fig. 3. It can grasp such high temperatures that are capable of making changes in

Fig. 3 Muffle furnace

the materials at the molecular level. After applying the boride paste over the En19 steel, it was kept in the muffle furnace to do heat treatment process [16, 17]. Due to high temperature, boride got diffused into steel and made it as highly resistance to wear.

4 Testing and Result

4.1 Pin-on-Disc Testing

Pin-on-disc is a method used to find the wear property of metal in which pin material is made to move against the rotating disc. This method is often preferred for ferrous material. Before start experiment make sure that the pin surface which cause wear on the disc should be flat. From the coefficient of friction, wear property of metal can be analysed. It is used to find the wear property of En19 steel subjected to boronizing process. Figure 3 shows the pin-on-disc apparatus for wear testing. In this method En19 steel was used as material for both pin and disc. During testing process, En19 disc was made to shear on the surface of En19 pin and loss of weight due to wear was calculated. By varying the load, speed and wear track diameter, the reading was calculated. From Table 2 it is observed that the loss of weight due to wear is less in boronized material [18, 19]. Using Tribo-X software, the material loss occurred by wear is measured and represented in Fig. 7. Figure 4 shows the graphical representation of wear property during testing of En19 steel using tribometer. Boronized En19 disc and pin after wear test are shown in Figs. 5 and 6 respectively.

Table 2 Hardened pin versus boronized disc

S. No.	Combination	Load (kg)	Speed (rpm)	Distance (m)	Weight of the En19 disc before testing D1 (gm)	Weight of the En19 disc after testing D2 (gm)	Total weight loss D1 − D2 (gm)	Weight of the En19 pin before testing P1 (gm)	Weight of the En19 pin after testing P2 (gm)	Total weight loss P1 − P2 (gm)
1	Hardened pin versus boronized disc	2	300	500	140.567	140.551	0.016	8.271	8.236	0.035
		2	600	500	148.358	148.343	0.015	8.308	8.274	0.034
		5	300	500	149.412	149.405	0.007	8.148	8.117	0.031
		5	600	500	147.229	147.226	0.003	8.260	8.227	0.033

Fig. 4 Pin-on-disc testing machine

Fig. 5 Boronized En19 disc after wear test

Fig. 6 Boronized En19 pin after wear test
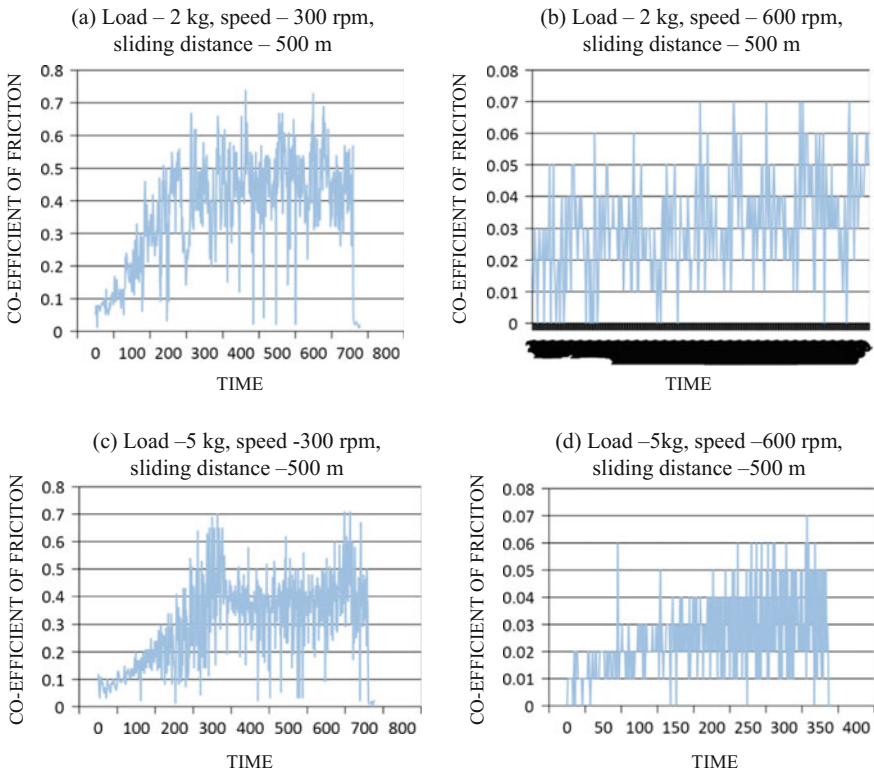
Fig. 7 Graph of friction versus time

5   Conclusion

In this experiment, En19 steel was exposed to boronizing process in order to increase the wear property. Boronizing by paste method was done on En19 steel, and its property was tested by pin-on-disc method. By using the tribometer, loss of material was analysed and wear property was measured. Tribo-X software is used to show the wear property in graphical method. From the experiment it is observed that material subjected to boronizing process seems to be enhanced in wear property. Hence, it is resolved that wear resistance property of En19 steel can be enriched by boronizing process.

References

1. Zou, C., Chen, Z.: Study of enhanced dry sliding wear behavior and mechanical properties of Cu-TiB$_2$ composites fabricated by in situ casting process. Wear **392**, 118–125 (2017)
2. Li, H., Lu, S.: Improving the wear properties of AZ31 magnesium alloy under vacuum low-temperature condition by plasma electrolytic oxidation coating. Acta Astronaut. **116**, 126–131 (2015)
3. Peng, J., Dong, H.: Improving the mechanical properties of tantalum carbide particle-reinforced iron-based composite by varying the TaC contents. J. Alloy. Compd. **726**, 896–905 (2017)
4. Nimura, K., Sugawara, T.: Surface modification of aluminum alloy to improve fretting wear properties. Tribol. Int. **93**, 702–708 (2016)
5. Gunda, R.K., Narala, S.K.R.: Evaluation of friction and wear characteristics of electrostatic solid lubricant at different sliding conditions. Surf. Coat. Technol. **332**, 341–350
6. Ochieze, B.Q., Nwobi-Okoye, C.C.: Experimental study of the effect of wear parameters on the wear behavior of A356 alloy/cow horn particulate composites. Def. Technol. (2017)
7. Abbasi, E., Luo, Q.: Wear mechanisms of NiCrVMo-steel and CrB-steel scrap shear blades. Wear **398–399**, 29–40 (2017)
8. Vikas, Shashikant: Effect and optimization of machine process parameters on MRR for EN19 & EN41 materials using Taguchi. Procedia Technol. **14**, 204–210 (2014)
9. Mu, D., Shen, B.-L.: Mechanical and dry-sliding wear properties of boronized pure cobalt using boronizing powders with SiC as diluent. Surf. Coat. Technol. **236**, 102–106 (2013)
10. Lei, J., Shi, C.: Enhanced corrosion and wear resistance properties of carbon fiber reinforced Ni-based composite coating by laser cladding. Surf. Coat. Technol. **334**, 274–285 (2018)
11. Li, Y., He, Y.: Wear and corrosion properties of AISI 420 martensitic stainless steel treated by active screen plasma nitriding. Surf. Coat. Technol. **329**, 184–192 (2017)
12. Wang, G., Gu, K.: Improving the wear resistance of as-sprayed WC coating by deep cryogenic treatment. Mater. Lett. **185**, 363–365 (2016)
13. Chen, Z.-K., Zhou, T.: Improved fatigue wear resistance of gray cast iron by localized laser carburizing. Mater. Sci. Eng. **644**, 1–9 (2015)
14. Yang, Q.: Wear resistance and solid lubricity of molybdenum-containing nitride coatings deposited by cathodic arc evaporation. Surf. Coat. Technol. **332**, 283–295 (2017)
15. Kommer, M., Sube, T.: Enhanced wear resistance of molybdenum nitride coatings deposited by high power impulse magnetron sputtering by using micropatterned surfaces. Surf. Coat. Technol. **333**, 1–12 (2017)
16. Lee, R.J.: Impact of muffle furnace preparation on the results of crystalline silica analysis. Regul. Toxicol. Pharmacol. **80**, 164–172 (2016)

17. Dirk, C.H.: Efficiency improvement for sulfated ash determination by usage of a microwave muffle furnace. J. Pharm. Biomed. Anal. **43**, 1881–1884 (2007)
18. Leonardi, M., Menapace, C.: Pin-on-disc investigation on copper-free friction materials dry sliding against cast iron. Tribol. Int. (2017); Bortoleto, E.M., Rovani, A.C.: Experimental and numerical analysis of dry contact in the pin on disc test. Wear **301**, 19–26 (2013)
19. Yang, L.J.: Pin-on-disc wear testing of tungsten carbide with a new moving pin technique. Wear **225–229**, 557–562 (1999)

Reduction of Wrinkling Defect in Deep Drawing Process

D. Kumaravel and K. Venkatesh

Abstract The aim of this experiment is to produce defectless component in deep drawing process and also to increase the quality of finished product. This process is to convert sheet metal into cup and cylindrical component. As the depth of the component is more as compared to diameter, this process is named as deep drawing. During this process, the sheet metal was cut into circular shape and kept on the die. If the die moves against the punch, sheet metal gets compressed and forms a required shape. Hydraulic press was used in this experiment to operate the punch and die set-up. Due to improper clearance and punch force, defect was occurred in drawing components. Most common defects occurred during this process are wrinkle and tear. In this experiment both steel and copper were taken as a base material and deep drawing process was finished with different parameters and defect was analysed.

Keywords Deep drawing · Wrinkling defect · Sheet metal · Drawing punch Drawing die

1 Introduction

Deep drawing is the sheet metal process used for making the required shapes which are not able to done by other machining process. If the depth of component is more, it is a suitable method to prepare that component. Complex shapes are also produced using deep drawing process. Hydraulic and mechanical press is used as an actuating system, but hydraulic press is preferred often due to smooth machining. In this experiment, 20-tonnage deep drawing hydraulic press was used to draw a sheet metal of 1 mm thickness to produce a cup of diameter 50 mm. At first, sheet metal was cut into the required shape and kept on the die. Punch is fixed on the top of

D. Kumaravel (✉) · K. Venkatesh
Department of Mechanical Engineering, Academy of Maritime Education
and Training, Chennai, India
e-mail: kevinkumaravel@gmail.com

machine which gives compressive force on the sheet metal. Due to high com-
pressive force, the sheet metal was deformed into the shape of die [1–3]. During this
process, if the force applied to the sheet metal is more, the wrinkling defect will
occur in the finished component. It was found that wrinkling occurs due to improper
punching speed also. Hence, to minimize the defect and enhance the product quality
[4, 5], deep drawing was done with different parameters and the suitable parameter
was found for drawing process.

2 Material

2.1 Base Material

In this experiment, copper and deep drawing steel were taken as a work material.
Copper is mainly used in the production of important alloys like bronze and brass. It
is a ductile metal with very high thermal and electrical conductivity [6–8]. Copper
has good corrosive property, and it is used as spark plug and electrical wires. Deep
drawing steel is a low-carbon-grade steel which has more drawability and ductility
as compared with commercial quality, and it is right for producing deep drawn
parts. It is mainly used for the applications such as roofs and doors. This material
has more ductility, and it is used often for drawing process [9]. At first, the sheet
metal of 1 mm thickness is cut into the dimension 100×100 mm and then made
as circular of diameter 90 mm as shown in Fig. 1.

2.2 Deep Drawing Die

In this experiment, mild steel was used as a die material which is shown in Fig. 2.
Drawing die should be designed such that the metal has to flow freely on the
circumference of die during drawing process. Metal begins to flow plastically by
draw ring and gets compressed on the outer side. If the radius of draw ring is large,

Fig. 1 Sheet metal for deep
drawing
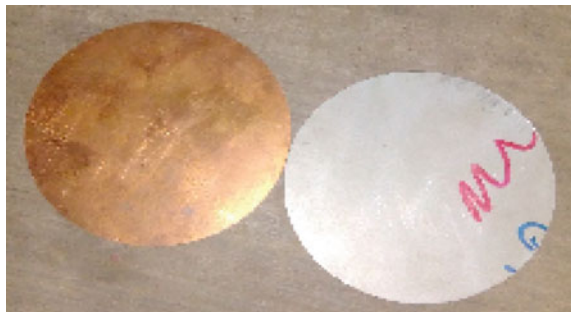
Fig. 2 Deep drawing die

then it leads to wrinkling defect. If the draw ring radius is sharp, then it leads to erring defect. Hence, the selection of suitable die is important in deep drawing process [10, 11].

2.3 Deep Drawing Punch

Deep drawing punch is made of mild steel, and it is used to compress the copper sheet into the die opening to form required shape which is shown in Fig. 3. Sharp radius of the punch will cause tearing defect during drawing. Hence, the sharp corner has to be avoided in drawing punch (Fig. 3).

Fig. 3 Deep drawing punch

3 Experimentation

Deep drawing process was finished with the help of hydraulic press as shown in
Fig. 4 which controls the operation of die and punch set-up. Die and punch were
arranged as shown in Fig. 5 such that the movement of punch to the die opening
makes the metal to flow freely and should have proper clearance [12, 13]. In deep
drawing process, the clearance among the die and punch should be larger than the
thickness of sheet metal. Tearing defect will occur when the clearance is lesser than
sheet metal thickness. Experimental detail of deep drawing process was given in
table 1. To avoid the tearing defect, 2 mm clearance was made between die and
punch. At first, the sheet metal of 1 mm thickness was made into circular shape of
diameter 90 mm and kept on the die cavity of inner diameter 105 mm. During this
process, the pressure of 500 kN/mm^2 was applied by the punch on the sheet metal.
If the punch moves towards the die cavity, workpiece gets compressed and

Table 1 Experimental detail

Die size and material	280 × 280 mm (mild steel)
Young modulus of elasticity	320 GPa
Materials used	Copper, deep drawing steel
Sheet metal thickness	1 mm
Cup diameter	50 mm
Blank size	Ø90 mm
Part draw height	20 mm
Machine capacity	20 tonnage

Fig. 4 Deep drawing machine

Fig. 5 Deep drawing fixture

converted into required shape. Cylindrical cup of diameter 50 mm and height 42.5 mm was made, and defect was analysed. In this experiment, four samples from both copper and steel were taken and deep drawing process was done with different parameters (Table 1; Figs. 4 and 5).

4 Result

Sheet metal fixed on the blank holder and deep drawing process was done with a force of 10 tonnage at 250 rpm. During this process the sheet metal got teared due to high speed. Second sheet metal was subjected to same force but reduced the speed to 225 rpm. In this process, cup-shaped component got more wrinkle defect. Third sheet which was subjected to 15 tonnage force at 210 rpm shows less wrinkle defect. Experiment is repeated with different parameters, and finally the defectless component was produced with the force of 20 tonnage at 200 rpm speed. Final product of deep drawing obtainted by various parameter for both copper and steel are shown in Figs. 6 and 7 respectively. Defect was analysed in both copper and deep drawing steel materials, and it is shown in Tables 2 and 3, respectively (Figs. 6 and 7).

Table 2 Result of copper sheet after deep drawing

Material (copper)	Force (tonnage)	Speed (m/min)	Clearance (mm)	Effect
Cu-1	10	250	2	Tearing
Cu-2	10	225	2	Wrinkle (more)
Cu-3	15	210	2	Wrinkle (less)
Cu-4	20	200	2	Safe part

Table 3 Result of steel sheet after deep drawing

Material (deep drawing steel)	Force (tonnage)	Speed (m/min)	Clearance (mm)	Effect
DDS-1	10	250	2	Tearing
DDS-2	10	225	2	Wrinkle (more)
DDS-3	15	210	2	Wrinkle (less)
DDS-4	20	200	2	Safe part
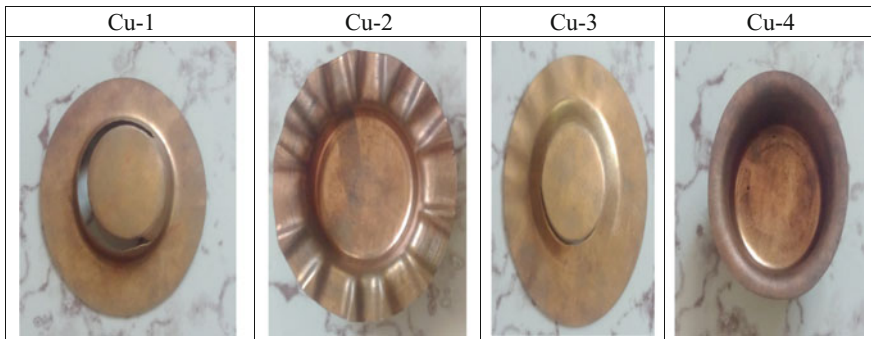
Fig. 6 Defect occurred on copper sheet
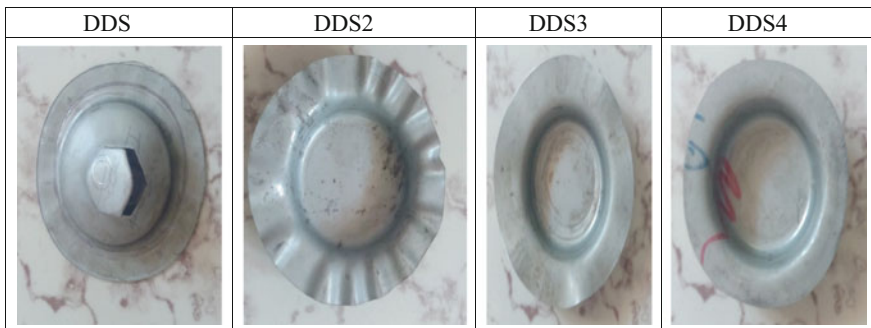
Fig. 7 Defect occurred on steel sheet

5 Conclusion

Deep drawing process was done on copper and drawing steel with different speed and force conditions, and the results were tabulated. From the experiment it is observed that with 10 tonnage of force at 250 rpm, sheet metal undergone tearing and wrinkling defect. After increasing the force to 20 tonnage and reducing the speed to 200 rpm, the defect got reduced. For deep drawing of 1 mm thickness of sheet metal, the force of 20 tonnage and speed of 200 rpm are suitable. By providing suitable parameter in deep drawing process, wrinkling defect can be reduced and obtained smooth surface finish.

References

1. Barthau, M.: New approach on controlling strain distribution manufactured in sheet metal components during deep drawing process. Procedia Eng. **207**, 66–71 (2017)
2. Zhang, L., Liu, H.: Numerical simulation and analysis of hydro mechanical deep drawing process for half-three-way tube. Procedia Eng. **174**, 524–529 (2017)
3. Lai, Z., Cao, Q.: Investigation on plastic deformation behavior of sheet workpiece during radial Lorentz force augmented deep drawing process. J. Mater. Process. Technol. **245**, 193–206 (2017)
4. Tropp, M., Tomasikova, M.: Concept of deep drawing mechatronic system working in extreme conditions. Procedia Eng. **192**, 893–898 (2017)
5. Long, A.: Forming methodology and mechanism of a novel sheet metal forming technology—electromagnetic superposed forming. Int. J. Solids Struct. (2017)
6. Lehtinen, P., Väisänen, T.: The effect of local heating by laser irradiation for aluminum, deep drawing steel and copper sheets in incremental sheet forming. Phys. Procedia **78**, 312–319 (2015)
7. Kurumada, A., Itoh, G.: Change of hardness of copper sheet by splitting process. Procedia Eng. **81**, 861–866 (2014)
8. Fu, M.W., Yang, B.: Experimental and simulation studies of micro blanking and deep drawing compound process using copper sheet. J. Mater. Process. Technol. **213**, 101–110 (2013)
9. Pratoori, R., Maddukuri, T.S.: Tensile testing of ultra-fine grained extra deep drawing steel sheets. Mater. Today **4**, 590–595 (2017)
10. Choubey, A.K., Agnihotri, G.: Analysis of die angle in deep drawing process using FEM. Mater. Today **4**, 2511–2515 (2017)
11. Lowrie, J., Ngaile, G.: Analytical modeling of hydrodynamic lubrication in a multiple-reduction drawing die. Procedia. Manuf **5**, 707–723 (2016)
12. Hassan, M., Hezam, L.: Deep drawing characteristics of square cups through conical dies. Procedia Eng. **81**, 873–880 (2014)
13. Isik, K., Gerstein, G.: Investigations of ductile damage in DP600 and DC04 deep drawing steel sheets during punching. Procedia Struct. Integrity **2**, 673–680 (2016)

Surface Roughness Evaluation of Milled Surfaces by Image Processing of Speckle and White-Light Images

J. Mahashar Ali, H. Siddhi Jailani and M. Murugan

Abstract An experimental approach for surface roughness measurement based on the speckle images caused by a laser beam on the milled surfaces and the white-light images of the same surfaces is presented. Since the surface slope at every point of the surface influences the speckle pattern, the surface roughness parameters R_{da} and R_{dq} were used for comparison. A CMOS camera, LASER and LED light sources were used for capturing speckle and white-light images of the milled surfaces. From the image pixel intensity matrix, a signal vector was generated and was used for the image metric. It is found that standard deviation and mean of the image signal vector correlate well with R_a, R_{da} and R_{dq} values measured by a standard Taylor Hobson surface roughness tester. The correlation was found to be better for speckle images than the white-light images.

Keywords Surface roughness · Machining · Vision system · Image processing
Speckle images · Statistical parameters

1 Introduction

Milling is a common machining operation and the lay pattern produced in the milling operation is the signature to the finish of any milled surface. The surface roughness is important when dealing with issues like friction, lubrication, wear,

J. Mahashar Ali (✉) · H. Siddhi Jailani
Department of Mechanical Engineering, B. S. Abdur Rahman
Crescent Institute of Science and Technology, Chennai 600048, India
e-mail: mahashar@crescent.education

H. Siddhi Jailani
e-mail: jailani@crescent.education

M. Murugan
School of Mechanical Engineering, Vellore Institute of Technology,
VIT, Vellore Campus, Vellore 632014, India
e-mail: murugan.m@vit.ac.in

fatigue and corrosion, and the control of surface roughness is imperative for the desired performance of the mechanical parts. The surface roughness of machined surface is traditionally being measured using a stylus instrument with high reliability. The stylus instrument has a up and down movement of the stylus for a desired horizontal travel. The limitation of the stylus instrument is its inability of reaching the bottom of the valleys of the surface due to the radius of the stylus tip [1]. Moreover, measurement using the stylus instrument is an offline process consuming substantial time. So, a reliable continuous online surface roughness measuring system in a non-contact type is one of the long-standing requirements of the industry [2]. None of the available optical techniques are reliable and economical for online surface roughness measurement in the unmanned manufacturing environments.

Over the years, substantial developments had taken place in the field of image processing for biometric and satellite imaging applications. Ma et al. [3] characterized the iris image by local sharp variation points, representing important image structure. For characterizing original two-dimensional images, a one-dimensional intensity signal was extracted from the iris features. Lighting variations were compensated by normalization of the image. In the iris image processing, the important idea was to capture the localized sharp variations along the x-direction. Keeping this in mind, the representation of five rows to a one-dimensional signal was obtained from averaging the intensity values of five rows. Therefore, from the entire two-dimensional normalized rectangular images a set of one-dimensional intensity signals were obtained. Using a wavelet transform, the position of localized sharp variation points were extracted and recorded as features. In this iris recognition methodology, to calculate the similarity and matching, the Hamming distance between the vectors was used.

The manufacturing industries concern regarding the measurement and control of roughness of machined surfaces is significant since the surface has a considerable influence on product quality and function [4]. Jiang and Whitehouse [5] in their review documented various challenges that the advances in manufacturing practices had posed on surface metrology. The evolution of structured, stochastic, and free-form surfaces had posed real challenges on surface roughness measurement. The multi-resolution analysis and various filtration techniques of surfaces are being used to characterize the surfaces. It is concluded that there is a lot of gap prevails between correlating the surface parameter with function. Zhao and Zhao [6] proposed theoretical and experimental spatial-average method (SAM) for the objective speckle pattern in the specular direction to overcome the limitation of the speckle contrast method (SCM) and the light scattering method (LSM) which are the most vital optical techniques for non-contact surface roughness measurement.

In industries, machine vision systems are being used for dimensional measurement and inspection with high reliability. For online inspection of machined surfaces, vision-based techniques are highly suitable for fast measurements. Kumar et al. [7] quantified the surface roughness of machined surfaces using machine vision system, by performing regression analysis of the images. In their work, they had magnified the original images by cubic convolution interpolation technique.

They had estimated a parameter called G_a and that was found to correlate well with the conventional surface roughness parameters. Al-kindi and Shirinzadeh [8] used vision-based data using two different light reflection models, intensity-topography compatible (ITC) and light diffuse, to enable suitable computation of surface roughness parameter. They had found the ITC model to be better and to correlate well with the values measured using stylus-based instrument. Kiran et al. [9] attempted to estimate quickly the roughness of medium rough surfaces using vision approach. They had found the direct imaging technique to be quicker than the light sectioning and phase shifting methods. Priya and Ramamoorthy [10] investigated the influence of the orientation angle of the workpiece in computing the surface roughness by image processing. They concluded that the surface roughness can be predicted with reasonable accuracy with machine vision and artificial neural network methodologies. Shahabi and Ratnam [11] used a CCD camera to capture the image of the nose area of the cutting tool and used this image to computationally generate the surface profile of the workpiece. The profile of the workpiece was generated for various feed rates. Surface roughness was estimated using the generated surface profiles. The method was shown to predict the surface roughness as well as dimensional deviation of the workpiece for various cutting conditions.

Leonard and Toal [12] used laser speckle contrast method for characterizing the surface roughness of lapped and ground surfaces. The angle of incidence of laser beam was set at 30° to the surface under investigation. The increase in angle of incidence was found to increase the measuring range by a factor of 4 for finish machined surfaces and by factor of 2 for polished surfaces. Persson [13] used angular speckle correlation technique for roughness measurements in the machined surfaces. The speckle pattern was captured from the surface by illuminating it by a coherent light. By changing the small angle of illumination altogether, a different pattern was obtained and it was also recorded. In this work, the characterization is done by correlating the two differently obtained speckle images. Jeyapoovan et al. [14] used the statistical parameters pertaining to the image intensity matrix of speckle images to quantify the surface roughness. The experiments were conducted using ground and milled specimens. They had demonstrated a strong correlation between the intensity parameters of captured speckle images and the roughness values R_a obtained using a stylus instrument.

In Engineering, measurement and evaluation of surface finish are very much important for many functional problems. The real surface topography is very much complicated to evaluate with the finite number of parameters. To designate a surface two or more surface roughness parameters usually used to calculate the roughness in the two-dimensional (2D) or in the three-dimensional (3D) forms. To evaluate a surface, many different roughness parameters are being used, including the hybrid parameters [15]. In this, the arithmetic average height R_a is the most widely used parameter. The parameters R_a, R_{da} and R_{dq} are defined as

$$R_a, \text{Roughness Average} = \sum_{i=1}^{N} \frac{|Y_i|}{N} \tag{1}$$

$$R_{da}, \text{Arithmetic Mean Slope} = \sum_{i=1}^{N} \frac{|\Delta_i|}{N} \tag{2}$$

$$R_{dq}, \text{Root Mean Square Slope} = \sqrt{\sum_{i=1}^{N} \frac{\Delta_i^2}{N}} \tag{3}$$

The Y_i is the vertical deviations from the average line. The hybrid parameter, R_{da} is the arithmetic mean slope of surface profile which is termed as the mean absolute profile slope over the measurement length. R_{dq} is the root mean square slope of the surface profile. Δ_i is deviations in the slope. In tribological analysis, surface slope, surface curvature and developed interfacial area are considered to be the important factors. Since the surface having peaks, valleys and slope, the image intensity variations will be the function of these slope parameters [16]. Since the image characteristics are also influenced by slope distributions, an attempt is made in the current work, to correlate R_{da} and R_{dq} with the statistical parameters derived from the speckle and white-light images of the milled surfaces by image processing and using a vision system.

2 Experimental Setup and Procedure

In the experiments, EN8 flat plain carbon steel was used as workpiece material. Five different workpieces were milled with different roughness values using dry milling. The cutter diameter used was 50 mm and fly milling was deployed. Since the significant process parameter that affects the surface roughness is feed, the feed values alone were varied, the depth of cut is kept constant at 0.14 mm and the cutting speed is kept at 95 m/min. The different feed rates used in the milling were 0.14, 0.146, 0.152, 0.159 and 0.165 mm/tooth.

The contact type mechanical stylus instrument was used for measuring the surface roughness. The surface roughness was measured on the milled surfaces using a Taylor and Hobson surface roughness tester. The instrument was having a stylus end radius of 2 μm. The cut-off length value of 0.5 mm is used for a surface data length of 5 mm. Approximately, the central region of the specimen was chosen for roughness measurement. The surface roughness parameters R_a, R_{da}, R_{dq} were measured for each specimen and were recorded. The Talysurf surface roughness tester used for surface roughness measurement and the representative profiles along with the roughness parameters R_a, R_{da} and R_{dq} is shown in Figs. 1 and 2. Table 1 shows the various roughness values of the milled specimens.

Fig. 1 Taylor and Hobson surface roughness tester
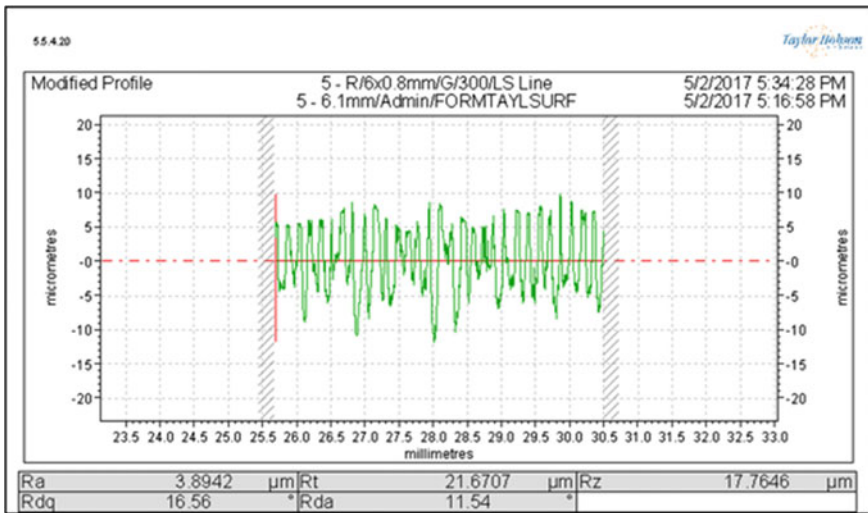
Fig. 2 A representative surface profile

Table 1 Roughness values of milled specimens

Specimen No.	Feed (mm/tooth)	R_a (µm)	R_{da}	R_{dq}
1	0.140	2.06	8.70	12.95
2	0.146	2.70	9.76	13.89
3	0.152	3.16	10.37	15.17
4	0.159	3.89	11.54	16.56
5	0.165	3.94	11.71	16.62
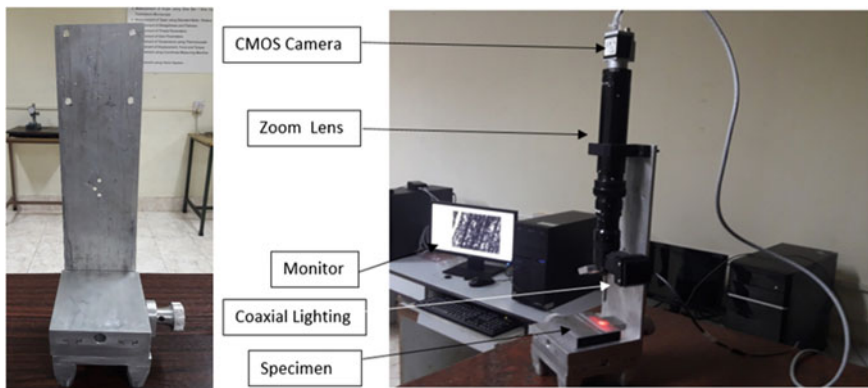
Fig. 3 The camera table and the experimental setup

A high-resolution CMOS camera which is fitted with an optical magnification is used for image acquisition. This setup along with the separately designed camera table is shown in Fig. 3. The lighting system with laser and white light was used to capture the speckle and white-light images, respectively. The camera and the specimen were placed on an adjustable table and the camera axis was set at an angle of 90° to the specimen surface. The same camera and lighting conditions were used for capturing the images of all surfaces. The coaxial white light is used with uniform illumination. A separate laser source is used for speckle image acquisition. Figure 4a, b shows the images obtained for milling specimens before normalization using white-light and laser source. After the image normalization is done to overcome the lighting variations. The normalization of the pixel intensity of the image matrix was obtained using mathematical transformation given by equation [17].

$$h(x, y) = \left(\frac{k(x, y) - \min(k)}{\max(k) - \min(k)} \right) \times 255 \tag{4}$$
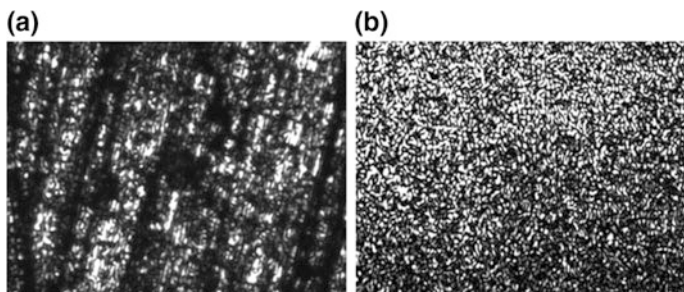
Fig. 4 Images of the specimens taken by **a** white light, **b** laser source

where $h(x, y)$ is the normalized pixel intensity of the image matrix, $k(x, y)$ is the pixel intensity of the image matrix, $\min(k)$ is the minimum value of the pixel intensity of image matrix and $\max(k)$ is the maximum value of the pixel intensity of image matrix.

This normalization was done to eliminate the effect of background lighting on the image matrix. It was done on all the images. The normalized white-light images and speckle images are shown in Fig. 5a, b. The stylus tip diameter corresponds to approximately three-pixel widths. Hence, a single line signal vector was generated by averaging the respective three columns from the three-pixel rows of the white-light image. This is done to the middle portion of the white-light images taken. Similarly for the speckle images, the whole image is considered for signal vector generation. All these images processing was done by MATLAB 2014. The one-dimensional image signal was generated for each surface image. The middle portion of the image was identified to derive the image signal for white-light images by selecting three-pixel rows of length 2400 pixels. The process of generating the signal vector is represented in Fig. 6.
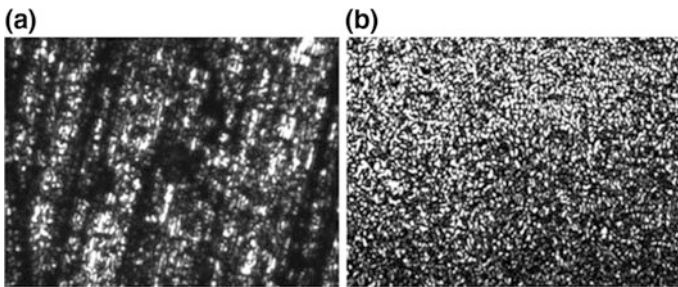
Fig. 5 Normalized images of the specimens **a** white light, **b** speckle
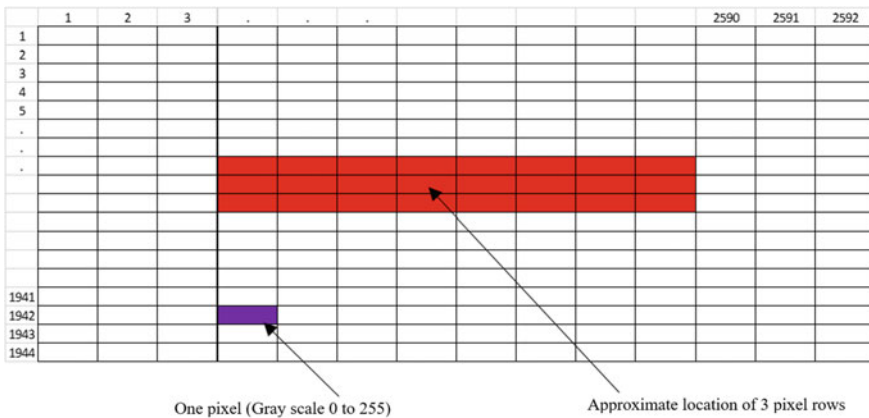
Fig. 6 Generation of one-dimensional image signal

3   Results and Discussion

The mean and standard deviation of the pixel intensity were obtained for each of the white-light images and speckle images from the image signal vectors. Table 2 shows the mean and standard deviation of image signal vector. This data is tabulated against the surface roughness R_a, arithmetic mean slope R_{da} and root mean square slope R_{dq} measured using the stylus instrument.

The plots between the mean and standard deviation of the image signal vector of white-light images and R_{da} is shown in Fig. 7a, b. It can be observed that the mean and standard deviation of white-light images have poor correlation with the roughness parameter R_{da}. A similar trend was observed with other roughness parameters also.

The poor correlation is primarily because of the shadow effect caused by the peaks of the surfaces on the neighbouring areas. Depending on the angle of incidence of a light ray the peaks tend to alter the intensity values of the neighbouring regions. The use of coaxial white-light source was to reduce this influence. But experiments demonstrate that this influence cannot be altogether eliminated.

Table 2 Statistical parameters of image pixel intensity

Specimen	R_a (µm)	R_{da}	R_{dq}	Speckle images		White-light images	
				Mean	Standard deviation	Mean	Standard deviation
1	2.06	8.70	12.95	73.00	31.64	73.71	30.90
2	2.70	9.76	13.89	73.29	31.45	74.00	30.70
3	3.16	10.37	15.17	73.43	31.30	74.29	30.41
4	3.89	11.54	16.56	73.57	31.01	74.29	30.40
5	3.94	11.71	16.62	73.71	30.90	73.71	30.90
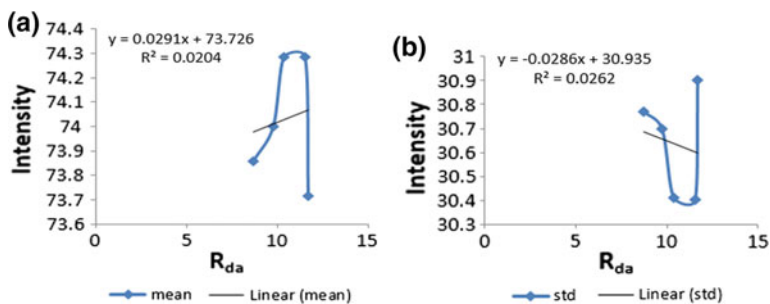
Fig. 7   a Mean image intensity of white-light images versus R_{da}, **b** standard deviation of image intensity of white-light images versus R_{da}

(a) $y = 0.336x + 72.341$
$R^2 = 0.9612$

(b) $y = -0.3789x + 32.455$
$R^2 = 0.9799$

(c) $y = 0.2151x + 71.159$
$R^2 = 0.9689$

(d) $y = -0.2424x + 33.785$
$R^2 = 0.9855$

(e) $y = 0.1643x + 70.93$
$R^2 = 0.9404$

(f) $y = -0.1868x + 34.069$
$R^2 = 0.9743$
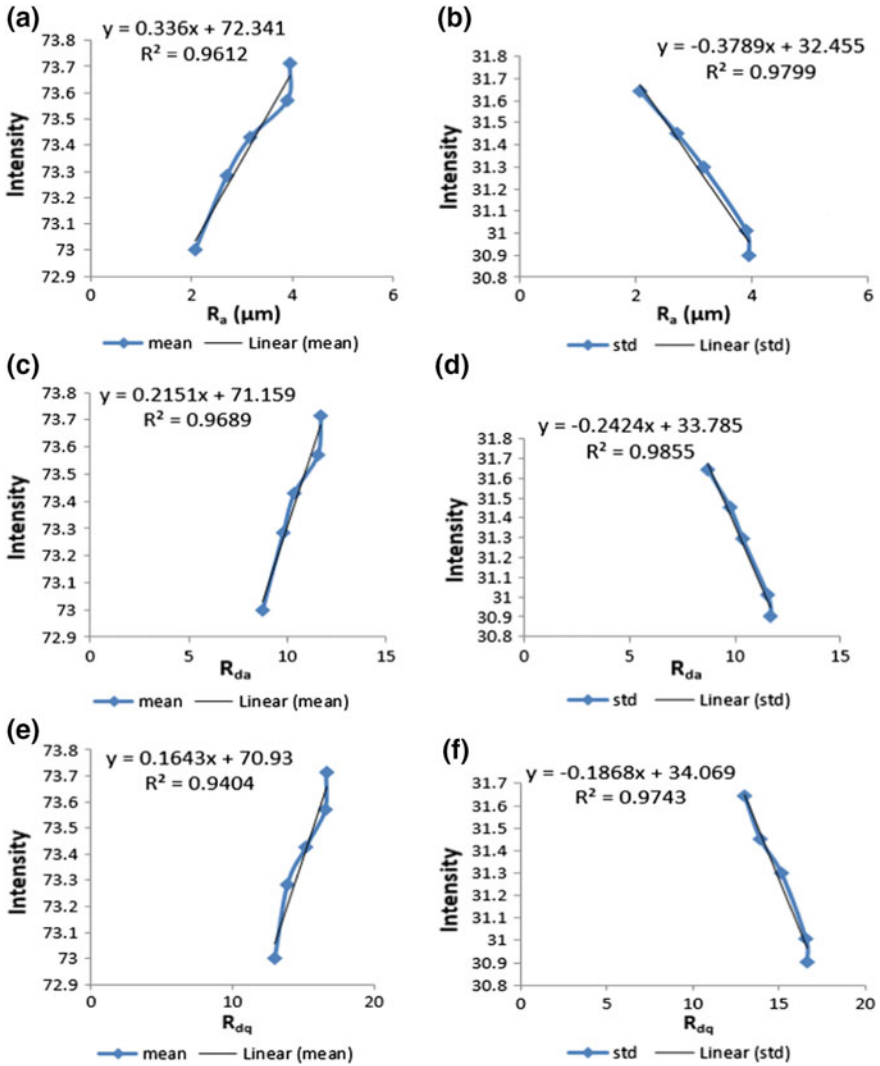
Fig. 8 Image intensity of speckle images with R_a, R_{da} and R_{dq} values **a** mean of image intensity versus R_a, **b** standard deviation of image intensity versus R_a, **c** mean of image intensity versus R_{da}, **d** standard deviation of image intensity versus R_{da}, **e** mean of image intensity versus R_{dq}, **f** standard deviation of image intensity versus R_{dq}

The plots between the mean and standard deviation of the image signal vector of speckle images on the Y-axis and R_a, R_{da} and R_{dq} in the X-axis are shown in Fig. 8a–f. It can be observed that the mean and standard deviation of the image signal vectors have very good correlation with the roughness parameter R_a for speckle images. The R^2 values, which show the effectives of correlation, between

the mean and standard deviation of the speckle image for R_a values are 0.9612 and 0.9799. It can also be noted from Fig. 8a, b that while the mean intensity of the speckle images varies directly with surface roughness parameter R_a, the standard deviation of speckle images vary inversely with R_a. A rough surface causes wider dispersion of the monochromatic light source, which leads to wider scattering and hence the speckle image intensities are dispersed more. This had led to the higher value of the standard deviation, which is in fact a measure of dispersion.

Similarly, the plots mean and standard deviation of intensity of speckle images with hybrid surface roughness parameters R_{da} and R_{dq} also show a good correlation. The R^2 values between the mean and standard deviation of the speckle image for R_{da} values are 0.9689 and 0.9855 and for R_{dq} values are 0.9404 and 0.9743 which indicate very good correlation. The direct–inverse relation for mean and standard deviation prevails for R_{da} and R_{dq} also. This is again because of higher roughness causing higher light scattering leading to higher dispersion of the image intensity.

Since, the interference of light is being influenced by the slope value of the various points on the surface profile, the surface roughness parameters arithmetic mean slope (R_{da}) and root mean square slope (R_{dq}) were used along with the R_a to evaluate the milled surface by speckle images in this work and they prove to relate better with the image parameters of speckle images of the surfaces.

4 Conclusion

- A non-contact vision-based image processing method for roughness evaluation of milled surfaces is attempted in this work. At first, a set of 2-D speckle and white-light images of milled surfaces was obtained. The mean and standard deviation of the image pixel intensity for speckle and white-light images were calculated from each surface image.
- With white-light imaging, the correlation between the image parameters and the stylus parameters were found to be very poor. This could probably be because of the influence of the angle of incidence of the light source on to the surface leading to the peaks causing shadows on the immediate vicinity.
- The speckle image intensity parameters correlate very well with the stylus parameters.
- The stylus parameters arithmetic mean slope (R_{da}) and root mean square slope (R_{dq}) were found to correlate well with the speckle image parameters as the slopes at various points on the free surface are responsible for the reflection of light rays.
- The technique of using the mean and standard deviation of the speckle images for non-contact evaluation of surface roughness is promising. The reliability of measurement can be established through experiments of bigger sample size.

References

1. Hamed, A.M., El-Ghandoor, H., El-Diasty, F., Saudy, M.: Analysis of speckle images to assess surface roughness. Opt. Laser Technol. **36**, 249–253 (2004)
2. Sodhi, M.S., Tiliouine, K.: Surface roughness monitoring using computer vision. Int. J. Mach. Tools Manufact. **36**(7), 817–828 (1996)
3. Ma, L., Tan, T., Zhang, D.: Efficient iris recognition by characterizing key local variations. IEEE Trans. Image Process. **13**, 739–750 (2004)
4. Dhanasekar, B., Mohan, N.K., Bhaduri, B., Ramamoorthy, B.: Evaluation of surface roughness based on monochromatic speckle correlation using image processing. Precis. Eng. **32**, 196–206 (2008)
5. Jiang, X.J., Whitehouse, D.J.: Technological shifts in surface metrology. CIRP Ann. Manufact. Technol. **61**, 815–836 (2012)
6. Zhao, X.Z., Zhao, G.: Surface roughness measurement using spatial-average analysis of objective speckle pattern in specular direction. Opt. Lasers Eng. **47**, 1307–1316 (2009)
7. Kumar, R., Kulashekar, P., Dhanasekar, B., Ramamoorthy, B.: Application of digital image magnification for surface roughness evaluation using machine vision. Int. J. Mach. Tools Manufact. **45**, 228–234 (2005)
8. Al-kindi, G.A., Shirinzadeh, B.:An evaluation of surface roughness parameters measurement using vision based data. Int. J. Mach. Tools Manufact. **47**, 697–708 (2007)
9. Kiran, M.B., Ramamoorthy, B., Radhakrishnan, V.: Evaluation of surface roughness by vision system. Int. J. Mach. Tools Manufact. **38**(5–6), 685–690 (1998)
10. Priya, P., Ramamoorthy, B.: The influence of component inclination on surface finish evaluation using digital image processing. Int. J. Mach. Tools Manufact. **47**, 570–579 (2007)
11. Shahabi, H.H., Ratnam, M.M.: Prediction of surface roughness and dimensional deviation of workpiece in turning: a machine vision approach. Int. J. Manufact. Technol. **48**, 213–226 (2010)
12. Leonard, L.C., Toal, V.: Roughness measurement of metallic surfaces based on the laser speckle contrast method. Opt. Lasers Eng. **30**, 433–440 (1998)
13. Persson, U.: Surface roughness measurement on machined surfaces using angular speckle correlation. J. Mater. Process. Technol. **180**, 233–238 (2006)
14. Jeyapoovan, T., Murugan, M., Clemend Bovas, B.: Statistical analysis of surface roughness measurements using laser speckle images. In: World Congress on Information and Communication Technologies, pp 378–382 (2012)
15. Gadelmawala, E.S., Koura, M.M.: Roughness parameters. J. Mater. Process. Technol. **123**, 133–145(2002)
16. Ali, J.M., Murugan, M.: Surface roughness characterisation of turned surfaces using image processing. Int. J. Mach. Mach. Mater. **19**(4), 394–406 (2017)
17. Gonzalez, R.C., Woods, R.E.: Digital Image Processing. Prentice Hall (2007)

On Processing of Ni–WC8Co-based Composite Clads on Austenitic Stainless Steel Through Microwave Energy

D. Singh, S. Kaushal, D. Gupta, H. L. Bhowmick and V. Jain

Abstract In the present investigation, composite clads of Ni + 20% WC8Co and Ni + 30% WC8Co were developed on austenitic stainless steel (SS-316) using microwave energy. Experiments trials were carried out inside a domestic microwave oven with a frequency range of 2.45 GHz and variable power level of 180–900 W. The exposure time and power level for developing clads were optimized. The microwave processed clads were further characterized through SEM/EDS, XRD, and measurement of Vicker's microhardness. Microstructural results revealed that the clads of approximately 0.7 mm thickness were free from any type of interfacial cracks and voids. WC particles were uniformly distributed inside soft Ni matrix. The presence of NiSi, Co_3W_3C, Fe_6W_6C, NiW, NiCr, and $FeNi_3$ phases was observed during phase analysis of developed composite clads. Microhardness of the Ni + 20% WC8Co and Ni + 30% WC8Co was found to be 810 ± 75 and 923 ± 65 HV, respectively.

Keywords Microwave cladding · Composite material · Microhardness Characterization

D. Singh · S. Kaushal (✉) · D. Gupta · H. L. Bhowmick · V. Jain
Department of Mechanical Engineering, Thapar Institute of Engineering
and Technology, Patiala, India
e-mail: sarbjeet.kaushal1988@gmail.com

D. Singh
e-mail: dilkaran22@gmail.com

D. Gupta
e-mail: dheeraj.gupta@thapar.edu

H. L. Bhowmick
e-mail: hiralal.bhowmick@thapar.edu

V. Jain
e-mail: vivek.jain@thapar.edu

S. Kaushal
Department of Mechanical and Automobile Engineering,
Guljar Group of Institutes, Ludhiana, India

1 Introduction

Surface modification of an engineering component is the cost-effective solution for enhancing the life of the component. Surface modification of the engineering surface is done by using cyaniding, nitriding, claddings/coatings, etc. The claddings/coatings are widely used in different industries throughout the world. There are many claddings/coatings techniques available such as vapor deposition techniques (PVD, CVD), plasma spraying, thermal spraying, laser cladding [1–4]. Among these techniques, the laser cladding method provides excellent metallurgical bonding between clad and substrate material. However, in case of laser cladding, the laser heat is directly applied to the material surface and transferred to the interior through conduction mode of heat transfer. This results in the setup of large thermal gradient within the material. This large thermal gradient causes thermal distortions and poor microstructure of the clads. Apart from this, laser cladding requires high initial setup cost [5, 6]. These problems of conventional processing methods arise the need of some alternative processing methods which can overcome these limitations. Recently, microwave cladding has been grown as the noble and versatile surface modification technique [7–10]. The microwave cladding is associated with a unique feature like volumetric heating. The volumetric heating provides the uniform thermal gradient across the material, and hence, an excellent microstructure of clad is obtained. Microwave cladding method offers more advantages like lower processing time, and lower installation and running costs. Austenitic stainless steels of SS-316 L grades are most commonly used in hydraulic components, food processing industries due to its corrosion-resistant characteristics. However, these grades of steels have poor working behavior under severe wear conditions and cavitation erosion environment. To improve the working life of these steels under wear environment, the surface prone to wear damage can be overlaid by some wear-resistant material through microwave cladding. Kaushal et al. [8, 9, 11] successfully developed the Ni/SiC- and Ni/Cr_3C_2-based composite claddings through microwave heating route at 2.45 GHz. These claddings were found very useful in antiwear applications. Ni/WC-based composite claddings are commonly used as wear-resistant claddings due to their high wear resistance and toughness [12, 13]. The present paper reports the development of Ni + 20% WC8Co and Ni + 30% WC8Co claddings on SS-316 L substrate through microwave hybrid heating methods. The clads were developed inside a domestic microwave oven working at 2.45 GHz and 900 W. Further, the characterization study of so developed clads was carried out using SEM/EDS, XRD, and Vicker's microhardness study.

2 Experimental Work

2.1 Material Details

The austenitic stainless steel (SS-316 L) was used as the substrate material in the current study. The rolled plates of SS-316 L steel were machined to dimensions 8 mm × 8 mm × 6 mm. The commercial available Ni-based EWAC powder (Make: L&T India) and WC8Co powder were used as cladding materials. The morphology and EDS analysis of raw clad powder are shown in Fig. 1a–d. SEM Fig. 1a, c depicts the spherical morphology of Ni powder and knife edge morphology of WC powder. EDS analysis results (Fig. 1b, d) confirmed the presence of Ni particles as a major element in EWAC powder and W, C as major elements of WC8Co powder. The chemical composition (wt%) of raw powder and substrate material is illustrated in Table 1. The raw clad powders were preheated at 180 °C to remove the presence of any moisture particles. The preheated powders were mixed in a mechanical mixture device to obtain the desired proportions (by wt%) of composite powders such as Ni + 20% WC8Co and Ni + 30% WC8Co.
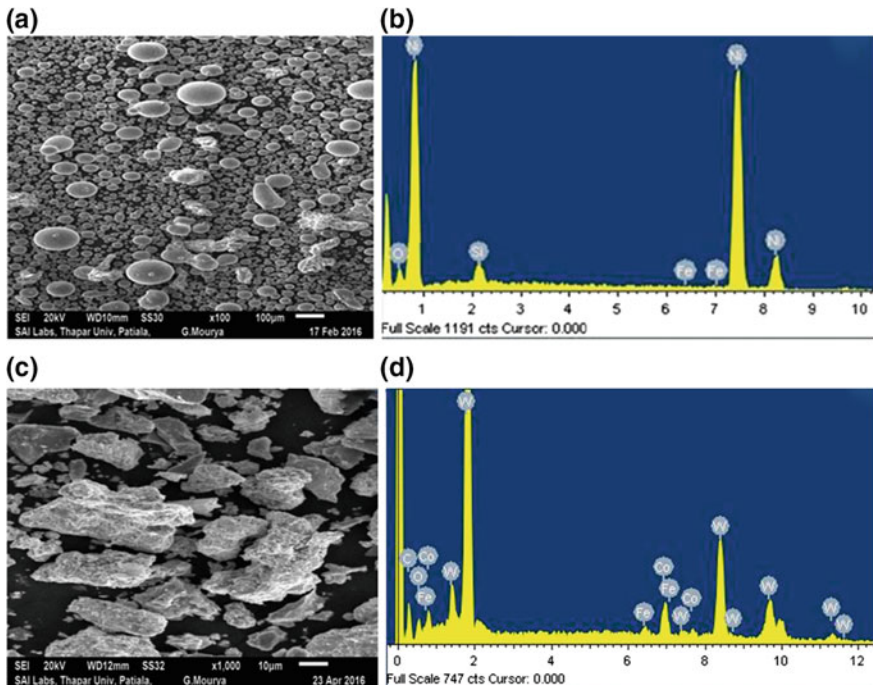
Fig. 1 **a** SEM morphology of Ni-based EWAC powder, **b** EDS analysis of Ni-based EWAC powder, **c** SEM morphology of WC8Co powder, **d** EDS analysis of WC8Co powder

Table 1 Chemical composition by wt% of raw materials

Material	Elements									
	Fe	Cr	Ni	C	Mo	W	Si	Mn	Co	Others
SS-316	Bal.	17.3	11.1	0.02	2.2	0.04	0.2	1.3	0.2	0.5
EWAC powder	–	0.17	Bal.	0.2		–	2.8	–	–	–
WC powder	–	–	–	14.19		72	–	–	7.32	6.49

2.2 Development and Characterization of Claddings

The premixed powder layers of Ni + 20% WC8Co and Ni + 30% WC8Co were placed manually on the SS-316 L base by maintaining a uniform thickness of 0.7 mm. The substrate was placed on the refractory brick in the microwave applicator (at 2.45 GHz and 900 W). The principle of microwave hybrid heating [7] was used to achieve the composite claddings. The complete mechanism of microwave hybrid heating (MHH) is shown in Fig. 2. The different parameters used in microwave heating were illustrated in Table 2. The composite clads of Ni + 20% WC8Co and Ni + 30% WC8Co were developed in 360 and 340 s of exposure times, respectively. The developed clads were sectioned across the thickness using low-speed diamond cutter prior to characterization. The sectioned specimens were then polished using different grits emery papers and lastly followed by diamond paste mirror polishing. The microhardness of the composite clads was evaluated using Vicker's microhardness tester. The different phases present in the composite clads were analyzed using X-ray diffractometer (XRD) study at $1°$ min^{-1} of scan
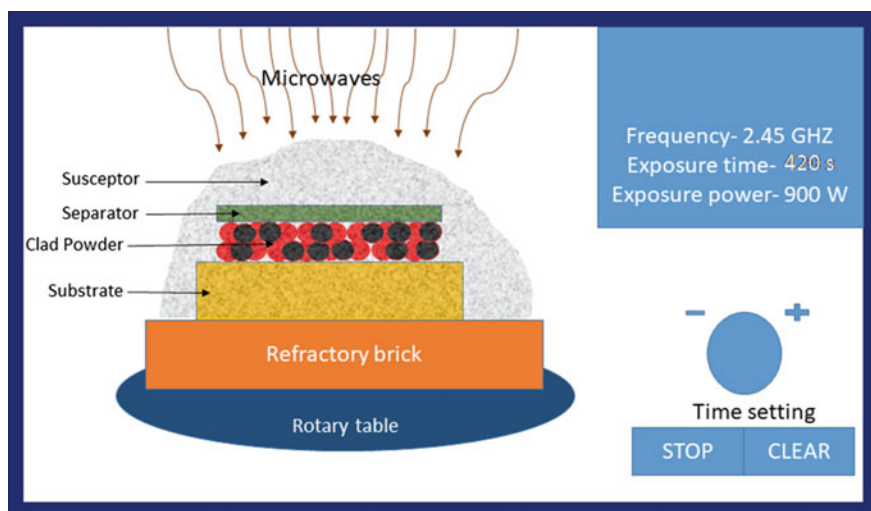
Fig. 2 Mechanism of microwave hybrid heating [10]

Table 2 Various process parameters used during microwave cladding

Parameters	Description
Applicator	Multimode (model: charcoal, make: LG)
Frequency	2.45 GHz
Exposure time	180–420 s
Exposure power	900 W
Powder preheating temperature	200 °C
Powder	Ni-based + 20% WC8Co, Ni-based + 30% WC8Co
Susceptor	Charcoal powder
Separator	99% pure alumina sheet (1 mm thick)

Table 3 Various observations during the pilot experiments with respect to time

Trial	Exposure time (s)	Observations	
		Ni + 20% WC8Co	Ni + 30% WC8Co
1	180	Only heating of powder	Melting of powder just started
2	240	Partial melting of the powder particles, poor bonding with substrate	Partial melting of the powder particles, poor bonding with substrate
3	300	Partial melting of the powder particles, poor bonding with the substrate	Presence of unmelted particles
4	380	Presence of unmelted particles	Desired cladding with strong metallurgical bonding
5	420	Desired cladding with strong metallurgical bonding	Melting of substrate started

rate and 20°–100° of scan range. The polished samples were etched using some suitable etchant solution (5 ml of each HCl, CH_3COOH, and HNO_3). The microstructural characterization of etched samples was carried out using backscattered electron (BSE) microscopy. The different elements present in the composite clads were verified using energy-dispersive spectroscopy (EDS). The various observations seen during the pilot experiments study were illustrated in Table 3.

3 Results and Discussion

3.1 Microstructure Study

The quality and behavior of clads depend upon their microstructures. The transverse sections of microwave processed Ni + 20% WC8Co and Ni + 30% WC8Co
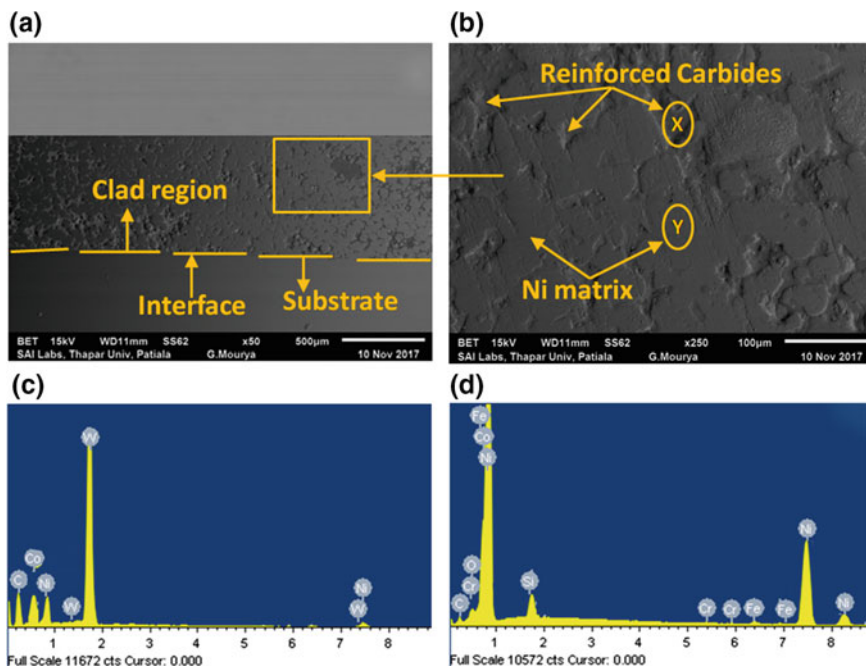
Fig. 3 BSE micrograph of **a** transverse section of Ni + 20% WC8Co clad, **b** clad region; EDS analysis **c** at point X, **d** at point Y corresponding to **b**

composite clads were shown in Figs. 3a and 4a, respectively. It was observed in Fig. 3a that clad of approximately 0.7 mm thickness was free from any interfacial voids and cracks. Further, the zoomed image of the clad region was shown in Fig. 3b, and it was seen that the reinforced carbide particles were randomly dispersed in the Ni matrix. To verify the presence of different elements in the clad region, the EDS analysis study was carried out at different points in the clad region. The EDS results (Fig. 3c, d) confirmed the presence of W, C elements in the carbide regions (point X in Fig. 3b) and Ni elements in the matrix region (point Y in Fig. 3b). Similarly, Fig. 4a showed that the composite clad of approximately 0.6 mm thickness was formed. Figure 4b showed the zoomed image of the clad region, which again revealed the presence of randomly dispersed carbide particles in the matrix region. EDS analysis results were shown in Fig. 4c and d which again confirmed the presence of carbide and Ni elements in the clad regions. The presence of hard carbide and soft Ni matrix results in higher toughness and hardness of the composite clad region.
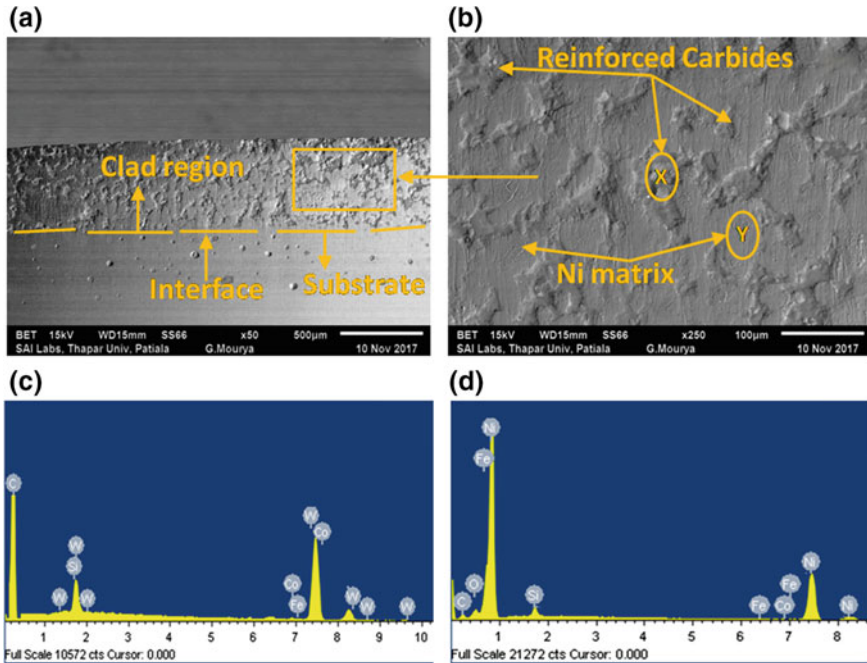
Fig. 4 BSE micrograph of **a** transverse section of Ni + 30% WC8Co clad, **b** clad region; EDS analysis **c** at point X, **d** at point Y corresponding to **b**

3.2　Phase Analysis Study

The XRD spectra of Ni + 30% WC8Co and Ni + 20% WC8Co composite clads were shown in Fig. 5a, b. The presence of Ni, W_2C, NiW, $FeNi_3$, $Cr_{23}C_6$ phases was observed in the clad regions of both claddings. During microwave hybrid heating, the formation of higher temperature results into dissociation of tungsten carbide into W and free C [11]. This free carbon might react with Ni and Cr to form NiW and $Cr_{23}C_6$. Further, free W elements result in the formation of W_2C during microwave heating. The presence of $FeNi_3$ could be due to the partial dilution of iron elements from SS-316 L region to the clad region and hence confirmed the metallurgical bonding formation between cladding and the substrate. In case of Ni + 30% WC8Co clad, there is a presence of Ni_2W_4C phase, which could be attributed to the reaction between Ni and WC particles.
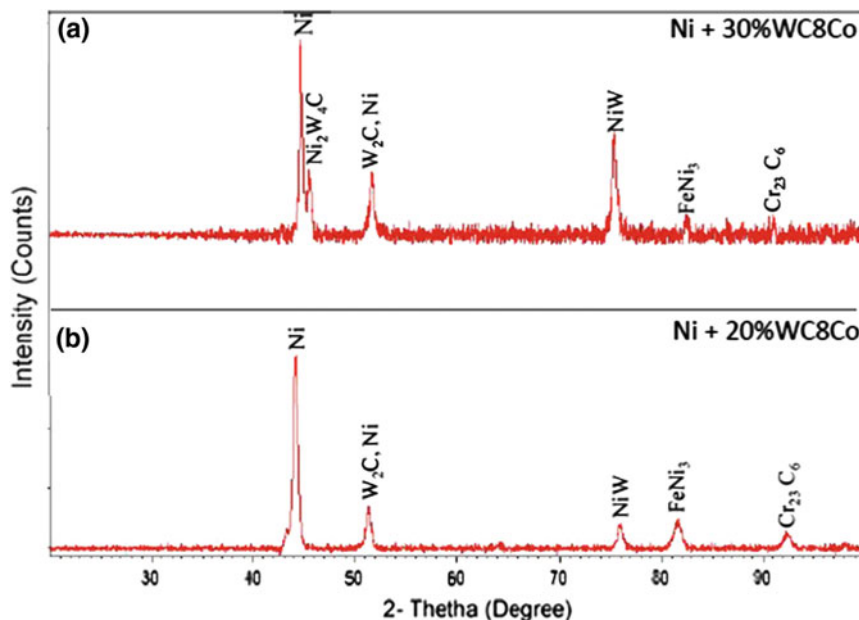
Fig. 5 XRD spectra of **a** Ni + 30% WC8Co clad, **b** Ni + 20% WC8Co

3.3 Vicker's Microhardness Study

The presence of hard carbides in the matrix region could be attributed to the higher microhardness of the clad region. To verify this fact, the Vicker's microhardness indentations across the lateral section of the composite clads were taken. The dwell time and load were kept at 20 s and 300 g, respectively. The microhardness results were shown in Fig. 6. It was observed that the Ni + 30% WC8Co exhibited the maximum value of microhardness of order 923 ± 65 HV. The value of microhardness of Ni + 20% WC8Co clad was observed as 810 ± 75 HV. The value of microhardness of Ni + 30% WC8Co and Ni + 20% WC8Co clads were approximately 3 times and 2.5 times higher than that of SS-316 L substrate, respectively. The higher deviation in the microhardness might be due to the fact that indentations were taken on hard carbide phases as well as soft Ni matrix phase. The higher microhardness of these claddings makes them suitable for antiwear applications.
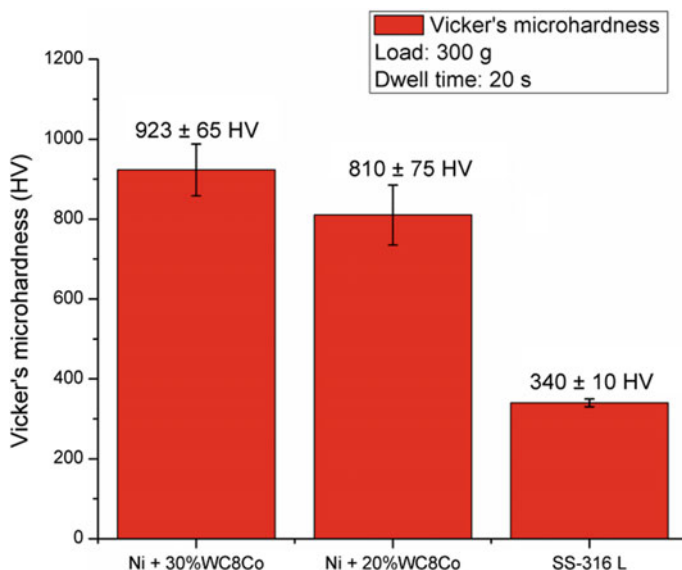
Fig. 6 Vicker's microhardness comparison of clads and SS-316 L

4 Conclusions

In the present investigation, a noble technique of microwave heating was successfully applied for the developing Ni + 20% WC8Co and Ni + 30% WC8Co composite clads on SS-316 L substrate. The following points have been concluded from the characterization study of the so developed clads:

- The clads of approximately 0.7 and 0.6 mm thickness were developed at exposure power of 900 W and 2.45 GHz microwave frequency.
- The microstructural results revealed that the reinforced carbide particles were randomly dispersed in the matrix region.
- The presence of NiW, $FeNi_3$, $Cr_{23}C_6$, W_2C phases was observed in the clad regions of both composite clads.
- The Vicker's microhardness value of Ni + 20% WC8Co and Ni + 30% WC8Co clads were 810 ± 75 and 923 ± 65 HV, respectively.

References

1. Adachi, S., Ueda, N.: Surface hardness improvement of plasma-sprayed AISI 316L stainless steel coating by low-temperature plasma carburizing. Adv. Powder Technol. **24**, 818–823 (2013)
2. M'Saoubi, R., Alm, O., Andersson, J.M., Engstorm, H., Larsson, T., Joesaar, M.P., Schwind, M.: Microstructure and wear mechanisms of texture-controlled CVD α-Al2O3 coatings. Wear **376–377**, 1766–1778 (2017)
3. Alidokht, S.A., Vo, P., Yue, S., Chromik, R.R.: Erosive wear behavior of cold-sprayed Ni-WC composite coating. Wear **376–377**, 566–577 (2017)
4. Krishna, N.G., Thinaharan, C., George, R.P., Parvathavarthini, N., Mudali, U.K.: Surface modification of type 304 stainless steel with duplex coatings for corrosion resistance in sea water environments. Surf. Eng. **31**, 39–47 (2015)
5. Kwok, C.T., Man, H.C., Cheng, F.T.: Cavitation erosion and pitting behaviour of laser surface-melted martensitic stainless steel UNS S42000. Surf. Coat. Technol. **126**, 238–255 (2000)
6. St-Georges, L.: Development and characterization of composite Ni−Cr+WC laser cladding. Wear **263**, 562–566 (2007)
7. Gupta, D., Sharma, A.K.: A method of cladding-coating of metallic and non-metallic powders on metallic substrate by microwave irradiation. Patent Application 527/Del, India (2010)
8. Kaushal, S., Gupta, D., Bhowmick, H.L.: Investigation of dry sliding wear behavior of composite cladding developed through microwave heating. J. Tribol. **139**, 041603-1-9 (2017)
9. Kaushal, S., Sirohi, V., Gupta, D., Bhowmick, H.L., Singh, S.: Processing and characterization of composite cladding through microwave heating on martensitic steel. Mater. Des. Appl. https://doi.org/10.1177/1464420715616139 (2015, in press)
10. Singh, S., Gupta, D., Jain, V., Sharma, A.K.: Microwave processing of materials and applications in manufacturing industries: a review. Mater. Manufact. Process. **30**, 1–29 (2014)
11. Kaushal, S., Gupta, D., Bhowmick, H.L.: On surface modification of austenitic stainless steel using microwave processed Ni/Cr_3C_2 composite cladding. Surf. Eng. https://doi.org/10.1080/02670844.2017.1362808 (2017, in press)
12. Kaushal, S., Gupta, D., Bhowmick, H.L.: On microstructure and wear behavior of microwave processed composite clad. J. Tribol. **139**, 061602-1-8 (2017)
13. Kaushal, S., Gupta, D., Bhowmick, H.L.: On processing of Ni-WC based functionally graded composite clads through microwave heating. Mater. Manufact. Process. https://doi.org/10.1080/10426914.2017.1401724 (2017, in press)

Application of TOPSIS to Optimize EDM Process Parameters for Small-Hole Drilling of Inconel 718

S. Rajamanickam and J. Prasanna

Abstract This work examines the best and worst input parameters such as current, capacitance, on-time, and off-time, which articulate the electrical discharge machining for small-hole drilling of Inconel 718. Inconel 718 is difficult to machine by usual machining processes and found applications in aircraft industries, rocket component, gas turbine parts, and cryogenic tanks. This work makes the use of commercial brass tube electrode having 300 µm diameter. The experimental campaign is prepared using RSM (central composite design), and a TOPSIS model is displayed to identify the best and worst process parameters in EDM, which influence several performance characteristics such as overcut, circularity, electrode wear rate, material removal rate, and taper angle. The intended technique can be used to select best and worst machining parameter among the various sets of combinations of machining parameter in EDM for small-hole drilling.

Keywords Inconel 718 · TOPSIS · EDM · Small-hole drilling
Brass tube electrode

1 Introduction

The small-hole drilling of superalloy with thickness/diameter ratio greater than 10 mm bargained new trend in microparts' fabrication industries. The Inconel 718 material was well-known superalloy which was rich in nickel content, which finds widespread applications. It offers very good strength and hardness and regains its

S. Rajamanickam (✉) · J. Prasanna
Department of Mechanical Engineering, College of Engineering, Guindy, Chennai, India
e-mail: manic1327@gmail.com

J. Prasanna
e-mail: prasanna@annauniv.edu

S. Rajamanickam
Department of Mechanical Engineering, Veltech Hightech Dr. Rangarajan Dr. Sakunthala
Engineering College, Chennai, India

original shapes at −423 to 1300 °F temperature due to its superior mechanical, physical, and chemical properties. Conventional machining of Inconel 718 has discomfort for microfeatures [1–5]. The important literatures of few when machining of Inconel 718 were coined to enrich this work. Biermann and Kirschner investigated conventional drilling of Inconel 718 using deep hole drilling machine TBT ML-200 [6]. Courbon et al. studied high-pressure jet-assisted turning of Inconel 718 with coated carbide tools [7]. Oezkaya et al. worked Inconel 718 of thickness 34 mm machined with cemented carbide twist drill of diameter 6.8 mm using horizontal machining center [8]. Kliuev et al. examined Inconel 718 material in EDM with a copper electrode of 1 mm diameter for cooling hole drilling applications [9]. Kuppan et al. performed electric discharge deep hole drilling of Inconel 718 using various tube electrodes, namely copper, copper tungsten, and graphite electrode tube of 3 mm diameter [10]. Rajesh et al. observed electric discharge machining of Inconel 718 with a hollow copper tool of inner diameter 9 mm and an outer diameter of 12 mm. Using RSM and regression techniques, input parameters, viz. pulse current, gap control, duty factors, sensitivity control, and flushing pressure, were analyzed for material removal rate and surface roughness [11]. Kumar et al. conducted WEDM of Inconel 718 with brass wire electrode. The MRR and SR of WEDM process parameter are optimized using NSGA II [12]. It is evident from the literature summarized that EDM with hollow tool gives better machining features.

In the recent time, multi-objective optimization of EDM input parameters is bringing the excitement of researcher to boost up the good quality of work. However, most of the optimization method fails to examine each input parameter. Shukla et al. reviewed TOPSIS which is suited for different machining processes for the various input parameters [13]. Gok used TOPSIS for turning ductile iron alloyed with Ni, Cu, and Mo [14]. Dewangan et al. employed TOPSIS for electrical discharge machining of AISI P20 tool steel using copper electrode [15]. By the overall literature review analysis, research gap, and interest, electrical discharge machining process parameter is optimized using TOPSIS when machining Inconel 718. The important process parameters used in this studies are current (1–5 A), capacitance (20–60 nF), on-time (6–10 μs), and off-time (1–9 μs).

2   Experimental Setup

The workpiece material used is Inconel 718 plate of thickness 5 mm. The tool material selected is a brass tube of diameter 300 μm. The experiments were conducted using numerical control Sparkonix EDM Drill: speed II machine. The photograph of the machine is illustrated in Fig. 1. The machine mainly consists of arc generator, coolant tank with pump, servo stand, slide mechanism, and work-table. The machine can be able to provide a maximum current of 35 A. The dielectric fluid prepared is deionized water with fluid pressure 100 kg/cm^2 for all experimental run. The machine rear panel is connected with 415 V/3 phase

electrical supply. It is seen from voltmeter, the gap voltage of maximum 85 V was observed. The workpiece is connected to the negative terminal, and tool is connected to the positive terminal of the machine. After performing the machining process, the performance characteristics such as material removal rate (MRR), electrode wear rate (EWR), overcut (OC), radial error (RE), and taper angle are calculated by employing Eqs. (1)–(5):

$$
\text{MRR} = \frac{\pi * \text{Height}\left(\begin{array}{c}\text{hole diameter at entrance}^2 + \text{hole diameter at exit}^2 \\ + \text{hole diameter at entrance } * \text{ hole diameter at exit}\end{array}\right)}{12 * \text{machining time}} \tag{1}
$$

$$
\text{EWR} = \frac{\text{Electrode wear observed directly in machine}}{\text{machining time}} \tag{2}
$$

$$
\text{OC} = \frac{\text{Diameter of the hole machined hole} - \text{Diameter of the tool}}{2} \tag{3}
$$

$$
\begin{aligned}
\text{RE} =(& \text{Diameter of the machined hole at the peak} \\
& -\text{Diameter of the machined hole at the valley})
\end{aligned} \tag{4}
$$

$$TA = \tan \left[\frac{(\text{Diamter of the hole at entrance} - \text{diameter of the hole at exit})}{2 * \text{ thickness of the workpiece}} \right] \qquad (5)$$

3 Experimentation by RSM and Optimization Using TOPSIS

3.1 Response Surface Methodology

The number of experimental runs is designed by RSM-CCD. The design of experiment—RSM is introduced in the year 1951 by George E. P. Box and K. P. Wilson. Central composite design (CCD) is most popular due to its simplicity, flexibility, and efficiency. Taking four machining parameters and five performance characteristics, CCD created 31 sets of experimental runs. Out of which dissimilar 25 sets of experimental runs were conducted. Those factors are based on a reference to machine manual book recommended by machine owner and various works of the literatures studied in EDM. Table 1 gives the machining parameter combinations along with corresponding response characteristics. These responses are taken into consideration for optimization of EDM process parameters to small-hole drilling.

3.2 TOPSIS Method

The technique for order of preference by similarity to ideal solution (TOPSIS) process is carried out as shown in Fig. 2. The EDM process small-hole drilling in Inconel 718 by commercial brass tube electrode, influenced by current, capacitance, on-time, off-time, and other factors (dielectric pressure, rotation of electrode, a polarity of machining, etc.). However, aptly choosing these machining parameters' combinations in favor of performance characteristics is not easy. Hence, employing TOPSIS method is highly positive for finding best and worst machining parameters along with corresponding performance characteristics. In this research paper, a systematic approach has been made to optimize EDM process parameters for small-hole drilling of Inconel 718 adopting TOPSIS Method. The first step of TOPSIS is to find the decision matrix. The decision matrix ($D_{27 \times 5}$) was prepared based on performance characteristics given in Table 1, and it is seen in the form of Eq. (6).

Table 1 Machining parameters' combinations along with corresponding performance characteristics

Run	Current (A)	Capacitance (nF)	On-time (µs)	Off-time (µs)	Material removal rate (mm³/s)	Electrode wear rate (mm/s)	Overcut (mm)	Radial error (mm)	Taper angle (°)
1	2	30	7	3	2.1040	4.6505	0.0830	0.0793	0.0328
2	4	30	7	3	0.0765	0.1378	0.1443	0.1245	0.1816
3	2	50	7	3	0.0785	0.2718	0.1811	0.0369	0.2728
4	4	50	7	3	0.0883	0.3305	0.1978	0.1019	0.0748
5	2	30	9	3	2.0873	4.1597	0.1406	0.0688	0.3914
6	4	30	9	3	0.0820	0.1519	0.1654	0.0519	0.1825
7	2	50	9	3	0.0854	0.2881	0.1718	0.0417	0.1478
8	4	50	9	3	0.1022	0.3442	0.2177	0.0764	0.2600
9	2	30	7	7	3.0146	4.2288	0.2712	0.1067	0.9944
10	4	30	7	7	0.0799	0.1706	0.1264	0.0541	0.0091
11	2	50	7	7	0.0781	0.2668	0.1533	0.0506	0.0967
12	4	50	7	7	0.0817	0.3267	0.1957	0.0430	0.1369
13	2	30	9	7	0.0464	0.0820	0.1548	0.0643	0.4470
14	4	30	9	7	0.0793	0.1777	0.1447	0.0707	0.1670
15	2	50	9	7	0.0765	0.2854	0.1715	0.0608	0.2956
16	4	50	9	7	0.0682	0.2932	0.1803	0.0768	0.3823
17	1	40	8	5	3.0999	7.9903	0.2070	0.1019	0.5319
18	2	40	8	5	0.0639	0.2240	0.1653	0.0525	0.3166
19	3	20	8	5	0.0732	0.1551	0.1664	0.0452	0.2217

(continued)

Table 1 (continued)

Run	Current (A)	Capacitance (nF)	On-time (µs)	Off-time (µs)	Material removal rate (mm³/s)	Electrode wear rate (mm/s)	Overcut (mm)	Radial error (mm)	Taper angle (°)
20	3	60	8	5	1.0306	37.8981	0.1718	0.0468	2.7013
21	3	40	6	5	0.0892	0.3138	0.1755	0.0376	0.2992
22	3	40	10	5	0.0880	0.2831	0.1790	0.0592	0.2983
23	3	40	8	1	0.0988	0.3050	0.1968	0.0510	0.2737
24	3	40	8	9	0.0823	0.2637	0.1704	0.0318	0.1587
25	3	40	8	5	0.0941	0.2643	0.2105	0.0484	0.4890

Fig. 2 TOPSIS process

$$D_{27 \times 5} = \begin{vmatrix} x_{11} & x_{12} & \ldots & x_{1j} \\ x_{21} & x_{22} & \ldots & x_{2j} \\ x_{31} & x_{32} & \ldots & x_{3j} \\ \ldots & \ldots & \ldots & \ldots \\ \ldots & \ldots & \ldots & \ldots \\ x_{i1} & x_{i2} & \ldots & x_{ij} \end{vmatrix} \quad (6)$$

From decision matrix, the normalization is done by using the formula indicated in Eq. (7) and the normalized values are mentioned in Table 2.

$$r_{ij} = \frac{y_{ij}}{\sqrt{\sum_{i=1}^{m} y_{ij}^2}} \quad j = 1, 2, \ldots, n. \quad (7)$$

Then, assuming suitable weight with the knowledge of field expertise to pull through weighted normalized value using Eq. (8), the weight for material removal rate = 0.15, electrode wear rate = 0.15, overcut = 0.2, radial error = 0.3, and taper angle = 0.2, respectively. The sum of all weight is assumed to be equal to one.

$$U = w_j r_{ij} \quad (8)$$

After calculating the weighted normalized values for each performance characteristic, point out the maximum value (U^+) and minimum value (U^-) by employing Eqs. (9) and (10). To the end of this step (Table 3), fix this value as the best $\left(U_J^+\right)$ or the worst $\left(U_J^-\right)$ for each performance characteristic separately by considering objective of interest. The objective is to optimize EDM parameters for maximizing material removal rate, minimum electrode wear rate, minimum radial error, minimum overcut, and minimum taper angle.

$$U^+ = \left(U_1^+, U_2^+, \ldots U_i^+\right) \text{ Maximum values}, \quad (9)$$

$$U^- = \left(U_1^-, U_2^-, \ldots U_i^-\right) \text{ Minimum values} \quad (10)$$

The next step is to arrive the separation measures from Eqs. (11) and (12).

Table 2 Normalized, separation measures, closeness coefficient, and rank values

	Normalized					Separation measures		Closeness coefficient	Rank
	Material removal rate (mm³/s)	Electrode wear rate (mm/s)	Overcut (mm)	Radial error (mm)	Taper angle (°)	S^+	S^-	CC	
1	0.3929	0.1178	0.0937	0.2346	0.0103	0.0534	0.2255	0.8084	1
2	0.0143	0.0035	0.1629	0.3684	0.0571	0.1194	0.2157	0.6437	24
3	0.0147	0.0069	0.2045	0.1093	0.0858	0.0892	0.2241	0.7154	10
4	0.0165	0.0084	0.2233	0.3015	0.0235	0.1080	0.2199	0.6705	22
5	0.3898	0.1054	0.1588	0.2035	0.1231	0.0535	0.2100	0.7969	2
6	0.0153	0.0038	0.1868	0.1536	0.0574	0.0890	0.2245	0.7160	9
7	0.0159	0.0073	0.1940	0.1234	0.0465	0.0877	0.2283	0.7225	5
8	0.0191	0.0087	0.2458	0.2261	0.0818	0.0990	0.2142	0.6840	20
9	0.5630	0.1071	0.3063	0.3156	0.3126	0.1015	0.1872	0.6484	23
10	0.0149	0.0043	0.1428	0.1602	0.0029	0.0874	0.2328	0.7270	3
11	0.0146	0.0068	0.1732	0.1498	0.0304	0.0879	0.2287	0.7223	6
12	0.0152	0.0083	0.2210	0.1272	0.0430	0.0892	0.2278	0.7186	7
13	0.0087	0.0021	0.1748	0.1903	0.1406	0.0958	0.2104	0.6873	19
14	0.0148	0.0045	0.1635	0.2092	0.0525	0.0930	0.2215	0.7043	15
15	0.0143	0.0072	0.1937	0.1799	0.0929	0.0925	0.2168	0.7009	17
16	0.0127	0.0074	0.2036	0.2271	0.1202	0.0992	0.2095	0.6788	21
17	0.5789	0.2024	0.2338	0.3015	0.1672	0.0815	0.1986	0.7092	12
18	0.0119	0.0057	0.1867	0.1555	0.0995	0.0910	0.2183	0.7056	14
19	0.0137	0.0039	0.1879	0.1338	0.0697	0.0887	0.2245	0.7168	8
20	0.1925	0.9601	0.1940	0.1385	0.8493	0.2308	0.0776	0.2516	25
21	0.0167	0.0079	0.1982	0.1112	0.0941	0.0889	0.2228	0.7147	11
22	0.0164	0.0072	0.2021	0.1752	0.0938	0.0923	0.2169	0.7016	16
23	0.0184	0.0077	0.2223	0.1507	0.0861	0.0911	0.2197	0.7069	13
24	0.0154	0.0067	0.1924	0.0942	0.0499	0.0873	0.2309	0.7256	4
25	0.0176	0.0067	0.2377	0.1432	0.1538	0.0951	0.2111	0.6894	18

Table 3 Best (Bold contents) and worst (Italics contents) values for each performance characteristic

Response	U^+	U^-	U_J^+	U_J^-
MRR	0.0868	0.0013	**0.0868**	*0.0013*
EWR	0.1440	0.0003	**0.0003**	*0.1440*
OC	0.0613	0.0187	**0.0187**	*0.0613*
RE	0.1105	0.0283	**0.0283**	*0.1105*
TA	0.1699	0.0006	**0.0006**	*0.1699*

$$S_i^+ = \sqrt{\sum_{j=1}^n \left(U_{ij} - U_J^+\right)^2} \tag{11}$$

$$S_i^- = \sqrt{\sum_{j=1}^n \left(U_{ij} - U_J^-\right)^2} \tag{12}$$

The closeness coefficient to a particular experimental run computed using Eq. (13) and the values of separation measures and closeness coefficient are also given in Table 2. Finally, it is ranked in order to obtain the best as well as worst process parameters.

$$CC = \frac{S_i^-}{(S_i^+ + S_i^-)} \tag{13}$$

4 Results and Discussion

The closeness coefficient has been calculated as discussed in the previous section. In Table 2, the highest closeness coefficient is measured for the experimental run 1 is 0.8084. The corresponding machining parameters are current 2A, capacitance 30 nF, on-time 7 µs, and off-time 3 µs. Hence, machining parameters, corresponding to the experimental run 1, are the optimal process parameters for small-hole drilling in EDM of Inconel 718 among the 25 dissimilar experiments as this has taken the best multi-performance characteristics. The machined hole at entry surface taken from optical microscope at $100 \times$ magnifications corresponding to the best setting is given in Fig. 3a, and the machined hole at exit surface for the same setting is presented in Fig. 3b. At the optimum setting, material removal rate is of 2.1040 mm³/s, electrode wear rate of 4.6505 mm/s, overcut of 0.0830 mm, radial error of 0.0793 mm, and taper angle of 0.0328°. From Table 2, the lowest closeness coefficient measured for the experimental run 20 is 0.2516. The responding machining parameters are current 3 A, capacitance 60 nF, on-time 8 µs, and off-time 5 µs. Hence, machining parameters, corresponding to the experimental run 20, are the least optimal process parameter for small-hole drilling in EDM of Inconel 718 among the 25 dissimilar experiments as this has taken the worst
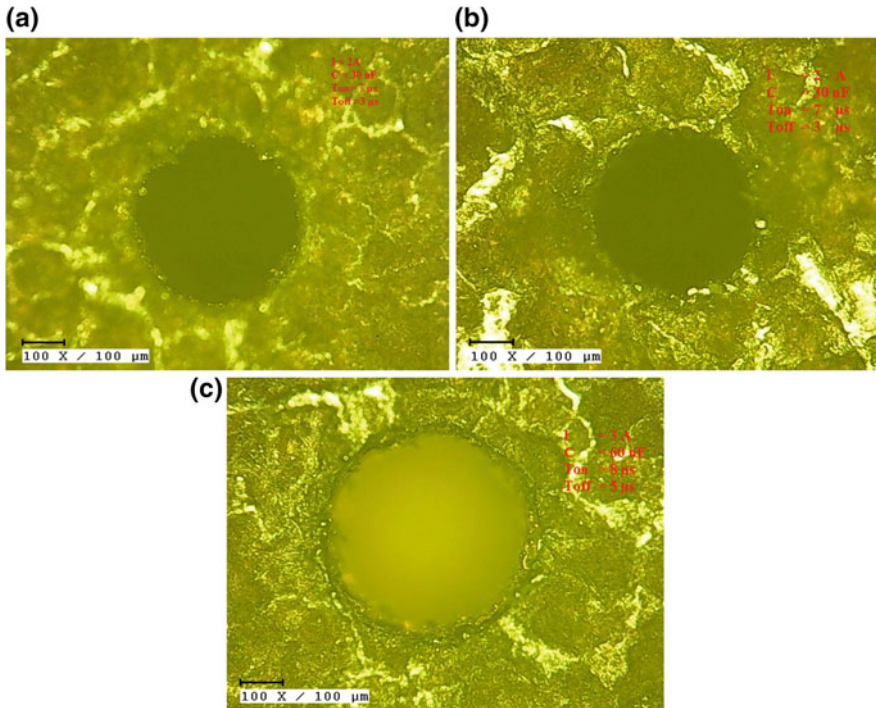
Fig. 3 Best and worst run machined holes

multi-performance characteristics. The blind machined hole is seen at entry surface corresponding to this setting, and it is given in Fig. 3c.

5   Conclusions

In this work, a new attempt has been applied to do justice small-hole drilling in EDM of aspect ratio greater than 15 on Inconel 718 using brass tube electrode of 300 μm. To optimize the machining parameters current, capacitance, on-time, off-time during small-hole EDM drilling on Inconel 718, TOPSIS method was used.

- RSM has been used to design experimental run, and TOPSIS has been used to select the optimum machining parameters for best and worst experimental run corresponding to machining parameters' combinations based on the analysis of closeness coefficient values and their ranking.
- The maximum values of material removal rate of 3.0999 mm³/s, electrode wear rate of 37.8981 mm/s, overcut of 0.2712 mm, radial error of 0.1245 mm, and taper angle of 2.7013° are documented. At the same time, minimum values of material removal rate of 0.0464 mm³/s, electrode wear rate of 0.0820 mm/s,

overcut of 0.0830 mm, radial error of 0.0318 mm, and taper angle of 0.0091°
are observed for small-hole drilling in EDM of Inconel 718.
- Future research work will fall on making microholes in EDM under ultra-high
aspect ratio with different electrode materials.

References

1. Lu, X., Jia, Z., Lu, Y., Feng, Y., Liang, S.Y.: Predicting the surface hardness of micro-milled nickel-base superalloy Inconel 718. Int. J. Adv. Manuf. Technol. **93**, 1283–1292 (2017)
2. Sredanovic, B., Lakic, G., Kramar, D., Kopac, J.: Study on the machinability characteristics of Inconel 718 superalloy during micro-milling. In: Proceedings of 5th International Conference on Advanced Manufacturing Engineering and Technologies, pp. 375–385 (2017)
3. Wang, F., Liu, Y., Shen, Y., Ji, R., Tang, Z., Zhang, Y.: Machining performance of Inconel 718 using high current density electrical discharge milling. Mater. Manuf. Process. **28**, 1147–1152 (2013)
4. Ulutan, D., Ozel, T.: Machining induced surface integrity in titanium and nickel alloys: a review. Int. J. Mach. Tools Manuf. **51**, 250–280 (2011)
5. Znidarsic, M., Junkar, M.: Deep small hole drilling with EDM. Adv. Manuf. Syst. Technol. 527–533 (1996)
6. Biermann, D., Kirschner, M.: Experimental investigations on single-lip deep hole drilling of superalloy Inconel 718 with small diameters. J. Manuf. Process. **20**, 332–339 (2015)
7. Courbon, C., Kramar, D., Krajnik, P., Pusavec, F., Rech, J., Kopac, J.: Investigation of machining performance in high-pressure jet assisted turning of Inconel 718: an experimental study. Int. J. Mach. Tools Manuf. **49**, 1114–1125 (2009)
8. Oezkaya, E., Beer, N., Biermann, D.: Experimental studies and CFD simulation of the internal cooling conditions when drilling Inconel 718. Int. J. Mach. Tools Manuf. **108**, 52–65 (2016)
9. Kliuev, M., Boccadoro, M., Perez, R., Dal Bo, W., Stirnimann, J., Kuster, F., Wegener, K.: EDM drilling and shaping of cooling holes in Inconel 718 turbine blades. Procedia CIRP **42**, 322–327 (2016)
10. Kuppan, P., Narayanan, S., Oyyaravelu, R., Balan, A.S.S.: Performance evaluation of electrode materials in electric discharge deep hole drilling of Inconel 718 superalloy. Procedia Eng **174**, 53–59 (2017)
11. Rajesha, S., Sharma, A.K., Kumar, P.: On electro discharge machining of Inconel 718 with hollow tool. JMEPEG, **21**, 882–891 (2012)
12. Kumar, A., Majumder, H., Vivekananda, K., Maity, K.P.: NSGA-II approach for multi-objective optimization of wire electrical discharge machining process parameter on Inconel 718. Mater. Today Proc. **4**, 2194–2202 (2017)
13. Shukla, A., Agarwal, P., Rana, R.S., Purohit, R.: Applications of TOPSIS algorithm on various manufacturing processes: a review. Mater. Today Proc. **4**, 5320–5329 (2017)
14. Gok, A.: A new approach to minimization of the surface roughness and cutting force via fuzzy TOPSIS, multi-objective grey design and RSA. Measurement **70**, 100–109 (2015)
15. Dewangan, S., Gangopadhyay, S., Biswas, C.K.: Study of surface integrity and dimensional accuracy in EDM using fuzzy TOPSIS and sensitivity analysis. Measurement **63**, 364–376 (2015)

Tool Wear Analysis While Creating Blind Holes on Float Glass Using Conventional Drilling: A Multi-shaped Tools Study

A. Sharma, V. Jain and D. Gupta

Abstract The present work is focused on the creation of blind holes on float glass using CNC conventional drilling (CD) by deploying multi-shape of tools. The selected tools are listed as a hollow abrasive tool, pinpointed conical tool, flat cylindrical tools, and concave circular tool. The experimental trials are performed by considering industrial conditions. The weight of the tools is estimated in two cases, i.e., fresh tool and after CD process to analyze the overall tool wear. Apparently, micrographs are aided to investigate the phenomena of lateral and end face tool wear while creating blind holes at two stages: (a) fresh tool and (b) after CD. Concave circular tool possessed a minimum percentage of weight loss, i.e., 4.92% after CD and is revealed as a most effective tool, which could be used for drilling purpose followed by the hollow abrasive tool.

Keywords Conventional drilling · Abrasive tools · Float glass
Tool wear · End face · Lateral face

1 Introduction

Float glass has vast scope in the application exemplify as metrological equipment, solar panel, and automobile toughened glass, owing to its superior properties like thermal, chemical, and wear resistance property [1]. Hard and brittle material such as glass is widely drilled using CNC conventional drilling (CD). Most of the research study is take place specifically related to efficient drilling and its working parameters. Yet, researchers are facing critical problem relevant to tool wear and selection of best tool shape for drilling purpose. In industries, the conventional diamond machining process is generally aided for glass drilling. However, during float glass drilling, few inadequacies are needed to be sought out.

A. Sharma (✉) · V. Jain · D. Gupta
Mechanical Engineering Department, Thapar University, Patiala 147001, India
e-mail: ankit.sharma@thapar.edu

Fig. 1 Schematic illustration of three-dimensional view of the RUM tool [2]
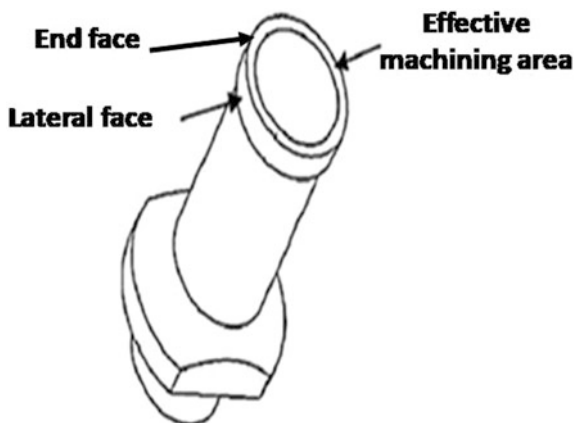
Kuruc et al. worked on ceramic drilling, where a hollow abrasive drill tool with metal-bonded diamond abrasives is equipped with it. Figure 1 shows the schematic illustration of three-dimensional view of the hollow abrasive tool [2].

In another study, hollow tool wear monitoring was carried out [3]. The digital microscope was used to observe tool wear [4]. In an article, the tool wear during drilling operation was discussed. It was found that the metal-bonded tool has lesser wear propensity, as the drilling tool is made-up of sintering type metal powder and diamond abrasive. It was revealed that the friction is a major which were affecting the tool wear during drilling operation [5]. Another researcher was aimed to reduce issues like surface topography by using a different shape of tools [6]. In an experimental work, a chamfered tool was used [7]. In a study, flat end shape tool with wax coating was equipped [8]. One more study discussed that tool geometry such as shape, tool's property limits the tool wear up to 20–30% [9]. In a research work, the chemical aspect of tool wear was declined [10]. In an experimental study, multiple shapes of tools were considered to analyze topography of a surface [11]. Popli and Gupta have been estimated the tool wear after machining. Abrasive size, spindle speed, and feed rate are the key parameters considered during the investigation [12]. One more study found that the as the shape of the tool change, it declines the tool wear rate of near about 20% [13].

After reviewing the past studies, the author found that the global scientists and glass industries are confronting tool wear problem on the major scale. Till now, less research was considered for the different shape of diamond-coated tools which were used in conventional diamond drilling. The present work is focused on the creation of blind holes on float glass using CNC conventional drilling (CD) by deploying multi-shape of tools. The selected tools are listed as a hollow abrasive tool, pin-pointed conical tool, flat cylindrical tools, and concave circular tool. The experimental trials are performed by considering industrial conditions. The weight of the tools is estimated in two cases, i.e., fresh tool and after CD process, to analyze the overall tool wear in case of each tool. Apparently, micrographs are aided to
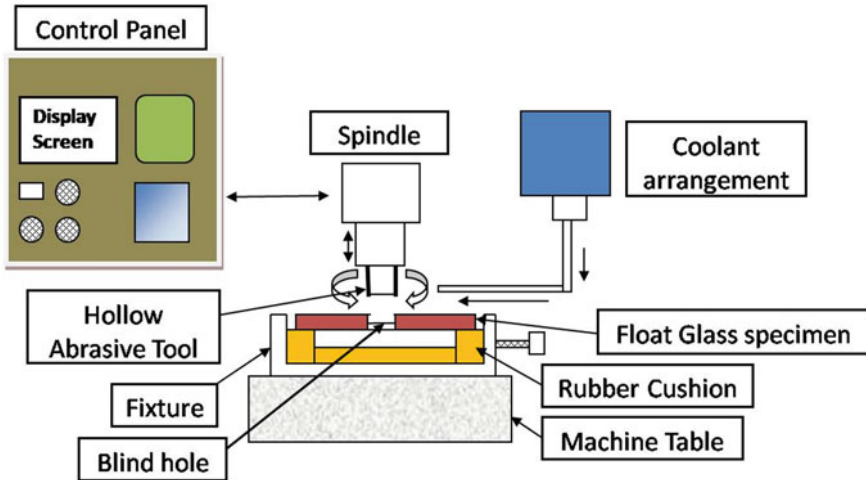
Fig. 2 Illustration of experimental setup

investigate the phenomena of lateral and end face tool wear while creating blind holes at two stages: (a) fresh tool and (b) after conventional drilling (CD).

2　Experimental Work

A CNC milling machine is used for experimental work after fixing attachments such as fixture, abrasive tools. Figure 1 shows the experimental setup which includes its major parts. These are (a) CNC machine, (b) controller unit, (c) fixture, (d) abrasive tool. Setup has spindle rotation power of 60–6000 rpm. While following industrial conditions, here spindle speed of 4500 rpm and feed rate (f) of 15 mm/min is considered.

Distilled water is used as a coolant. The float glass work specimen is installed on a special fixture to maintain constant clamping pressure. The drilling depth opts as 3 mm. The whole working parameters will be similar for creating blind holes by CD. The float glass sample is a chemical composition of silica (60%), limestone (10%), dolomite (10%), soda ash (10%), salt cake (10%), and cullet pieces (Table 1).

Five multi-shaped tools opt for the experiment work as mentioned in Table 2. As shown in Figs. 3 and 4 solid and one hollow abrasive-coated tools with different shapes are used for generating blind holes. Each tool makes four holes by CD process to attain more accurate result outcomes. Thus, a total of 20 blind holes are produced. As shown in Fig. 2, Tool 2 and Tool 3 both have different heights and diameters. Therefore, there could be the possibility of deviation in tool wear results. The specification and measurements of the abrasive tools are mentioned in Table 2.

Table 1 Mechanical properties of workpiece material

S. No.	Properties	Value
1.	Density	2500 kg/m^3
2.	Compressive strength	212 MPa
3.	Elastic modulus (tensile)	70 GPa
4.	Tensile strength (UTS)	50 MPa
5.	Impact strength	800 MPa
6.	Vickers hardness	4.59
7.	Poisson's ratio	0.23

Table 2 Detail specifications of abrasive tools

S. No.	Tool Name	Type	Tool shank material	Tool abrasive mesh size	Dimensions (mm)
1	Pinpointed conical tool	Solid	EN 31	90–140	Dia.—7.94
2	Flat cylindrical tool (height > dia.)	Solid	EN 31	90–140	Dia.—4.92
3	Flat cylindrical tool (height < dia.)	Solid	EN 31	90–140	Dia.—7.92
4	Hollow abrasive tool	Hollow	EN 31	90–140	O.D.—5.90 I.D.—4.21
5	Concave circular tool	Solid	EN 31	90–140	Dia.—9.94

Fig. 3 List of tools used in experimentation
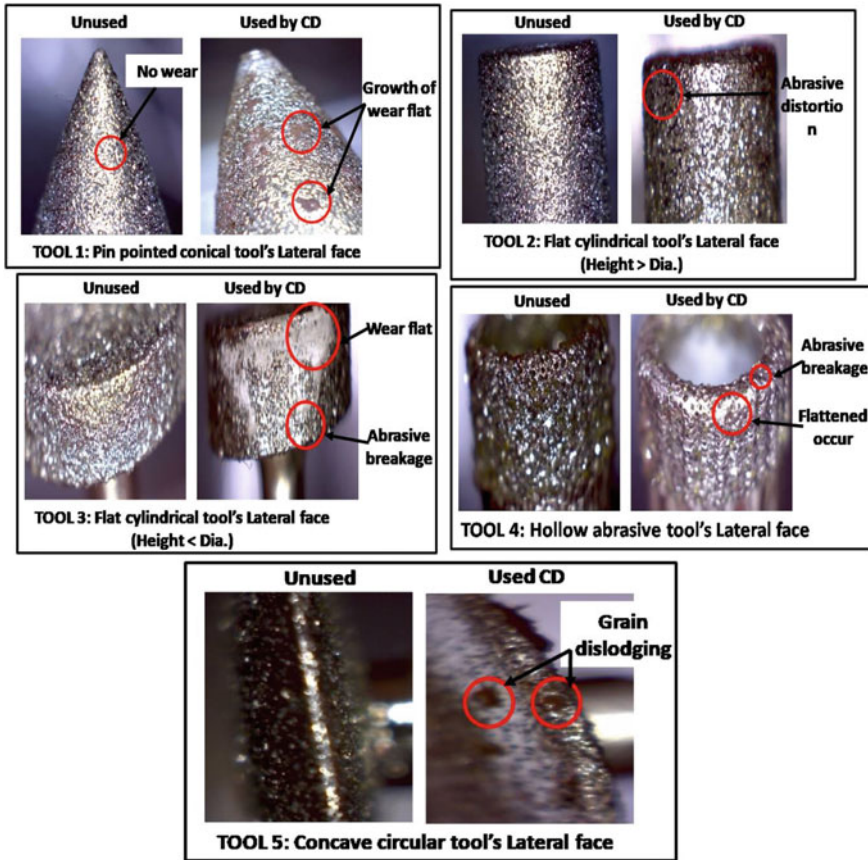
Fig. 4 Microscopic images of the lateral face of all the tools at two stages

After considering all the working factors such as tool, workpiece, and drilling parameters, the blind holes are produced. The complete process of blind hole making is completed in an order of using multiple tools. Afterward, the multiple abrasive tool samples are further carried out for examination as well as quantification.

Weighing balance is used to weigh the different multi-shaped tools. The weight loss (%) estimation between fresh tool and a used tool (after CD process) is attained. A digital microscope is equipped to observe the tool wear of various multi-shaped tools at two stages, i.e., when the tool in fresh and after CD. Wear is further estimated and analyzed at lateral and end faces of the tool.

3 Results and Discussion

3.1 Tool Wear

Individual tools lateral and end faces are visualized in Figs. 4 and 5. Figure 4 shows the microscopic images of the lateral face of all the tools at two stages, i.e., (a) fresh tool and (b) after CD process. Figure 5 depicts the microscopic images of the end face of all the tools at two stages. During the drilling process, the lateral face of the tool is not in direct contact with the drilling surface. Therefore, stress generation near this region is lesser. The reason of lesser stress generation at the lateral face of the tool is because of occurrence of lesser cutting force that subsequently provides lesser tool wear [5, 14]. On a flip side, the lateral face of the pinpointed conical tool (Tool 1) is continuously in contact with the machined
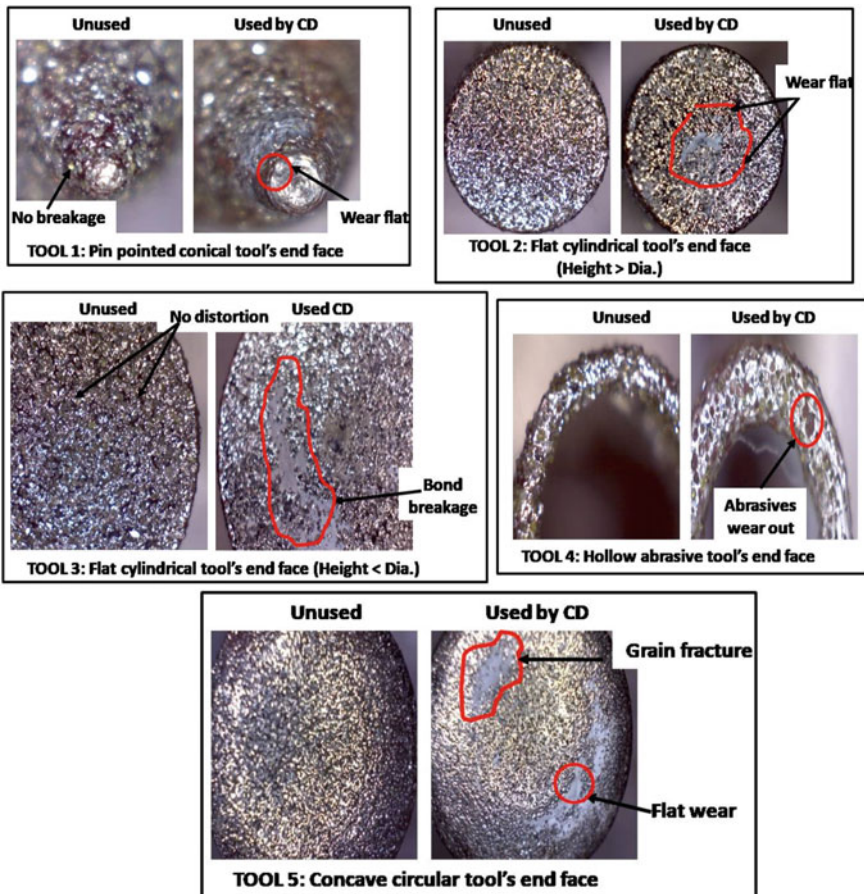
Fig. 5 Microscopic images of the end face of all the tools: **a** unused, **b** used by CD

Table 3 Weight loss (%) between new tool and used tool by CD process

Tool no.	Tool type	New tool weight (gm)	Used tool weight after CD (gm)	Weight loss between new tool and CD (%)
Tool 1	Pinpointed conical tool	5.772	5.150	10.78
Tool 2	Flat cylindrical tool (height > dia.)	2.772	2.546	8.15
Tool 3	Flat cylindrical tool (height < dia.)	2.238	2.085	6.84
Tool 4	Hollow abrasive tool	3.826	3.580	6.43
Tool 5	Concave circular tool	2.234	2.124	4.92

surface. So, it could also generate heavy chipping and crack over hole periphery. Similarly, Fig. 4 shows that after CD operation, there is a noticeable difference in the microstructure of the diamond grains on the tool lateral faces of five tools.

As a comparison to tools ends faces (Fig. 5), lateral faces are carried out less amount of wear flat and grains dislodging. However, a little grain dislodging (Fig. 4) is visualized at the tool corners (close to the end face). Hence, there is not much requirement of diamond grains over the lateral face of the tool. Correspondingly, length of the lateral face can be reduced. Also, it could lead to limits in the tool's fabrication cost. Microscopic images are helped to visualize the tool wear before drilling (unused tool) and after drilling.

At the tool's end face, few diamond grains are dislodged and washed away after drilling because of bond fracture action. Figure 5 illustrates the end face of the tools in different stages. Some grains were pulled out of the metal bond too soon, before finishing their effective working lives. It was stated that the impact force leads to deterioration of the grains. It will further lead to the occurrence of chipping over the workpiece.

To compute the tool wear after CD process, weight (in gm) of the five tools is computed. In Table 3, weight loss (in %) between the unused (new) tool and used tool by CD process is estimated.

Figure 6 depicts the weight loss (%) after conventional drilling (CD) process. The maximum percentage of tool weight reduction because of wear is in the case of tool 1, i.e., 10.78%, whereas, Tool 5 carried out least amount of weight loss, i.e., 4.92%. Subsequently, the reason behind lesser tool wear for Tool 5 is because of lesser friction and correspondingly least stress generation [10]. Therefore, it is stated that the design of the tool's lateral face should be optimum. It is because the tool which possesses the smaller lateral face, need a lesser quantity of grains and consequently, lesser fabrication cost could achieve.
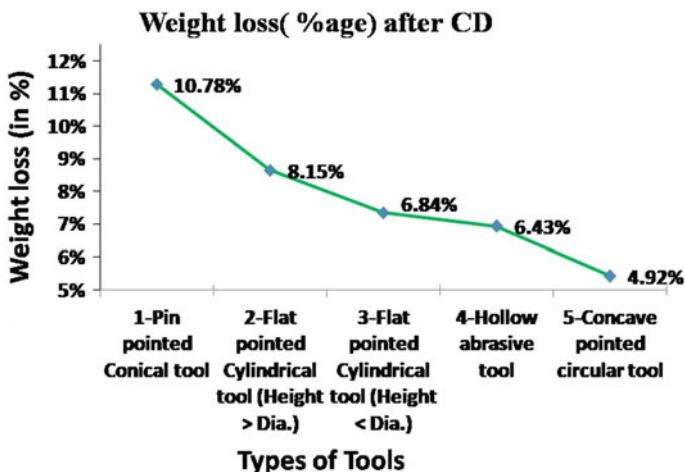
Fig. 6 Weight loss (%) after conventional drilling (CD) process

4 Conclusions

The following conclusion is carried out on the basis of the current experimental study about multi-shaped tool wear:

- Tool 5 (Concave circular tool) has generated least wear, and Tool 1 (Pinpointed conical tool) has produced highest wear amount. Added, the maximum quantity of the wear flat and grain fracture was observed on tool's end face.
- After CD process, the concave circular tool has possessed least weight loss, i.e., 4.92%.
- Tool 5 is recommended for drilling purpose, and it helps to limit the extra monetary loss.

References

1. Zweibel, K.: Issues in thin film PV manufacturing cost reduction. Solar Energy Mater. Solar Cells **59**, 1–18 (1999)
2. Zeng, W.M., Li, Z.C., Pei, Z.J., Treadwell, C.: Experimental observation of tool wear in RUM of advanced ceramics. Int. J. Mach. Tools Manuf. **45**, 1468–1473 (2005)
3. Kuruc, M., Vopat, T., Peterka, J.: The surface roughness of poly crystalline cubic boron nitride after rotary ultrasonic machining. Procedia Eng. **100**, 877–884 (2015)
4. Liu, L.P., Lin, B., Fang, F.Z.: Monitoring of tool wear in rotary ultrasonic machining of advanced ceramics. Adv. Mater. Res. **314–316**, 1754–1759 (2011)
5. Jain, A.K., Pandey, P.M.: Experimental studies on tool wear in μ-RUM process. Int. J. Adv. Manuf. Technol. **85**, 2125–2138 (2016)

6. Li, Z.C., Jiao, Y., Deine, T.W., Pei, Z.J., Treadwell, C.: Rotary ultrasonic machining of ceramic matrix composites: feasibility study and designed experiments. Int. J. Mach. Tools Manuf. **45**, 1402–1411 (2005)
7. Singh, R.P., Singhal, S.: Rotary ultrasonic machining: a review. Mater. Manuf. Process. **31**, 1795–1824 (2016)
8. Wang, Q., Cong, W., Pei, Z.J., Gao, H., Kang, R.: Rotary ultrasonic machining of potassium dihydrogen phosphate (KDP) crystal: an experimental investigation on surface roughness. J. Manufact. Process. **11**(2), 66–73 (2009)
9. Ghahramani, B., Wang, Z.Y.: Precision ultrasonic machining process: a case study of stress analysis of ceramic (Al_2O_3). Int. J. Mach. Tools Manuf. **41**, 1189–1208 (2001)
10. Paul, E., Evans, C., Mangamelli, A., McGlauflin, M., Polvani, R.: Chemical aspects of tool wear in single point diamond turning. Precis. Eng. **18**, 4–19 (1996)
11. Li, Z.C., Jiao, Y., Deine, T.W., Pei, Z.J., Treadwell, C.: Rotary ultrasonic machining of ceramic matrix composites: feasibility study and designed experiments. Int. J. Mach. Tools Manuf. **45**, 1402–1411 (2005)
12. Popli, D., Gupta, M.: Experimental investigation of tool wear and machining rate in rotary ultrasonic machining of nickel alloy. Mach. Sci. Technol. **32**, 1–27 (2017)
13. Ghahramani, B., Wang, Z.Y.: Precision ultrasonic machining process: a case study of stress analysis of ceramic (Al_2O_3). Int. J. Mach. Tools Manuf. **41**, 1189–1208 (2001)
14. Singh, R.P., Singhal, S.: Rotary ultrasonic machining of advanced materials: a review. Int. J. Technol. Res. Eng. **2**, 777–785 (2015)

Effect of Surface Modification Using GTAW as Heat Source and Cryogenic Treatment on the Surface Hardness and Its Prediction Using Artificial Neural Network

M. K. Chaanthini and Sanjivi Arul

Abstract High-wear-resisting EN 31 bearing steel has been widely used to make components such as roller bearing, ball bearing, spline shaft, and other components like tiller blades, punches and dies are subjected to severe abrasion to require high surface hardness. To obtain high surface hardness, EN 31 steel is usually surface modified using various methods like conventional heat treatment (591 HV), cryogenic treatment (688 HV) and GMAW. But, there are no studies on surface modification of EN 31 using gas tungsten arc (GTA) heat source followed by cryogenic treatment. To improve the hardness further, surface alloying using gas tungsten arc followed by cryogenic treatment is done in this study. EN 31 steel is surface-hardened by using GTA heat source by varying the welding current, electrode tip angle and shallow and deep cryogenic treatments (SCT & DCT) by varying soaking time and temperature. Microstructures were studied and microhardness was measured. It is found that cryogenic treatment leads to formation of carbide particles in martensite matrix with reduced retained austenite which improves the microhardness from 258 to 898 HV after SCT and 1856 HV for DCT. Further, in this work, a back-propagation artificial neural network (ANN) which uses gradient descent learning algorithm is used to predict the microhardness of EN 31 steel for the entire ranges of parameters used in the experiments. The ANN model is trained and tested using 200 experiments done. The input parameters of the ANN model are 4 variables (welding current, electrode tip angle, cryogenic soaking time and temperature). Using MATLAB, a programme was developed and by varying the transfer function (tansig and logsig) different ANN models are constructed for the prediction of microhardness. This study shows that

M. K. Chaanthini · S. Arul (✉)
Dept of Mechanical Engineering, Amrita School of Engineering,
Amrita Vishwa Vidyapeetham, Coimbatore, India
e-mail: s_arul@cb.amrita.edu

M. K. Chaanthini
e-mail: sugan.saravanan@gmail.com

back-propagation artificial neural network (ANN) which uses gradient descent learning algorithm is very efficient for predicting the microhardness of EN 31 steel.

Keywords Surface hardness · EN 31 · GTAW · Shallow cryogenic treatment Deep cryogenic treatment · Artificial neural network

1   Introduction

EN 31 is a high-carbon steel used commonly in the automotive industry for producing components such as bearing that has wear-resisting nature which was explained by Harish et al. [1]. EN 31 is also used to produce components including roller bearing, ball bearing, spline shaft, tiller blades used for ploughing the fields in agricultural industry [2], extruders, slurry pumps, and pipes carrying slurry of minerals and ores which are subjected to severe abrasion [3]. They are also used for some engineering applications where high hardness, increased dimensional stability and reduced residual stress [4] are required. Hence, these components should have high surface hardness. Either conventional heat treatment (CHT) or cryogenic treatment (CT) or both can be used for surface modification of EN 31 steel or any other steels. CHT which includes quenching and tempering of X12CrMoWVNbN10-1-1 steel for enhancing hardness and impact toughness [5], also for increasing fatigue behaviour of 56SiCr7 spring steel [6] and improving the surface hardness in H13 tool steel nitrogen diffusion [7] and carbon diffusion [8]. High-speed tool steel HS 6-5-2 was austenitized for martensitic transformation which increases the hardness [9], and the abrasion resistance was increased by quenching which was studied by Suchanek et al. [10]. Gas tungsten arc(GTA) heat source is also a kind of CHT used for refining the surface of Al–Si alloys which improves hardness and wear resistance [11, 12]. From the literature, it has been found that cryogenic treatment shows greater improvement in mechanical properties compared to conventional heat treatment processes. Many steels have undergone cryogenic treatment for the enhancement of mechanical properties such as H13 tool steel which was analysed by Perez et al. [13] to increase fracture toughness, also [14] for improving wear resistance [14] and toughness [15]. AISI M2 steel was studied for increasing tool life and wear resistance by Firouzdor et al. [16] and for improving wear and toughness by Molimari et al. [14]. AISI 440C bearing steel was investigated for hardness improvement [17]. EN 8 steel was studied by Murugappan et al. [18] which shows reduced surface roughness in turning. Also, CT has been performed in AL 6063 and its machinability in turning [19] and the improvement in hole quality during drilling by reducing the surface roughness [20]. Cryogenic treatment (shallow and deep) includes annealing, cooling at −50 or −196 °C using dry ice or liquid nitrogen, respectively, and tempering.

In this work, EN 31 steel is surface-hardened by both conventional heat treatment (gas tungsten arc heat source) and cryogenic treatment (shallow at −50 °C,

deep at −196 °C) by varying the welding current, electrode tip angle, soaking time and temperature. Predicting the hardness is difficult since various parameters are involved in surface treatments. It requires a lot of experimental work for obtaining the microhardness which leads to loss of time, material and money. In order to reduce the time and cost immensely, artificial neural network (ANN) can be used for prediction of properties.

Artificial neural network is a nonlinear mapping structures based on the function of the human brain. The network is composed of a large number of neurons (processing elements) highly interconnected with each other to solve a specific problem [21]. It has been widely used for data processing, data mining, regression analysis, pattern recognition, medical diagnosis, etc. Nowadays, neural network is used in materials field for the prediction of mechanical properties of various metal alloys. The hardness of the high-speed steel [22] and low-carbon steel [21] for the given chemical composition is predicted by using back-propagation and radial basis function algorithm. Similarly, Zahran [23] uses feed forward back-propagation to predict the hardness of the aluminium alloy for the given alloying elements. Yield strength, ultimate tensile strength and elongation of aluminium cast alloy, Al-357 is predicted as a function of T6 heat treatment variables. Similarly, hot-rolled low-carbon steel predicted the same properties as a function of thermo-mechanical process parameters by using back-propagation algorithm [24]. For different welding periods and temperature, the shear strength is predicted by using back-propagation algorithm for Ni–Ti alloy [25]. Using neural network back-propagation algorithm, martensite start and austenite start temperatures for iron-based shape-memory alloys were predicted for the given weight percentages of seven elements and three different treatment conditions explained by Eyercioglu et al. [26]. Also, ductile cast iron properties such as tensile strength, elongation and Brinell hardness were predicted for nine chemical components and five melting temperatures investigated by Perzyk et al. [27].

Mechanical properties have been predicted for many steels and alloys. But there is no literature found for the prediction of mechanical properties for EN 31 steel. In this study, EN 31 steel is surface-treated using gas tungsten arc (GTA) heat source followed by both shallow and deep cryogenic treatments. The microhardness is predicted using the given inputs of welding current, electrode tip angle, cryogenic temperature and soaking time by using ANN back-propagation algorithm.

2 Experimental Work

2.1 Surface Treatment Using GTA Heat Source

The experiments were conducted using Lincoln electric V205T TIG welding machine, a servo-motor-driven manipulator controlled by a PLC which has *X* axis control. GTA heat source is applied using thoriated tungsten electrode on EN 31

Fig. 1 EN 31 welded sample

specimen of dimension 150 mm $\times$ 25 mm $\times$ 6 mm shown in Fig. 1. The chemical composition of EN 31 steel is 96.65% Fe, 0.964% C, 0.258% Si, 0.6215 Mn, 0.011% P, 0.012 S, 1.10% Cr, 0.071% Mo, 0.082% Ni and 0.001% Pb. The electrode diameter, electrode tip distance and welding speed were made constant to 2.4 mm, 3 mm and 5 mm/s. The welding current of 100, 125, 150, 175, 200 A and the electrode tip angle of 30°, 60°, 180°, 45° were varied to perform the experiment which is followed by SCT and DCT.

2.2 Cryogenic Treatment

After surface GTA surface treatment, shallow cryogenic treatment is done by using dry ice at −50 °C for 100 samples. The workpieces are kept inside the cryogenic chamber. The temperature inside the cryogenic chamber was monitored using a thermocouple. EN 31 welded samples were subjected to SCT for five different soaking periods of 3, 6, 9, 12 and 15 h. Once the SCT is over, the workpieces were allowed to reach the room temperature and then the microhardness was taken. The next 100 samples were subjected to deep cryogenic treatment by using liquid nitrogen at −196 °C in a 50 L tank. EN 31 welded samples are kept inside the tank for five different time intervals 3, 6, 9, 12 and 15 h. Once DCT was over, the samples were tested for microhardness.

2.3 Microhardness Measurement

The hardness value of the sample is obtained from Vickers microhardness tester. Microhardness is measured 200 samples with the load value of 1000 gf. Microhardness values are taken at the top surface of the weld pool with the dwell time of 15 s.

3 Modelling of Artificial Neural Network

In this work, ANN model is trained using gradient descent back-propagation which is shown in Fig. 2 with four different input parameters, namely welding current, electrode tip angle, soaking time and temperature, two hidden layers with the combinations of two transfer functions, i.e. tansig-tansig, tansig-logsig, logsig-tansig and logsig-logsig, and one output which is the predicted hardness. Hyperbolic tan-sigmoid (tansig) is a neural transfer function, and it calculates a layer's output from its net input as given in Eq. (1) [28].

$$a = \text{tansig}(n) = 2/(1 + \exp(-2 \times n))^{-1}. \tag{1}$$

This is mathematically equivalent to tanh (N). It differs in that it runs faster than the MATLAB implementation of tanh, but the results can have very small numerical differences. This function is a good trade-off for neural networks, where speed is important and the exact shape of the transfer function is not. Log-sigmoid is a transfer function, and it calculates a layer's output from its net input as given in Eq. (2) [28].
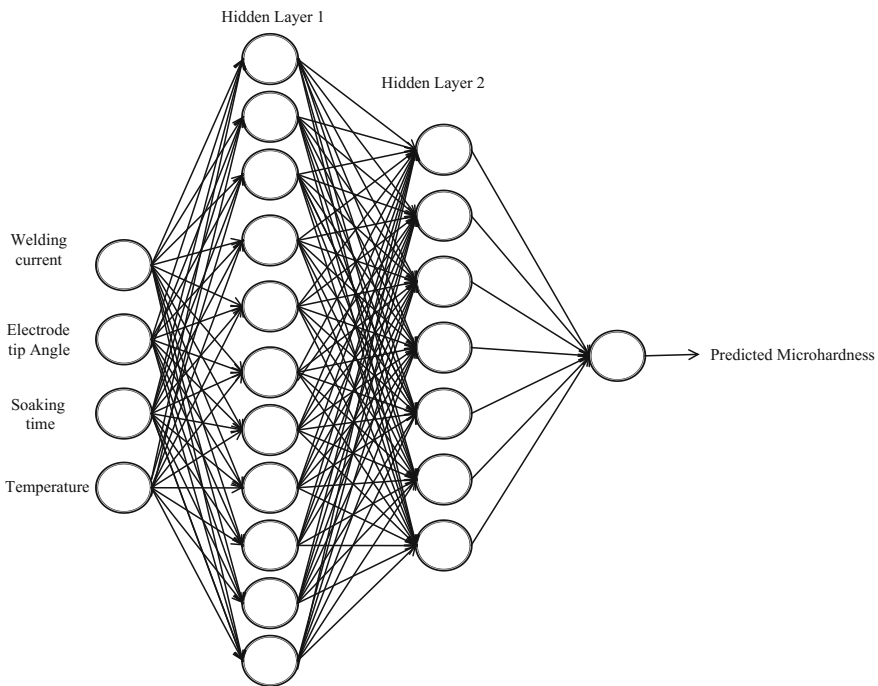
Fig. 2 ANN model with two hidden layers for predicting microhardness

$$\text{logsig}(n) = 1/(1 + \exp(-n)). \tag{2}$$

This network model uses traingd as training function with 1000 number of epochs i.e., 1000 forward and backward passes for training a single data and MSE as performance function. The learning rate is fixed at 0.01. The network has four input layers, one output layer, two hidden layers [26, 29],with neurons ranging from 5 to 12 [23]. The traingd can train any network as long as its weight, net input and transfer functions have derivative functions. Back-propagation is used to calculate derivatives of performance (perf) with respect to the weight, and bias variable X is given in Eq. (3) [28]. Each variable is adjusted according to gradient descent:

$$\mathrm{d}X = lr \times d\text{perf}/\mathrm{d}x. \tag{3}$$

The welding current, electrode tip angle, soaking time and cryogenic temperature are given as inputs, and the microhardness is taken as the output. The input layer receives information from the experiments and transmits them to the neurons of the hidden layer without performing any calculation. The hidden layer then processes the received information and extracts useful features for constructing the network. Finally, the output layer produces the predicted values. Before training, the experimental data were divided into three data sets: 70% training data set, 15% validation data set and 15% testing data set.

4 Results and Discussion

4.1 Experimental Results

The microhardness values started to increase as the welding current increases from 100 to 200 A, the soaking period increases from 3 to 15 h, and the electrode tip angle increases from 30° to 180°. DCT samples show higher microhardness compared to SCT samples. Also, the microhardness values were higher at 15 h of soaking time due to long-time cooling cycle which gives rise to martensite structure with carbide precipitates and reduced retained austenite. The hardness of the samples is more in the case of DCT than SCT due to complete transformation of austenite to martensite for any given set of input parameter values. A sample of experimental microhardness values with 60° electrode tip angle (20 samples out of 200) for both SCT and DCT is given in Table 1.

Table 1 Experimental microhardness for SCT and DCT samples (for 60° electrode tip angle)

S. No.	Current (A)	Soaking time (h)	Temperature (°C)	Microhardness (HV)
1.	100	3	−50	577
2.	100	6	−50	720
3.	100	9	−50	743
4.	100	12	−50	770
5.	100	15	−50	781
6.	125	3	−50	639
7.	125	6	−50	731
8.	125	9	−50	748
9.	125	12	−50	786
10.	125	15	−50	798
11.	100	3	−196	780
12.	100	6	−196	816
13.	100	9	−196	922
14.	100	12	−196	1161
15.	100	15	−196	1288
16.	125	3	−196	825
17.	125	6	−196	846
18.	125	9	−196	928
19.	125	12	−196	1117
20.	125	15	−196	1292

4.2 Prediction Using ANN

The artificial neural network model is constructed for four input parameters, two hidden layer and one output layer. Each hidden layer varied from 5 to 12 neurons. Trial-and-error method was conducted 10 times for 8×8 set of neurons, so for each network combination there are 640 runs. Out of that, 64 best runs were selected for each neuron combination. And it has been identified that each network combination with 4-11-8-1(tansig-tansig), 4-10-11-1(tansig-logsig), 4-11-11-1 (logsig-tansig) and 4-6-10-1(logsig-logsig) shows the best correlation coefficient (R). Tansig-tansig is found to be optimized from the above network combinations. Table 2 shows the R-value for training and testing for 5–12 neurons. R-testing values are comparatively higher than R-training values for all given neurons. The highest R-testing values for different combinations of transfer functions are shown as bold values. It is clearly seen from Table 2 that the highest correlation coefficient (R) for microhardness prediction was obtained for tansig-tansig network, which has two hidden layers with 11 and 8 neurons, respectively. Based on this analysis, the optimal architecture of the ANN was constructed as 4-11-8-1.

The statistical values of predicted microhardness are given in Table 3. The overall performances of predicted microhardness are evaluated through mean percentage error, maximum percentage error, sum of square error (SSE), the

Table 2 R-value for training, testing for two-layer hidden neurons

S. No.	Hidden neurons		Tansig-Tansig		Tansig-Logsig		Logsig-Tansig		Logsig-Logsig	
	Layer 1	Layer 2	Testing	Training	Testing	Training	Testing	Training	Testing	Training
1.	6	10	0.97357	0.94581	0.98484	0.93944	0.97217	0.93088	**0.98823**	0.95336
2.	10	11	0.98037	0.9731	**0.98881**	0.97522	0.98277	0.93324	0.95211	0.91159
3.	11	8	**0.99219**	0.9756	0.97074	0.96979	0.95253	0.93436	0.96401	0.89186
4.	11	11	0.98102	0.97266	0.97773	0.96182	**0.98708**	0.96999	0.96962	0.92687

Table 3 Statistical values for microhardness

	Tansig-Tansig	Tansig-Logsig	Logsig-Tansig	Logsig-Logsig
% min error	0	4.94615E−06	1.05855E−06	6.10509E−06
% max error	0.003278255	0.003526192	0.002963253	0.004618504
% mean error	0.00057751	0.000488841	0.000529832	0.001062983
MSE	0.006346931	0.005819027	0.005932456	0.019464978
RMS	0.079667631	0.076282544	0.077022437	0.139516946
SSE	9.51258419	10.26023434	10.14169377	12.13717675
COV	0.036789694	0.03811546	0.037455976	0.04082674
R-Training	0.975604694	0.97521901	0.969989152	0.953355211
R-Validation	0.987196985	0.979940379	0.963647087	0.97766329
R-Testing	0.992188414	0.988808418	0.987081896	0.988232371
Performance	0.005059633	0.005633414	0.008220062	0.009037116

root-mean-square error (RMSE), the correlation coefficient (R) and the coefficient of variation in per cent (COV). The tansig-tansig combination shows high correlation coefficient in which R-testing is 0.9921, corresponding R-training is 0.9756, minimum percentage error is 0, maximum percentage error is 0.00327, mean percentage error is 0.0005, MSE is 0.0063, and RMSE is 0.079. The training set performance is shown in Fig. 3 indicating the predicted and experimental hardness
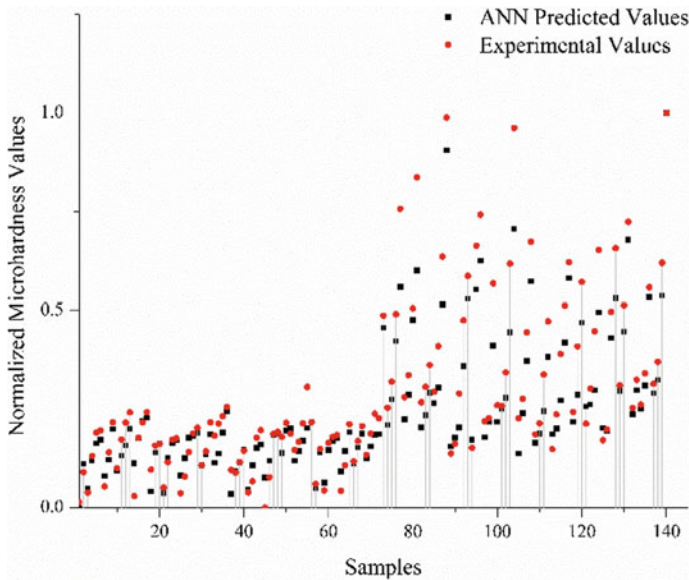
Fig. 3 Performance of proposed ANN model for microhardness of training set
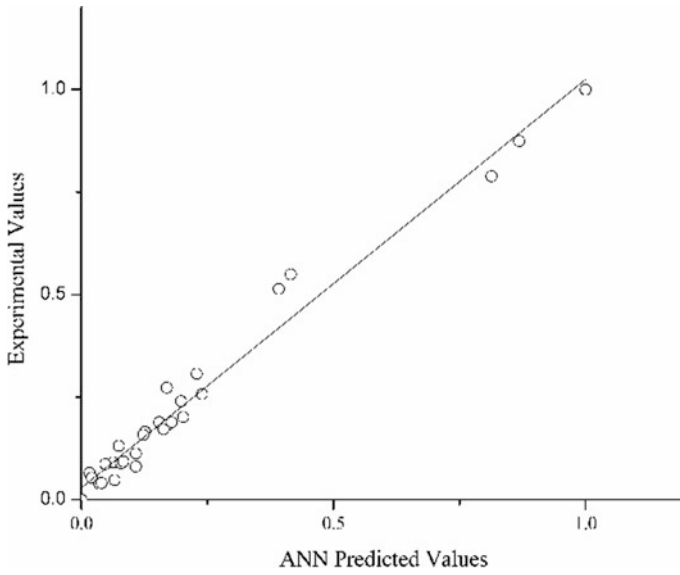
Fig. 4 Test set performance of EN 31 steel microhardness
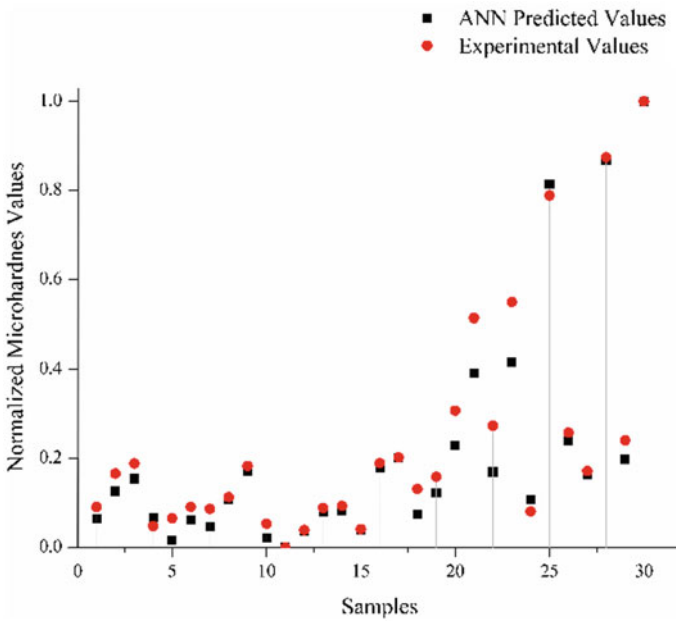
Fig. 5 Performance of proposed ANN model for microhardness of test set

values. Thus, the relationship between the input and output parameters is successfully demonstrated in this ANN model. Comparison of ANN-predicted microhardness with experimental microhardness for testing set is shown in Figs. 4 and 5. The predicted values of microhardness for both training and testing sets correlate very well with the experimental values.

5 Conclusions

The ANN with back-propagation algorithm was developed to predict the mechanical property of EN 31 steel, which was surface-hardened by GTA heat source (welding current 100, 125, 150, 175 and 200 A and electrode tip angles 30°, 45°, 60°, 180°) and cryogenic treatment (temperature −50 °C, −196 °C and soaking time 3, 6, 9, 12, 15 h). The following conclusions are obtained from this work:

- The ANN model can be used for determining the microhardness.
- The input parameters efficiently influence the microhardness.
- ANN can be used as a highly effective tool for predicting microhardness with appropriate combination of training functions.
- Training function with tansig-tansig combination gives the highest correlation coefficient (R) value.

References

1. Harish, S., Bensely, A., Mohan Lal, D., Rajadurai, A., Lenkey, G.B.: Microstructural study of cryogenically treated En 31 bearing steel. J. Mater. Process. Technol. **209**, 3351–3357 (2009)
2. Kocher, G., Parkash, O., Vardhan, S.: Hardfacing by welding to increase wear resistance properties of EN31 by MR 3LH electrode. Int. J. Emerg. Technol. Adv. Eng. **2**, 102–105 (2012)
3. Sapate, S.G., Chopde, A.D., Nimbalkar, P.M., Chandrakar, D.K.: Effect of microstructure on slurry abrasion response of En-31 steel. Mater. Des. **29**, 613–621 (2008)
4. Kamei, K., William, A.G., Koveile, L., Ahmad, N., Chakravorty, A., Davis, R.: An experimental study of the effect of thermal treatments & charpy impact test parameters on impact toughness of EN31 steel. IOSR J. Mech. Civ. Eng. **11**, 17–22 (2014)
5. Tao, X., Li, C., Han, L., Gu, J.: Microstructure evolution and mechanical properties of X12CrMoWVNbN10-1-1 steel during quenching and tempering process. J. Mater. Res. Technol. **5**, 1–13 (2015)
6. Fragoudakis, R., Karditsas, S., Savaidis, G., Michailidis, N.: The effect of heat and surface treatment on the fatigue behaviour of 56SiCr7 spring steel. Proc. Eng. **74**, 309–312 (2014)
7. Cho, K.T., Song, K., Oh, S.H., Lee, Y.K., Lee, W.B.: Surface hardening of shot peened H13 steel by enhanced nitrogen diffusion. Surf. Coatings Technol. **232**, 912–919 (2013)
8. Ramezani, M., Pasang, T., Chen, Z., Neitzert, T., Au, D.: Evaluation of carbon diffusion in heat treatment of H13 tool steel under different atmospheric conditions. J. Mater. Res. Technol. **4**, 114–125 (2015)

9. Sackl, S., Kellezi, G., Leitner, H., Clemens, H., Primig, S.: Martensitic transformation of a high-speed tool steel during continuous heat treatment. Mater. Today Proc. **2**, S635–S638 (2015)
10. Suchanek, J., Kuklik, V.: Influence of heat and thermochemical treatment on abrasion resistance of structural and tool steels. Wear **267**, 2100–2108 (2009)
11. Saravanan, R., Sellamuthu, R.: Determination of the effect of Si content on microstructure, hardness and wear rate of surface-refined Al-Si alloys. Proc. Eng. **97**, 1348–1354 (2014)
12. Saravanan, R., Sellamuthu, R.: An Investigation of the effect of surface refining on the hardness and the wear properties of Al-Si alloy. Appl. Mech. Mater. **592–594**, 53–57 (2014)
13. Pérez, M., Rodríguez, C., Belzunce, F.J.: The use of cryogenic thermal treatments to increase the fracture toughness of a hot work tool steel used to make forging dies. Proc. Mater. Sci. **3**, 604–609 (2014)
14. Molinari, A., Pellizzari, M., Gialanella, S., Straffelini, G., Stiasny, K.H.: Effect of deep cryogenic treatment on the mechanical properties of tool steels. J. Mater. Process. Technol. **118**, 350–355 (2001)
15. Patil, P.I.: Comparison of effects of cryogenic treatment on different types of steels : a review. Int. J. Comput. Appl. 10–29 (2012)
16. Firouzdor, V., Nejati, E., Khomamizadeh, F.: Effect of deep cryogenic treatment on wear resistance and tool life of M2 HSS drill. J. Mater. Process. Technol. **206**, 467–472 (2008)
17. Idayan, A., Gnanavelbabu, A., Rajkumar, K.: Influence of deep cryogenic treatment on the mechanical properties of AISI 440C bearing steel. Proc. Eng. **97**, 1683–1691 (2014)
18. Murugappan, S., Arul, S., Campus, C.: A study on effect of sub zero temperature cooling on surface roughness of turned EN8 steel rod. Int. J. Appl. Eng. Res. **10**, 21549–21563 (2015)
19. Murugappan, S., Arul, S., Narayanan, S.K.: An experimental study on turning of AL6063 under cryogenic pre cooled condition. Proc. CIRP **35**, 61–66 (2015)
20. Murugappan, S., Arul, S.: Quality assessment of drilled holes in Al 6063 plate at sub zero temperature. Int. J. Appl. Eng. Res. **10**, 31329–31340 (2015)
21. Somkuwar, V.: Use of artificial neural network for predicting the mechanical property of low carbon steel. **2**, 43–49 (2013)
22. Somkuwar, V.: Prediction of hardness of high speed steel using artificial neural network. **2**, 93–98 (2013)
23. Zahran, B.M.: Using neural networks to predict the hardness of aluminum alloys. **5**, 757–759 (2015)
24. Esmaeil, A., Jamal Rajabi, J.R.: Prediction of mechanical properties of T6 heat treatment by artificial neural network. J. Asian Sci. Res. **2**, 742–746 (2010)
25. Taskin, M., Dikbas, H., Caligulu, U.: Artificial neural network (ann) approach to prediction of diffusion bonding behavior (shear strength) of ni-ti alloys manufactured by powder metalurgy method. Math. Comput. Appl. **13**, 183–191 (2008)
26. Eyercioglu, O., Kanca, E., Pala, M., Ozbay, E.: Prediction of martensite and austenite start temperatures of the Fe-based shape memory alloys by artificial neural networks. J. Mater. Process. Technol. **200**, 146–152 (2008)
27. Perzyk, M., KochaÅ ski, A.: Prediction of ductile cast iron quality by artificial neural networks. J. Mater. Process. Technol. **109**, 305–307 (2001)
28. Sivanandam, S., Sumathi, S., Deepa, S.: Introduction to Neural Networks Using MATLAB 6.0. Tata McGraw-Hill Education India (2005)
29. Reddy, N.S.: Neural networks model for predicting corrosion depth in steels. Indian J. Adv. Chem. Sci. **2**(3), 204–207 (2014)

Laser Cladding of Nickel Powder on AISI 202 Stainless Steel and Optimization of the Process Parameters

S. Martin Vinoth, P. Dinesh Babu, P. Marimuthu
and Sandesh S. Phalke

Abstract Laser cladding is a build-up manufacturing or layer by layer process in which the laser interacts with the powder and deposited on the substrate. In this study, the nickel powder was melted and deposited on the stainless steel SS202 substrate. The process parameters used are laser power, travel speed and powder feed rate. The microhardness of the clad layer was measured, and the macrostructure of the clad area was analysed. The influences of the laser process parameters are observed, and optimum parameters were obtained to improve the clad quality.

Keywords Laser cladding · Laser power · Microhardness · Macrostructure
Optimization

1 Introduction

Laser cladding is the method of adding one material over another to generate a layer. It is a process of depositing a powder or wire material over the substrate in which the laser source interacts with the powder and deposits over the substrate. Figure 1 shows the schematic figure of the laser cladding. It can be widely used in production of fabricate metal matrix composites, repairing of worn-out parts, remanufacturing and repairing of dies and tools. Due to this process, the tribological

S. Martin Vinoth (✉) · P. Dinesh Babu · P. Marimuthu · S. S. Phalke
School of Mechanical Engineering, SASTRA Deemed
to be University, Thanjavur 613401, India
e-mail: martinvinoth@mech.sastra.edu

P. Dinesh Babu
e-mail: dineshbabu@mech.sastra.edu

P. Marimuthu
e-mail: marimuthu@mech.sastra.edu

S. S. Phalke
e-mail: sanamigo002@gmail.com
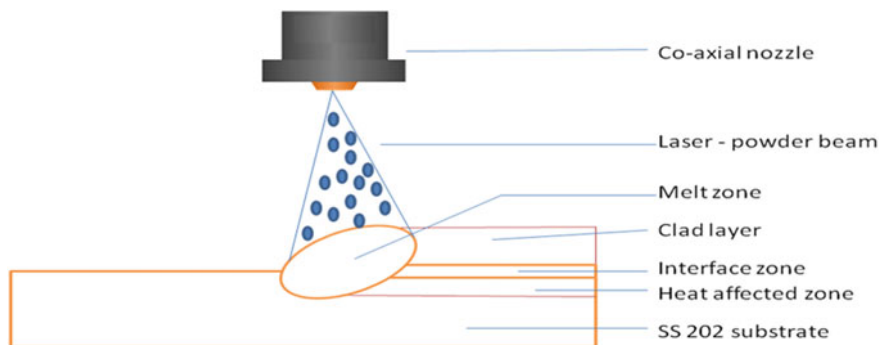
Fig. 1 Laser cladding schematic diagram

properties are also improved. This paper investigates the cladding layer of NiTi particles on H13 steel substrate with the parameters such as laser power, travel speed and pulse repetition frequency. The microhardness of the coated layer was 684 HV which is 2.5 times of its base [1]. They found that the graded layers were built up without cracks and low porosity [2]. The bonding strength can be attained in Ni60 + 50 wt%Cr_3C_2 composite outside layer with a laser power of 1.7 kW [3]. Also found that the sprocket was repaired using laser cladding and the optimal process parameters such as laser power, powder feed rate and travel speed [4]. They analysed the microstructure and fatigue fracture behaviour of EA4T steel after remanufacturing [5]. The behaviour of geometric characteristics of the aluminium coatings was examined [6]. In this study, the auto cast-iron mould was repaired by using gradient material powder technology [7]. Many engineering components need excellent surface properties such as high hardness, wear resistance, elevated temperature resistance and high corrosion resistance. A nickel-based alloy coating gives elevated metallurgical bonding strength, excellent resistance to wear and enhanced corrosion behaviour.

2 Experimental Work

In this study, nickel powder with particle size—100 mesh—was deposited on the SS202 substrate. The trials were carried out in Magod laser Pvt. The system involved of continuous-wave CO_2 laser (make Trumpf TLC 1005) with the extreme output power of 4 kW. It has a 5-axis motion systems with independent rotary axis. The diameter of laser beam was set to 3 mm, and the base was positioned 8 mm from the coaxial nozzle. Nickel powder was fed through coaxial feeder. The substrate is pre-cleaned with nitric acid to remove grease and dust particles. In order to change the power, the bonding strength between the clad layer and the substrate was increased. The laser cladding process was obtained over SS202 plate of size (160 × 120 × 5 mm) with variable travel speed, laser power and powder feed rate

Table 1 Process parameters

S. No.	Parameter	1-level	2-level	3-level
1.	Laser power (kW)	1.7	2.1	2.5
2.	Travel speed (mm/min)	500	650	800
3.	Powder feed (g/min)	8	10	12

Table 2 Experimental data with L9 orthogonal array

S. No.	Laser power— LP (kW)	Travel speed—TS (mm/min)	Powder feed rate —PFR (g/min)	Clad width (W) (mm)	Clad height (H) (mm)	Aspect ratio (W/H) %	SNRA1	Microhardness at interface zone (HV)
1.	1.7	500	8	3.3491	0.5660	5.917	−15.4420	360
2.	1.7	650	10	3.4561	0.5316	6.501	−16.2596	390
3.	1.7	800	12	3.7500	0.5189	7.226	−17.1780	410
4.	2.1	500	10	3.2601	0.5201	6.268	−15.9426	370
5.	2.1	650	12	3.4211	0.6368	5.372	−14.6027	402
6.	2.1	800	8	4.0330	0.5189	7.772	−17.8107	448
7.	2.5	500	12	3.3210	0.5125	6.480	−16.2315	398
8.	2.5	650	8	3.8591	0.5238	7.367	−17.3458	404
9.	2.5	800	10	3.8916	0.6373	6.106	−15.7151	430

to find the optimal parameter for quicker and effective laser cladding. The parameters and the levels are planned in Table 1.

To reduce the more number of trials, the trials were designed against a three level L9 orthogonal array that required nine runs. The process parameters of laser power, powder feed rate and travel speed have been varied to examine the process responses of clad quality. The process parameters were analysed based on L9 orthogonal array and are presented in Table 2.

The specimen was cut from the transversal cross sections after the cladding process. Figure 2 shows the samples with multitracks. The samples for micrograph observations were prepared using regular polishing procedures etching with the combination of copper ammonium chloride 9 g, ferric chloride 45 g, hydrochloric acid 150 ml and distilled water 75 ml solution. Figure 3 shows the geometrical quantities of a clad track with different parameters.

3 Results and Discussion

In Fig. 5, micrograph of the interface was analysed with different parameters. The cross-sectional view can be divided into three layers such as cladding zone, interface zone and substrate. The microhardness was increased with the increase in scanning speed. The interface zone has higher hardness compared to the cladded layer and substrate. In Fig. 4, the microhardness was measured with an indenter
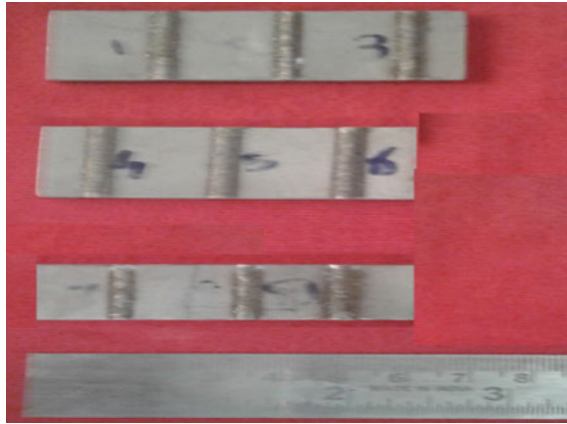
Fig. 2 Laser cladded samples with multitracks
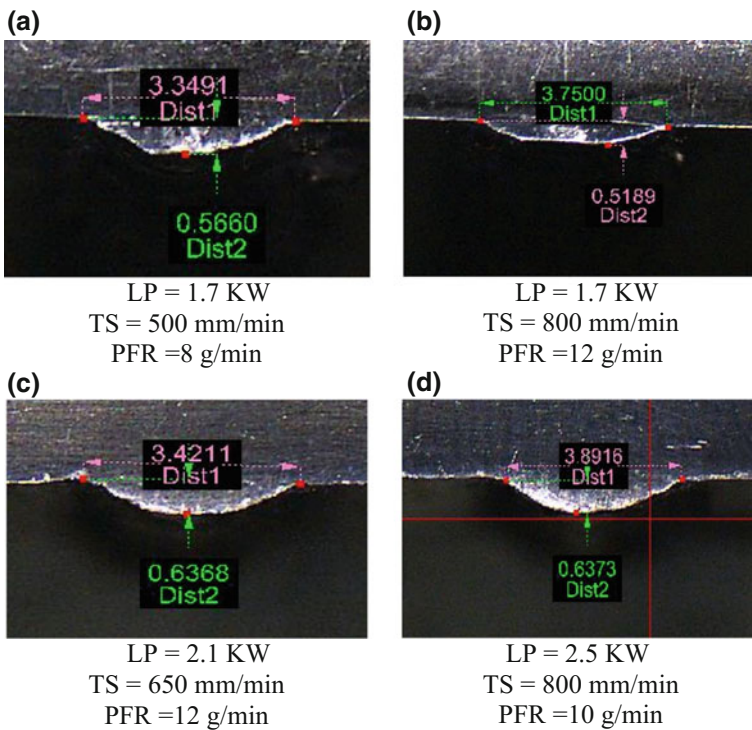
Fig. 3 Geometrical quantities of a clad track with different parameters

Fig. 4 Microhardness distribution of the clad specimen for laser power 2.1 kW, travel speed 500 mm/min and powder feed rate 10 g/min
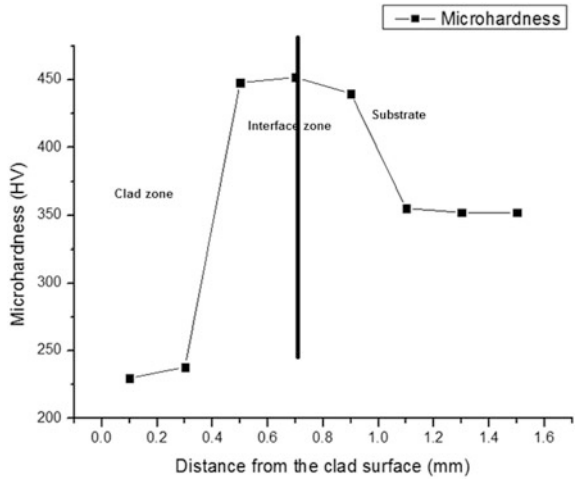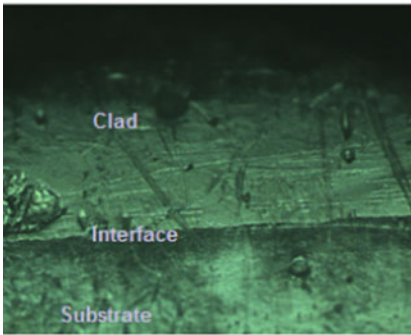
LP = 1.7 KW
TS = 500 mm/min
PFR = 8 g/min
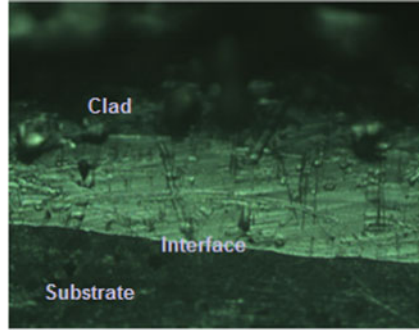
LP = 1.7 KW
TS = 800 mm/min
PFR =12 g/min
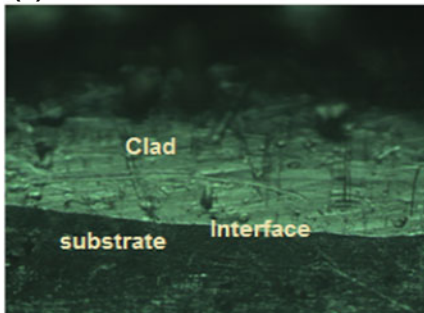
LP = 2.1 KW
TS = 650 mm/min
PFR =12 g/min
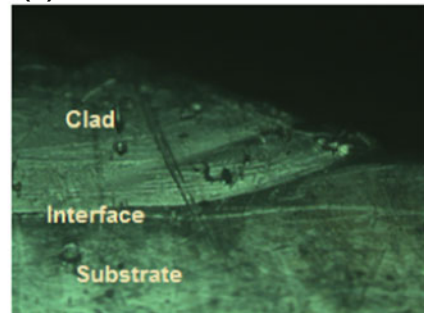
LP = 2.5 KW
TS = 800 mm/min
PFR =10 g/min

Fig. 5 Micrograph of the interface with different parameters

load of 4.903 N and the graph plotted between the microhardness and distance from the clad surface. The results indicate the hardness value was greater at the interface zone compared to the clad zone. From the Taguchi's orthogonal array, it is knowledgeable that travel speed was the most important parameter in laser cladding process.

4 Conclusions

In this experimental investigation of laser cladding of nickel powder over stainless steel 202 substrate in which the microhardness at the interface was increased. The clad layer was shaped without any cracks and only little porosity. The metallurgical bonding was realized between the layer and the substrate. The microhardness and macrostructure were analysed in detail. The high hardness was obtained in the interface zone so the bonding strength was enriched. This is implication of hardening capability of the base material. The clad height is increased with the rise of the powder feed rate. The clad width also increases with the increase in power. The main effect of every process parameters on the S/N ratio is obtainable in Fig. 6. The clad height was mostly controlled by the travel speed. In this investigation, the best possible process parameters of laser cladding are laser power 2.1 kW, powder feed rate 10 g/min and travel speed 500 mm/min and were obtained from the resulting response graph (Fig. 6), in order to get better clad without crack.
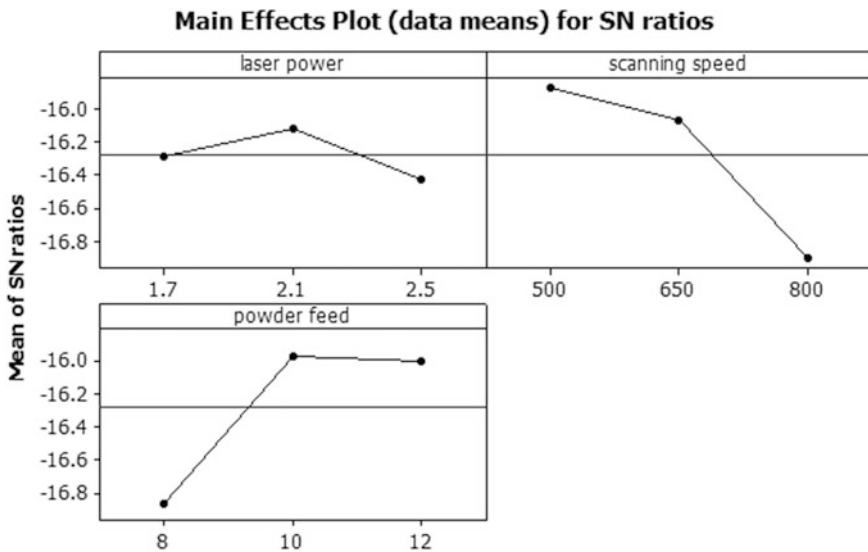
Fig. 6 Response graph for optimum aspect ratio

References

1. Norhafzan, B., Aqida, S.N., Chikarakara, E., Brabazon, D.: Surface modification of AISIH13 tool steel by laser cladding with NiTi powder. Appl. Phys. A Mater. Sci. Process. **122**, 384 (2016)
2. Ocylok, S., Weisheit, A., Kelbassa, I.: Functionally graded multi-layer by laser cladding for increased wear and corrosion protection. 359–367 (2010)
3. Pan, C., Wang, H., Wang, H., Chang, Q., Wang, H.: Microstructure and thermal physical parameters of Ni60-Cr_3C_2 composite coating by laser cladding. J. Wuhan Univ. Technol. (2010)
4. Liu, H., Hu, Z., Qin, Z., Wang. Y., Zhang, J.: Parameter optimization and experimental study of the sprocket repairing using laser cladding. Int. J. Adv. Manuf. Technol. (2017)
5. Chen, W., Chen, H., Li, C., Wang, X., Cai, Q.: Microstructure and fatigue crack growth of EA4T steel in laser cladding remanufacturing. Eng. Fail. Anal. 120–129 (2017)
6. Riveiro, A., Mejias, A., Lusquinos, F., del Val, J., Comesana, R., Pardo, J., Pou, J.: Optimization of laser cladding for Al coating production. In: Lasers in Manufacturing Conference (2013)
7. Wei, F., Qilin, D., Peng, C., Dianbing, C.: Experimental research and engineering application of laser cladding reparations. In: International Conference on Mechatronics, Electronics, Industrial and Control Engineering (2014)

Damage Sensing Through Electrical Resistive Measurement Using Electrospun PVDF-CNF Sensor

M. S. Nisha and P. Siva Kota Reddy

Abstract In this present investigation, the electrospun PVDF-CNF material was embedded between the top layers of conductive laminates which is carbon fiber-reinforced polymer (CFRP) in order to improve the multi-function property. In this study, the manufactured specimen was characterized in two ways, namely material characterization and mechanical characterization. The scanning electron microscope (SEM) and X-ray diffraction (XRD) were used for material characterization in order to determine the dispersion of CNF with the polymer and the crystalline structure of polymer, respectively. Mechanical characterization is done in two ways, namely tensile incremental–decremental loading and three-point bending test in order to determine the sensitivity of material during loading conditions, and initialization of damage to the materials was analyzed.

Keywords PVDF-CNF · CFRP · Structural health monitoring
Electrospun and damage sensing

1 Introduction

Composites are nothing but combining of two or more materials to form a structure with different properties that differ from individual elements. This plays an important role in the development of aircraft industry. Due to its enhanced properties such as tensile strength, high stiffener-to-weight ratio, these are used in aircraft structures. Nowadays, composites are used in many engineering applications mainly in aerospace and aeronautical industries because of their good physical properties such as less structural weight, good corrosion resistance, and good resistance to damage [1]. Carbon fiber-reinforced polymer composites are widely used in aerospace industry due to its very high specific strength and stiffness

M. S. Nisha (✉) · P. Siva Kota Reddy
School of Aeronautical Sciences, Hindustan Institute of
Technology and Science, Chennai 603103, India
e-mail: msnisha@hindustanuniv.ac.in

properties. [CFRP] composites are quite susceptible to various forms of damage, and common damages within CFRP composites include matrix cracking, delamination, fiber breakage [2]. Delamination is the major defect which affects the load-carrying capacity of the laminate [3]. CFRP composites are often joined by epoxy resins to prevent the stress concentration, and aggressively bonded composite materials can be found in some private aircraft. Damage that can occur in adhesive bonded material includes porosity poor bond adhesion and reduces cohesive strength of adhesive [4]. These defects can be identified by using non-destructive testing. NDT is used in this technique because the defect is identified without damaging the surface or interior part of the material. NDT is widely used in aerospace industries. There are many NDT techniques to find the defect in a material [5]. The main NDT techniques used in aerospace industries are ultrasonic testing [6], radiography testing [7], visual inspection [8], shearography testing [9], electromagnetic testing [10], and ultrasonic testing to determine the crack and damage to the aircraft. Structural health monitoring plays a major role in aerospace industry for damage monitoring in the structure. It focuses research on producing multi-functional materials which reduce weight by increasing its mechanical properties, and by means of sensing capabilities it monitors the structural health [11–13]. SHM provides information about the current state information and project performance of the structural system that enable the decision to maintain safety. A change in material (or) geometric properties of the structure that adversely affect its current and future performance can be defined as damage. Various techniques were adopted to integrate the sensors to obtain the information regarding temperature, stress, strain and vibration by means of various sensors such as strain gauge, optical fiber sensor, Micro electromechanical system (MEMS) sensor and piezoelectric sensor are used [14]. Each technique has its own limitations where the fiber optic and piezoelectric sensor are cost-intensive, embedding sensor (or) MEMS sensor downgrades the mechanical property of the structure, and even sensor will damage during different manufacturing processes. With the existing sensor manufacturing processes, introduction of health monitoring systems should be compatible. So in this study, PVDF-CNF sensor was used to monitor the damage in which it has the self-sensing capability and does not degrade its mechanical properties through embedding in the CFRP laminates. As a semi-crystalline polymer, PVDF is a versatile polymer and posses excellent piezoelectric and pyroelectric properties which makes it useful in various field such as sensor, actuators and transducer [15–17]. The crystalline structure in PVDF intensively affects its properties. PVDF consists of different crystalline phases depending on its conformation. Among these phases, α, β are common. β-phase has large spontaneous polarization per unit cell, thus exhibiting high electroactive properties which are responsible for most of the piezoelectric properties in PVDF [18]. The β-phase content in PVDF can increase by electrospinning and blending PVDF with carbon nanotube (CNT) [19]. Here, CNF is used to increase the beta phase content in PVDF. However, due to CNF structure and dimensions which facilitates dispersion during composite preparation and due to their availability in large quantities with consistent quality at price lower than CNT, CNF is interesting for large-scale application. To a better accessibility

and to improve interaction with surrounding matrix, CNF can be easily functionalized because of their stacked cup structure [20, 21]. Embedding nanofiber in CFRP reduces the internal damage to the structure. Identifying internal damage to carbon fiber-reinforced polymer (CFRP) laminates by electrical resistance change method had been firstly used [22] for sensing the damage to structure of the structural health monitoring application. The dispersion of carbon powder in the CFRP matrix [23, 24] can be used for self-diagnosing purposes. Vacuum-assisted resin transfer molding process (VARTM) used to produce modified glass fiber-reinforced epoxy composite from nanoparticles reports its electrical and mechanical properties [25].

2 Material Selections

The materials used for manufacturing sensor are (a) poly vinylidene fluoride (pvdf) molecular weight of 180,000 by sigma Aldrich (b) carbon nano fibre (CNF) of diameter 100 nm and length 20–200x/m by sigma Aldrich (C) epoxy resin araldite LY 556/hardener HY 651 (ratio 100:12 parts by weight) and carbon fibre 12 k unidirectional dry woven fabric.

3 Experimental Procedure

3.1 Polymer Solution Preparation

The PVDF-CNF polymer solution preparation has been shown in Fig. 1. A mixture of (50:50 wt% ratio) dimethyl sulfoxide (DMSO) and acetone was used as solvent for preparing solution. PVDF was dissolved in solvent and stirred for 2 h at 60 °C

Fig. 1 PVDF-CNF solution preparation steps

Fig. 2 Schematic representation of electrospinning process
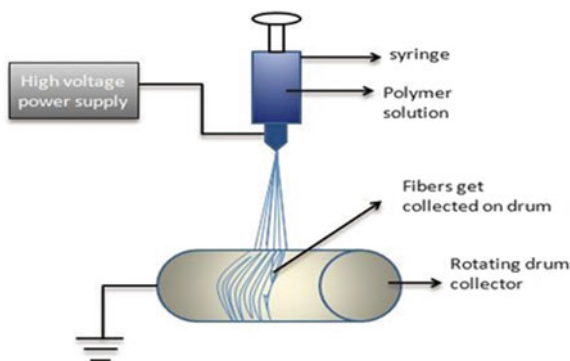
at concentration of 18 wt%, and CNF was dispersed in solvent for one hour in sonicator. The surfactant sodium dodecyl sulfate (SDS), used to stabilize CNFs, was dissolved in acetone and added along with solution. Because we need homogeneous and relatively concentration suspension for spinning process, both solutions were mixed together and stirred for 2 days to prepare a perfect solution for electrospinning process at various concentrations of CNF. Solution preparation has been done in CENCO at Hindustan University. The prepared polymer solution has been shown in Fig. 2.

3.2 Fabrication of Fiber Mat

The PVDF/CNF polymer solution prepared was now processed to form fibers using the technique of electrospinning, shown in Fig. 3. A rotating collector drum was used for fabricating aligned ultrafine PVDF/CNF. The prepared polymer solution was inserted into a syringe which has a thin needle connected to the positive electrode of a high-voltage DC power supply. The rotating drum collector was attached to the negative electrode of the high-voltage DC power supply. The vertical distance from the spinneret to the collector was about 17 cm, and high voltage of 20 kV is applied to get an aligned fiber.

According to the principle of the electrospinning process [17, 18], the polymer solution gets drained from jet and deposited on rotating drum collector to form a fiber mat of nanofiber-based composite. Figure 3 shows the prepared PVDF-CNF mat with CNF wt% of 0.5 and 1. The fiber mats have been manufactured at Research Park in IIT Madras by using the ESPIN-NANO equipment.

Fig. 3 PVDF-CNF mat of 0.5 and 1 wt%

3.3 Embedding Fiber Sensor in CFRP

For embedding PVDF-CNF sensor in carbon fiber, vacuum-assisted resin transfer molding (VARTM) is used. Ten plies of carbon fiber have been cut with dimension of 300×300 nm. And the PVDF-CNF sensor has been cut with dimension according to ASTM standards. The process of embedding sensor is shown in Fig. 4.

In order to keep CNF sensor in place and to create conductive path, conductive silver paste adhesive is used. The PVDF-CNF fiber sensor was placed in ninth plate center, which makes it easy to cut the specimen. Finally after placing glass fiber ply over ninth ply, silver adhesive was placed over the visible silver mark which provides conductive path to metal surface and cables were placed over it, to monitor the resistance changes during testing. Then, vacuum bag was placed and vacuum was supplied followed by resin infusion. Finally, the manufactured plate was allowed to cure in room temperature for 24 h and was cut according to ASTM standard specification of 25 mm $\times$ 50 mm for tensile test. For gripes, aluminum end tabbing was provided while testing.
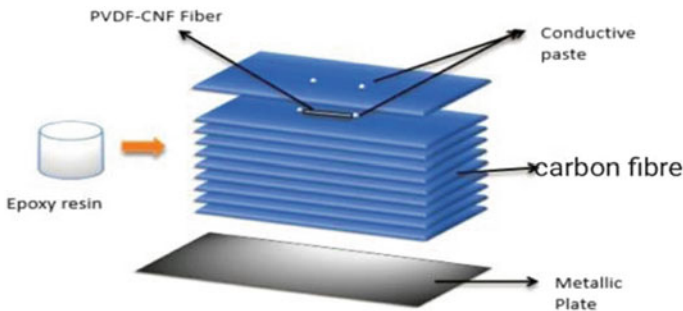
Fig. 4 Schematic representation of embedding CNF sensor in CFRP
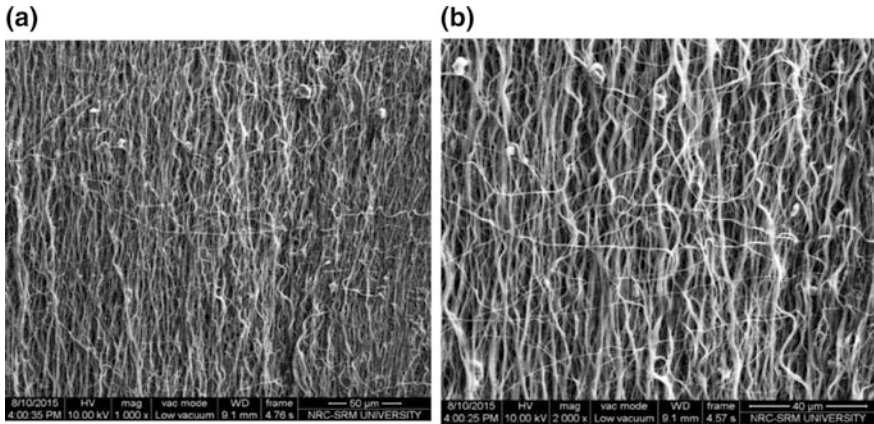
Fig. 5 SEM morphology of CNF-PVDF electrospun fiber mat (**a** 0.5 wt% and **b** 1 wt%)

4 Test Performed on Sensor

To know the characteristics like surface morphology and size of electrospun fibers, in PVDF-CNF fiber a scanning electron microscope (SEM) is used and too identifies crystalline phase present in the fiber mats and X-ray diffraction (XRD) is used. The tensile test was performed on the specimen to measure its mechanical properties and piezoresistive behavior of the fiber sensor. According to American Society for Testing and Materials (ASTM D3039), specimen was taken in of 250 mm × 25 mm dimension. The tests were conducted to evaluate sensor response in longitudinal loading axis. The load was applied to opposite arms of the specimen, while sensor response was monitored from electronic multimeter attached to the specimen. Three-point bending test is performed in UTM, where CNF faces bottom wards so tensile stress is developed in the region of fiber. Initially, the bending testing was conducted to the specimen till fracture.

5 Results and Discussion

5.1 SEM Results

Above images are the SEM images of CNF and PVDF-CNF composites. The SEM images of CNF were long and uniform in structure. The electrospun PVDF-CNF composites, the CNF, were homogenously spread in PVDF matrix. The synthesized PVDF-CNF composite has a diameter of 9.1 mm. The electron conductivity of composite is increased because it has smooth, continuous, and interconnected structure as shown in Fig. 5.

5.2 XRD Results

Above images are the results of XRD for a different weight% of CNF. In this, XRD for CNF is tested for 0, 0.5, 1 wt% of CNF composite. Among above samples for 1 wt% of CNF in composite, the β-phase is high so the electrical conductivity is also high. In 0 wt% of CNF in the composite, there is no β-phase so the electrical conductivity is very less. In 0.5 wt% of CNF in composite, the β-phase is less compared to 1 wt% of CNF so the electrical conductivity is also less compared to electrical conductivity for 1 wt% on CNF (Figs. 6, 7, and 8).

Fig. 6 0 wt% of CNF
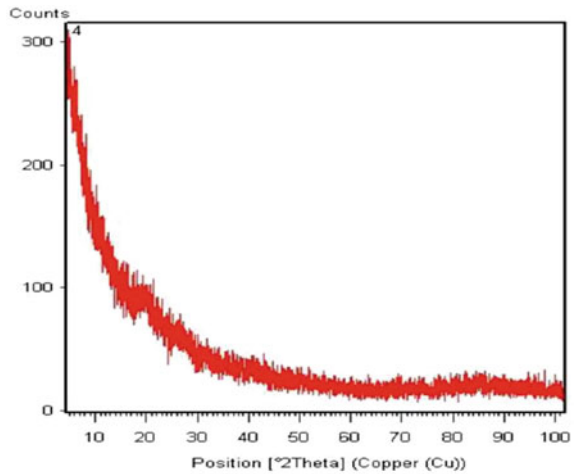
Fig. 7 0.5 wt% of CNF
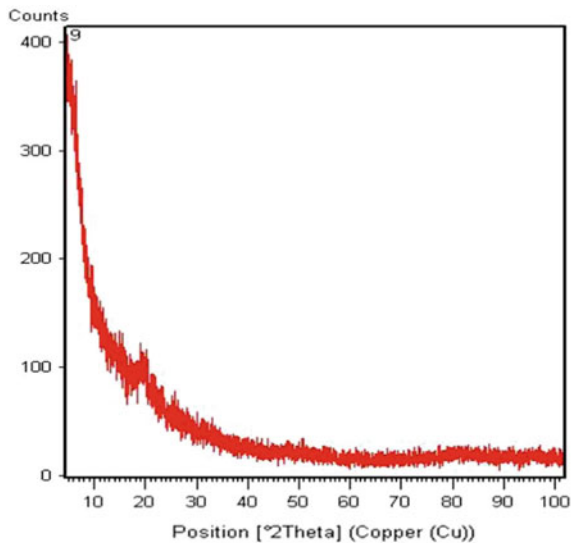
Fig. 8 1 wt% of CNF
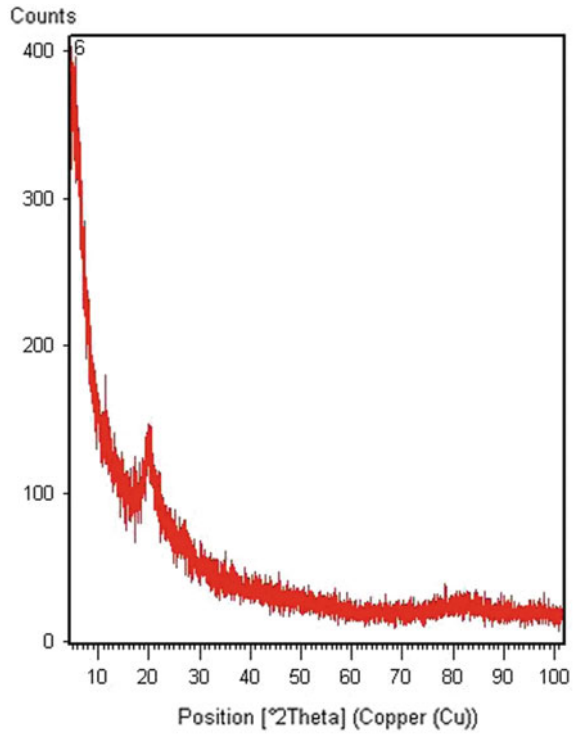
5.3 Tensile Test

The results of various weights of CNF embedded between the CFRP are shown in Figs. 9, 10, and 11. In the figures, the mechanical stress as well as the CNF fiber's electrical response $\Delta R/R_0$ variations are shown. The direct correlation between the mechanical loading and its corresponding electrical resistance was determined. The CNF can be used for tensile sensing by means of electrical resistance measurement in which the electrical resistance readings of the CNF are proportional to the loading conditions and it creates the lower value of modulus of elasticity due to damage accumulation during different loading conditions. Simultaneously, the embedded CNF resistance measurement slope will decrease during the applied strain. Thus, the performance of the CNF during damage to the composite material will inherit poor where that is simple from the tensile test.
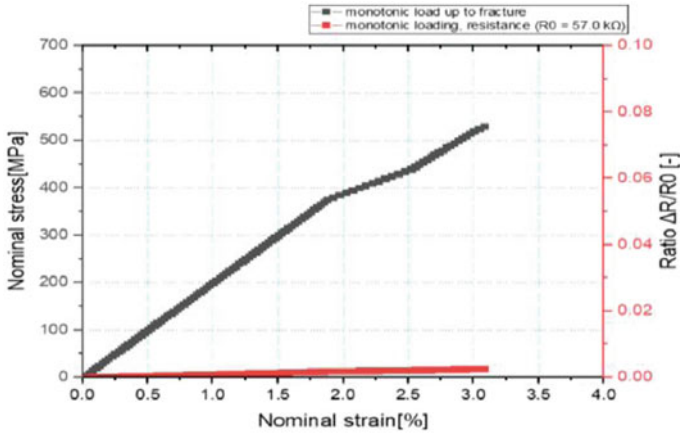
Fig. 9 0 wt% CNF
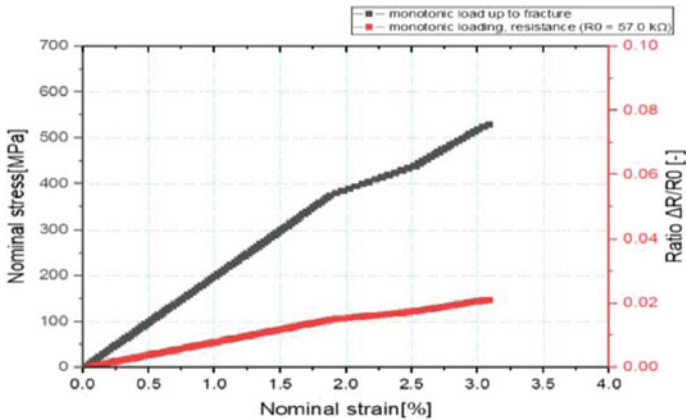
Fig. 10 0.5 wt% CNF

5.4 Three-Point Bending Moment Result

The three-point bending test was conducted by placing the embedded PVDF-CNF mat at the bottom of the specimen where if it experiences the tensile stress due to this the tensile stress has developed in the region at the fiber.

Figure 12 shows the results of the mechanical stress/strain as well as the ratio of $\Delta R/R_0$ of the monotonic test till the specimen fracture during monotonic test, the mechanical load has converted to the mechanical stress, this load is applied till the specimen fracture, and its corresponding stress and change in electrical resistance were analyzed by exponential curve fit. In this case, the exponential linear curve fit resulted in a poor correlation where $R^2 = 0.89$, but the better exponential curve fit
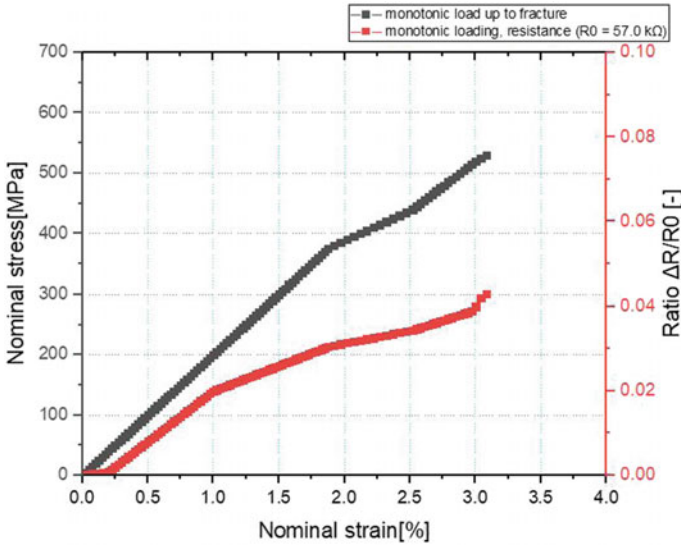
Fig. 11 1 wt% CNF
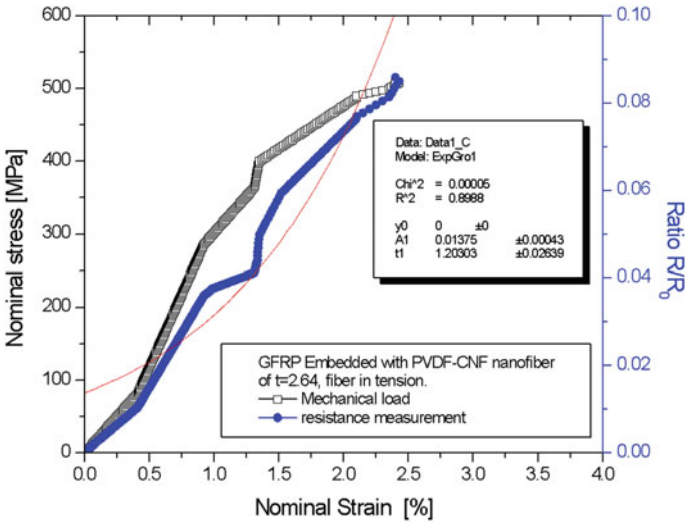
Fig. 12 Monotonic tensile test

will be $R^2 = 0.98$. So that, every specimen was tested by various incremental loading and unloading conditions to determine the exact loading step where the specimen was initiated to damage. The values for the incremental loading were distributed in different ranges from the maximum mechanical stress values of
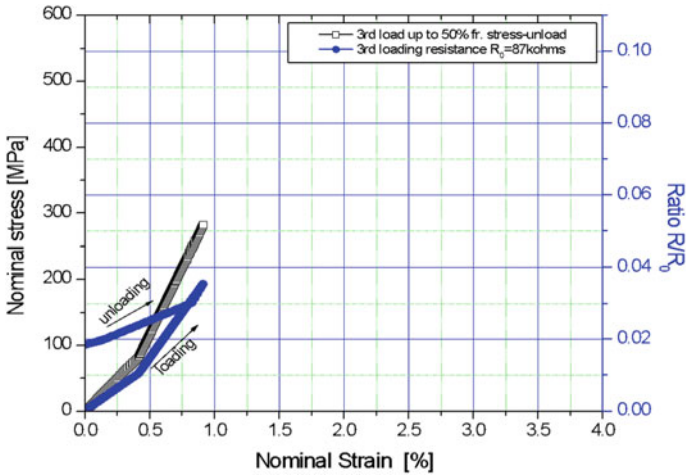
Fig. 13 Three-point bending test

monotonic test results. The 16, 38, 50, 68, 87, and 100% of fracture stresses as the 1st, 2nd, 3rd, 40th, 5th and 6th loading condition.

Figure 13 shows the 50% of fracture stress result where the third loading and unloading work processed, while unloading the sensor embedded between the laminate's response was very distinctive and created the hysteresis loop. The hysteresis loop was created due to the $\Delta R/R_0$ measurement.

When the mechanical stress comes to zero, the change in resistance did not return to zero where the residual resistance was created. In the next loading step, the residual resistance was resulting which is in the range of 4 KΩ which can be interpreted that after 200 MPa of mechanical structure, the material damage has been initiated.

6 Conclusion

In this paper, the ultrafine fibers of PVDF-CNF were fabricated via modified electrospinning technique and embedded between the CFRP. The electrical resistance was measured during the mechanical test to monitor damage to aerospace structure.

Thus, the conclusions are:

- CNF helps to improve the electrical conductivity on CFRP composites.
- Linear changes were seen with electrical resistance of fiber at different tensile loading conditions during mechanical stress applied in order to prove that there is no degrading of mechanical property of sensor.

- CNF can be used in aircraft structure like fuselage and wing to detect the damage to structure, due to overload or malfunction.
- From the three-point bending test, the embedded PVDF-CNF specimen effectively identified the instructive of damage to the specimen during the 50% of fracture stress which results as the hysteresis loop is created during the unloading condition due to the residual resistance.
- The PVDF-CNF conductive sensor has enough sensitivity to detect the damage to the matrix cracks before failure occurs, due to its small size and large surface area, its increase sensitivity of damage to structure by using electrical resistance measurement.

References

1. Chou, T.-W.: Microstructural Design of Fiber Composites. Cambridge University Press (2005)
2. Todoroki, A., Kobayashi, H., Matuura, K.: Application of electric potential method to smart composite structures for detecting delamination. JSME Int. J. Ser. A, Mech. Mater. Eng. **38**(4), 524–530 (1995)
3. Todoroki, A., Tanaka, Y.: Delamination identification of cross-ply graphite/epoxy composite beams using electric resistance change method. Compos. Sci. Technol. **62**(5), 629–639 (2002)
4. Karapappas, P., et al.: Enhanced fracture properties of carbon reinforced composites by the addition of multi-wall carbon nanotubes. J. Compos. Mater. **43**(9), 977–985 (2009)
5. Adams, R., Cawley, P., Pye, C., Stone, B.: A vibration technique for non-destructively assessing the integrity of structures. J. Mech. Eng. Sci. **20**(2), 93–100 (1978)
6. Aggelis, D.G., Paipetis, A.S.: Monitoring of resin curing and hardening by ultrasound. Constr. Build. Mater. **26**(1), 755–760 (2012). https://doi.org/10.1016/j.conbuildmat.2011.06.084
7. Bull, D.J., Spearing, S.M., Sinclair, I., Helfen, L.: Three-dimensional assessment of low velocity impact damage in particle toughened composite laminates using micro-focus X-ray computed tomography and synchrotron radiation laminography. Compos. A Appl. Sci. Manuf. **52**, 62–69 (2013). https://doi.org/10.1016/j.compositesa.2013.05.003
8. Kalinichenko, N.P., Kalinichenko, A.N., Lobanova, I.S., Borisov, S.S.: Methods for the manufacture of nonmetallic reference specimens for liquid-penetrant inspection. Russ. J. Nondestr. Test. **49**(11), 668–672 (2013)
9. Hung, Y.Y., Yang, L.X., Huang, Y.H.: 5-Non-destructive evaluation (NDE) of composites: digital shearography. In: Karbhari, V.M. (ed.) Non-Destructive Evaluation (NDE) of Polymer Matrix Composites, pp. 84–115. Woodhead Publishing
10. Koyama, K., Hoshikawa, H., Kojima, G.: eddy current nondestructive testing for carbon fiber-reinforced composites. J. Press. Vessel Technol. **135**(4), 041501 (2013). https://doi.org/10.1115/1.4023253
11. Newswire, P.: Global non-destructive testing (NDT) equipment market—by technology (Ultrasonic, Eddy Current, Electromagnetic, Radiography, Thermography), Verticals (Manufacturing, Petrochemical, Aerospace, Automotive, Power Generation) & Geography (2013–2018), PR Newswire (2013)
12. Balageas, D., Fritzen, C.-P., Güemes, A.: Structural Health Monitoring. Wiley-ISTE, London (2006)
13. Cai, J., Qiu, L., Yuan, S., Shi, L., Liu, P., Liang, D.: Structural health monitoring for composite materials. In: Composites and its applications Chap. 3 (2012)

14. Farrar, C.R., Worden, K.: An introduction to structural health monitoring. Philos. Trans. R. Soc. V:365 (2007)
15. Belouadah, R., Kendil, D., Bousbiat, E., Guyomar, D.: Guiffard B 2009 electrical properties of two-dimensional thin films of the ferroelectric material Polyvinylidene Fluoride as a function of electric field. Phys. B **404**, 1746 (2009)
16. Broahurst, M.G., Davis, G.T., McKinney, J.E., Collins, R.E.: Piezoelectricity and pyroelectricity in polyvinylidene fluoride—a model. Appl. Phys. **49**(10), 4992 (1978)
17. Chen, Q.X., Payne, P.A.: Industrial applications of piezoelectricity polymer transducers. Meas. Sci. Technol. **6**, 249–267 (1995)
18. Chang, J., Dommer, M., Chang, C., Lin, L.: Piezoelectric nanofibers for energy scavenging applications. Nano Energy **1**, 356–371 (2012)
19. Huang, S., Yee, W.A., Tjiu, W.C., Liu, Y., Kotaki, M., Boey, Y.C.F., Ma, J., Liu, T., Lu, X.: Electrospinning of polyvinylidene difluoride with carbon nanotubes: synergistic effects of extensional force and interfacial interaction on crystalline structure. Langmuir **24**, 13621–13626 (2008)
20. Kang, I., et al.: Introduction to carbon nanotube and nanofiber smart materials. Wren Compos. Part B **37**, 382–394 (2006)
21. Feng, L., Xie, N., Zhong, J.: Carbon nanofibers and their composites: a review of synthesizing, properties and applications. Materials **7**, 3919–3945 (2014)
22. Wichmann, M.H.G., Sumfleth, J., Gojny, F.H., Quaresimin, M., Fiedler, B., Schulte, K.: Glass-fibre-reinforced composites with enhanced mechanical and electrical properties—benefits and limitations of a nanoparticle modified matrix. Eng. Fract. Mech. **73**(2346–59), 626 (2006)
23. Muto, N., Arai, Y., Shin, S.G., Matsubara, H., Yanagida, H., Sugita, M., et al.: Compos. Sci. Technol. 61, 875–883 (2001)
24. Lee, J.-J., Seo, D.-C.: Damage detection of CFRP laminates using electrical resistance measurement and neural network. Compos. Struct. **47**, 525–530 (1999)
25. Nisha, M.S., Singh, D.: Manufacturing of smart nanomaterials for structural health monitoring (SHM) in aerospace application using CNT and CNF. J. Nano Res. (2016)

Investigations on Fabrication Techniques of Aluminium-Based Porous Material

Daljeet Singh, Ankesh Mittal, Vivek Jain, Dheeraj Gupta and V. K. Singla

Abstract The intention of this paper is to investigate the fabrication of aluminium-based porous material. The fabrication is done by two methods: the conventional drilling method and a non-conventional gas-releasing blowing agent technique. The experiments were conducted to compare the optimum value of porosity, compressive strength and metallurgical values. The non-conventional technique results in the aluminium foam with lightweight. The results show that the energy absorption capacity due to constant plateau stress and porosity is high in aluminium foam whereas compressive strength is low in this case. The conventional method has a great advantage to control the pore morphology such as the uniformity of pores, structure of pores. Energy diffraction X-ray spectroscopy and scanning electron microscope techniques are used for characterizing the aluminium metal foam.

Keywords Pure aluminium · $CaCO_3$ · Gas-releasing blowing agent
CNC drilling · SEM

1 Introduction

The porous material is basically the skeletal portion of the material. The pores are generally filled with a liquid or gas. In the previous decade, the porous material and its advantages captivate the many researchers. The application area of the porous material is very broad, and the fabrication of porous material directly depends upon the applications of the particular material [1]. Porous materials are used for energy and sound absorbing, filters, heat insulating, lightweight structure, biomedical implants with different properties [2]. There are several methods for the fabrication

D. Singh (✉) · V. Jain · D. Gupta · V. K. Singla
Department of Mechanical Engineering, Thapar University, Patiala 147004, India
e-mail: er.daljeetsandhu93@gmail.com

A. Mittal
SLIET Longowal, Sangrur 148106, India

of porous material like selective laser sintering, 3D fibre deposition method, hydrofluoric acid, radio frequency (RF) magnetron sputtering, injection moulding. These methods are widely used for the fabrication of porous material, but the conventional techniques (when tool physically touches the work piece) are not used in these days. Basically, foams are fabricated according to applications and purpose in the industries [3]. Cost-efficient production processes enabled their acceptance in several industrial sectors. So, based on the applications, the fabrication can be classified into two categories: fabrication of porous material using conventional method and fabrication of aluminium foam using non-conventional technique [4]. The properties are seriously depending upon the porosity, fabrication methods and material that is used [5, 6]. The porous material has different physical and chemical properties, and it behaves unlike due to alveolate structure [7]. So, the traditional tensile testing method substitute with compression test can give significant results. The alternative conventional drilling method is used for unidirectional pores, and if it is compared with non-conventional machining method, its eco-friendly process like no chemical reaction is there. The uniform porous structure is not only used for energy absorption but also used in heat exchanger/sinks and other heavy applications [8]. The fabrication of porous material with CNC drilling can be realized in the absence of any kind of chemical reaction because of its pure machining process, and it is best to control pore morphology with different parameters [9]. The pore size, structure, position and porosity can also be decided by the shape and size of the tool. Therefore, the method of CNC drilling is easier and simple than non-conventional ones.

In this research, the author tries to explore the possibility of fabrication to inaugurate this new fabrication method and exchange view about the properties with non-conventional technique.

2   Experimental Work

The method used for the fabrication of aluminium metal foam is gas-releasing particle decomposition. The blowing agents like NaCl and $MgCO_3$ are added in the molten aluminium for the fabrication of aluminium foam. When these foaming agents are heated above the melting temperature, they release gasses, which help to create pores in metal. For the experimental procedure, 500-gm solid-state aluminium is placed inside the furnace and set the melting temperature of furnace between 670 and 690 °C. Add 5–10% silica carbide and 2–3% calcium carbonate to increase the viscosity. The powder foam $MgCO_3$ (1–2%) is added uniformly and stirred with the help of graphite stirrer continuously. When the media is heated above 465 °C, magnesium carbonate decomposes into Mg and CO_2. So, when $MgCO_3$ particles are added with molten aluminium, the large amount of carbon dioxide is produced which helps to fabricate pores. The media (Aluminium+ $MgCO_3$) heated above the melting temperature for 7–10 minutes to evaporate the $MgCO_3$ and again cooled it for solidifying the foam. The fabrication of aluminium

foam has been done after the solidification of heated media. The porosity of aluminium porous material based on the content of foaming agent can change this particular property after changing the quantity of $MgCO_3$. The experimental procedure is shown in Fig. 1.

The other approach used for the fabrication of pores in solid aluminium is conventional drilling method, which helps to control pore morphology and uniformity of pores. During this process, drilling tool physically touches the work piece and fabricates holes. For the experiment, cut the pure aluminium work piece in cube shape with 10 mm dimensions (shown in Fig. 2). The tool used for drilling is 1 mm diameter and should have more strength so high-speed steel tool with little bit drift and chatter is used which provided better accuracy. The drilling operation is performed with the help of vertical drilling machine which is computer numerical control with some specifications, like spindle speed should vary from 60 to 6000 rpm, feed rate from 1 to 5000 mm/min and tool changing time up to 2.5 s. Execute the program as per the requirement with the help of G and M codes. The tool should have more strength than the sample material, so high speed steel drills are selected with tittle bit drift and chatter to work easly. The centre distance between the holes is 1.8 mm. Select the feed rate for aluminium as 10, 8 and 5 mm/min with spindle speed 1200, 1500 and 1800 rpm, respectively. The tool was sticking in the workpiece with high feed rate and low spindle speed. but with 5 mm/min feed rate and 1800 rpm spindle speed the tool is go through the workpiece with cycle time 240 seconds. Figure 3 shows the unidirectional pores are fabricated in solid aluminium and made it porous material. The fabrication of aluminium porous material by this method has many keys, like changing the drilling tool can change the pore morphology.
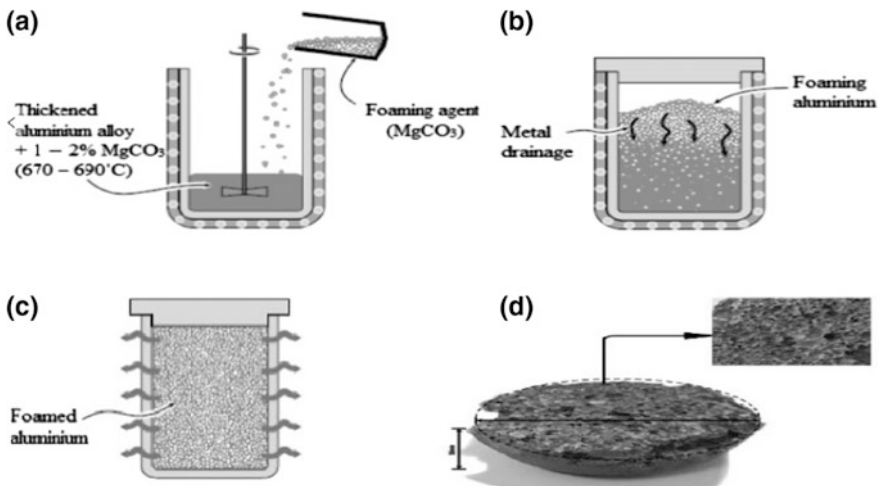
Fig. 1 Particle decomposition in liquid aluminium: **a** adding forming agent, **b** isothermal forming, **c** cooling of aluminium porous and **d** shows the surface of aluminium porous material
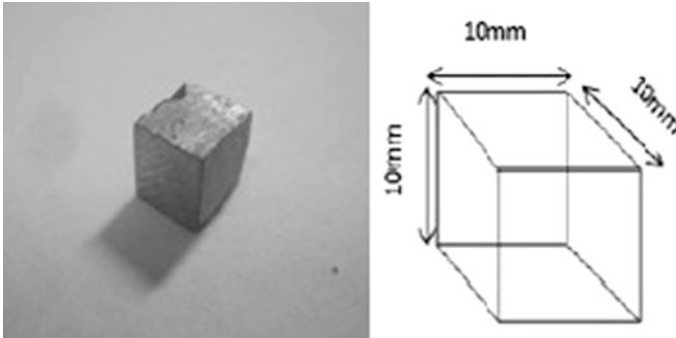
Fig. 2 Pure aluminium work piece

Fig. 3 Aluminium work
piece after drilling

To investigate the behaviour of both types of porous material, we need to perform some experiments on it. Due to the alveolate structure, foam behaves differently in testing. So, traditional tensile testing method is replaced with compression testing. The plateau stress in case of metal foam is the main property because tensile strength of foams is nearly the same as the stress, where plateau stress occurs. The compression tests are conducted by 1000 kN compression testing machine. The load has been applied gradually in a controlled manner of 1–1.5 kN by manually operated hydraulic jack. To find the porosity of both samples, use the Archimedes principle. The measuring tube filled up to certain level and find the volume of sample after immersed in fluid. The change in volume of fluid helps to findout the porosity level. Scanning electron microscope is used to diagnose the wall thickness, crack on surface and pore uniformity. Energy diffraction X-ray spectroscopy characterizes the presence of different elements and finds the percentage contribution of different elements in metal foam.

3 Results and Discussions

3.1 Compressive Strength

The stress–strain curve for aluminium metal foam is shown in Fig. 4. The foam behaves elastically with less strain rate in starting and cross-head travel approximate 1 mm with load less than 1 kN. Then, start the brittle crushing of porous wall with increasing cross-head travel distance (3–6 mm) as shown in Fig. 5 and show the constant or slightly increasing value of strain. The 70% deformation of the object was done with 1.8 kN load. Deformation shows constant plateau stress through collapse area that means high energy absorption capacity is available in metal foam. The behaviour of aluminium foam at different cross-head travel distances under the compression testing machines is shown in Fig. 5.

Figure 6 shows the graphical representation for compressive strength of aluminium porous material. Load is continuously increasing with increasing of cross-head travel distance. Deformation with load shows an increasing plateau stress, which means energy absorption capacity is low and compressive strength is high. Figure 7 shows the behaviour of aluminium porous material under
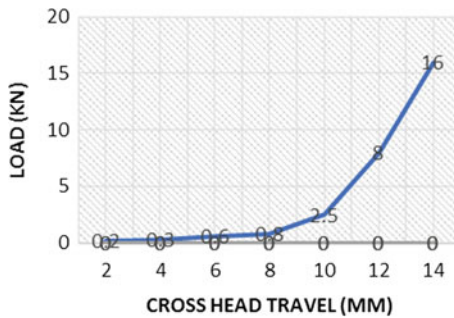
Fig. 4 Stress–strain curve for aluminium foam
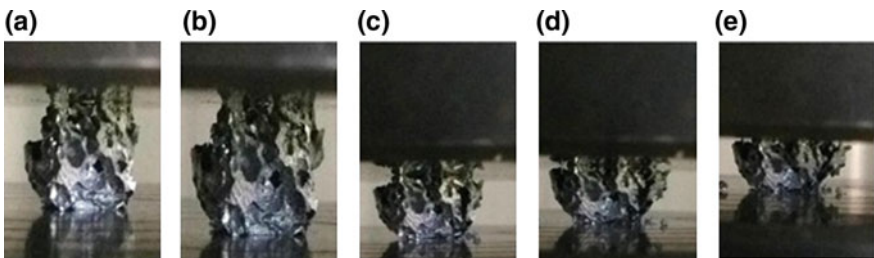
Fig. 5 Behaviour of metal foam **a** at 0 mm, **b** at 1 mm, **c** at 3 mm, **d** at 6 mm, **e** at 8 mm cross-head travel
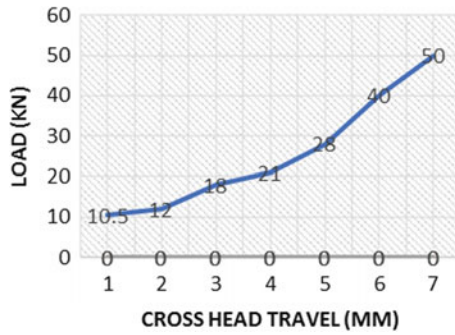
Fig. 6 Stress–strain curve for aluminium porous
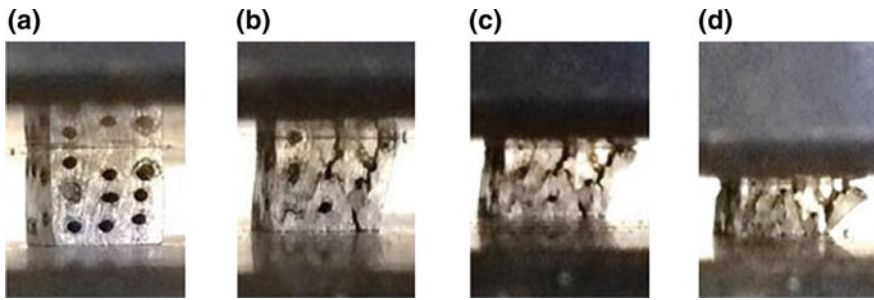
Fig. 7 Behaviour of aluminium porous: **a** at 0 mm, **b** at 1 mm, **c** at 3 mm, **d** at 5 mm cross-head travel

compression testing machine at different load conditions. The load during testing continuously increases and crushes the sample at different cross-head distances. The maximum travel distance will show the high compressive load.

3.2 Porosity

It is essential to behave multiple functions in addition to pore size, shape and surface area, such as porosity and metallurgical values of the sample. The porosity of aluminium metal foam and aluminium porous material is measured by Archimedes principle. Find out the volume of samples and apparent volume for mathematical calculations. The results are shown in Table 1; the aluminium metal foam has high porosity value followed by aluminium porous material.

Table 1 Mathematical values of the porosity

Sample	Volume of sample (SV) (cm^3)	Apparent volume (AV) (cm^3)	Voids volume (VV) = AV-SV (cm^3)	Porosity = VV/AV	Porosity (%)
Aluminium metal foam	1.32	4.574	4.574 − 1.32 = 3.254	3.254/ 4.57 = 0.71	71
Aluminium porous material	0.216	0.585	0.585 − 0.216 = 0.368	0.368/ 0.585 = 0.629	62.9

3.3 Metallurgical Tests

3.3.1 Scanning Electron Microscope

SEM inspection is basically used to analyse the surface shape, cracks and porosity, which provide the high magnification image (up to 50000×) with an acceleration voltage of 10 kV. Figure 8 shows the non-uniformity of pores and metal oxide filaments remaining in the edges of pores. The boundaries between the actual particles and matrix generated between the walls are clearly shown. These oxide filaments may reduce the thermal conductivity of the aluminium foam.

3.3.2 Energy Diffraction X-Ray Spectroscopy

The energy diffraction X-ray spectroscopy shows the aluminium and oxygen with maximum surface area because the aluminium is parent metal, and it is cooled in open atmosphere, where the oxygen was mixed with the aluminium foam. Figure 9 shows the different contribution of metals and alloys in aluminium foam. Yellow line shows the participation of oxygen with maximum contribution, and purple line shows the calcium with minimum contribution. Table 2 represents the presence of different elements in aluminium foam with weight and atomic percentage. The oxygen has maximum contribution followed by aluminium and carbon.
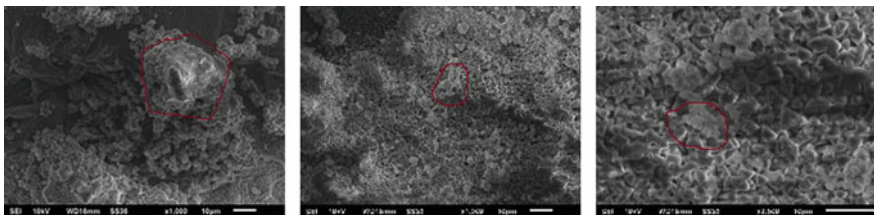
Fig. 8 SEM images of aluminium metal foam at different magnifications
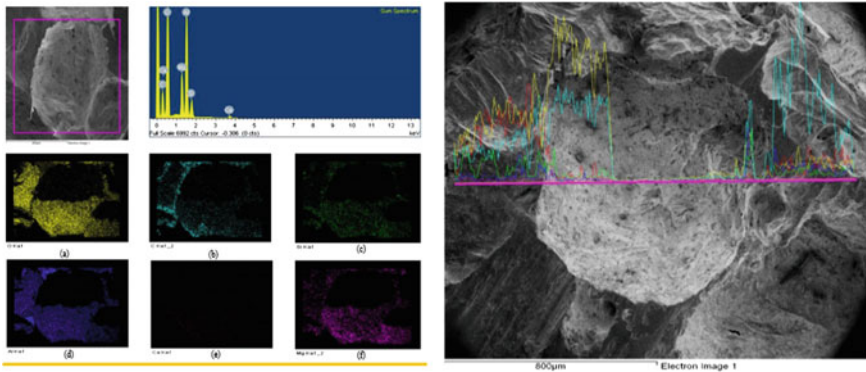
Fig. 9 Spectrum and line mapping of entire elements on selected surface of aluminium foam

Table 2 Weight and atomic percentage of different elements in aluminium foam

Elements	Weight (%)	Atomic (%)
C	15.97	22.85
O	41.75	55.70
Mg	4.82	3.16
Al	35.33	16.11
Si	1.91	1.08
Ca	0.29	0.12
Total	100	

4 Conclusion

The simple fabrication method is used in order to develop aluminium porous material which has unidirectional pores. The following conclusions were obtained.

(1) The behaviour of aluminium metal foam is totally different from aluminium porous material during compression test. Aluminium metal foam has more constant plateau stress, so it can absorb more energy. The highly porous and light weight material can use in automoblies crash boxes to absorb energy during collision. The weight and density ratio in aluminium foam is very less as compared to conventional technique.

(2) The compressive strength is low in aluminium foam as compared to parent metal, but in case of aluminium porous material the compressive strength is close to parent material with lightweight. So, the aluminium porous material can be used for high strength applications like self-lubricating bearing.

(3) The metallurgical test shows oxide formation on pore cells, which effects the conductivity of metal foam.

(4) In future, the assistance of blowing agents could cause change in strength and relative density of metal foam. Porosity could change with change in formation

time, and simple drilling tool can replace with gang drill; wherever no requirement of large NC programming and repeating operations, it would be less time-consuming.

References

1. Izakishi, K.: Porous material. In: Process Technology and Applications. London (1998)
2. Louis-Philippe, L.: Porous metals and metallic foams, current status and recent developments. Adv. Eng. Mater. **10**(9), 775–787 (2008)
3. John, Banhart: Manufacture, characterisation and application of cellular metals and metal foams. Prog Mater. Sci. **46**(6), 559–632 (2001)
4. Noh, R., Razali1, M., Abdullah, B., Muhammad Hussain, I.: Mechanical properties of aluminium foam by conventional casting combined with NaCl space holder. Appl. Mech. Mater. **393**, 156–160 (2013)
5. Andy, T.: Fabrication of porous material for micro component application by direct X-ray lithography and sintering. Microelectron. Eng. **98**, 297–300 (2012)
6. Michailidis, N., Maliaris, G.: Computational-experimental investigation of milling porous aluminium. CIRP Ann Manuf. Technol. **66**, 121–124 (2017)
7. Chen, C.H., Takita, K., Honda, S., Awaji, H.: Fracture behaviour of cylinderical porous alumina with pore gradient. J. Eur. Ceram. Soc. **25**(4), 385–391 (2005)
8. Hokamoto, K., Shimomiyab, K.: Fabrication of unidirectional porous-structured aluminium through explosive compaction using cylindrical geometry. J. Mater. Process. Tech. **251**, 262–266 (2018)
9. Shinsuke, S.: Fabrication of porous aluminium alloys with aligned unidirectional pores by dipping pipes into liquid semi-solid base material. Proc. Mater. Sci. **4**, 85–89 (2014)

Optimization of Electrical Parameters for Machining of Ti–6Al–4V Through TOPSIS Approach

T. Praveena and J. Prasanna

Abstract This paper deals with improvisation of electrical parameters which are necessary for working of micro-electrical discharge machining (micro-EDM/μ-EDM). TOPSIS formulation was used for the evaluation purpose. The advancement of electrical parameters was done to increase the material removal rate (MRR) and understate the tool wear rate (TWR) and overcut (OC). A prototype has been built up to carry out the investigations. Being difficult to cut material, Ti–6Al–4V was used for the assessment. The experiments were conducted by the design of experiments through Taguchi's orthogonal array with three electrical factors, viz., peak current (I_p), pulse on time (T_on), and duty factor (DF) at three levels. The results were analyzed by TOPSIS method. It leads to better results than other optimization methods. Finally, ANOVA test was performed to accomplish the contributions of the working parameters toward the quality characteristics.

Keywords Micro-EDM · Micro-hole · Optimization · Taguchi TOPSIS

1 Introduction

The emergence of micro-machining gives rise to extensive advances in the microelectromechanical systems (MEMS) and semiconductor industry. It also is used variedly in the production of micro-parts in automotive, electronics and communication, environmental, and in general healthcare products [1]. Micro-holes are used in various applications like inkjet printer nozzle, fuel injection nozzle, cooling channels in turbine blades, microsensors, drug delivery orifice [2]. Many techniques are there in the market to carry out the making of micro-holes and structures [3]. The micro-EDM is such a magnificent machine work on the same principle of electrical discharge machining (EDM). Due to the scaling down of

T. Praveena (✉) · J. Prasanna
Department of Mechanical Engineering, CEG, Anna University, Chennai, India
e-mail: tpraveena.au@gmail.com

EDM, the system leads to the modification in circuit design and hence the process parameters [4]. The dissimilarity between conventional EDM and μ-EDM is the pulse generator, tool range, and axes movement. The pulse produced by the μ-EDM is in microseconds; hence, the discharge produced in the gap by μ-EDM is of the order of 10^{-9}–10^{-5} J. Tool size (thickness or dia) ranges from 1 to 999 μm. The three-axis (X, Y, and Z) movements allow the job to produce complex and precision structures [3]. Various μ-EDM researches were studied through [5–7].

A small hole (0.4 mm) dry drilling of titanium alloy had done by Prasanna et al. [8]. Pradhan et al. [9] tried out to make micro-hole on titanium alloy (Ti–6Al–4V) to examine the issues of operating parameters on the execution parameters of micro-EDM. Ti–6Al–4V alloy has been widely used in the production of turbine blades, aeronautical wings, biomedical instruments, and many consumer products [1] where it desires high corrosion resistance. Besides this, Ti–6Al–4V is an electrically conductive material, high strength-to-weight ratio and withstands high temperature. Consequently, it can be easily machined by EDM process [10, 11]. Optimization of process parameters is done through various techniques like Taguchi, ANOVA, gray relational analysis (GRA) [12], response surface methodology (RSM) [13], artificial neural networks (ANNs) [14, 15], and TOPSIS [16]. Prasanna et al. [8] carried out optimization of machining parameters by means of Taguchi and gray relational investigation for small hole dry drilling. Tiwary et al. [13] analyzed the action of various control parameters on machining of Ti–6Al–4V. They have used central composite design (CCD) for the experiments. Athawale et al. [17] selected the appropriate CNC machine with the use of TOPSIS algorithm, which is an efficient multi-criteria decision matrix (MCDM) tool for finding such type of complex conclusion-making problems in industrialized domain [18]. Senthil Kumar et al. [16] used the TOPSIS method for optimizing the control parameters. They have found that the optimized process parameters give better results.

The literature survey shows the importance of micro-holes in various systems. This paper presents the optimization of electrical machining parameters on micro-hole of Ti–6Al–4V. A multi-response optimization (TOPSIS) method is used here to explore the optimum working condition for the developed μ-EDM.

2 Experimental Details

2.1 Experimental Setup

This experimental work uses an internal model, which produces micro-discharges for various ranges of operating parameters. The experimental setup of the developed μ-EDM has been illustrated in Fig. 1. A centrical flushing was made with the help of the submergible pump. The tool is made anode, and the workpiece is made

Fig. 1 Experimental setup of μ-EDM process
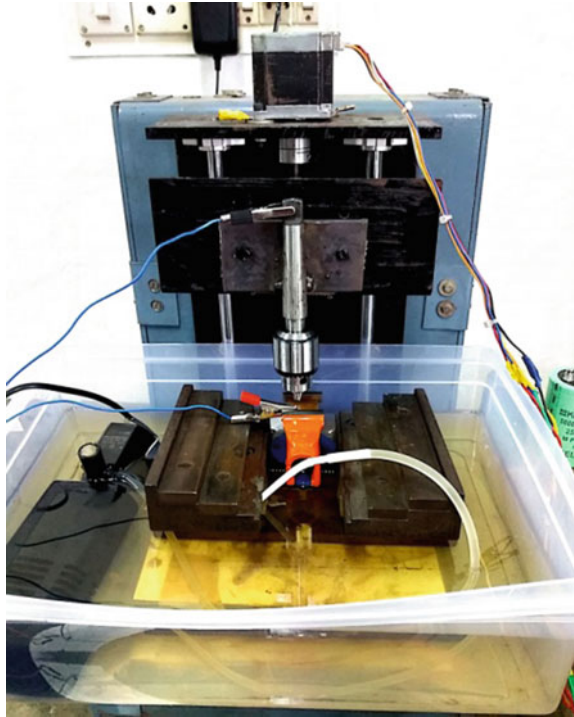
Table 1 Operating conditions of the developed micro-EDM

Operating parameters	Operating condition (V)
Working voltage	150
Gap voltage	40
Servo voltage	5

Table 2 Materials and dimensions

Accessories	Materials	Dimension (mm)
Tool	Copper	φ 0.25
Workpiece	Ti–6Al–4V	2.5 × 2.5 × 0.5
Dielectric	Commercial EDM oil	–

cathode (reverse polarity). The working conditions of the machine have been given in Table 1. The working materials and its dimensions are given in Table 2.

2.2 Methodology

In this experiment, micro-hole of 0.25 mm dia is machined on the Ti–6Al–4V. The elemental composition of Ti–6Al–4V has been given in Table 3. It considered three

Table 3 Elemental composition of Ti–6Al–4V

Element	C	Al	V	Fe	Ti
Weight (%)	0.012	6.07	4.2	0.02	89.698

Table 4 Experimental parameters and their stages

Process parameters	Symbols (Unit)	Levels		
		1	2	3
Peak current	I_p (A)	0.5	1	1.5
Pulse on time	T_{on} (μs)	50	500	1000
Duty factor	DF (%)	0.3	0.5	0.7

Table 5 L_9 orthogonal array and experimental results

Ex. No.	Process parameters			Experimental results		
	I_p	T_{on}	DF	MRR	TWR	OC
1.	0.5	50	0.3	0.00226	0.00035	0.15
2.	0.5	500	0.5	0.00270	0.00098	0.16
3.	0.5	1000	0.7	0.00345	0.00155	0.16
4.	1	50	0.5	0.00222	0.00061	0.12
5.	1	500	0.7	0.00319	0.00104	0.15
6.	1	1000	0.3	0.00241	0.00079	0.14
7.	1.5	50	0.7	0.00332	0.00173	0.13
8.	1.5	500	0.3	0.00338	0.00098	0.16
9.	1.5	1000	0.5	0.00409	0.00327	0.18

factors at three levels and is given in Table 4. The experiments were carried out through the design of experiments with the use of L_9 orthogonal array based on Taguchi's design matrix given in Table 5. The length of the tool has been measured before and after each experiment using the scale. Extra machining time was given to each experiment for complete piercing of the tool electrode through the workpiece. This could avoid the tapering of the holes. The machining time of each experiment was recorded.

The images of the machined holes have been captured through the Dewinter optical microscope. The diameter of the entry and exit side of hole has been measured using the Dewinter Material Plus Software. MRR, TWR, OC are the performance parameters calculated using the formulae given below.

Calculation of MRR

MRR is the volume of material removed over the machining time.

$$D_a = \frac{D_t + D_b}{2} \tag{1}$$

$$V_m = \frac{\pi}{4} D_a^2 h \tag{2}$$

$$\text{MRR} = \frac{V_m}{t} \text{ mm}^3/\text{min} \tag{3}$$

where

D_a The average diameter of the entry (D_t) and exit (D_b) side of the machined hole,
h Depth of the machined hole, and
t   Machining time.

Calculation of TWR

The tool wear rate has been obtained by the volume of material removed out over the machining time.

$$V_e = \frac{\pi}{4} D_e^2 L_e \tag{4}$$

$$\text{TWR} = \frac{V_e}{t} \text{ mm}^3/\text{min} \tag{5}$$

where

D_e Diameter of the tool electrode and
L_e Length of the eroded tool.

Calculation of OC

The overcut of the machined hole has been calculated by the difference of average diameter of the machined hole by the electrode dia.

$$\text{OC} = D_a - D_e \text{ mm} \tag{6}$$

2.3 *Implementation of TOPSIS*

Technique for Order Preference by Similarity to an Ideal Solution is TOPSIS. It is one of the multi-criteria models in making decision. This technique is employed for its simplicity and rationality. It has the ability to compute the relative performance for each alternative by its good computational efficiency and present it in a simple mathematical form [18]. In TOPSIS, the units of all outcomes are erased and the measures are converted into normalized values. The normalized value (N_{ij}) is achieved by using Formula (7). The specific normalized efficiency values are shown in Table 6.

$$N_{ij} = \frac{X_{ij}}{\sqrt{\sum_{i=1}^{9} X_{ij}^2}}; \quad i = 1, 2, \ldots, 9; \quad j = 1, 2, 3 \tag{7}$$

S. No.	MRR	TWR	OC
Table 6 Valuation of normalized decision value			
1.	0.246111	0.077936	0.331711
2.	0.294165	0.218222	0.360742
3.	0.375609	0.344561	0.347219
4.	0.241376	0.134649	0.263873
5.	0.347199	0.232237	0.324464
6.	0.262756	0.174578	0.310928
7.	0.361499	0.385098	0.282828
8.	0.367751	0.218222	0.360797
9.	0.445018	0.727406	0.396891

where

i Number of choices,

j   Number of measures, and

X_{ij} Real value of the ith value of jth experimental run.

The weighted normalized value (W_{ij}) is computed by multiplying the normalized value (N_{ij}) with its associated weights (w_j) and is given by Formula (8),

$$W_{ij} = w_j * N_{ij}; \quad i = 1, 2, \ldots, 9; \quad j = 1, 2, 3 \tag{8}$$

Here, equal weightage is given to all the output response. Therefore, $w_j = 0.50$. The positive ideal solution (Y^+) and negative ideal solution (Y^-) are computed using Eq. (9).

$$
\begin{aligned}
Y^+ &= \left\{ \left(\text{Max}(W_{ij}) \big| j \in P \right), \left(\text{Min} \, (W_{ij}) \big| j \in P' \right) \big| i = 1, 2, \ldots, 9 \right\} \\
Y^- &= \left\{ \left(\text{Min}(W_{ij}) \big| j \in P \right), \left(\text{Max} \, (W_{ij}) \big| j \in P' \right) \big| i = 1, 2, \ldots, 9 \right\}
\end{aligned} \tag{9}
$$

where P is a set of valuable properties and P' is a set of non-valuable properties.

The partition of each alternative has been calculated by using Eqs. (10) and (11).

$$D_i^+ = \sqrt{\sum_{i=1}^{9} \left(W_{ij} - Y_j^+ \right)^2} \quad i = 1, 2, \ldots, 9 \quad j = 1, 2, 3 \tag{10}$$

$$D_i^- = \sqrt{\sum_{i=1}^{9} \left(W_{ij} - Y_j^- \right)^2} \quad i = 1, 2, \ldots, 9 \quad j = 1, 2, 3 \tag{11}$$

The nearness coefficient value (C_i) for every alternative is calculated as per Formula (12).

$$C_i = \frac{D_i^-}{D_i^- + D_i^+} \tag{12}$$

Table 7 Determination of closeness coefficient to the ideal solution

S. No.	MRR	TWR	OC	D_i^+	D_i^-	C_i	Rank
1.	0.081217	0.025719	0.109465	0.225266	0.021566	0.087371	9
2.	0.097074	0.072013	0.119045	0.178142	0.050882	0.222168	6
3.	0.123951	0.113705	0.114582	0.131311	0.099862	0.431980	3
4.	0.079654	0.044434	0.087078	0.206832	0.047719	0.187464	7
5.	0.114576	0.076638	0.107073	0.167760	0.066208	0.282980	4
6.	0.086709	0.057611	0.102606	0.192719	0.043262	0.183327	8
7.	0.119295	0.127082	0.093333	0.116444	0.115164	0.497237	2
8.	0.121358	0.072013	0.119063	0.172938	0.063437	0.268374	5
9.	0.146856	0.240044	0.130974	0.043896	0.224614	0.836520	1
S^+	0.146856	0.240044	0.087078				
S^-	0.079654	0.025719	0.130974				

Table 8 Calculated average coefficient value

Level	Factor		
	I_P	T_{on}	DF
Level 1	0.247173	0.257357	0.179691
Level 2	0.217924	0.257841	**0.415384**
Level 3	**0.534044**	**0.483942**	0.404066

Table 7 shows the calculation of nearness coefficient values from the positive and negative ideal solutions. From the nearness coefficient measure, the mean outcome for each stage of machining parameters has been calculated and is given in Table 8. Additionally, a comparative graph for various process parameters is established in Fig. 2.

3 Result and Discussion

From the nine nearness coefficients value, experiment 9 depicted the top multi-response characteristics because it gives the highest nearness coefficient value. A greater nearness coefficient indicates that the corresponding experiment is closer to the ideal value; by the way, the optimum level of process parameter combination was recognized in accordance with the highest average nearness coefficient values (bold values in Table 8). The corresponding process parameters are peak current (I_p) (level 3): 1.5 A; pulse on time (T_{on}) (level 3): 1000 μs; duty factor (DF) (level 2): 0.5. The results show that optimal setting is same as the best setting (rank 1) for this set of experiments. The corresponding response values for
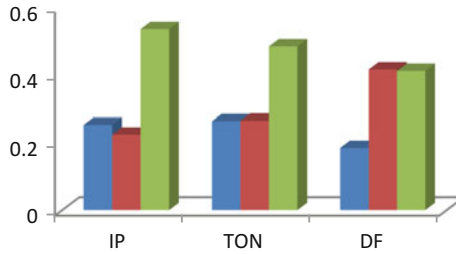
Fig. 2 Nearness coefficient results for various process parameters
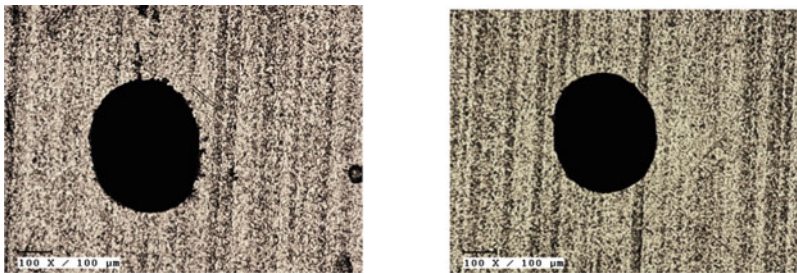
(a) Entry dia of the micro hole at the optimum condition   (b) Exit dia of the micro hole at the optimum condition

Fig. 3 Microscopic images for the optimum setting

the optimum setting are MRR = 0.00409 mm^3/min, TWR = 0.00327 mm^3/min, and average overcut (OC) = 0.18 mm. It is observed that the TOPSIS method is more efficient in solving micro-EDM multi-response difficulties than the formerly used methods. The microscopic images of the optimal setting are shown in Fig. 3.

Table 9 shows that the values of ANOVA test are conducted with 95% confidence interval to recognize the most important strength of each process parameter and its cause on the response characteristics. The % contributions of input parameters are shown in Fig. 4. It is found that the peak current contributes more, and the pulse on time and duty factor contributes equally.

Table 9 ANOVA results of coefficient value

Factor	Process parameters	Sum of squares	Degrees of freedom	Mean sum of squares	F-test	% contribution
A	I_p	0.183082	2	0.091541	8.471	44
B	T_{on}	0.102463	2	0.0512315	4.741	25
C	DF	0.106024	2	0.053012	4.906	26
Error		0.021613	2	0.0108065	–	5
Total		0.4132	8			100

Fig. 4 % contribution of process parameters
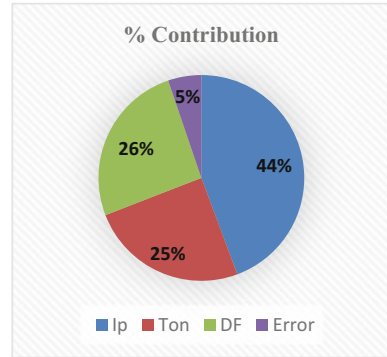
4 Conclusion

In this paper, a breakthrough model of μ-EDM is used for the experiments. Micro-holes of 0.25 mm dia on Ti–6Al–4V have established by using the developed μ-EDM setup. An array of experiments has conducted through Taguchi's L_9 orthogonal array. The peak current (I_p), pulse on time (T_{on}), and the duty factor (DF) are the electrical parameters which have optimized for the responses of MRR, TWR, OC. This multi-response optimization of control parameter in terms of response parameter has been evaluated by means of TOPSIS method. It is observed that the TOPSIS method gives best results at the optimum condition. ANOVA test was performed to calculate the % contributions of input parameters toward the output parameters.

References

1. Liu, K., Lauwers, B., Reynaerts, D.: Process capabilities of Micro-EDM and its applications. Int. J. Adv. Manuf. Technol. **47**, 11–19 (2010)
2. Diver, C., Atkinson, J., Helmi, H.J., Li, L.: Micro-EDM drilling of tapered holes for industrial applications. J. Mater. Process. Technol. **149**, 296–303 (2004)
3. Masuzawa, T.: State of the art of micromachining. Ann. CIRP **49**(2), 473–488 (2000)
4. Xiao, Z., Dahmardeh, M., Moghaddam, M.V., Nojeh, A., Takahat, K.: Scaling approach toward nano electro-discharge machining: nanoscale patterning of carbon nanotube forests. Microelectron. Eng. **150**, 64–70 (2016)
5. Braganca, I.M.F., Rosa, P.A.R., Dias, F.M., Martins, P.A.F., Alves, L.L.: Experimental study of micro-EDM discharges. J. Appl. Phys. **113**, 1–14 (2013)
6. Ho, K.H., Newman, S.T.: State of the art electrical discharge machining (EDM). Int. J. Mach. Tools Manuf. **43**, 1287–1300 (2003)
7. Shao, B., Rajurkar, K.P.: Modelling of the crater formation in micro-EDM. Proc. CIRP **33**, 376–381 (2015)
8. Prasanna, J., Karunamoorthy, L., Raman, M., Prashanth, S., Chordia, D.R.: Optimization of process parameters of small hole dry drilling in Ti–6Al–4V using Taguchi and grey relational analysis. Measurement **48**, 346–354 (2014)

9. Pradhan, B.B., Masanta, M., Sarkar, B.R., Bhattacharyya, B.: Investigation of electrodis-charge micro-machining of titanium super alloy. Int. J. Adv. Manuf. Technol. (2008)
10. Hasçalık, A., Çaydaş, U.: Electrical discharge machining of titanium alloy (Ti–6Al–4V). Appl. Surf. Sci. **253**, 9007–9016 (2007)
11. Lin, Y.C., Yan, B.H., Chang, Y.S.: Machining characteristics of titanium alloy (Ti–6Al–4V) using a combination process of EDM with USM. J. Mater. Process. Technol. **104**, 171–177 (2000)
12. Natarajan, N., Arunachalam, R.: Optimization of micro-EDM with multiple performance characteristics using Taguchi method and grey relational analysis. J. Sci. Ind. Res. **70**, 500–505 (2011)
13. Tiwary, P., Pradhan, B., Bhattacharyya, B.: Application of multi-criteria decision making methods for selection of micro-EDM process parameters. Int. J. Adv. Manuf. Technol. **2**, 251–258 (2014)
14. Rahman, M.M.: Modeling of machining parameters of Ti-6Al-4 V for electric discharge machining: a neural network approach. Sci. Res. Essays **7**(8), 881–890 (2012)
15. Somashekhar, K.P., Ramachandran, N., Mathew, J.: Optimization of material removal rate in Micro-EDM using artificial neural network and genetic algorithms. Mater. Manuf. Process. **25**, 467–475 (2010)
16. Senthil Kumar, V.S., Lokesh, R., Rathinasuriyan, C., Sankar, R.: Multi response optimization of submerged friction stir welding process parameters using topsis approach. In: Proceedings of the ASME 2015 International Mechanical Engineering Congress and Exposition, 13–19 Nov 2015
17. Athawale, V.M., Chakraborty, S.: A TOPSIS method-based approach to machine tool selection. In: Proceedings of the 2010 International Conference on Industrial Engineering and Operations Management Dhaka, Bangladesh, 9–10 Jan 2010
18. Roszkowska, E.: Multi-criteria decision making models by applying the topsis method to crisp and interval data

A Study on Machinability of Leather Using CO_2-Based Laser Beam Machining Process

S. Vasanth and T. Muthuramalingam

Abstract The utilization of laser technology on machining leather has grown significantly during recent years due to number of advantages such as flexibility, high production speed, possibility to cut complex geometries, easier cutting over conventional cutting methods of slitting knifes, die press techniques and manual cutting. In the present work, an endeavor has been proposed to analyze the machinability of leather using CO_2-based laser beam machining (LBM) process. Buffalo leather has been taken as specimens in the present study. It has been inferred that LBM can produce less dross compared to conventional machining while cutting leather.

Keywords Leather · LBM · CO_2 · Surface

1 Introduction

In the present scenario, the usage of leather materials is being increased in different industrial sectors such as shoes and fashion, furniture and automotive. Owing to the growth of higher utilization of such materials, it is needed an advancement in the machining of those materials to produce the final product. Conventionally manual cutting of leather material using scissors and draw-gauge knives was performed. However, the quality of such technique is not noteworthy [1]. Hence it is necessary to introduce untraditional cutting processes such as water jet machining (WJM) process and laser beam machining (LBM) process [2]. Nevertheless, WJM process could produce the jamming of top layer of leather. Hence it is proposed to use LBM process to cut the leather material with complex geometry shape [3].

S. Vasanth · T. Muthuramalingam (✉)
Department of Mechatronics Engineering, SRM Institute
of Science and Technology, Kattankulathur 603203, India
e-mail: muthu1060@gmail.com

S. Vasanth
e-mail: mails2gautham@gmail.com

LBM is a non-traditional machining process in which a controlled laser is directed toward the workpiece for removing the material. This process utilizes the thermal energy to remove material from the workpiece by the sequence of heating, melting or vaporization of the material. There are many different types of lasers including gas, solid-state lasers, and excimer lasers are available [4]. Gas lasers are mostly preferred among which owing to its ability of low maintenance and operating costs. It is very essential to analyze the effect of input process parameters on response parameters in LBM process to improve the efficacy of the system [5]. Hence an attempt has been made to analyze the machinability of leather using CO_2-based LBM process in the present study [6].

2 Experiments and Methods

Buffalo leather has been taken as specimens in the present study owing to higher usage among the leather material. The leathers have been cut using the Trumpf TLF 1200 HQ CO2 LBM process as the rectangular specimens with size of 45 × 10 mm. Surface quality can be considered as the primary performance measures in any machining process [7, 8]. Surface quality has been evaluated using Firefly gt800-handheld USB digital microscope. The surface morphology has been acquired using scanning electron microscope (SEM). Laser power (W) and cutting speed (m/min) have been taken as input process parameters to access the surface quality [1]. The process variables of cutting process have been chosen on expert knowledge of experienced machining operator in the present study. The cutting experiments have been performed using CO_2 LBM under the design of experiments as per Table 1.

Table 1 Design layout in LBM

Trial no	Power (W)	Cutting speed (m/min)
1	20	20
2	20	25
3	25	20
4	30	25
5	30	30
6	30	35
7	35	40
8	35	50
9	35	65

3 Results and Discussion

The buffalo leathers have been machined using CO$_2$ LBM process as the rectangular specimens as shown in Fig. 1.

3.1 Influence of Parameters on Surface Quality

Figure 2 shows the surface quality of machined leather using LBM process. The LBM process can reduce dross formation in the leather during machining process. It has also been observed that there is no sign taper formation owing to the machining process. However, the top layer of the machined surface has been observed with unwanted carbonization layer. Since the LBM process has been associated with the formation of higher thermal energy, it has been reflected in the machined surface of leather. Nevertheless, it is very essential to reduce the carbonization effect as much as possible. The thickness and nature of carbonization layer depend on the concentration of the thermal energy over the surface.

It has been known that the duration of laser concentration over the surface has been determined by the cutting speed of the laser source movement on LBM process. Laser power can directly influence thermal energy produced during the machining process in LBM. The higher thermal energy can vaporize more leather material as that of lower laser electrical power. Hence the higher thermal energy can vaporize the material in a faster manner. This has resulted in unwanted dross formation over the machined surface layer in LBM process. From Fig. 2, it has been observed that higher carbonization effect has been observed in specimens 1, 2 and 3 owing to the lower cutting speed of the laser. However, it has been observed that the higher cutting speed with higher laser power could able to produce better surface quality of leather with lower carbonization effect. It has been observed that trial number 9 can produce the optimal level of surface quality with less dross formation.

Fig. 1 Machined buffalo leather using LBM
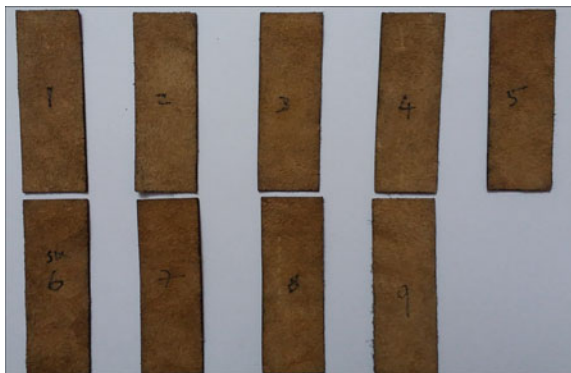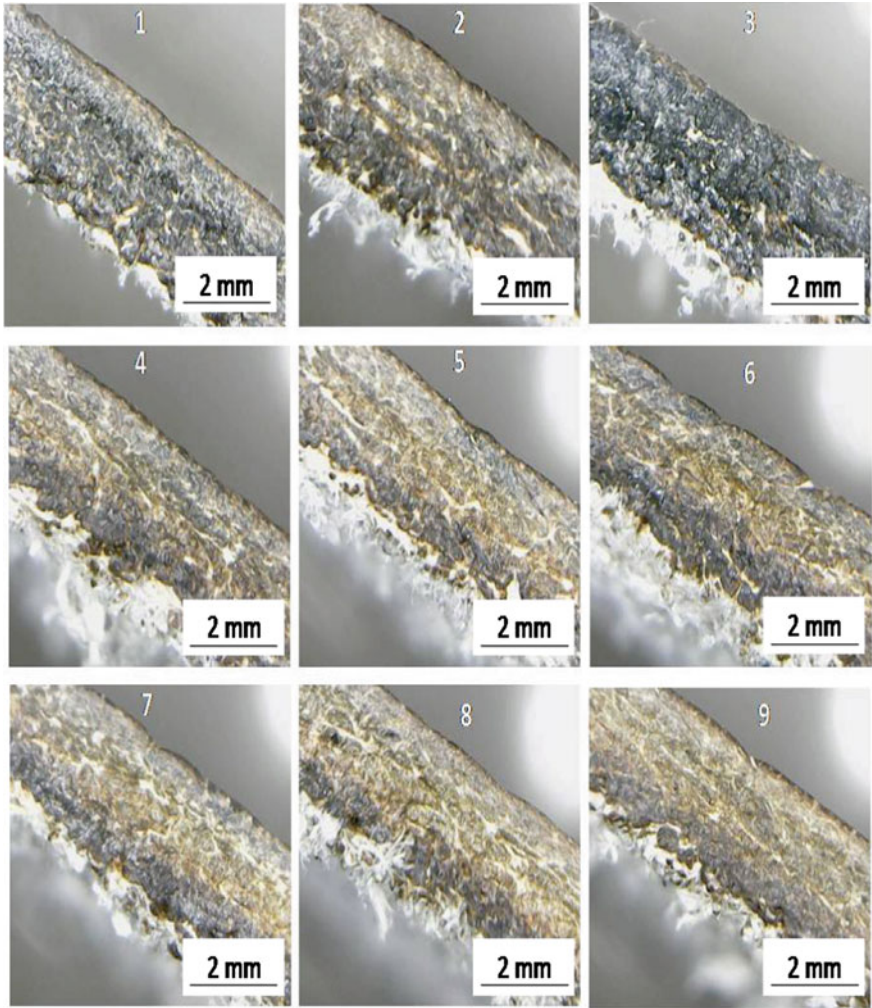
Fig. 2 Surface quality of machined leather

3.2 Influence of Laser on Dross Formation

Dross is a redundant layer in the layer formation. It has been known that dross formation can reduce the surface quality as well as the life of the final product [1]. It is very essential to prove that the LBM process can produce less dross than the conventional manual cutting. Since the conventional manual cutting such as scissors and knife cutting can cut the material using the mechanical power with less thermal energy, it can able to produce higher dross. This has resulted in the lower product quality of final leather product. In LBM process, the material removal is

happened owing to the higher thermal energy produced by the laser source. The thermal plasma can vaporize the unwanted material from the machining zone. This mechanism has resulted on reducing the dross formation over the machined surface in LBM process. Nevertheless, the heat-affected zone would be more in LBM process. This effect can be nullified by the proper selection of optimal process parameters in LBM process. Figure 3 shows the SEM images of machined surface of leather using manual cutting and laser cutting of the process. It has been inferred that the manual cutting has produced dross whereas laser cutting can produce dross

Fig. 3 SEM images of machined leather using LBM process
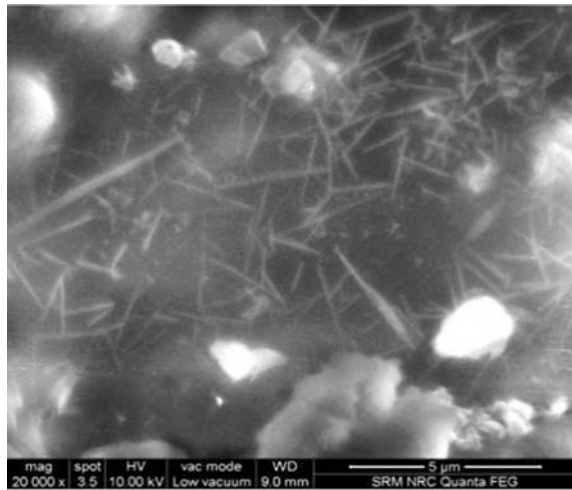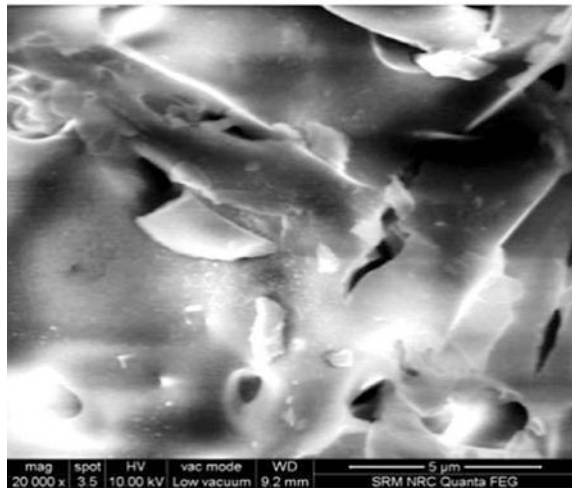
surface. It has been considerable heat-affected zone observed in machined layer using LBM process.

4   Conclusion

The experimental investigation for analyzing the effects of process parameters on the performance measures has been conducted while machining buffalo leather using LBM process. Based on the experimental results, the following conclusions have been made.

(a) The lower cutting speed can increase the carbonization layer formation over the machined leather in LBM process.
(b) LBM process can reduce the dross formation on the machined specimen owing to its ability of removing material by high thermal energy.

References

1. Stepanov, A., Manninen, M., Parnanen, I., Hirvimaki, M., Salminen, A.: Laser cutting of leather: tool for industry or designers. Phys. Proc. **78**, 157–162 (2013)
2. Muthuramalingam, T., Mohan, B.: A review on influence of electrical process parameters in EDM process. Arch. Civil. Mech. Eng. **15**, 87–94 (2015)
3. Patowari, P.K., Mishra, U.K., Saha, P., Mishra, P.K.: Surface integrity of C-40 steel processed with WC-Cu powder metallurgy green compact tools in EDM. Mater. Manuf. Process. 26, 668–676 (2011); Kim, I.W., Lee, C.M.: A study on the machining characteristics of specimens with spherical shape using laser-assisted machining. Appl. Therm. Eng. 100, 636–645 (2016)
4. Nasim, H., Jamil, Y.: Diode lasers: From laboratory to industry. Opt. Laser Technol. **56**, 211–222 (2014)
5. Ayed, Y., Germain, G., Salem, W.B., Hamdi, H.: Experimental and numerical study of laser assisted machining of Ti-6Al-4 V titanium alloy. Finite Elem. Anal. Des. **92**, 72–79 (2014)
6. Caiazzo, F., Curcio, F., Daurelio, G., Minutolo, F.M.C.: Laser cutting of different polymeric plastics (PE, PP and PC) by a CO_2 laser beam. J. Mater. Process. Technol. **159**, 279–285 (2015)
7. Muthuramalingam, T., Mohan, B.: Influence of discharge current pulse on machinability in electrical discharge machining. Mater. Manuf. Process. **28**, 375–380 (2013)
8. Muthuramalingam, T., Mohan, B., Rajadurai, A., Prakash, M.D.A.A.: Experimental investigation of iso energy pulse generator on performance measures in EDM. Mater. Manuf. Process. **28**, 1137–1142 (2013)

Structural Health Monitoring of Glass Fiber Reinforced Polymer Using Nanofiber Sensor

M. S. Nisha, P. Faruk Khan and K. V. Ravali

Abstract Nowadays, GFRP, i.e., glass fiber reinforced polymer composites, are widely used in manufacturing process especially in aircraft industries and automobiles due to their beneficial mechanical and thermal properties such as specific strength and better resistance to corrosion. In this present research, the electrostatic-bonded PVDF-MWCNT fiber composition and GFRP had been used for structural health monitoring (SHM) of composite material. PVDF-MWCNT had been embedded to upper-most layer of the nonconductive materials which is GFRP, i.e., glass fiber reinforced polymers for the undertaking process. This research takes place mainly to improve the multifunction ability. Mainly, the manufacture specimen was characterized into two types; they are mechanical load characterization and material characterization. It is the first time this fiber composition is used in composite materials for monitoring purposes. MWCNT fiber easily penetrates and does not decrease the mechanical properties of material. In this investigation, SEM, i.e., scanning electron microscope and XRD (X-ray diffraction) were used for material characterization process to determine the dispersion of MWCNT with polymer, crystalline structure. The manufactured specimen another characterization namely mechanical load characterization it had done in two ways are incremental–decremental tensile loading and three-point loading testing in order to determine the sensitivity of the material during loading and unloading, material damage identification. The MWCNT fiber worked as a sensor in both tensile and compression loadings. So we mainly used the MWCNT for this process.

Keywords GFRP · SEM · XRD · PVDF-MWCNT · Electrical resistance SHM

M. S. Nisha (✉) · P. Faruk Khan · K. V. Ravali
School of Aeronautical Sciences, Hindustan Institute
of Technology and Science, Chennai 603103, India
e-mail: msnisha@hindustanuniv.ac.in

1   Introduction

In the present aviation and aerospace industries, composites are vigorously employing due to their esteemed properties such as low structural weight, high stiffness, corrosion resistance, higher resistance to defect or damage and thermal, physical properties which reduce the current uncertainties in the aviation terrain [1]. Nowadays, composites are used in different applications for lightweight, strength and have improved structural performance [2], so that glass fiber reinforced polymer (GFRP) will be used in aircraft structures like in landing gears, engine parts, fuselage and wings [3] due to its high strength-to-weight ratio, low maintenance cost, excellent corrosion resistant, high specific strength, high specific and good resistant to chemical agents [4]. At present, the failure of an aircraft is due to structural deterioration and the most probably failure in an aircraft is fatigue damage, buckling, scratches, notches, etc. The fatigue damage is caused due to the high stress concentration point when a load is applied in localized zone [5] and the buckling also leads the failure of aircraft, reducing the bending stiffness and shear stiffness [6]. There are many techniques which were adopted to identify the damages on the aircraft structures [7], such as visual inspection, ultrasonic testing, thermography and tomography. All these damage sensing methods were adopted for the composite structures where the sensors were embedded between the structures. And all techniques have its own advantages and disadvantages based on their applications, such as visual inspection can only detect the surface cracks and damages. It will be useful to identify the flaws on the surface but not underneath the surface. In general, visual inspection practice depends heavily on the vision (or) experience of the inspector [8]. Embedding ultrasonic sensor, piezoelectric sensor and acoustic emission in the literature to detect the damages on the aircraft structures [9–11]. This technique has two units in which one unit generates the wave field and other unit receives the signal. These generated waves penetrate the composite structure if there is any damage which delays propagation of signals. However, they have some drawbacks: embedding sensor downgrades the mechanical property of the specimen [12]. Meanwhile, during the manufacturing process, the embedding sensor itself gets damage due to the high pressure and temperature applied to the sensor. And even in the optical fiber sensor, the signal ion may be found when the damage has realized on the structure. The detection of this damage by using the above-mentioned techniques is known as structural health monitoring (SHM). SHM illustrates the system that can monitor the virtue of a design [13]. It is programmed condition computation of the design through examination and analysis of the data collected on-site by sensing system. This approach will determine the location of damage by using sensors which are sensitive to changes in single parameter and in sensitive to change other parameters [14]. The aircraft SHM system appears in landing gear monitoring, engines and composite structures. While most of the aircraft structures other than composite structures are made from ductile alloys that can endure crack growth over time, brittle alloys have high strength where these differences will effect the SHM [15].

The nanotechnology plays a vital role in SHM where the material itself acts as the sensor so that it will not degrade the mechanical property of aircraft structures. The implementation of carbon nanotubes in the sensor technology (SHM) of the aircraft composite structures by embedding the PVDF and MWCNT in the GFRP to detect the damages in the aircraft composites. As a nanotube is a surface structure, its whole weight is concentrated in the surface of its layers. The extremely high adsorption capacity of the MWCNT and the excellent sensitivity of the MWCNT properties to atoms and molecules adsorbed on their surface provide the possibility of designing sensors on the basis of nanotubes. Several types of gas sensors (detectors) on the basis of the MWCNT are listed here: (1) *Sorption gas sensors*, (2) *Ionization gas sensors*, (3) *Capacitance gas sensors* and (4) *Resonance frequency shift gas sensors* [16].

2 Materials and Methods

2.1 Materials

(a) **PVDF**. PVDF427152-BULK used in this experiment is provided by sigma-Aldrich (Bangalore, India) in pellets form. The material characteristics as provided by the supplier are: the number average M_n is 71×10^3 and weight average is 180×10^3 by GPC, respectively; transition temperature (brittleness temp. −62 °C ASTM D 746 and T_m 155–165 °C; hardness (76–80 shore D, ASTM D 2240); solubility (some polar solvents such as organic esters and amines: soluble).

(b) **MWCNT**. MWCNT 704113-250MG (89% carbon basis; MP: 3652–3697 °C (lit), $\geq$ 99% carbon nanotubes), 0.7–1.3 nm diameter as details provided by the supplier Sigma-Aldrich (Bangalore, India) is considered.

(c) **DMSO**. DMSO 472301-500ML(dimethyl sulfoxide) ACS reagent 99.9% having the characteristics; BP (189 °C), MP (16–19 °C), formula weight: 78.13 g/mol, molecular weight M_w: 78.13 $(CH_3)_2SO$ as detailed by the supplier Sigma-Aldrich (Bangalore, India).

(d) **SDS**. SDS 862010 (sodium dodecyl sulfate); molecular weight M_w: 288.38 $CH_3(CH_2)_{11}OSO_3Na$, $\geq$ 98.5% (GCP): assay 98%, melting point m_p: 204–207 °C(lit), flash point: 170 °C are the characteristics detailed by the supplier Sigma-Aldrich (Bangalore, India).

(e) **Acetone**. acetone (Product ID: 32201-1L) ACS reagent, $\geq$ 99.5% (by GCP). It is also used for identification of ester groups in lipids by spectrophotometric methods having the characteristics; BP: 56 °C/760 mmHg (lit), MP: −94 °C (lit) and flash point: −17 °C as given by the supplier Sigma-Aldrich (Bengaluru, India).

2.2 Solution Preparation

The materials obtained for the experimental study are PVDF, MWCNT and DMSO. The piezoelectricity characteristic of the PVDF material has been used in sensor manufacturing. The master batches of the PVDF and CNT have been mixed with solvent and melted. This molten solution has been used for preparing composite fibers. According to the procedure in Fig. 1, in a beaker placed on the magnetic stirrer PVDF pellets of mass mentioned in Table 1 were added to the beaker. PVDF is insoluble in water. Solvents which are SDS in nature have to be selected for to dissolve them. In this sensor preparation method, DMSO is taken as a solvent for PVDF. After the addition of PVDF pellets into the beaker, the DMSO solvent of ML mentioned in Table 1 is added to the beaker and the magnetic stirrer is set at temp 70 °C. Let the pellets to dissolve in the solvent for at least 3 h, the DMSO itself cannot dissolve completely the PVDF, so we are adding one more SDS to quick the reaction as additive. After the PVDF pellets are dissolved in acetone $(CH_3)_2CO$, the multiwalled carbon nanotubes here considered are in black powder format. It should be added as batch-wise of mentioned MG in Table 1 for better results. Give some gap between each batch for correct rate of mixture. After completing the addition of MWCNT to the solution, add the remaining PVDF pellets for easy dissolvation. The whole solution preparation needs nearly 8 h of time and strict attention for the preparation process. SDS is used as anionic surfactant and for resisting the molecular bonding among PVDF and MWCNT.

2.3 Sensor Preparation

To spun the fiber mat, the electrospun technique was used which converts the polymer solution into fine threads of required diameters such as (hundreds of nanometers (~ 250 nm)—hundreds of micrometers (~ 250 μm)) which uses strong voltage of electricity (nearly in tens of kV) to deposit the threads on the target (mold). In the melt electrospinning technique, the solution is fed in the solution depositor. The spinneret is attached to cathode (+) of 25 kV, and the target mold is connected to anode (−) at other end. It is considered as most difficult and highly precise method for fiber fabrication which uses the combined properties of both
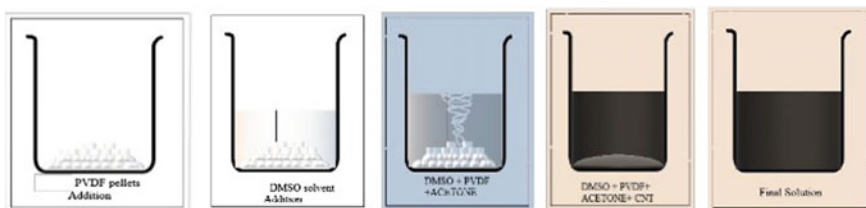
Fig. 1 Sensor solution preparation by the batch-wise addition of composite materials

Table 1 Material quantity details of the samples

Sample	MWCNT (GMS)	PVDF (GMS)	DMSO (GMS)	SDS (GMS)	ACETONE (GMS)
1.	0	0.8	2.5	0.3	2.5
2.	0.2	0.6	2.5	0.3	2.5
3.	0.4	0.4	2.5	0.3	2.5

Fig. 2 Sensor preparation on rotating cylindrical drum by ES method
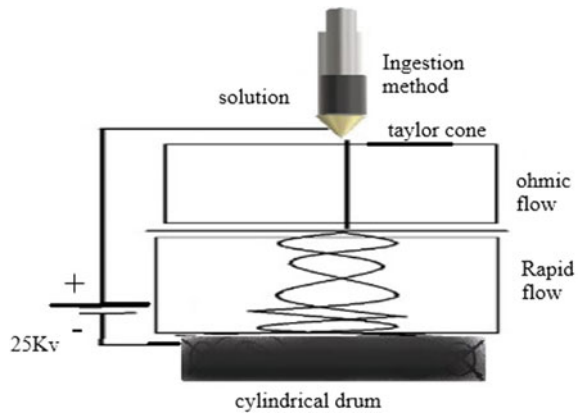
electrospraying and conventional dry spinning of fibers. Due to whipping instability at the initial stage, the fiber is stretched and absent for the process because of low melt conductivity and high viscosity of the melt to overcome this condition 0.05 ml/h feed rate were adopted (Fig. 2).

2.4 Embedding Sensor

The following steps were involved for fabricating the composites plates which embedded with PVDF-MWCNT fiber mat. The 10 layered glass fiber laminates were cut in the dimensions of 300×300 mm which is oriented at 0°/90°. By using vacuum infusion resin transfer molding (VARTM) technique, the laminate was manufactured. The resin and hardener used for this study are epoxy resin LY556/ Hardener HY951, respectively. The sensor fiber mat was orientated at 0° to its axial direction, and its performance was monitored during the mechanical test of the nanofiber sensors mat which was placed between 9th and 10th layered sheets by using silver paste. The dimensions of the sensors will be 50×2 mm, and it is placed in the center position between the sheets. Now, cover the sheets with a mesh cover to avoid the leakage of resign and cover this with vacuum bag and seal all the portion of the structure. Now, small tubes are inserted into the vacuum bag and some are coming out of it and connected to pressure gauge and vacuum pump. Now, vacuum infusion takes place, the resin and hardener are taken in the

100:12 ratio and allowed to flow in vacuum bag at 25 mm/Hg pressure and at room temperature. After the resin flow over all part of sheet, the process will be stopped. It will be dried for 24 h and after that remove the vacuum bag and mesh cover and take the GFRP laminate from the mold [17].

3 Experimental Procedure

3.1 Characterization of PVDF-MWCNT Fiber

To study the surface morphology and size of electrospun fibers, a scanning electron microscope (SEM) was used. Crystalline phase present in the fiber mats was identified by XRD (X-ray diffraction).

3.2 Incremental Loading and Unloading Tensile Test

Tensile test is done on the samples to find the maximum flexural stress. After finding the maximum flexural stress, the mechanical behavior and matrix composition of the specimen are observed at 25, 35, 45% and also its related stress at that condition. This testing is done as prescribed by the ADTM D3039 standards for tensile properties of polymer matrix composite materials which shows the specimen dimensions as (250 × 25 × 3 mm) is also provided the aluminum tabs to hold by the UTM grips and pulled up to failure observed. Universal testing machine (UTM M-100) considered here has the maximum capacity of 100 kN. The graph of force and displacement is plotted according to the nominal strain (MPa) and nominal stress (%). The curve does not increase constantly because of matrix composite properties. Incremental loading and unloading give the graph which is shown as retrograde.

3.3 Three-Point Bending Test

Three-point bending test is used to find the flexural properties from bending displacement of the samples. The maximum flexural stress is found by the bending displacement and also the condition of fiber mat at different percentage of maximum flexural stress. This testing is done according to the ASTM D790 bending test of unreinforced and reinforced plastics and an electrical insulating material which shows the specimen dimensions as (150 × 25 × 3 mm) placed on the two knife edges at equal distance from the tip. The load is applied at the center of the fiber mat in incremental and decremental loading condition. The graph is plotted as flexural stress (MPa) versus flexural strain (%). The maximum flexural stress of the fiber

mat is also finding out in this bending method. Due to this, the maximum flexural stress at 25, 30, 45% and also the failure in the fiber mat are observed at particular percentage of the load.

4 Result and Discussion

4.1 Morphological and Phase Behavior Analysis

From SEM image, homogeneously dispersed MWCNT was observed in PVDF matrix. SEM image of PVDF fiber mat and PVDF-MWCNT fiber mat is shown in Fig. 3.

And in order to determine the reinforcement effect, such as mechanical behaviors, crystallization and piezoelectricity of MWCNT in aligned PVDF fibers, interfacial adhesion between MWCNT and PVDF chains are two major factors. The crystalline structure of PVDF/MWCNT fiber mat is characterized by XRD spectrum. The diffraction peak at $2\theta = 21°$ is observed, which generally represents the β-crystalline PVDF formation, as shown in Fig. 4.
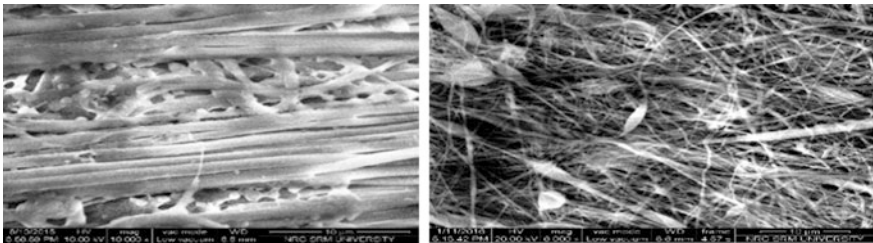
Fig. 3 SEM images of PVDF fiber mat and PVDF-MWCNT fiber mat
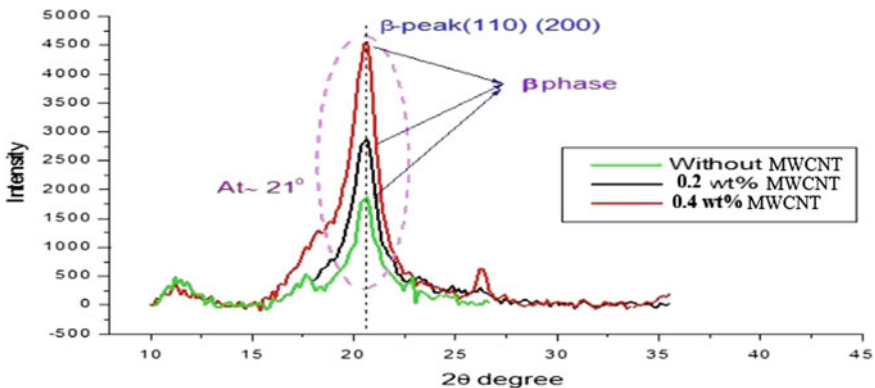
Fig. 4 XRD diffraction of PVDF-MWCNT fiber

4.2 Tensile Test

The tensile test has been conducted for three types of samples in which, one set of sample was embedded such as 0, 0.2 and 0.4 wt% of MWCNT. Initially, the tensile testing was conducted on the specimen untill it fractures. From that, the fracture stress was found out, and the four incremental loading–unloading procedures were done for all the specimen according to the fracture stress obtained in order of 20, 35, 45 and 100%. Figure 5 represents the typical mechanical response of different MWCNT wt%.

For the initial tensile test, glass fiber without MWCNT specimen has been taken and the first mechanical load of 120 MPa stress has been applied on the specimen, which shows the increase in strain according to the load (stress) applied. Then, the second mechanical load of 310 MPa and third mechanical load of 493 MPa stress show the gradual level of increase according to the stress fracture which can be seen in graph, and the curve does not follow the same growth which shows the matrix crack or debonding that occurs in fiber. During fourth mechanical load of 613 MPa on the specimen, further increase in the load tends to be fiber damage or material damage. In the graph, it is shown that GFRP without MWCNT withstands the stress level of (445MPa) and GFRP with MWCNT of 0.2 wt% withstands (535MPa) and GFRP with MWCNT of 0.4 wt% withstands (650 MPa), and show that the increase in MWCNT concentration increases the strength of the material. In aerospace designing, mechanical stress has been widely preferred due to its mechanical property. During mechanical load, its resistance has been monitored and shows the electrical resistance reading of MWCNT fiber which is proportional to the applied stress. Thus, MWCNT has an essential attribute in calculating the inherent damage in composite material by performing simple tension test.

4.3 Three-Point Bending Moment Result

PVDF-MWCNT sensor in tension region

The ability of the embedded sensor which is PVDF-MWCNT fiber mat to sense the damage on the composite structures during loading conditions was analyzed by using the three-point bending test. The damages such as matrix crack, fiber breakage and debending can be detected by measuring the change in electrical resistance which can be related to the residual strain stored in the material during different loading condition which could result in damage. In the present study, the plot was drawn between the change in electrical resistance versus nominal strain of the FRP specimen embedded with PVDF-MWCNT fiber mat. Figure 6 shows that the ratio of $\Delta R/R_0$ and nominal strain for the different wt% of MWCNT such as 0, 0.2 and 0.4wt%. When the nominal strain increases the corresponding change in electrical resistance increases for all the wt% of MWCNT else 0 wt% does not change in path toward change in electrical resistance. It is clearly understood that the 0 wt% of MWCNT fiber mat embedded between the GFRP has no variation in resistance increasing the value of nominal strain.
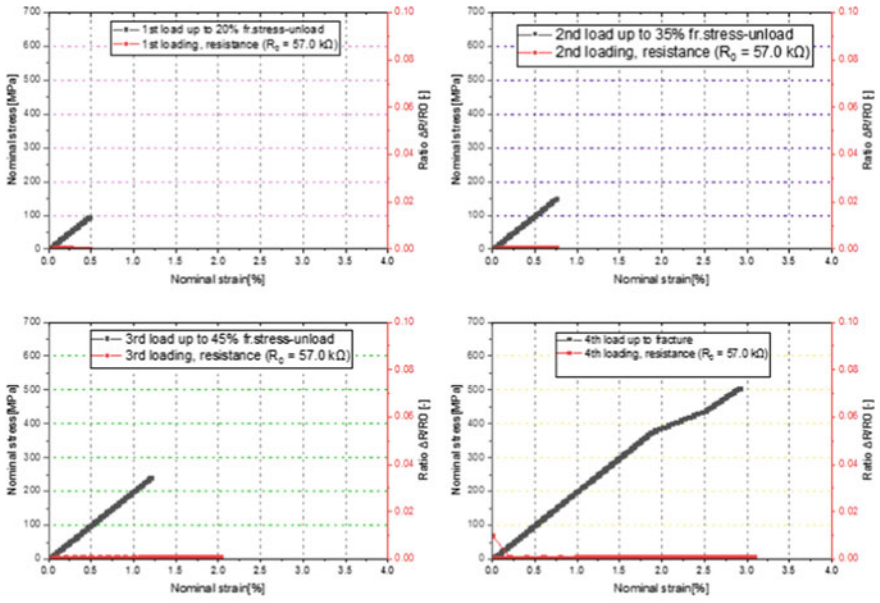
(a) 0 wt.% MWCNT
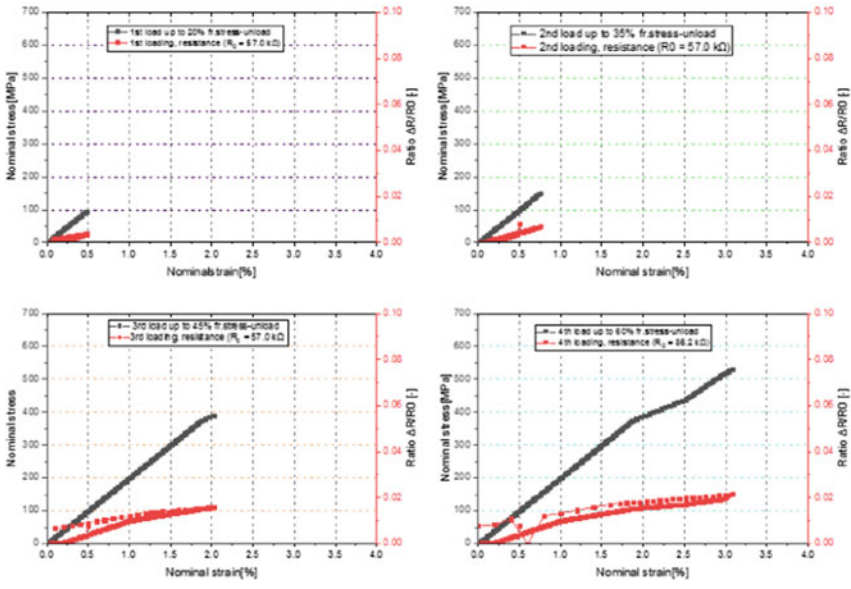
(b) 0.2 wt.% MWCNT

Fig. 5 Typical tensile mechanical and resistance results of GFRP specimen with embedded PVDF-MWCNT with electrical resistance change of **a** 0 wt% MWCNT, **b** 0.2 wt% MWCNT, **c** 0.4 wt% MWCNT
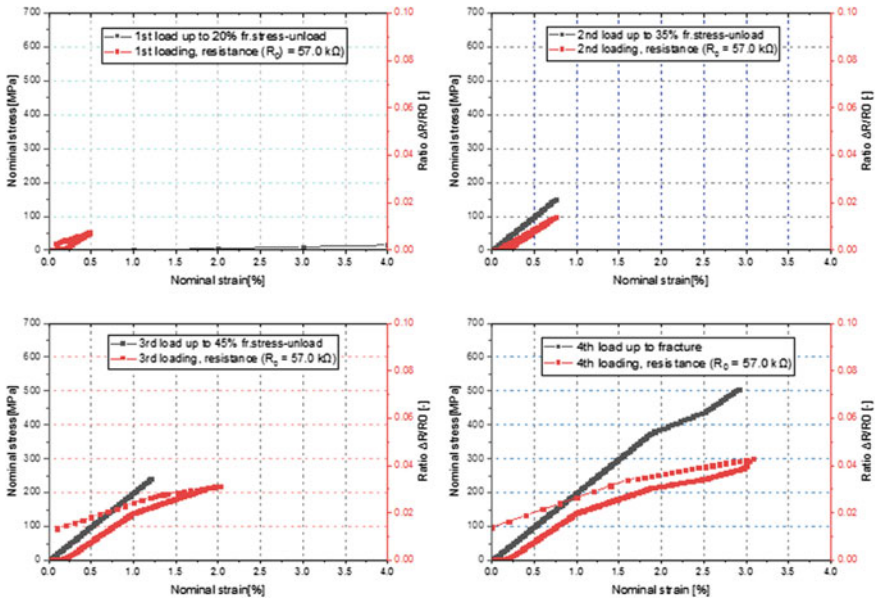
(c) 0.4 wt.% MWCNT

Fig. 5 (continued)
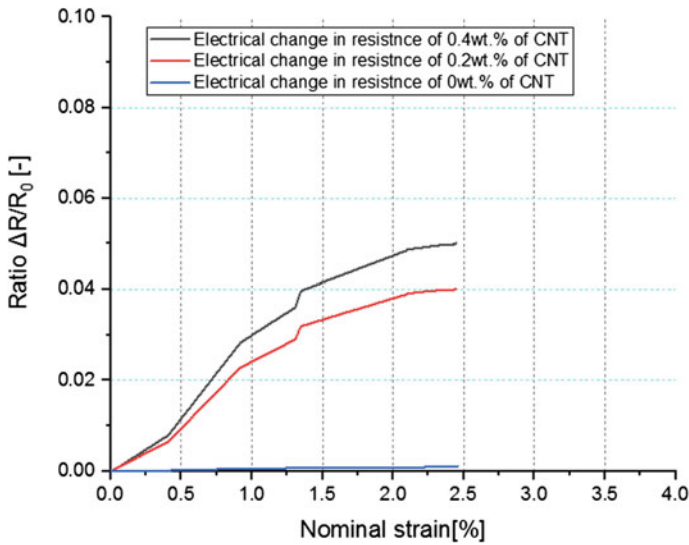
Fig. 6 Typical electrical resistance result of different MWCNT wt% in nominal strain region

5   Conclusion

The glass fiber reinforced polymer (GFRP) samples embedded with PVDF-MWCNT fiber mat has manufactured in order to determine the damages on the aircraft structure through its electrical resistance measurement. In the present study, the following conclusions were obtained: MWCNT has electrical conductive property when PVDF-MWCNT fiber mat embedded between the nonconductive GFRP laminate. The GFRP specimen becomes conductive in order to measure the change in resistance through silver paste and conductive cables. The dispersion of MWCNT and PVDF was analyzed by using SEM technique and its electrical conduct property was analyzed by XRD. Electrospinner technique was adopted to obtain the ultra-thin fiber mat sensor which will not degrade the mechanical property of manufactured specimen. The VARTM process was adopted in order to obtain the smoothly finished sample. Two types of mechanical test were carried out such as tensile test and three-point bending test. In both the test, it has proved that when the mechanical loading was applied its corresponding change in electrical resistance was monitored. When the change in electrical resistance varies abnormally the specimen leads to damage in the structure.

References

1. Composite materials. Royal Society of Chemistry/Advancing the chemical science. www.rsc.org/Education/Teachers/Resources/Inspirational/Resources/4.3.1.pdf
2. Composites in aerospace applications by Adam Quilter on Oct 1, 2004. www.avaitionpros.com/article/1038644/compOsites
3. Deo, R.B., Starner, J.H., Holzwarth, R.C.: Low-cost composite materials and structures for aircraft applications, May 2001
4. Witten, E., Kraustkuhnel, M.: Composites market report 2017. http://www.euciaeu/userfiles/composites-Market%20report-2015pdf.
5. Determination of fracture causes in an aircraft motor cylinders. Eng. Fail. Anal. **82**, 812–822 (2017)
6. Hu, H., Belouettar, S., Potier-Ferry, M., Makradi, A., A novel, finite element for global and local buckling analysis of sandwich beams. Comp. Struct. **90,** 270–278 (2009)
7. Katunin, A., Dragon, K., Dziendzikowski, M.: Damage identification in aircraft composite structures: a case study using a various non-destructive testing techniques. Comp. Struct. **127**, 1–9 (2015)
8. Soyoz, S., Feng, M.Q.: Instantaneous damage detection of bridge structure and experimental verification. Struct. Control Health Monit. **15**(7), 958–973 (2008)
9. Boller, C., Chang, F.-K., Fujino, Y.: Encyclopedia of structural health monitoring. Wiley, New York (2009)
10. Balageas, D., Fritzen, C., Guemes, A. (eds.): Structural health monitoring. ISTE, London, Newport Beach, CA (2006)
11. Giurgiutiu, V.: Structural health monitoring with piezoelectric wafer active sensors. Elsevier, Oxford (2008)
12. Garg, D.P., Zikry, M.A., Anderson, G.L., Stepp, D.: Struct Health Monit **1**, 23–39 (2002)

13. Farrar, C.R., wooden, K.: Structural health monitoring: a machine warning prospective. Willey, Chichester, UK (2013)
14. Friswell, M.I., Adhikari, S.: Structural health monitoring using shape sensors, Mech. Syst. Signal Process. **24**, 623–635 (2010)
15. Focus on landing gear via SHM & sensors. In: 6th European workshop on SHM, detect tolerant, safe life
16. Zaporotskova, I.V., Boroznina, N.P., Parkhomenko, Y.N., Kozhihor, L.V.: Carbon nanotubes: sensor properties. A review. Mod. Electron. Mater. **2**, 95–105 (2016). National University of Science and Technology Misis, 10th Jan 2017
17. Nisha, M.S., Singh, D.: Manufacturing of smart nanomaterials for structural health monitoring (SHM) in aerospace application using CNT and CNF. J. Nano Res. **37**, 42–50 (2016)

A Sensitization Studies on the Metallurgical and Corrosion Behavior of AISI 304 SS Welds

M. Kumar, A. Sharma and A. S. Shahi

Abstract Experimental investigation is performed to study the effect of sensitization on metallurgical and corrosion behavior of thermally aged 10 mm thick AISI 304 SS butt joints fabricated by gas tungsten arc welding (GTAW) process. The welded joint was subjected to different post-weld thermal aging (PWTA) treatments for studying the impact of carbide precipitation on its corrosion and metallurgical properties. Microstructural studies show that the weld metal exhibits largely skeletal morphology of δ-ferrite. The welded joint when subjected to different PWTA treatments showed precipitation of carbides which occurred interdendritically along the δ–γ interface in its weld metal, whereas precipitation occurred intergranularly in its heat-affected zone (HAZ). DLEPR studies of the weldments show that the PWTA of joints led to relatively higher DOS as compared to as-welded condition. It was further concluded that DOS values were higher in HAZ region as compared to welded joints of the weld specimen.

Keywords AISI 304 SS · GTAW · Sensitization · PWTA · Butt joints
DOS · Corrosion behavior

1 Introduction

Stainless steels are iron-based alloys significantly resistant to rusting in different environments, especially in ambient atmosphere. The main component of stainless steel is chromium and to prevent the rust formation at least 11% (in weight) of chromium concentrations is required [1]. The invisible and adherent chromium-rich oxide film is formed on the surface which allows steel to obtain their stainless characteristics. Also, corrosion resistance property may be improved by the addition

M. Kumar (✉) · A. Sharma
Mechanical Engineering Department, Thapar University, Patiala 147001, India
e-mail: mohit.dhiman349@gmail.com

A. S. Shahi
Mechanical Engineering Department, SLIET University, Longowal 148106, India

of molybdenum and nickel. Austenitic stainless steels (ASS) help in establishing the biggest stainless family in account of applications. ASS have so many applications, from household utensils, domestic appliances, electronic and electrical appliances to the nuclear, chemical, food industries, petrochemical, architecture industries and transportation owing to its excellent combination of mechanical properties, oxidation and corrosion resistance under the cyclic loading and monotonic states [2–4]. Besides the different grades of stainless steel, ASS are stable in the ambient temperature to the melting temperature because of face-centered cubic (fcc) lattice structure.

In today's era, welding becomes one of the major fabrication technologies that play an important role in the different industrial applications, and the several weldability issues and concern that arises during welding have much importance in deciding about the consistency and acceptable performance of such fabrications [5, 6]. These steels are prone to intergranular corrosion because the welding temperature of these steels ranges from 450 to 850 °C which gives rise to the problem of sensitization, which is a process of formation of chromium carbides at the grain boundaries surrounded alongside by the chromium-depleted zones [7, 8]. Welding causes microstructural changes across the weld zones and heat-affected zones (HAZs), which in turns, influences the kinetics and thermodynamic of definite corrosion processes leading to fracture and/or accelerated corrosion of the welds [9–11]. The austenitic stainless steel (ASS) fabrications, for example, nuclear waste containment vessels and pipelines in petrochemical industry when processed to service environments lying between the temperature range of 450–850 °C for longer time become prone to carbide precipitation. This susceptible nature toward carbide formation affects the corrosion and mechanical properties of such weld fabrications. In other words, the quantity of carbide precipitation occurring during welding and different PWTA conditions both play an important role in affecting the overall corrosion and metallurgical behavior of these welds.

From the literature survey, it is found that sensitization in AISI 304 SS welds possesses serious problems during working applications and in view of this aspect it becomes important to investigate the role of sensitization on the metallurgical and corrosion behavior of the sensitized AISI 304 SS welded joints.

2 Experimental Work

The base plates from the hot-rolled sheets of AISI 304 SS having thickness of 10 mm were cut into required sizes and edges were machined to double-V groove butt design. AISI 308L SS was selected as the filler material showing compatibility with the base material, having electrode diameter of 2.4 mm that was used for root pass and the weld passes, respectively, for completing welds using gas tungsten arc welding (GTAW) process. The composition of the base material and the filler material used in the present work is shown in Table 1.

Table 1 Composition of the base material and filler material used in the present work (%wt.)

Alloying element	C	Si	P	Mn	Cr	S	Ni	Fe
Base material 304 SS	0.054	0.68	0.026	1.21	18.54	0.00	8.16	Balance
Filler material 308L SS	0.024	0.98	0.045	2.03	19.39	0.03	11.67	Balance

The due consideration was given to weld quality-related aspects, and it was also ensured that proper positioning of the base plates was sustained using tack welds, whereas to minimize distortion effects in the plates, suitable clamping arrangements were used. According to the joint design and welding heat input levels selected for achieving the joints, one root pass and two main cover passes used on each side of the plate to fill the grooves for each joint. Table 2 shows the detailed experimental conditions used in the welding procedure. Proper care and attention were given during welding where all required safety measures like interpass cleaning between consecutive weld passes and precleaning of the grooved edges were followed to ensuring defect-free welds. Visual inspection was done to provide best quality and it was checked that all the weld beads possessed very good geometrical constancy and were free from any visible defects, for example, porosity and blowholes. To ensure that there is no welding defect and to provide proper shielding argon gas with 10–15 l/min was used during welding.

After the accomplishment of GTAW process, the welded joints (comprises the weld zone and HAZ) have a variety of material conditions depending on heat inputs given to the welded joints. The weld specimens were then subjected to different post-weld thermal aging (PWTA) treatments (650 °C temperature for the soaking period of 30 and 120 min and then normalizing it) to induce the forced sensitization effect.

The test samples were then mounted and grounded to 2500 mesh on silicon carbide papers, and finally suspension of alumina powder on velvet cloth is used for polishing. For revealing, microstructure of different zones of welds manual etching was used. Etchant was a mixture of 8.5 g ferric chloride; 2.4 g cupric chloride; 122 ml alcohol; 122 ml hydrochloric acid; 6 ml nitric acid. After complete immersion of the specimen into the etchant solution up to 35 s, etched surface of

Table 2 Parametric combination and heat input used

Type of passes	Current (I)	Voltage (V)	Welding speed (S) (mm/s)	Heat input per unit length per weld pass (kJ/mm)
Root pass	120	13	1.56	0.700
Middle pass	145	15	1.43	1.064
Cover pass	145	13	1.39	0.949
Root pass	120	13	1.49	0.732
Middle pass	145	14	1.44	0.986
Cover pass	140	15	1.38	1.065
Overall heat input (kJ/mm)				5.496

the specimens was rinsed in water, then in methanol and dried up so as to remove any source of moisture. Optical microscopy was used to investigate the microstructural views of the different zones of the welds like weld metal (WM), fusion zone (FZ) and heat-affected zone (HAZ).

In order to found the sensitization nature of the welded joints, double-loop electrochemical potentiokinetic reactivation (DLEPR) test was done with similar conditions as used in the previously reported studies [12–14]. The testing samples were subjected to a standard polishing method that included polishing using emery papers of different grit sizes starting from 100 to 1000 grit size papers and followed by lapping using aluminum paste on a velvet cloth so as to remove any micro-scratches present on the surface. The polished specimens were then used to generate DLEPR plots. An electrochemical cell as shown in Fig. 1 consisting of an elec-trolyte, a graphite counter electrode, specimen as the working electrode and a calomel reference electrode were used for this work.

The DLEPR testing was carried out to evaluate the degree of sensitization (DOS) of the following samples:

1. Specimen (for weld metal as well as HAZ region) in as-welded conditions.
2. Specimens (for weld metal as well as HAZ region), post-weld thermally aged (PWTA), 650 °C temperature for 30 min.
3. Specimens (for weld metal as well as HAZ region), post-weld thermally aged (PWTA), 650 °C temperature for 120 min.

The DLEPR testing was done in three stages:

1. A delay of 5-min at VOC.
2. For as-welded specimens and PWTA specimens, scanning rate of 100 mV/min (i.e., 1.67 mV/s) was used and for an anodic polarization scanning rate ranging from 50 mV below VOC to 310 mV was used.

Fig. 1 Photograph showing potentiostat and electrodes used for DOS studies
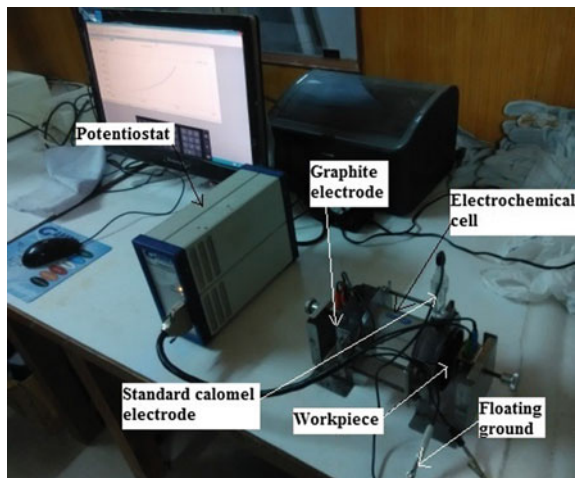
3. For as-welded specimens and PWTA specimens a cathodic reactivation scans from 300 mV to VOC at the same scan rate.

In the present work, electrolyte used was a mixture of 0.01 M KSCN + 0.5 M H_2SO_4 solutions, prepared by using distilled water. The whole testing including generation of the DLEPR curves was obtained with the galvanostat/potentiostat, which was controlled by the dedicated software (as shown in Fig. 1). A ratio of reactivated current (I_r) to the activated current (I_a) generated in the double-loop test (I_r/I_a) is used as a term degree of sensitization (DOS). It can be evaluated by using the following formula: DOS = I_r/I_a [15].

3 Results and Discussion

3.1 Microstructure of the Welded Joints

Ferrite studies were done in order to check hot fissuring propensity of weldment. It was observed that the weld metal consists 6.3–6.8% of the ferrite content, which is in the recommended range showing that these welded joints was not susceptible to hot fissuring and cracking. The weld metal microstructure showed a δ-ferrite phase and dendritic structure the placed in the interdendritic regions. It was clearly seen that the weld metal holds skeletal and ferrite morphology. Figure 2 indicates that the precipitation of the carbides takes place interdendritically, i.e., along the δ/γ interface, when the welded joint was subjected to different PWTA, i.e., 650 °C for 30 min and 650 °C for 120 min.

Figure 3 indicates the HAZ microstructure in the as-welded condition and different PWTA conditions. It could be seen that during welding HAZ experiences grain coarsening [16]. This grain coarsening was further responsible for the carbide precipitation on the HAZ region of the welded joint. From Fig. 3, it was found that as the welded joint was given to different PWTA treatments, i.e., 650 °C for 30 min and 650 °C for 120 min, the carbide precipitation occurred in the HAZ
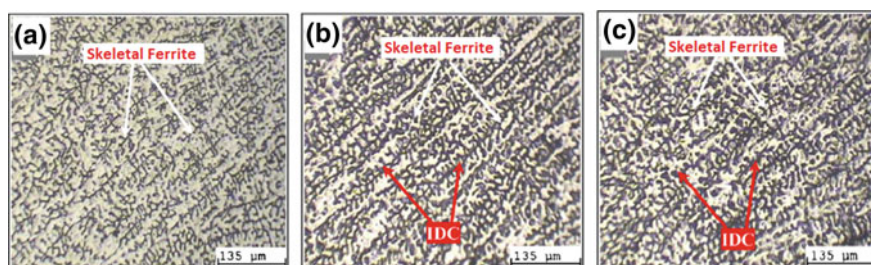
Fig. 2 Microstructural views of the weld metal in the: **a** as-welded condition; **b** 650 °C for 30 min and **c** 650 °C for 120 min
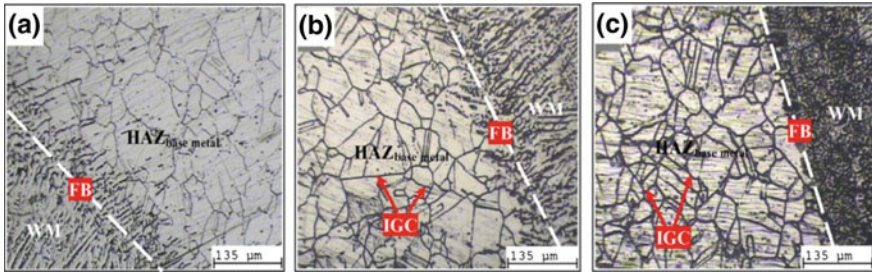
Fig. 3 Microstructural views of the HAZ in the: **a** as-welded condition; **b** 650 °C for 30 min and **c** 650 °C for 120 min

intergranularly [17]. Also, it was seen that carbide precipitation is more in case of PWTA treatment, i.e., 650 °C for 120 min.

3.2 Sensitization Studies of the Welded Joints

For evaluating DOS in the welded joint as well as HAZ of the weld specimens, DLEPR technique was used and the DOS results were measured, in the as-welded conditions as well as in different PWTA conditions are shown in Tables 3 and 4, and the related DLEPR curves are shown in Figs. 4 and 5.

Degree of Sensitization (DOS) in the Welds
In the as-welded conditions, the degree of sensitization values of the welded joint was 0.02. However, it was further observed that when the welded joint was subjected to different PWTA treatments (i.e., 650 °C for 30 min and 650 °C for

Table 3 DOS results of the welded joints in the weld specimens

S.No.	Specimen condition	Reactivated current, I_r (A/cm^2)	Activated current, I_a (A/cm^2)	DOS = I_r/I_a
1	As-welded	754.6×10^{-6}	32.59×10^{-3}	0.02
2	PWTA, i.e., 650 °C for 30 min	2.051×10^{-3}	33.11×10^{-3}	0.06
3	PWTA, i.e., 650 °C for 120 min	4.446×10^{-3}	38.37×10^{-3}	0.12

Table 4 DOS results of the HAZ in the weld specimens

S. No.	Specimen condition	Reactivated current, I_r (A/cm^2)	Activated current, I_a (A/cm^2)	DOS = I_r/I_a
1	As-welded	4.026×10^{-3}	38.25×10^{-3}	0.10
2	PWTA, i.e., 650 °C for 30 min	8.767×10^{-3}	36.33×10^{-3}	0.22
3	PWTA, i.e., 650 °C for 120 min	10.88×10^{-3}	32.08×10^{-3}	0.34
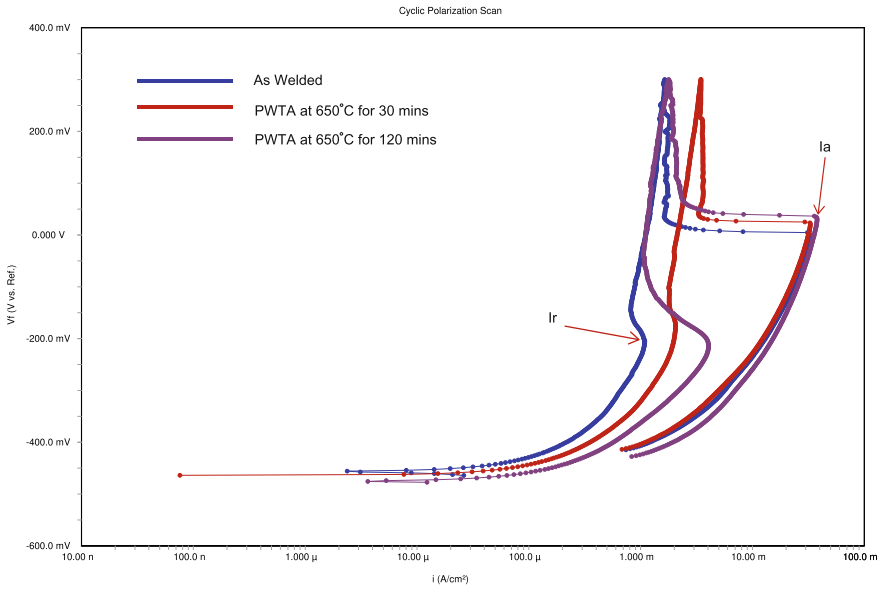
Fig. 4 DLEPR curves for welded joints in the weld specimens for **a** as-welded, **b** PWTA at 650 °C for 30 min and **c** PWTA at 650 °C for 120 min conditions
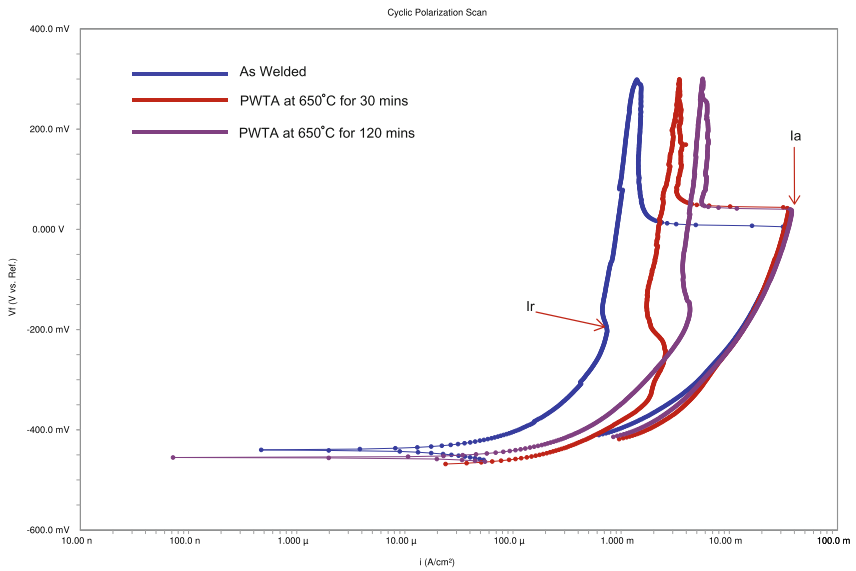
Fig. 5 DLEPR curves for HAZ in the weld specimens for **a** as-welded, **b** PWTA at 650 °C for 30 min and **c** PWTA at 650 °C for 120 min conditions

120 min), the DOS value was increased (Table 3). This increment in the DOS value of the welded joint is attributable to the carbide precipitation along $\delta–\gamma$ interfaces in the weld specimen.

Degree of Sensitization (DOS) the HAZ

In the as-welded conditions, the degree of sensitization value of the HAZ in the weld specimen was 0.10. However, it was further observed that when the welded joint was subjected to different PWTA treatments (i.e., 650 °C for 30 min and 650 °C for 120 min), the DOS value was increased (Table 4). This increment in the DOS value of the welded joint is attributable to the carbide precipitation along the intergranularly in the HAZ.

4   Conclusions

- Microstructural observations show that the weld metal of the joints comprised largely of austenite containing a small amount of δ-ferrite with skeletal morphology. Under different PWTA conditions, the $\delta–\gamma$ interface showed carbide precipitation, which occurred interdendritically.
- HAZ of the joints showed grain coarsening during welding, which when subjected to different PWTA showed carbide precipitation that was found to occur intergranularly.
- DLEPR studies of the weldments show that the PWTA of joints resulted into higher DOS as compared to the as-welded condition, as aging leads to carbide formation occurring intergranularly in the HAZ and interdendritically in the weld zone.
- DLEPR studies also show that DOS values were higher in HAZ region as compared to the welded joints of the weld specimen.

References

1. Khatak, H.S., Raj, B.: Corrosion of Austenitic Stainless Steels. Narosa Publishing House, India (2002)
2. Sedrics, A.J.: Corrosion of Stainless Steels, 2nd edn. Wiley, New York (1996)
3. Kuang, W., Han, E.H., Wu, X., Rao, J.: Microstructural characteristics of the oxide scale formed on 304 stainless steel in oxygenated high temperature water. Corros. Sci. **52**, 3654–3660 (2010)
4. Liu, W., Wang, R.J., Han, J.L., Xu, X.Y., Li, Q.: Microstructure and mechanical performance of resistance spot welded cold-rolled high strength austenitic stainless steel. J. Mater. Process. Technol. **210**, 1956–1961 (2010)
5. Yan, J., Gao, M., Zeng, X.: Study on microstructure and mechanical properties of 304 stainless steel joints by TIG, laser and laser-TIG hybrid welding. Opt. Lasers Eng. **48**, 512–517 (2010)
6. John C.L., Damian, J.K.: Welding Metallurgy and Weldability of Stainless Steels. Wiley, New York (2005)

7. Bruemmer, S.M., Charlot, L.A.: Development of grain boundary chromium depletion in type 304 and 316 stainless steels. Scr. Metall. **20**, 1019–1024 (1986)
8. Tuthill, A.H.: Corrosion testing of austenitic stainless-steel weldments. Weld. J. **5**, 36–40 (2005)
9. Cui, Y., Lunding, C.D.: Austenite-preferential corrosion attack in 316 austenitic stainless-steel weld metals. Mater. Des. **28**, 324–328 (2007)
10. Cui, Y., Lunding, C.D.: Evaluation of initial corrosion location in E316 austenitic stainless-steel weld metals. Mater. Lett. **59**, 1542–1546 (2005)
11. Dadfar, M., Fathi, M.H., Karimzadeh, F., Dadfar, M.R., Saatchi, A.: Effect of TIG welding on corrosion behavior of 316L stainless steel. Mater. Lett. **61**, 2343–2346 (2007)
12. Lopez, N., Cid, M., Puiggali, M., Azkarate, I., Pelayo, A.: Application of double loop electrochemical potentiodynamic reactivation test to austenitic and duplex stainless steels. Mater. Sci. Eng., A **229**, 123–128 (1997)
13. Cihal, V., Stefec, R.: On the development of the electrochemical potentiokinetic method. Electrochem. Acta **46**, 3867–3877 (2001)
14. Gracia, C., de Tiedra, M.P., Blanco, Y., Martin, O., Martin, F.: Intergranular corrosion of welded joints of austenitic stainless steels studied by using an electrochemical minicell. Corros. Sci. **50**, 2390–2397 (2008)
15. Kain, V., Chandra, K., Adhe, K.N., De, P.K.: Effect of cold work on low-temperature sensitization behaviour of austenitic stainless steels. J. Nucl. Mater. **334**, 115–132 (2004)
16. Kumar, S., Shahi, A.S.: Effect of heat input on the microstructure and mechanical properties of gas tungsten arc welded AISI 304 stainless steel joints. Mater. Des. **32**, 3617–3623 (2011)
17. Kumar, S., Shahi, A.S.: Studies on metallurgical and impact toughness behavior of variably sensitized weld metal and heat affected zone of AISI 304L welds. Mater. Des. **89**, 399–412 (2016)

A Study on Friction Stir Welding of Al6061-ZrB$_2$ Metal Matrix Composites

T. V. Christy, D. Emmanuel Sam Franklin,
R. Nelson and S. Mohanasundaram

Abstract Over the past few decades, various attempts have been made in fabricating aluminum matrix composites (AMCs) reinforced with several ceramic particles for various applications in aircraft, automotive and marine industries. Al6061 reinforced with (10 wt%) ZrB$_2$ composite is a metal matrix composite (MMC) manufactured by the in situ salt–metal reaction. Friction stir welding (FSW), a solid-state welding, overcomes the setbacks associated with conventional fusion welding processes. The primary objective of this work is to adapt FSW process in joining Al6061/ZrB$_2$ with various weld parameters like tool rotational speed (1200, 1300, 1400, 1500, 1600 and 1700 rpm), welding speed (20, 30, 40, 50, 60 and 70 mm/min) and axial force maintained between 2.5 and 3.5 kN. With the addition of ZrB$_2$, the properties of Al6061 are highly improved. An attempt has been made to study the mechanical properties and the microstructure of Al6061-ZrB$_2$ MMC welded by FSW method. The evaluation of microstructure in the welded joints showed various zones like welded nugget zone (WNZ), thermomechanically affected zone (TAZ) and heat-affected zone (HAZ). The weld zone was characterized with homogeneously distributed ZrB$_2$ particles. Samples 3 and 4 showed comparatively good mechanical properties than the remaining samples with different weld parameters.

T. V. Christy (✉) · D. Emmanuel Sam Franklin · S. Mohanasundaram
Department of Mechanical Engineering, Karunya Institute
of Technology and Sciences, Coimbatore, India
e-mail: christy@karunya.edu

D. Emmanuel Sam Franklin
e-mail: emmanuelsam@karunya.edu

S. Mohanasundaram
e-mail: mohanasundaram@karunya.edu

R. Nelson
Department of Mechanical Engineering, Sri Krishna College
of Technology, Coimbatore, India
e-mail: nelson.90.mech@gmail.com

1 Introduction

Aluminum alloys reinforced with different hard ceramic particles are called as aluminum matrix composites (AMCs). The advantages of AMCs include that of the aluminum alloys and also the special properties of ceramic properties like greater strength, improved stiffness, low density, improved high-temperature properties, controlled thermal expansion coefficient, thermal/heat management, good abrasion and wear resistance and improved damping capabilities [1–5]. They are likely to play a prominent role in aircraft, automobile and marine industries in enhancing their product capabilities. Apart from the SiC and Al$_2$O$_3$, which were predominantly used as reinforcements in the earlier decades in developing AMC [6–8], different other reinforcements like titanium boride [9], silicon nitride [10], boron carbide [11] and titanium oxide [12] are also used. Among all such reinforcements, zirconium diboride (ZrB$_2$) is preferred being a high covalent refractory ceramic material with hexagonal crystal structure and possess high strength, melting temperature, hardness, electrical and thermal conductivity, to exist as a suitable material in aerospace industry [13]. In situ method is preferred in manufacturing Al-ZrB$_2$ composite to meet the demands of industrial applications [15–17]. Limitations like poor wettability, bonding and non-uniform distribution have restricted the use of ex situ method in various engineering applications [14].

A procedure for the secondary processes like machining and joining is to be established to expand the applications of AMCs in the above-mentioned industries [18]. Welding of AMCs through conventional fusion methods produces poor joint properties due to the solidification-induced structure and chemical reactions. It is reported that such processes produce deteriorating effects such as coarse microstructure, porosity, segregation and decomposition of ceramic particles and formation of several brittle intermetallic compounds [19–21]. Friction stir welding (FSW), a solid-state welding method, provides homogeneous distribution of ceramic particles in the weld zone and found to be the potential choice in overcoming the defects in fusion welding. FSW invented by The Welding Institute in 1991 uses a non-consumable rotating tool, harder than the base material to join the edges without melting the metal. The tool, consisting of two parts, namely shoulder and pin, moves along the line of the joint with sufficient axial force. The heat generated by the tool rotation leads to a very soft region closer to the FSW tool pin. Advancement of the tool further mechanically intermixes the two pieces of metal at the place of the joint by pushing the deformed material from the front to the back of the tool and forges to complete the process.

The present work focuses on the application of different set of FSW parameters in joining Al6061/10 wt% ZrB$_2$ and to evaluate the microstructure and various mechanical properties of the welded joints.

2 Experimental Procedure

The Al6061-T6 rods (Ø20 mm) were melted in an electrical furnace using a graphite crucible. The AMC for this work, namely 10% by weight ZrB_2 particulates in Al6061 matrix through the in situ process involving the salt–metal reaction between the zirconium-containing K_2ZrF_6 and the boron-containing KBF_4 salts in the presence of molten Al6061 alloy [8, 22].

$$K_2ZrF_6 + 2KBF_4 \rightarrow ZrB_2 + 4KF + Heat$$
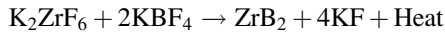
The weighed quantities of inorganic salts K_2ZrF_6 and KBF_4 were added into the molten Aluminum to produce ZrB_2. The temperature of the melt was maintained at 750 °C and thoroughly stirred using a graphite rod at regular intervals of 10 min. The melt was poured into a preheated die (100 mm × 100 mm × 10 mm) after the slag is removed. Castings with 10% wt of ZrB_2 were obtained. The casted samples were of poor surface finish due to the shrinkage of material while pouring into die. Casted samples were machined to the 100 mm × 50 mm × 6 mm size using vertical milling machine (Figs. 1 and 2).

Fig. 1 Casted sample before machining

Fig. 2 Casted sample after machining
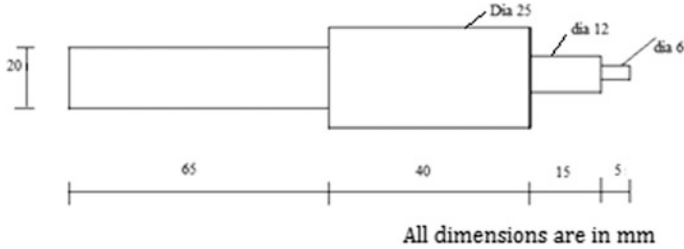
Fig. 3 Dimensions of FSW tool

A threaded cylindrical profile tool required for friction stir welding is made from the high carbon high chromium steel by turning operation. The thread present in the tool helps in good friction between the weldable samples (Fig. 3).

During welding process, the material tends to expand due to the heat produced and the welding speed. The plates were clamped in order to restrict the expansion and movement of the material while welding. The samples were being kept on FSW machine and held by the clamps on both the sides as shown in Fig. 4. FSW was done in the samples for different parameters like tool rotational speed, welding speed and axial force. The axial force was maintained between 2.5 and 3.5 kN in order to apply pressure on the samples, which further develops the friction and heat. The tool rotational speed for six samples is taken as 1200, 1300, 1400, 1500, 1600 and 1700 rpm. Similarly, the welding speed for FSW samples was taken as 20, 30, 40, 50, 60 and 70 mm/min. Specimens were cut from the welded samples for the required dimensions to carry out microstructural and mechanical characterization.

Tensile test was carried out on the welded samples (machined in ASTM E8 standard dimension of gauge length 40 mm, gauge width 6 mm and thickness 6 mm by electrical discharge machining) using universal testing machine to determine their tensile strength. Microhardness test is done to find the hardness using HI-113 Mitutoyo microhardness tester at 500 g load applied for 10 s. The test surface was highly polished, and the test was conducted at 10 different locations of the specimen. In two lens with $10\times$ and $50\times$ magnification, Vickers indenter was

Fig. 4 FSW on the sample

used. The smaller the force applied, the higher the metallographic finish required. Bend test, i.e., compression test, was conducted in the welded specimen with the dimension of 100 mm × 10 mm using universal testing machine. The failure occurs when the load applied exceeds the specimen's compression load. The specimens (30 mm × 30 mm × 10 mm) were prepared as per the standard procedure for microstructural analysis and roughly polished using emery sheets of 1200 grade. They were fine polished in a twin disk polisher machine. Diamond paste of 3 and 1μ was used and color etched with 3 g of NaOH, 2 g of KMnO$_4$ in 100 ml of distilled water. The etched specimens were viewed under an optical microscope to observe the microstructure of fabricated MMC's.

3 Results and Discussion

3.1 Tensile Properties of Welded Joints

Tensile test was carried out on the six welded samples with different welding parameters. Figure 5 shows the tensile properties of the welded joint in sample 3, which yielded the best tensile strength, i.e., 94 N/mm^2. The corresponding
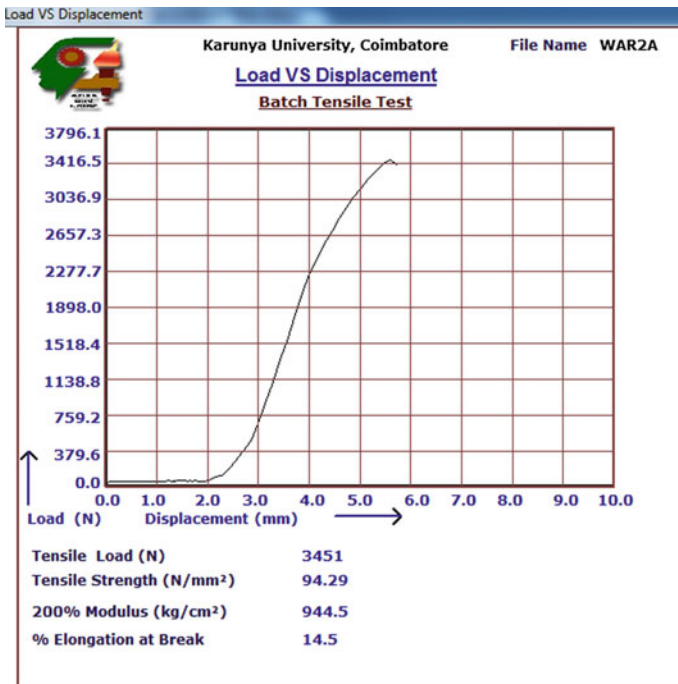
Fig. 5 Tensile test in sample 3

Table 1 Tensile test results

Sample	Tensile load (N)	Tensile strength (N/mm²)	200% modulus (kg/cm²)	% elongation at break
1	2187	60	195.3	9
2	3041	83	763.7	18.8
3	3451	94	944.5	14.5
4	3403	93	922.5	15
5	2681	73	720.5	12.5
6	2515	69	694	11.5

rotational speed and weld speed were 1400 rpm and 40 mm/min, respectively. This can be attributed to the reinforcement offered by the homogeneously dispersed fine ZrB_2 particles. This is also evidenced by the microstructural analysis, the images of which are presented in Sect. 3.4. Also the specimen welded at 1500 rpm and 50 mm/min possessed a joint strength of 93 N/mm². Table 1 lists the percentage elongation of different specimens along with the loads applied for conducting the tensile tests. The optimum rotational speed and weld speed were found to be 1400 rpm and 40 mm/min. This combination led to the breaking up of reinforcement into finer particles and also their homogeneous distribution in the matrix.

3.2 Microhardness Analysis of Welded Joints

The microhardness profiles obtained along various points in the welded joints are shown in Fig. 6. The Vickers hardness values were measured from the weld joint center (0 mm) progressively in the horizontal Y-axis for both the samples up to 5 mm in length from the joint center. Hardness values were taken from weld face, midway through the weld nugget and near to the root of the welded nugget. Table 2

Fig. 6 Microhardness profile across the FSW joint
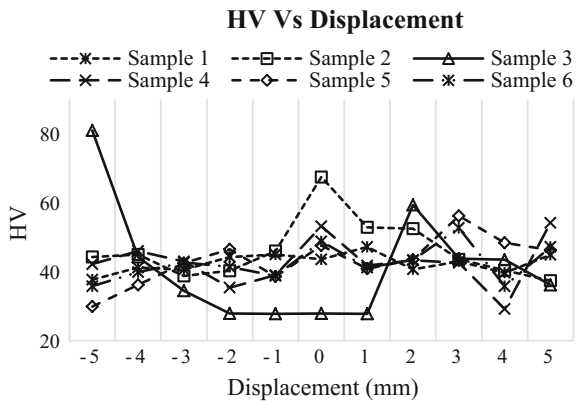
Table 2 Microhardness reading for the welded samples

Sample	Avg. ind. dia. (mm)	Hardness (HV)
1	46.095	43.6
2	43.61	48.8
3	37.33	67.5
4	41.74	53.2
5	44.12	47.6
6	57.62	27.9

lists the Vickers hardness values for the various samples with indentor diameters 1 and 2. The hardness is found to be higher in the weld zone with the increased weight percentage of ZrB$_2$ particles. This was due to the shear stress induced by the tool workpiece interface at the FSW region which leads to the generation of strong grain structure and also due to the friction produced in that particular region.

3.3 Analysis on the Bend Test

The study was conducted on the bend strength of the weldments. The failure of the specimen during bend test occurs when the load applied exceeds the specimen compression load. Figure 7 shows the failed samples under compression load. The compressive stress for the welded samples is tabulated in Table 3, which also compares the results taken from the tensile test and microhardness test.

The best compressive stress property was achieved in sample 3 as 11 N/mm^2, withstanding the compressive load up to 710 N, whereas the compressive stress in sample 4 was 10 N/mm^2 with the compressive load up to 695 N. The reason for the better joint efficiency in samples 2, 3 and 4 can be attributed to the optimum FSW process parameters. It was also found that the cracks originated exactly in the advancing side. This proves that unlike tensile strength, the breakage of the sample occurred in the advancing side. It was due to the reason that in the bottom of the FS

Fig. 7 Tested samples under compression load

Table 3 Bend test results

Sample No.	Bend angle (in °)	Compressive stress (N/mm^2)
1	137.75	8
2	147.6	10
3	157.25	11
4	149.8	10
5	146.85	8
6	166.5	5

weldments the strength is low on the advancing side, whereas in the top of the weldment the strength is good on the advancing side. The mechanism of the material during FSW of the weldment attributed to such behavior.

When all the mechanical test results were compared, it was observed that sample 3 with 1400 rpm tool rotational speed and 40 mm/min weld speed yielded higher tensile strength and good hardness properties, whereas the sample 4 with 1500 rpm rotational speed and 50 mm/min weld speed yielded the tensile strength closer to that of the sample 3.

3.4 Microstructure Analysis

The butt joining of Al6061/10 wt% ZrB$_2$ composites was accomplished successfully through FSW. The crown with semicircular features had no defects and presents smooth quality with no prominences or depressions.

The macrostructure of the friction stir welded Al6061/10 wt% ZrB$_2$ consisted of parent composite (BM), heat-affected zone (HAZ), thermomechanically affected zone (TMAZ) and welded nugget zone (WNZ). The zone adjacent to the weld zone was TMAZ, affected thermally and deformed plastically. TMAZ and HAZ together constituted the transition zone. Figures 8 and 9 reveal the microstructure of the friction stir welded Al6061/10 wt% ZrB$_2$ composites (samples 1 and 3) and the distribution of reinforcement in the matrix. ZrB$_2$ particles are observed to be mostly
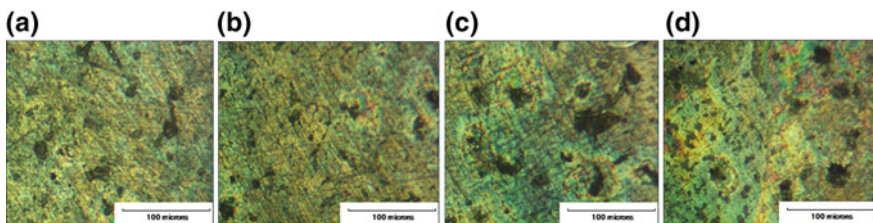
Fig. 8 Optical micrographs of friction stir welded Al6061/10 wt% ZrB$_2$ composites—sample 1. **a** Parent composite, **b** heat-affected zone, **c** transition zone and **d** welded nugget zone
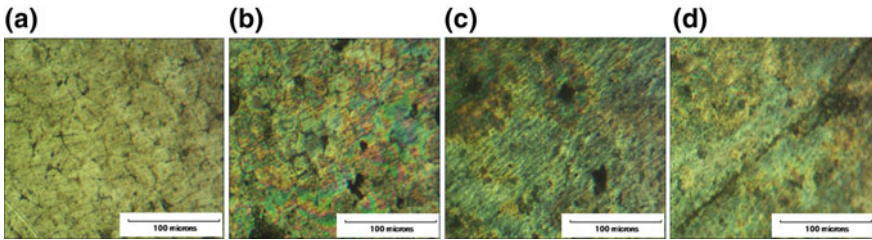
Fig. 9 Optical micrographs of friction stir welded Al6061/10 wt% ZrB$_2$ composites—sample 3. **a** Parent composite, **b** heat-affected zone, **c** transition zone and **d** welded nugget zone

spherical and dispersed homogeneously in the aluminum matrix as revealed for the parent composites and similarly for all the samples. It was found that the ZrB$_2$ particles refined the dendritic structure due to the constitutional super cooling during solidification of the matrix composite. ZrB$_2$ particles were produced in varying sizes due to the reaction of K$_2$ZrF$_6$ and KBF$_4$ salts with molten aluminum. The particles, roughly of size 2 μm, agglomerate to form clusters depending on the working temperature, holding time, reaction rate and cooling rate [23]. The average thermal expansion coefficient of Al6061 is 24×10^{-6}/°C, whereas that of ZrB$_2$ is 6.6×10^{-6}/°C. Such difference in their thermal expansion coefficient tends to append dislocations with high density around ZrB$_2$ during solidification.

Figures 8b and 9b show the microstructure of welded sample 1 in HAZ where its grain size does not have much difference when compared to that of the parent composite. But, in the transition zone, the clear boundary between TMAZ and WNZ is revealed. Due to the frictional heat by the rotating tool and stresses induced, there is plastic deformation in TMAZ and stretched ZrB$_2$ particles along the shear stress directions. TMAZ showed similar structure on both sides. The microstructure of the weld zone showed a homogeneous distribution of ZrB$_2$ particles with no welding defects like porosity and segregation as seen in the fusion welding. The number of particles in this zone seemed to be larger than that of the parent composite zone. No reaction was found to occur between the matrix and ZrB$_2$ composites due to the frictional heat applied. The nucleation sites with the presence of reinforcement particles were found to be increased, which further led to the reduction in aluminum matrix grain size [24]. Due to the stirring action of the tool, several clusters were fragmented.

From the microstructure of all welded samples, it was observed that when the tool rotational speed and weld speed are less in samples 1 and 2, the ZrB$_2$ particles are coarse but distributed evenly. When both the parameters were increased in samples 5 and 6, the particles were finer, but agglomeration was more pronounced. ZrB$_2$ particles were spread more along the boundaries. Figure 9 reveals that the microstructure of the samples 3 and 4 was observed with the ZrB$_2$ particles evenly distributed in the Al6061 matrix with finer refinement, which indicates the parameters considered to be optimum.

4   Conclusions

FSW was carried out successfully in joining Al6061/10 wt% ZrB_2 composites. Tensile, microhardness, and bend test were conducted, and the microstructure was analyzed on the welded joints. The results are summarized as follows:

- Tensile strength, compressive strength and hardness in the welded sample FS welded with tool rotational speed 1400 rpm and weld speed 40 mm/min were found to be more compared to other samples with different parameters.
- The microstructure of FS welded Al6061/10 wt% ZrB_2 composites was categorized into four zones: (i) parent composite, (ii) heat-affected zone, (iii) thermomechanically affected zone and (iv) welded nugget zone. Weld zone in the sample 3 and also in sample 4 displayed a homogeneous distribution of ZrB_2 particles. The hardness in the weld zone was higher than the parent composite as a result of the fragmentation of ZrB_2 particles and grain refinement. In these samples, the particles were distributed uniformly with finer refinement.

References

1. Akbari, M.K., Baharvandi, H.R., Shirvanimoghaddam, K.: Tensile and fracture behavior of nano/micro TiB$_2$ particle reinforced casting A356 aluminum alloy composites. Mater. Des. **66**, 150–161 (2015)
2. Sivananth, V., Vijayarangan, S., Rajamanickam, N.: Evaluation of fatigue and impact behavior of titanium carbide reinforced metal matrix composites. Mater. Sci. Eng. **597**, 304–313 (2014)
3. Xiu, Z., Yang, W., Chen, G., Jiang, L., Mac, K., Wu, G.: Microstructure and tensile properties of Si$_3$N$_{4p}$/2024Al composite fabricated by pressure infiltration method. Mater. Des. **33**, 350–355 (2012)
4. Chen, H.S., Wang, W.X., Li, Y.L., Zhang, P., Nie, H.H., Wu, Q.C.: The design, microstructure and tensile properties of B$_4$C particulate reinforced 6061Al neutron absorber composites. J. Alloy. Compd. **632**, 23–29 (2015)
5. Hemanth, J.: Abrasive and slurry wear behavior of chilled aluminum alloy (A356) reinforced with fused silica (SiO$_{2p}$) metal matrix composites [J]. Compos. B **42**, 1826–1833 (2011)
6. Kang, Y.C., Chan, S.L.I.: Tensile properties of nanometric Al$_2$O$_3$ particulate reinforced aluminium matrix composites. Mater. Chem. Phys. **85**, 438–443 (2004)
7. Miracle, D.B.: Metal matrix composites—from science to technological significance. Compos. Sci. Technol. **65**, 2526–2540 (2005)
8. Dinaharan, I., Murugan, N., Parameswaran, S.: A influence of in situ formed ZrB$_2$ particles on microstructure and mechanical properties of AA6061 metal matrix composites. Mater. Sci. Eng. **528**, 5733–5740 (2011)
9. Ramesh, C.S., Pramod, S., Keshavamurthy, R.: A study on microstructure and mechanical properties of Al6061–TiB$_2$ in-situ composites. Mater. Sci. Eng. **528**, 4125–4132 (2011)

10. Ramesh, C.S., Keshavamurthy, R.: Slurry erosive wear behaviour of Ni–P coated Si$_3$N$_4$ reinforced Al6061 composites [J]. Mater. Des. **32**, 1833–1843 (2011)
11. Kalaiselvan, K., Dinaharan, I., Murugan, N.: Characterization of friction stir welded boron carbide particulate reinforced AA6061 aluminum alloy stir cast composite [J]. Mater. Des. **55**, 176–182 (2014)
12. Ramesh, C.S., Anwar Khan, A.R., Ravikumar, N., Savanprabhu, P.: Prediction of wear coefficient of Al6061–TiO$_2$ composites [J]. Wear **259**, 602–608 (2005)
13. Sonber, J.K., Murthy, T.S.R.C., Sunramanian, C., Kumar, S., Fotedar, R.K., Suri, A.K.: Investigation on synthesis of ZrB$_2$ and development of new composites with HfB$_2$ and TiSi$_2$. Int. J. Refract. Metal. Hard Mater. **29**, 21–30 (2011)
14. Kumar, S., Chakraborthy, M., Subramanya Sarma, V., Murty, B.S.: Tensile and wear behaviour of in situ Al–7Si/TiB$_2$ particulate composites [J]. Wear **265**, 134–142 (2008)
15. Pramod, S.L., Bakshi, S.R., Murty, B.S.: Aluminum based cast in situ composites: a review [J]. J. Mater. Eng. Perform. **24**, 49–113 (2015)
16. Chen, F., Chen, Z., Mao, F., Wang, T., Cao, Z.: TiB$_2$ reinforced aluminum based in situ composites fabricated by stir casting [J]. Mater. Sci. Eng., A **625**, 357–368 (2015)
17. Shorowordi, K.M., Laoui, T., Haseeb, A.S.M.A., Celis, J.P.: Microstructure and interface characteristics of B$_4$C, SiC and Al$_2$O$_3$ reinforced Al matrix composites: a comparative study [J]. J. Mater. Process. Technol. **142**(3), 738–743 (2003)
18. Dinaharan, I., Murugan, N.: Metallurgical and mechanical characterization of stir cast AA6061/ZrB$_2$ in situ composite butt joints. Met. Mater. Int. **18**, 135–142 (2012)
19. Lean, P.P., Gil, L., Urena, A.: Dissimilar welds between unreinforced AA6082 and AA6092/SiC/25p composite by pulsed-MIG arc welding using unreinforced filler alloys (Al–5Mg and Al–5Si). J. Mater. Process. Technol. **143–144**, 846–850 (2003)
20. Huang, R.Y., Chen, S.C., Huang, J.C.: Electron and laser beam welding of high strain rate superplastic Al 6061/SiC composites. Metall. Mater. Trans. A **32**, 2575–2584 (2001)
21. Storjohann, D., Barabash, O.M., Babu, S.S., David, S.A., Sklad, P.S., Bloom, E.E.: Fusion and friction stir welding of aluminum-metal-matrix composites. Metall. Mater. Trans. A **36**, 3237–3247 (2005)
22. Dinaharan, I., Murugan, N.: Microstructure and some properties of aluminium alloy AA6061 reinforced in situ formed ZrB$_2$ particulate stir cast composite. J. Cast Met. Res. **27**(2), 115–121 (2014)
23. Ni, D.R., Wang, J.J., Zhou, Z.N., Ma, Z.Y.: Fabrication and mechanical properties of bulk NiTip/Al composites prepared by friction stir processing. J. Alloy. Compd. **586**, 368–374 (2014)
24. Hashemi, R., Hussain, G.: Wear performance of Al/TiN dispersion strengthened surface composite produced through friction stir process: a comparison of tool geometries and number of passes [J]. Wear **324–325**, 45–54 (2015)

Analysis of Machinability on WEDM Processed Titanium Alloy with Coated Electrodes

A. Ramamurthy and T. Muthuramalingam

Abstract In the present study, an attempt has been made to analyze the effects of wire electrical machining process on machining high-strength titanium alloy with the coated wire electrodes under different process parameters combinations. Brass wire electrode and zinc diffused coated electrode have been taken as electrodes to investigate material removal rate and surface roughness. From the experimental investigation, it has been observed that the conventional brass wire electrode has produced higher material removal rate. Histogram analysis shows that the zinc diffused brass wire electrode can produce lower surface roughness.

Keywords Alloy · WEDM · Electrode · Histogram

1 Introduction

It is extremely difficult to machine such high-strength materials with complex shapes using conventional machining processes. The average surface roughness (R_a) is influenced by the craters formed during any machining process [1]. Wire electrical discharge machining (WEDM) process is one of the significant unconventional machining processes in which the material removal is occurred owing to the electrical plasma discharges happened between the wire electrode and the workpiece separated by constant air gap [2]. The melted material is ejected from the machining zone using flushing process by allowing insulating medium flow through it. The accuracy of the optimal process parameters combination is limited in any machining process [3]. The utilization of optimization techniques can also be used

A. Ramamurthy (✉)
Department of Mechanical Engineering, Saveetha Engineering College, Thandalam, India
e-mail: ramapec@gmail.com

T. Muthuramalingam
Department of Mechatronics Engineering, SRM Institute of Science and Technology, Kattankulathur, India
e-mail: muthu1060@gmail.com

for improving the surface characteristics moderately [4]. The enhancement of wire electrode is an essential one to modify the machining characteristics in WEDM process [5]. It has been observed that the surface finish of the workpiece can be enhanced while utilizing the wire electrode with lower electrical conductivity such as tungsten carbide [6]. The suitable coating deposited over the conventional wire electrode such brass wire can significantly improve the machining characteristics in wire EDM process [7].

Very few studies are available to discuss about the effect of the coated electrodes on the performance measures in WEDM process. In the present investigation, an attempt has been made to analyze the effects of brass wire electrode and zinc diffused coated electrode on machining high-strength titanium alloy in WEDM process.

2 Experiments and Methods

Due to its importance in aircraft structures, titanium (Ti-6Al-4V) alloy has been chosen as workpiece material in the present study. The specimens have been machined using Electronica Sprintcut Electra ELPULS 40A WEDM machine. The conventional brass wire tool electrode (BWE) and zinc diffused brass wire tool electrode (DWE) with diameter of 0.25 mm have been utilized for machining workpiece specimens based on their diverse nature of the electrical conductance and the melting point. The experiments have been performed with various combinations of process parameters such as pulse-on duration (T_{on}), pulse-off duration (T_{off}), servo gap voltage (SV) and wire tension (WT). The selection process variables of the present study are shown in Table 1. The ranges of process variables have been selected based on lower, medium and higher ratings available in the WEDM to analyze the effects of electrode coatings on the performance measures during the machining process. The surface roughness (R_a) of the machined specimen has been evaluated by portable surf tester of model SJ-201P manufacture by Mitutoyo with the cutoff length of 0.8 cm [8].

Table 1 Selection of process variables in the present study

S. No.	Process parameters	Notation	Units	Process variables
1.	Pulse-on duration	T_{on}	μs	110, 120, 130
2.	Pulse-off duration	T_{off}	μs	30, 40, 50
3.	Servo voltage	SV	V	40, 60, 80
4.	Wire tension	WT	kg	5, 7, 9

3 Results and Discussion

The work piece specimens have been machined with dissimilar coated wire electrodes under selected process parameter combinations in WEDM process. In the present section, the various studies regarding the significance of wire electrodes on material removal rate and surface roughness have been explained.

3.1 Material Removal Rate Analysis of Machined Titanium Alloy Specimens

The material removal rate of machined titanium alloys with different wire electrodes is shown in Table 2. The plasma energy depends on the plasma current, discharge duration and occurrence of plasma formation per second in WEDM process. The value of MRR is mainly determined by the melting point of the workpiece, and the plasma current flows through the wire electrode and workpiece during the machining in WEDM process. It has been understood that the plasma current can be modified by the electrical conductance between specimen and electrode in WEDM process. From the experimental investigation, it has been clearly understood that the MRR has been affected by the melting point and electrical resistivity of the electrodes in WEDM. Since DWE has the zinc content, the electrical conductance of such electrode is lower than the BWE. Hence, it has produced lower MRR than BWE. From the experimental investigation, it has been inferred that the BWE has removed more material than DWE owing to its higher electrical conductivity in WEDM process. Tables 3 and 4 show the ANOVA tables for material removal rate using BWE and DWE, respectively.

Table 2 MRR obtained in WEDM process under different process variables settings

Trial No.	T_{on} (µs)	T_{off} (µs)	SV (V)	WT (kg)	Material removal rate (mm³/min)	
					BWE	DWE
1.	110	30	40	5	104.730	30.329
2.	110	40	60	7	149.047	62.358
3.	110	50	80	9	158.472	120.119
4.	120	30	60	9	149.746	40.518
5.	120	40	80	5	175.720	90.272
6.	120	50	40	7	178.458	158.650
7.	130	30	80	7	173.046	52.289
8.	130	40	40	9	163.601	135.803
9.	130	50	60	5	247.058	216.504

Table 3 ANOVA table for MRR using BWE

Source	Degree of freedom	Sum of square	Mean square	F	P	% contribution
T_{on}	1	0.00322	0.00322	2.686	0.176591	0.318821
T_{off}	1	0.97607	0.97607	814.086	0.000009	96.64346
SV	1	0.02483	0.02483	20.712	0.010410	2.458489
WT	1	0.00465	0.00465	3.877	0.120313	0.46041
Error	4	0.00480	0.00120			0.118815
Total	8	1.01356				

Coefficient of determination: $R^2 = 97.45\%$

Table 4 ANOVA table for MRR using DWE

Source	Degree of freedom	Sum of square	Mean square	F	P	% contribution
T_{on}	1	0.00390	0.00390	0.1416	0.725815	0.296616
T_{off}	1	1.27513	1.27513	46.2752	0.002440	96.9806
SV	1	0.00082	0.00082	0.0296	0.871675	0.062365
WT	1	0.00742	0.00742	0.2693	0.631201	0.564332
Error	4	0.11022	0.02756			2.096088
Total	8	1.39749				

Coefficient of determination: $R^2 = 95.11\%$

3.2 Histogram Analysis of Machined Workpiece

Figure 1 shows the histogram analysis of the machined workpiece using WEDM process with different wire electrodes such as brass wire electrode (BWE) and diffused wire electrode (DWE). The histogram graph is utilized to evaluate the number of occurrence over the range. In the study, the surface roughness has been taken as the occurrence to access the surface quality of the machined workpiece using wire EDM process with different wire electrodes. From Fig. 1, it has been observed that the diffused coated wire has produced lesser amount of occurrence of higher surface roughness than brass wire electrodes, whereas DWE has produced high amount of occurrence of lower surface roughness. Since the average surface roughness is mostly influenced by the occurrence of the surface roughness values, it is one of the methods to evaluate the surface quality. From the histogram analysis, it has been proved that the diffused brass wire electrode has produced better surface finish owing to its ability of producing lower average surface roughness. Tables 5 and 6 show the ANOVA tables for surface roughness using BWE and DWE, respectively. It has been confirmed that T_{off} has dominant nature on determining surface roughness in WEDM process.
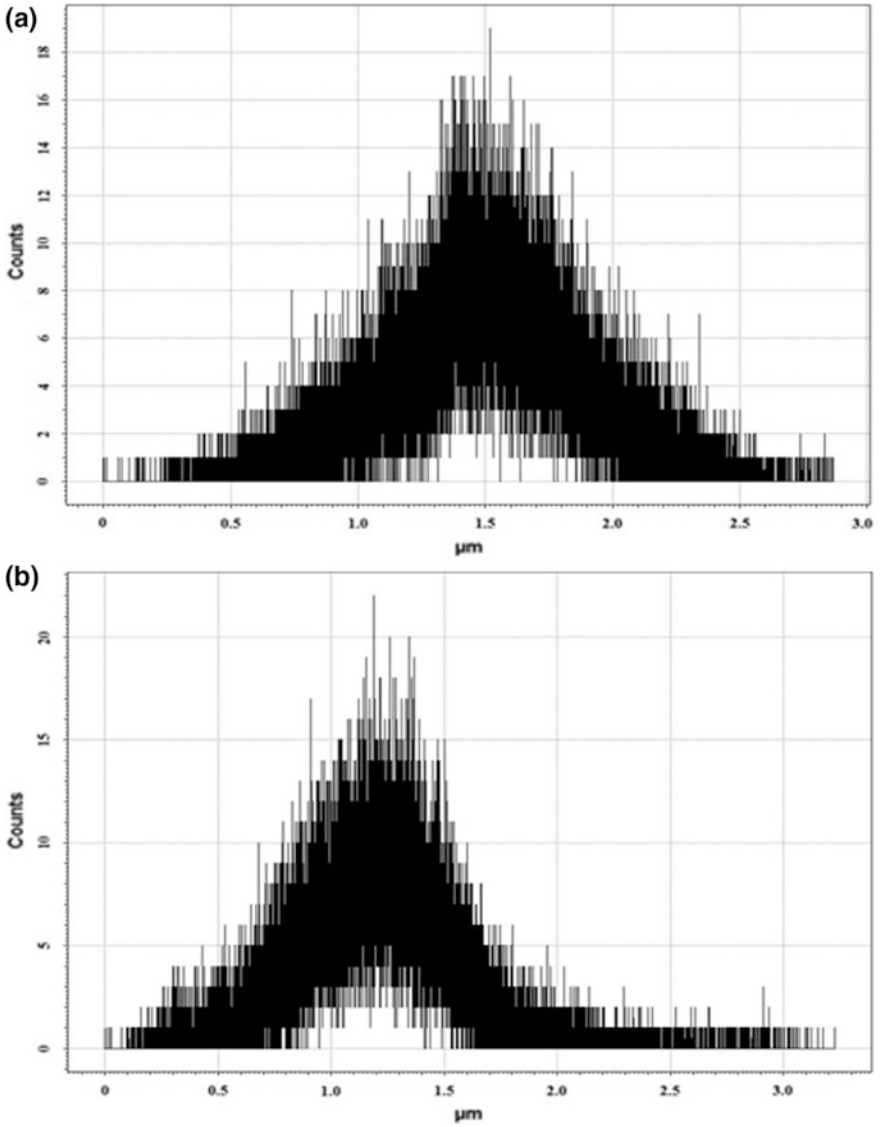
Fig. 1 Histogram analysis of Ti-6Al-4V alloy machined with various wire electrodes **a** BWE and **b** DWE

Table 5 ANOVA table for surface roughness using BWE

Source	Degree of freedom	Sum of square	Mean square	F	P	% contribution
T_{on}	1	0.00322	0.00322	2.686	0.176591	0.318821
T_{off}	1	0.97607	0.97607	814.086	0.000009	96.64346
SV	1	0.02483	0.02483	20.712	0.010410	2.458489
WT	1	0.00465	0.00465	3.877	0.120313	0.46041
Error	4	0.00480	0.00120			0.118815
Total	8	1.01356				

Coefficient of determination: $R^2 = 97.45\%$

Table 6 ANOVA table for surface roughness using DWE

Source	Degree of freedom	Sum of square	Mean square	F	P	% contribution
T_{on}	1	0.00390	0.00390	0.1416	0.725815	0.296616
T_{off}	1	1.27513	1.27513	46.2752	0.002440	96.9806
SV	1	0.00082	0.00082	0.0296	0.871675	0.062365
WT	1	0.00742	0.00742	0.2693	0.631201	0.564332
Error	4	0.11022	0.02756			2.096088
Total	8	1.39749				

Coefficient of determination: $R^2 = 95.11\%$

4 Conclusion

The experimental investigation for analyzing the effects of coated electrodes on the performance measures has been conducted while machining titanium alloy using WEDM process. Based on the experimental results, the following conclusions have been made.

(a) Conventional brass wire electrode has produced higher material removal rate in WEDM process.
(b) Pulse-off time can considerably affect the surface roughness.
(c) Histogram analysis shows that the zinc diffused brass wire electrode can produce lower surface roughness.

References

1. Muthuramalingam, T., Mohan, B.: Performance analysis of iso current pulse generator on machining characteristics in EDM process. Arch. Civil Mech. Eng. **14**, 383–390 (2014)

2. Ho, K.H., Newman, S.T., Rahimifared, S., Allen, R.D.: State of the art in wire electrical discharge machining. Int. J. Mach. Tools Manuf. **44**, 1247–1259 (2004)
3. Rajendran, S., Marimuthu, K., Sakthivel, M.: Study of crack formation and resolidified layer in EDM process on T90Mn2W50Cr45 tool steel. Mater. Manuf. Process. **28**, 664–669 (2012)
4. Muthuramalingam, T., Mohan, B.: Application of Taguchi-grey multi responses optimization on process parameters in electro erosion. Measurement **58**, 495–502 (2014)
5. Muthuramalingam, T., Mohan, B.: Influence of tool electrode properties on machinability in spark erosion machining. Mater. Manuf. Process. **28**, 939–943 (2013)
6. Jahan, M.P., Wong, Y.S., Rahman, M.: A study on the fine finish die-sinking micro-EDM of tungsten carbide using different wire electrode. J. Mater. Process. Technol. **209**, 3956–3967 (2009)
7. Ramamurthy, A., Sivaramakrishnan, R., Muthuramalingam, T., Venugopal, S.: Performance analysis of wire electrodes on machining Ti-6Al-4V alloy using electrical discharge machining process. Mach. Sci. Technol. **19**, 577–592 (2015)
8. Muthuramalingam, T., Mohan, B., Rajadurai, A., Prakash, M.D.A.A.: Experimental investigation of iso energy pulse generator on performance measures in EDM. Mater. Manuf. Process. **28**, 1137–1142 (2013)

Multi-response Optimization of Machining Parameters in EDM Using Square-Shaped Nonferrous Electrode

S. Ganapathy, P. Balasubramanian, T. Senthilvelan and R. Kumar

Abstract Productivity has a vital role in industry which leads to enhance the overall profit. In most of the processes, properties of end product should be same as the property of raw materials which shows the necessity of non-conventional machining method. The electrical discharge machining (EDM) is widely used for machining hard and complex shaped parts in industries. In this study, EN-8 material has been chosen as workpiece and it has been machined by conventional copper electrode of having the shape of square. Various influencing parameters have been selected as input parameters, viz. peak current, pulse on time, dielectric pressure and size of electrode. Totally, 29 experiments were conducted using design of experiments (DOE) and analyzed with the output responses. Multi-response optimization was carried out using desirability function, and analysis of three-dimensional model graph was observed. Input parameters were optimized in order to obtain maximum metal removal rate (MRR) and minimum tool wear rate (TWR). The significant parameters have been identified using analysis of variance (ANOVA). Coefficient of correlation is also been evaluated. Interactions of parameters against the outputs are analyzed.

Keywords EDM · DOE · MRR · TWR · RSM · ANOVA

S. Ganapathy (✉)
Department of Mechanical Engineering, Sri Sairam Engineering College, Chennai, India
e-mail: ganapathy.mech@sairam.edu.in

P. Balasubramanian · R. Kumar
Department of Mechanical Engineering, A.V.C College of Engineering, Mayiladuthurai, India
e-mail: balaprof8@gmail.com

R. Kumar
e-mail: kumarramalingam62@gmail.com

T. Senthilvelan
Department of Mechanical Engineering, Pondicherry Engineering College, Pondicherry, India
e-mail: senthilvelan@pec.edu

1   Introduction

The EDM is identified as the futuristic machining process [1]. It has amazing resources on account of adaptability of its applications and known to be useful in modern industries. The material removal in EDM is related to the erosive effect that is being produced along with the partial discharge which occurs between two electrolytic conductive materials. In a spark of short duration a liquid dielectric gap is generated separating tool and workpiece electrodes. The high-frequency electrical discharge is used to melt the workpiece material in a particular area to produce external shapes, holes, profiles in an electrically conductive workpiece by means of tool which is conductive. The result of controlled pulses of current occurs between the workpiece (anode) and tool electrode (cathode) as shown by the EDM plots [1, 2].

The present work aims at finding the optimal level of the parameters for the EDM process using design of experiments (DOE). This work was done with EN-8 as a work piece and copper as tool electrode. Using the Box–Behnken method response surface methodology (RSM) was applied to obtain the optimal values of the process parameters for machining is obtained [3]. The work of the process is mainly determined by many electrical parameters, viz. peak current, pulse on time, dielectric fluid and the size of the tool. All the parameters which are electrical and non-electrical have influence on the EDM output parameters namely material removal rate (MRR) and tool wear rate (TWR) [4].

2   Experimental Details

2.1   Design of Experiments

Careful planning is required for adopting the design of experiments (DOE), and sensible layout of the experiment and expert analysis of results is also necessary. A proper selection of the variables (input factors) and their communications are involved in design of experiments (DOE). A proper selection of the variables (input factors) and their communications are involved in design of experiments (DOE) for determining the optimal parameters for minimum tool wear rate (TWR) and maximum material removal rate (MRR). A Box–Behnken approach has emerged as

Table 1 Machining parameters and their levels

Sl. No.	Machining parameters	Units	Low level	Medium level	High level
1	A. Peak current	A	9	21	34
2	B. Pulse on time	μs	100	500	1000
3	C. Dielectric pressure	kg/cm^2	0.8	1.2	1.6
4	D. Tool size	mm	10	12	15

an advanced tool for enthusiastic engineers and scientists. Table 1 gives the actual values used for the machining of EN-8 steel based on the low, medium and high level of current, pulse time and dielectric pressure set for this experiment for the EDM machine.

2.2 Experimental Plan

In this experiment, four parameters are chosen and three levels have been selected. Totally, 29 experiments were conducted and corresponding output responses are found out.

   The specimen used for this study is conventional EN-8 steel (low-carbon steel) of size $60 \times 80 \times 10$ mm, and top surface was machined in a shaper. Chemical composition of this material is given in Table 2. The electrode material is used were cast square copper electrode with the different dimension of 10, 12 and 15 mm square. An electrical discharge machine model grace V5030 **(die sinking type)** was used to conduct experiments, and grade 3 EDM oil was used with the following specifications of kinematic viscosity 3.0–4.0 cst, 108 °C flash point and 45 kVA of dielectric strength. The machining was done for the duration of 5 min. The electrode and workpiece wear were found by taking the difference of the electrode weights and workpiece before and after machining with the aid of weighing scale OMEGA with capacity of 250 g and accuracy of 1 mg and CIBI weighing scale with a capacity of 500 g and accuracy of 1 mg. The process is shown in Fig. 1.

Table 2 Chemical composition of EN 8 material in wt%

	C	Mn	Si	P	S
Min	0.35	0.60	0.05	0.015	0.015
Max	0.45	1.00	0.35	0.06	0.6

Fig. 1 Parts of EDM: (1) electrode holder, (2) electrode, (3) work piece and (4) magnetic chuck

Side Flushing
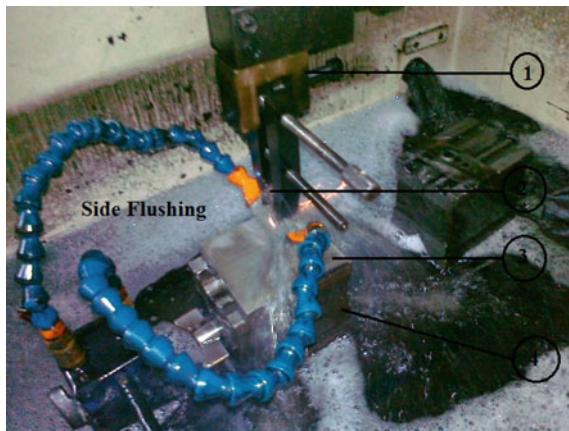
Table 3 shows the design matrix with input parameters and corresponding output responses for 29 trials (Figs. 2 and 3).

3   Result and Discussion

The analysis was made using the Design Expert 7.0.0 software specifically used for response surface methodology applications [5]. This study uses four factors and three levels with 29 trials as shown in Table 3 [6].

Table 3 DOE matrix and result for the EDM process parameters

Std	Run	Peak current	Pulse on time	Dielectric pressure	Tool square	MRR	TWR
		A	μs	kg/cm^2	mm	mm^3/min	mm^3/min
1	4	9	100	1.2	12	21.6741	4.9452
2	9	34	100	1.2	12	100.007	6.4787
3	23	9	1000	1.2	12	3.979	1.1958
4	11	34	1000	1.2	12	45.2959	1.8321
5	17	21	500	0.8	10	45.9431	3.2705
6	27	21	500	1.6	10	50.8221	1.3079
7	15	21	500	0.8	15	65.417	0.0705
8	7	21	500	1.6	15	59.417	4.0584
9	28	9	500	1.2	10	10.837	1.5452
10	8	34	500	1.2	10	65.7698	2.531
11	19	9	500	1.2	15	14.2002	1.2705
12	22	34	500	1.2	15	85.644	2.3695
13	21	21	100	0.8	12	72.1225	5.988
14	25	21	1000	0.8	12	35.5112	1.2705
15	5	21	100	1.6	12	75.728	5.9596
16	1	21	1000	1.6	12	35.5007	2.2331
17	2	9	500	0.8	12	18.0792	1.3736
18	18	34	500	0.8	12	70.897	1.6816
19	14	9	500	1.6	12	14.2002	1.1584
20	3	34	500	1.6	12	85.25	2.831
21	12	21	100	1.2	10	60.1644	7.0448
22	10	21	1000	1.2	10	26.1584	1.0331
23	16	21	100	1.2	15	78.4753	4.8295
24	13	21	1000	1.2	15	39.3587	3.1584
25	26	21	500	1.2	12	55.3064	1.2331
26	29	21	500	1.2	12	58.6696	1.2705
27	20	21	500	1.2	12	55.6801	1.2705
28	24	21	500	1.2	12	54.1853	1.1958
29	6	21	500	1.2	12	57.1748	1.2331

Fig. 2 Electrode after wear
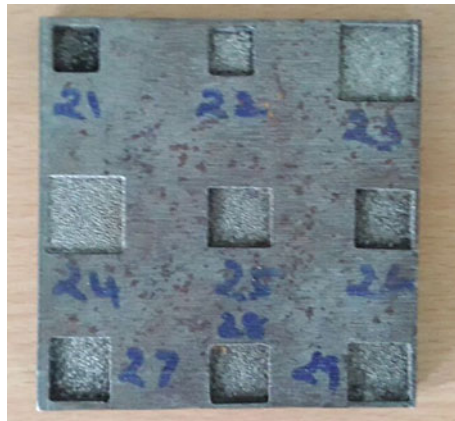
Fig. 3 Workpiece after machining

3.1 Significant Parameter

Significance for MRR depends on tool size, peak current and pulse on time variation of which is directly proportional. The parameters that are significant for TWR are peak current, pulse on time and dielectric pressure variation of which is directly proportional [3].

3.2 Collateral of Explanation

The value of R^2 for workpieces is more than 0.95 [3–7]. The adjusted R^2 is good agreement with R^2 which is used for the terms in the model. The R^2 values are formulated in Table 4.

Table 4 ANOVA table for MRR and TWR

(a) MRR

Source	SS	DF	MS	F value	Prob > F	
Model	17429.8098	14	1244.98642	452.56342	<0.0001	Significant
Residual	38.5135192	14	2.75096566			
Lack of fit	26.3365795	10	2.63365795	0.8651297	0.6141	Not significant
Pure error	12.1769398	4	3.04423494			
Cor. total	17468.3233	28				
Std. dev.	1.65860353		R^2		0.997795237	
Mean	50.3954483		Adj. R^2		0.995590473	
C.V. %	3.29117725		Pred. R^2		0.990427005	
Press	167.224165		Adeq. precision		81.44099936	

(b) TWR

Source	SS	DF	MS	F value	Prob > F	
Model	102.546331	14	7.32473791	4228.8061	<0.0001	Significant
Residual	0.02424948	14	0.00173211			
Lack of fit	0.02034192	10	0.00203419	2.0823138	0.2499	Not significant
Pure error	0.00390756	4	0.00097689			
Cor. total	102.57058	28				
Std. dev.	0.04161857		R^2		0.999763583	
Mean	2.60827241		Adj. R^2		0.999527165	
C.V. %	1.59563741		Pred. R^2		0.99865996	
Press	0.13744871		Adeq. precision		232.2767067	

3.3 Effect of Parameters Interaction

Figure 4 implies the interaction parameters on the EN-8 steel using conventional square copper electrode. Whenever the peak current increases and pulse on time
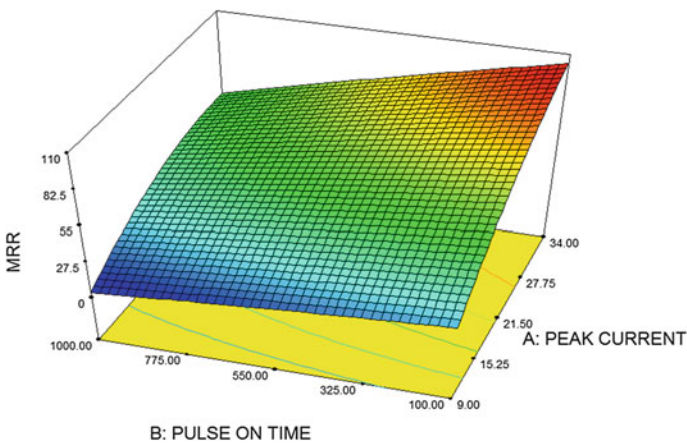
Fig. 4 Interaction plot for MRR
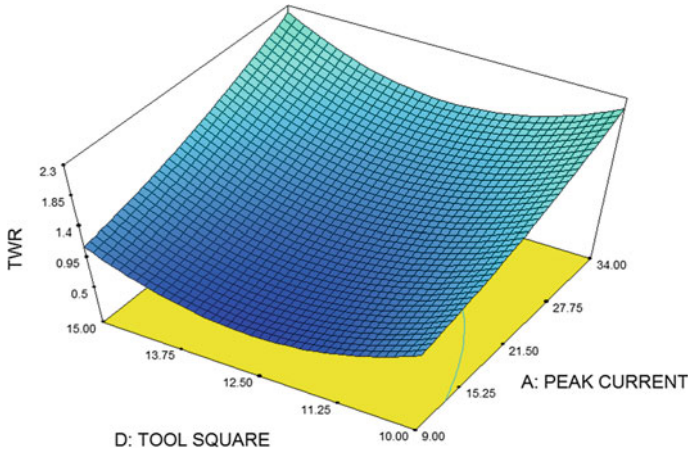
Fig. 5 Interaction plot for TWR

decreases, the MRR will be maximum. Figure 5 shows the decrease in the peak current along with the tool square that decreases the TWR to the minimum.

4　Optimist Exploration

Now the intendment is carried out under the control of electrical discharge machining, and the best consolidation is from the different inconsistent effects along the machining parameters such as TWR values and MRR values which could be studied based on the mathematical models. Optimal exploration has been developed for that different variable condition depending on maximizing the values of MRR and minimizing the TWR values. The optimal solution of different variables is achieved in the control of the developed precise models. The optimal value results have been tabulated, as exposed in Table 5 [8, 9].

Table 5 Optimum parameters

Std	Peak current	Pulse on time	Dielectric pressure	Size of the tool	MRR (mm^3/min)	TWR (mm^3/min)	Desirability
1	34	472.33	0.8	15	87.216477	0.5225625	0.900344065
2	33.94	466.68	0.8	15	87.526726	0.5477734	0.900275406
3	34	478.27	0.8	15	86.848042	0.494674	0.900267826

5 Conclusion

The following conclusion is arrived at based on the experiments conducted on EN-8 steel for EDM machining.

Considering EN-8 steel which has been machined by cast square electrode, the mean value of material removal rate (MRR) is (maximum) 87.2 mm^3/min and tool wear rate (TWR) is (minimum) 0.52 mm^3/min. The two values of machining is found to be very effective and efficient.

Further to the above, the following are observed while machining.

- The material removal rate and tool wear rate are mainly influenced by the tool size and peak current.
- The value of collateral of explanation (R^2) is above 0.95.
- The predicted value R^2 is in good agreement with Adj. R^2.
- The input parameters have been optimized in order to get maximum material removal and minimum tool wear rate.
- Peak current of 34 A with 472 μs of pulse on time, dielectric pressure of 0.8 kg/cm^2 and 15 mm size tool yield maximum MRR of 87.2 mm^3/min and minimum TWR of 0.52 mm^3/min.

References

1. Kansal, H.K., Sehijpal Singha, B., Kumara, P.: Parametric optimization of powder mixed electrical discharge machining by response surface methodology. J. Mater. Process. Technol. **169**, 427–436 (2005)
2. Mir, M.J., Sheikh, K., Singh, B., Malhotra, N.: Modelling and analysis of machining parameters for surface roughness in powder mixed EDM using RSM approach. Int. J. Eng. Sci. Technol. **4**, 45–52 (2012)
3. Balasubramanian, P., Senthilvelan, T.: Optimization of machining parameters in EDM process using cast and sintered copper electrodes. Procedia Mater. Sci. **6**, 1292–1302 (2014)
4. Chandramouli, S., Shrinivas Balraj, U., Eswaraiah, K.: Optimization of electrical discharge machining process parameters using Taguchi method. Int. J. Adv. Mech. Eng. **4**, 425–434 (2014)
5. Amrish Raj, D., Senthilvelan, T.: Empirical modelling and optimization of process parameters of machining titanium alloy by wire-EDM using RSM. Mater. Today Proc. **2**, 1682–1690 (2015)
6. Gopalakannan, S., Senthilvelan, T., Ranganathan, S.: Modeling and optimization of EDM process parameters on machining of Al 7075–B$_4$C MMC using RSM. Procedia Eng. **38**, 685–690 (2012)
7. Cheke, P.R., Khedekar, D.S., Pawar, M.S., Kandam, R.S.: Comparative performance of wet of and dry EDM process for machining of oil hardened non sinking steel material. Int. J. Mech. Eng. Technol. **3**, 13–22 (2012)

8. Jangra, K., Grover, S., Aggarwal, A.: Simultaneous optimization of material removal rate and surface roughness for WEDM of WC-Co composite using grey relational analysis along with Taguchi method. Int. J. Ind. Eng. Comput. **2**, 479–490 (2011)
9. Kumar, A., Kumar, V., Kumar, J.: Prediction of surface roughness in wire electric discharge machining (WEDM) process based on response surface methodology. Int. J. Eng. Technol. **2**, 708–719 (2012)

Analysis and Optimization on Functionally Graded Rotating Disk Using Grey Relational Method

P. Tharun, M. Dharshan Siddarth, D. Prakash and K. Babu

Abstract In the present study, optimization on rotating functionally graded disk is made through Taguchi's *S/n* ratio and grey relational technique. Initially, the stress components and the displacement of the rotating disk are analyzed by analytical technique and finite element analysis (FEA) and observed that the results of the FEA analysis have a good coincidence with analytical method. Later, multi-objective optimization techniques are employed in the structural analysis of rotating disk to minimize the maximum stress, displacement, and mass of the disk. Rotating disk's outer and inner radius ratio, *b/a*, material property gradient index, *n*, thickness index, *m*, angular speed, *w*, the temperature difference, *T* and constraints at the inner and outer surface of the rotating disk are included as the control parameters. These parameters are varied to three levels of value, and the L27 orthogonal matrix is used. The twenty-seven cases are analyzed through FEA technique, and as an outcome, maximum stress and displacement are determined. From the multi-objective optimization, the best value for the control parameters is identified as *b/a* = 2; *n* = 1; *m* = 0; speed = 5000 rpm; temperature difference = 300 °C and clamped constraint at inner and outer surface of rotating disk and the corresponding maximum stress = 0.567 Mpa, deflection = 0.113 μm, and mass = 0.84 kg.

Keywords Functionally graded material · Analytical method · Numerical simulation · Optimization · Grey relation

P. Tharun · M. Dharshan Siddarth · D. Prakash (✉)
School of Mechanical Engineering, SASTRA Deemed to be University, Thanjavur 613401, India
e-mail: prakash@mech.sastra.edu

K. Babu
Department of Mechanical Engineering, SSN College of Engineering, Chennai 603110, India
e-mail: babuk@ssn.edu.in

1 Introduction

For the last two decades, functionally graded materials (FGM) are finding many applications in the engineering and biomedical field due to a gradual change in the volume fraction of constituents from one surface to another surface. The continuous material property variation along any direction causes reduced stress at sharp boundaries in comparison with laminated composites. The material properties are varied in accordance with power law or exponential function. It is also essential to study the behavior of stress components like radial, tangential, thermal stress and strain components for the given speed and thermal conditions. In this context, FGM has high scope in rotating disk components like turbine rotor, ship propeller, turbojet engines, compressor, flywheel, brakes, and gears. For these components, the selection of material constituents is based on the functional requirement. Components that are working in high-temperature environment, ceramic and metal constituents are used in which ceramic is used at the hot surface to prevent heat transfer. Al_2O_3/ZrO_2 combination is used where good hardness, wear resistance, toughness, and strength are required. Yongming et al. [1] used titanium silicon carbide (Ti_3SiC_2) and alumina (Al_2O_3) in which Ti_3SiC_2 is having excellent electrical and thermal conductivity, thermal shock resistance, high melting point, high strength and high toughness with low density, whereas Al_2O_3 has excellent hardness and insulation characteristics. The structural behavior of the above said FGM materials had been studied by various approaches and some of them are listed as follows. Hassani et al. [2] employed three methods, Runge–Kutta's method, variable material property, and finite element method in the stress–strain behavior of a non-uniform rotating disk under thermos mechanical loading and reported that Runge–Kutta's method is more accurate than variable material property method. Mahdavi et al. [3] used VMP method and FEA through ANSYS software in the thermo-plastic analysis of FGM disk with varying disk thickness and noticed that temperature gradient, thickness profile, and boundary conditions have a significant impact on stress behavior. Çallıoğlu et al. [4] obtained the radial and tangential stress components for an FGM disk rotating at constant angular velocity through the analytical and numerical method and validated the numerical solution with analytical method. Gupta et al. [5] studied the creep characteristics of rotating disk made of silicon carbide particle in the pure aluminum matrix. Durodola and Attia [6] performed a comparison between FEM and direct numerical integration with the prediction of stresses and deformation in FGM subjected to centrifugal body load for both solid and hollow disks. The analysis was performed on uniform thickness disk profile, and the results showed that strain and stresses in solid disks were not significantly modified by choice of gradation as it was in the case of hollow disks. Bhowmick et al. [7] proposed a numerical method to analyze stress and deformation on rotating solid disk by the variational approach by considering the radial displacement as an unknown variable. Similarly, many researchers employed semi-analytical method [8–10], finite element method [11], direct numerical integration [12] in the analysis of stress and strain in rotating FGM disk.

In most of the research works, it is noticed that the stress and strain behavior is studied by varying the diameter of rotating disk, thickness profile index, material property variation index, type of constraint at the inner and outer surface of the disk, temperature gradient, angular speed, angular acceleration and observed their impact. In addition to the above studies, high strength to weight ratio is also an essential factor to be considered in designing the FGM disk. To the best of the authors' knowledge, such a kind of study is very limited, and hence in this study, optimization of geometrical and physical properties of FGM disk is made for optimum strength and weight. This study is organized with analytical and FEA analysis on FGM disk, multi-objective optimization by grey relational analysis and to study the percentage effect of each factor on stress and deflection by analysis of variance (ANOVA) technique is included.

2 FGM Disk Configuration

In this study, the disk is analyzed for uniform and varying thickness with an inner radius, a and outer radius, b. Under varying thickness disk, convergent and divergent shapes are included. The thickness is varying along the radial direction in accordance with Eq. (1).

$$t(r) = t_o \left(\frac{r}{b}\right)^{-m} \tag{1}$$

$$E(r) = E\left(\frac{r}{b}\right)^{n1} \tag{2}$$

$$\rho(r) = \rho\left(\frac{r}{b}\right)^{n2} \tag{3}$$

$$\alpha(r) = \alpha\left(\frac{r}{b}\right)^{n3} \tag{4}$$

$$T(r) = T_o \left(\frac{(b^2 - r^2)}{b^2 - a^2}\right) \tag{5}$$

where m is the varying thickness index and t_o is the thickness of the disk at the axis. The value of m is positive for convergent thickness disk, negative for divergent thickness, and zero for uniform thickens. Figure 1 shows the geometry of rotating disk with various thickness profiles. The physical properties like Young's modulus, density, and thermal expansion coefficient are varied along the radial direction as per the equations from (2) to (5). However, the Poisson's ratio is considered as constant since its variation is expected to be insignificant on stress.

Where $n1$, $n2$, and $n3$ are the property gradient index. In this study, the elastic modulus, E = 72,000 MPa; ρ = 2800 kgm^{-3}; Poisson's ratio, υ = 0.3 and the

Fig. 1 Geometry of rotating
disk
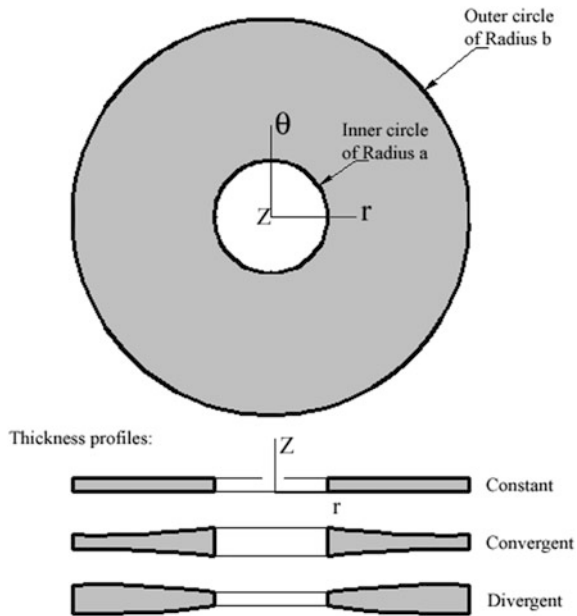
thermal expansion coefficient, $\alpha = 25 \times 10^{-5}$ 1/°C. The disk is rotating about its centroidal axis, Z with a constant speed of w rpm. For this rotating disk, the radial stress, tangential stress, and deflection are calculated from analytical and numerical analysis.

2.1 Stress Analysis—Analytical Method

In the analytical method, rotating disk with uniform thickness is considered, the thickness of the rotating disk is comparatively small, and hence, the static analysis is made under plane stress condition. The inertial force due to constant angular velocity is the only body force acting on the disk and because of axial symmetry, shear stress component $\tau_{r\theta}$ gets vanished. The governing differential equation for the above conditions is given in Eq. (6).

$$\frac{d}{dr}(r\sigma_r) - \sigma_\theta + \rho(r)\omega^2 r^2 = 0 : \ \sigma_r = \frac{F}{r}; \ \sigma_\theta = \frac{dF}{dr} + \rho(r)\omega^2 r^2 \qquad (6)$$

σ_r and σ_θ are the radial and tangential stress, ρ is the density varying as the function of radius, r ($a \leq r \leq b$). Above Eq. (1) is satisfied for the stress function F.

The strain–displacement relation under rotating symmetry condition is given as $\varepsilon_r = \frac{du}{dr}; \ \varepsilon_\theta = \frac{u}{r}; \ \varepsilon_{r\theta} = 0.$

ε_r and ε_θ are the radial and tangential strain components, and u is the radial displacement.

Then, the strain compatibility equation is written as $\varepsilon_r = \dfrac{d}{dr}(r\varepsilon_\theta)$.

The stress–strain relationship is given by using Hooke's law under plane stress condition.

$$\varepsilon_r = \frac{1}{E(r)}(\sigma_r - v\sigma_\theta) + \alpha(r)T(r) : \ \varepsilon_\theta = \frac{1}{E(r)}(\sigma_\theta - v\sigma_r) + \alpha(r)T(r)$$

$E(r)$ is the radially varying elastic modulus, v is the poisson ratio assumes to be constant, and $T(r)$ is the variation of temperature along the radial direction as given in Eq. (5).

Using the above relations, the strain compatibility equation is rewritten as Eq. (7).

$$r^2 F'' + rF'\left(1 - r\frac{E'(r)}{E(r)}\right) - F\left(1 - vr\frac{E'(r)}{E(r)}\right) = -\rho(r)\omega^2 r^3\left(3 + v - r\frac{E'(r)}{E(r)}\right)$$
$$- \rho'(r)\omega^2 r^2 - E(r)r^2(\alpha'(r)T(r) + \alpha(r)T'(r)) \tag{7}$$

The above equation is reduced to Eq. (8).

$$r^2 F^n + rF'(1 - n1) - F(vn1 - 1) = -\rho\omega^2 \frac{(3 + v - n1 + n2)}{b^{n2}} r^{n2+3}$$
$$- \frac{E\alpha T_o n3}{b^{n1+n2}(b^2 - a^2)} r^{n1+n2+1} + \frac{E\alpha T_o(n3 + 2)}{b^{n1+n2}(b^2 - a^2)} r \tag{8}$$

For homogeneous isotropic material $n1$, $n2$, and $n3 = 0$ and Eq. (8) are simplified as Eq. (9).

$$r^2 F^n + rF' - F = -\rho\omega^2 r^2(3 + v) \tag{9}$$

The stress function F can be written as:

$$F = C_1 r^{(n1+m)/2} + C_2 r^{(n1-m)/2} + C_3 r^{(n2+3)} + C_4 r^{(n1+n3+1)} + C_5 r^{(n1+n3+3)}$$
$$\text{where } m = \sqrt{(n1^2 - 4vn1 + 4)}$$

$$C_3 = -\frac{\rho\omega^2(3 + v - n1 + n2)}{b^{n2}(n2^2 + 6n2 - n1n2 - 3n1 + vn1 + 8)} C_4$$
$$= \frac{E\alpha T_o n3}{b^{(n1+n2-2)}(b^2 - a^2)(n3^2 + 2n3 - n1n3 + n1 + vn1)}$$

$$C_4 = \frac{E\alpha T_o n3}{b^{(n1+n2-2)}(b2-a2)(n3^2+2n3-n1n3+n1+\upsilon n1)} \tag{10}$$

Then, the radial stress component is given as

$$\sigma_r = C_1 r^{(n1+m-2)/2} + C_2 r^{(n1-m-2)/2} + C_3 r^{(n2+3)} + C_4 r^{(n1+n)} + C_5 r^{(n1+n3+2)} \tag{11}$$

$$\sigma_\theta = \frac{(n1+m)}{2} C_1 r^{(n1+m-2)/2} + \frac{(n1+m)}{2} C_2 r^{(n1-m-2)/2} + (n2+3)C_3 r^{(n2+3)}$$
$$+ (n1+n3+1)C_4 r^{(n1+n)} + (n1+n3+3)C_5 r^{(n1+n3+2)} + \rho(r)\omega^2 r^2 \tag{12}$$

$$C_1 = \frac{D_2 b^{\frac{-n1+m+2}{2}} - D_1 a^{\frac{-n1+m+2}{2}}}{b^m - a^m} : \quad C_2 = \frac{D_1 b^m a^{\frac{-n1+m+2}{2}} - D_2 a^m b^{\frac{-n1+m+2}{2}}}{b^m - a^m}$$

where $\qquad D_1 = -C_3 a^{n2+2} - C_4 a^{n1+n3} - C_5 a^{n1+n3+2}$:
$D_2 = -C_3 b^{n2+2} - C_4 b^{n1+n3} - C_5 b^{n1+n3+2}$.

Radial displacement component is given as

$$u = \frac{r}{E(r)}(\sigma_\theta - \upsilon\sigma_r) + r\alpha(r)T(r) \tag{13}$$

2.2 Numerical Analysis

The rotating disk of functionally graded material is numerically analyzed through finite element technique. The geometry of the rotating disk is modeled in the ANSYS APDL platform in 2-dimensional geometry under plane stress considerations. The geometry is created in the cylindrical coordinate system with an inner radius of $a = 40$ mm and outer radius $b = 100$ mm with uniform thickness as shown in Fig. 1.

The disk rotates at a constant angular speed of 5000 rpm about its centroidal axis Z. The geometry is divided into 30 annular strips, and the material properties are defined in accordance with Eqs. (2)–(4) with the constant Poisson ratio of 0.3. The disk is modeled with aluminum material at in the inner surface and ceramic material at the outer surface with $E = 72$ GPa, $\rho = 2800$ kgm^{-3}, and $\alpha = 23 \times 10^{-6}$ 1/°C. Plane 42-2D structural element is used to mesh the geometry, and each annular strip is meshed with 60 elements. The following boundary conditions are specified to solve the finite element domain. Inner and outer circles of the rotating disk constrained as free–free condition. The temperature at each strip is defined in accordance with Eq. (5), and the temperature at the inner surface of the disk is 300 °C. The angular velocity of ω rad/s is specified about its centroidal axis, Z. From the outcome of the numerical analysis, the radial stress and tangential stress along the radial

direction are plotted, compared with analytical solutions and noticed that numerical solution is having a good agreement with analytical results as shown in Fig. 2. Also, the stress plots and deflection plot for the same case are shown in Fig. 3.
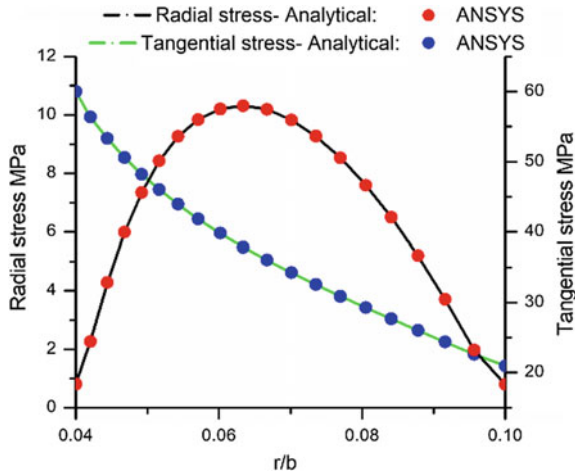
Fig. 2 Validation of numerical result with analytical prediction
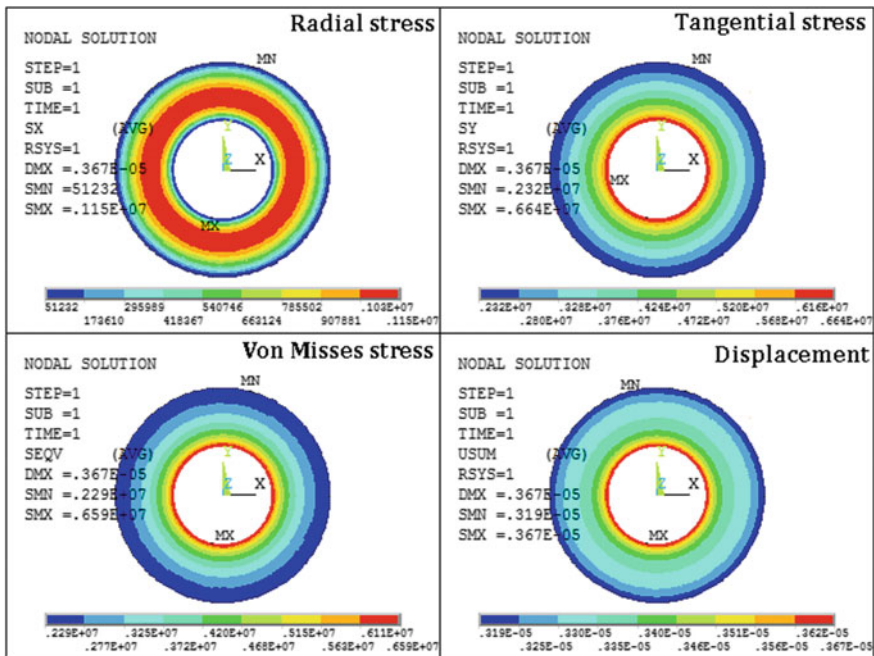
Fig. 3 Stress and deflection plot

2.3 Multi-Objective Optimization

Taguchi's grey relational analysis is the widely used method for multi-objective optimization since it provides an efficient solution for uncertainty, multi-input, and discrete data problem. It analyzes the relationship between sequences with fewer data and can examine many factors in comparison with statistical method [15]. This technique is employed in this study for minimization of deflection, stress, and mass of disk with equal weightage function. The control parameters considered in this optimization are inner to outer diameter ratio (b/a), material property gradient index n, thickness index m, angular speed, w, temperature difference, T and constraints at the inner and outer circle of rotating disk. The constraints C and F represent "Free" and "Clamped" condition, respectively. The above-stated parameters are changed to three different values and are given in Table 1.

In this optimization study, the L27 orthogonal matrix is employed which is the standard pattern available. The L27 orthogonal matrix is shown in Table 2 with the assigned design parameter values. The 27 cases are analyzed numerically in the ANSYS software with the above-discussed procedure, and as an outcome, stress, deflection, and weight of the disk are predicted and given in Table 2.

The deflection, stress, and mass for the 27 cases are normalized between zero and one by using Eq. (14) and given in Table 2.

$$x_i(k) = \frac{\max y_i(k) - y_i(k)}{\max y_i(k) - \min y_i(k)} \tag{14}$$

$$\xi_i(k) = \frac{\Delta_{\min} - \psi \Delta_{\max}}{\Delta_{0i}(k) + \psi \Delta_{\max}} \tag{15}$$

$$\sum_{k=1}^{n} \xi_i(k) \gamma_i = \frac{1}{n} \tag{16}$$

where $\max y_i(k)$ and $\min y_i(k)$ is the largest value of $y_i(k)$ for the kth response and $x_i(k)$ is the value after grey relational generation. The grey relation coefficient is calculated from Eq. (14). $\Delta_{0i}(k)$ is the difference between absolute value $x_0(k)$ and $x_i(k)$, ψ is the identification coefficient ranging between 0 and 1, and generally it is taken as 0.5. $\Delta_{\min}$ and $\Delta_{\max}$ are the minimum and maximum value among the Δ_{0i} for the respective kth response. Next, the grey relation grade (GRG) is calculated from Eq. (15) and given in Table 2. Where n is the number of process responses.

Table 1 Level values of parameters

Parameter	Level 1	Level 2	Level 3	Parameter	Level 1	Level 2	Level 3
b/a	2	3	4	N (rpm)	5000	10,000	15,000
n	−1	0	1	T(°C)	300	400	500
m	−0.5	0	0.5	C	FF	CF	CC

Table 2 L27 orthogonal array and output responses

| Case No. | Design parameters | | | | | | δ (μm) | Output responses | | Normalized data | | | Grey relation |
	b/a	n	m	N	T	C		σ (Mpa)	Weight (kg)	δ (μm)	σ (Mpa)	Weight (kg)	
1	2	−1	−0.5	5000	300	FF	2.24	8.19	0.981	0.98	0.97	0.97	0.95
2	2	−1	−0.5	5000	400	CF	0.411	3.77	0.981	1.00	0.99	0.97	0.97
3	2	−1	−0.5	5000	500	CC	0.109	1.79	0.981	1.00	1.00	0.97	0.98
4	2	0	0	10,000	300	FF	9.55	17.59	0.844	0.91	0.92	0.99	0.89
5	2	0	0	10,000	400	CF	1.83	9.38	0.844	0.98	0.96	0.99	0.96
6	2	0	0	10,000	500	CC	0.444	3.88	0.844	1.00	0.99	0.99	0.98
7	2	1	0.5	15,000	300	FF	22.9	21.36	0.733	0.78	0.90	1.00	0.84
8	2	1	0.5	15,000	400	CF	4.61	13.65	0.733	0.96	0.94	1.00	0.94
9	2	1	0.5	15,000	500	CC	1.01	4.77	0.733	0.99	0.98	1.00	0.98
10	3	−1	0	15,000	300	CF	15.6	95.84	3.440	0.85	0.51	0.68	0.63
11	3	−1	0	15,000	400	CC	4.81	52.88	3.440	0.95	0.73	0.68	0.73
12	3	−1	0	15,000	500	FF	34.9	192.90	3.440	0.66	0.00	0.68	0.51
13	3	0	0.5	5000	300	CF	2	5.12	2.728	0.98	0.98	0.77	0.87
14	3	0	0.5	5000	400	CC	0.555	2.37	2.728	1.00	1.00	0.77	0.89
15	3	0	0.5	5000	500	FF	4.53	8.51	2.728	0.96	0.97	0.77	0.85
16	3	1	−0.5	10,000	300	CF	12.6	21.04	1.39	0.88	0.90	0.92	0.83
17	3	1	−0.5	10,000	400	CC	2.25	5.15	1.39	0.98	0.98	0.92	0.93
18	3	1	−0.5	10,000	500	FF	27.1	17.24	1.39	0.74	0.92	0.92	0.79
19	4	−1	0.5	10,000	300	CC	5.42	39.48	9.241	0.95	0.80	0.00	0.65
20	4	−1	0.5	10,000	400	FF	23.9	138.97	9.241	0.77	0.29	0.00	0.48
21	4	−1	0.5	10,000	500	CF	15.6	60.83	9.241	0.85	0.69	0.00	0.57
22	4	0	−0.5	15,000	300	CC	14.4	55.07	3.49	0.86	0.72	0.68	0.68
23	4	0	−0.5	15,000	400	FF	103	193.76	3.49	0.00	0.00	0.68	0.42

(continued)

Table 2 (continued)

Case No.	Design parameters						Output responses			Normalized data			Grey relation
	b/a	n	m	N	T	C	δ (μm)	σ (Mpa)	Weight (kg)	δ (μm)	σ (Mpa)	Weight (kg)	
24	4	0	−0.5	15,000	500	CF	67.1	168.59	3.49	0.35	0.13	0.68	0.47
25	4	1	0	5000	300	CC	1.65	1.95	2.902	0.99	1.00	0.75	0.88
26	4	1	0	5000	400	FF	13.9	7.41	2.902	0.87	0.97	0.75	0.80
27	4	1	0	5000	500	CF	9.01	8.17	2.902	0.91	0.97	0.75	0.82

Table 3 Response table for the grey relational grade

Parameter	Level 1	Level 2	Level 3	Parameter	Level 1	Level 2	Level 3
b/a	0.94393	0.78141	0.64072	N (rpm)	0.88889	0.7881	0.68907
n	0.71929	0.77853	0.86825	T (°C)	0.80243	0.7901	0.77353
m	0.78133	0.79926	0.78547	C	0.72604	0.78433	0.8557

Higher value of grey relation grade corresponds to intense relational degree between the reference sequence $x_0(k)$ and $x_i(k)$ [16].

Finally, the optimum control factors value is predicted from the grey relational grade response Table 3. The best value for the control parameters is identified as $b/a = 2$; $n = 1$; $m = 0$; speed = 5000 rpm; temperature difference = 300 °C and clamped constraint at the inner and outer circle of rotating disk. For this combination of parametric values, a confirmation analysis is conducted in the ANSYS and the stress, deflection, and mass are predicted as 0.567 Mpa and 0.113 μm, 0.84 kg, respectively.

3   Conclusion

In this study, rotating disk of functionally graded material is analyzed for stress and deflection using the analytical and numerical method. The numerical simulation method is employed in the ANSYS software and validated with analytical solutions. The material properties like Young's modulus, density, and thermal expansion coefficient are radially orthotropic. Also, the disk is analyzed for uniform and varying thickness. As an outcome of the analysis, maximum radial stress, maximum tangential stress, deflection is predicted and shown as contour plots. Later optimization technique is employed to identify the optimum values for inner to outer diameter ratio (b/a), material property gradient index n, thickness index m, angular speed (w), temperature difference, T and constraints at the inner and outer circle of rotating disk for minimum stress and deflection. The multi-objective optimization is carried out for minimization of stress, deflection, and mass of disk with equal weightage. The best value from the multi-objective optimization is found as $b/a = 2$; $n = 1$; $m = 0$; speed = 5000 rpm; temperature difference = 300 and clamped constraint at the inner and outer circle of rotating disk. For the corresponding control parameter value, the stress = 0.567 Mpa, deflection = 0.113 μm, and mass = 0.84 kg. Finally, ANOVA technique is employed to study the percentage influence of each control factor on stress and deflection, found that angular speed and b/a ratio are the most significant factors on both displacement and total stress and temperature is the lest significant factor on both output responses.

References

1. Yongming, L., Wei, P., Shuqin, L., Ruigang, W., Jianqiang, L.: A novel functionally graded material in the Ti–Si–C system. Mater. Sci. Eng. A **345**(1), 99–105 (2003)
2. Hassani, A., Hojjati, M.H., Mahdavi, E., Alashti, R.A., Farrahi, G.: Thermo-mechanical analysis of rotating disks with non-uniform thickness and material properties. Int. J. Pres. Ves. Pip. **98**, 95–101 (2012)
3. Mahdavi, E., Ghasemi, A., Alashti, R.A.: Elastic–plastic analysis of functionally graded rotating disks with variable thickness and temperature-dependent material properties under mechanical loading and unloading. Aerosp. Sci. Technol. **59**, 57–68 (2016)
4. Çallıoğlu, H., Sayer, M., Demir, E.: Elastic–plastic stress analysis of rotating functionally graded discs. Thin Wall Struct. **94**, 38–44 (2015)
5. Gupta, V.K., Chandrawat, H.N., Singh, S.B., Ray, S.: Creep behaviour of a rotating functionally graded composite disc operating under thermal gradient. Metall. Mater. Trans. A **35**(4), 1381–1391 (2004)
6. Durodola, J.F., Attia, O.: Deformation and stresses in functionally graded rotating disks. Compos. Sci. Technol. **60**(7), 987–995 (2000)
7. Bhowmick, S., Misra, D., Saha, K.N.: Approximate solution of limit angular speed for externally loaded rotating solid disk. IJMS **50**(2), 163–174 (2008)
8. Kordkheili, S.H., Naghdabadi, R.: Thermoelastic analysis of a functionally graded rotating disk. Compos. Struct. **79**(4), 508–516 (2007)
9. Asghari, M., Ghafoori, E.: A three-dimensional elasticity solution for functionally graded rotating disks. Compos. Struct. **92**(5), 1092–1099 (2010)
10. Bayat, M., Saleem, M., Sahari, B.B., Hamouda, A.M.S., Mahdi, E.: Analysis of functionally graded rotating disks with variable thickness. Mech. Res. Commun. **35**(5), 283–309 (2008)
11. Damircheli, M., Azadi, M.: Temperature and thickness effects on thermal and mechanical stresses of rotating FG-disks. JMST **25**(3), 827–836 (2011)
12. Zenkour, A.M.: Analytical solutions for rotating exponentially-graded annular disks with various boundary conditions. Int. J. Struct. Stab. Dy. **5**(04), 557–577 (2005)
13. Chang, C.L., Tsai, C.H., Chen, L.: Applying grey relational analysis to the decathlon evaluation model. Int. J. Comput. Internet Manag. **11**(3), 54–62 (2003)
14. Datta, S., Mahapatra, S.: Modelling, simulation and parametric optimization of wire EDM process using response surface methodology coupled with grey-Taguchi technique. IJEST **2**(5), 162–183 (2010)

Investigation on the Process Parameters of Double-Sided Friction Stir Welded AA6082-T$_6$ Joints with Different Tool Pins Using Response Surface Methodology

S. Vignesh, P. Dinesh Babu, M. Nalla Mohamed, S. Martin Vinoth, G. Surya and S. Dinesh

Abstract Aluminium alloys are of much use in several vital areas including aerospace, marine, defence and railways, which becomes obligatory to have a welded joint of high strength. The input considerations of the friction stir welding process of double-sided type play an imperative part in identifying the performance and characteristics of the joints. This research is a novel approach to investigate the influence of weld input parameters on the output responses of aluminium 6082-T$_6$ alloy using tapered square and tapered pentagonal tool pin profiles. The double-sided friction stir welding (FSW) was chosen for the research work, as it gives better strength joint than single-sided ones. Response surface methodology (RSM) was used to establish the interactions through mathematical relationships, considering the FSW process parameters and output responses. The influence of tapered square (TSP) and tapered pentagonal pin (TPP) profiles on the welding

S. Vignesh (✉) · G. Surya · S. Dinesh
Department of Mechatronics, Bannari Amman Institute
of Technology, Sathyamangalam 638401, India
e-mail: vignesh@bitsathy.ac.in

G. Surya
e-mail: surya.mc15@bitsathy.ac.in

S. Dinesh
e-mail: dinesh.mc16@bitsathy.ac.in

P. Dinesh Babu · S. Martin Vinoth
School of Mechanical Engineering, SASTRA University,
Thanjavur 613401, India
e-mail: dineshbabu@mech.sastra.edu

S. Martin Vinoth
e-mail: martinvinoth@mech.sastra.edu

M. Nalla Mohamed
Department of Mechanical Engineering, SSN College of Engineering,
Chennai 603110, India
e-mail: nallamohamedm@ssn.edu.in

309

characteristics was analysed. Also, an extended investigation was carried out in achieving the welding parameters in optimum level, so as to maximize the output responses.

Keywords Aluminium alloys · Double-sided friction stir welding Tapered square pin · Tapered pentagonal pin · Desirability approach Response surface methodology

1 Introduction

Al–Mg–Si alloy conforming to AA6082-T$_6$ is a common alloy for extrusions, plate and sheet from stock which has quite good weldability in comparison with high strength Al alloys [1]. It is increasingly used in the marine structures and aircraft applications with the fully heat-treated condition, as it has 0.2% proof stress (f_o) about equal to the yield of mild steel. Also, it can be readily welded with nearly 50% loss of strength in the heat-affected zone [2, 3]. Though these alloys are known for their weldability, they undergo problems such as softening, etc. in the heat-affected area. At the time of weld thermal cycle, Mg$_2$Si precipitate substances get reversed [4]. This mechanical disability is an important issue in the design aspects of engineering [5]. Friction stir welding (FSW) is chosen in spite of having many fusion welding processes, because it could be a solid-state welding approach where the material to be welded does not melt throughout the process [6]. This process is widely preferred due to the absence of parent metal melting [7]. The investigation on the improvement in double-sided friction stir welded joint in terms of strength is important for describing its performance. The main intention of any manufacturer is to select the welding process parameters that would yield a joint of high strength. Response surface methodology (RSM) is a type of approach that is used to predict the process parameters for producing a high strength joint with excellent characteristics. This particular method is widely preferred as it reduces the time required for the design of experiments and the effort needed from labours.

Ram Kumar et al. [8] made a comparative analysis on the improvement in the strength of aluminium joints using single- and double-sided friction stir welding processes and concluded that superior welds can be acquired by double-sided friction stir welded joints such that the welding regions are reachable from both sides for the process. Elatharasana et al. [9] conducted an experimental analysis and optimization of process parameter on FSW of AA 6061-T6 aluminium alloy using RSM. With the help of Taguchi design approach, Lakshminarayanan et al. [10] performed a study to investigate the influences of FSW process parameters on the tensile strength of AA7039 butt joints and concluded that the spindle speed, welding speed and axial force are the most significant parameters in deciding the tensile strength of the joint. Tiwari et al. [11] conducted a parametric analysis of FSW using RSM and suggested that it is necessary to investigate the mechanical aspects of the welded joint for describing its performance. Hence, in our research,

the responses such as tensile strength, hardness, toughness were taken to assess the characteristics of double-sided FSW aluminium alloy 6082 joints. The main intention is to utilize RSM to establish mathematical relationships, considering the FSW input parameters such as spindle speed measured in rpm, welding speed measured in mm/s, two different pin profiles, and the output responses such as tensile strength measured in MPa, hardness in HV, toughness in kg(f) m. The other objective is to determine the optimal welding location which would maximize the output responses using desirability approach.

2 Experimentation

2.1 Materials

In this research, the aluminium 6082-T_6 alloy was chosen as the base metal due to its common usage in marine parts and aircraft structures [1]. In order to confirm the various elements present in as-received aluminium alloy, the chemical analysis test was conducted as per ASTM-E1251 standard. The chemical compositions of the base metal are formulated in Table 1. The base metal 6082-T_6 aluminium alloy has been cut into the required size (150 mm $\times$ 75 mm $\times$ 8 mm). The mechanical properties of the base material are given in Table 2. It is evident that when the tapered pin profile is used, it produces a higher welding force than the straight pin profile [12]. Hence, the welding of joints of 6082-T_6 aluminium alloy has been carried out in computer numerical controlled FSW machine using tools with two different pin profiles such as tapered square and tapered pentagonal. The tools which are made of tungsten carbide are used in experimentation due to its strength rather than steel with a Young's modulus of 550 GPa and maintains a sharp edge better than other tools. The process parameters such as spindle speed (N), welding speed (S) and tool pin profiles (tapered square or tapered pentagonal) were considered as an important aspect which influences the quality of the weld joint produced. The effects of tool pin profile on metallurgical and mechanical properties of the weldments were evaluated. The changes in the microstructure of the weld zones were observed using scanning electron microscope (SEM).

2.2 Methods

The welding process was performed using special friction stir welding equipment shown in Fig. 1. The machine is capable of welding 50-mm-thick Al alloys plates. The double-sided friction stir welding application is shown schematically in Fig. 3. The double-sided friction stir welded joints are found to have much better strength joints when compared with single-sided friction stir welded joints [13]. Thus, better

Table 1 Chemical composition of the 6082-T$_6$ alloy (wt%)

Reference	Si	Fe	Cu	Mn	Mg	Cr	Ni	Zn	Ti	Pb
Typical	0.7–1.3	≤ 0.50	≤ 0.10	0.4–1.0	0.6–1.2	≤ 0.25		≤ 0.20	≤ 0.10	
Actual batch	1.0	0.20	<0.02	0.48	0.65	<0.01	<0.01	0.01	0.02	<0.01

Table 2 Mechanical properties of the 6082-T$_6$ alloy

Yield strength (MPa)	Ultimate strength (MPa)	Elongation (%)	Hardness (HRB)	Density (g/cm^3)	Melting point (°C)
168.33	300	11.5	70	2.70	555
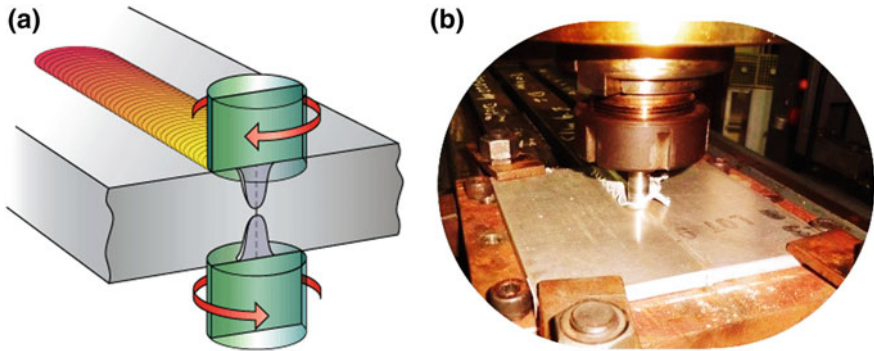
Fig. 1 Schematic illustration and equipment of double-sided friction stir welding
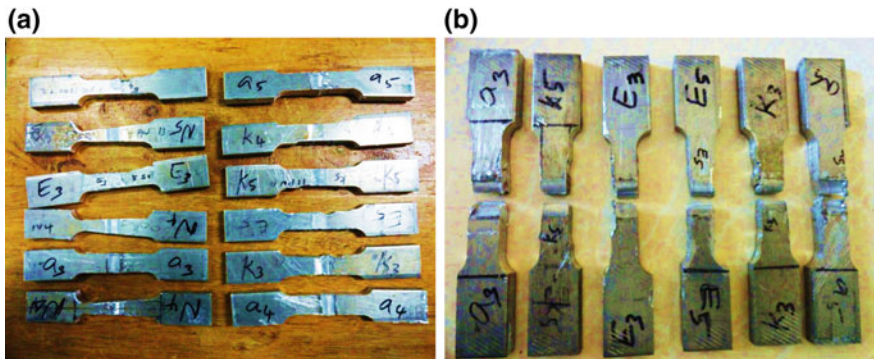
Fig. 2 Tensile specimens **a** before test and **b** after test

weld joints can be obtained in the case of double-sided FSW process [8, 13]. A rotating tool with a specially designed pin and shoulder is inserted into the butting edges of plates to be joined and then traversed along the joint line as shown in Fig. 1a. The test was performed by varying the various process parameters.

After performing the test, the tensile test specimen was cut as per ASTM standard. The tensile specimens before and after the tensile test are shown in Fig. 2. The Vicker's micro-hardness testing machine was used for calculating the hardness of the weld portion. The specimens were prepared for the microstructure study with fine polishing and etching. The polishing of the specimens was done by successive

grinding of specimens with the use of emery sheets of decreasing grain size. With the help of disc polisher, the specimens were polished to mirror finish by applying diamond polisher. For the sake of better visibility of the microstructural zones, the mirror-finished specimens were said to undergo etching with Keller's reagent for producing surface relief as well as contrast among the different phases and grains when viewed through the scanning electron microscope.

3   Approach

The acceptability of the developed mathematical relationship was tested using ANOVA methodology [14]. These test results for the improvement in mechanical properties of the two different pin profiles are shown in Tables 3 and 4, respectively. According to this methodology, if the F-ratio which is calculated for the developed model is less than the standard F-ratio at a preferred confidence level, the model is said to be satisfactory. The test results of tensile strength, hardness and toughness for the tapered square pin profile are shown in Table 3. The test results of tensile strength, hardness and toughness for the tapered pentagonal pin profile are shown in Table 4.

Table 3 ANOVA test results for tapered square pin profile

Terms involved	Tensile strength (TS)	Hardness (H)	Toughness (T)
Model			
Sum of squares	272.1016357	252.2086207	0.058931664
Degrees of freedom	5	5	5
Mean squares	54.42032714	50.44172414	0.011786333
F-value	258.2156543	107.9336987	35.30890499
Prob > F	<0.0001	<0.0001	<0.0001
Outcome	Significant	Significant	Significant

Table 4 ANOVA test results for tapered pentagonal pin profile

Terms involved	Tensile strength (TS)	Hardness (H)	Toughness (T)
Model			
Sum of squares	298.3174359	462.7658267	0.097357449
Degrees of freedom	5	5	5
Mean squares	59.66348718	92.55316534	0.01947149
F-value	58.05992728	52.65137613	27.19600323
Prob > F	<0.0001	<0.0001	0.0002
Outcome	Significant	Significant	Significant

4 Results and Discussion

The influence of double-sided FSW process and tool considerations on the micro-hardness is shown in Fig. 3. From the hardness trend, it is observed that the hardness in FSZ is less than the advancing and retreating side in all the different tool and process parameters due to the slow cooling occurred in the solid-state welding process. In the case of tapered pentagonal pin profile, the maximum hardness of

AS – Advancing side FSZ – Friction stir zone RS – Retreating side
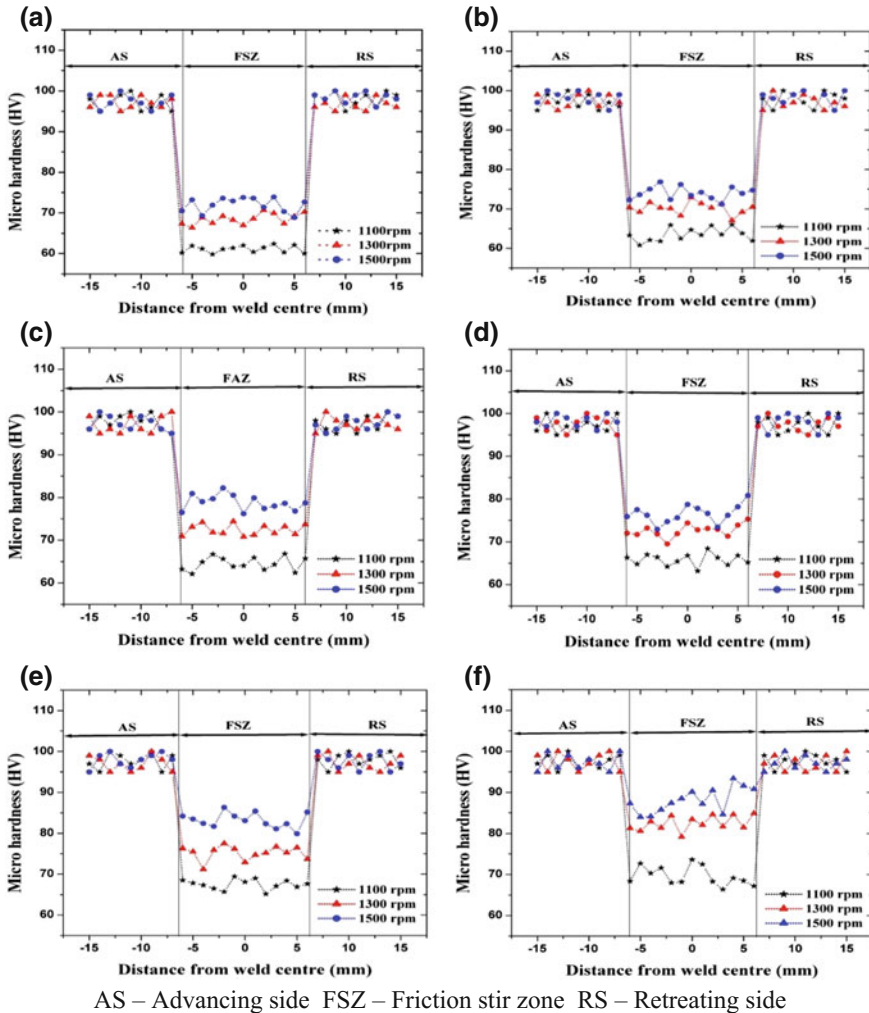
Fig. 3 Effect of process and tool parameters on micro-hardness of AA6082-T_6 aluminium alloy for the tool rotational speeds at 1100, 1300, 1500 rpm; **a** TSP; $S = 2.4$ mm/s, **b** TSP; $S = 3.2$ mm/s, **c** TSP; $S = 4$ mm/s, **d** TPP; $S = 2.4$ mm/s, **e** TPP; $S = 3.2$ mm/s, **f** TPP; $S = 4$ mm/s

88.1 HV is for the spindle and welding speeds of 1500 rpm and 4 mm/s, respectively. When the hardness for tapered square and tapered pentagonal pins is compared, the maximum hardness of 88.1 HV is obtained in the case of a tapered pentagonal pin.

4.1 Optimization using Desirability Approach

The tensile strength, hardness and toughness are related for developing an optimized model. The optimal range of the welding limits at which the preferred mechanical properties can be achieved is identified based on the optimization study carried out. Once the models are developed, we need to set the optimization criteria for which the optimum welding conditions can be achieved. The optimization criteria for two pin profiles have been implemented. In the event of tapered square pin tool, the criteria were set to achieve the maximum output responses with the input parameters spindle speed and welding speed at maximum limits. The developed optimization results show that for optimization criteria that is set to maximize, the input parameter spindle speed must be in the range of 1300 rpm for achieving the maximum tensile strength and hardness. The result gives the optimal welding conditions which would provide a maximum tensile strength of 149 MPa, maximum hardness of 75 HV and maximum toughness of 1.83 kg(f) m. The overlay plot is the result of the optimization obtained through graphical method. Figure 4 gives the overlay plot in which the yellow-shaded areas are the sections that come under the recommended criteria.

In the event of tapered pentagonal pin tool, the criteria were set to achieve the maximum output responses with the input parameters spindle speed and welding speed at maximum limits. The developed optimization results show that for optimization criteria that is set to maximize, the spindle speed must be in the range of 1400 rpm for achieving the maximum tensile strength and hardness. The result

Fig. 4 Overlay plot shows the optimum working conditions for a tapered square pin profile
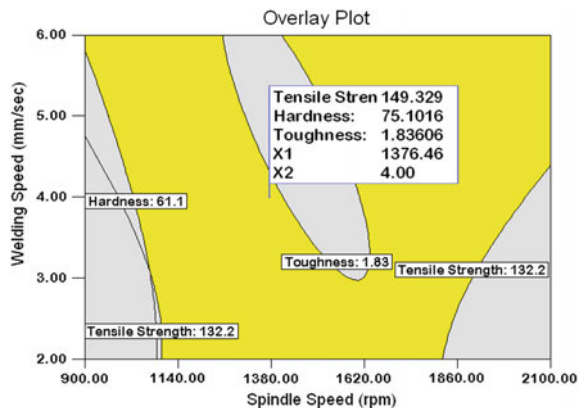
Fig. 5 Overlay plot shows the optimum working conditions for a tapered pentagonal pin profile
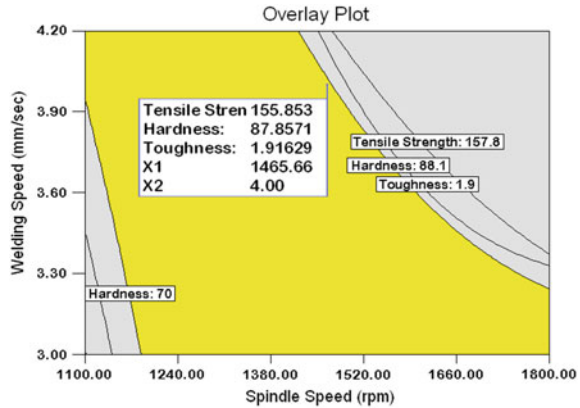
gives the optimal welding conditions which would provide a maximum tensile strength of 155 MPa, maximum hardness of 87 HV and maximum toughness of 1.91 kg(f) m. Figure 5 gives the overlay plot in which the yellow-shaded areas are the sections that come under the recommended criteria.

Now, when we compare the optimized results for tapered square and tapered pentagonal pin profiles, it is evident that the tensile strength, hardness, toughness are all maximum, when the pentagonal pin profile is adopted. Thus, we can conclude by using tapered pentagonal pin profile, the maximum tensile strength, hardness and toughness can be obtained. It is evident from the above results that the tapered pentagonal pin profile tends to produce a metallurgically defect-free weld compared with other type of tool pin profiles. It is evident that the determined results for the models are acceptable, and the predicted values are said to be in good agreement with the experimentally calculated results.

5 Conclusions

In this research, by using the double-sided FSW technique in the recommended input parameter limits considered in the work, the below-mentioned opinions can be concluded.

- Optimization using the desirability approach with the help of RSM is an advantageous approach for optimizing the double-sided FSW parameters to attain an improved model with good mechanical properties.
- When the tapered square pin profile is used, a spindle speed of 1375–1377 rpm is said to be the optimum range which will give an admirable welded module obtained from AA6082-T_6 aluminium alloy. When the tapered pentagonal pin profile is used, a spindle speed of 1464–1466 rpm is said to be the optimum range which will give an admirable welded module obtained from AA6082-T_6

aluminium alloy. Now, when comparing both, the maximum tensile strength, hardness and toughness can be obtained only when the tapered pentagonal pin profile is used.

- The tapered pentagonal pin profile with welding speed of 4 mm/s and spindle speed of 1500 rpm produces a better tensile strength than a square tool pin profile.
- Fine grains are observed in the FSZ when tapered pentagonal pin profile used, these grains are finer than the square tool pin profile.
- The spindle speed has been acknowledged as the most noteworthy factor. Further, it is followed by the influence of difference tool pin profiles and the welding speed. The monitoring of the interaction of welding speed with the spindle speed has to be done.

References

1. Thomas, W.M.: Friction stir welding. International patent application No. PCT/GB92/02203 and GB patent application No. 9125978.8. US Patent No. 5 (1991)
2. Blake, L.S.: Civil Engineer's Reference Book. Reed Educational and Professional Publishing Ltd (1989)
3. Doran, D., Cather, B.: Construction Materials Reference Book. Routledge (2014)
4. Dawes, C.J.: An introduction to friction stir welding and its development. Weld. Met. Fabr. **63**, 2–16 (1995)
5. Thomas, W.M., Nicholas, E.D.: Friction stir welding for the transportation industries. Mater. Des. **18**, 269–273 (1997)
6. Oosterkamp, A., Oosterkamp, L.D., Nordeide, A.: A kissing bond phenomena in solid state welds of aluminium alloys. Weld. J. 225–231 (2004)
7. Flores, O.V.: Micro structural issues in a friction stir welded aluminium alloy. Scripta Mater. **38**, 703–708 (1998)
8. Ram Kumar, A., Varghese, S., Sivapragash, M.: A comparative study of the mechanical properties of single and double sided friction stir welded aluminium joints. Procedia Eng. **38**, 3951–3961 (2012)
9. Elatharasana, G., Senthil Kumar, V.S.: An experimental analysis and optimization of process parameter on friction stir welding of AA 6061-T$_6$ aluminium alloy using RSM. Procedia Eng. **64**, 1227–1234 (2013)
10. Lakshminarayanan, A.K., Balasubramanian, V.: Process parameters optimization for friction stir welding of RDE-40 aluminium alloy using Taguchi technique. Trans. Nonferr. Met. Soc. China **18**, 548–554 (2008)
11. Tiwari, S., Chelladurai, H., Shukla, A.K.: Parametric analysis of friction stir welding. In: 5th International & 26th All India Manufacturing Technology, Design and Research Conference (AIMTDR), IIT Guwahati. **528**, pp. 1–6 (2014)

12. Bilici, M.K.: Effect of tool geometry on friction stir spot welding of polypropylene sheets. Exp. Polym. Lett. **6**, 805–813 (2012)
13. Mehra, S., Dhanda, P., Khanna, R., Goyat, N.S., Verma, S.: Effect of tool on tensile strength in single and double sided friction stir welding. Int. J. Sci. Eng. Res. **3**, 1–6 (2012)
14. Montgomery, D.C.: Design and Analysis of Experiments. John Wiley and Sons (1984)

RETRACTED CHAPTER: Interfacial Science in Metal–Ceramic Joining for Thermoelectric Module

S. Stalin, K. Kalaichelvan and T. Sujitha

Abstract Achieving high reliable metal–ceramic joint is dependent on both interfacial bond strength and favorable stress gradient in the interface. The work is based on comparative study of the various metal–ceramic combinations, copper with aluminum nitride and nickel with nitride to identify the best for the required operating temperature of thermoelectric module. The use of CuSil ABA alloy in paste form and a brazing alloy was prepared in-house with the same composition as that of CuSil ABA alloy was separately used for bonding metal interconnect and ceramic substrate. The microstructural analysis and study of thermal loss of the bonded substrate were studied. The comparisons of microstructures of different combinations suggest that the bonding of Cu with alumina is more effective when compared to AlN, since the interface forms a continuous TiO_X reaction layer over the ceramic surface. The microstructure of post-thermal gradient tested sample is evaluated for the presence of flaws when the hot side temperature is 300 °C, which is significant suggesting the quality of the interface needs further improvement.

Keywords Metal–ceramic bonding · Brazing · Microstructure characterization Thermal gradient measurement

1 Introduction

Thermoelectric (TE) module [1, 2] consists of p-type and n-type semiconductor legs, connected by metal interconnect, and the full assembly is packaged between ceramic base plates. In the fabrication process of the TE module, there are two main

---

S. Stalin (✉) · K. Kalaichelvan · T. Sujitha
Department of Ceramic Technology, ACT Campus—Anna University,
Chennai 600025, India
e-mail: stalingodson@yahoo.com

interfaces in this module: one is between TE legs and interconnect metal, and the other is between metal interconnect and ceramic substrate (also referred as base plate). TE legs are normally connected in parallel by means of copper interconnect, which allows the current to pass through them without any loss because of its high electrical conductivity [3]. On either sides of the TE leg-metal interconnect assembly, normally alumina is used as ceramic substrate which is electrically insulating and thermally conductive [3]. To bond metal with ceramic substrate, vacuum brazing technique is the one possible method for its low cost and feasible to join complex geometries for large-scale production [4]. Brazing of metal with ceramic has difficulties occurring while joining them reliably due to thermal expansion coefficient mismatch between metal and ceramic and poor wettability behavior of molten metal over ceramic substrate [5, 6]. These limitations can be overcome by use of two types of brazing alloys: one is conventional brazing alloy, and other is active brazing alloy. The use of conventional brazing alloy requires metallization process (Mo–Mn metallization) to improve the wettability of ceramic surface by the liquid filler metal alloy which is costly and requires lots of time. But commercial active brazing alloy [7–9] such as CuSil ABA (63% Ag + 35.25% Cu + 1.75% Ti) has been successfully utilized to form adherent metal ceramic joining by the use of reactive elements like titanium or zirconium for various applications [5, 6, 10].

This work is aimed at developing defect-free interfacial metal–ceramic bonding by the use of CuSil ABA alloy in paste form which was commercially available, and a brazing alloy was prepared in-house with the same composition as that of CuSil ABA alloy. Both these alloys were separately used for bonding metal with ceramic substrate. Comparison of various metal-ceramic interface adhesions with respect to reaction layer formation have been analysed. Finally, the microstructure of post-thermal gradient tested metal–ceramic combination is evaluated.

2 Experimental Work

The ceramic base plate and the metal interconnect pairs have been chosen in such a way that it should form defect-free interface with least thermal resistance and stable at the operating temperature of the module. To select the best pair, different combinations of plate and interconnect materials were examined and its microstructures were studied. Four different combinations were prepared as shown in Fig. 1. The bonding between metal and ceramic was carried out by vacuum brazing technique.

COPPER	COPPER	COPPER	NICKEL
BRAZING ALLOY (prepared)	BRAZING ALLOY (CuSil ABA)	BRAZING ALLOY (CuSil ABA)	BRAZING ALLOY (CuSil ABA)
ALUMINA	ALUMINA	ALUMINIUM NITRIDE	ALUMINIUM NITRIDE

Fig. 1 Four different combinations of metals, brazing alloys and ceramics

Two types of brazing alloys were employed in the experiments: one prepared by in-house melting route and other commercially available CuSil ABA paste. The vacuum-brazed sample was characterized for its structural integrity and the microstructure. The metallographically polished samples were characterized by optical microscope, SEM and EDX. Thermal losses across the interface between interconnect and base plates are evaluated using an in-house made arrangement.

2.1 Bonding Metal and Ceramic Using In-House Prepared Alloy

The overall process for the preparation of the brazing alloy and bonding the copper with alumina is shown in the form of flowchart in Fig. 2. The composition of
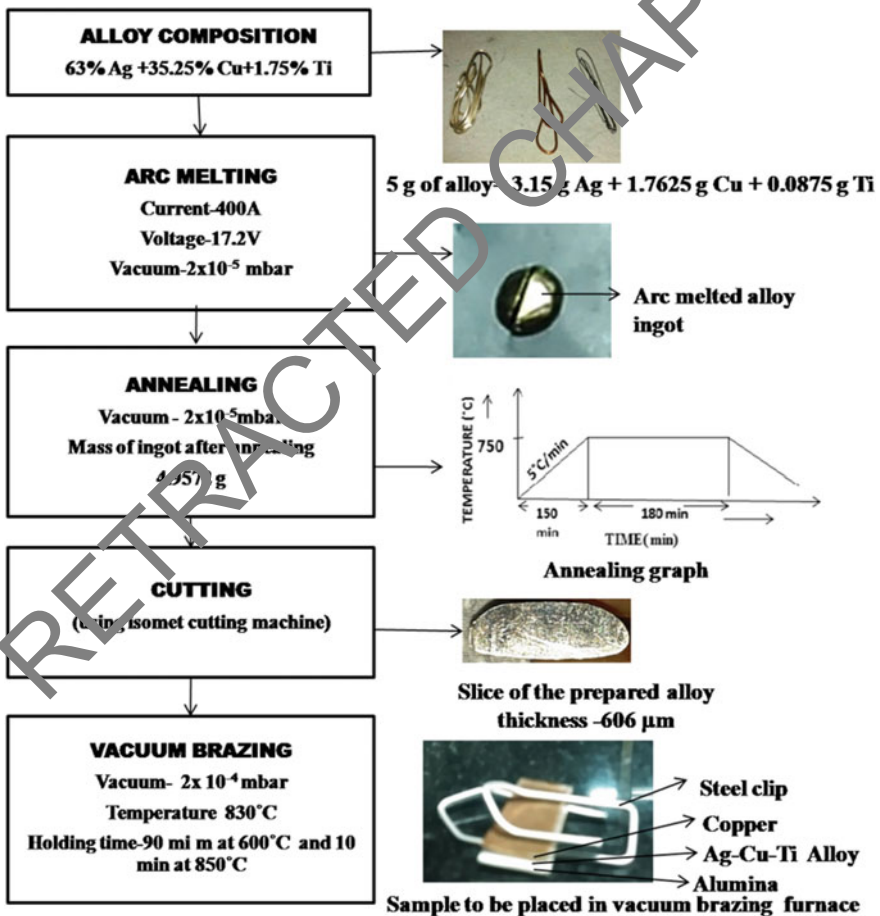
Fig. 2 Flowchart showing the steps involved in bonding copper and alumina using the prepared brazing alloy

in-house prepared brazing alloy is 63% Ag, 33.25% Cu and 1.75% Ti same as the composition of CuSil paste and melted in vacuum arc melting furnace [5, 11].

2.2 Vacuum Arc Melting

The vacuum arc melting furnace heats the material by means of an electric arc. The three weighed wires of Cu, Ag and Ti were placed in the copper hearth. The melting chamber was evacuated to 2×10^{-5} mbar and back-filled to 300 torr flowing argon atmosphere before melting. About 400 A current and 17.6 V were applied to create the arc and the temperature was above 2000 °C. Melting was done for about 5 min, and the process was repeated for three to four times.

2.3 Bonding Metal and Ceramic Using CuSil ABA Filler Paste

Copper and nickel were chosen as the metal, and alumina (Al_2O_3) and aluminum nitride (AlN) were chosen as the ceramic base plate [12, 13]. The reason for selecting aluminum nitride as one of the base plate materials is that, compared to Al_2O_3, AlN has low thermal coefficient of expansion and high thermal conductivity. These properties are very desirable for TE module performance. About three samples were prepared by using copper/nickel metal sheet and Al_2O_3/AlN in three different combinations as shown in Fig. 1. The temperature schedule used is given in Fig. 3.

Fig. 3 Temperature profile graph for vacuum brazing
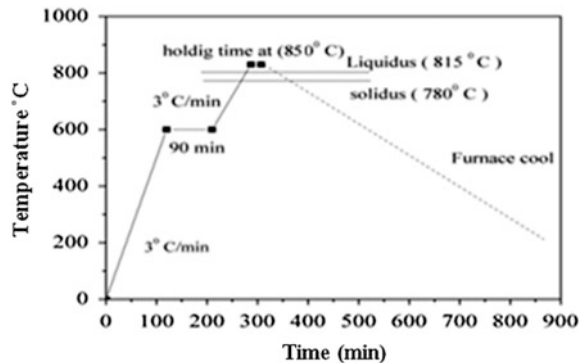
2.4 Vacuum Brazing

The sample was vacuum-brazed in a furnace after evacuating the chamber to 2.5×10^{-4} mbar. The temperature profile used for brazing ceramic and metal is shown in Fig. 3. The sample was heated at a rate of 3 °C/min till it reaches 600 °C and the holding time of 90 min was given. Further the temperature was increased to 850 °C with heating rate of 3 °C/min. The sample was cooled in the furnace itself [14].

3 Results and Discussion

3.1 Characterization of Copper + CuSil ABA + Al$_2$O$_3$ Interface

The spot EDS analysis carried out at the different region (Fig. 4) shows Cu-rich and Cu + Ag-rich region in the Cu interconnect layer. The weight percentage of the
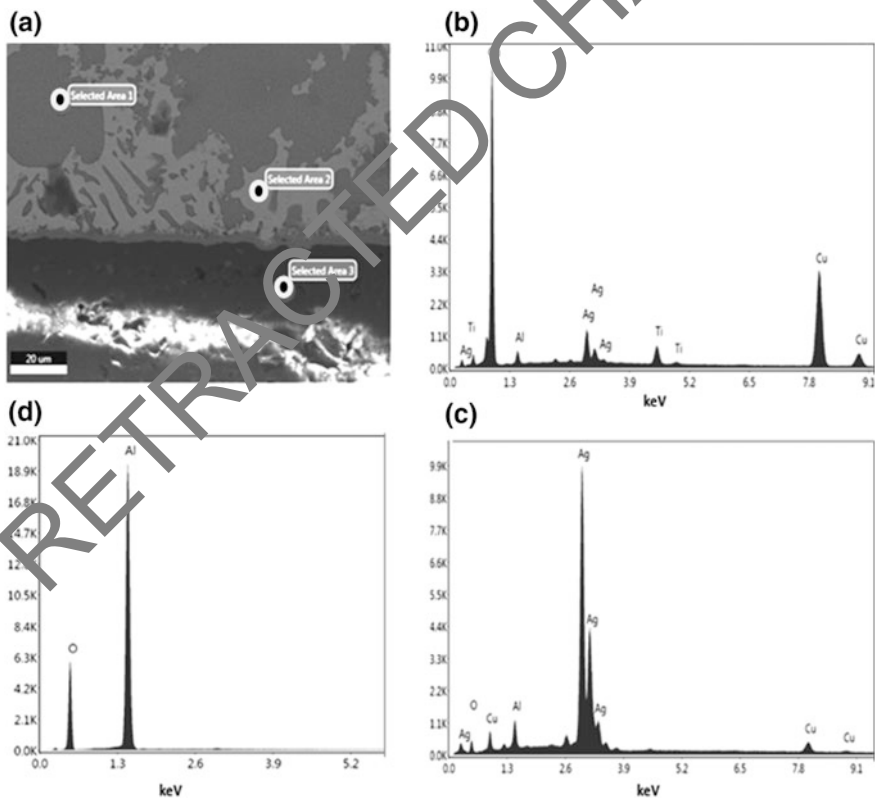
Fig. 4 Spot analysis **a** microstructure showing three spot analysis selected areas, **b** area 1, **c** area 2, **d** area 3

elements in the Cu-rich area is 83.30 Cu, 4.17 Ti and 9.57 Ag. In the Cu + Ag region, the weight percentage is 79.78 Ag and 7.76 Cu. The elemental mapping done at the area around the interface (Fig. 5) clearly shows that the melted brazing alloys wet the grain boundary of copper and the titanium reactive element present in the filler alloy reacts with the alumina surface forming the TiO_X and/or Ti–Al–O compound. This mapping also shows the presence of titanium in the copper-rich region rather than silver-rich region. Titanium has more affinity toward copper compared to silver.

The SEM-EDX analysis of SS/CuSil/alumina stated by Kar et al. [15] that titanium has a solubility of 67 wt% at 1150 °C in copper, whereas it is only 2% in silver. In the presence of silver, the tendency of titanium to associate with the molten alloy gets reduced, thereby increasing the activity of titanium in the filler alloy. Nicholas [16] observed that the addition of silver to copper enhances the ability of titanium solutes to induce wetting and cause TiO_X reaction layer to be formed, and the extent of wetting will be greater for a liquid metal with low surface energy.
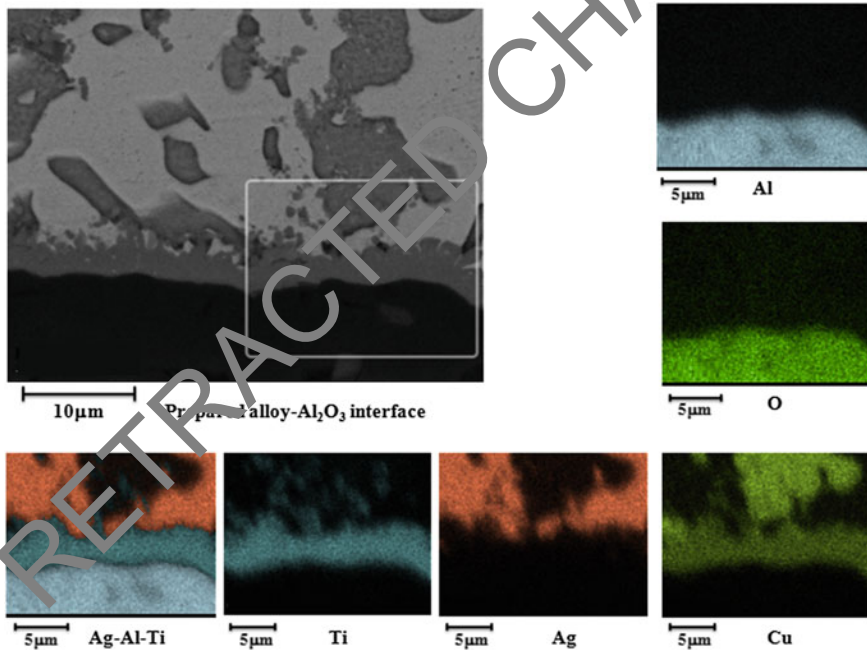
Fig. 5 Elemental mapping on the prepared alloy–Al_2O_3 interface

3.2 Characterization of Cu + CuSil ABA + AlN and Ni + CuSil ABA + AlN Interfaces

The diffusion kinetics of CuSil ABA in copper/nickel with AlN is not same as that in copper/Al_2O_3 (Figs. 6 and 7). The reaction layer is not continuous, uniform along the surface of the AlN substrate. The EDS mapping is clear that the elements such as silver, copper and titanium in the CuSil ABA alloy were segregated into Ag-rich, Cu + Ni-rich phases and the presence of titanium was found rarely over the AlN surface. Further line-scan investigation across the interface (Fig. 8) confirms that there is no titanium enrichment on the surface of the ceramic base plate, unlike in Al_2O_3. Instead, high amount of silver is present on the AlN base plate.
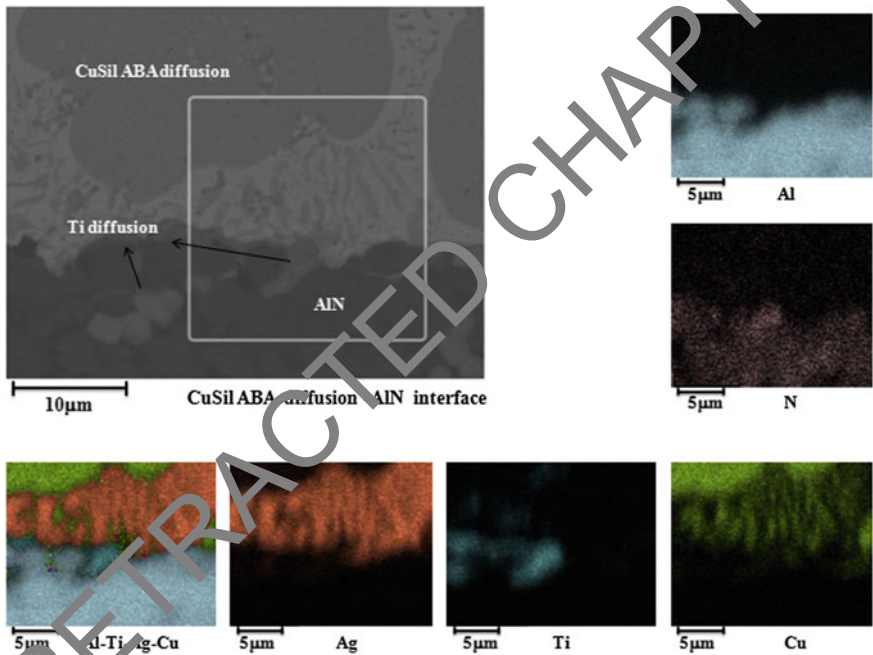
Fig. 6 Elemental mapping of CuSil ABA + AlN interface on the Cu + CuSil ABA + AlN bond
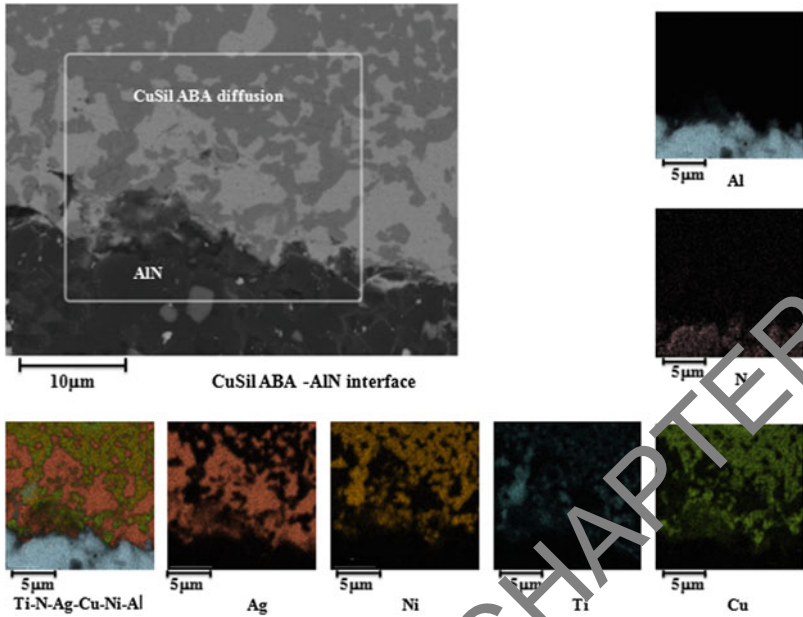
Fig. 7 Elemental mapping of CuSil ABA + AlN interface of the Ni + CuSil ABA + AlN bond
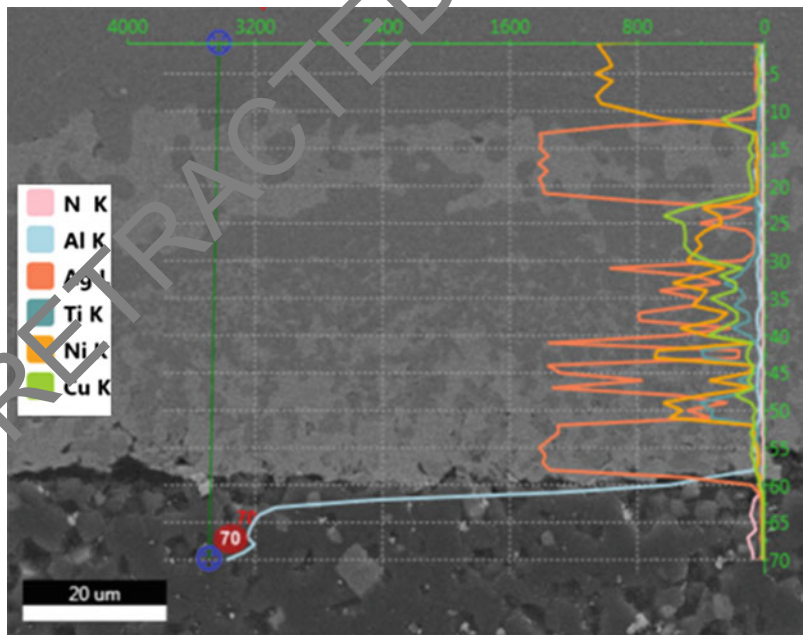
Fig. 8 Line scan of the elements presents in the diffusion layer

3.3   Comparison of the Microstructure

From the comparison of microstructure of the brazed samples (Fig. 9), the reactive titanium and copper phase formed on the interface are responsible for bonding ceramic substrate with metal interconnect. The titanium-rich continuous uniform diffusion layer is prominently seen in alumina compared to AlN. So, this study implies bond strength in metal with alumina will be greater compared to that of AlN since the bonding between copper and alumina mainly attributed to the titanium-rich uniform reaction layer, resulting in wetting of ceramic surface and also binding the metal with ceramic substrate.
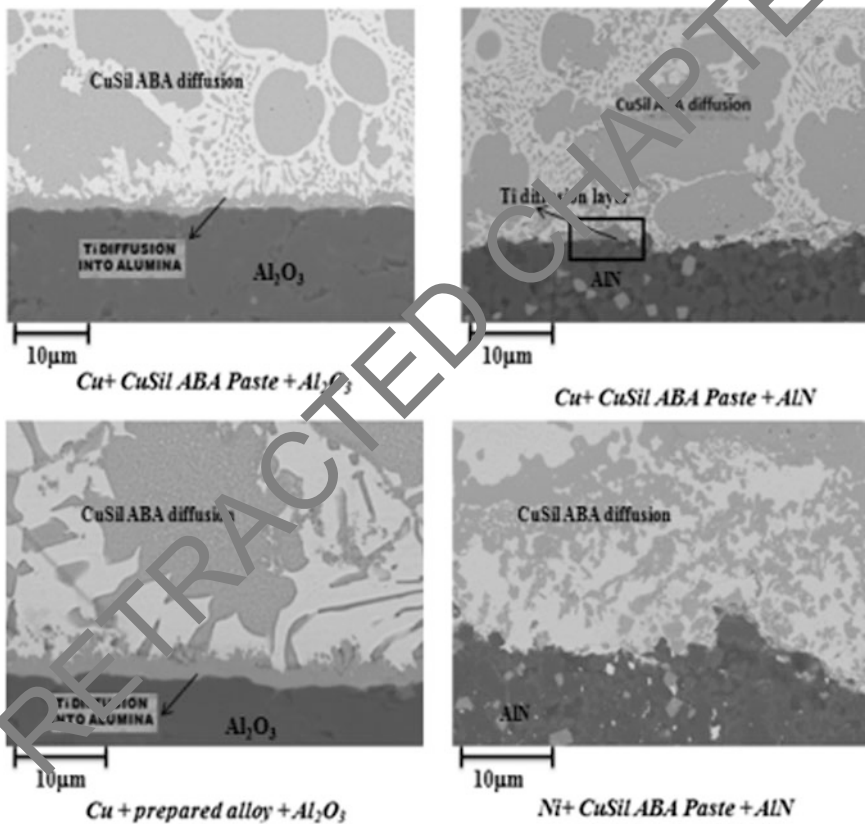
Fig. 9 Comparison of microstructures of the bonded samples showing the difference in the Ti diffusion layer in Al_2O_3 and AlN interface
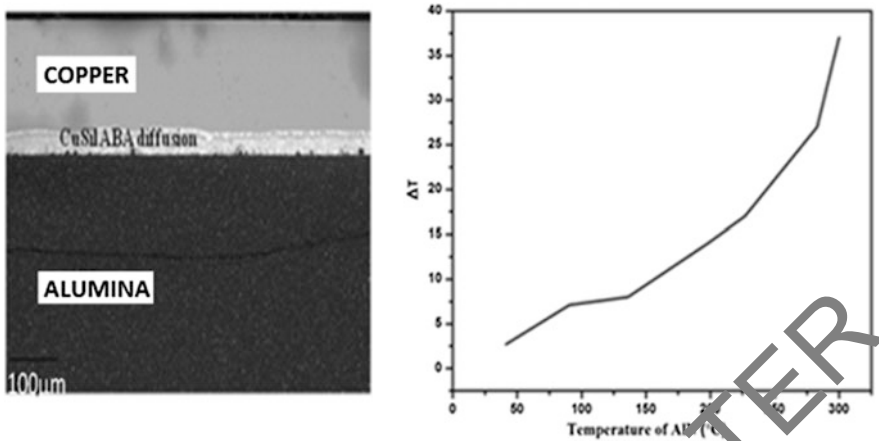
Fig. 10 Microstructure of the thermally heated sample Al_2O_3/CuSil ABA/copper

3.4 Microstructural Evaluation Post-thermal Gradient Test

As the copper/alumina brazed sample is subjected to thermal gradient testing heated to temperature at 300 °C at regular interval of about 30 min, respectively. Upon post-thermal gradient testing, the microstructural evaluation of interfacial zone is observed to be defect-free along the interface, but indication of crack is observed to be on the ceramic substrate, microscopically (Fig. 10). Thus, the defect-free interfacial bond is observed to withstand thermal shock which creates a thermal loss of up to 40 °C when the hot side temperature is 300 °C. Thereby, better heat transfer is achieved.

4 Conclusions

The bonding between Al_2O_3 with copper and AlN with nickel and copper interconnect materials has been successfully brazed using CuSil ABA filler alloy at 850 °C for 5 min, respectively. The comparisons of microstructures of different combinations suggest that the bonding of Cu with alumina using CuSil ABA filler alloy (prepared in-house and commercially available) is more effective when compared to AlN. As copper/CuSil ABA/Al_2O_3 is comparatively producing better bonding since it forms titanium-rich reaction layer over the alumina surface. Similar layer is also observed in Cu/AlN. Based on the experimental results obtained and analysis of studies, the bond strength of metal with alumina will be greater compared to that of AlN since the bonding between copper and alumina mainly attributed to the titanium-rich uniform reaction layer, resulting in wetting of ceramic surface and also binding the metal with ceramic substrate.

The microstructural evaluation of post-thermal gradient measurement suggests that the interface region is found to be defect-free bonding. There is no indication such as crack or delamination found along the interface. Hence, the joint can withstand temperature up to 300 °C, which is significant suggesting the quality of the interface needs further improvement.

References

1. LeBlanc, S.: Thermoelectric generators: linking material properties and systems engineering for waste heat recovery applications. Sustain. Mater. Technol. **12**, 26–35 (2014)
2. Barako, Michael T., Park, Woosung, Morconnet, Amy M., Asheghi, Mehdi, Goodson, Kenneth E.: A reliability study with infrared imaging of thermoelectric modules under thermal cycling. IEEE Xplore (2012). https://doi.org/10.1109/ITHERM.2012.6231417,86-92
3. Liu, G.W., Li, W., Qiao, G.J., Wang, H.J., Yang, J.F., Lu, T.J.: J. Alloys Compd. **470**, 163–167 (2009)
4. Rice, R.W.: Advances in Joining, vol. 69. Brook Hiu Publications, Chestnut Hill, MA (1976)
5. Schilm, J., Pönicke, A., Kluge, M., Sichert, I., Martin, N.-P., Michaelis, A.: TiO$_x$ based thermoelectric modules—manufacturing. Prop. Oper. Beh. Mater. Today Proc. **2**, 770–779 (2015)
6. Akselsen, O.M.: Advances in brazing of ceramics. J. Mater. Sci. **27**, 1989–2000 (1992)
7. Mondal, S., Pathak, L.C., Venkateswaran, K., Das, S.K., Ray, A.K.: Development and characterization of Ag-Cu-Ti alloys for ceramic brazing. Trans. Indian Ceramic Soc. **63**, 9–13 (2004)
8. Kozlova, O., Voytovych, R., Eustathopoulos, N.: Initial stages of wetting of alumina by reactive CuAgTi alloys. Scripta Mater. **65**, 13–16 (2011)
9. Yadav, D.P., Kaul, R., Ganesh P., Ram Shiroman, Sridhar, R., Kukreja, L.M.: Study on vacuum brazing of high purity alumina for application in proton synchrotron. Mater. Des. **64**, 415–422 (2014)
10. Beeranur, R., Waghmare, K.K., Kumar Singh, R.: Characterization of vacuum brazing of SS304 and alumina ceramics with active brazing alloy. Proc. Mater. Sci. **5**, 969–977 (2014)
11. Rongti, L., Wei, P., Jian, C., Jie, L.: Thermodynamic properties of Ti in Ag–Cu–Ti alloys. Mater. Sci. Eng., A **335**, 21–25 (2002)
12. Wu, M., Cao, C., Xin-bo, H., Qu, X.: Brazing diamond/Cu composite to alumina using reactive Ag-Cu-Ti alloy. Trans. Nonferrous Met. Soc. China **23**, 1701–1708 (2013)
13. Ismail, F.I., Ahmed, W.H.: Recent Pat. Electrical Eng. **2**, 27–39 (2009)
14. Roberts, P.M.: Introduction to Brazing Technology, pp. 158–165. Taylor & Francis, CRC (2016)
15. Kar, A., Palit Sagar, S., Ray, A.K.: Characterization of interface of Al$_2$O$_3$-SS braze joint. J. Mater. Charact. **58**, 555–562 (2007)
16. Nicholas, M.G.: Active Metal Brazing, 1st edn, pp. 73–92. Springer US (1990)

Experimental Investigation of Spherical Core Sandwich Structure by Beam Flexure

V. Pandyaraj and A. Rajadurai

Abstract Honeycomb structures are the most widely used sandwich structures as it provides material with minimal density and relative high out-of-plane compression properties and out-of-plane shear properties. Though the properties are substantial, the manufacturing of honeycomb structure is difficult. In this study, GFRP sandwich was selected for investigation as it is widely used in aerospace structural applications due to its high strength-to-weight ratio. A novel (spherically cored) sandwich structure of two different models, namely regular spherical and inverted spherical, was designed and fabricated. The sandwich structures were made with vinyl ester resin and two different GF reinforcements, namely woven glass fiber fabric and chopped strand fabric by hand lay method. The diameter of the spherical core was fixed as 16 mm, whereas two different pitch distances of 24 and 32 mm were used. The core shear properties and facing fracture stress of these eight variants of spherical cored sandwich specimens were tested using three-point bend test. The test result indicated that the regular spherical structure model with chopped strand and pitch of 24 mm possess a high core shear strength of 427 kPa which is more or less equivalent to honeycomb sandwich structure and facing fracture stress of 34 MPa. Whereas the regular spherical sandwich structure made with woven 24 mm pitch shows a low core shear strength of 79 kPa and facing fracture stress of 6.37 MPa.

Keywords Spherical sandwich structure · Woven GFRP · Inverted Regular · CSM

V. Pandyaraj (✉) · A. Rajadurai
Department of Production Technology, MIT-Anna University, Chennai 600044, India
e-mail: pandyaraj.raj1@gmail.com

1 Introduction

A sandwich structure is fabricated by attaching two thin stiff skins to a light-weight thick core. The core material is usually low density material, but its higher thickness provides high bending stiffness to the structure. In sandwich structure, the face sheet carries the bending load while the core carries the shear load. The face sheets are strong and stiff in tension and compression compared to the core material whose primary function is to keep the face sheets separated in order to maintain a high section modulus. The core material has high flexural strength and stiffness properties relative to overall panel density. Therefore, sandwich panels are more efficient while carrying bending loads. In addition to it, they provide buckling resistance to shear panels and compression members. The sandwich panels are analyzed based on their effective properties rather than consideration of actual structure. A lot of experiments and analyses had been carried out to predict the effective continuum properties of the core based on its geometric and material characteristic. Bart-smith et al. [1] carried out the bending performance of sandwich structure fabricated by using Al alloy 6061-0 as core material and Al alloy 6061-T6 as the facing sheet material. FM-300 is used as adhesive material for bonding the core material and the facing sheet. Based upon the collapse load criteria for face yielding, core shear and indentation, a mechanism map was generated. The yield load and limit load were found experimentally, numerically and analytically, and the results were validated. Kang et al. investigated the mechanical behavior of sandwich panels by using tetrahedral and kagome truss cores fabricated from wires. In his study, the sandwich panels were fabricated with perforated face sheet and solid face sheet and kagome truss core was fabricated by using copper sheets. Three-point bending load test was carried out to find the flexural strength. Based on the compression test, it is found that the kagome truss core exhibited double peaks on the load–displacement curve, which indicates that it is possible to absorb much more energy during deformation.

Wang and Gao [2] investigated the bearing capacity of double rhombic honeycomb and double hexagonal honeycomb using finite element analysis. Both the structural core had been fabricated by using paper board. By using the Ansys software, the deflection and von-mises stress were found at different loads. From the analyses, it is found that the compression performance of double rhombic honeycomb was better. Venugopal et al. [3] performed the static four-point bending load of nomex flex core and carbon-reinforced polymer face sheet combination. 2D and 3D models were modeled using orthographic material properties. The finite element results were compared with the experimental data for studying bending properties. 2D and 3D FE model results correlate with experimental results of sandwich specimen, and the maximum percentage error was 11.27% only. Chen et al. [4] investigated the mechanical behavior of hollow cylindrical joint honey comb sandwich structures. Here the three edge point joint was replaced by a hollow cylindrical joint. The Young's modulus, Poisson's ratio fracture strength and stress intensity factor were calculated by deriving a theory for hollow cylindrical joint honeycomb. From the result, it is found that the Young's modulus and fracture strength of honeycomb

structure improved by 76 and 30.3%. Foo [5] conducted the failure of panel using low-velocity impact test and came to the conclusion that the response of the impact depends upon the strain hardening of the material and core density. Jan [6] investigates the flexure behavior of the honeycomb structure experimentally and analytically and compares them both. In this study, a novel spherical sandwich had been considered for investigation purpose. The orientation of spherical structure had been altered in two different ways, namely regular, inverted. They were fabricated by using GFRP material. The core shear ultimate stress properties and facing fracture stress of each orientation were tested and analyzed.

2 Modeling of the Specimen

In the present study, two different models of spherical sandwich structure, namely regular and inverted, were considered. The specimens are modeled using the software Pro-e-creo. Figure 1 shows the regular and inverted models of spherical cored sandwich structures.

3 Fabrication of the Specimen

The GFRP spherical structures were fabricated by using hand molding process. The reinforcement used in the study was woven 300 glass fiber cloth (W) and chopped strand mat (CSM) of 450 grade. Eight variants of sandwich structures were fabricated using W and CSM. Two pitch distances of 24 and 32 mm were taken as the spacing between centers of hemispheres. The length of the specimen is taken as 300 mm, and the width of the specimen is considered to be 44 mm. Table 1 gives the geometrical parameters of the spherical sandwich structure.
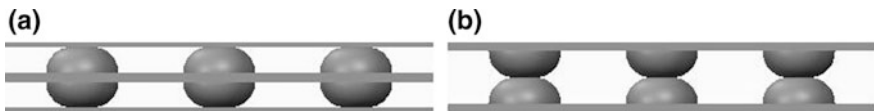
Fig. 1 Different models of spherical cored sandwich structure. **a** Regular, **b** inverted

Table 1 Geometrical parameters of the spherical sandwich structure

S. No.	Parameter	Dimension (mm)
1	Facing sheet thickness	1
2	Core height	16
3	Sphere diameter	16
4	Flatness at the sphere top	8
5	Wall thickness	1 (W)/2(CSM)
6	Pitch	24/32
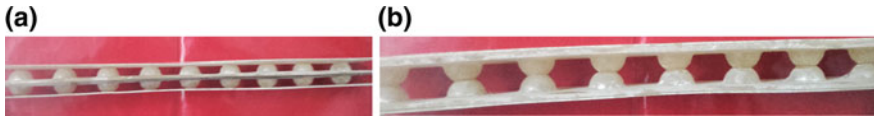
Fig. 2 Specimens of 32 mm pitch spherical cored sandwich structure. **a** Regular CSM, **b** inverted CSM

Figure 2a, b shows the photographs of the sandwich specimen prepared for taking the three-point bend test.

4 Three-Point Bend Test

The three-point bend test experiments were carried out, and the behavior of load versus deflection was recorded. The core shear ultimate stress properties and facing fracture stresses were calculated according to ASTM C-393. Figure 3 shows the three-point bend test setup for loading the specimen. Rajadurai and Pandyaraj [7] conducted the flexural test and compared the properties for different orientation of spherical structure.

For every model of the sandwich structures, three experiments were conducted and the mean value was taken for investigation. The core shear ultimate stress and facing fracture stress were calculated using the following formula as given in ASTM C-393.

$$F_s^{ult} = P_{max}/(d+c)b \tag{1}$$

$$\sigma = P_{max}S/2t(d+c)b \tag{2}$$

where F_s^{ult} is the core shear ultimate strength, P_{max} is the maximum force prior to failure, d is the sandwich thickness, c is the core thickness, b is the sandwich width, σ is the facing stress, t is the facing thickness and S is the span length.

Fig. 3 Three-point bend test setup for loading the specimen

Table 2 Comparison of core shear and facing stress for different orientations of spherical model

Sample name	Sample reference	Core shear ultimate stress 'kPa'	Facing stress 'MPa'
REGULAR	RW-24	79	6.37
	RW-32	101	8.13
	RC-24	427	34.19
	RC-32	317	25.39
INVERTED	INW-24	123	9.88
	INW-32	129	10.36
	INC-24	223	17.88
	INC-32	311	24.96

5   Result and Discussion

The core shear ultimate stress and facing fracture stress calculated for all the models are listed in Table 2.

Here the notation R for regular, IN for inverted, W for woven and C for CSM.

5.1   Comparison of Core Shear Ultimate Stress for Different Models

The core shear ultimate stress is more for regular CSM 24 mm pitch (RC24) and it is minimum for woven regular 24 mm pitch (RW24) among regular model. For inverted model, the core shear ultimate stress of chopped strand mat 32 mm pitch (INC32) is maximum and woven 24 mm pitch (INW24) is minimum. However, for overall analysis, it is found that the core shear ultimate stress is maximum for regular (RC24) spherical model. Whereas the core shear ultimate stress of (RW24) is very less. The CSM model has high strength because the core thickness is 2 mm greater than woven model. The regular model has high value because of the surface bonding between core and the facing sheet (Fig. 4).

5.2   Comparison of Facing Stress for Different Models

Figure 5 illustrates the facing fracture stress comparison for different spherical models. The facing stress is more for regular CSM 24 mm pitch (RC24), and it is minimum for woven regular 24 mm pitch (RW24) among regular models. For inverted, the facing fracture stress of chopped strand mat 32 mm pitch (INC32) is maximum and woven 24 mm pitch (INW24) is minimum. On comprehensive analysis, it is found that the facing stress is maximum for regular spherical model and minimum for inverted model. In pitchwise comparison, the facing fracture stress is higher for 24 mm pitch than 32 mm pitch. Table 3 shows the different failure identification codes for the spherical models.

Comparison of core shear ultimate stress of Spherical Sandwich Models
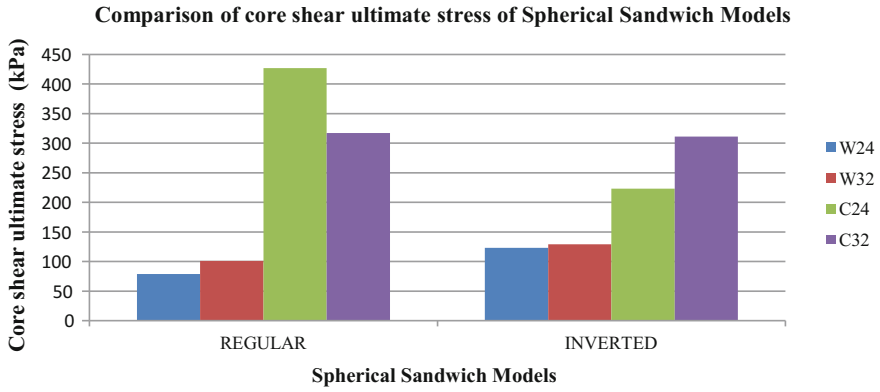
Fig. 4 Core shear ultimate shear stress comparison for different spherical models

Comparison of facing stress of Spherical Sandwich Models
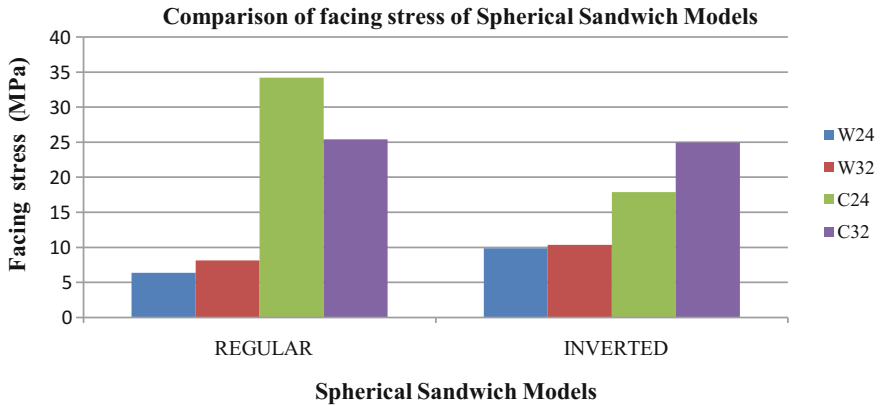
Fig. 5 Facing fracture stress comparison for different spherical models

Table 3 Sandwich panel failure identification code

Sample name	Sample reference	Failure type	Code
Regular	RW24	Facing failure	F
	RW32	Skin-to-core delamination	D
	RC24	Transverse shear	S
	RC32	Facing failure	F
Inverted	INW24	Core crushing	C
	INW32	Transverse shear	S
	INC24	Facing failure	F
	INC32	Skin-to-core delamination	D

6 Conclusions

- A novel spherical GFRP sandwich structure was taken for the investigation purpose.
- The orientation of spherical structure was altered in two different models, namely regular and inverted.
- From experimental results, it is found that the core shear ultimate stress and facing stress are maximum for regular and minimum for inverted model.
- On overall analysis, it is found that the regular C24 mm pitch has high core shear ultimate stress value of 427 kPa and the facing fracture stress value of 34.19 MPa.
- The increased core shear stress and facing sheet facture stress in RC24 could be attributed to the distributed load sharing by closely placed spheres and the effective contact between the apex of spheres with the facing sheet in view of short pitch distance.
- This structure can be used for light load application where strength-to-weight ratio should be high.

References

1. Bart-smith, H., Hutchinson, J.W., Evans, A.G.: Measurement and analysis of the structural performance of cellular metal sandwich construction. Int. J. Mech. Sci. **43**, 1945–1963 (2000)
2. Wang, B., Gao, S.: Based on the ANSYS double rhombic honeycomb paperboard finite element analysis. In: International Conference on Education Technology and Management Science (ICETMS 2013)
3. Venugopal, M.M., Maharana, S.K., Badarinarayan, K.S.: Finite element evaluation of composite sandwich panel under static four point bending load. Jest-M **2**, 1–6 (2013)
4. Chen, Q., Pugno, N., Zhao, K., Li, Z.: Mechanical properties of a hollow-cylindrical-joint honeycomb. Compos. Struct. **109**, 68–74 (2014)
5. Foo, C.C., Seah, L.K., Chai, G.B.: Low-velocity impact failure of aluminium honeycomb sandwich panels. Compos. Struct. **85**, 20–28 (2008)
6. Jan, S., Khan, R.U., Ahmad, S., Amjad, M.: Flexural strength of honeycomb sandwich structures. IJASER **4**(1) (2015)
7. Pandyaraj, V., Rajadurai, A.: Experimental study on core shear properties and facing sheet of fracture of spherical core sandwich structure. ICMTS, pp. 70–74 (2017)

Parameter Design and Analysis in Friction Welding of Brass Material Using Grey Relational Analysis

C. Shanjeevi, J. Thamilarasan and N. Balaji

Abstract In today's context, joining of dissimilar materials is experiencing a huge development which finds applications in different fields of interest. This study focuses on optimization of process parameters in friction-welded joint on similar brass material. A L_9 (3^4) orthogonal array of Taguchi design is considered for welding parameters to maximize and minimize in tensile strength and weld time. Since the parameters are considered with multi-outputs, grey relational (GRA) is used to identify the optimal parameter. Analysis of Variance (ANOVA) is performed on the measured data and S/N (signal-to-noise) ratio. By utilizing multi-objective optimization, the value of prediction observed from grade mean value 0.831 is increased further to 0.845 through an additional evidence of test. Consequently, the Taguchi method was found to be promising technique to obtain the optimum conditions for such studies.

Keywords Friction welding · Brass · Grey relational analysis (GRA)

1 Introduction

Due to the unique properties of brass like excellent corrosion resistance, strength and distinct colour it is widely used in miscellaneous industries [1]. Special properties of brass such as high malleable and good flow characteristics for casting have made it an excellent applicant for its bright gold-like appearance. During fusion welding, brass material causes porosity during melting and zinc produces large amount of zinc oxide

C. Shanjeevi (✉) · J. Thamilarasan · N. Balaji
Department of Mechanical Engineering, Vel Tech Rangarajan
Dr. Sagunthala R&D Institute of Science and Technology, Chennai, India
e-mail: dr.c.shanjeevi@veltech.edu.in

J. Thamilarasan
e-mail: thamilarasan@veltech.edu.in

N. Balaji
e-mail: nbalaji@veltech.edu.in

which causes health and safety issues. Moreover, brass material is difficult to transfer zinc across the welding arc. Fortunately, friction welding is one of the techniques which overcomes this issue due to solid-state welding. The dissimilar welding of brass and high-carbon steel is studied by Luo et al. using inertia friction welding. Luo et al have investigated dissimilar welding of brass and high carbon steel and studied weld behavior and its intermetallic elements [2]. Sassani et al. approach focused on feasibility and practicality of incompatible materials. The dissimilar materials such as titanium to nickel, bronze to steel, brass to copper with varying welding parameters are experimentally investigated [3]. Gao et al. investigated a dissimilar lap joint of commercial brass-to-plain carbon steel using friction stir welding. The effect of welding speed and heat input during welding was discussed based on their microstructural and mechanical properties. Consequently, the author have also examined the outputs of tensile shear strength and shear fracture on the welded joint [4, 5]. Esmaeilia et al. analysed the effect of performance observed under dissimilar joints and studied the mechanical properties [6]. However, many studies related to brass material are focused on mechanical properties of dissimilar materials. The prediction of optimal parameter with respect to multi-outputs is very limited. The novelty of this work is to investigate the optimal condition of weld parameter using grey relational analysis.

2   Experimental Work

Taguchi method consists of three stages (system, parameters and tolerance designs) by developing the concept of engineering knowledge, improving quality characteristics and analysing the optimal parameters [5]. By applying Taguchi method, cost and time considered for conducting the experiments are reduced at the minimum.

The elements observed in brass material are shown in Table 1. The experiment was done with a similar joint of brass material by friction welding of three different levels with three parameters which are listed in Table 2, and response of tensile

Table 1 Chemical elements of leaded brass

Elements	Cu	Pb	Fe	Zn
wt%	68.7	0.7	0.6	30

Table 2 Factors and their levels

Factors	Levels		
	1	2	3
Friction pressure [MPa]	104	121	139
Upset pressure [MPa]	151	173	195
Rotational speed [rpm]	1500	1750	2000

Table 3 Experimental results

Experiments	Friction welding parameters			Tensile strength [MPa]	Weld time [s]
	Friction pressure [MPa]	Upset pressure [MPa]	Rotational speed [r/min]		
1	1	1	1	340	9.5
2	1	2	2	371	8.52
3	1	3	3	375	8.53
4	2	1	3	362	7.31
5	2	2	1	345	8.19
6	2	3	2	344	7.31
7	3	1	2	364	7.13
8	3	2	3	344	6.77
9	3	3	1	349	7.34

Fig. 1 Friction-welded joint

strength and weld time is listed in Table 3. The physical appearance of friction-welded joints is shown in Fig. 1. Burn-off length is kept constant at 2.5 mm.

3 Results and Discussion

The tensile test was performed on a welded specimen as per the ASTM standard and fractured specimen as shown in Fig. 2. The tensile strength of the weld region is varied from 340 to 375 MPa. The higher the upset pressure and rotational speed, the weld bond of the tensile strength is increased. However, it was necessary to find the optimal parameter to attain the effective way for further consideration. In order to find the optimal parameter for two outputs such as tensile test and weld time, grey relational analysis (GRA) is chosen to make more effective method and simplify the welding parameter. The data that are either deficient or undetermined is called grey and a framework having incomplete data is called grey system. The grey

Fig. 2 Tensile fractured specimen

number speaks to a complete number with less information. The utilization of Taguchi technique with GRA is assigned to improve the welding tasks with multi-performance objectives [7].

The following are the procedures to be used for calculating grey relational grade with larger-the-better characteristics.

Step 1: The S/N ratio for the corresponding response is calculated by using the following formula.

(i) Larger the better

$$S/N \text{ ratio}(\eta) = -10 \log_{10}\left(\frac{1}{n}\right) \sum_{i=1}^{n} \frac{1}{y_{ij}^2} \tag{1}$$

(ii) Smaller the better

$$S/N \text{ ratio}(\eta) = -10 \log_{10}\left(\frac{1}{n} \sum_{i=1}^{n} \frac{1}{y_{ij}^2}\right) \tag{2}$$

where n = number of replications, y_{ij} = observed response value, where $i = 1, 2, \ldots n; j = 1, 2, \ldots k$.

In order to maintain the better quality output, tensile strength is assigned with maximization and minimization of weld time.

Step 2: Normalized value is determined in a single input rather than different output to make even data in an acceptable range of less than or equal to one. Similar to the *S/N* ratio formula, quality characteristics are assigned for normalizing the original

sequence as shown below in Eqs. (3) and (4) for larger and lower the better quality, respectively.

$$x_i^*(k) = \frac{x_i^{(0)}(k) - \min x_i^{(0)}(k)}{\max x_i^{(0)}(k) - \min x_i^{(0)}(k)} \tag{3}$$

$$x_i^*(k) = \frac{\max x_i^{(0)}(k) - x_i^{(0)}(k)}{\max x_i^{(0)}(k) - \min x_i^{(0)}(k)} \tag{4}$$

Step 3: Grey relational coefficient was then calculated based on the normalized values by giving 0.5 weightage.

$$\gamma = \frac{\Delta_{\min} + \varepsilon \Delta_{\max}}{\Delta_{oi}(k) + \varepsilon \Delta_{\max}} \tag{5}$$

where $\Delta_{oi}(k) = \left| x_0^*(k) - x_i^*(k) \right|$ is the absolute value of the difference between $x_o^*(k)$ and $x_i^*(k)$.

$\Delta_{\min} = \displaystyle\min_{\forall j \in i} \min_{\forall k} \left| x_0^*(k) - x_j^*(k) \right|$, smallest value of $x_i(k)$

$\Delta_{\max} = \displaystyle\max_{\forall j \in i} \max_{\forall k} \left| x_0^*(k) - x_j^*(k) \right|$, largest value of $x_i(k)$

ε $(0 \le \varepsilon \le 1)$ is the distinguishing coefficient and the value is taken as 0.5.

Step 4: Generating the grey relational grade by sum of the grey relational coefficients. The higher the grey relational grade means the parameter combination is closer to the optimal setting.

$$\gamma_i = \frac{1}{n} \sum_{k-1}^{n} \xi i(k) \tag{6}$$

where γ is the grey relational grade and k is the number of performance characteristics.

The normalized values were then calculated to monitor the value of coefficient obtained from GRA. From Table 4, it is evident that the setting of weld parameter 3 elevated with the highest grade. The combination of A_1, B_3 and C_3 shows the largest value of the grey relational grade 0.807. From the measured response grade, it demonstrates that increase in tensile strength and decrease in weld time were achieved in 104 MPa friction pressure, 195 MPa upset pressure and 2000 rpm rotational speed.

Based on the grade response, the measured mean value of prediction is calculated under the mentioned equation.

Table 4 Calculated grey relational grades

Exp. No	S/N ratio of TS	S/N ratio of WT	Normalized		Grey relational analysis		Grey relational coefficient		Grade	Grade order
1	50.6295	−19.554	0.001	1.001	0.999	0.001	0.333	1.001	0.667	3
2	51.3874	−18.608	0.891	0.679	0.109	0.321	0.821	0.609	0.715	2
3	51.4806	−18.618	1.001	0.683	0.001	0.317	1.001	0.612	0.807	1
4	51.1741	−17.278	0.641	0.227	0.359	0.773	0.582	0.393	0.487	5
5	50.7563	−18.265	0.150	0.562	0.850	0.438	0.370	0.533	0.452	6
6	50.7311	−17.278	0.120	0.227	0.880	0.773	0.362	0.393	0.378	8
7	51.2220	−17.061	0.697	0.153	0.303	0.847	0.623	0.371	0.497	4
8	50.7311	−16.611	0.120	0.000	0.880	1.000	0.362	0.333	0.348	9
9	50.8565	−17.313	0.267	0.239	0.733	0.761	0.406	0.396	0.401	7

Table 5 Response table for grey relational grade

Factors	Levels			Max–Min	Rank
	1	2	3		
Friction pressure [A]	**0.7297**	0.4390	0.4153	0.3143	1
Upset pressure [B]	**0.5503**	0.5050	0.5287	0.0453	3
Rotational Speed [C]	0.4643	0.5343	**0.5853**	0.1210	2

$$\hat{\gamma} = \gamma_m + \sum_{i=1}^{q} (\bar{\gamma}_i - \gamma_m) \tag{7}$$

The optimal combination of respective parameters (A_1, B_1 and C_3) resulted to 0.809. The predicted optimized value calculated from the above equation is 0.809 with an optimal welding parameter as shown in Table 5 and variations in each welding parameter are shown in Fig. 2. It indicates that with decrease in friction and upset pressure and increase in rotational speed, the weld quality is increased in tensile strength (Fig. 3).

For identifying the significant factor in friction welding, analysis of variance (ANOVA) test was performed. The parameter with a friction pressure of 83.47% shows a major contribution in friction welding followed by rotational speed 12.73% and upset pressure with 3.37 under 95% confidence level as listed in Table 6. For the confirmation experiment, the experiment is conducted with optimal parameter. From this parameter, the value of 377 MPa was achieved with weld time of 8.24 s. The improvement of grade is increased to 0.5% when compared to mean of predicted value which is tabulated in Table 7.

Main Effects Plot for SN ratios
Data Means
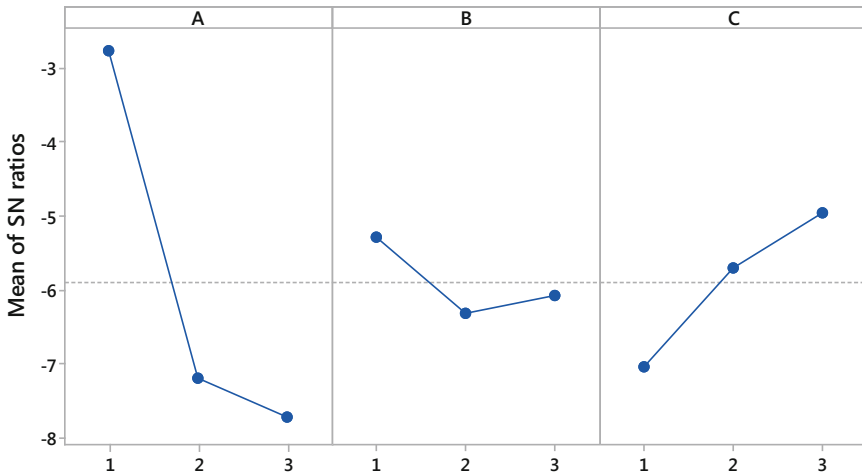
Signal-to-noise: Larger is better

Fig. 3 Main effect plot for *S/N* ratio

Table 6 Significant factor for GRA

Welding parameter	DF	SS	MS	F	p-value	% Contribution
Friction pressure (A)	2	44.5575	22.2788	199.55	0.005	83.47
Upset pressure (B)	2	1.7999	0.8999	8.06	0.110	3.37
Rotational speed (C)	2	6.7958	3.3979	30.44	0.032	12.73
Error	2	0.2233	0.1116			
Total	8	53.3765				

Table 7 Optimal values of individual welding characteristics

Welding characteristics	Initial design	Optimal welding parameters	
		Prediction	Experiment
	$A_1B_3C_3$	$A_1B_1C_3$	$A_1B_1C_3$
Tensile strength	375		377
Weld time	8.53		8.41
GRA	0.807	0.809	0.814

4 Conclusions

- Friction welding of similar leaded brass alloys was welded successfully and strength of the weld is reasonable.
- Grey relational analysis was statistically performed using Taguchi's L_9 orthogonal array to optimize the tensile strength and weld time.
- The optimized values of the process parameters are found as friction pressure 101 MPa, upset pressure 151 MPa and rotational speed 2000 rpm.
- Based on the optimal parameter, with decrease in friction and upset pressure and increase in rotational speed, tensile strength is increased with decrease in weld time.
- By using GRA, the weld parameter is increased by 0.814 with increase in grade value of 0.5%.
- In this study, the application of GRA was successful and improved the multiple quality characteristics for increasing the strength of welded joint.

References

1. ASM: Properties and selection: nonferrous alloys and special purpose materials. ASM, Cleveland (1990)
2. Luo, J., Xiang, J., Liu, Dejia, Li, F., Xu, K.: Radial friction welding interface between brass and high carbon steel. J. Mater. Process. Technol. **212**, 385–392 (2012)
3. Sassani, F., Neelam, J.R.: Friction welding of incompatible materials. Welding Research Supplement, Nov 1988, pp. 264–270-s
4. Gao, Y., Nakata, K., Nagatsuka, K., Matsuyama, T., Shibata, Y., Amano, M.: Microstructures and mechanical properties of friction stir welded brass/steel dissimilar lap joints at various welding speeds. Mater. Des. **90**, 1018–1025 (2016)
5. Gao, Y., Nakata, K., Nagatsuka, K., Matsuyama, T., Shibata, Y., Amano, M.: Optimizing tool diameter for friction stir welded brass/steel lap joint. J. Mater. Process. Technol. **229**, 313–321 (2016)
6. Esmaeilia, A., Besharati Givia, M.K., Zareie Rajanib, H.R.: A metallurgical and mechanical study on dissimilar Friction Stir welding of aluminum 1050 to brass (CuZn30). Mater. Sci. Eng. A **528**, 7093–7102 (2011)
7. Taguchi, G.: Introduction to quality engineering. McGraw-Hill, New York (1990)

Multi-objective Optimization Using Taguchi's Loss Function-Based Principal Component Analysis in Electrochemical Discharge Machining of Micro-channels on Borosilicate Glass with Direct and Hybrid Electrolytes

Jinka Ranganayakulu and P. V. Srihari

Abstract Machining of hard and brittle materials like borosilicate glass has imposed challenges due to its low machinability. Among various non-traditional machining methods, electrochemical discharge machining (ECDM) or spark-assisted chemical engraving (SACE) is proved as a potential method to machine such low machinable and non-conducting engineering materials. ECDM combines the features of electric discharge machining (EDM) and electrochemical machining (ECM) to machine electrically non-conducting materials. In the present study, direct (NaOH) and hybrid (NaOH + KOH) electrolytes were used to machine micro-channels on borosilicate glass with in-house developed prototype constant velocity tool-feed ECDM experimental set-up. The experiments were conducted based on L_9 orthogonal array with electrolyte concentration, voltage and duty factor as control factors. The overcut (OC) and heat-affected zones (HAZ) were considered as responses. Taguchi's loss function-based principal component analysis (PCA) was utilized for simultaneous optimization of responses. Analysis of variance (ANOVA) was performed, and electrolyte concentration was found as the most significant factor for both the cases. Confirmation tests with three replications were conducted at optimum factor levels and validated experimental results.

Keywords ECDM · Borosilicate glass · Hybrid electrolyte · Principal component analysis · ANOVA

J. Ranganayakulu (✉) · P. V. Srihari
Department of Mechanical Engineering, R. V. College of Engineering,
Bengaluru 560059, Karnataka, India
e-mail: jinka.ranganayakulu@gmail.com

P. V. Srihari
e-mail: pvsrihari@gmail.com

349

1   Introduction

Borosilicate or Pyrex glass finds application in MEMS and medical devices like drug delivery devices due to its anodic bonding capability with silicon, chemical inertness and optical properties. The low machinability of borosilicate glass has imposed challenges to incorporate it into micro-devices. Electrochemical discharge machining (ECDM) has emerged as a potential method to machine hard-to-machine materials [1]. Various tool-feeding mechanisms in spark-assisted chemical engraving (SACE) were discussed with their merits and demerits [2]. The effect of thermal conductivity of the tool materials like stainless steel, copper, tungsten, and high carbon steel was studied with gravity-feed mechanism to machine 50 micro-holes on borosilicate glass of thickness 1 mm and NaOH 30 wt% electrolyte. A considerable increase in initial drilling speeds was noticed with tungsten tool electrode at 35 V [3]. Attempts were made to model gas film formation to machine micro-channels with a carbide tool and a side-insulated carbide tool with 20% wt. NaOH at 35 V. Side-insulated tool has resulted in the channels with sharper contours, smooth surface texture and reduced width [4]. Variable inter-electrode gaps were used to machine micro-channels on glass substrate with steel tool and NaOH electrolyte. Based on response surface methodology (RSM), optimum values for control factors were obtained as applied voltage 55 V, electrolyte concentration 20 wt% and inter-electrode gap 40 mm [5]. Gravity tool feed was used to machine micro-holes on borosilicate glass substrates with KOH and NaOH electrolytes at 30 wt% and found that the use of a KOH electrolyte has produced more entrance diameter, 991.0 ± 40.4 µm compared to NaOH, 976.5 ± 20.5 µm [6]. 3D micro-structures were demonstrated by layer-by-layer micro-milling ECDM machining on Pyrex glass of 500 µm with KOH as electrolyte at 27.5% (w/v, 5 M) with tool rotation, significant reduction in groove width at higher rotational rates [7]. Rotary abrasive-coated electrode was used to drill Al_2O_3 with equal wt% mixed electrolyte of NaOH and KOH. An increase in electrolytic conductivity was noticed with mixed electrolyte than that of NaOH or KOH at the same concentration and has resulted in an increased volume of material removal [8]. Minimum amount of comparative study was done with direct and hybrid electrolytes to machine micro-channels on borosilicate glass. Hence, this paper presents the machining of micro-channels on borosilicate glass with NaOH and NaOH + KOH electrolytes and compares the machining performance in terms of overcut (OC) and heat-affected zones (HAZ).

2 Experimental Work

2.1 ECDM Experimental Set-up

An indigenously developed ECDM experimental set-up with constant velocity tool-feed mechanism shown in Fig. 1 was utilized to machine micro-channels. It consists of three modules, tool and work feed, processing chamber and power circuit modules. Two stepper motors of bipolar, $1.8°$ step angle, 200 steps per revolution, 20 V, 2 A, 9 kg-m were incorporated for tool- and table-feed mechanism. An acrylic processing chamber with Ø120 mm and height 70 mm was used to accommodate electrolyte, auxiliary electrode and work table. The power circuit consists of regulated D.C. power supply (0–300 V, 3 A) for machining purpose, D.C. power supply (0–32 V, 2 A) to operate controlled pulse circuit at 5 V input, function generator and oscilloscope. Tool immersion depth of 1.5 mm from the surface of the workpiece and inter-electrode distance of 40 mm were maintained for all the experiments. Due to electrolysis, water decomposes into H_2 and O_2, and H_2 bubbles accumulate at cathode (tool) and O_2 bubbles at anode. The spark initiated across the tool and electrolyte interface is shown in Fig. 1c. The technical specifications for the ECDM and properties of borosilicate glass were presented in Tables 1 and 2.

2.2 Taguchi's Loss Function-Based Principal Component Analysis for Multi-response Optimization

The methodology given by [9–11] was used to optimize multi-response characteristics with the following steps.
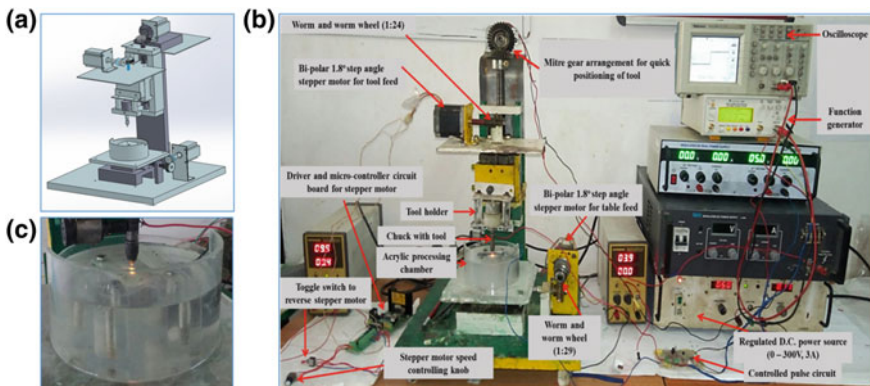
Fig. 1 ECDM experimental set-up. **a** 3D CAD model, **b** photographic view, and **c** close-up view of spark

Table 1 Technical specifications

Parameter	Value
Anode—Graphite	20 mm × 20 mm × 5 mm
Cathode—Tool	Stainless steel, Ø300 μm
Borosilicate glass	10 mm × 10 mm × 1 mm
Tool and work feed	0.06 and 0.04 mm/min
Pulsed D.C. power	333 Hz, total time 3 ms

Table 2 Properties of borosilicate glass

Parameter	Value
Density	2.23 g/cm^3
Young's modulus	64 GPa
Thermal conductivity	1.14 W/m K
Thermal expansion	3.3×10^{-6} K
Dielectric strength	5.0–34 kV/mm

Step 1: Identification of factors for the experiment.
Step 2: Selection of responses for the experiment.
Step 3: Compute the quality loss for each response.

Let L_{ij} be the quality loss for ith response at jth trial. L_{ij} can be computed based on Taguchi's loss function.

$$L_{ij} = k_1 \frac{1}{n_i} \sum_{k=1}^{n_i} y_{ijk}^2 \quad \text{for the smaller-the-best response} \tag{1}$$

$$L_{ij} = k_1 \frac{1}{n_i} \sum_{k=1}^{n_i} \frac{1}{y_{ijk}^2} \quad \text{for the larger-the-best response} \tag{2}$$

where L_{ij} = quality loss for ith response at jth trial, y_{ijk} = observed data for ith response at jth trial and kth repetition, n_i = replications for ith response and k_1, k_2 = quality loss coefficients.

Step 4: Normalize L_{ij}.

To reduce the variability, the scale of the quality loss for each response is normalized. L_{ij} is transformed into Y_{ij} ($0 < Y_{ij} < 1$) by using Eq. (3).

$$Y_{ij} = \frac{L_i^+ - L_{ij}}{L_i^+ - L_i^-} \tag{3}$$

where Y_{ij} = the normalized quality loss (NQL) for ith response at jth trial $L_i^+ = \max\{L_{i1}, L_{i2}, \ldots, L_{ij}\}$; $L_i^- = \min\{L_{i1}, L_{i2}, \ldots, L_{ij}\}$.

Step 5: Perform the principal component analysis (PCA) on the basis of the computed data, Y_{ij} [12].

Step 6: Evaluate the number of principal components, k, and find Ω, a multi-response performance index (MRPI).

$$\Omega_{kj} = \sum_{i=1}^{p} a_{ki} Y_{ij} \qquad (4)$$

where $a_{k1}, a_{k2}, \ldots, a_{kp}$ are the elements of the eigenvector corresponding to the kth largest eigenvalue.

Step 7: Determination of significant factor effects and optimal settings.

Step 8: Perform a confirmatory experiment.

2.3 Experimental Procedure

Electrolytes of NaOH were prepared with 15, 20 and 25 wt%, respectively. A hybrid electrolyte of NaOH + KOH was prepared with 15, 20 and 25 wt% which includes 5 wt% KOH in each case. Experiments were conducted with the factors and their levels for direct and hybrid electrolytes as presented in Tables 3 and 4.

Table 3 Factors and levels with direct electrolyte

Factors	Levels		
	1	2	3
[a]EC wt% (A)	15	20	25
Voltage, V (B)	50	55	60
Duty factor, DF % (C)	60	65	70

[a]*EC* Electrolyte concentration

Table 4 Factors and levels with hybrid electrolyte

Factors	Levels		
	1	2	3
EC wt% (NaOH + KOH), (A)	10 + 5	15 + 5	20 + 5
Voltage, V (B)	50	55	60
Duty factor, DF % (C)	60	65	70

3 Results and Discussion

Experiments were conducted based on L_9 orthogonal array as shown in Table 5, for direct (NaOH), and Table 6, for hybrid (NaOH + KOH) electrolytes with overcut (OC) and heat-affected zone (HAZ) as responses. The HAZ and OC were measured with trinocular stereo microscope images at 4×, 1 mm scale. OC and HAZ calculations were carried out using Eqs. (5) and (6). Figure 2 shows optical images of a machined borosilicate workpiece representing OC and HAZ and optical images of micro-channels machined at optimum process parameters.

$$OC = B - TD \tag{5}$$

$$HAZ = A - B \tag{6}$$

where A = width across HAZ, µm; B = width across machined channel, µm; TD = tool diameter, µm.

Taguchi's quality loss (TQL) values for OC (L_1) and HAZ (L_2) were calculated based on smaller-the-best option using Eq. (1) with direct and hybrid electrolyte as shown in Tables 5 and 6. Normalized quality loss (NQL) values with direct and hybrid electrolytes for OC (Y_1) and HAZ (Y_2) were calculated using Eq. (3) as listed in Table 7.

Eigenvalues, principal components and explained variation were obtained with MINITAB 17 and listed in Table 8 with direct electrolyte and in Table 9 with hybrid electrolyte. The eigenvector for the first largest eigenvalue for both direct and hybrid electrolytes was [0.707, 0.707]. Consequently, from Eq. (4), we have, MRPI,
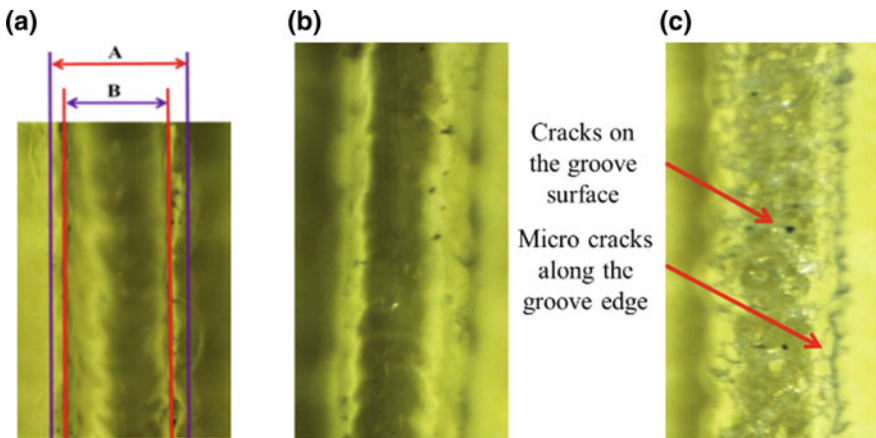
Fig. 2 Optical images of micro-channels at 4×, 1 mm scale. **a** OC and HAZ measurements, **b** at optimum values with direct electrolyte, and **c** at optimum values with hybrid electrolyte

Table 5 Experimental results and quality loss values with direct electrolyte

Trial no.	Factors			OC, µm	HAZ, µm	TQL values	
	A	B	C			L_1	L_2
1	1	1	1	50.448	36.675	2545.026	1345.042
2	1	2	2	83.048	76.609	6896.984	5869.033
3	1	3	3	127.872	77.425	16,351.468	5994.571
4	2	1	2	125.427	63.569	15,732.151	4041.104
5	2	2	3	188.997	65.199	35,720.076	4250.997
6	2	3	1	148.248	114.099	21,977.398	13,018.679
7	3	1	3	156.398	118.174	24,460.246	13,965.191
8	3	2	1	164.548	97.799	27,075.938	9564.744
9	3	3	2	197.147	89.649	38,867.142	8037.042

Table 6 Experimental results and quality loss values with hybrid electrolyte

Trial no.	Factors			OC, µm	HAZ, µm	TQL values	
	A	B	C			L_1	L_2
1	1	1	1	70.008	60.309	4901.141	3637.259
2	1	2	2	93.643	63.569	8769.017	4041.104
3	1	3	3	140.098	73.349	19,627.393	5380.169
4	2	1	2	143.358	38.305	20,551.454	1467.258
5	2	2	3	173.512	59.495	30,106.634	3539.619
6	2	3	1	149.878	83.945	22,463.340	7046.692
7	3	1	3	164.548	75.795	27,075.938	5744.825
8	3	2	1	167.808	75.795	28,159.411	5744.825
9	3	3	2	188.998	81.499	35,720.076	6642.184

Table 7 Normalized quality loss values with direct and hybrid electrolytes

Trial	NQL values with direct electrolyte		NQL values with hybrid electrolyte	
	Y_1	Y_2	Y_1	Y_2
1	1.00000	1.00000	1.00000	0.61107
2	0.88018	0.64153	0.87449	0.53869
3	0.61988	0.63158	0.52217	0.29869
4	0.63694	0.78637	0.49219	1.00000
5	0.08664	0.76974	0.18214	0.62857
6	0.46499	0.07500	0.43015	0.00000
7	0.39664	0.00000	0.28048	0.23333
8	0.32463	0.34868	0.24533	0.23333
9	0.00000	0.46974	0.00000	0.07250

Table 8 Eigenvalues for the principal components with direct electrolyte

Principal components	Eigenvalue	Explained variation	Cumulative variation	Eigenvector
PC_1	1.4017	0.701	0.701	[0.707, 0.707]
PC_2	0.5983	0.299	1.000	[0.707, −0.707]

Table 9 Eigenvalues for the principal components with hybrid electrolyte

Principal components	Eigenvalue	Explained variation	Cumulative variation	Eigenvector
PC_1	1.4252	0.713	0.713	[0.707, 0.707]
PC_2	0.5748	0.287	1.000	[0.707, −0.707]

Table 10 Calculated MRPI (Ω) values with direct and hybrid electrolytes

Trial	MRPI (Ω)-direct electrolyte	MRPI (Ω)-hybrid electrolyte
1	**1.41400**	**1.13903**
2	1.07585	0.99912
3	0.88479	0.58035
4	1.00628	1.05497
5	0.60546	0.57317
6	0.38178	0.30412
7	0.28043	0.36327
8	0.47603	0.33841
9	0.33210	0.05126

$$\Omega_{1j} = 0.707Y_{1j} + 0.707Y_{2j} \qquad (7)$$

From Eq. (7), MRPI values with direct and hybrid electrolytes were calculated as presented in Table 10. Higher MRPI (Ω) value indicates that the corresponding factor combination is closer to the optimum values.

The results for OC and HAZ with direct and hybrid electrolytes were presented in Fig. 3. An increase in OC and significant reduction in HAZ was identified with hybrid electrolyte. Individual molar conductivity of Ka^+ ion (50.1 Ω^{-1} cm^2 mol^{-1}) is higher than that of Na^+ ion (38.7 Ω^{-1} cm^2 mol^{-1}) in water at 25 °C [1]. The increase in OC was attributed due to high electrical conductivity of hybrid electrolyte. High conducting electrolyte has enhanced the gas-forming tendency at cathode and resulted in the increase in volume of material removal [8, 13]. The reduction in HAZ with hybrid electrolyte was noticed, due to OC overlapped with the HAZ as shown in Fig. 2c.
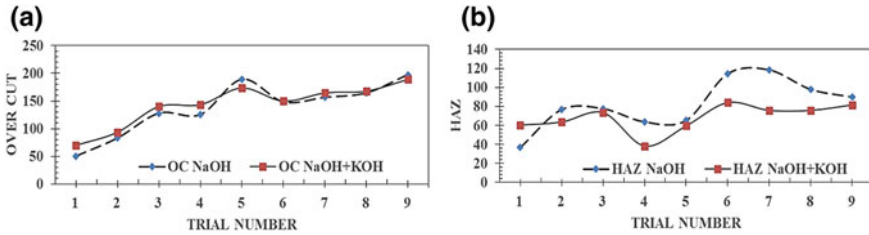
Fig. 3 **a** Overcut and **b** heat-affected zones with direct and hybrid electrolytes

4 Determination of Significant Factors and Optimal Factors

4.1 Determination of Significant Factors with Analysis of Variance (ANOVA)

From ANOVA electrolyte, concentration was found to be the most influencing factor as shown in Tables 11 and 12 with 70.80 and 55.72% for both the direct and hybrid electrolytes.

4.2 Determination of Optimal Factors

The calculated values of main effects on MRPI (Ω) with direct electrolyte and hybrid electrolytes were presented in Tables 13 and 14. The optimum-level parameters with direct and hybrid electrolytes were identified as $A_1B_1C_2$. Figures 4 and 5 show the corresponding factor effects on MRPI (Ω) values with direct and hybrid electrolytes.

Table 11 Analysis of variance on MRPI with direct electrolyte

Source of variation	DoF	Sum of squares	Mean square	F	P value	% contribution
EC	2	0.88362	0.44181	**10.30***	0.089	**70.80***
V	2	0.20243	0.10121	2.36	0.298	16.22
DF	2	0.07618	0.03809	0.89	0.530	6.10
Error	2	0.08581	0.04291			6.88
Total	8	1.24804				100

$F_{0.1,2,2} = 9.00$, *EC is significant at 10% significant level, coefficient of determination, R^2–93.12%, DoF—Degree of freedom

Table 12 Analysis of variance with hybrid electrolyte

Source of variation	DoF	Sum of squares	Mean square	F	P-value	% contribution
EC	2	0.65249	0.326245	**39.68***	0.025	**55.72***
V	2	0.44423	0.222115	**27.01***	0.036	**37.93***
DF	2	0.05793	0.028964	3.52	0.221	4.95
Error	2	0.06213	0.03107			1.4
Total	8	1.08558				100

$F_{0.05,2,2} = 19.00$, *EC and V are significant at 5% significant level, R^2–98.60%

Table 13 Main effects on MRPI (Ω) with direct electrolyte

| Factors	Levels			Max.–Min.
	1	2	3	
EC wt% (A)	**1.12488**[a]	0.66451	0.36285	0.76202
V (B)	**0.90023**[a]	0.71911	0.53289	0.36734
DF (C)	0.75727	**0.80474**[a]	0.59022	0.21452

[a]$A_1B_1C_2$ optimum process parameters

Table 14 Main effects on MRPI (Ω) with hybrid electrolyte

| Factors	Levels			Max.–Min.
	1	2	3	
EC wt% (A)	**0.90617**[a]	0.64409	0.25098	0.65519
V (B)	**0.85242**[a]	0.63690	0.31191	0.54052
DF (C)	0.59385	**0.70178**[a]	0.50559	0.19619

[a]$A_1B_1C_2$ optimum process parameters

Fig. 4 Factor effects with direct electrolyte
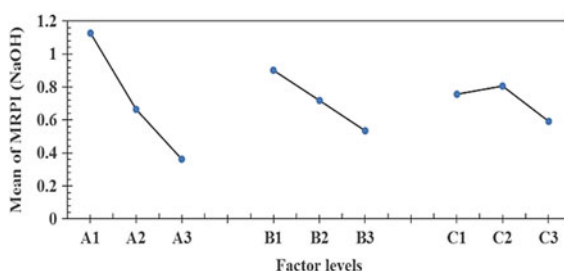
5 Confirmation Experiments

Confirmation experiments were carried out for three replications by setting the factors at their optimal values $A_1B_1C_2$, electrolyte concentration, 15 wt%, applied voltage, 50 V, duty factor, 65%, with both the direct and hybrid electrolytes.

Fig. 5 Factor effects with hybrid electrolyte
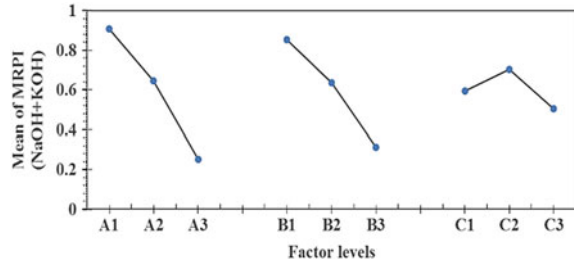
The average values of OC and HAZ from confirmation experiments with direct electrolyte were found to be 76.26 and 66.30 μm. These values were within the limits of trial 1 and trial 2 responses (50.448 and 83.048 μm for OC and 36.675 and 76.609 μm for HAZ), near the maximum MRPI value. Similarly, average values of OC and HAZ from confirmation experiments with hybrid electrolyte were found to be 76.26 and 62.29 μm. These values were within the limits of trial 1 and trial 2 responses (70.008 and 93.643 μm for OC and 21.189 and 63.569 μm for HAZ), near the maximum MRPI value. Hence, the optimal values were confirmed.

6 Conclusions

- The optimum-level parameters with direct and hybrid electrolytes were identified as $A_1B_1C_2$.
- From ANOVA, for both direct and hybrid electrolytes, electrolyte concentration was found to be the most influencing factor with 70.80 and 55.72%.
- Increase in OC due to high electrical conductivity of hybrid electrolyte and significant reduction in HAZ was identified due to OC overlapped with the HAZ.
- Smooth and well-defined micro-channels were machined with NaOH electrolyte at optimum values.
- Micro-cracks along the edges and channel surface were noticed on channels machined with hybrid electrolyte.

References

1. Wuthrich, R., Abou Ziki, J.D.: Micromachining Using Electrochemical Discharge Phenomenon, 2nd edn. William Andrew. ISBN 978-0-323-24142-7 (2015)
2. Wuthrich, R., Spaelter, U., Wu, Y., Bleuler, H.: A systematic characterization method for gravity-feed micro-hole drilling in glass with spark assisted chemical engraving (SACE). J. Micromech. Microeng. **16**, 1891–1896 (2006)
3. Mousa, M., Allagui, A., Ng, H.D., Wuthrich, R.: The effect of thermal conductivity of the tool electrode in spark-assisted chemical engraving gravity-feed micro-drilling, J. Micromech. Microeng. **19**, 015010, 7 p (2009)
4. Han, M.S., Min, B.K., Jo Lee, S.: Modelling gas film formation in electrochemical discharge machining processes using a side-insulated electrode. J. Micromech. Microeng. **18**, 045019 (2008)
5. Mallik, B., Sarkar, B.R., Doli, B., Bhattachryya, B.: Multi criteria optimization of electrochemical discharge micro-machining process during micro-channel generation on glass, Appl. Mech. Mater. 592–594, 525–529 (2014)
6. Jonathan, W., Amol, J.: ECDM methods for fluidic interfacing through thin glass substrates and the formation of spherical microcavities. J. Micromech. Microeng. **17**, 403–409 (2007)
7. Zhi-Ping, Z., Wei-Hsin, C., Fuang-Yuan, H., Biing-Hwa, Y.: 3D micro structuring of Pyrex glass using the electrochemical discharge machining process. J. Micromech. Microeng. **17**, 960–966 (2007)
8. Sanjay, K.C., Venkateswara Rao, P.: The drilling of Al_2O_3 using a pulsed DC supply with rotary abrasive electrode by the electrochemical discharge process. Int. J. Adv. Manuf. Technol. **39**, 633–641 (2008)
9. Chao-Ton, S., Lee-Ing, T.: Multi-response robust design by principal component analysis. Total Qual. Manag. **8**(6), 409–416 (1997)
10. Antony, J.: Multi-response optimization in industrial experiments using Taguchi's quality loss function and principal component analysis. Qual. Reliab. Eng. Int. **16**, 3–8 (2000)
11. Basanta Kumar, B., Vinod, Y.: Experimental modeling and multi-objective optimization of traveling wire electrochemical spark machining (TW-ECSM) process. J. Mech. Sci. Tech. **27** (8), 2467–2476 (2013)
12. Ranganayakulu, J., Somashekhar, S.H., Lijo, P.: Parametric analysis and a soft computing approach on material removal rate in electrochemical discharge machining. Int. J. Manuf. Technol. Manag. **24**(1/2/3/4), 23–39 (2011)
13. Sanjay, K.C., Venkateswara Rao., P.: Machining of SiC by ECDM process using different electrode configurations under the effect of pulsed DC. Int. J. Manuf. Technol. Manag. **28** (1/2/3), 39–56 (2014)

Flutter Analysis of Supersonic Low Aspect Ratio Composite Wings Using FSI Methodology

T. Babin and N. Sangeetha

Abstract A two-dimensional plate model for the aeroelastic flutter of low aspect ratio composite wing is taken based on the classical plate theory and fluid–structure interaction methodology and is adapted for further studies. The domain model and the corresponding supersonic loads are defined in accordance with Hamilton principle and first-order piston theories, respectively. Natural frequencies and flutter velocity are analysed and verified using the differential quadrature method (DQM) literatures, in comparison with the fluid–structure interaction method. Based on the parametric study carried out, the results show that the flutter characteristics are strongly dependent on cross-ply laminates and these kinds of vibration in the low aspect ratio composite wings can occur only in the high circumferential frequencies. The effects of the aspect ratio on supersonic flutter characteristics of laminated wings are investigated, with constant surface area and constant thickness, and all the layers are of equal thickness.

Keywords Flutter · Low aspect ratio wings · Fluid–structure interaction
Composite wings · Ply angle

1 Introduction

Fibre-reinforced composite materials are being mostly used in the design of aerospace vehicles, since they have high stiffness, high strength-to-weight ratio and anisotropy composite in the heat exchange. When these thin-walled structural components are subjected to the action of a high-speed airflow on the outer surface, they may become dynamically unstable at a certain critical speed of the vehicle.

T. Babin (✉) · N. Sangeetha
Department of Mechanical Engineering, Kumaraguru College of Technology,
Coimbatore, India
e-mail: babinn4340@gmail.com

N. Sangeetha
e-mail: Sangeetha.n.mec@kct.ac.in

This phenomenon is known as flutter. The flutter behaviour of composite laminated sheets has attracted many researchers because of its continuous growth towards the problem. Karpouzian [1, 2] was the first to give the detailed flutter analysis on anisotropic composite cantilevered wing structures based on the Laplace transform method, while the Giles [3, 4] studied the flutter analysis with equivalent plate models of planform geometry. Later on, Meirovitch [5] derived the equations governing the static and dynamic aeroelastic displacement equations of cantilevered wing structures based on the plate theories.

One of the proven methods to solve the flutter problem is the differential quadrature method (DQM). Shu [6, 7] in his book gave the detailed application of DQM in various engineering applications including compressible fluid flows and other aeroelastic applications. And Liu and Wu [8] were the first to derive the DQM for boundary value problems to obtain the solution. Fluid–structure interaction is a recently developed method for analysing the effect of fluid forces on structural components. Out of some of the ways to couple both the mechanics such as one-way and two-way coupling strategies, two-way coupling methodology is adapted where both the fluid and structural analysis take place at same time successively. From the recent researches in bridge and piping vibration analysis [9–11] made through FSI, showed the way to solve the flutter problem by the same technique. FSI technique has shown the improved accuracy and reliability over compressible flows. Kamakoti [12] was the first to use the FSI in aeroelastic application; he predicted the flutter for a wing at different Mach numbers based on moving grid technique. In addition, Kwon et al. [13] studied the impact on composite plates with FSI by conducting a real-time experiment and showed the application of FSI on composite plates. This paper is majorly concerned with the study on aeroelastic flutter characteristics of low aspect ratio composite wings at compressible flow condition using FSI technique. The results are compared with DQM method based on the literatures [6, 7]. At last, a detailed parametric study has been conducted to study the influences of aspect ratios, ply angle and stacking sequence on the supersonic flutter behaviour of composite laminate panel.

2 Theoretical Formulations

2.1 Low Aspect Ratio Wing Model

For simplifying the problem, 2D shear deformable plate model is chosen for the study. Wing structure is idealized as a fibre-reinforced laminated composite plate whose constituent laminates are located by different angles in cross-ply and stacking sequence with constant surface area and constant layer thickness. Two-dimensional plate model is developed such that x and y are the coordinates representing the chord-wise and span-wise coordinates, respectively. The point O is the origin located at the intersection of the mid-plane chord with the leading edge of

Fig. 1 2D plate model with displacement
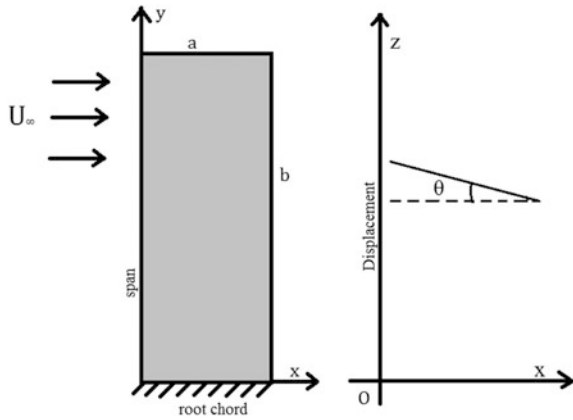
wing structure. The 2D plate model representing low aspect ratio composite wing is assumed to act as an elastic plate which is clamped at the root chord and set to free at other three boundaries as shown in Fig. 1.

According to Kirchoff's hypothesis, the displacements (u, v, w) are given by [2]:

$$u(x, y, z, t) = u_0(x, y, t) - z\frac{\partial w}{\partial x},$$
$$v(x, y, z, t) = v_0(x, y, t) - z\frac{\partial w}{\partial y}, \tag{1}$$
$$w(x, y, z, t) = w(x, y, t).$$

Since the displacement along $w(x, y, z, t)$ is independent of transverse coordinate z and assumption made that root chord is fixed, the transverse normal and shear strains due to plunge and pitch are zero. u_0 and v_0 are the mid-plane elastic deflections in the x and y directions, respectively. Partial derivatives refer to the corresponding angular displacements.

2.2 Supersonic Aerodynamic Load

In the compressible supersonic flight region, the aerodynamic load is unsteady in nature which can be evaluated by the first-order theory. These aerodynamic loads on the faces of the composite wing can be expressed by:

$$\Delta F = \frac{2\rho V}{Ma}\left[\left(V\frac{\partial w}{\partial x} + \frac{\partial w}{\partial t}\right) + V\frac{\partial H}{\partial x}\right] = \frac{4q}{Ma}\left(\frac{\partial w}{\partial x} + \frac{1}{V}\frac{\partial w}{\partial t} + \frac{\partial H}{\partial x}\right).$$

The dynamic pressure is given by $q = \frac{\rho V^2}{2}$.

Where ρ is the air density, Ma is the Mach number, V is the velocity of the wing, $w(x, y, t)$ is the transverse displacement of the wing, q is the dynamic pressure, and $H(x, y)$ is the wing thickness function.

2.3 Energy Expression as Governing System

The dynamical problem of flutter can be formulated as strain energy expression of plate segment, and it can be expressed as [3]:

$$\Delta E = \int_{t_0}^{t_1} (\delta P - \delta T - \delta W).dt = 0 \tag{3}$$

where P is the potential energy, T is the kinetic energy, and the W is the virtual work performed by the wing due to non-conservative forces. Potential energy of the wing is the total strain energy stored in the wing along the respective directions.

$$\varepsilon_x = \frac{\partial u}{\partial x} = \frac{\partial u_0}{\partial x} - z\frac{\partial^2 w}{\partial x^2} = -z\frac{\partial^2 w}{\partial x^2}, \quad \varepsilon_y = \frac{\partial v}{\partial y} = \frac{\partial v_0}{\partial y} - z\frac{\partial^2 w}{\partial y^2} = -z\frac{\partial^2 w}{\partial y^2},$$
$$\gamma_{xy} = \frac{\partial u}{\partial y} + \frac{\partial v}{\partial x} = \frac{\partial u_0}{\partial y} + \frac{\partial v_0}{\partial x} - 2z\frac{\partial^2 w}{\partial x.\partial y} = -2z\frac{\partial^2 w}{\partial x.\partial y}. \tag{4}$$

In order to get the simple form, the mid-plane elastic deflections are assumed zero, such that the partial derivatives containing u_0 and v_0 were eliminated. ε_x and ε_y are the normal strains in their respective directions, and γ_{xy} is the engineering shear strain.

For the nth general orthotropic layer of composite wing with principle axes, the constitutive equation of stresses takes the form,

$$\left\{ \begin{array}{c} \sigma_x^n \\ \sigma_y^n \\ \tau_{xy}^n \end{array} \right\} = \left[\begin{array}{ccc} \overrightarrow{Q_{11}} & \overrightarrow{Q_{12}} & \overrightarrow{Q_{16}} \\ \overrightarrow{Q_{12}} & \overrightarrow{Q_{22}} & \overrightarrow{Q_{26}} \\ \overrightarrow{Q_{16}} & \overrightarrow{Q_{26}} & \overrightarrow{Q_{66}} \end{array} \right] \left\{ \begin{array}{c} \varepsilon_x^n \\ \varepsilon_y^n \\ \gamma_{xy}^n \end{array} \right\} \tag{5}$$

The values of the elements $[Q]^n$ in the above-discussed matrix are related to material properties of the nth layer by [6],

$$Q_{11} = \frac{E_1}{\left(1 - \vartheta_{12}^2\left(\frac{E_2}{E_1}\right)\right)}, \quad Q_{12} = \frac{\vartheta_{12}E_2}{\left(1 - \vartheta_{12}^2\left(\frac{E_2}{E_1}\right)\right)}, \quad Q_{22} = \frac{E_2}{\left(1 - \vartheta_{12}^2\left(\frac{E_2}{E_1}\right)\right)}, \tag{6}$$
$$Q_{66} = G_{12}.$$

where v_{ij}, E_i and G_{ij} are Poisson's ratio, Young's modulus and shear modulus, respectively. The relationship between local material expressions discussed above and the global ones can be related as follows:

$$\begin{Bmatrix} \overrightarrow{Q_{11}} \\ \overrightarrow{Q_{22}} \\ \overrightarrow{Q_{12}} \\ \overrightarrow{Q_{66}} \\ \overrightarrow{Q_{16}} \\ \overrightarrow{Q_{26}} \end{Bmatrix} = \begin{bmatrix} m^4 & n^4 & 2m^2n^2 & 4m^2n^2 \\ n^4 & m^4 & 2m^2n^2 & 4m^2n^2 \\ m^2n^2 & m^2n^2 & m^4+n^4 & -4m^2n^2 \\ m^2n^2 & m^2n^2 & -2m^2n^2 & (m^2-n^2)^2 \\ m^3n & -mn^3 & mn^3-m^3n & 2(mn^3-m^3n) \\ mn^3 & -m^3n & m^3n-mn^3 & 2(m^3n-mn^3) \end{bmatrix} \begin{Bmatrix} Q_{11} \\ Q_{22} \\ Q_{12} \\ Q_{66} \end{Bmatrix} \quad (7)$$

where $m = \cos\theta$ and $n = \sin\theta$.

It is assumed that the laminate consists of $2k$ symmetrical layers of constant thickness and it is a continuous function of x and y. The laminate strain energy for a single layer n is given by:

$$P_n = \int_{t_{n-1}}^{t_n} \left\{ \sigma_x^n \varepsilon_x^n + \sigma_y^n \varepsilon_y^n + \sigma_{xy}^n \varepsilon_{xy}^n \right\} .dz \quad (8)$$

The laminate strain energy for all the layers is given by integrating the above equation over the domain of the plate extended in x-direction as wing chord and in y-direction as wingspan.

$$\delta P = 2 \int_0^a \int_0^b \sum_{n=1}^k \left\{ \int_{t_{n-1}}^{t_n} \left[\sigma_x^n \varepsilon_x^n + \sigma_y^n \varepsilon_y^n + \sigma_{xy}^n \varepsilon_{xy}^n \right] .dz \right\} \quad (9)$$

where a is the wing chord breadth and b is the wingspan length.

To simplify the above strain energy expression, the material properties along with thickness are related to a single equation of total laminate bending stiffness coefficient D_{mn} which is defined as:

$$D_{mn} = \frac{2}{3} \sum_{n=1}^k \left(t_n^3 - t_{n-1}^3 \right) \overrightarrow{Q_{ij}^n} \quad (10)$$

The non-conservative virtual work is mainly due to fluid forces on the face of the wing. The unsteady aerodynamic load multiplied by corresponding virtual displacement yields non-conservative virtual work density. By integrating it over the entire domain of the wing. The obtained non-conservative virtual work is given by:

$$\delta W = \int_0^a \int_0^b \Delta F .\delta w .dy .dx = \int_0^a \int_0^b \frac{4q}{Ma} \left(\frac{\partial w}{\partial x} + \frac{1}{V} \frac{\partial w}{\partial t} + \frac{\partial H}{\partial x} \right) \delta w .dy .dx . \quad (11)$$

Also, the kinetic energy of the wing takes the following equation:

$$\delta T = \int\limits_0^a \int\limits_0^b \rho h \ddot{w} \delta w \, .dy.dx. \tag{12}$$

By substituting (9), (11) and (12) in the extended Hamilton's principle Eq. (3), the governing system equation based on the energy conservation can be obtained as:

$$D_{11}w_{xxxx} + 4D_{16}w_{xxxy} + 2(D_{12} + 2D_{66})w_{xxyy} + 4D_{26}w_{xyyy} + D_{22}w_{yyyy} + \rho h \ddot{w}$$
$$+ \frac{4q}{Ma}\left(\frac{\partial w}{\partial x} + \frac{1}{V}\frac{\partial w}{\partial t} + \frac{\partial H}{\partial x}\right) = 0 \tag{13}$$

For the flutter problem, the boundary condition of the low aspect ratio composite wing is:

(a) Fixed support at the root:

$$w(x, y, t) = 0; \quad \frac{\partial w}{\partial y} = 0;$$

(b) Free at the other ends:

$$M_n = 0; \quad P_n = 0;$$

Here,

$$P_n = Q_n + \frac{\partial M_s}{\partial s}, \quad \text{where } M_s = n_x n_y \left(M_y - M_x\right) + \left(n_x^2 - n_y^2\right)M_{xy};$$
$$M_n = n_x^2 M_x + 2n_y M_{xy,y} n_x + n_y^2 M_y;$$

where the subscripts n and the s represent the normal and the tangential directions of the edge, respectively. And the M_n and the M_s represent the normal bending moment and twisting moment, respectively. Also, n_x and n_y denote the direction cosines of unit normal vector at a point.

3   FSI for Flutter Analysis

3.1   Fluid Solver

A semi-spherical domain of radius 5 m is chosen as fluid zone, and the origin is located at the intersection of trailing edge with root chord. Hexagonal block mesh is created using ICEM CFD with 445,864 elements and 82,398 nodes. Fluent 18.2 is used as fluid solver with density-based Navier–Stokes equation and k–ε turbulence

model. The pressure far field is the condition given to outer walls in an assumption that the wing is a cantilevered structure at open atmosphere. Implicit scheme and second-order upwind scheme are used to solve the governing equations.

3.2 Structural Solver

Finite element method is used to solve the structural equations. ACP (pre) from ANSYS 18.2 models the composite laminates. Figures 2 and 3 show the finite element model and the laminate model of the composite wing, respectively. The geometrical specifications and material properties are given in Table 1. Closed coupling of fluid forces into structural faces results in mechanical deformations, which is further directed to modal analysis to obtain the excitation frequencies, so-called flutter frequencies.
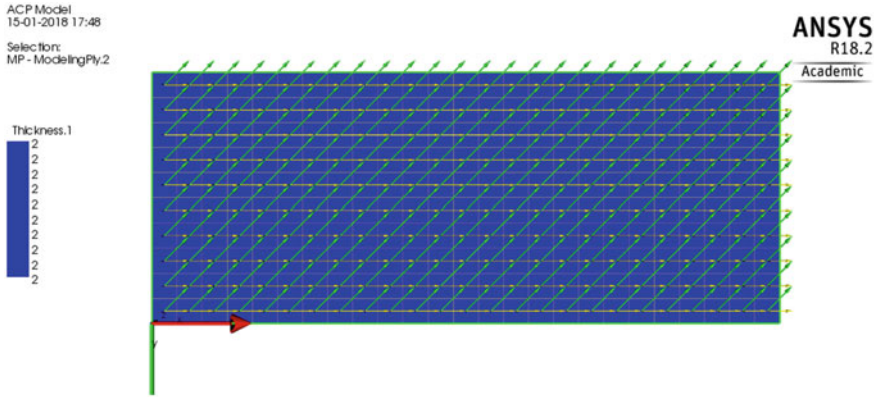
4 Results and Discussion

4.1 Verification with DQM

In this section, the aeroelastic flutter characteristics of the cross-ply $[\theta/-\theta/\theta/-\theta]s$ laminated low aspect ratio composite wing are analysed using FSI method. The

Fig. 2 Finite element model of the composite wing
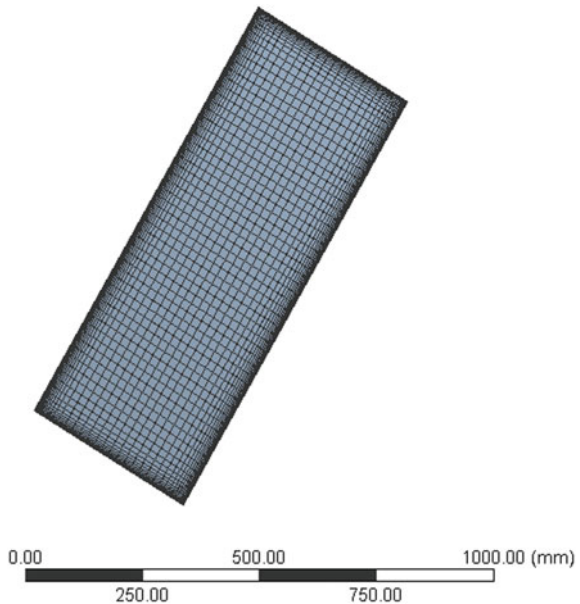
Fig. 3 Second ply of the stacking sequence—45° oriented ply

Table 1 Baseline parameters of composite wing

Parameters	Value
a	0.4 m
b	1 m
t	0.002 m
ρ	1490 kg/m^3
E_x	4×10^{10} N/m^2
E_y	8.6×10^9 N/m^2
Poisson ratio XY	0.25
Strain Z	0.0032

comparison between the excited frequencies of FSI method and the DQM method is discussed in Table 2, and the graph shows the deviation between the two methods.

The convergence of the FSI and DQM results is represented in the graph form in Fig. 4. The values plotted in each case are the excited frequencies obtained at speed of 600 m/s. For several structural models and the flutter velocity with variation in ply angle, the listed table and the graph show that the results obtained using fluid–structure interaction method have good solution in comparison with the results obtained by DQM [9]. These results show that the flutter analysis can be carried out further for parametric analysis such as stacking sequence and other aspect ratios.

4.2 Aeroelastic Characteristics

Aeroelastic characteristics of composite wings are highly dependent upon the structural parameters such as aspect ratios, ply angle and stacking sequence. Based on the dynamic stability, the flutter coalescence occurs at critical dynamic pressure

Table 2 Excited frequencies of the cross-ply [$\theta/-\theta/\theta/-\theta$]s laminated wings at Mach number 1.8

θ		FSI				DQM			
		15	30	45	60	15	30	45	60
Frequency (Hz)	Mode 1	5.435	8.81	16.318	23.8	6.012	9.132	16.32	25.33
	Mode 2	31.42	50.412	62.845	58.989	32.20	51.61	62.86	61.01
	Mode 3	35.62	52.189	92.762	114.65	37.42	54.04	92.45	117.8
	Mode 4	104.78	153.24	160.15	165.42	101.6	152.8	161.0	162.1
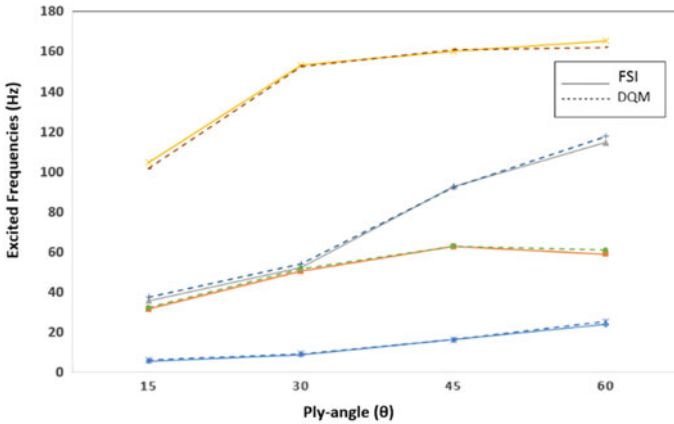
Fig. 4 Excited frequencies of composite wing versus ply angle

Table 3 Coalescence of frequencies for various stacking sequence

Stacking sequence	[−45/45/90/0]	[−45/90/0/45]	[45/90/−45/0]	[90/−45/45/0]
Flutter velocity (m/s)	986	826	916	687

Table 4 Flutter velocities of composite panel at different ply angles with different aspect ratios

Flutter velocity (m/s)	[15/−15/15/−15]	[30/−30/30/−30]	[45/−45/45−45]	[60/−60/60−60]
$\lambda = 1.25$	615	765	859	958
$\lambda = 1.50$	584	721	784	809
$\lambda = 1.75$	569	648	704	749

by frequency coincidence theory. However, flutter characteristics of supersonic low aspect ratio wings can occur with higher circumferential frequencies. Hence, the frequency coincidence should be assured to accurately describe certain higher frequencies for flutter prediction of cantilevered wings using fluid–structure interaction method. Frequency coalescence is calculated based on the coincidence of bending and torsion mode at different flight speeds. The excited frequency coalescence of frequencies for different stacking sequences is discussed in Table 3. Also, the flutter velocity of the composite panel with varied aspect ratios and ply angle was analysed and the results are plotted for discussion in Table 4.

The influence of aspect ratios on supersonic aeroelastic characteristics is investigated, with constant thickness, surface area and unit layer thickness. From the results, it is inferred that the flutter characteristics are highly dependent on the cross-ply angle and the aspect ratio. When aspect ratio is greater than one, the corresponding flutter velocity also increased with ply angle.

5   Conclusion

A two-dimensional plate model of low aspect ratio composite wing is developed for aeroelastic flutter analysis from the extended Hamilton principle. And a solution of flutter analysis is given based on the fluid–structure interaction method. From the study, the effects of aeroelastic characteristics such as cross-ply, aspect ratio and stacking sequence on the supersonic aerodynamic load condition were investigated. The following conclusions can be made from the results obtained:

(a) Fluid–structure interaction method provides a better solution for the flutter and aeroelastic characteristics of low aspect ratio composite wings, in comparison with DQM. Also, the computational time for this analysis is comparatively less in case of two-dimensional models.
(b) Supersonic aeroelastic characteristics of low aspect ratio composite wings can occur with very high circumferential frequencies. This proves that the plate model is better than the beam model in the case of low aspect ratio wings, because in case of beam model the aerodynamic flutter occurs by the coalescence between the bending mode and the torsional mode.
(c) Comparative analysis of flutter characteristics at different aspect ratio, cross-ply and the stacking sequence shows the influence of such parameters over the flutter speed. It is to be noted that the flutter characteristics of the composite laminates vary complicated with the ply angle and aspect ratios.

Since the problem is simplified by CPT into a 2D model, the computational time taken by the commercial software is comparatively less. However, the computational power required to couple the two solvers is more to perform simulations.

References

1. Karpouzian, G., Liberscu, L.: Exact flutter solution of advanced anisotropic composite cantilevered structure. AIAA-93-1535 (1993)
2. Karpouzian, G., Liberscu, L.: Comprehensive model of anisotropic composite aircraft wings suitable for aeroelastic analysis. J. Aircraft. **31**, 703–712 (1994)
3. Giles, G.L.: Equivalent plate analysis of aircraft wingbox structures with general planform geometry. J. Aircraft. **23**, 859–864 (1986)
4. Giles, G.L.: Further generalization of an equivalent plate representation for aircraft structural analysis. J. Aircraft. **26**, 67–74 (1989)
5. Meirovitch, L., Seitz, T.J.: Structural modeling of low-aspect ratio composite wings. AIAA-93-1371 (1995)
6. Shu, C., Richards, B.E.: Application of generalized differential quadrature to solve two dimensional incompressible Navier-Stokes equations. Int. J. Numer. Methods Fluids **15**, 791–798 (1992)
7. Shu, C.: Differential Quadrature and Its Application in Engineering, pp. 206–224. Springer, London (2000)
8. Liu, G.R., Wu, T.Y.: Multipoint boundary value problems by differential quadrature method. J. Math. Comput. Model. **35**, 215–227 (2002)

9. Hua, X.G., Chen, Z.Q., Ni, Y.Q., Ko, J.M.: Flutter analysis of long-span bridges using ANSYS. J. Wind Struct. **10**, 61–82 (2007)
10. Tateishi, A., Watanabe, T., Himeno, T., Inoue, C.: Multimode flutter analysis of transonic fan using FSI simulation. In: Proceedings of ASME Turbo Expo-26702 (2014)
11. Parameshwaran, R., Jathin, S., Rao, D.: Fluid-structure interactions and flow induced vibrations: a review. Proc. Eng. **144**, 1286–1293 (2016)
12. Kamakoti, R., Shyy, W.: Fluid structure interaction studies for aeroelastic application. J. Progress Aerosp. Sci. **40**, 535–558 (2004)
13. Kwon, Y.W., Owens, A.C., Kwon, A.S., Didoszak, J.M.: Experimental study of impact on composite plates with fluid structure interaction. Int. J. Multiphys. **4**, 259–271 (2010)

Experimental Analysis of Surface Roughness of Duplex Stainless Steel in Milling Operation

D. Philip Selvaraj

Abstract Duplex stainless steel materials are widely used in various industrial sectors due to its excellent stress corrosion cracking resistance and higher strength levels. The present work presents the results of experimental investigation carried out in end milling operation of cast nitrogen alloyed duplex stainless steel ASTM A 995 Grade 5A. The end milling operations were carried out with coated carbide cutting tool inserts. The experiments were conducted at three different spindle speeds, three different feed rates, and three different axial depth of cuts. The cutting parameters are optimized using Taguchi method. The effects of cutting speed, feed rate, and depth of cut on the surface roughness were analyzed using mean and analysis of variance. It is found out that the significant variable affecting the surface roughness is the feed rate, then the spindle speed, and the axial depth of cut.

Keywords Duplex stainless steel · End milling · Optimization
Surface roughness · Taguchi method

1 Introduction

Duplex stainless steel materials are widely used in various industrial applications due to its excellent stress corrosion cracking resistance and higher strength levels. The duplex stainless steel (DSS) alloys are used in oil and gas, marine, chemical, petrochemical, pulp and paper, medical, civil construction, process and pollution control industries [1]. Milling is an operation for making curved and flat surfaces by employing multipoint milling cutters. For making slots and surface profiles, end milling cutters are widely used [2]. Surface finish is one of the most important quality characteristics to check the machinability of the work material. Surface finish is influenced by several cutting variables including geometry of the tool and

D. Philip Selvaraj (✉)
Department of Mechanical Engineering, Karunya Institute of Technology
and Sciences (Deemed to-be University), Coimbatore, India
e-mail: de_philip@rediffmail.com

machine tool, material of the tool and workpiece and cutting parameters [3]. Taguchi technique is extensively used in industries for production processes' optimization. Orthogonal array (OA) is employed to study the production process by conducting less number of experiments. By using the Taguchi method, the experimental cost and time are reduced and profit increased. Taguchi technique is used for cutting parameters optimization and to find optimum cutting conditions for achieving the required output parameters [4–7]. Zhang et al. optimized surface roughness in a CNC face milling operation of aluminum alloy by using Taguchi technique. They considered feed, spindle speed, and depth as input parameters. They reported that the influences of cutting speed and feed on surface quality were greater than depth for the milling process. They also found that the tool wear influence on the surface quality was statistically significant [8]. Lin developed an optimization method for milling operation of stainless steel using Taguchi technique. The cutting parameters were optimized with consideration of metal removal rate and height of burr. They reported that spindle speed has most significant, and feed has insignificant effect on removed volume. The contribution order for burr height was cutting speed followed by feed and depth [9]. Bagci and Aykut used Taguchi technique for optimizing surface roughness during the milling operation of the stellite 6. They indicated that surface finish was significantly affected by spindle speed, feed, and depth. The optimum surface finish was obtained at low level of depth of cut and feed rate and high level of spindle speed [10]. Tsao applied the gray Taguchi technique to optimize the cutting parameters of aluminum alloy. He reported that the optimal cutting parameters reduced the flank wear and the surface roughness [11]. Ghani et al. used Taguchi technique to optimize machining parameters in end milling operation when machining AISI H13 steel using coated carbide tool insert. They reported that the optimal machining conditions for obtaining lower cutting force and better surface quality were higher spindle speed, lower feed, and lower axial depth [12]. Sai et al. conducted investigations of carbon steels and DSS alloy in milling operation. They were chosen lower feed rate and higher spindle speed for improving surface quality. The effect of depth of cut was not significant on the surface quality. Formation of built-up edge was the reason for poor surface quality at lower spindle speed [13]. Selvaraj et al. used Taguchi technique for optimize the cutting parameters during the milling process of DSS alloy. The cutting variables considered were spindle speed and feed rate [14]. Xavior et al. applied Taguchi method to optimize surface roughness and tool wear of AISI 304 stainless steel using carbide tool in wet turning operation. Coconut oil was found to be a better cutting fluid than the conventional mineral oils in reducing the tool wear and surface roughness. They conducted wet turning operation using different types of cutting fluids [15]. Selvaraj et al. optimized the cutting force, surface finish, and tool wear of DSSs in turning process. They suggested higher level of cutting velocity and lower level of feed for minimizing surface roughness and cutting force. The two input factors used were cutting velocity and feed rate. They used Taguchi's signal to noise ratio method for optimization [16]. Karunya et al. optimized the surface finish of AISI 304 austenitic stainless steel (ASS) in turning process. They reported that the cutting speed, the feed, and depth are

affecting the surface finish by about 81, 10, and 5%, respectively. They used Taguchi's signal to noise ratio method for optimization [17]. From the literature cited above, it is confirmed that very less works have been reported in milling operation of duplex stainless steels. Hence, in the current work an effort has been taken to find out the optimum cutting parameters to minimize the surface roughness during dry milling operation of 5A grade DSS using Taguchi's average of results methodology.

2   Experimental Work

The material selected for this investigation is DSS ASTM A 995 grade 5A with the compositions as shown in Table 1.

   The milling experiments are carried out in a HMT column and knee-type milling machine. The workpiece used is a rectangular block of 120 mm × 100 mm 30 mm. The diameter of the end mill cutter used in this experiment is 20 mm. Milling tool inserts used are tungsten carbide inserts coated with TiCN. The end mill cutter and the milling tool insert are shown in Figs. 1 and 2, respectively. The surface roughness is measured using TR-100 surface roughness tester. The surface roughness is measured using piezo-electric stylus. The measurements were taken at three different places of the machined surfaces and the average was calculated.

   The cutting parameters considered for milling operation are spindle speed, feed, and axial depth. The quality characteristic identified is surface roughness. Taguchi's OA is used to design the experimental plan. Three factors and three-level experiments are carried out based on L_9 OA. The milling tests are carried out at three different spindle speeds (500, 710, and 1000 rpm), three different feed rates (40, 100, and 160 mm/min), and three different axial depth of cuts (0.4, 0.8, and 1.2 mm).

Table 1   Chemical composition of ASTM A 995 grade 5A DSS (wt%)

C	Si	Mn	S	P	Cr	Ni	Mo	N	Fe
0.028	0.67	0.87	0.005	0.028	25.10	6.63	4.16	0.26	Bal

Fig. 1   End mill cutter
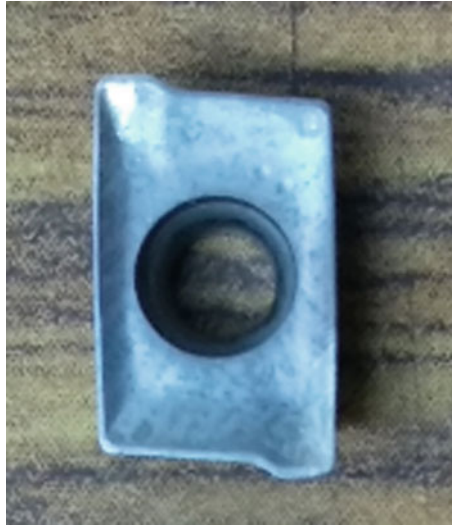
Fig. 2 Milling insert

Table 2 Cutting parameters and their levels for milling studies

Symbol	Cutting parameters	Level 1	Level 2	Level 3
N	Spindle speed (rpm)	500	710	1000
f	Feed rate (mm/min)	40	100	160
d	Axial depth of cut (mm)	0.4	0.8	1.2

The levels of cutting parameters for milling studies are indicated in Table 2. The experimental layout using L_9 OA for milling studies is given in Table 3.

3   Results and Discussion

3.1   *Effect of Machining Parameters*

The results of the experiments for surface finish during dry milling operation of 5A grade DSS are given in Table 4. In the current work, Taguchi analysis is conducted using means. Qualitek-4 software is used for analyzing the experimental results.

The overall mean or average surface roughness (*m*) is determined by using Eq. (1).

Table 3 Experimental layout using L₉ OA for milling studies

Experimental number	Cutting parameter level		
	N	f	d
1	1	1	1
2	1	2	2
3	1	3	3
4	2	1	2
5	2	2	3
6	2	3	1
7	3	1	3
8	3	2	1
9	3	3	2

Table 4 Experimental results for surface roughness of 5A grade DSS

Exp. No.	Parameter level			R_a (µm)
	N	f	d	
1	1	1	1	0.80
2	1	2	2	1.25
3	1	3	3	1.71
4	2	1	2	0.86
5	2	2	3	1.14
6	2	3	1	1.19
7	3	1	3	0.76
8	3	2	1	0.79
9	3	3	2	1.07

$$m = \frac{1}{n} \sum_{i=1}^{n} S_i$$
$$= 1.0633 \text{ µm}$$

(1)

where n is the number of tests, and S_i is the values of the surface roughness for the ith test.

The main effect of spindle speed, N at first level (i.e., = 500 rpm), on surface roughness is determined by using Eq. (2).

$$\text{Mean surface roughness for } N \text{ at first level} = \frac{S1 + S2 + S3}{3}$$
$$= 1.253 \text{ µm}$$

(2)

The main effects and their variations among levels associated with the surface finish of 5A grade DSS during dry milling operation are given in Table 5.

Table 5 Main effects and their differences on the surface roughness

Factors	Level 1 (L_1)	Level 2 (L_2)	Level 3 (L_3)	Difference between levels		
				$L_2 - L_1$	$L_3 - L_1$	$L_3 - L_2$
N (rpm)	1.253	1.063	0.873	−0.190	−0.380	−0.190
f (mm/min)	0.806	1.059	1.323	0.252	0.516	0.264
d (mm)	0.926	1.060	1.203	0.134	0.277	0.143

During dry milling operation, the change of spindle speed from 500 to 710 rpm decreases the surface roughness main effects mean value from 1.253 to 1.063 μm. The increase of spindle speed from 710 to 1000 rpm decreases the surface roughness main effects mean value from 1.063 to 0.873 μm. At higher spindle speed, the heat generation is increased so the material becomes soft at the sheer zone. Hence, lower cutting force is required for machining operation which decreases the surface roughness. At higher spindle speed, the cutting forces decreased due to the reduction of chip thickness which results lower surface roughness [18]. The increase of feed rate from 40 to 100 mm/min increases the surface roughness main effects mean value from 0.806 to 1.059 μm. The increase of feed rate from 100 to 160 mm/min increases the surface roughness main effects mean value from 1.059 to 1.323 μm. The increase of depth of cut from 0.4 to 0.8 mm increases the surface roughness main effects mean value from 0.926 to 1.060 μm. The increase of depth of cut from 0.8 to 1.2 mm increases the surface roughness main effects mean value from 1.060 to 1.203 μm. At lower feed and depth, the volume of material removed is decreased so the lower cutting force is required for machining operation which decreases the surface roughness. At lower feed and depth, the contact area between work and tool is decreased which reduces the cutting force; hence, surface finish is improved. The main effects and their variation among levels of the cutting variables on the surface finish of 5A grade DSS during dry milling operation is shown in Fig. 3. The feed rate line slope is larger compared with the spindle speed line slope and depth of cut line slope. Hence, the feed rate is the most significant cutting parameter for surface roughness followed by the spindle speed and the depth of cut. The lowest main effect for surface roughness is attained at spindle speed level 3, feed rate level 1, and depth of cut level 1. Therefore, the optimal milling parameters for surface quality are the level 3 cutting speed (1000 rpm), the level 1 feed (40 mm/min), and level 1 axial depth (0.4 mm).

3.2 Analysis of Variance

The ANOVA is carried out to find out the input parameters that affect the response significantly. The grant total sum of the squares, sum of squares due to mean and
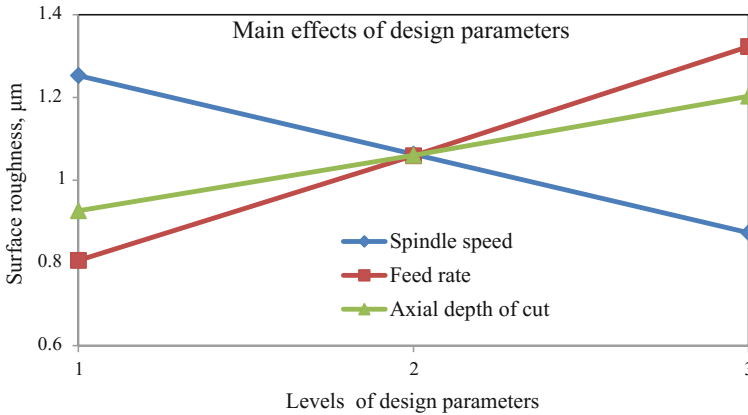
Fig. 3 Main effects of the design parameters on surface roughness of 5A grade DSS during dry milling operation

the total sum of squares can be calculated by using the following equations discussed by Xavior et al. [15].

$$\text{Grand total sum of squares} = \sum_{i=1}^{n} (S_i)^2$$

$$\text{Sum of squares due to mean} = n \times m^2 \tag{4}$$

$$\text{The total sum of the squares (SST)} = \text{grand total sum of squares} \\ - \text{sum of squares due to mean} \tag{5}$$

The SS_T contains two sources. They are sum of the squares (SS_d) due to each design parameter and the sum of the squares due to error (SS_e). The sum of squares due to design parameter spindle speed is calculated by using Eq. (6) discussed by Xavior et al. [15].

$$\text{Sum of squares due to spindle speed} = 3\left[(A1 - m)^2 + (A2 - m)^2 + (A3 - m)^2\right] \tag{6}$$

where $A1$, $A2$, and $A3$ are the mean surface roughness values at first, second, and third levels of spindle speeds, respectively.

Similarly, sum of squares due to other two factors feed and depth are also calculated. The variance, F-ratio, and percentage of contribution are calculated by using the following equations.

Table 6 ANOVA results for surface roughness of DSS during dry milling operation

Cutting parameter	DOF	Sum of squares (S)	Variance (V)	F-Ratio (F)	Pure sum of squares (S')	Percentage contribution (%)
N	2	0.216	0.108	10.582	0.196	26.07
f	2	0.400	0.200	19.565	0.379	50.50
d	2	0.114	0.057	5.612	0.094	12.55
Error	2	0.022	0.011			10.88
Total	8	0.752				100

$$\text{Mean squares or Variance}(V) = \frac{\text{Sum of squares due to each factor}}{\text{Degrees of freedom for each factor}} \quad (7)$$

$$F \text{ ratio} = \frac{\text{Mean squares due to the factor}}{\text{Mean squares due to error}} \quad (8)$$

$$\text{Percentage contribution} = \frac{\text{Sum of squares for each factor}}{\text{Total sum of squares}} \times 100 \quad (9)$$

The results of the ANOVA for the surface roughness of 5A grade DSS in dry milling operation are given in Table 6. The confidence level of ANOVA is 95%. It is observed that the feed is the most important milling parameter influencing the surface quality in dry milling operation of 5A grade DSS. The order of significance of the milling parameters affecting the surface quality is feed, spindle speed, and depth. ANOVA table shows that the feed rate, spindle speed, and depth affect the surface quality by about 51, 26, and 13%, respectively.

3.3   Optimum Machining Conditions

Table 7 gives the optimum machining conditions for achieving lowest surface roughness for 5A grade DSS during dry milling operation. It reveals that for optimal surface roughness, the spindle speed should be at level 3, the feed should be at level 1, and the depth should be at level 1. The total contribution from the three input parameters is −0.585. It provides the improvement obtained in the expected response from the parameters. The grand mean of predicted response is 1.063 μm. It is the overall mean of all experiments. The value of surface roughness predicted at optimum condition is 0.48 μm. Confirmation test is carried out at optimum machining condition. The experimental value of surface roughness at this condition is 0.52 μm. The predicted surface roughness at optimum machining condition is compared with experimental surface roughness obtained from confirmation test and the error is about 8%. Optimum levels of machining parameters ensured significant reduction in the surface roughness.

Table 7 Optimum condition for minimum surface roughness for 5A grade DSS

Factor	Level description	Level	Contribution
N	1000	3	−0.191
f	40	1	−0.257
d	0.4	1	−0.137

4 Conclusions

The Taguchi technique is implemented to identify the optimal milling conditions and minimize the surface roughness of 5A grade DSS during dry milling operation.

- Surface roughness is decreased with increase in spindle speed and it is increased with increase in feed rate and axial depth of cut.
- 1000 rpm spindle speed, 40 mm/min feed rate and of 0.4 mm axial depth of cut are found to give the lowest surface roughness during dry milling operation.
- ANOVA results indicate that for dry milling of DSS, the feed, the spindle speed, and the axial depth are affecting the surface finish by about 50, 26, and 12%, respectively.
- The predicted surface roughness at optimum machining condition is compared with experimental surface roughness obtained from confirmation test and the error is about 8%.
- Optimum levels of machining parameters ensured significant reduction in the surface roughness.

References

1. Davis, J.R.: ASM Specialty Handbook Stainless Steels. ASM International, Ohio (1996)
2. Shaw, M.C.: Metal Cutting Principles. Oxford University Press, New York (2005)
3. Juneja, B.L., Sekhon, G.S., Seth, N.: Fundamentals of Metal Cutting and Machine Tools, New Age International Publishers, New Delhi (2003)
4. Taguchi, G., El Sayed, M., Hashing, T.C.: Quality Engineering and Quality Systems. McGraw Hill, New York (1989)
5. Ross, J.: Taguchi Technique for Quality Engineering. McGraw Hill, New York (1993)
6. Phadke, M.K.: Quality Engineering Using Robust Design. Prentice-Hall, New Jersey (1989)
7. Roy, K.R.: A Primer on Taguchi Method. Van Nostrad Reinhold, New York (1990)
8. Zhang, J.Z., Chen, J.C., Kirby, E.D.: Surface roughness optimization in an end-milling operation using the Taguchi design method. J. Mater. Process. Technol. **184**, 233–239 (2007)
9. Lin, T.R.: Optimization technique for face milling stainless steel with multiple performance characteristics. Int. J. Adv. Manuf. Technol. **19**, 330–335 (2002)
10. Bagci, S.E., Aykut, E.: A study of Taguchi optimization method for identifying optimum surface roughness in CNC face milling of cobalt-based alloy (stellite 6). Int. J. Adv. Manuf. Technol. **29**, 940–947 (2006)

11. Tsao, C.C.: Grey-Taguchi method to optimize the milling parameters of aluminum alloy. Int. J. Adv. Manuf. Technol. **40**, 41–48 (2009)
12. Ghani, J., Chodhury, I.A., Hassan, H.H.: Application of Taguchi method in the optimization of end milling parameters. J. Mater. Process. Technol. **145**, 84–92 (2004)
13. Sai, W.B., Salah, N.B., Lebrun, J.L.: Influence of machining by finishing milling on surface characteristics. Int. J. Mach. Tools Manuf. **411**, 443–450 (2001)
14. Philip Selvaraj, D., Chandramohan, P., Mohanraj, M., Rajesh, P.K.: Experimental investigations on surface roughness, cutting force and tool wear of duplex stainless steel in end milling using Taguchi method. Int. Review Mech. Eng. **7**, 1133–1141 (2013)
15. Anthony Xavior, M., Adithan, M.: Determining the influence of cutting fluids on tool wear and surface roughness during turning of AISI 304 austenitic stainless steel. J. Mater. Process. Technol. **209**, 900–909 (2009)
16. Philip Selvaraj, D., Chandramohan, P., Mohanraj, M.: Optimization of surface roughness, cutting force and tool wear of nitrogen alloyed duplex stainless steel in a dry turning process using Taguchi method. Measurement **49**, 205–215 (2014)
17. Karunya, G., Ravikumar, P., Geeta Krishna, P., Shiva Krishna, P.: Optimization of the surface roughness by applying the Taguchi technique for the turning of AISI 304 austenitic stainless steel. Int. J. Mech. Eng. Technol. **8**, 694–701 (2017)
18. Thakur, G., Ramamoorthy, D.B., Vijayaraghavan, L.: Study on the machinability characteristics of super alloy Inconel 718 during high speed turning. Mater. Des. **30**, 1718–1725 (2009)

Optimization of Machining Parameters of Inconel 718 by WEDM Using Response Surface Methodology

S. Senkathir, R. Aravind, R. Manoj Samson and A. C. Arun Raj

Abstract WEDM is considered to be a unique form of the traditional EDM process, where an electrode is used to start the ignition process. Here, the material is dissolved before of the wire and there is no straight contact between the working component and the tool(wire), removing the mechanical tension during machining. The main outcome from this work is to find out the effects which different machining parameters have on the machining standards of Inconel 718 and to acquire the optimum sets of machining parameters so that the standard of working components can be optimized. The response surface methodology is applied here to learn about the impact of the WEDM process parameters and also to get sets of optimal parameters for optimum output attributes. The effect of the parameters are to be studied, viz. peak current (Amps), pulse time on (μs) and feed (m/s) on the responses, viz. machining time, surface roughness, material removal rate. Molybdenum has high strength at elevated temperatures making it suitable in furnace, aerospace and similar applications, and hence, molybdenum wire is used here as cutting tool. Series of experiments were conducted by machining INCONEL 718 blocks using molybdenum wire under different parameters of input current, pulse on time and feed rate got from response surface method table. By plotting the results got from material removal rate (MRR), circularity and surface roughness of these experiments, the results for optimum parameters to be applied which are needed to get minimum machining time, circularity error and surface roughness could be achieved.

S. Senkathir · R. Manoj Samson · A. C. Arun Raj
Department of Mechanical Engineering, SRM University, Kattankulathur,
Chennai 603203, India
e-mail: senkathir.s@ktr.srmuniv.ac.in

R. Manoj Samson
e-mail: manojsamson.r@ktr.srmuniv.ac.in

A. C. Arun Raj
e-mail: arunraj.c@ktr.srmuniv.ac.in

R. Aravind (✉)
Design & Development Department, Gedee Weiler Pvt. Ltd, Coimbatore, India
e-mail: aravindravindran9@gmail.com

1 Introduction

Inconel and its alloys are used extensively in industries due to high strength and thermal resistance, and due to its excellent mechanical properties at low and intermediate temperatures (−250 to 700 °C), it plays an excellent role in recent times in petroleum, aerospace and nuclear energy industries. Likewise, refractory metals and alloys like molybdenum are extremely heat resistant and have different physical characteristics. Because of these properties, molybdenum is excellent in many elevated temperature applications where high melting points are required. Molybdenum has good strength at high temperatures making it suitable in furnace, aerospace and similar applications. The paper by Dhanabalan [1] shows the observations and inferences on electrical discharge machining (EDM) of Inconel 718 using copper electrodes. Hence, molybdenum having more strength than copper at higher temperatures can be used as the tool in these series of experiments. Thomas Newton [2] experiments to find the main EDM parameters which contribute to the formation of recast layer in Inconel 718 alloy show that average recast layer thickness increased primarily with energy per spark, peak discharge current and current pulse duration. This recast layer formed decreases the strength of the alloy, and hence, the recast layer must be kept in check during these series of experiments. Satyanarayana [3] paper on multi-response optimization of CNC WEDM process for machining Inconel 718 using Taguchi Grey relational analysis investigates the effects which various machining parameters have on the machining standards of Inconel 718 and to get the optimum sets of machining parameters which optimizes that the standard of working components. But these papers have not investigated the effects Inconel 718 alloy had when machined with molybdenum wire which is stronger than the other relative tools used. As per the principle of WEDM, the stronger the metal, the easier it will be to machine. Hence, it was decided to study the Effects of Molybdenum wire on Inconel 718 alloy. The working range of process parameters and their levels is found using one factor at a time approach. The effects of the WEDM process parameters are studied using response surface methodology. Optimal parameters for optimum output characteristics are predicted using this method. For multi-response optimization, the response surface methodology has been very useful. Confirmation experiments are done further to validate the result.

2 Experimental Work

The experiment is carried out by taking optimal parameter values, which were obtained by conducting experiments on INCONEL 718 of dimensions 120 mm 80 mm × 10 mm as workpiece using molybdenum electrode wire of 5 m length for 20 experiments. Basically, machining time, material removal rate, surface roughness are strongly correlated with machining parameters such as peak current, pulse on time and feed. These three input parameters are selected out of the working parameters of WEDM such as pulse time on, off time, gap, input current and feed time as MRR is directly proportional to the amount of energy exerted during pulse on time which is given by input current and pulse on time. Maximum wire feed gives less wire breakage, better machining stability and slightly more cutting speed [4]. Hence, optimized values of machining parameters based on the response surface method are adopted in this work to improve the machining time, material removal rate, surface roughness of EDM process (Table 1).

Machining has been carried out on an EDM machine for INCONEL plate using the molybdenum wire. The timing is calculated for each of 20 experiments. Machining time is taken to determine the material removal rate.

Table 1 Experimental layout using response surface method

Ton	Ip	Feed	Run order	Ton (μs)	Ip (A)	Feed (mm/s)
1	1	1	1	26.1	2.7	86.8
0	0	−1.682	2	17.5	2.5	35
−1.682	0	0	3	3	2.5	67.5
1	−1	−1	4	26.1	2.2	48.1
−1	−1	−1	5	8.8	2.2	48.1
0	0	0	6	17.5	2.5	67.5
0	1.682	0	7	17.5	3	67.5
0	0	0	8	17.5	2.5	67.5
0	0	0	9	17.5	2.5	67.5
−1	1	−1	10	8.8	2.7	48.1
−1	−1	1	11	8.8	2.2	86.1
1.682	0	0	12	32	2.5	67.5
1	−1	1	13	26.1	2.8	86.8
1	1	−1	14	26.1	2.7	48.17
0	0	0	15	17.1	2.5	67.5
0	0	0	16	17.5	2.5	67.5
0	−1.682	0	17	17.5	2	67.5
0	0	1.682	18	17.5	2.5	100
−1	1	1	19	8.1	2.7	86.8
0	0	0	20	17.5	2.5	67.5

Fig. 1 Cubical machined
sample
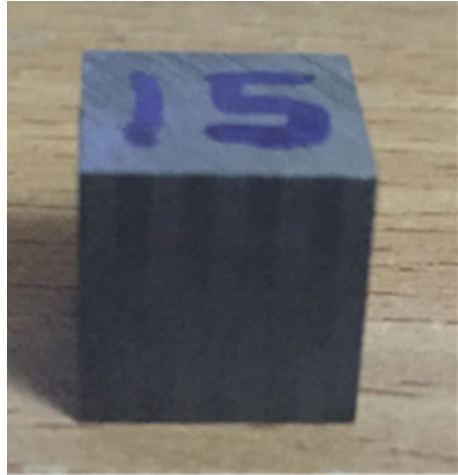
Fig. 2 Cylindrical sample

Material removal rate = Volume removed/Time taken mm^3/s. Totally, 20
experiments are done on each workpiece. In one workpiece, 20 cubical holes of
dimension 10 mm are cut in order to calculate the surface roughness using Talysurf
instrument and 20 cylindrical holes of 10 mm diameter are cut in another workpiece
to calculate the circularity or roundness using coordinate measuring machine into
samples as shown in Figs. 1 and 2.

3 Results and Discussion

3.1 Machining Measurement

3.1.1 Determination of MRR from Experimental Layout

See Table 2.

3.1.2 Plots of MRR

From the experimental values of Volume *V*, the value of MRR is calculated and the graphs are plotted as shown in Figs. 3 and 4. From these graphs, the optimization plot for MRR is calculated.

From these graphs, we can calculate the optimization plot of MRR as shown in Fig. 5.

Table 2 Determination of process parameters

| S. No.	Ton (μs)	Ip (A)	Feed (mm/s)	Volume (mm³)	MRR 10^{-4} (mm³/s)	Circularity (μm)	*Ra* (μm)
1	26	3	87	0.101	8.34	0.051	2.461
2	18	3	35	0.057	4.71	0.038	2.108
3	3	3	68	0.046	3.8	0.122	3.499
4	26	2	48	0.051	4.23	0.066	2.78
5	9	2	48	0.045	3.75	0.079	1.088
6	18	2	68	0.06	4.98	0.051	1.262
7	17	3	67	0.083	6.86	0.068	1.992
8	17	2	68	0.059	4.89	0.033	1.247
9	18	3	67	0.079	6.53	0.066	2.085
10	9	3	48	0.063	5.17	0.1	1.116
11	9	2	87	0.058	4.82	0.111	1.954
12	32	3	68	0.092	7.6	0.061	1.904
13	26	2	87	0.076	6.29	0.037	2.444
14	26	3	48	0.068	5.65	0.028	1.822
15	17	3	67	0.079	6.49	0.046	1.335
16	17	2	68	0.059	4.84	0.064	1.717
17	18	3	68	0.098	8.05	0.037	1.598
18	18	3	100	0.082	6.76	0.77	2.22
19	9	3	87	0.081	6.65	0.065	1.705
20	17	3	68	0.083	6.87	0.036	4.978
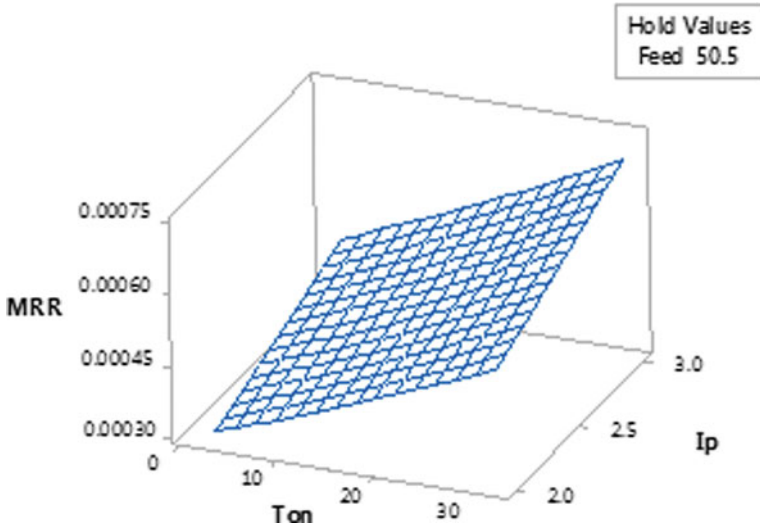
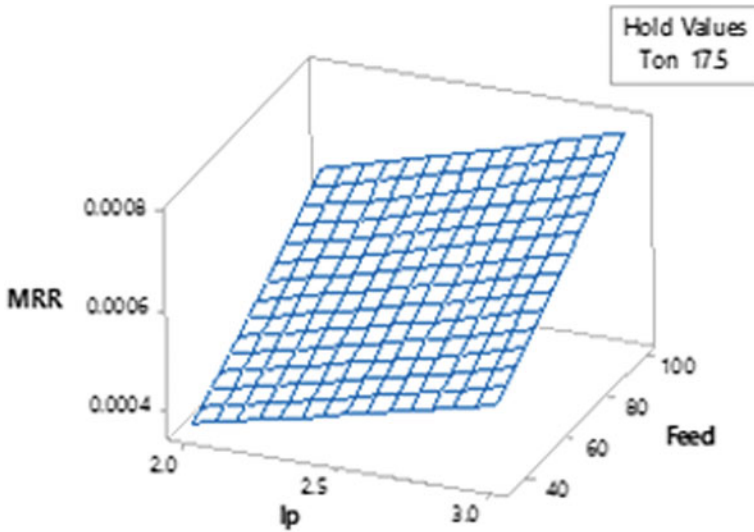**Fig. 3** Surface plot of MRR versus Ip, Ton
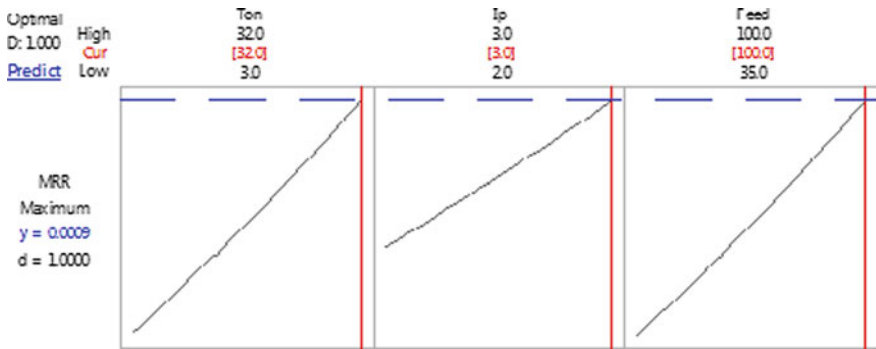

Fig. 4 Surface plot of MRR versus feed, Ip

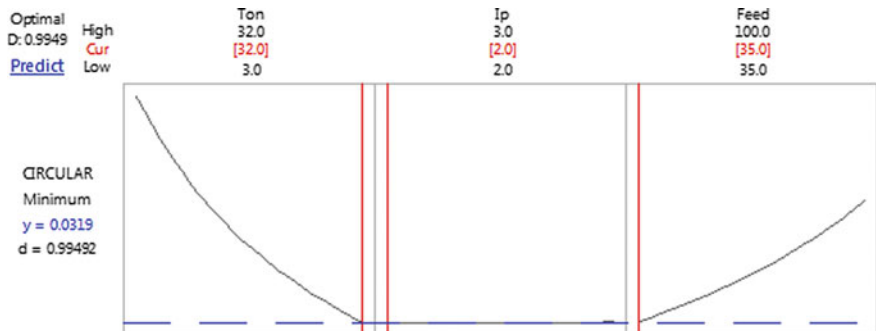**Fig. 5** Optimization plot of MRR

Fig. 6 Optimization plot of circularity

3.2 Measuring Circularity Using CMM

3.2.1 Circularity Measurement

From the given results got from CMM graphs, Table 2 is tabulated with the actual value as the roundness or circularity value. Then, the graphs are plotted using the given roundness value and the parameters. It can be seen from the surface plots that the circularity error increases with increased feed rate and decreasing pulse time [5]. Similarly, circularity error increases with increased feed rate and does not change with input current. From these graphs, we can plot the optimization plot for circularity as shown in Fig. 6.

Fig. 7 Optimization plot of *Ra* (surface roughness)

3.3 Surface Roughness Measurement

3.3.1 Measuring Surface Roughness

From the average *Ra* values got from the Talysurf instrument, the tabulation is done. The tabulation is complete with these *Ra* values and the graphs can be plotted using these values from Table 2. From these values, we can plot and it can be seen from the plots that the *Ra* value increases with increases with increase in input current and pulse time [6]. Similarly, the *Ra* value increases with increase in feed rate. Hence using the surface plot graphs, we can optimize the plot from that graphs as shown in Fig. 7.

From these graphs, we can plot the optimization plot for MRR, circularity and surface roughness, and hence, we could find the entire optimization of the parameters as shown in Fig. 8.

4 Conclusions

- Machining time can be reduced by increasing the input current, pulse time on and feed.
- Circularity is very less and surface roughness could be reduced when pulse time on is increased and the feed and input current are maintained at minimum value.
- Machining time and circularity error can be reduced when the pulse time on and input current is kept at maximum and the feed is kept around 78 mm/s.
- Machining time, circularity error and surface roughness can be reduced when pulse time on is 32 μs, peak input current is 2.6 A, and feed rate is around 92.77 mm/s.
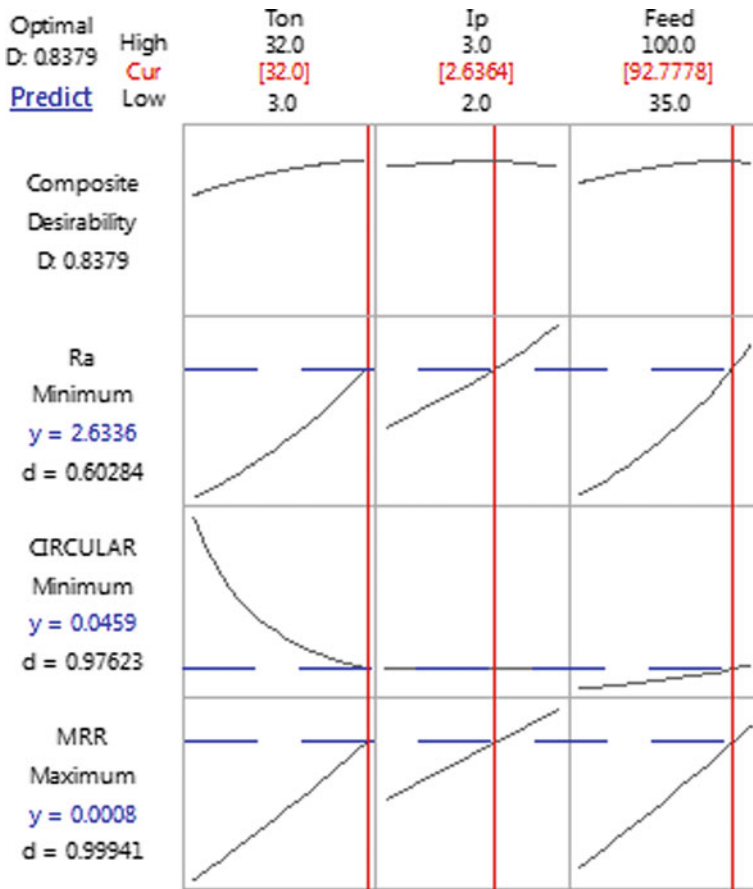
Fig. 8 Optimization plot of MRR, circularity and *Ra*

References

1. Dhanabalan, S., Sivakumar, K., Sathiya Narayanan, C.: Optimization of Machining Parameters in EDM of Inconel 718 for Form Tolerance Using Grey Relational Analysis. IJEMS **20**(5) (October 2013)
2. Newton, T.R., Melkote, S.N.: Investigation of the effect of process parameters on the formation and characteristics of recast layer in wire-EDM of Inconel 718. Materials Science and

Engineering A-structural Materials Properties Microstructure and Processing—Mater Sci Eng A-Struct Mater **513**, 208–215 (2009)

3. Satyanarayana, B., Srikar, G.: Multiresponse optimisation of CNC WEDM process for machining Inconel 718 using Taguchi Grey relational analysis. Int. J. Mech. Prod. Eng. (IJMPE) **2**(10) (Oct 2014). IJMPE—IRAJ

4. Garg, R.: Effect of process parameters on performance measures of wire cut electrical discharge machining. Ph.D. thesis, National Institute of Technology, Kurukshetra (May 2010)

5. Maiyar, L.M., Ramanujam, R.: Optimization of machining parameters for end milling of Inconel 718 super alloy using Taguchi based Grey relational analysis. Proc. Eng. **64**, 1276–1282 (2013)

6. Li, L., Guo, Y.B.: Surface Integrity characterstics in Wire–EDM of Inconel 718 at different discharge energy. Proc CIRP **6**, 220–225 (2013)

Analysis and Evaluation of Different Heat Treatment Fixture Designs Inspired from 3D Infill Patterns

P Sasikiran and J Nagarjun

Abstract The heat treatment fixture is a work holding device used to secure the workpiece during heat treatment. Those fixtures fail prematurely due to high thermal and fatigue loads. Thus, alternative fixture design is required in order to improve the life of the fixture. In this paper, the alternative designs that are analysed are inspired from 3D infill patterns. The infill patterns considered and evaluated for the fixture design are honeycomb structure, diamond structure and concentric circular structure. The patterns are modelled with the help of solid works with constant mass and diameter. It is further analysed with coupled thermal structural analysis, factor of safety and fatigue life with the help of ANSYS workbench 18.0 and the best-suited design for the fixture is evaluated.

Keywords Heat treatment fixture · 3D printing patterns · Coupled thermal structural analysis · Factor of safety · Fatigue life · Solid works ANSYS

1 Introduction

Heat treatment is a discipline of materials and measurement which deals with the change in physical properties of materials when heated above the re-crystallization temperature [1]. The paper deals with the heat treatment fixture made of steel 1010 which supports the suspended grey cast iron jobs subjected to normalizing. A heat treatment fixture is a work holding device used to securely locate and support the position of a workpiece during the heat treatment process. The fixture analysed in this paper is used specifically for normalizing heat treatment process. Normalizing

P. Sasikiran (✉) · J. Nagarjun
Department of Mechanical Engineer, PSG Institute of Technology
and Applied Research, Coimbatore, India
e-mail: umasasikiran@psgitech.ac.in

J. Nagarjun
e-mail: nagarjun@psgitech.ac.in

is one of the predominant heat treatment processes used to decrease the internal stresses and refine the grain structure which increases the ductility and toughness. The temperature commonly used for normalizing is around 1173 K since the recrystallization temperature is above 1073 K. Grey cast iron is one of the important materials used in automobiles and aerospace industries for its low cost and easy manufacturability [2]. The heat treatment fixture, when analysed the working stress, is lesser than the yield strength, and the failure takes place due to fatigue. Fatigue is weakening of the material when it is subjected to repeated loads. Fatigue strength of an object decreases due to grain size, geometry and type of loading [3–6]. Thus, the heat treatment fixtures are replaced frequently which leads to high production cost. Hence, there is a need for finding alternative design which will perform for longer duration. This paper will focus on the alternative design analysis and evaluation which are inspired from the infill patterns of 3D printing [7, 8]. The major constraint of design deals with the dimensions of the pit furnace and weight of the fixture. The alternative designs are designed with equal mass and same fixture diameter. The designs are analysed using finite element analysis (FEA) because it is difficult to use sensors in this kind of application where the temperature can reach as high as 1200 K [9, 10]. The paper initially analyses fatigue life of the current working model (circular design) using FEA, and then it compares with the actual average life of the heat treatment fixture. Then if the accuracy of the FEA is satisfactory, then it is further used for analysing the 3D infill patterns. This paper compares three different standard 3D infill patterns based on its von Mises stress, deformation, factor of safety and fatigue life [11]. Weifang Chen analysed the fixture layout design to optimize the deformation due to clamping force. But analysing heat treatment fixture is uncommon, and further, there is no research on design of heat treatment fixture that is influenced by 3D infill pattern and analysis of the same. Hence, this paper focuses on design and analysis of heat treatment fixture inspired from 3D infill patterns in order to obtain higher life.

2 Design Methodology

The height and diameter of the furnace are 1800 and 700 mm, respectively. The fixture is to be placed in the bath of height 1400 mm and the diameter 650 mm, respectively. The minimum clearance to be maintained between the bath and outer diameter of the fixture is 60 mm. Figure 4a shows that the workpiece in the fixture is suspended away from the central axis of support, and this makes the fixture to act like a cantilever. The loading material for heat treatment is initially moulded with the help of shell moulding, and these parts are tied up in mild steel wires and then hung on the fixture. The fixture designs were modelled using solid works, and it was further imported, meshed and analysed in ANSYS. The concentric circular fixture was meshed into 196,082 elements which were shown in Fig. 1a. And each fixture has 24 points in order to suspend workpieces, and each point is subjected to a load of 70 N which has been shown in Fig. 1b.
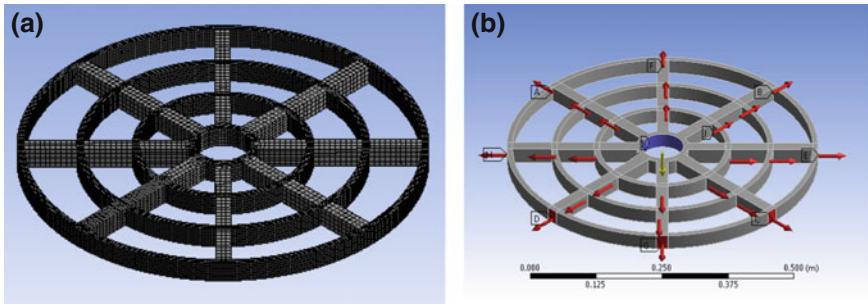
Fig. 1   **a** Meshed concentric circular pattern, **b** forces acting on the fixture

(a) Circular fixture with suspended
grey cast iron rocker arm

(b) Circular fixture just after
Heat-treatment

Fig. 2   Fixture at work in Indo Shell Cast Company

This heat treatment process is carried out in a pit furnace, where the cast iron is heated to 1173 K. Figure 2b shows the fixture and workpiece at red-hot condition during the heat treatment process. Then the fixture containing the cast iron products is taken out and hung on a rotating shaft which has a prime mover whose rated rpm is 400 rpm. The cooling method used here is blast hair cooling with the help of fans. The fixture is used for heating and cooling alternatively; hence, it is subjected to fatigue. During the process, the fixture is made to rotate at the speed of 400 rpm along with the suspended workpieces due to which the centrifugal force acts on the

fixture. The thermal load along with static structural load is also applied, and analysis is carried out for the fixture. It is carried out using ANSYS software which is widely used finite element analysis (FEA) software package. The FEA is a kind of numerical method for solving complex problems of engineering with complicated geometries, different loadings and various material properties where analytical solutions are very difficult to obtain. Thus, the ANSYS is used for the finding the minimum number of revolution that could be attained by the fixture which is 278,220 cycles. The average life of the existing fixture as per the company records is 247,500 cycles. And it is found that the difference between the actual value and ANSYS analysed value is 30,720 cycles which is equal to 12.41%. Thus, the computation method is found effective in the analysis of the fixture.

3 Results and Discussion

3.1 Coupled Thermal Structural Analysis

The existing model fails in shorter duration due to adverse working conditions. In order to increase the life of the fixture, different designs of the fixture are considered. The alternative designs are based upon the patterns of 3D printing. The patterns are analysed for its strength, deformation, factor of safety and fatigue life.

3.2 Equivalent Stress Analysis

The fixture subjected to heat treatment is affected by both thermal and static stress. A design may commonly fail at the critical position where it is subjugated to maximum stress. Figure 3 shows the difference between the total stress that acting on concentric circle pattern is 26.8% lesser than diamond pattern and 17.23% lesser than honeycomb pattern.

3.3 Deformation Analysis

Figure 4 indicates the amount of deformation experienced by the different patterns. Since the bending strength of the design is indirectly proportional to the bending strength of the material, the result indicates that circular pattern experiences the lesser deformation in comparison with the honeycomb and diamond pattern considered.
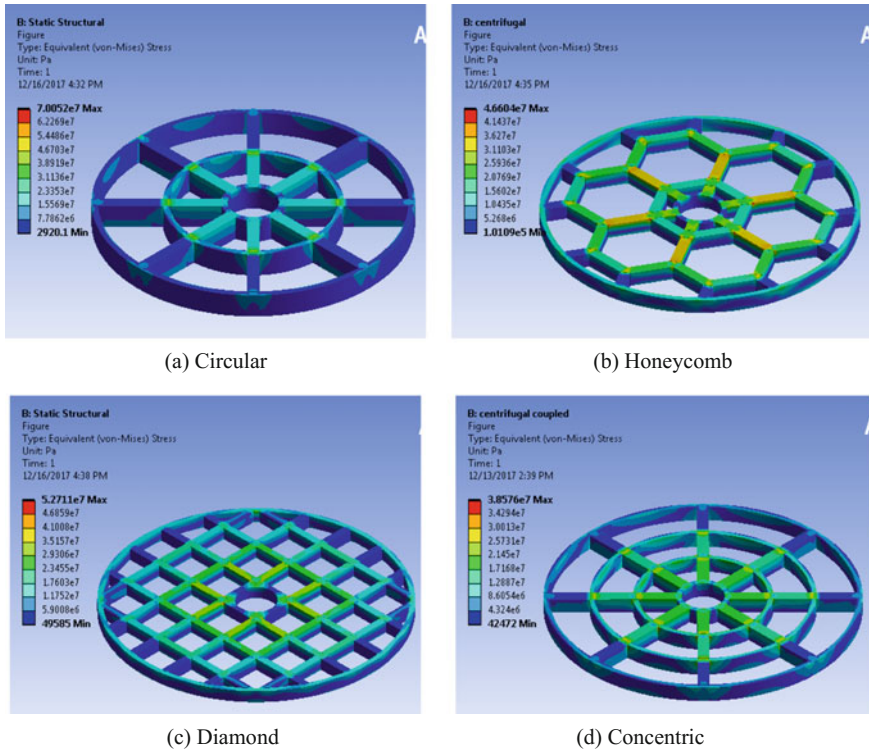
(a) Circular

(b) Honeycomb

(c) Diamond

(d) Concentric

Fig. 3 Equivalent von Mises stress for various designs

3.4 Safety Factor Evaluation

Safety factor is the ratio between yield strength and the maximum stress acting over the material. Hence, it can be used to evaluate the reliability of the design. From Fig. 5, it is further evidence that the circular design is more safe, the safety factor of 7.90 which is 81% more safe compared to the existing design, and also 21 and 37% more safe than honeycomb and diamond, respectively.

3.5 Fatigue Life Analysis

The fatigue life will indicate number of revolutions the fixture will able to withstand before the evidence of first crack or failure. There are a few assumptions to be made before doing the analysis in ANSYS software. The assumptions made are: (i) the surface of the fixtures are finely machined and (ii) the load acting on the fixture is purely axial in nature. As the heat treatment temperature will be as high as 1200 K, here the working temperature is considered the maximum, and reliability factor was
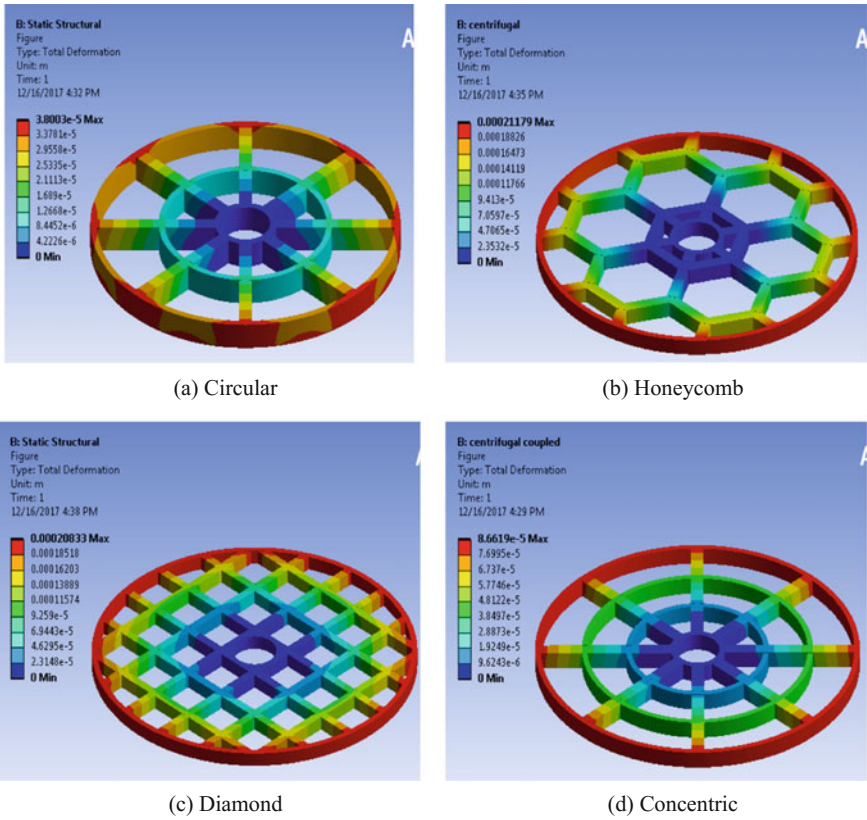
(a) Circular

(b) Honeycomb

(c) Diamond
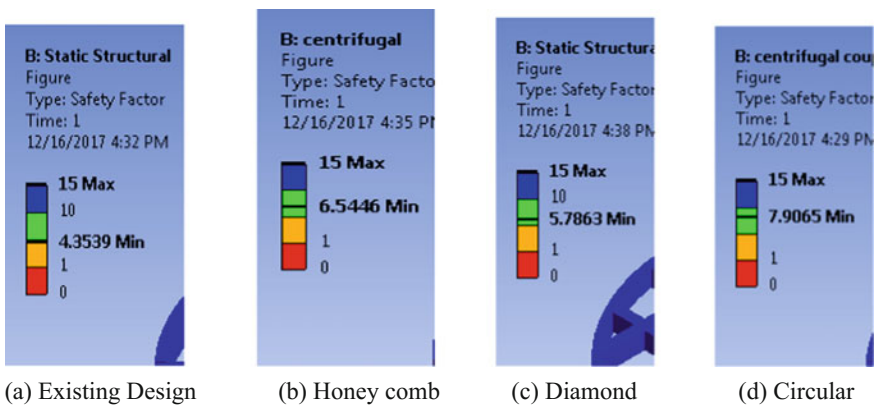
(d) Concentric

Fig. 4 Deformation of different designs

(a) Existing Design

(b) Honey comb

(c) Diamond

(d) Circular

Fig. 5 Safety factor evaluated for various designs

(a) Circular

(b) Honeycomb
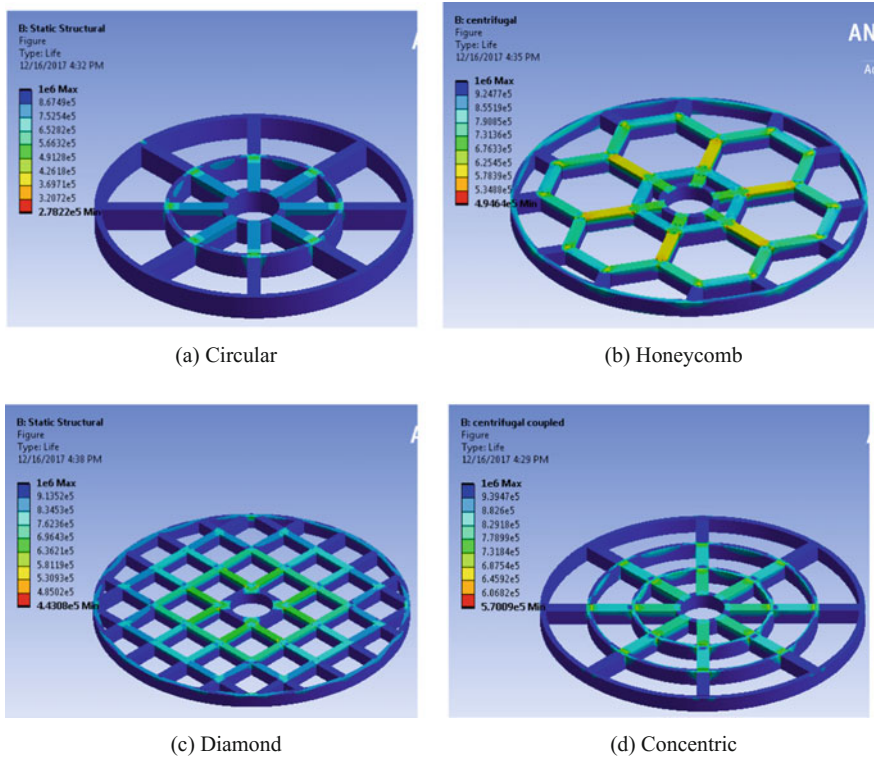
(c) Diamond

(d) Concentric

Fig. 6 Fatigue life analysis of different designs

chosen as 90%. Based on the equation below, various modification factors were considered and the final fatigue limit was found to be 3.4 MPa. Figure 6 indicates the fatigue life of various designs, it infers the current design will have the minimum revolution of 2,78,220 cycles, whereas the honeycomb and diamond design fixtures have the predicted life of 4,94,640 and 4,43,080 cycles, respectively. The circular pattern when analysed showed the maximum predicted life of 5,70,090 cycles which is 104% more than the current design being used.

$$S_e = k_a k_b k_c k_d k_e k_f S'_e.$$

k_b represents the size modification factor,
k_c represents the load modification factor,
k_d represents the temperature modification factor,
k_e represents the reliability factor,
k_f represents any other miscellaneous effects,
S'_e is the endurance limit,
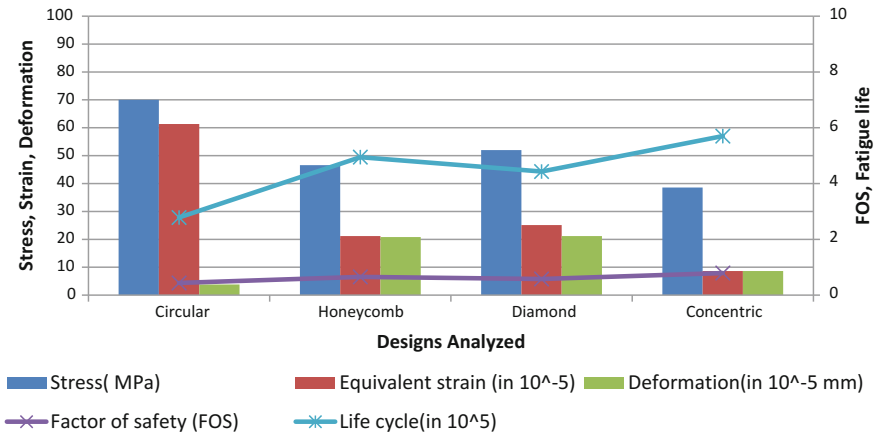S_e is the fatigue limit.

Fig. 7 Consolidated results of various analyses

4 Conclusion

The results of the analysis are consolidated in the graph as shown in Fig. 7. From the graphs, it is evident that the stress, strain and deformation are less for concentric circular design fixture in comparison to other considered designs for the heat treatment fixture. The results are further justified by the safety factor and fatigue life evaluation which also inferred that concentric circular design is the most safest and reliable structure. The research can be further extended by analysing other types of 3D infill patterns such as Archimedean chords, Cast fill, Moroccan star patterns, etc., in finding the robust design for the heat treatment fixture.

References

1. Moonesan, M., Honarbakhsh, A., Madah, F., Habibollah, A.: Effect of alloying elements on thermal shock resistance of gray cast iron. J. Alloys Compd. **520**, 226–231 (2012)
2. Thornton, R., Slatter, T., Jones, A.H., Lewis, R.: The effects of cryogenic processing on the wear resistance of grey cast iron brake discs. Wear **271**, 2386–2395 (2011)
3. Park, B.H.: Bogie frame design in consideration of fatigue strength and weight reduction. J. Rail Rapid Transit **220**(3), 201–206 (2006)
4. Fouvry, S., Kapsa, P., Vincent, L.: A multiaxial fatigue analysis of fretting contact taking into account the size effect. Fretting fatigue: current technology and practices, ASTM STP 1367, PA, pp. 167–182 (2000)
5. Araújo, J.A., Nowell, D.: The effect of rapidly varying contact stress fields on fretting fatigue. Int. J. Fatigue **24**, 763–775 (2002)

6. Araújo, J.A., Nowell, D., Vivacqua, R.C.: The use of multiaxial fatigue models to predict fretting fatigue life of components subjected to different contact stress fields. Fatigue Fract. Eng. Mater. Struct. **27**, 967–978 (2004)
7. Meisel, N, Williams, C.: An investigation of key design for additive manufacturing constraints in multimaterial three-dimensional printing. J. Mech. Des. **137**(11), 111406 (2015)
8. Gopsill, J.A., Shindler, J., Hicks, B.J.: Using finite element analysis to influence the infill design of fused deposition modelled parts, Progress in Additive Manufacturing, Springer International Publishing, pp. 2363–9512 (2017)
9. Yoon, Y.-J., Moon, S.K., Hwang, J.: 3D printing as an efficient way for comparative study of biomimetic structures—trabecular bone and honeycomb. J. Mech. Sci. Technol. **28**(11), 4635–4640 (2015)
10. Mosekilde, L., Ebbesen, E.N., Tornvig, L., Thomsen, J.S.: Trabecular bone structure and strength—remodeling and repair. J. Musculoskelet. Neuronal Interact. **1**(1), 25–30 (2000)
11. Neelakandan, V., Kumar, B., Ganesan, T., Rao, P.C.: Analysis and design optimization for improved fatigue life of one-way clutch drive used in starter motor. In: Seetharamu, S., Rao, K., Khare, R. (eds.) Proceedings of Fatigue, Durability and Fracture Mechanics. Lecture Notes in Mechanical Engineering. Springer, Singapore, 978-981-10-6001-4 (2018)

Stress Analysis on Functionally Graded Spur Gear

V. Aravind, S. Adharsh, D. Prakash and K. Babu

Abstract Gear is an essential power transmitting element used extensively in all kinds of machines, and among the many gear types, involute spur gear is comparatively simple to design and manufacture. However, predominant failure occurs at the gear root portion as a consequence of high bending stress. Several research works have been done in replacing the gear materials to reduce the stress and to improve the load carrying capacity. In this context, this study employs a functionally graded material (FGM) for the gear tooth and the respective stress analysis is carried out through finite element analysis (FEA) technique. The finite element analysis method is verified for grid independence and validated with benchmark problem. FGM materials, namely Al–SiC, Al–Si$_3$N$_4$, Al–Al$_2$O$_3$, Al–Steel, Steel–Zirconia are included in this investigation, and the variation in the material property is considered in the radial direction as exponential, linear, elliptical and power law equations. As an outcome of the analysis, the variation of stress, strain and displacement is documented for various FGM materials and the best equation for the material property variation is identified under uniform and varying face width value of gear tooth.

Keywords Spur gear · Functionally graded material · Finite element analysis

V. Aravind · S. Adharsh · D. Prakash (✉)
School of Mechanical Engineering, SASTRA Deemed to be University,
Thanjavur 613401, India
e-mail: prakash@mech.sastra.edu

K. Babu
Department of Mechanical Engineering, SSN College of Engineering,
Chennai 603110, India
e-mail: babuk@ssn.edu.in

1 Introduction

Gear is the most frequently and widely used element in power transmissions since the design is simple, reliable and compact with good positive drive. Spur gear generally fails due to bending and contact stresses at the gear root portion. The bending stress in gear is determined by Lewis equation by considering as a parabolic beam [1]. The influence of radial stress, stress concentration is neglected and assumed the tangential component of stress is distributed uniformly for a pair of the tooth at contact at any time. Timokhuko [2] used the photoelastic method to determine bending stress at the root portion and observed that it was higher than the values obtained by Lewis equation. However, the success of numerical simulation technique with the assistance of computer facility made FEA technique as a popular method for the accurate analysis of the gear strength. Proveer used numerical simulation—FEA techniques to estimate the fatigue life along with the stress at the root portion of gear [3]. Panwar and Abhay [4] analysed the composite gear using ANSYS software and reported that composite gear provides improved properties than alloy steels. Timoty [1] determined the root is bending stress through FEA technique and the strain gauge measurement and compared with ISO 6336:2006, AGMA 2001-DO4 method. The above literature adds the proficiency on numerical simulation technique in the structural analysis of gear.

Secondly, in the research of gear materials, composite materials are emerging in the manufacture of many engineering components [5]. MMC has unique advantages like lightweight, higher stability, higher strength and are corrosion resistant [6]. Pawar and Abhay [4] prepared aluminium silicate composite with 18% of Sic and improved the hardness, tensile strength over base metal and also observed that 60% less weight in comparison with steel gears, for the same power rating. Anand Mohan and Senthilvelan improved the bending load carrying capacity by adding 20% of glass fibre reinforced polypropylene materials for gear. Imbaby and Jiang fabricated the stainless steel–titania composite micro-spur gear and reported that adding of Titania increases the microhardness and decreases the sintered density and linear shrinkage by varying the percentage of Titania from 2.5 to 10%. However, in these gears, the physical property and the mechanical property are discontinuous at the interface of two different layers of material [7]. In this context, FGM materials are widely used in the engineering components, since physical behaviour is changing gradually without discontinuity. FGM is an innovative material designed to execute the desired function by providing in-depth composition and properties [8].

The non-homogenous pattern of material gradation offers good hardness, wear resistance and supports as a good thermal barrier for many applications such as piezoelectric actuators and electromagnetic sensors [9–11]. Even though many research works are available in the stress analysis of functionally graded rotating disc [12–15], such as turbojet engines, rotors, brake discs, flywheels, jet engines, pumps automobiles and turbines [16], a specific study on gears is very limited.

From the above-reviewed literature, it is observed that gear made of composite material is the latest research work has been done and in that case, the sharp discontinuity in the material composition creates a critical stress concentration at the metal interface zone, and this can be overcome by the functionally graded. Hence in this research, an initial attempt is made to investigate the stress analysis on spur gear tooth made of functionally graded material.

2 Spur Gear Design and Model

The spur gear is designed using Lewis method for the power of 1500 W and speed of 1400 rpm. The determined geometric parameter values are provided in Table 1. The geometry of the spur gear is modelled using ANSYS APDL module for the determined values and shown in Fig. 1. A single tooth from the gear is modelled by considering it as a cantilever beam.

3 Numerical Simulation Procedure

The gear model is created as a two-dimensional geometry and divided into 20 equal radial segments as shown in Fig. 2a. Each radial segment is assigned with a material property which was governed by the laws (elliptical, power, linear, exponential) and also the variation of material property is piecewise. The geometry is meshed with PLANE 183 element having 8 nodes with 2 degrees of freedom on each node. The two degrees of freedom is a translation in x-direction and y-direction. This element has a capability to analyse the behaviour of plasticity, creep, hyperelasticity, stress stiffening, large strain capabilities and large deflections [17]. The geometry is solved under plane stress with thickness consideration option. The thickness of the gear tooth is specified through real constant option. The geometry is meshed as shown in Fig. 2b.

Table 1 Design values for the spur gear tooth	Geometric parameter	Values
	Module	10 mm
	No of teeth	18
	Pressure angle	20°
	Addendum	10 mm
	Dedendum	11.57 mm
	Pitch circle diameter	180 mm
	Tooth thickness	15.71 mm
	Whole depth	22.5 mm
	Face width	100 mm
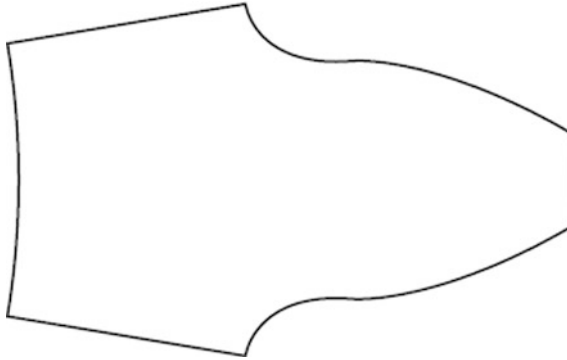
**Fig. 1** Geometry of the spur gear tooth
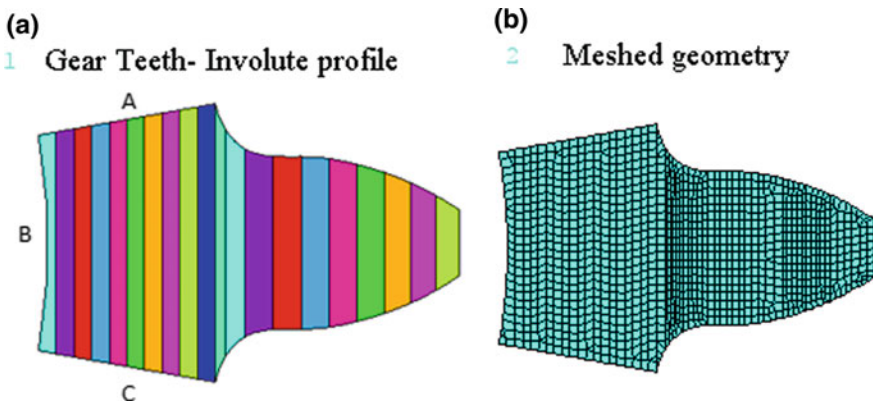
Fig. 2 FEA model of gear

As boundary conditions, the gear edges A, B and C are constrained in both *x*-direction and *y*-direction, and a tangential load of 113.68 N is applied at the tooth tip for deflection testing. The edge B is alone constrained for testing the gear with angular velocity. Material combinations like Al–SiC, Al–Si$_3$N$_4$, Steel–Zr and Al–Al$_2$O$_3$ materials are the functionally graded materials included in this work, and its mechanical properties are mentioned in Table 2.

As an outcome of the analysis, the stress and the deflection are determined for the gear domain and the results are shown in Fig. 3 for a sample case of steel–Zr material, and the physical property is varied linearly. No contact test is performed on the designed spur gears.

For the above gear, the bending stress and the deflection are determined theoretically from Eqs. (1) and (2).

Table 2 Material properties

Material	Young's modulus (Gpa)	Density (kg/m^3)	Poisson ratio
Al–SiC	$E_A = 68.9$ [20] $E_B = 410.47$	$\rho_{A=}2700$ [20] $\rho_B = 3210$	$\mu_A = 0.33$ [20] $\mu_B = 0.183$
Al–Si$_3$N$_4$	$E_A = 68.9$ $E_B = 310$ [21]	$\rho_{A=}2700$ $\rho_B = 3440$ [21]	$\mu_A = 0.33$ $\mu_B = 0.27$ [21]
Al–Al$_2$O$_3$	$E_A = 68.9$ $E_B = 353.1$ [22]	$\rho_A = 2700$ $\rho_B = 3950$ [22]	$\mu_A = 0.33$ $\mu_B = 0.21$ [22]
Steel–Zr	$E_A = 200$ [23] $E_B = 250$ [23]	$\rho_A = 8000$ [23] $\rho_B = 5680$ [23]	$\mu_A = 0.3$ [23] $\mu_B = 0.22$ [23]
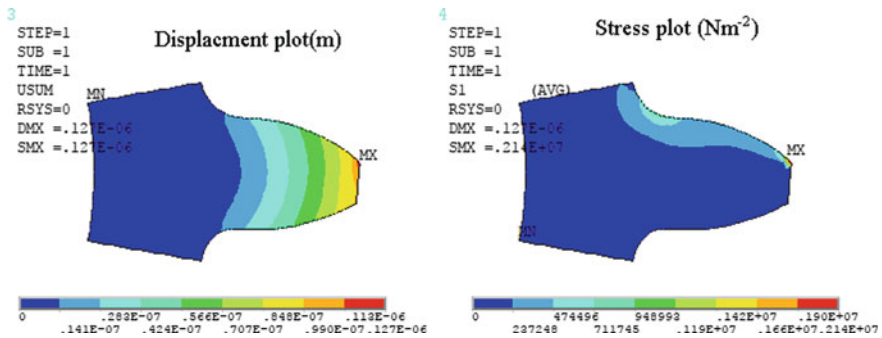
Fig. 3 Structural analysis contour plots

$$\sigma_b = \left(\frac{6F_t h}{t^2} - \frac{F_t}{t}\tan\alpha\right)\left(0.18 + \left[\left(\frac{t}{r}\right)^{0.15} + \left(\frac{t}{h}\right)^{0.45}\right]\right) \tag{1}$$

$$\delta = \frac{F_t \times h^3}{3\text{EI}} \tag{2}$$

The maximum the bending stress and the deflection are calculated as 2.1×10^6 Nm^{-2} and 0.12×10^{-6} m and the determined values are in good agreement with FEA results.

4 Results and Discussions

The above gear is analysed for a different pair of FGM such as aluminium–silicon carbide, Aluminium–silicon nitride, Aluminium–aluminium oxide and steel–zirconium. Also, the variation of material properties is governed by the liner, power law, exponential and elliptical equation. The gear is analysed for uniform face

Table 3 Material property variation equations

Laws	Young's modulus	Density	Poisson ratio
Exponential	$E(r) = E_0\, e^{\beta r}$	$\rho(r) = \rho_0\, e^{\gamma r}$	$v(r) = v_0\, e^{\mu r}$
Linear	$E(r) = (m \times r) + c$	$\rho(r) = (m_1 \times r) + c_1$	$v(r) = (m_2 \times r) + c_2$
Power	$E(r) = E^0(r/b)^{\beta 1}$	$\rho(r) = \rho^0(r/b)^{\beta 2}$	$v(r) = v^0(r/b)^{\beta 3}$
Elliptical	$E(r) = (1 - r/a^2) \times b^2$	$\rho(r) = (1 - r/a_1^2) \times b_1^2$	$v(r) = (1 - r/a_2^2) \times b_2^2$
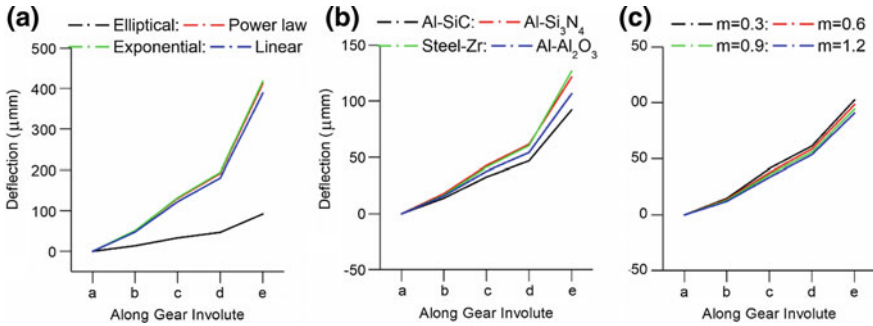
Fig. 4 Variation of deflection

width and varying face width value. For the examined cases, the displacement and stress along the gear involute and stress at the teeth root are predicted from finite FEA and submitted for comparative discussion. The material property is varied along the radial direction of the gear as linear [18], power law [17], exponential [19] and elliptical equation as mentioned in Table 3.

E_0, ρ_0, v_0 are the mechanical properties, subscript of the materials at the outer end. m, c, m_1, c_1, m_2, c_2 are the slope and the constant variable, respectively, β_1, β_2, β_3 are the gradient indices of Young's modulus, density and the Poisson ratio. a, b, a_1, b_1, a_2, b_2 are the semi-major and the semi-minor axis of the ellipse.

In the first study, the gear is analysed for steel zirconium with constant face width value. The material gradient equation is changed, and the resulted displacement variation along the gear involute is shown in Fig. 4a. The deflection is gradually increasing from the gear root to the gear tip for all the material gradient equations. The variation of deflection along the involute is almost same for all the equations except elliptical equation. The elliptical equation shows low defection along the involute. In the second study, the FGM pairs are varied, and the deflection along the involute is shown in Fig. 4b for the elliptical equation. From this figure, it is observed that the deflection is comparatively less for the FGM pair Al–SiC and Al–Al$_2$O$_3$, Al–Si$_3$N$_4$ and steel–Zr stand next. In the third study, the face width of gear is varied in the radial direction in accordance with Eq. (3) and its influence on deflection is shown in Fig. 4c.

$$h_r = h_o \left(\frac{r}{b}\right)^{-m} \tag{3}$$

where h_o is the gear thickness at $r = b$ and m is the geometric parameter index. The geometric parameter index is varied as 0.3, 0.6, 0.9 and 1.2 [14], and the gear teeth are analysed for the material steel–Zr with an elliptical pattern of material variation. From this figure, it is observed that increasing the geometric parameter index (m), decreases the deflection, and however, the difference is insignificant.

For the above-analysed cases, the average stress at the gear root portion is determined and shown in Fig. 5. The stress at the gear root potion is comparatively minimum for the geometric parameter index, $m = 1.2$ and increases significantly by decreasing m. While changing material property equation, the stresses at root portion are almost same for the linear, exponential and the power law equation and a significant increase is noticed for the elliptical equation. Also, steel–Zr shows low stress among the other analysed materials. Finally, the influence of angular speed is also investigated for a constant and varying the face width of gear teeth. The speed of rotation is varied as 250, 500, 750 and 1000 rpm, and as an outcome deflection and stress along the gear involute are shown in Fig. 6. In Fig. 6, the deflection and the stress are significantly influenced by the speed of rotation. Also, variable thickness gear index $m = 1.2$ indicates comparatively low deflection and stress values than uniform thickness gear. For all the cases, the stress is maximum at the gear root portion and deflection is maximum at the gear tip portion.
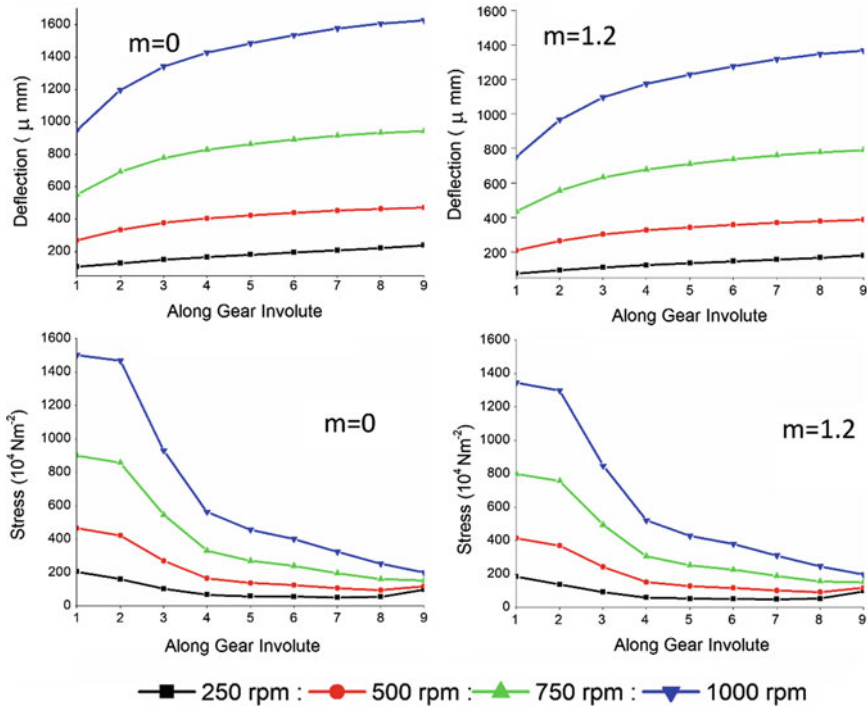

Fig. 5 Root stress
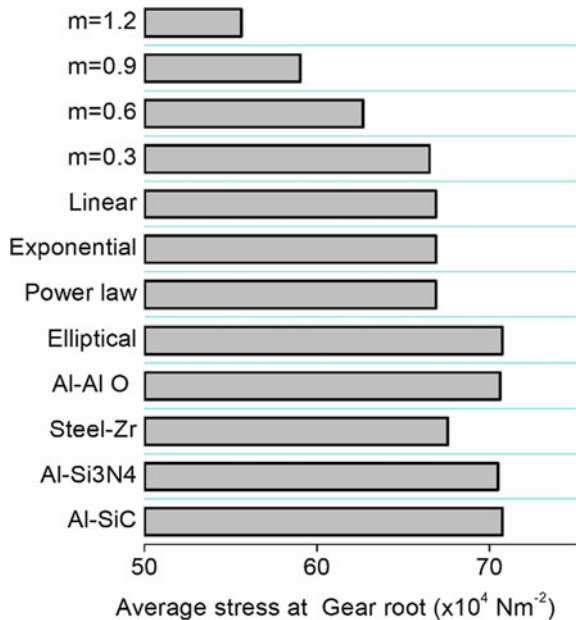
Fig. 6 Variation of deflection and stress

5 Conclusion

In this work, the gear made of the functionally graded material is analysed for the stress and deflection through FEA methods. The gear teeth is treated as a cantilever beam and modelled as two-dimensional geometry in ANSYS APDL.15 software. The FGM pair such as Al–SiC and Al–Al$_2$O$_3$, Al–Si$_3$N$_4$ and steel–Zr are included in this study, and its material behaviour is varied linearly, exponentially, power law and elliptically. Among the pairs of FGM Al–SiC showed the least deflection because of its high Young's modulus value. Among the analysed materials, steel–Zr shows reduced stress at the gear root portion, and material property variation by elliptical equation shows less deflection comparatively. Also, it is noticed that gear of variable face width creates less stress and deflections in comparison with constant face width gear and hence offers good load carrying capability. Especially at the gear root portion, the induced stress by variable face width gear ($m = 1.2$) is almost 20% lesser than constant face width gear. Finally, the influence of speed on the stress and the deflection is studied and noticed that variable face width gear shows comparatively less stress and deflection for all speeds of rotation in comparison with constant face width gear.

References

1. Lisle, T.J., Shaw, B.A., Frazer, R.C.: External spur gear root bending stress: a comparison of ISO 6336: 2006, AGMA 2101-D04, ANSYS finite element analysis and strain gauge techniques. Mech. Mach. Theory **111**, 1–9 (2017)
2. Timoshenko, S., Baud, R.V.: Strength of gear teeth. Mech. Eng. **48**(11), 1105–1109 (1926)
3. Silori, P., Shaikh, A., Kumar, K.C.N., Tandon, T.: Finite element analysis of traction gear using ANSYS. Mater. Today: Proc. **2**(4–5), 2236–2245 (2015)
4. Pawar, P.B., AbhayUtpat, A.: Analysis of composite material spur gear under static loading condition. Mater. Today: Proc. **2**(4–5), 2968–2974 (2015)
5. Pankaj, C., Amit, B.: Design and analysis of composite material gear box. IOSR-JMCE **1**(1), 15–25 (2012)
6. Devi, N.C., Mahesh, V., Selvaraj, N.: Mechanical characterization of aluminium silicon carbide composite. IJAER 4 (2011)
7. Navazi, H.M., Haddadpour, H.: Nonlinear cylindrical bending analysis of shear deformable functionally graded plates under different loadings using analytical methods. IJMS **50**(12), 1650–1657 (2008)
8. Kawasaki, A., Watanabe, R.: Concept and P/M fabrication of functionally gradient materials. Ceram. Int. **23**(1), 73–83 (1997)
9. Abbas, M.R., Uday, M.B., Noor, A.M., Ahmad, N., Rajoo, S.: Microstructural evaluation of a slurry based Ni/YSZ thermal barrier coating for automotive turbocharger turbine application. Mater. Des. **109**, 47–56 (2016)
10. Dhineshkumar, S.R., Duraiselvam, M., Natarajan, S., Panwar, S.S., Jena, T., Khan, M.A.: Enhancement of strain tolerance of functionally graded LaTi 2 Al 9 O 19 thermal barrier coating through ultra-short pulse based laser texturing. Surf. Coat. Tech. **304**, 263–271 (2016)
11. Naga, S.M., Awaad, M., El-Maghraby, H.F., Hassan, A.M., Elhoriny, M., Killinger, A., Gadow, R.: Effect of La 2 Zr 2 O 7 coat on the hot corrosion of multi-layer thermal barrier coatings. Mater. Des. **102**, 1–7 (2016)
12. Zheng, Y., Bahaloo, H., Mousanezhad, D., Mahdi, E., Vaziri, A., Nayeb-Hashemi, H.: Stress analysis in functionally graded rotating discs with non-uniform thickness and variable angular velocity. IJMS **119**, 283–293 (2016)
13. Mahdavi, E., Ghasemi, A., Alashti, R.A.: Elastic-plastic analysis of functionally graded rotating discs with variable thickness and temperature-dependent material properties under mechanical loading and unloading. Aerosp. Sci. Technol. **59**, 57–68 (2016)
14. Hassani, A., Hojjati, M.H., Mahdavi, E., Alashti, R.A., Farrahi, G.: Thermo-mechanical analysis of rotating discs with non-uniform thickness and material properties. Int. J. Pres. Ves. Pip. **98**, 95–101 (2012)
15. Hosseini, M., Shishesaz, M., Tahan, K.N., Hadi, A.: Stress analysis of rotating nano-discs of variable thickness made of functionally graded materials. IJES **109**, 29–53 (2016)
16. Nejad, M.Z., Rastgoo, A., Hadi, A.: Exact elasto-plastic analysis of rotating discs made of functionally graded materials. IJES **85**, 47–57 (2014)
17. Peng, X.L., Li, X.F.: Elastic Analysis of rotating Functionally graded polar orthotropic discs. Int. J. Mech. Sci. **60**, 84–91 (2012)
18. Callioglu, H., Bektas, N.B., Sayer, M.: Stress analysis of functionally graded rotating discs: analytical and numerical solutions. Acta. Mech. Sin. **27**, 950–955 (2011)
19. Verma, R.K., Sarda, A.: Analysis of functionally graded material spur gear under static loading condition. Adv. Phys. Lett. **3**, 2349–1108 (2016)
20. Bayat, M., Saleem, M., Sahari, B.B., Hamouda, A.M.S., Mahdi, E.: Analysis of functionally graded rotating disks with variable thickness. Mech. Res. Commun. **35**, 283–309 (2008)
21. Ziegler, G., Heinrich, J., Wötting, G.: Relationships between processing, microstructure and properties of dense and reaction-bonded silicon nitride. J. Mater. Sci. **22**, 3041–3086 (1987)

22. Sazgar, A., Movahhedy, M.R., Mahnama, M., Sohrabpour, S.: Development of a molecular dynamic based cohesive zone model for prediction of an equivalent material behaviour for Al/ Al_2O_3 composite. Mater. Sci. Eng. A **679**, 116–122 (2017)
23. Kordkheili, S.H., Livani, M.: Thermoelastic creep analysis of a functionally graded various thickness rotating disk with temperature-dependent material properties. Int. J. Press. Vessels Pip. **111**, 63–74 (2013)

Experimental Investigation on Heat Transfer Analysis of Fins

A. S. Ramana and J. Arun Jacob Packianathan

Abstract Fins are extended surfaces that find use in variety of applications for heat transfer enhancement. Proper design and manufacturing of fin are essential for effective and efficient heat removal. Arrangement of fins, fin perforations, and surface property are some of the key parameters that impact heat transfer. Heat flow through fins depends on temperature distribution through it. Hence in the present experimental investigation, a comparison of temperature variations in in-line/ staggered arrangement of fins, fin perforations, and fins of smooth/rough surface profile was studied. Higher heat dissipation was observed for three holes configuration compared to two holes configuration. Further, knurled fin surfaces offered better heat dissipation. In addition, staggered fin arrangement enhances heat transfer compared to in-line arrangement. Comparison was undertaken for both the cases of fins with/without heat generation.

Keywords Staggered fins · In-line fins · Knurled fins · Heat dissipation

1 Introduction

Pin fins of varying pitch, perforation diameters, and material have long been researched worldwide for heat transfer enhancement studies. Yet the complexities of the heat transfer in variety of fin applications demands further study. In a study to determine the heat transfer enhancement, multiple pin perforations not only increased heat transfer but also reduced pressure drop [1] and square cross-sectional perforated pin fin was more effective [2]. Inter-fin pitch to pin fin diameter and fin material also influences heat transfers [3]. Researchers have predicted fin performance and compared numerical solutions with thermal camera measurement readings [4]. Kim et al. [5] showed that optimized pin fin heat sinks have lower

A. S. Ramana (✉) · J. Arun Jacob Packianathan
Department of Mechanical Engineering, SSN College of Engineering,
Chennai 603110, India
e-mail: ramanaas@ssn.edu.in

thermal resistance than optimized plate-fin heat sinks for a smaller pumping power and larger dimensionless length. High heat transfer coefficient was noticed for perforated fin arrays in a study undertaken by Huang et al. [6], and it increased with increasing perforation length. Tanda et al. [7] in their studies for a duct with in-line and staggered arrangement of fins revealed improvement in heat transfer due to presence of diamond-shaped elements induct. Haldar et al. [8] studies underscored the importance of the convection mode rather than the conduction for short fins and thus fin thermal conductivity requires little attention for such fins. Increased heat transfer and pressure drop were observed in analysis on oblong pin fins by Metzgeret al. [9]. Sara et al. [10] in their analysis on perforated staggered cylindrical fins achieved high heat transfer characteristics and pressure drop. Increased fin efficiency was noticed by Senthilkumar et al. [11] in their investigation on fins coated with CNT. Tzer-Ming Jeng and Sheng-Chungzeng [12] showed that in-line square pin fin array has lesser heat transfer than in-line circular pin fin array. Enhanced heat transfer coefficient was attained by Umesh et al. [13] in perforated fins at an angle of orientation as opposed to the solid fin array. Vanfossen and Brigham [14] observed that the average heat transfer coefficient on the pin surface was larger than that on the end walls. Kuzma-Kichta et al. [15] have reported better thermal performance in tubes in tubes with two-thread screw knurling.

Though there exists several works on pin fins, the combined effect of knurling and perforations on pin fins have not yet been discussed at length in previous studies. The objective of the present work is to investigate the heat transfer aspects on combination of perforations and knurling in pin fins.

2 Experimental Investigation

Fins temperature rise and decrease during heating and cooling periods were investigated with/without perforation and in symmetrical and staggered arrangements. The detailed test set up and procedures are explained in subsequent subsections.

2.1 Experimental Test Setup

The experiment setup as shown in Figs. 1 and 2 was designed to measure the difference in rates of temperature increase/decrease in staggered and staggered arrangement of fins of cylindrical nature. The experiment consists of the following parts a heater unit, cylindrical fins in symmetrical/staggered configuration, and a data display unit. The heater unit is a rectangular chamber of dimensions 350 mm × 350 mm × 450 mm. It incorporates heaters that heat fin base plate and thermocouples that measure the temperature of the fin. The chamber is lined with glass wool to minimize the heat loss between chamber and atmosphere.
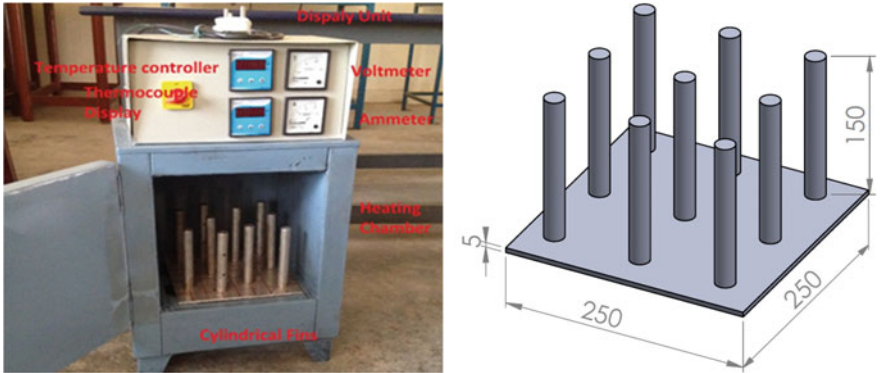
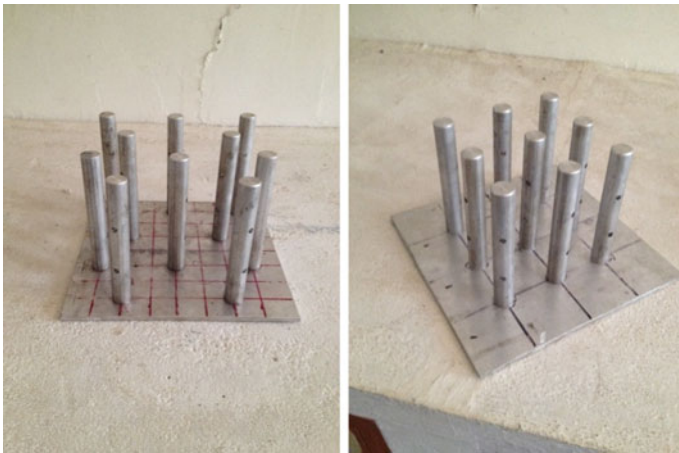**Fig. 1** Experimental setup and fin dimensions in mm

Fig. 2 Staggered and symmetric arrangement

Thermocouples of "K" type are fixed at a distance of 50 mm vertically above the fins attached to the back wall of the chamber and few other thermocouples are placed near the fins at different locations. These are present to measure the temperature inside the chamber. The unit has an insulated door to open and close the chamber. The insulated door minimizes heat losses during its operation. The heater is of 1800 W capacity plate heater type. Roughness was done on fin surface to study its effect on heat transfer. A pattern of crossed lines with a diamond-shaped cut on the pin fin surface using double roller cross-knurling tool was done using lathe.

2.2   Experimental Procedure

Initially, the heater unit is turned on with a particular fin arrangement inside. It is heated for a certain time and is allowed to cool in the setup itself. The cooling period is kept constant and the readings are noted. The readings are compared for both the symmetrical and staggered arrangements. The experiment was further carried out for detailed analysis of heat transfer through fins in both symmetrical and staggered arrangements by increasing the number of holes and increasing the roughness on the surface of the fins.

3   Results and Discussion

The temperature increase/decrease during heating/cooling period presented in further subsections. The following section figures are plotted based on average of different sets of experiments. In the figures, various parameters of form UF(ij) are involved, where i represents row number in the array, j represents column number in the array. The readings are taken for both top and bottom surface of the fin. The top surface is represented as "U" and the bottom is represented as "B". The conditions applied for obtaining readings, "O" represents open door setup and "Cl" represents closed-door setup conditions.

Figures 3 and 4 show the temperature variation with time for in-line/staggered arrangement of fins with thermocouples placed in the top surface holes of the fins. They represent the heating of the fins in both open and closed arrangements. The curve at the top is obtained due to closed-door setup as the fin is heated to higher temperatures with little space for heat dissipation than open door setup. Due to closed-door condition, sufficient heat is not dissipated; hence, the temperature of the fin increases rapidly during the initial heating period.
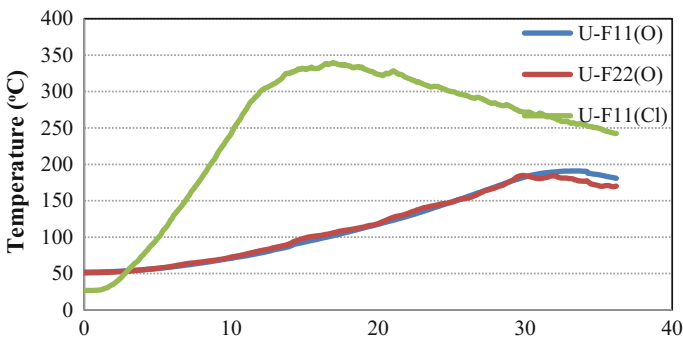

Fig. 3 Temperature rise in in-line arrangement during open and closed condition
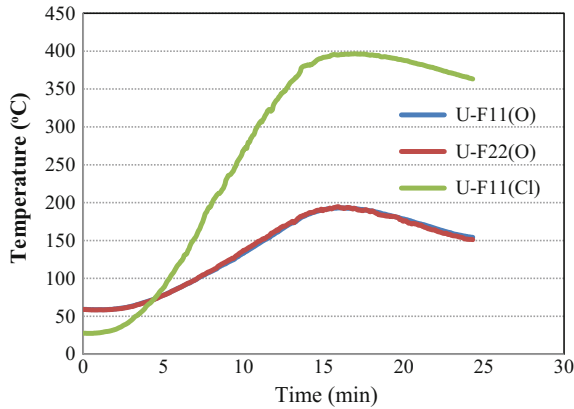
Fig. 4 Temperature rise in staggered arrangement during open and closed condition
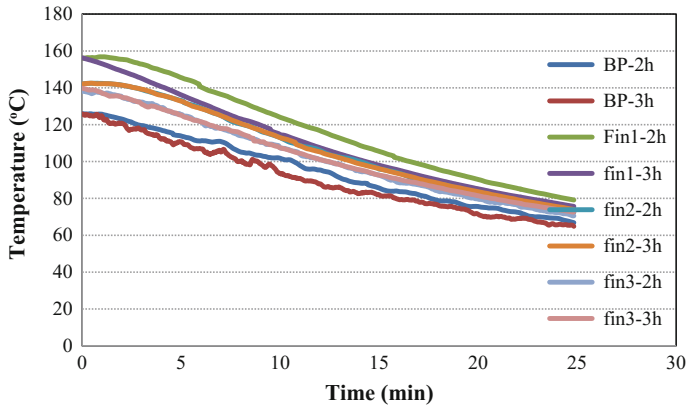

Fig. 5 Temperature variations in 2 holes (2 h) versus 3 holes (3 h)

The temperature variation with time for fins 2 and 3 holes is shown in Fig. 5. Two holes fins show higher temperature than 3 holes fins. BP represents base plate and fin 1, 2, 3 represents fins in different locations with 2 holes and 3 holes. The temperature variation with time for fins with 3 holes and knurled surfaces is shown in Fig. 6. Knurled surfaces show better heat dissipation during cooling. Better performances are attributed to disturbances in thermal boundary layer and higher heat transfer coefficient (Fig. 6).

The random air flow movement in knurled surfaces coupled with continuous mixing of air at different temperatures through perforations accelerates heat transfer. This aids in better heat transfer coefficient and, hence, the improvement in performance of fin with perforation and roughened pin surface.
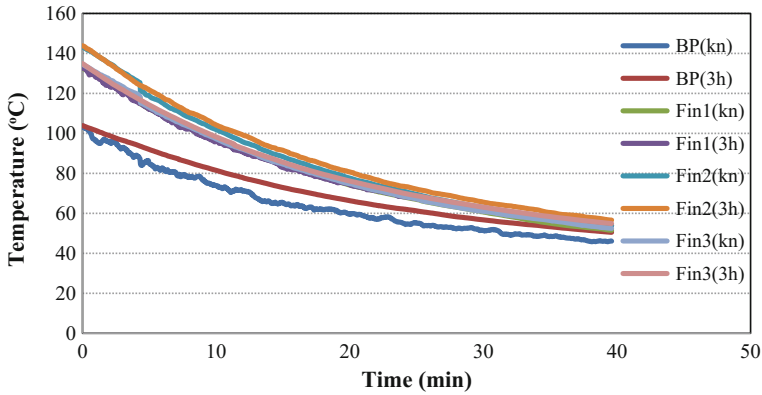
Fig. 6 Temperature variations in 3 holes (3 h) versus knurled (kn) surface

4 Conclusion

Based on experimental results, the staggered fin arrangement has a higher heat dissipation rate compared to in-line arrangement. When the door of the heater is in open condition, there is a considerable variation in heat dissipation rate between in-line and staggered arrangement. However, the temperature rise/drop in case of the closed condition is more or less similar in both in-line and staggered arrangement. The heat dissipation rate is higher in the three holes arrangement when compared to two holes arrangement of pin fins. The heat dissipation rate is higher in the knurled surface compared to three-holed plain surface of pin fins.

References

1. Al-Damook, A., Kapur, N., Thompson, H.M.: An experimental and computational investigation of thermal air flows through perforated pin heat sinks. Appl. Therm. Eng. **89**, 365–376 (2015)
2. Sahin, B., Demir, A.: Performance analysis of a heat exchanger having perforated square fins. Appl. Therm. Eng. **28**, 621–632 (2008)
3. Babus'Haq, R.F., Akintunde, K., Probert, S.D.: Thermal performance of a pin-fin assembly. Int. J. Heat Fluid Flow **16**, 50–55 (1995)
4. Huang, C.-H., Liu, Y.-C., Ay, H.: The design of optimum perforation diameters for pin fin array for heat transfer enhancement. Int. J. Heat Mass Transf. **84**, 752–765 (2015)
5. Kim, D.-K., Kim, S.J., Bae, J.K.: Comparison of thermal performances of plate-fin and pin-fin heat sinks subject to an impinging flow. Int. J. Heat Mass Transf. **52**, 3510–3517 (2009)

6. Huang, G.-J., Wong, S.-C., Lin, C.-P.: Enhancement of natural convection heat transfer from horizontal rectangular fin arrays with perforations in fin base. Int. J. Therm. Sci. **84**, 164–174 (2014)
7. Tanda, G.: Heat transfer and pressure drop in a rectangular channel with diamond shaped elements. Int. J. Heat Mass Transf. **44**, 3529–3541 (2001)
8. Haldar, S.C.: Natural convection about a cylindrical pin element on a horizontal plate. Int. J. Therm. Sci. **49**, 1977–1983 (2010)
9. Metzger, D.E., Fan, C.S., Haley, S.W.: Effects of pin shape and array orientation on heat transfer and pressure loss in pin fin arrays. J. Eng. Gas Turbines Power **106**, 252–257 (1984)
10. Sara, O.N., Pekdemir, T., Yapici, S., Yılmaz, M.: Heat-transfer enhancement in a channel flow with perforated rectangular blocks. Int. J. Heat Fluid Fl. **22**, 509–518 (2011)
11. Senthilkumar, R., Nandhakumar, A.J.D., Prabhu, S.: Analysis of natural convective heat transfer of nano coated aluminium fins using Taguchi method. Heat Mass Transf. **49**(1), 55–64 (2013)
12. Jeng, T.-M., Tzeng, S.-C.: Pressure drop and heat transfer of square pin-fin arrays in in-line and staggered arrangements. Int. J. Heat Mass Transf. **50**, 2364–2375 (2007)
13. Awasarmol, U.V., Pise, A.T.: An experimental investigation of natural convection heat transfer enhancement from perforated rectangular fins array at different inclinations. Exp. Therm. Fluid Sci. **68**, 145–154 (2015)
14. Vanfossen, G.J., Brigham, B.A.: Length to diameter ratio and row number effects in short pin fin heat transfer. ASME J. Eng. Gas Turbines Power **106**, 241–244 (1984)
15. Kuzma-Kichta, Y.A., Savelev, P.A., Koryakin, S.A., Dobrovol'skii, A.K.: Studying of heat-transfer enhancement in tubes with screw knurling. Therm. Eng. **54**(5), 407–409 (2007)

Multi-response Optimization of Process Parameters in Laser Drilling of AA6061-TiB$_2$/ZrB$_2$ In Situ Composite Produced by K$_2$TiF$_6$-KBF$_4$-K$_2$ZrF$_6$ Reaction System

A. Mahamani and V. V. Anantha Chakravarthy

Abstract The major involvement of this experimental work is to drill the holes of microsize on AA6061-TiB$_2$/ZrB$_2$ composite using fiber laser marking machine setup with input parameters as speed of the laser, laser power and standoff distance. The input parameters are optimized by Grey relational analysis method to identify the parameters to minimize the entry diameter, exit diameter and taper. The outcome of the Grey relational analysis indicates that higher laser speed, lower laser power and higher standoff distance are favorable range of parameters to attain minimum entry diameter, exit diameter and taper within the selected level of parameters. Laser power has significant influence on the multi-performance characteristics than the standoff distance and laser speed. The result of confirmation experiment illustrates that the response values obtained from the experiments and grey relational grade equation are with good correlation. Outcome of this experimental work helps to prefer the optimum laser drilling parameters in machining of AA6061-5% TiB$_2$/ZrB$_2$ composite.

Keywords In situ composites · Laser drilling · Entry diameter
Exit diameter · Taper · Grey relational analysis

A. Mahamani (✉) · V. V. Anantha Chakravarthy
Department of Mechanical Engineering, Sri Venkateswara College
of Engineering and Technology (Autonomus), Chittoor 517127, Andhra Pradesh, India
e-mail: mahamanisudhan@gmail.com

V. V. Anantha Chakravarthy
e-mail: vv.ananth001@gmail.com

1   Introduction

The effort on developing aluminum-based composites is increased thanks to its superior mechanical properties at the lowest weight. Existence of corrosion resistance, higher elevated mechanical strength, thermal and electrical properties of the composites make them suitable for aircraft, electronic and automotive industries [1]. In situ synthesis of the making composite is considered as an economic route to attain the improved properties by reinforcing relatively lower volume fraction of the reinforcements. Aikin [2] reported the various advantages of in situ composites. Coarse-free, small, oxide-free, fine and dust-free reinforcement drawn from the exothermic chemical reaction offers excessive interfacial strength and enhanced wettability in turn increasing the mechanical properties and high-temperature bearing ability of the composites. The conventional drilling is associated with considerable force on the material around the hole. Drilling small size holes on the brittle materials and obtaining the close tolerances at economic machining rate are a herculean task [3]. Laser drilling is believed as suitable machining processes to conquer the above said challenge. In this process, the material removal is carried out by melting, vaporization and ablation by means of focusing the thermal or photochemical energy on top of the work piece [4]. This process is widely employed to make small orifices in the nozzles and cooling channels in air turbine blades [5]. Mishra and Yadava [6] developed an artificial neural network-based model to envisage the hole taper, rate of material removal and dimension of the HAZ in laser beam percussion drilling of thin aluminum sheet. The result from the study exemplifies that the pulse width is a most significant parameter factor which is persuading the hole taper and rate of material removal than the pulse frequency. Yue and Lau [7] investigated the pulsed laser cutting ability of an Al–Li/SiC composite by using scanning electron microscopy and energy-dispersive spectroscopy analysis. From the experimental results, an empirical model was developed for attaining the minimal thermally affected zone by relating the laser machining parameters. Lau et al. [8] developed a modernistic ultrasonic enabled laser machining system to upgrade the quality of the drilled holes on aluminum matrix composites in terms of enhanced depth of drill, lower taper and minimal recast layer. The experimental result demonstrates that the anticipated laser drilling system not only offer extended depth of drill but also hole quality. They also proposed a mathematical model to gauge the shape of the drilled hole. Ezeddini et al. [9] presented an experimental work on laser cutting of Al-(TiN + Al_2O_3) composite made by pooled powder metallurgy and thixoforming method. Influence of laser operating parameters like power and speed of cutting and cutting surface are investigated. Microhardness and surface roughness are premeditated to gauge the quality of the cutting exterior. They also aimed to optimize laser operating parameters to curtail the surface roughness. Sharma and Kumar [10] examined the laser-based machining behavior of aluminum matrix composites reinforced with SiC, Al_2O_3 and ZrO_2 particles. The variation in tallness of the dross, kerf, and angle of striations of various composites are evaluated under different range of

parameters. It is found from the analysis the speed of cutting, reinforcement particles and profile of cutting are identified as most noteworthy factors which are influencing the machining responses. Further, the comparative study illustrates that the SiC particle reinforced composite has enhanced machining characteristics than other composites. Mahamani and Chakravarthy [11] studied influence of reinforcement content and laser machining parameters on entry diameter, exit diameter and taper. It is seen from results the way in and way-out diameters and taper of AA6061 alloy is not as much as that of the composites for all the machining conditions. At higher laser speed the way in and way-out diameters are reduced whereas the slope of the laser drilled hole is increased. Higher laser power widens the way in and way-out diameters, and diminishes the slope of the hole. For the growing industry need, multiple characteristics are premeditated to gauge the product quality. Multi-response optimization is an effectual way to handle situation where multiple responses are involved [12]. Grey relational analysis is a significant task of grey theory by which to appraise the different level of development trends among various factors and widely recognized by researchers for achieving the research results [13]. The literature review clears that, the laser drilling of ex situ aluminum-based composites widely reported. However, the studies on laser drilling of in situ composites are extremely limited. Therefore, the current paper proposes multi-response optimization of laser drilling parameters in machining of AA6061-TiB$_2$/ZrB$_2$ in situ composites. The intention of the work is to optimize the laser parameters in machining of AA6061-TiB$_2$/ZrB$_2$ in situ composites using Grey relational analysis for multi-response optimization including entry diameter, exit diameter and taper.

2 Material Synthesis and Characterization

AA6061-5% TiB$_2$/ZrB$_2$ in situ composite is fabricated via mixed salt reaction [14] and used for the experimental work. The energy-dispersive X-ray analysis (EDAX) pattern and quantitative elemental analysis description are offered in Figs. 1 and 2. The elements like aluminum, titanium and zirconium are detected in the EDAX pattern. The quantitative analysis confirms the presence of 4.31% TiB$_2$ and 2.42% ZrB$_2$ in the sample. Scanning electron microscopic examination is conducted and illustrated in Fig. 3. The result shows that TiB$_2$ and ZrB$_2$ reinforcement particles are found in hexagonal and round shape, respectively. It is observable from the analysis that the reinforcements are homogenous distributed in the matrix. The thickness of the composite plate is decreased via horizontal milling process and made into 0.5 mm thickness.
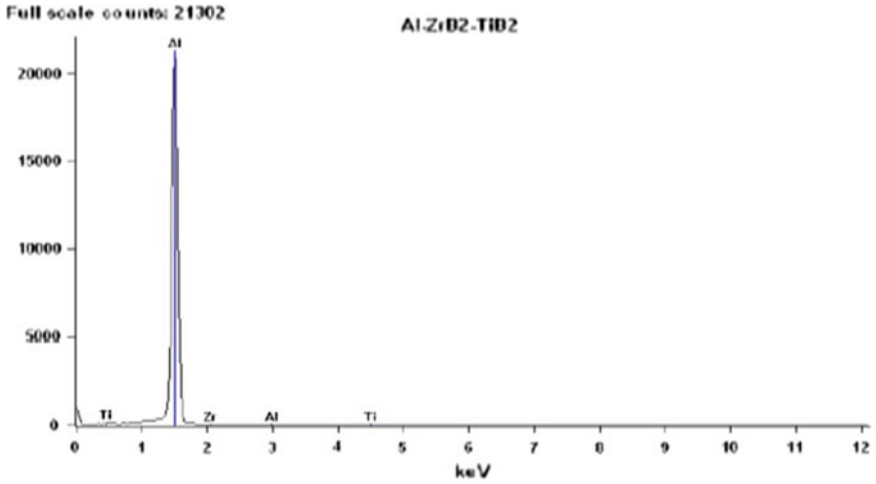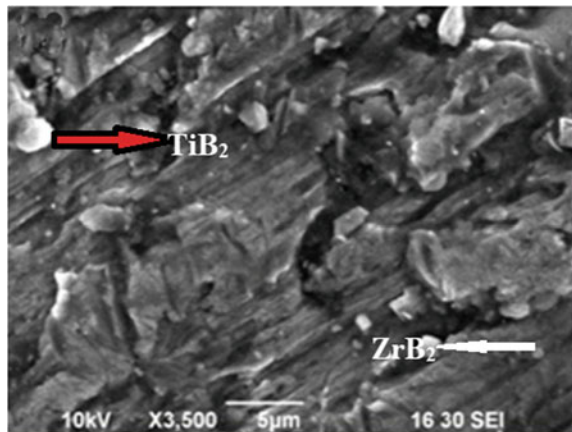
Fig. 1 EDAX of the composite

Fig. 2 Quantitative analysis of the composite

| Element	Net Counts	Weight %	Atom %
Al	204336	93.27	96.63
Ti	9442	4.31	2.60
Zr	5301	2.42	0.77
Total		100.00	100.00

Fig. 3 Microstructure of the composite

3   Experimental Work

A YB fiber laser machining setup is used (Meera Laser, Chennai) to carry out the experimental investigation. Speed of laser, laser power and standoff distance are chosen as machining parameters, whereas entry diameter, exit diameter and taper are preferred as responses. Factors and their level of the experimental work are presented in Table 1. Taguchi L_{27} layout is followed for experimental work. The other parameters are selected as follows: wave length is 1074 nm, pulse frequency is 20 Hz, and diameter of the beam is 50 µm. Entry diameter, exit diameter and taper are measured by using Metallurgical microspore (Metzer Optical Instruments Mathura, India) and reported. Some of holes made by laser machining process are exposed in Fig. 4.

Table 1 Laser parameters and their levels

Factors	Notation	Units	Levels		
Laser speed	LS	mm/sec	20	30	40
Laser power	LP	watt	80	85	90
Standoff distance	SOD	mm	194	195	196
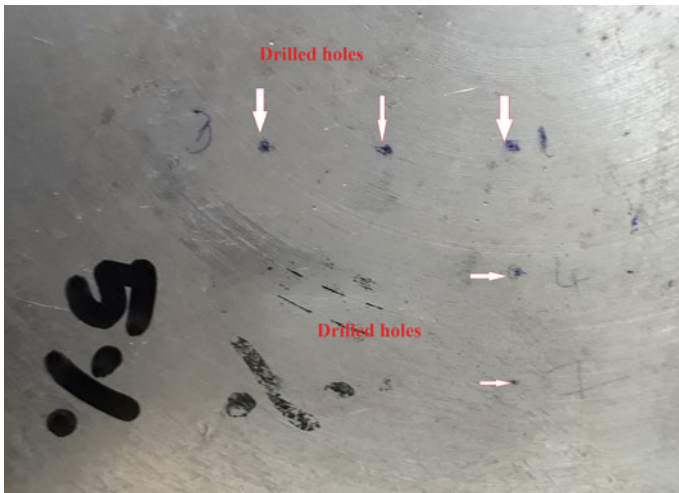
Fig. 4 Laser drilled holes

4   Results and Discussion

Grey relational analysis is applied to optimize the entrance diameter, exit diameter and taper in laser drilling of Al6061-5% TiB_2/ZrB_2 in situ composite. The deviation sequence and grey relational coefficient for entry diameter, exit diameter and taper are evaluated [14]. Grey relational grade value evaluated for each trail [14] and reported in Table 2.

It obvious from Table 2 the trial number 21 has the uppermost value of grey relational grade. Consequently, trail number 21 is optimal machining parameters among the 27 trails, which yields smallest entry diameter, exit diameter and taper in laser drilling composite. Response graph also generated for grey relational grade and illustrated in Fig. 5. As seen from Fig. 5, the laser power has the strongest influence on multi-performance characteristics than the laser speed and standoff distance. Further, higher level laser speed (A_3), lower level laser power (B_1) and higher level standoff distance (C_3) have maximum grey relational grade. Therefore, optimal level of parameters in laser drilling of AAl6061-TiB_2/ZrB_2 in situ composite can be given as A_3, B_1 and C_3. The analysis of variance also performed to categorize the significant parameters which influence multi-performance characteristics and presented in Table 3. It is seen from Table 3, the percentage of involvement of laser power is more when compared to laser speed and standoff distance. At higher laser speed, the entry diameter of the drilled hole is reduced, and consequently the interaction time is declined. Heat-affected zone in the region of the hole is minimized; therefore, entry diameter reduced [15]. A raise in laser speed also lessens the laser power availability to smack irradiated area. This effect accelerates the expulsion of small droplet of melt from the work piece; therefore, the way-out diameter of the drilled hole is minimized. At higher laser power, the heat supplied to the point of focus is relatively more. Excessive heat addition maximizes the thermal damage in the region of the hole, in turn increasing the diameter of the entry and exit of the hole. Hence, lower power is preferred to curtail the HAZ and attain the preferred dimensions [16]. As the standoff distance increases, the entrance diameter of the hole decreases. At higher standoff distance, the diameter of the beam is lowered. This effect diminishes the entry diameter of the laser drilled hole. The exit diameter is decreased by rising the standoff distance. It might be credited that the thermal stress on the composite is negligible at longer standoff distance. Thermal conductivity of aluminum and reinforcements are entirely different. The presence of reinforcement condenses the thermal conductivity and preserves the heat input for long time. Further, the melting point of the aluminium alloy is 650 °C, while the melting point of the TiB_2 and ZrB_2 reinforcements is 3230 and 3246 °C, respectively. Existence of larger deviation in the melting point of the aluminum alloy matrix and reinforcements leads to uneven in melting during machining. When the heat input is subjected to the composites, the aluminum will melt at beginning than the heat is carry forward until the melting of reinforcements. This effect maximizes the thermal damage and heat-affected zone. The thermal damage of the composites under laser speed of 40 mm/sec, laser power

Table 2 Grey relational analysis

S. no.	Levels			Responses			Deviation table			Grey relational coefficient			Grey relational grade	Order
	LS	LP	SOD	Entry (μm)	Exit (μm)	Taper (Rad)	Entry (μm)	Exit (μm)	Taper (Rad)	Entry (μm)	Exit (μm)	Taper (Rad)		
1.	1	1	1	307	157	0.299	0.433	0.568	0.572	0.567	0.432	0.428	0.515	11
2.	1	1	2	306	153	0.306	0.595	0.730	0.727	0.405	0.270	0.273	0.616	7
3.	1	1	3	305	152	0.305	0.909	0.753	0.701	0.091	0.247	0.299	0.714	4
4.	1	2	1	308	168	0.281	0.099	0.140	0.148	0.901	0.860	0.852	0.365	25
5.	1	2	2	307	163	0.288	0.240	0.311	0.317	0.760	0.689	0.683	0.413	20
6.	1	2	3	306	162	0.288	0.595	0.356	0.308	0.405	0.644	0.692	0.470	15
7.	1	3	1	308	171	0.274	0.000	0.001	0.009	1.000	0.999	0.991	0.334	27
8.	1	3	2	308	166	0.282	0.182	0.189	0.190	0.818	0.811	0.810	0.381	23
9.	1	3	3	306	166	0.281	0.515	0.203	0.150	0.485	0.797	0.850	0.421	19
10.	2	1	1	306	157	0.298	0.504	0.554	0.545	0.496	0.446	0.455	0.518	10
11.	2	1	2	306	153	0.305	0.708	0.730	0.709	0.292	0.270	0.291	0.637	6
12.	2	1	3	305	152	0.305	1.000	0.770	0.706	0.000	0.230	0.294	0.772	3
13.	2	2	1	307	167	0.281	0.193	0.158	0.153	0.807	0.842	0.847	0.375	24
14.	2	2	2	307	162	0.289	0.375	0.347	0.335	0.625	0.653	0.665	0.436	17
15.	2	2	3	306	161	0.289	0.708	0.406	0.345	0.292	0.594	0.655	0.507	13
16.	2	3	1	308	171	0.274	0.047	0.000	0.000	0.953	1.000	1.000	0.337	26
17.	2	3	2	307	166	0.283	0.275	0.208	0.195	0.725	0.792	0.805	0.393	22
18.	2	3	3	306	165	0.282	0.587	0.234	0.173	0.413	0.766	0.827	0.440	16
19.	3	1	1	306	151	0.310	0.532	0.802	0.818	0.468	0.198	0.182	0.655	5
20.	3	1	2	306	147	0.318	0.716	0.991	1.000	0.284	0.009	0.000	0.874	2
21*.	3*	1*	3*	305*	146*	0.317*	0.967*	1.000*	0.969*	0.033*	0.000*	0.031*	0.960*	1*
22.	3	2	1	307	161	0.292	0.240	0.392	0.408	0.760	0.608	0.592	0.435	18

(continued)

Table 2 (continued)

S. no.	Levels			Responses			Deviation table			Grey relational coefficient			Grey relational grade	Order
	LS	LP	SOD	Entry (μm)	Exit (μm)	Taper (Rad)	Entry (μm)	Exit (μm)	Taper (Rad)	Entry (μm)	Exit (μm)	Taper (Rad)		
23.	3	2	2	307	156	0.301	0.402	0.595	0.608	0.598	0.405	0.392	0.523	9
24.	3	2	3	306	158	0.296	0.716	0.541	0.495	0.284	0.459	0.505	0.552	8
25.	3	3	1	308	164	0.287	0.118	0.266	0.286	0.882	0.734	0.714	0.393	21
26.	3	3	2	307	159	0.296	0.322	0.487	0.500	0.678	0.513	0.500	0.473	14
27.	3	3	3	306	159	0.294	0.614	0.482	0.446	0.386	0.518	0.554	0.51	12

Main Effects Plot for SN ratios
Data Means

Signal-to-noise: Smaller is better
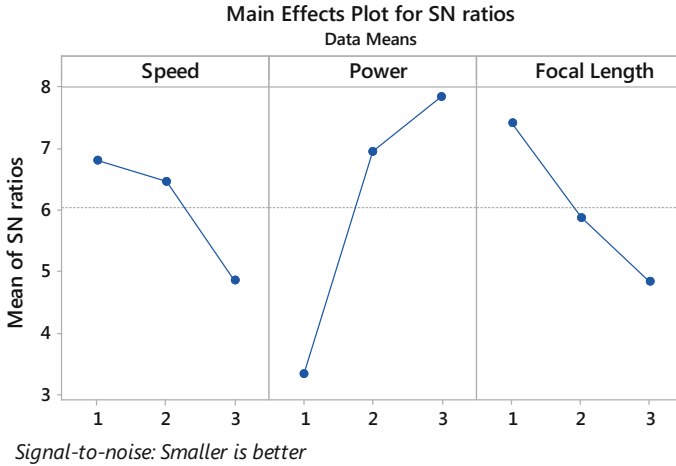
Fig. 5 Response graph

Table 3 Analysis of variance (ANOVA)

Source	DF	Adj SS	Adj MS	% of Contribution
Laser speed	2	0.084	0.042	13.33
Laser power	2	0.428	0.214	68.05
Stand off distance	2	0.112	0.056	17.85
Error	20	0.047	0.002	0.75
Total	26	0.673	0.315	100

of 80 W and standoff distance 196 mm is exposed in Fig. 6. The heat-affected zone and thermal damage induced by the heat input are designated in Fig. 6. At lower laser speed, the interaction time of the laser with workpiece is increased. Higher laser power maximizes the heat input to the machining zone [17]. Shorter standoff distance also enhances the heat influence to the workpiece. Therefore, the combination of the lower laser speed, higher power and shorter standoff distance maximizes the entry diameter, exit diameter and taper of the hole. Laser hole drilled by 20 mm/s laser speed, 90 W laser power and 194 mm standoff distance is displayed in Fig. 7. Wider heat-affected zone and more thermal damage are evident from Fig. 7, which indicates the influence of excessive heat input at the top of the hole.

A authentication test was conducted to confirm the multi-performance characteristics at the optimal level of the parameters. By using these levels of parameter, a couple of trails are conducted and the average value of the response is reported in Table 4. The approximate Grey relational grade (ζ) using the optimal level of the Laser parameters can be articulated as
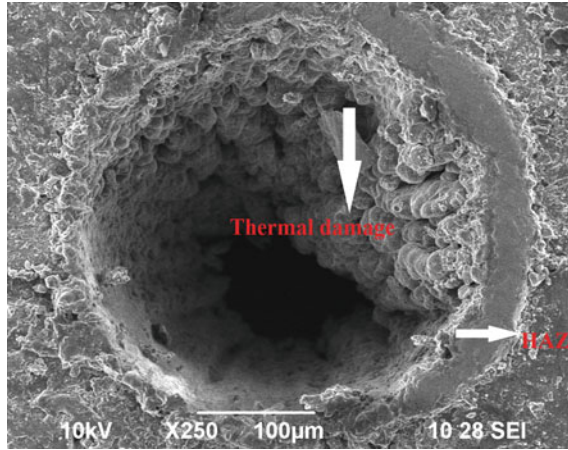
Fig. 6 Microscopic view of drilled hole (Trail 21)
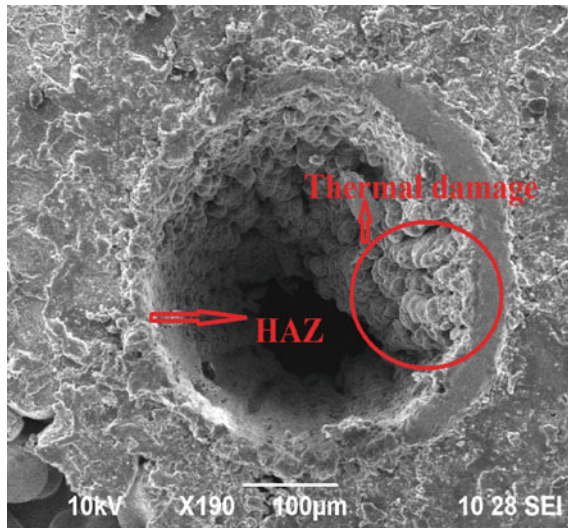
Fig. 7 Microscopic view of drilled hole (Trail 7)

Table 4 Result of confirmation test

Level	Initial machining parameters	Optimal machining parameters	
		Prediction (Eq. 1)	Experiment
Setting level	$A_1\ B_1\ C_1$	$A_3\ B_1\ C_3$	$A_3\ B_1\ C_3$
Entry diameter, μm	306.6	–	304.66
Exit diameter, μm	157	–	146.34
Taper, radians	0.2992	–	0.3166
Grey relational grade (GRG)	0.5145	0.9116	0.9596
Improvement in GRG	0.4450		

$$\zeta = \zeta_{\mathrm{m}} + \Sigma\,\zeta_{\mathrm{i}} - \zeta\,\mathrm{m} \tag{1}$$

$i = 1$ where 'ζ_{m}' is the entirety signify of the Grey relational grade, 'ζ_{i}' is the mean of the Grey relational rank at the optimal level, and 'q' is the numeral of laser parameters that considerably affect the multiple performance characteristics.

Table 4 depicts that the envisaged value acquired from Eq. (1) is 0.9116. The grade obtained from the confirmation experiment is 0.9596 with exit diameter 146.34 µm, entry diameter 304.66 µm and taper 0.31664 rad. There is 4.8% enhancement in the Grey relational grade over the predicted value. The enhancement in Grey relational grade is also evaluated by comparing the initial and optimal setting of the parameters and tabulated in Table 4. It is found from Table 4 the enhancement in the grey relational grade is 46.7% and evidently shows the upgrading in responses.

5 Conclusion

Multi-response optimization of process parameters in laser drilling of AA6061-TiB$_2$/ZrB$_2$ in situ composite using Grey relational analysis was discussed. From the result and analysis, the subsequent conclusions are drawn.

- Grey relational analysis method was successfully applied for the optimization of the laser parameters to progress the overall responses. Higher level laser speed (A_3), lesser level laser power (B_1) and higher level standoff distance (C_3) within the selected range have maximum Grey relational grade.
- The laser power has strongest persuade on the multi-performance characteristics than laser speed and standoff distance. Analysis of variance demonstrates that the laser power has 68.05%, standoff distance has 17.85%, and laser speed has 13.33% contribution on the multi-performance characteristics.
- The outcome attained from the authentication test is good agreement with experimental value and estimated value from the Grey relational analysis.
- This experimental investigation guides to choose the optimum laser drilling parameters in machining of AA6061-5% TiB$_2$/ZrB$_2$ composite. This Grey relational analysis can be applied to optimize the parameters of any machining operation with multi-performance characteristics.

References

1. Kaczmar, J.W., Pietrzak, K., Włosiński, W.: The production and application of metal matrix composite materials. Mater. Process. Tech. **106**, 58–67 (2000)
2. Aikin, R.M.: The mechanical properties of in-situ composites. JOM **49**, 35–39 (1997)
3. Stephena, A., Schrauf, G., Mehrafsuna, S., Vollertsenc, F.: High speed laser micro drilling for aerospace applications, Proc. CIRP **24**, 130–133 (2014)
4. Dhar, S., Nishant Saini, N., Purohit, R.: A review on laser drilling and its techniques. In: International Conference on Advances in Mechanical Engineering: pp. 1–3. AME (2006)
5. Padhee, S., Pani, S., S Mahapatra, S.: A parametric study on laser drilling of Al/SiCp metal-matrix composite. Eng. Manuf. **226**, 76–91 (2011)
6. Mishra, S., Yadava, V.: Modeling and optimization of laser beam percussion drilling of thin aluminum sheet. Opt. Las. Tech. **48**, 461–474 (2013)
7. Yue, T.M., Lau, W.S.: Pulsed Nd:YAG Laser cutting of Al/Li/SiC metal matrix composites. Mater. Manuf. Pro. **11**, 17–29 (1996)
8. Lau, W.S., Yue, T.M., Wang, M.: Ultrasonic-aided laser drilling of aluminum-based metal matrix composites. CIRP Ann. **43**, 177–180 (1994)
9. Ezeddini, S., Bayraktar, D.K.E., Miskioglu, I.: Laser cutting of the TiN + Al_2O_3 reinforced aluminium matrix composites through semisolid sintering. In: Mechanics of Composite and Multi-functional Materials. Springer International Publication (2018)
10. Sharma, V., Vinod Kumar, V.: Comparison of machining characteristics of metal matrix composites using CO_2 laser curve cutting process. https://doi.org/10.1177/0954408917710145 (2017)
11. Mahamani, A., Chakravarthy, A.V.V.: Investigation on laser drilling of AA6061-TiB_2/ZrB_2 in situ composites. Mater. Manuf. Proc. **32**, 1700–1706 (2016)
12. Šibalija, T.V., Majstorović, V.D.: Novel approach to multi-response optimization for correlated responses. FME Trans. **38**, 39–48 (2010)
13. Dai, J., Liu, X., Hu, F.: Research and application for grey relational analysis in multigranularity based on normality grey number. Sci. World J. (2014). https://doi.org/10.1155/2014/312645
14. Mahamani, A., Jayasree, A., Mounika, K., Reddi Prasad, K.,Sakthivelan, N.: Evaluation of mechanical properties of AA6061-TiB_2/ZrB_2 in-situ metal matrix composites fabricated by K_2TiF_6-KBF_4-K_2ZrF_6 reaction system. Micro. Mater. Prop. **10**, 185–200 (2015)
15. Mahamani, A., Muthukrishnan, N., Anandakrishnan, V.: Determination of optimum parameters for multi performance characteristic in turning of Al6061-6% ZrB2 in-situ metal matrix composite using Grey relational analysis. Manuf. Mater. Mech. Eng. **2**, 19 (2012)
16. Chien, W.T., Hou, S.C.: Investigating the recast layer formed during the laser trepan drilling of Inconel 718 using the Taguchi method. Adv. Manuf. Tech. **33**, 308–316 (2007)
17. Pak, A.M., Moradi, M.: Hole geometry features analysis in fiber laser percussion drilling process. Adv. Mech. Auto. Eng. **2**, 18–21 (2015)

Influence of Nanoparticles-Suspended Electrolyte on Machinability of Stainless Steel 430 Using Electrochemical Micro-machining Process

T. Geethapriyan, T. Muthuramalingam, S. Vasanth, J. Thavamani and Vignesh Hariharan Srinivasan

Abstract In this present work, the experimental studies have been carried out on the electrochemical micro-machining (ECMM) process of stainless steel 430 by varying the process parameters such as electrolyte concentration, applied voltage, micro-tool feed rate and duty cycle. Microscopic image and SEM analysis have been characterised in the ECMM process. Therefore, the micro-level hole has been produced in the stainless steel 430 for the applications of fuel injectors and medical equipments. The detailed study on the influence of nanoparticles-suspended electrolyte analyses the response measurements such as material removal rate, overcut, circularity and cylindricity. Of the two machining conditions, the copper nanoparticles-suspended electrolyte enhances the performance measures of the machining surface, increases localisation region and reduces the stray current effect, while obtaining a uniform circularity profile, higher material removal rate and lesser overcut due to its high electrical and thermal conductivity compared to the without nanoparticles suspended in the electrolyte. The experimental results indicate the influence of variations in the electrolyte concentration, and the duty cycle has been most significant parameters in the cutting condition for copper nanoparticles-suspended electrolyte by ECMM process.

Keywords Stainless steel 430 · Copper tool electrode · Copper nanoparticles Orthogonal machining · Taguchi method · SEM analysis

T. Geethapriyan (✉) · J. Thavamani · V. H. Srinivasan
Department of Mechanical Engineering, SRM University, Kattankulathur 603203, India
e-mail: devimani.priyan18@gmail.com

T. Muthuramalingam · S. Vasanth
Department of Mechatronics Engineering, SRM Institute of Science and Technology,
Kattankulathur 603203, India

1 Introduction

Electrochemical machining is the process of removing metal using an electro-chemical process. ECMM is carried out when difficulties occur in machining of miniature components and parts with conventional techniques. It is also one of the most precise techniques used. The experimental investigation indicates most effective zone of major process parameters such as applied voltage and concentration of electrolyte, giving the significant amount of material removal rate (MRR) with low overcut [1]. Machining voltage, micro-tool feed rate, concentration of electrolyte and duty cycle (input process parameters) have vital role in the ECMM process to evaluate the performance measures such as surface roughness, overcut and material removal rate in this study [2]. In ECMM process, the experiments are conducted based on L18 orthogonal array to find the effect of response parameters on material removal rate (MRR). The analysis of variance is performed to find out the percentage contribution of input process parameters on MRR. Among the assorted factors investigated, duty cycle is found to be the foremost important factor and contributes regarding 42% to the MRR because the duty cycle increases, and the pulse on time conjointly increases that contributes to a higher MRR [3]. The electrochemical micro-machining (ECMM) of stainless steel work-piece with acidified sodium nitrate. The sulphuric acid of 0.05 m/L is additional to the quality solution specifically sodium nitrate to solubilise by-products. The most significant characteristics of ECMM square measure researched through theme of experiments involving varied parameters like applied voltage, pulse on time and concentration of electrolyte. The performance measures are compared with that of sodium nitrate and acidified sodium nitrate on ECMM process [4]. Through this research, we hope to find out the effect of nanoparticles in ECMM.

2 Experimental Work

The experiment was conducted on the basis of Taguchi method. Based on this method, the number of trials to be conducted was calculated to be 9. Stainless steel 430 was chosen as the work piece and was cut into specimens of size 40 mm $\times$ 40 mm so as to fit inside the electrochemical machining machine. $NaNO_3$ solution was used as the electrolyte, for it is a non-passivating electrolyte. The tool chosen for machining was a copper tool of 0.4 mm diameter. Copper was chosen as the nanoparticle due to its high thermal and electrical conductivity. Copper nanoparticles reveal an awfully sturdy catalytic activity, a property that can be attributed to their massive chemical process extent. Copper nanoparticles that are very tiny and have a high surface-to-volume ratio also can function of antibacterial agents.

3 Results and Discussion

3.1 Analysing the Effect of Nanoparticles on MRR

Figure 1 shows that the material removal rate is increased on suspending the nanoparticles on the electrolyte. When the nanoparticles are suspended in the electrolyte, the overall electrical conductivity of the experiment increases which makes sure that material is being removed at a much faster rate.

The nanoparticle improves the process parameters due to its high conductivity and thus increases the accuracy of the machining. This is done because of the high electrical and thermal conductivity of the electrolyte. Another reason for better rate of removal is the metal ions of the nanoparticles. These ions hit the work piece during the machining process, thus improving the rate of machining.

3.2 Effect of Nanoparticles on Overcut

From Fig. 2, it can be seen that the use of nanoparticles has helped decrease the overcut when compared with the values of machining without the use of nanoparticles. The nanoparticle improves the process parameters due to its high conductivity and thus increases the accuracy of the machining. This is because the nanoparticles increase the electrical conductivity of the electrolyte when being suspended in it. When nanoparticles are suspended in the electrolyte, a thermal localised effect is induced; because of this effect, the accuracy of the machining process is better when compared to that without the use of nanoparticles. Lesser values of overcut prove that the use of nanoparticles provides higher degree of machining.
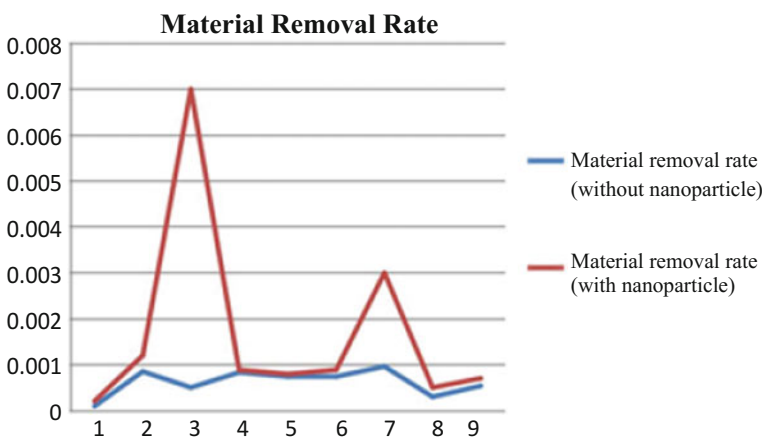

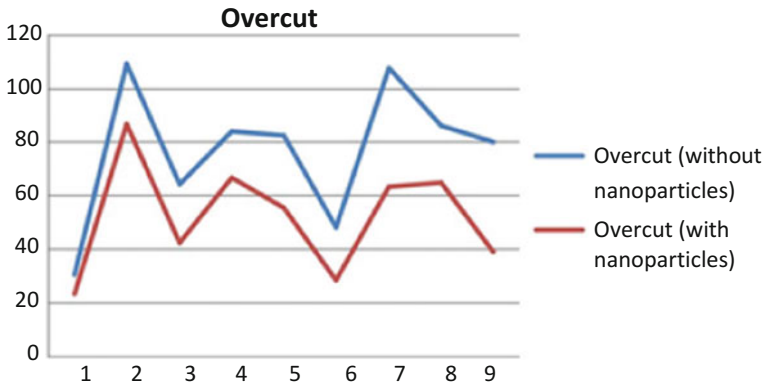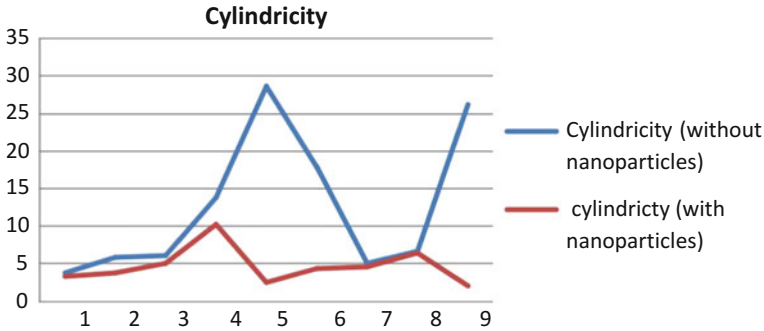**Fig. 1** Graph comparing MRR with and without nanoparticles

Fig. 2 Graph showing overcut with and without nanoparticles

3.3 Effects of Nanoparticles on Circularity

Figure 3 shows the influence of nanoparticles-suspended electrolyte. Tolerance zones are values which are closer to zero. When the nanoparticles are suspended in the electrolyte, the overall conductivity of the experiment increases. This is because during machining stray current effect is produced on the sides of the tool, in order to reduce the stray current effect the electrolyte concentration must be reduced so that the rate of machining occurs in a more accurate manner. The values which were acquired without the use nanoparticles-suspended electrolyte deviate further more from its tolerance zone.
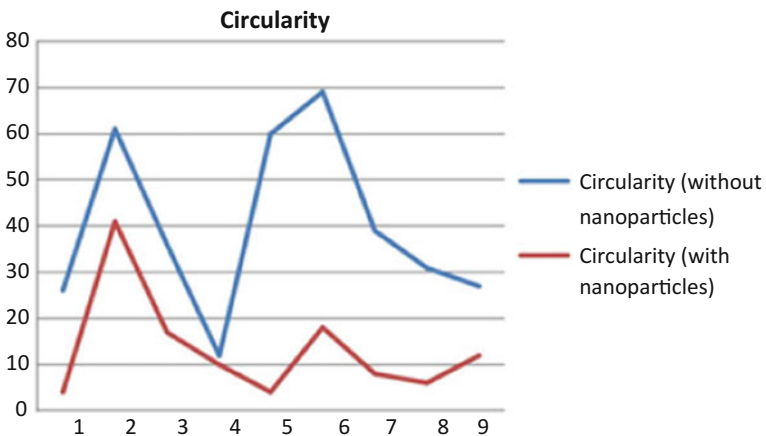
Fig. 3 Graph comparing circularity with and without nanoparticles

Fig. 4 Graph comparing cylindricity with and without nanoparticles

3.4 Effect of Nanoparticles on Cylindricity

Figure 4 shows the influence of nanoparticles-suspended electrolyte. From the graph, we could see that the variation in process parameters gives variation in the values of cylindricity. Closer values to the tolerance range mean accuracy in machining. The nanoparticles influence the process parameters which help in getting values closer to the tolerance range. This happens due to the localisation of current which occurs when nanoparticles are suspended. This increases the electrical conductivity of the experiment. This increase in electrical conductivity makes sure that the machining occurs at a much faster rate. This along with an optimal duty cycle gives a final output with faster rate of machining and a more accurate machining.

3.5 Effect of Nanoparticles on Machining Accuracy

From Fig. 5, it is seen that the accuracy of the machining process for the experiments is found to be less than the accuracy of the experiments which use nanoparticles. This is because when the nanoparticles are suspended in the electrolyte, the metal ions strike the surface of the workpiece and improves conduction. Localisation of current takes place by reducing the stray current effect, thereby directing current to one particular point on the workpiece. In the experiments which were conducted without the use of nanoparticles, the stray current effect is found to be relatively higher which reduces the precision during machining.
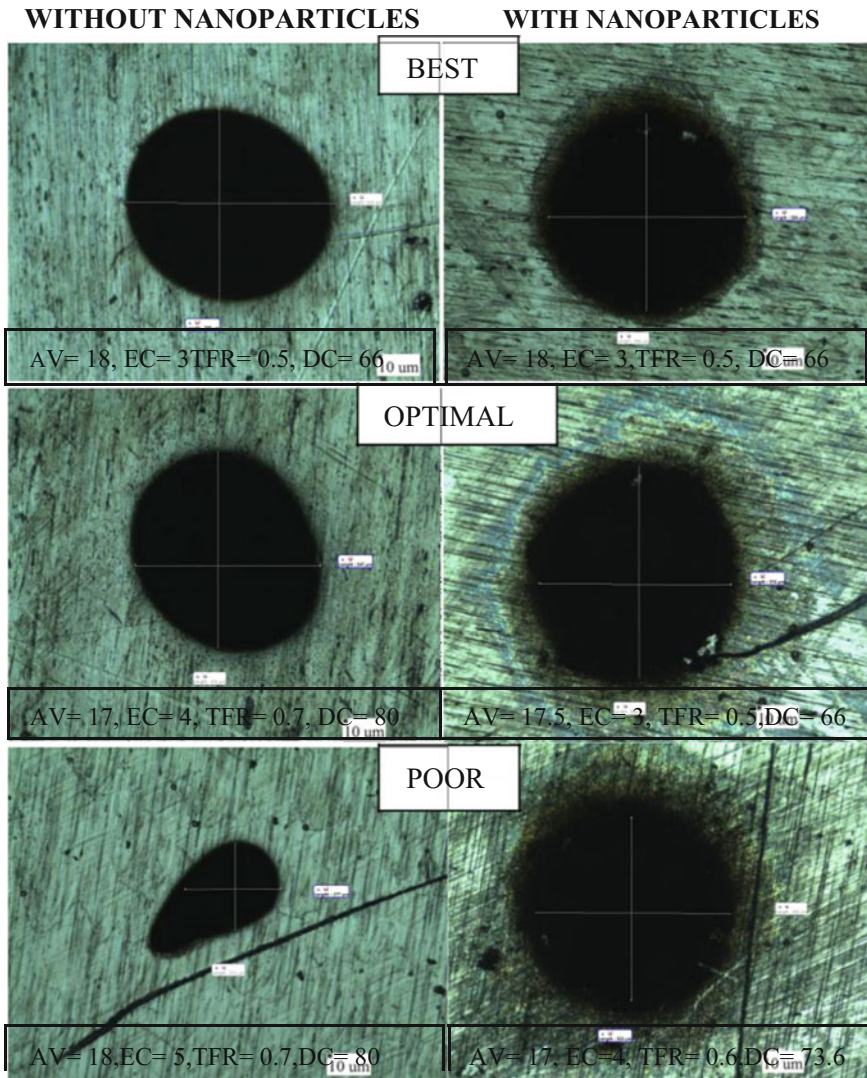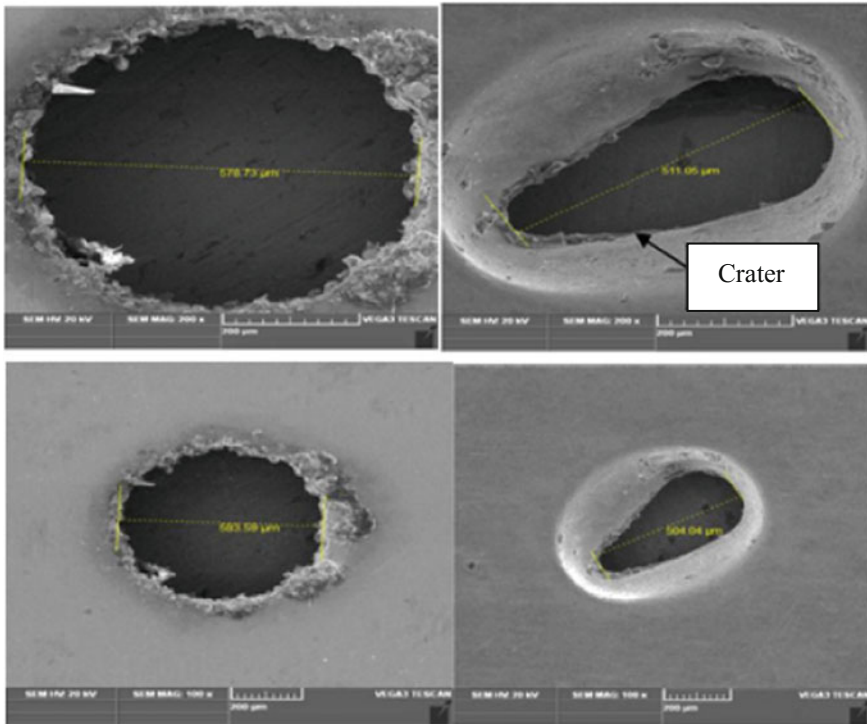
WITHOUT NANOPARTICLES   **WITH NANOPARTICLES**

BEST

AV= 18, EC= 3TFR= 0.5, DC= 66   AV= 18, EC= 3,TFR= 0.5, DC= 66

OPTIMAL

AV= 17, EC= 4, TFR= 0.7, DC= 80   AV= 17.5, EC= 3, TFR= 0.5, DC= 66

POOR

AV= 18,EC= 5,TFR= 0.7,DC= 80   AV= 17, EC= 4, TFR= 0.6,DC= 73.6

Fig. 5 Comparison of machining accuracy with and without nanoparticles

3.6 Scanning Electron Microscope

Figure 6 shows the images obtained from a scanning electron microscope with magnification of over 250×. The image is obtained by concentrating a beam of electrons over the surface of the work piece to obtain an image. The electrons interact with the work piece to produce a signal which helps in obtaining the topography of the surface. From the two images obtained, it can be clearly seen that

Fig. 6 SEM image of workpieces

the hole that is machined by suspending the nanoparticles in the electrolyte is more accurate than the one where there is no nanoparticle.

In machining process without nanoparticles, it can be seen that the formation of clatter occurs along the sides of the machined region. By suspending nanoparticles in the electrolyte, we can see that the formation of such defects does not occur due to presence of metal ions and localisation of current, thus increasing the level of machining.

4   Conclusion

- The MRR obtained from the experiments using nanoparticles is better than those experiments without the presence of nanoparticles. The presence of nanoparticles increases the electrical conductivity, and the metal ions of those particles strike the surface of the work piece and increase the rate of material removal.
- The circularity, cylindricity and overcut are found to be more in the experiments without nanoparticles as the conductivity is lesser when compared to the

experiments with nanoparticles. The nanoparticles help in localising the current in a particular direction towards the surface of the work piece by reducing the stray current effect and thereby improving machining.

- By suspending nanoparticles in the electrolyte, the surface of the work piece becomes free of corrosion, chemical reactions and crater formation when compared to the work pieces without nanoparticles suspended in the electrolyte.

References

1. Bhattacharyya, B., Doloi, B., Sridhar, P.S.: Electrochemical micro-machining: new possibilities for micro-manufacturing. J. Mater. Process. Technol. **113**(1–3), 301–305 (2001)
2. Geethapriyan, T., Kalaichelvan, K., Muthuramalingam, M.: Performance analysis of process parameters on machining α–β titanium alloy in electrochemical micromachining process. J. Eng. Manuf. 1–13 (2016)
3. Saravanan, D., Arularasu, M., Ganesan, K.: A study on electrochemical micromachining of super duplex stainless steel for biomedical filter. Proc. CIRP 6 **7**(5), 116–122 (2012)
4. Thanigaivelan, R., Arunachala, R., Karthikeyan, B.: Electrochemical micromachining of stainless steel with acidified sodium nitrate electrolyte. Int. J. Appl. Eng. Res. **6**, 351–355 (2013)

Influence of Tool Electrodes on Machinability of Stainless Steel 420 Using Electrochemical Micromachining Process

T. Geethapriyan, Poovazhagan Lakshmanan, M. Prakash, U. Mohammed Iqbal and S. Suraj

Abstract The machining of stainless steel 420 using conventional machining techniques creates many problems such as tool wear, poor surface roughness, lesser dimensional accuracy and high heat-affected zone. These problems can be overcome by non-conventional machining techniques like ECM, EDM, LBM, PAM. Even in some non-conventional machining techniques, problems such as mechanical stress, heat-affected zone still prevail. Electrochemical machining (ECM) is a technology where there is no heat-affected zone and no thermal stresses. ECM uses the same principle of electrolysis for its operation. Using ECM difficult to machine materials can be machined which is almost impossible by conventional machining methods. Micromachined stainless steel 420 finds the application in the modification of implants in biomedical field. In this present work, the experiment has been conducted to study the machinability of stainless steel 420 using electrochemical micromachining process. The influence of two different tool electrodes (copper and brass) in micromachinability by varying process parameters such as applied voltage, electrolyte concentration, microtool feed rate and duty cycle using Taguchi method. The responses such as Material Removal Rate, Surface Roughness and Radial Overcut are analyzed using gray relational analysis. It is observed that the copper tool electrode has removed 20.91% more material than brass tool electrode; the surface roughness of brass tool electrode has produced 23.62% less than the copper tool electrode; and the radial overcut of copper tool electrode has generated 29.65% more than the brass tool electrode.

Keywords Stainless steel 420 · Copper and brass tool · $NaNO_3$
Optimization · Orthogonal machining · Taguchi–gray method

T. Geethapriyan (✉) · M. Prakash · U. Mohammed Iqbal · S. Suraj
Department of Mechanical Engineering, SRM University,
Kattankulathur 603203, India
e-mail: devimani.priyan18@gmail.com

P. Lakshmanan
Department of Mechanical Engineering, SSN College of Engineering, Chennai 603203, India

1 Introduction

Electrochemical micromachining is used for applications where only a small part is getting machined. It is nothing but electrochemical machining with all of its parameters is stepped down for required material removal rate. It uses a microtool for microlevel machining. Electrochemical machining (ECM) is a technology where there are no heat-affected zone and no thermal stresses.

The working of ECM is based on the principle of Faraday's laws of electrolysis. Michael Faraday stated two laws which are as follows

1. The first law states that the amount of any material dissolved or deposited is directly proportional to the quantity of electricity passed.
2. The second law states that the amount of change produced in the material is proportional to its electrochemical equivalent of the material.

Electrochemical micromachining has been done on various materials, but only very few research works have been done by using stainless steel 420 as the workpiece.

Moreover, the material used as workpiece in our experiment is stainless steel 420. It is selected based on many factors, and one of them is that it is a hard material; despite its advantages, only a very few papers have used this material and they are not electrochemical machining so taking these into account we chose this as our workpiece. The main tools used in ECMM are copper and brass, and hence, analyzing both the tools will give us clear knowledge of which tool has more advantages [2].

The main application of the workpiece material is in the body modification implants, and it is also used in surgical equipments where a sharp cutting edge is required. In case of any fractures, the holes in the body modification implants were mechanically drilled and they tend to develop mechanical cracks which lead to weakening of the structure of the implant, but when we use electrochemical micromachining to drill holes, the problem of mechanical cracks can be eliminated [3].

1.1 *Consturction*

A fundamental ECMM setup has the following part such as DC power supply unit that is also used to power the electrodes as well. Then, the controller, tool driving unit, electrolyte chamber, sludge filter, electrolyte tank, pump, filter, tool feedback unit (Fig. 1).
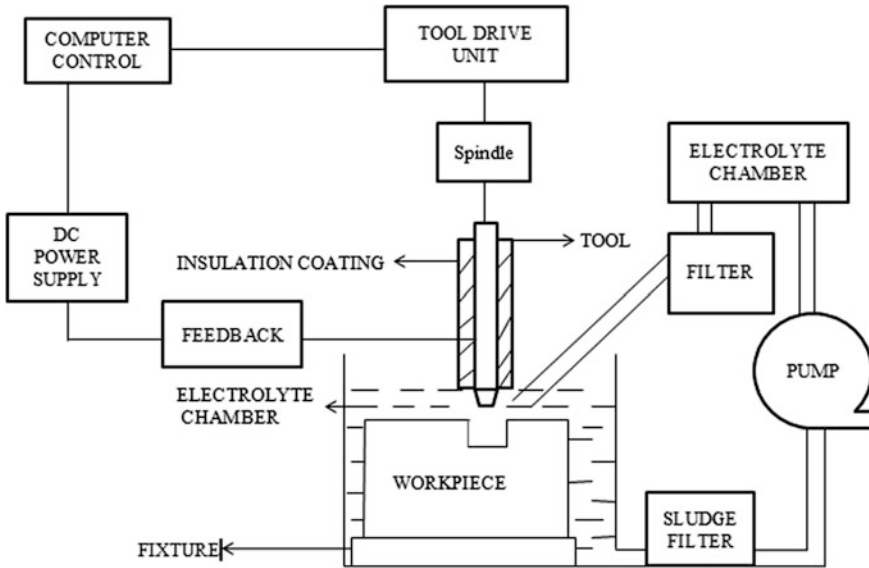
Fig. 1 Schematic diagram of ECMM setup

1.2 Working Process

The machine setup consists of a regulator that regulates power supply by controlling various parameters such as applied voltage, current, pulse-on and pulse-off time. It also consists of a The ECMM setup has the following parts in its system they are:

- Tool feed control
- Electrolyte bath containing tool and workpiece
- Pump
- Filter

Tool feed control in the system is used to control the tool movement toward the workpiece. For every three rotations given to the rod-connecting tool holder and the top slab the tool moves one millimeter. A constant feed should be given to maintain interelectrode gap.

Electrolyte bath containing tool and workpiece give the picture of tool and electrode immersed in the bath of electrolyte when the machining process is carried out.

Pump is used to transfer the electrolyte from electrolyte chamber to the filter; it is powered by a electric motor inside.

Filter is used to remove the contaminants from electrolyte. When electrolyte is pumped to filter, the filter containing tiny pores stops the particles and allows only the liquid with the salt dissolved in it to pass through (Fig. 2).

Fig. 2 Machining of workpiece

2 Objective

To identify the effect of process parameter on electrochemical micromachining of Stainless steel 420.

To find the influence of various characteristics of tools on the response parameters such as Material removal rate, Surface roughness, Overcut.

To analyze the effect of copper and brass tool electrodes on electrochemical micromachining of Stainless steel 420 [1].

3 Experimental Design

3.1 Workpiece Selection

The material used as workpiece in our experiment is stainless steel 420. It is selected based on many factors, and one of them is that it is a hard material; despite its advantages, only a very few papers have used this material and they are not electrochemical machining so taking these into account we chose this as our workpiece. The composition of stainless steel is stainless steels do not corrode in normal environment as it has a passive layer of chromium oxide protecting the

Table 1 Composition of stainless steel 420

Element	C	Si	Mn	P	S	Cr	Fe
Composition (%)	0.18	0.55	0.57	0.018	0.029	12.579	86.093

surface from forming iron oxides and then get peeled away. But it is not fully corrosion proof in high salinity conditions or poor air circulation environment (Table 1) [4].

3.2 Tool Selection

Copper

Copper has good thermal and electrical conductivity, and it offers corrosion resistance. It can be easily machined, and it is stiff enough to withstand the electrolytic pressure without vibrating and it is available at an economically viable cost.

Brass

Brass has good thermal and electrical conductivity, and it has electrical conductivity slightly lower than copper. It offers corrosion resistance, and it can be easily machined.

It is stiff enough to withstand the electrolytic pressure without vibrating, and it is available at an economically viable cost.

3.3 Electrolyte Selection

The electrolyte selected for our experiment is aqueous $NaNO_3$ solution. Maximum feed rate can be achieved with sodium nitrate electrolyte. Sodium nitrate is more advantageous than the other electrolytes due to its lower throwing power, and high and controlled metal removal, which leads to high speed and accuracy in machining [6].

3.4 Selection of Process Parameters

3.4.1 Applied Voltage

The voltage applied for the electrochemical micromachining is 3–10 V. A voltage less than 5 V would lead to a very large time-consuming process, and the voltage higher than the mentioned level means macromachining.

3.4.2 Current

The current used in electrochemical micromachining is 1–5 A. A current less than 1 A means very slow processing and a current above that means macromachining.

3.4.3 Electrolyte Concentration

The electrolyte concentration can be taken from 10 to 200 g/L maximum. A concentration less than this means the electrolyte is poor conductor and a higher concentration cannot be sustained by water as it has limit for being a solution.

3.4.4 Duty Cycle

The duty cycle used in the ECM process is in the range of 10–90%. If a duty cycle value is given less than 10%, it will not undergo machining and a duty cycle above 90% is impossible for pulsed power supply unit [7].

4 Results and Discussion

4.1 Material Removal Rate

By dividing the machining time of each workpiece from the corresponding volume of material removed, the material removal rate for each workpiece can be calculated (Fig. 3).

4.1.1 Analyzing the Effect of MRR with Copper and Brass Tool

From these graphs it is inferred that when applied voltage and current increase along with them, MRR also increases and similar relation is also displayed for duty cycle. But for the electrolyte concentration, it increases for a certain level and then decreases after reaching a high MRR. This type of reaction by parameters for brass tool is observed (Fig. 4) [8].

In terms of applied voltage slight variations are observed as the graph suggests that a steady increase in MRR is observed with the steadily increasing applied voltage, whereas in terms of current it is similar to that of the brass graph. In the graphs of electrolyte concentration, it is different to that of brass as the line keeps going upward, and at maximum concentration, maximum MRR is achieved and with respect to duty cycle 50% is proven to be the optimum negative value and 40% has the higher MRR. It shows more variations to that of the brass tool.
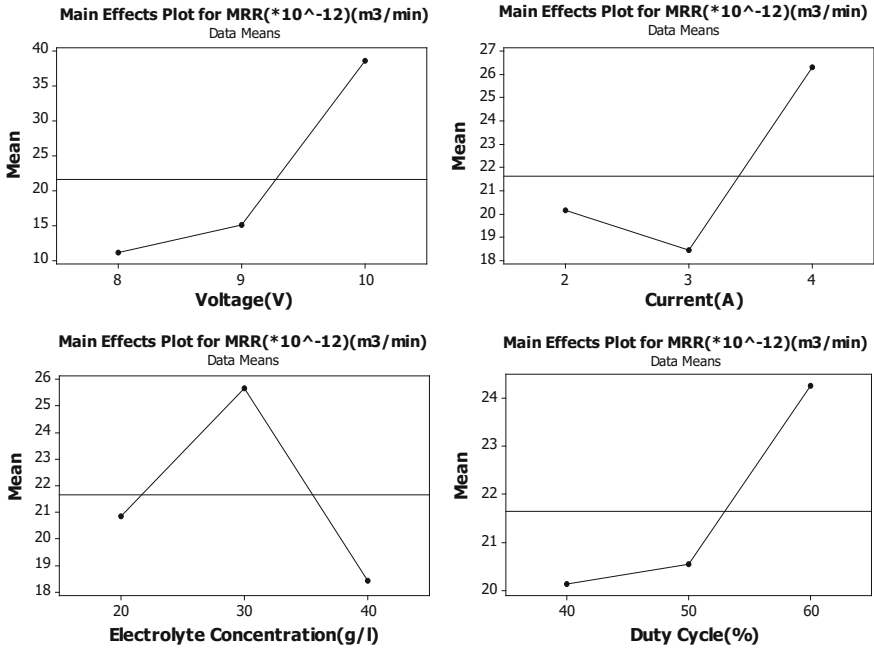
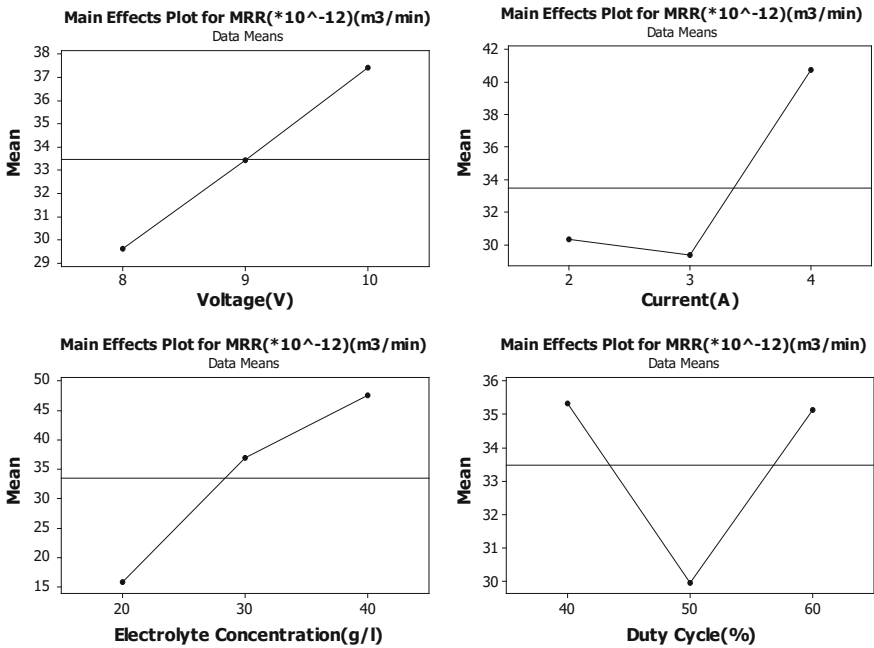**Fig. 3** Main effects plot for MRR using brass tool

Fig. 4 Main effects plot for MRR using copper tool

Overall, copper has better metal removal rate to that of the brass tool as it makes use of the conductive property for its advantages. Overall, copper has better metal removal rate to that of the brass tool as it makes use of the conductive property for its advantages.

4.2 Effect of Tool Electrodes on MRR

Series 1 curve represents the MRR of copper, and Series 2 curve represents the MRR of brass. From the graphs, it is evident that series 1 curve dominates the graph with most of the values being higher than series 2 curve, i.e., brass curve (Fig. 5).

4.3 Effect of Process Parameters on Surface Roughness for Copper and Brass Tool

When it comes to surface roughness, the one with the lower value is always preferred because the surface that is smooth is the one to be preferred because of better properties of smooth surface due to lower friction. The graphs show that with respect to applied voltage surface roughness increases, but in a nonlinear fashion, for current it is almost a straight line that means that with respect to increasing current surface roughness increases because of material removal. In terms of electrolyte concentration, it reaches a peak at the second stage, and at final value, it reaches the lowest value meaning that the electrolyte concentration must be increased for better surface roughness (Figs. 6 and 7).

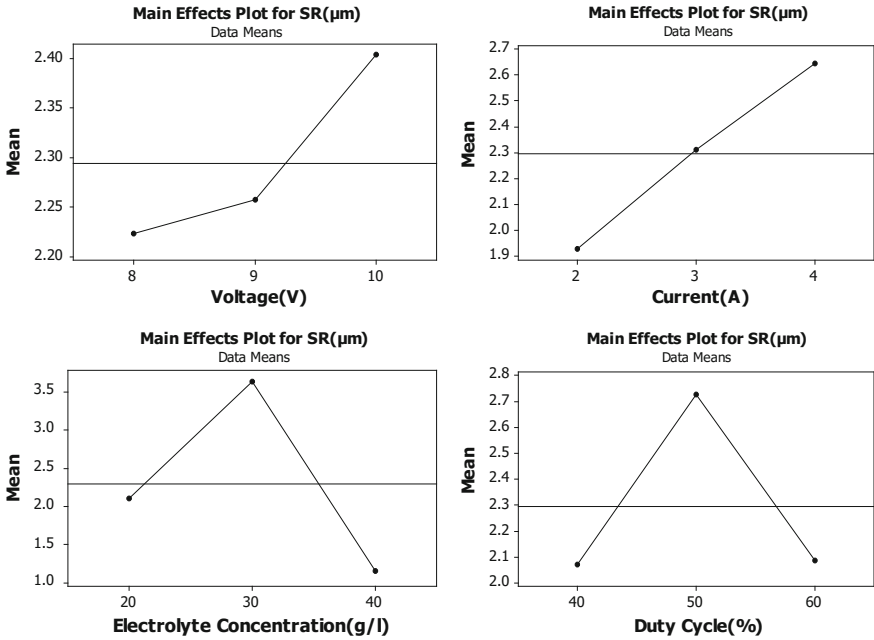**Fig. 5** Plot for MRR using copper and brass tool
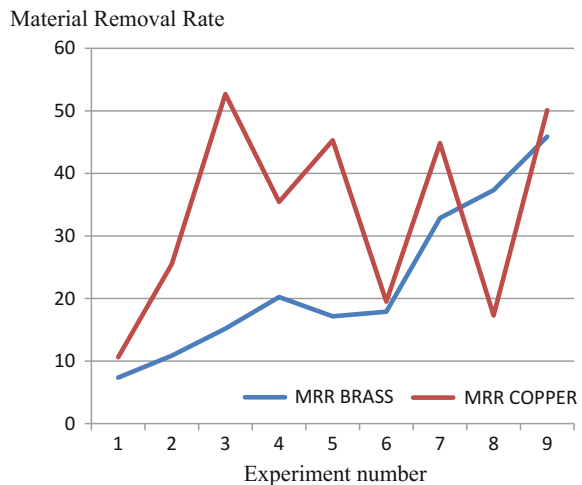
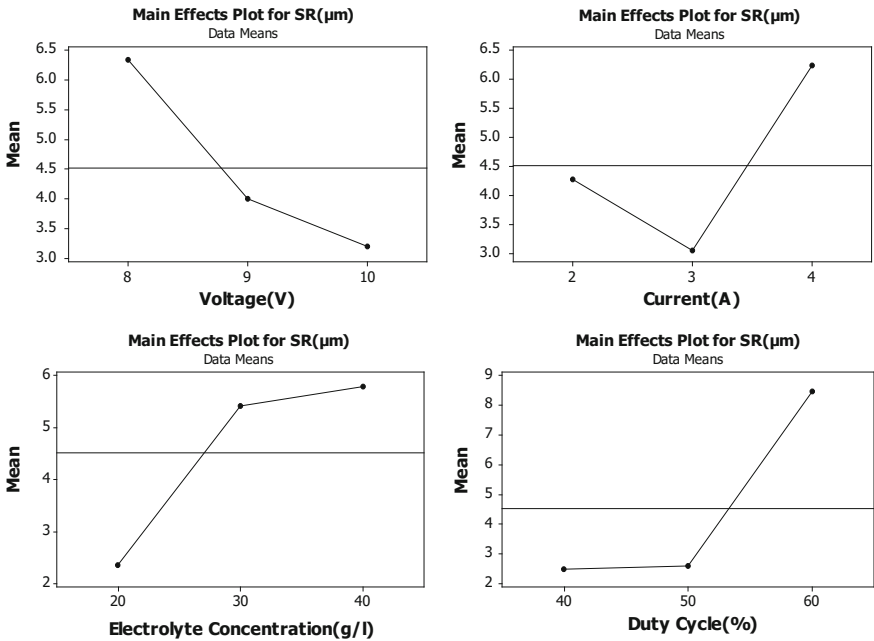Fig. 6 Main effects plot for SR using brass tool

Fig. 7 Main effects plot for SR using copper tool

When brass has lower conductivity, copper has better conductivity; various results are being influenced by their properties. In the above given graph, it shows that increase in applied voltage surface roughness decreases which is quite contrast to that of the brass graph for the same. For current, it reaches a low at 3 A and then increases drastically showing us the optimum point for better surface roughness. In terms of electrolyte concentration, surface roughness increases with respect to electrolyte concentration [9].

4.4 Overcut

Overcut can be defined as the difference between tool size or required size and the size that was actually obtained. The overcut for our specimen can be measured by using metallurgical microscope, and the difference between tool size (400 µ) can be calculated (Fig. 8).

For overcut, there is no constant increase with respect to that of other parameters; it shows deviations with applied voltage and current in a directly opposite way. When current increase overcut decreases, opposite happens to that of the applied voltage. Overcut is at its peak for the electrolyte concentration of 30 g/L, and it is least for 20 g/L in terms of duty cycle lowest overcut is observed at 50% duty cycle and maximum at 60%.
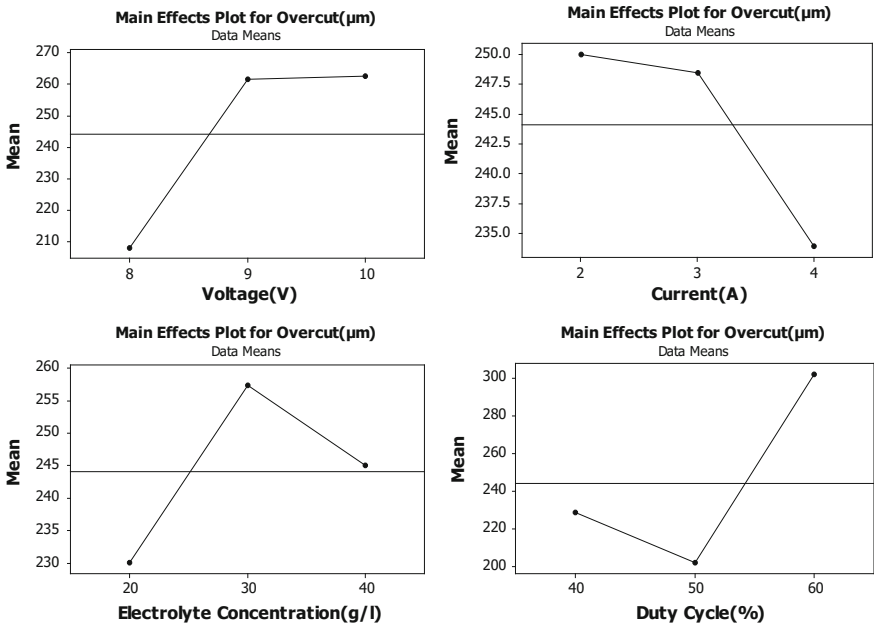

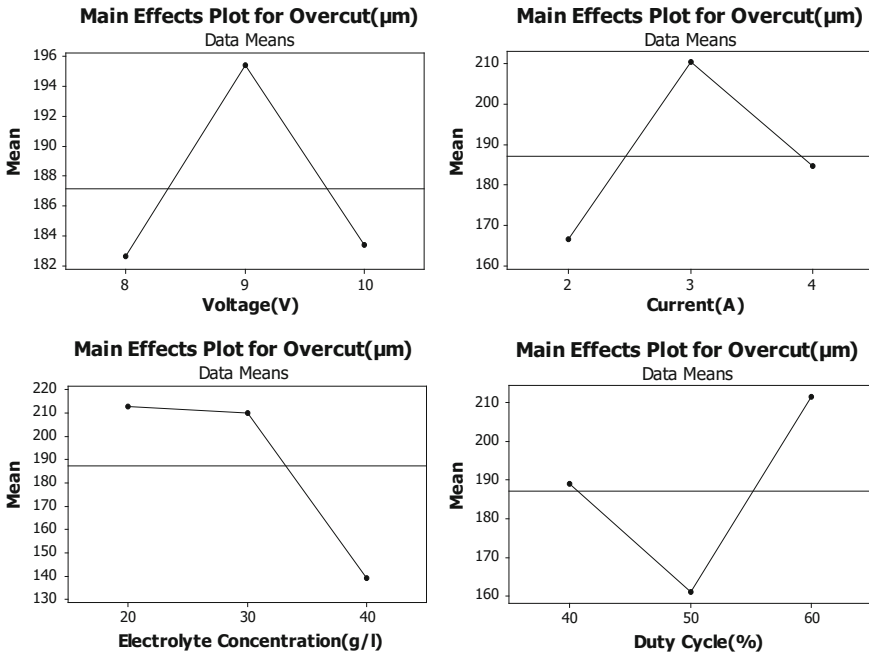**Fig. 8** Main effects plot for ROC using brass tool

Fig. 9 Main effects plot for ROC using copper tool

The overcut reaches its max. at 9 V, it has its lowest at 8 V, and a similar kind of behavior is observed for current which gives maximum overcut at its second stage and the lowest at its first value which is the same sequence for the applied voltage. When it comes for electrolyte concentration, the overcut decreases with increasing electrolyte concentration in a nonlinear fashion. The duty cycle of the system influencing the overcut has the lowest value at its value of 50% and has the maximum overcut at its maximum duty cycle (Fig. 9).

4.5 Effect of Tool Electrodes on ROC

The radial overcut graph has the similar effect to that of previous tables. In this graph, series 1 curve represents brass and series 2 curve represents copper. Again copper dominates the graph with higher values, i.e., copper produces higher overcut than graph (Fig. 10).

4.6 SEM Analysis of Specimens

SEM (scanning electron microscope) is a type of electron microscope that uses a focused electron beam to produce images.

Fig. 10 Plot for ROC using copper and brass tools
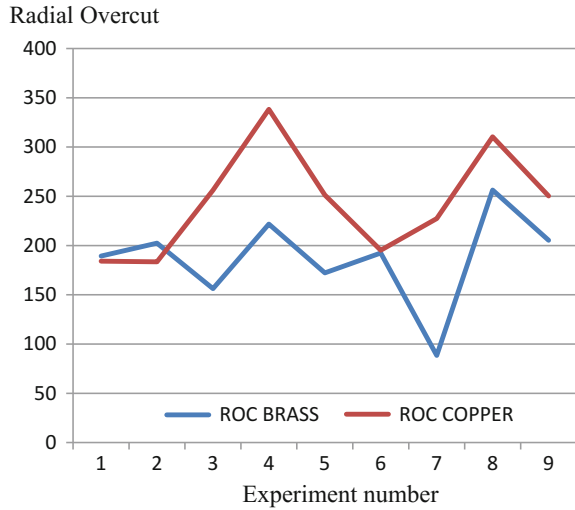
4.6.1 With Brass Tool

The specimen mentioned above B1 has the parameters from the DOE that has the applied voltage of 8 V and 2 A current and an electrolyte concentration of 20 g/L and a duty cycle of 40%. The image shows that scratches are coming out of the machined portion and the center of portion has small blunts and tiny holes in them and a small line of scratch on the right side, and the overall shape is somewhat an irregular oval shape (Figs. 11 and 12).

The specimen mentioned above B7 has the parameters from the DOE that has the applied voltage of 10 V and 3 A current and an electrolyte concentration of 40 g/L and a duty cycle of 50%. The image shows that scratches are coming out of the machined portion and the center of portion has small blunts and tiny holes in them and it also has some of the scratches in the center. It has a dark zone in the top left side, and the overall shape is round.

4.6.2 For Copper Tool

The workpiece C2 is the first workpiece to be worked, and it follows the first set of parameters from the DOE. The parameters are applied voltage 8 V, current 2 A, electrolyte concentration 20 g/L and the last parameter duty cycle 40%. The image shows blunts and tiny holes in them, but the number of scratches is more and it has two black dark spots in the machined portion and the shape of the machined zone is mostly circular and it also has a layer of machined zone outside the focused part or the machined part (Figs. 13 and 14).
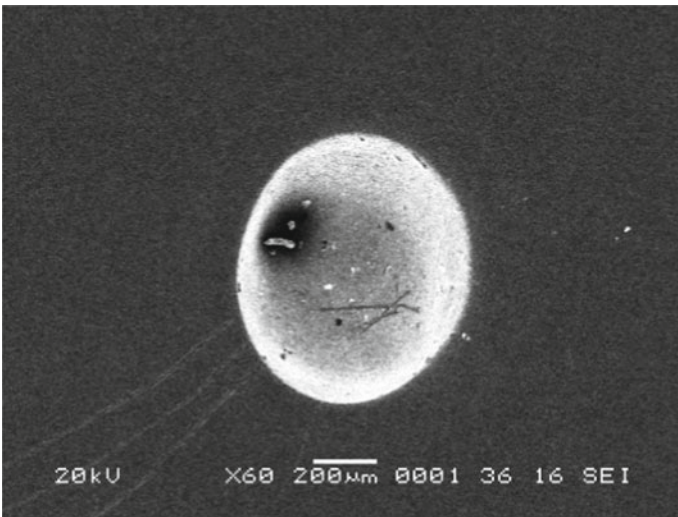
The workpiece C3 is the second workpiece to be worked, and it follows the second set of parameters from the DOE. The parameters are applied voltage 8 V,
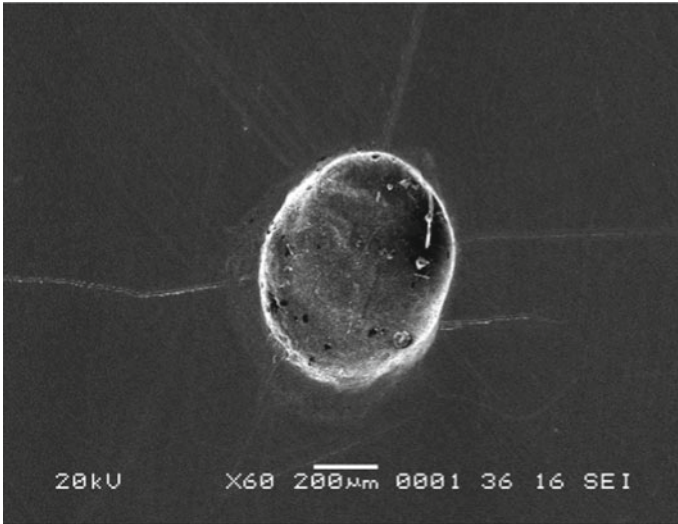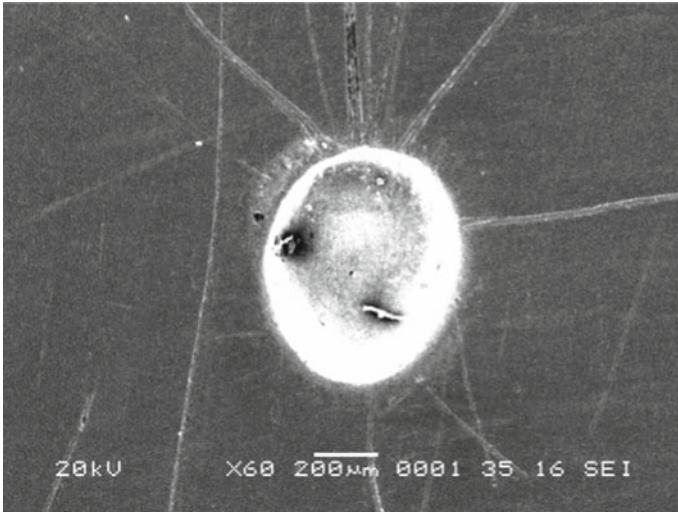
8V – 2A – 20g/l – 40%

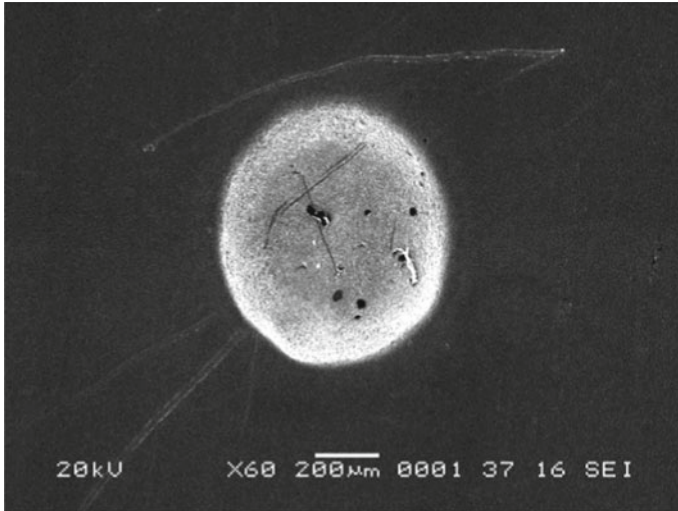**Fig. 11** SEM image of less accuracy surface with brass tool

10V – 2A – 40g/l – 50%

Fig. 12 SEM image of better surface with brass tool

8V – 2A – 20g/l – 40%

Fig. 13 SEM image of less accuracy surface with copper tool

8V – 3A – 30g/l – 50%

Fig. 14 SEM image of better surface with copper tool

current 3 A, electrolyte concentration 30 g/l and the last parameter duty cycle 50%. The image shows that scratches are coming out of the machined portion and the center of portion has small blunts and tiny holes. Overall shape of the machined zone is circular, and it seems to be smoother than the other specimens [5].

5 Conclusion

By varying input parameters we have found and discussed the influence of various input parameters as well as the characteristics of the tool. All the above results and discussions show that copper has better material removal rate than brass as it has the highest amount of electrical and thermal conductivity and it is the best tool for ECM. Results show that copper has more material removal rate compared to brass, while brass on the other hand has a good conductivity second only to copper. Combining all the other properties for the optimum response like a good surface smoothness as copper-machined surfaces are more rough than brass-machined surfaces. The copper-machined surfaces have more radial overcut than brass-machined surfaces. Despite the advantages of copper such as more conductivity and chemically inert nature of copper, brass has some chemical advantages that improves all those properties as it is an improved alloy of copper and it can be called as the best tool for electrochemical micromachining (ECMM). The final output comparison between brass tool and copper tool is pointed below.

Material Removal Rate of copper tool-machined samples is 20.91% more than brass tool-machined samples.
Surface roughness of brass tool-machined samples is 23.62% less than copper tool-machined samples.
Radial overcut of copper tool-machined samples is 29.65% more than brass tool-machined samples.

References

1. Bhattacharyya, B., Mitra, S., Boro, A.K.: Electrochemical machining: new possibilities of micromachining. Rob. Comput. Integr. Manuf. **18**, 283–289 (2002)
2. Bhattacharyya, B., Malapati, M., Munda, J., Sarkar, A.: Influence of tool vibration on machining performance in electrochemical micro-machining of copper. Int. J. Mach. Tools Manuf. **47**, 335–342 (2007)
3. Bhattacharyya, B., Munda, J., Malapati, M.: Advancement in electrochemical micro-machining. Int. J. Mach. Tools Manuf. **47**, 335–342 (2007)
4. De Silva, A.K.M., Altena, H.S.J., McGeough, J.A.: Precision ECM by Process Characteristic Modelling. Department of Engineering, Glasgow Caledonian University, Cowcaddens Road, Glasgow, UK (2000)

5. De Silva, A.K.M., Altena, H.S.J., McGeough, J.A.: Influence of Electrolyte Concentration on Copying Accuracy of Precision- ECM. School of Engineering Science & Design, Glasgow Caledonian University, UK
6. Dharmalingam, S., Marimuthu, P., Raja, K., Pandyrajan, R., Surendar, S.: Optimization of process parameters on MRR and overcut in electrochemical micro machining on metal matrix composites using grey relational analysis. Int. J. Eng. Technol. (IJET) **6**(2), 975–4024 (2014)
7. Gowri, S., Ranjith Kumar, P., Vijayaraj, R., Balan, A.S.S.: Micromachining: technology for the future. Int. J. Mater. Struct. Integrity **1**(1–3) (2007)
8. Kozak, J., Rajurkar, K.P., Makkar, Y.: Selected problems of micro-electrochemical machining. J. Mater. Process. Technol. **149**, 426–431 (2004)
9. Kozak, J., Rajurkar, K.P., Makkar, Y.: Study of Pulse Electrochemical Micromachining. Center Nontraditional Manuf. Res., J. Manuf. Process. **6**(1) (2004)

Parametric Optimization of Abrasive Water jet Machining Process on Inconel 600 Using Two Different Abrasive Grain Sizes

T. Geethapriyan, R. Manoj Samson, A. C. Arun Raj, S. Senkathi and C. Gunasekar

Abstract Abrasive water jet machining is one of the widely used unconventional machining processes to machine complicated shapes for difficult-to-machine materials like titanium alloy, Inconel, alloy steel, tool steel, marble. Inconel 600 is used as a material for machining considering its applications for engine seal of the rocket engine, marine, aerospace industries. In this present work, the predominant process parameters like pressure, abrasive flow rate, transverse speed, and stand-off distance which are varied to obtain optimum values of response parameters like material removal rate and surface finish. Since the multi-response optimization cannot be performed by conventional Taguchi method, it has performed with Grey–Taguchi methodology. Pressure and stand-off distance are the most influence process parameters to obtain the higher MRR and better surface finish. Finally, the results indicate that the abrasive grain size of 100 mesh for machining Inconel 600 has produced higher MRR and better surface finish than the abrasive grain size of 80 mesh. The optimized results attained from this grey relational approach indicate that higher MRR and lower surface roughness were achieved with the process parameters' combinations such as pressure of 275 Mpa, mass flow rate of 0.24 kg/min, transverse speed of 150 mm/min, and stand-off distance of 3 mm. The experimental results show that the multi-response performance of the Inconel 600 used in the electrochemical micro-machining process has been enhanced through the grey relational approach.

Keywords Inconel 600 · AWJM · Two different abrasive grain sizes Orthogonal machining · Taguchi–Grey method

T. Geethapriyan (✉) · R. Manoj Samson · A. C. Arun Raj · S. Senkathi · C. Gunasekar
Department of Mechanical Engineering, SRM University, Kattankulathur,
Chennai 603203, India
e-mail: devimani.priyan18@gmail.com

1 Introduction

Water jet machining (WJM) perhaps energy-based non-traditional machining methodology accustomed machining soft and non-metallic materials. It involves the employment of high-speed water jet to smoothly cut a soft work piece. It is like abrasive jet machining (AJM). In water jet machining, high-speed water jet is allowed to hit a given work piece. Throughout this method, its K.E. is regenerated to pressure energy [1]. This induces a stress on the specimen. Once this stress is high enough, unwanted particles of the piece of work unit of measure are automatically removed [2].

Abrasive water jet machining (AWJM) unit of activity unconventional machining processes. They belong to mechanical cluster of unconventional processes such as ultrasonic machining (USM) and abrasive jet machining (AJM). In these processes, the energy of water and abrasive phase unit of activity would not deliver the good material removal or machining [3]. AWJM will be achieved mistreatment completely different approaches and methodologies as enumerated below: AWJM—entrained—three part—abrasive, air and water AWJM—suspended—two part—water and abrasive in AWJM, abrasive particles like sand (SiO_2) glass beads unit of measurement added to the water jet to spice up its cutting ability by many folds. AWJ unit of measurement is mainly of two varieties—entrained and suspended kinds as mentioned earlier. In entrained kind of AWJM, the abrasive particle unit of measurement allowed to induce on water jet to make abrasive water jet with important speed of 800 m/s. Such high-speed abrasive jet can machine nearly any material [4]. "Harder" and "difficult-to-cut" materials like thick steel plates, Al and different manufacturing materials, ceramic matrix and metal matrix composites, reinforced plastics, stratified composites unit of measurement reserved for AWJM [6].

2 Experimental Work

Nowadays, the abrasive water jet machining is employed to machine the materials like non-ferrous alloys, steels, titanium alloys, nickel-based superalloys, polymers, honeycombs, composite, concrete, stone—granite, wood, bolstered plastics, metal compound laminates, fibre metal laminates alloy could be a family of primary solid solution nickel–chromium-based superalloys. Alloy alloys unit of measurement reaction and corrosion-resistant materials like minded for service in extreme environments subjected to pressure and heat once heated, and alloy forms a thick, stable, passivation matter layer protecting the surface from any attack. Alloy retains strength over a decent temperature variation, partaking for high temperature applications where number 13 and steel would succumb to creep as a result of thermally induced crystal vacancies alloy is heat strength is developed by primary

Table 1 Composition of Inconel 600

Elements	Ni	Cr	Fe	Mn	Cu	Si	C	S
Composition	72	14-17	6-10	1	0.5	0.5	0.15	0.015

Table 2 Levels of process parameters

Parameters/levels	Level-1	Level-2	Level-3
Pressure (Mpa)	235	255	275
Transverse speed (mm/min)	90	120	150
Stand-off distance (mm)	2	3	4
Mass flow rate (kg/min)	0.24	0.34	0.44

solid solution twenty-one strengthening or precipitation hardening, hoping on the alloy. Alloy alloys area unit generally employed in warm the applications (Table 1).

Inconel's warm temperature strength is developed by solution strengthening or precipitation strengthening, reckoning on the alloy. In precipitation-strengthening or age-hardening varieties, a small amount of niobium is combined with nickel to form the intermetallic compound Ni_3Nb or gamma prime (γ'). Gamma prime forms tiny cubic crystals that inhibit slip and creep effectively at elevated temperatures. The formation of gamma prime crystals will increase over time, particularly when 3 h of a heat exposure of 850 °C, and continue to grow when seventy-two hours of exposure (Table 2).

2.1 Selection of Performance Measure

2.1.1 Material Removal Rate (MRR)

In AWJM takes place because brittle fracture of the work surface because of high-speed abrasive particles. Modelling has been finished the subsequent assumptions: Abrasives square measure spherical in form and rigid. The particles area unit is defined by the mean grit diameter. The K.E. of the abrasives area unit is completely employed in removing material. Brittle materials' area unit is thought about to fail because of brittle fracture, and thus, the volume of fracture is taken into consideration to be figured with diameter adequate note indentation length. For ductile material, volume of removal is assumed to be adequate for the volume of indentation because of particulate impact.

$$MRR = \frac{\text{Initial weight} - \text{final weight } (mm^3/min)}{\text{Time taken for machining}}$$

2.2 Surface Roughness

The effect of water pressure on the surface finish in conjunction with the thickness of the cut. The study shows that at the higher portion of the kerf, the result of water pressure on surface roughness is insignificant. However, with the rise within the cutting depth, the effect of water pressure will increase. High water pressure will increase the K.E. of the abrasive particles and prolongs their capability for removal of material through the cutting depth. As a result, the surface finish may be belittled by increasing water pressure.

2.2.1 Design of Experiment

DOF victimization Taguchi approach will economically satisfy the requirement of downside finding and products or method style optimization project. The process parameters and so the levels were selected supporting the literature review of some studies that had been documented on abrasive water jet machining (Table 3).

$$DOF = C{-}1 * F + (T{-}1 * P{-}Q) + 1\,C{-}\text{Levels}\,Q{-}\text{No. of. Interaction}$$

3 Result and Discussion

3.1 Optimization

It is an associate degree of act, process, or methodology of creating one thing (as a design, system, or decision) as absolutely good, functional, or effective as possible; Particularly, the numerical procedures (as finding the largest of a function) involved in this.

Table 3 L9 orthogonal array

Ex. no	Pressure (Mpa)	Mass flow rate (kg/min)	Transverse speed (mm/min)	Stand-off distance (mm)
1.	235	0.24	90	2
2.	235	0.34	120	3
3.	235	0.44	150	4
4.	255	0.24	120	4
5.	255	0.34	150	2
6.	255	0.44	90	3
7.	275	0.24	150	3
8.	275	0.34	90	4
9.	275	0.44	120	2

3.1.1 Taguchi Optimization

Dr. Taguchi of Asian Nation Telephones and Telegraph Company, Japan, has developed a technique supporting orthogonal array experiments, which provides a lot of reduced variance for the experiment with optimum settings of process parameters (Table 4).

3.2 Grey Relational Analysis

Grey relational technique is used for solving interrelationships among the multiple responses. This analysis consists of following rules.

Grey relative technique is employed for determination interrelationships among the multiple responses. This method consists of following steps (Table 5).

$$s/n \text{ ratio of MRR} = -10 * \log(1/y)\Sigma\left(1/X^2\text{nj}\right) s/n \text{ ratio of SR} = -10 * \log(1/y)\Sigma X^2\text{nj}$$
$$\text{GCnj} = (\Psi\text{min} + \delta\Psi\text{max})/(\Psi\text{nj} + \delta\Psi\text{max})$$

where it is grey coefficient for nth trial of jth dependent response, d is the quality loss, and Ψ is the unique coefficient which has value from 0 to 1.

Table 4 L9 orthogonal array with MRR and SR

Ex. no	Pressure	Mass flow rate	Transverse speed	Stand-off distance	MRR grain size 80 (µm)	MRR grain size 100 (µm)	SR grain size 80 (µm)	SR grain size 80 (µm)
1.	235	0.24	90	2	24.972	22.857	3.81	2.87
2.	235	0.34	120	3	30.55	30.386	2.13	1.79
3.	235	0.44	150	4	42.25	34.482	4.4	3.90
4.	255	0.24	120	4	30.219	32.972	4.71	3.58
5.	255	0.34	150	2	41.095	42.567	4.24	2.05
6.	255	0.44	90	3	22.357	46.37	1.74	2.48
7.	275	0.24	150	3	38.462	79.31	1.76	2.26
8.	275	0.34	90	4	24.390	21.774	3.02	2.91
9.	275	0.44	120	2	32.967	62.162	3.03	2.08

Table 5 Values of grey relational grade and rank

Ex. no	Grey relational coefficient				Grey relational grade		Rank	
	MRR		SR					
	Grain size 80 (μm)	Grain size 100 (μm)	Grain size 80 (μm)	Grain size 100 (μm)	Grain size 80 (μm)	Grain size 100 (μm)	Grain size 80 (μm)	Grain size 100 (μm)
1.	0.37386	0.34189	0.38848	0.45199	0.38117	0.39694	9	6
2.	0.49532	0.40253	0.63730	1	0.56631	0.70126	5	3
3.	1	0.43696	0.34925	0.3333	0.67642	0.38513	2	9
4.	0.48706	0.42412	0.3333	0.35969	0.41018	0.39190	8	7
5.	0.91878	0.49963	0.35856	0.74167	0.63922	0.62065	4	4
6.	0.3333	0.54642	1	0.54426	0.66665	0.54534	3	5
7.	0.77209	1	0.97927	0.62548	0.87568	0.81274	1	1
8.	0.36676	0.3333	0.47452	0.44484	0.42064	0.38907	7	8

Table 6 Average grey relational grade for 80 grain size

Factors	Average grey grade			Lag-Low
	Level-1	Level-2	Level-3	
Pressure	0.54071	0.572	0.60460	0.0638
Transverse speed	0.48951	0.49799	0.72984	0.2435
Stand-off distance	0.51262	0.70288	0.50182	0.20106
Mass flow rate	0.55568	0.542062	0.61958	0.07752

3.3 Average Grey Grade for Each Input Process Parameters for 80 Grain Size

The highest Large-Low grade worth shows that the transversal speed because the most significant parameter on determinative response characteristic (Table 6).

## 3.4 Average Grey Grade for Each Input Process Parameters for 100 Grain Size

See Table (7).

Table 7 Average grey relational grade for 100 grain size

Control factor	Average grey grade			Lag-Low
	Level-1	Level-2	Level-3	
Pressure	0.49645	0.51930	0.64197	0.14552
Transverse speed	044378	0.60576	0.60617	0.16239
Stand-off distance	0.58056	0.68645	0.3887	0.29775
Mass flow rate	0.53388	0.57033	0.55152	0.03674

3.5 Effect of Input Process Parameters on MRR

The result of jet pressure on MRR was tested in various pressures from forty-five to 275 MPa. During this vary it had been found that once the jet pressure accrued the MRR was virtually of a set worth. The tests were continual at two abrasive flow rates. Therefore, it completes that jet pressure has no result on MRR within the range. Take a look at results of the jet pressure on the MRR at completely different abrasive flow rates (Fig. 1).

The influence factor in the graph is transverse speed due to pressure (80 mesh). A number of experiments were carried out to find the relation between the traverse speed and MRR. During these tests, the traverse speed is varied from 40 to 220 mm/min and the testes were repeated for abrasive flow rates of 0.24 and 0.74 kg/min. It shows that MRR decreases with the increase in traverse speed. In the main effects of grain size 80 mesh, when the pressure is high, mass flow rate is low, transverse speed is low, and the stand-off distance is low which gives high material removal rate. The varying transverse speed and pressure give low MRR then grain size 100 mesh (Fig. 2).
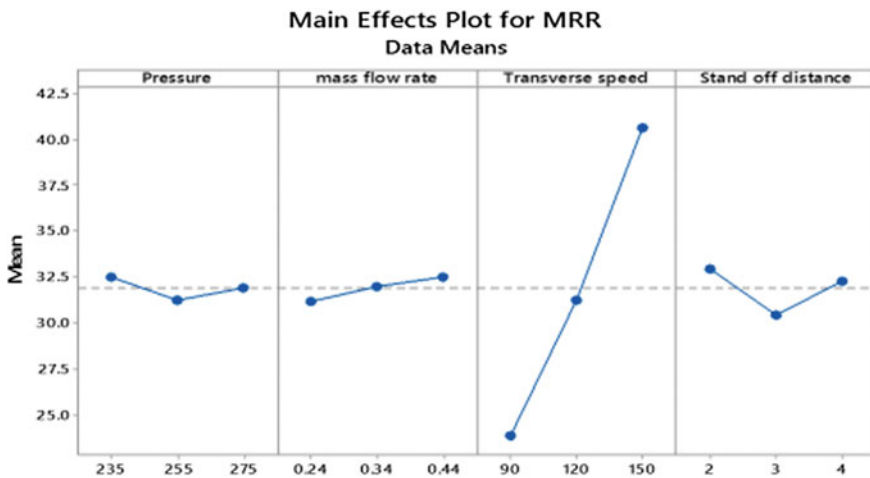
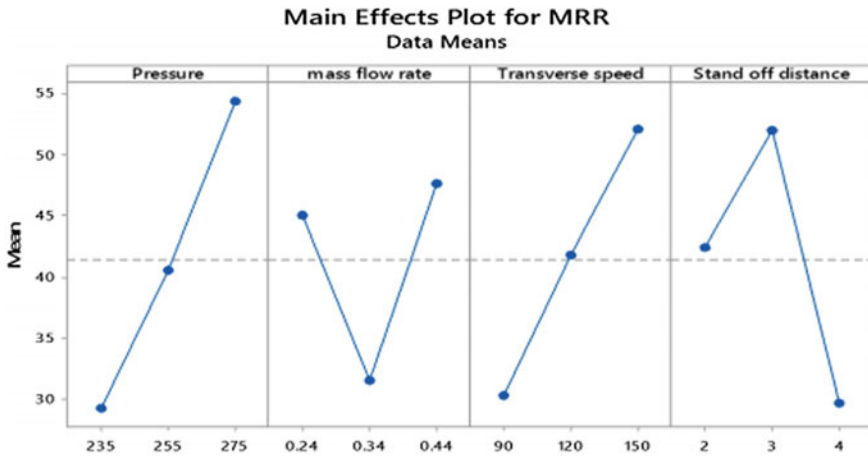
Fig. 1 Main effects of MRR for 80 grain size

Fig. 2 Main effects of MRR for 100 grain size

3.5.1 Influence of Abrasive Grain Size on MRR

Comparing grain size 80 and 100 mesh, the grain size 100 mesh shows high influence of MRR. The high pressure, high mass flow rate, low speed, and low stand-off distance give high MRR. The grain size 80 mesh gives low surface. The grain size 80 mesh gives low material removal rate compared to grain size 100 mesh because of small grain size. In the comparison, the grain size 100 gives high material removal rate due to large grain size compared to grain size 80 mesh (Fig. 3).
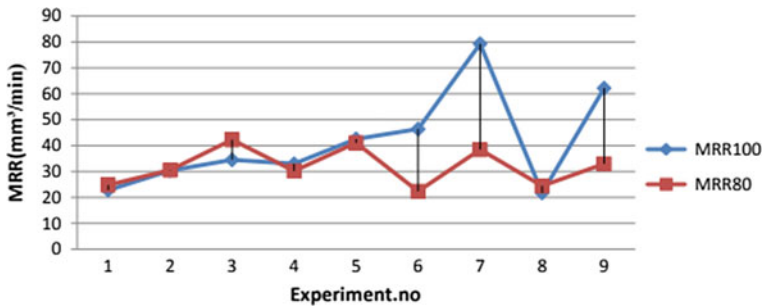
Fig. 3 Comparison of MRR for 80 and 100 grain sizes

3.6 Effect of Input Process Parameters on SR

The effect of jet pressure on surface finish Ra parameter was tested under ranges of pressures from 45 to 275 MPa. In this range, it was found that when the jet pressure increased, the surface roughness Ra parameter was almost of a fixed value. The tests were repeated at two abrasive flow rates.

The surface roughness Ra parameter values were measured at different traverse speeds in the range from 40 to 200 mm/min and the two different abrasive flow rates. Due to the increase in traverse speed, surface roughness decreases. The relation trend is of a power function with medium regression ratio. The surface roughness Ra parameter values were tested at a range of abrasive flow rate from 0.24 to 0.74 kg/min (Fig. 4).

The factor influencing in the graph is stand-off distance which gives surface roughness (80 mesh). The surface finish Ra values are nearly constant at different abrasive flow rates.

The higher the traverse speed yields that the surface finish is decreasing by increasing the abrasive flow rate. The main effect is caused by stand-off distance for 80 grain size (Fig. 5).

3.7 Influence of Abrasive Grain Size of SR

The figure which shows that the influence of grain size of compared 80 and 100 abrasive grain sizes. The better surface roughness value of 80 grain size because of high mass flow rate and low transverse speed and there parameters (Fig. 6).
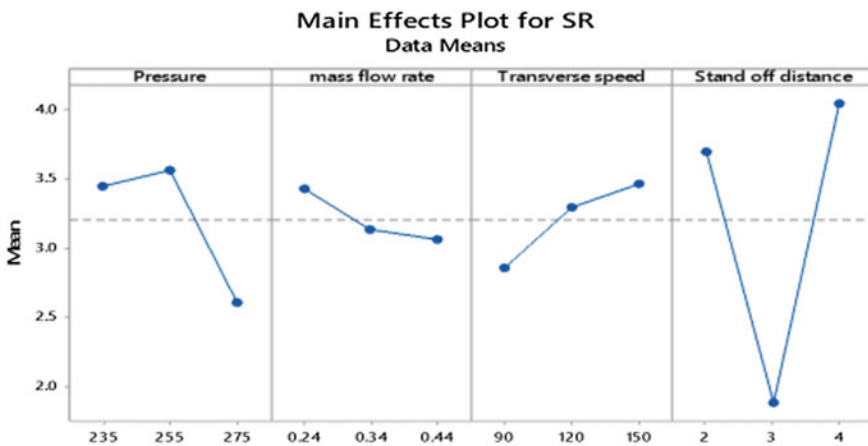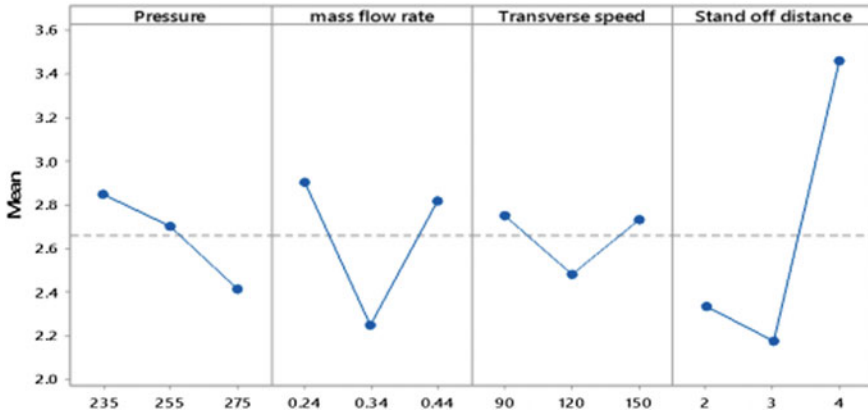

Fig. 4 Main effects of SR for 80 grain size

Fig. 5 Main effects plot for SR data means
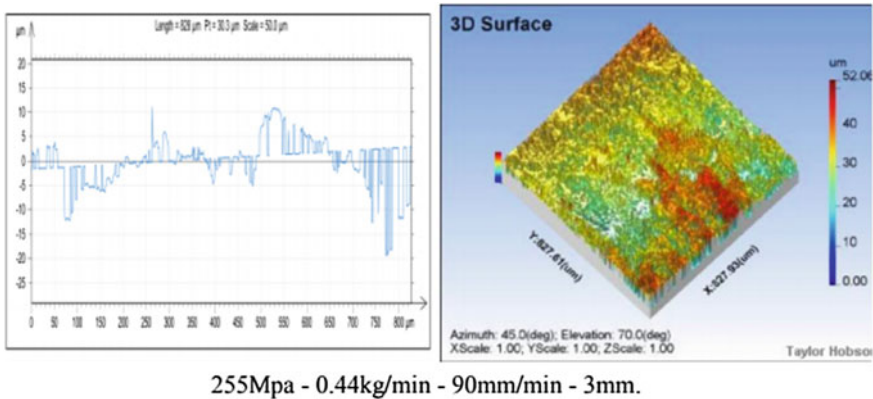

255Mpa - 0.44kg/min - 90mm/min - 3mm.

Fig. 6 Better surface roughness for 80 grain size

Due to the high mass flow rate and low transverse speed, we get better surface roughness. The poor surface roughness value of 80 grain size because of low abrasive flow rate and stand-off distance and there parameters (Fig. 7).

Due to the low mass flow rate and high stand-off distance we get better surface roughness. The better surface roughness value of 100 grain size because of low pressure and low stand-off distance and there parameters (Fig. 8).

Due to the low pressure and mass flow rate, we get better surface roughness. The poor surface roughness value of 100 grain size because of high transverse speed gives and stand-off distance and there parameters.

The optimized graph of both 80 and 100 grain sizes is shown in Fig. 9.

255Mpa - 0.24kg/min - 120mm/min - 4mm.

Fig. 7 Poor surface roughness for 80 grain size

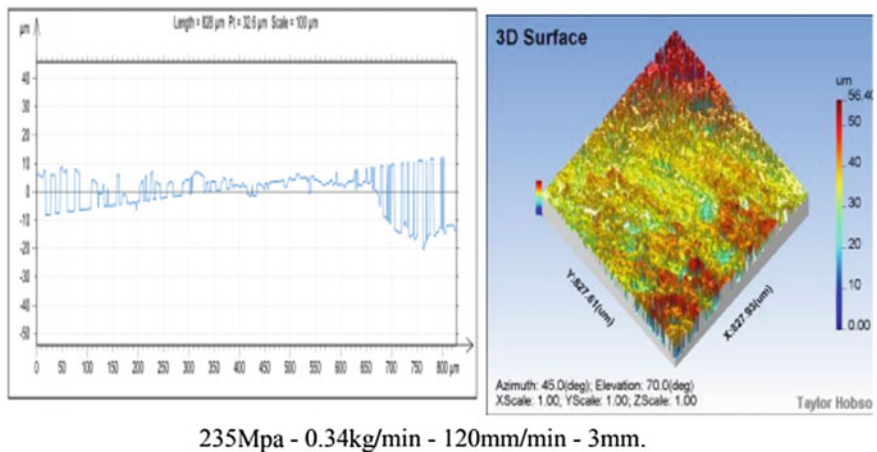235Mpa - 0.34kg/min - 120mm/min - 3mm.
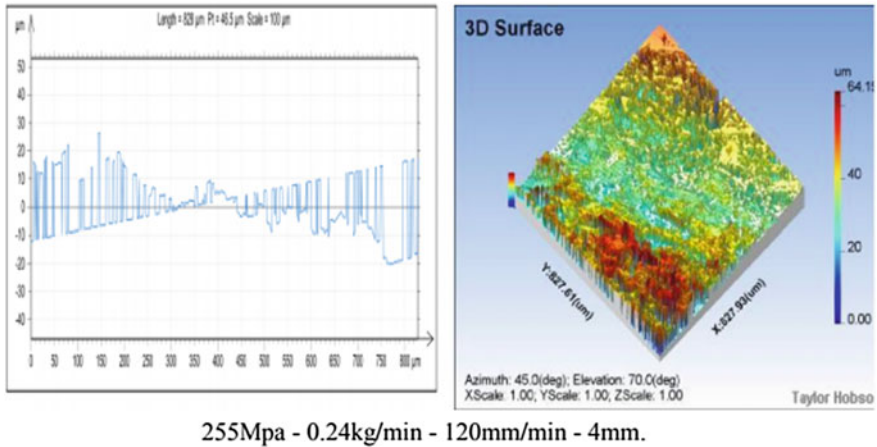
Fig. 8 Better surface roughness for 100 grain size

The optimized satisfactory value of material removal rate is 79.31 mm^3/min and surface roughness is 2.26 μm under the condition of pressure (275 Mpa), mass flow rate (0.24 kg/min), transverse speed (150 mm/min), stand-off distance (3 mm) (Fig. 10).

The grain size 80 mesh gives high surface roughness in high pressure, low mass flow rate, high speed, and high stand-off distance. The grain size 80 μm gives low surface roughness in low pressure, high mass flow rate, low speed, and low stand-off distance. The grain size 100 mesh gives high surface roughness in high pressure, low mass flow rate, high speed, and high stand-off distance. The grain size
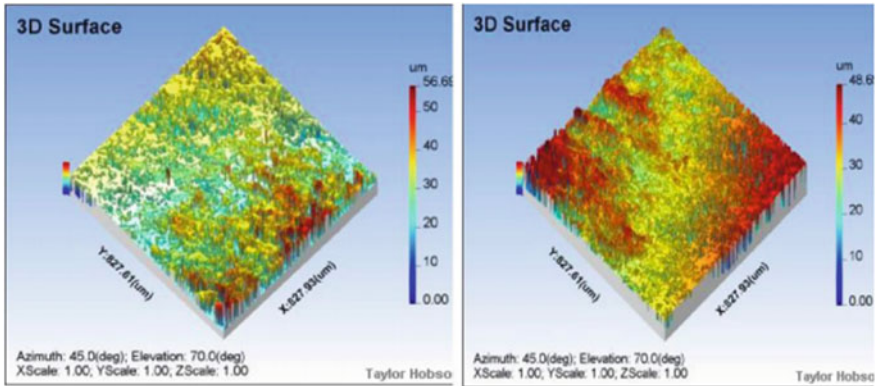
275Mpa - 0.24kg/min - 150mm/min - 3mm

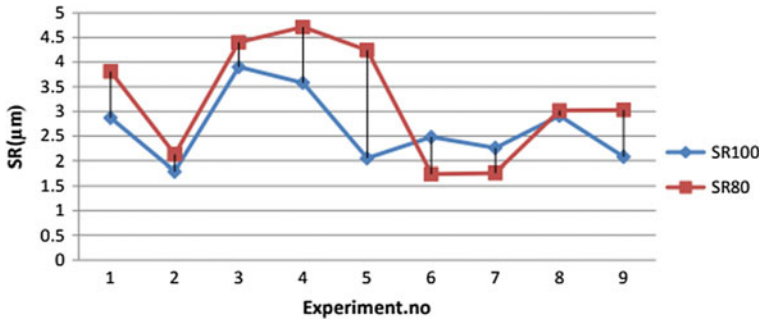**Fig. 9** Optimized value for 80 and 100 grain sizes

Fig. 10 Comparison of SR for 80 and 100 grain sizes

100 μm gives low surface roughness in low pressure, high mass flow rate, low speed, and low stand-off distance. Comparing grain sizes 80 and 100, the grain size 100 mesh shows low surface roughness.

4 Conclusions

In this present work, Inconel grade 600 is machined using abrasive water jet machining. Inconel is chosen based on its applications in engine seal, rocket engine, aerospace. The predominant parameters like pressure (Mpa), abrasive flow rate (kg/mm), stand-off distance (mm), transverse speed (mm/min), which suitably varied to get the optimum values of response parameter's like material removal rate and surface finish. These machining parameters are optimized using Taguchi-Grey

relational approach. The optimum combination of process parameter for obtaining better response parameters is found.

The grain size of 100 mesh produces 11% higher material removal rate than grain size of 80 mesh because the grain size 80 mesh gives low material removal rate compared to grain size 100 mesh because of small grain size. Actually pressure also plays a huge role in this when pressure combines with abrasive. The grain size of 100 mesh produces 27% better surface roughness than grain size of 80 mesh because the grain size 100 mesh gives low surface roughness compared the grain size 80 mesh because of large grain size. Again pressure plays a huge role. The most influence process parameters for getting better response parameters is the pressure and stand-off distance because increasing pressure and decreasing the stand-off distance increase the material removal rate and decrease the surface roughness.

The optimized satisfactory value of MRR is 79.31 mm^3/min, and surface roughness is 2.26 μm under the condition of pressure (275 Mpa), mass flow rate (0.24 kg/min), transverse speed (150 mm/min), stand-off distance (3 mm).

References

1. Olsen, J., Zeng, J.: The state of the art precision abrasive waterjet cutting OMAX Corporation Kent, Washington, U.S.A. 98032. In: The 8th Pacific Rim International Conference on Water Jet Technology Oct. 10–12, 2006 Qingdao, China Paper (2006)
2. Korat, M.M., Acharya, G.D. Dr., Korat, M.M.: A review on current research and development in abrasive waterjet Machining. Int. J. Engineering Res. Appl. **4**(1) (Version 2) (2014)
3. Liu, H., Wang, J., Kelson, N., Brown, R.J.: A study of abrasive waterjet characteristics by CFD simulation. J. Mater. Process. Technol. 153–154, 488–493 (2004). (School of Mechanical, Manufacturing and Medical Engineering, Queensland University of Technology, Australia)
4. Akkurt, A., Kulekci, M.K., Seker, U., Ercan, F.: Effect of feed rate on surface roughness in abrasive waterjet cutting applications. J. Mater. Process. Technol. **147**, 389–396 (2004)
5. Selvan, M.C.P., Raju, N.M.S. Dr.: Analysis of surface roughness on abrasive water jet cutting on cast iron. Int. J. Sci. Environ. Technol. **1**(3), 174–182 (2012). (Research Scholar, Karpagam University, Coimbatore, India. Principal, Mahendra Institute of Technology, Namakkal, India)
6. Badgujar, P.P., Rathi, M.G.: Analysis of surface roughness in abrasive water jet cutting of stainless steel. Int. J. Eng. Res. Technol. (IJERT) **3**(6), (2014)
7. Shanmugha sundaram, P.: Influence of abrasive waterjet machining parameters on the surface roughness of eutectic Al-Si alloy–graphite composites (2014). (Department of Automobile Engineering, Karpagam University, Coimbatore-641021)

Experimental Investigation of Electrochemical Micro-machining Process Parameters on Stainless Steel 316 Using Sodium Chloride Electrolyte

T. Geethapriyan, R. Manoj Samson, J. Thavamani, A. C. Arun Raj and Bharadwaj Reddy Pulagam

Abstract In this paper, the experimental investigation of electrochemical micro-machining (ECMM) process on stainless steel 316 by varying the effect of applied voltage, electrolyte concentration, micro-tool feed rate and duty cycle. The machining performance such as material removal rate (MRR) and overcut (OC). Taguchi design of experiment has been used to carry out the design of input process parameters and their levels. Microscopic image has been used to study the surface topography of the electrochemical micro-machined work piece surface. The experimental results attain that the effect of electrolyte concentration and duty cycle has most significant factors for the machining of stainless steel 316 by electrochemical micro-machining (ECMM) process. The optimize process parameters for higher material removal rate and lower overcut are found out using grey relational approach, and finally, the confirmation tests were carried out in the electrochemical micro-machining process.

Keywords Stainless steel-316 · NaCl electrolyte · Copper tool electrode
Orthogonal machining · Taguchi method

1 Introduction

Electrochemical machining (ECM) was developed to machine difficult-to machine materials, regarding associate degree anodic dissolution methodology supported the event of electrolysis, whose laws were recognized by chemist. In ECM, electrolytes perform as conductivity of electricity. The speed of machining does not suppose the metal hardness. ECM offers variety of blessings over different machining ways in which and along has many disadvantages. The benefits area unit there is no tool

T. Geethapriyan (✉) · R. Manoj Samson · J. Thavamani
A. C. Arun Raj · B. R. Pulagam
Department of Mechanical Engineering, SRM University,
Kattankulathur, Chennai 603203, India
e-mail: devimani.priyan18@gmail.com

wear; machining is completed at low voltage compared to various processes with high metal removal rate; no burr formation; taxing semiconducting materials may additionally be machined into difficult profiles; work-piece structure suffer no thermal damages; acceptable for production work and low labour wants. The disadvantages area unit an outsized quantity of energy is consumed that is some 100 times that needed for the drilling or turning of steel; issues with safety on removing and doing away with the explosive element gas generated throughout machining; not fitted to non-conducting materials and issue in handling and containing the answer. The applications area unit electronic countermeasures is wide utilised in manufacturing of moulds and dies; along used for making tough variety of rotary engine blades and it's presently habitually used for the machining of region elements, vital deburring, mechanical system parts, ordnance parts etc. Once chemical science machining method is applied to micro-machining vary (i.e. from 0.1 to 1 mm) for manufacturing radical preciseness shapes and producing small structures then it's referred to as chemical science micro-machining (EMM). Electrochemical micro-machining (ECMM) appears to be terribly distinguished as a future micro-machining technique, since in several areas of applications it offers several merits. Their are no thermal and mechanical stresses on work piece, no heat affected layer on work piece, no tool wear, high machining rate, stress-free surface, controlled material removal, utilized for removal and patterning of metal film and foils.

2 Experimental Design

The electrolyte should be chosen according to the nature of the specimen and the specimen that is chosen must be conductive in nature for the EMM process.

2.1 Selection of Work Piece

For this EMM process, stainless steel 316 was chosen as the work piece. For EMM process, the chosen work piece should have good corrosive resistance, electrical conductivity and low electrical resistivity. It is used as die material, used for jewellery making, cutting, carving, sanding, shaping, cutting tools for machining, surgical instruments, sports and dentulous applications. Also, tungsten carbide with micro-holes is used for producing printed circuit boards. Since tungsten carbide with micro-holes is used for various applications, machining tungsten carbide with EMM and determining the optimum parameters will be very helpful for producing low-cost tungsten carbide with micro-holes for commercial purposes. The properties are low electrical resistivity ($\sim 2 \times 10^{-7}$ Om) and resistance to scratching. Another important reason for selecting tungsten carbide as the work piece is that from the literature survey, it is inferred that more amount of EMM work has not been done on tungsten carbide materials.

2.2 Selection of Electrolyte

EMM electrolytes are primarily classified into two teams, like electrolytes of passive containing oxidizing anions, i.e. binary compound (NaCl), and electrolytes of non-passive containing aggressive ions, i.e. binary compound. Electrolytes of passive are noted to relinquish higher machining accuracy. This is because of development of compound films and atomic number 8 evolution within the region of stray current. It is usual to figure with NaCl which can improve the dissolution of fabric while not poignant the micro-tool. By decreasing the answer concentration, lay to rest conductor gap may be reduced to a lower limit for up the micro-machining potential. For this project, soda nitre ($NaNO_3$) was chosen because of the solution. The properties that create $NaNo_3$ because of the appropriate solution for EMM method are low cost, simply accessible, non-toxic.

2.3 Selection of Tool

The micro-tool accuracy and surface finish directly affect the specimen accuracy. The micro-tool materials need to be compelled to possess sensible thermal and electrical natural phenomenon, corrosive resistant and high machinability, stiffness to resist answer pressure, whereas not vibration and fewer stray current implications. However, various micro-tool materials within the main depend on natural science and mechanical properties and a type to be created. For reducing the results of stray current, the micro-tool got to be insulated properly so as that flows of current solely through the front face, which in turn causes less side gap. Insulated materials like attack, Si_3N_4 could also be coated on the sidewall of the little tool by chemical vapour deposition (CVD) technique. For this project, copper tool was used as a result of the properties of copper square measure; high electrical, thermal, physical phenomena; high corrosion resistance; low cost; ease of convenience.

3 Experimental Work

Orthogonal array diminishes the entire variety of trials. Total nine experimental are conducted for Taguchi design to obtained the MRR, and overcut of the specimen is calculable. Total twenty experimental trials are conducted, and MRR, overcut and surface roughness were measured.

3.1 Specifications of Specimen Materials and Experimental Methods

For this experiment, chrome steel is chosen as the operating material. Taguchi design (L9 orthogonal array) is usually recommended for copper specimen, which has a dimension of length 1.5 mm, width 8 and 3 mm. One piece of delicate metallic element inorganic compound material is taken, and trial square measure administered by varied the parameters. The calculation of MRR is finished by taking initial and final weight of labour piece before and after the machining (Table 1).

3.2 Taguchi Design

Taguchi's philosophy was developed by Dr. Genichi Taguchi and will be an outstanding tool for the design of top-quality production system. Taguchi's orthogonal array (OA) provides a collection of experiments with less vary of experimental runs, and Taguchi's *S/N* ratios, that square measure power functions of necessary output, assist as objective functions among the advanced technique. It uses a maths live of performance named as signal to noise magnitude relation. The *S/N* magnitude relation takes into thought of every mean and variability. The *S/N* magnitude relation is that the magnitude relation of the mean (signal) to the standard deviation (noise). The relation depends on the standard characteristics of the product/process to be optimized. The standard *S/N* ratios sometimes used square measure nominal is best (NB), lower the upper (LB) and higher the better (HB). Once experimental data (quality attribute price) is normalized exploitation NB/LB/HB criteria; normalized price lies ranges from zero to one. Zero indicates worst quality to be rejected, and one indicates most satisfactory quality. Since *S/N* magnitude relation is taken into account mean (signal) to the noise (deviation from the target); increasing *S/N* magnitude relation implies minimum deviation and

Table 1 Properties and composition of stainless steel 316

Composition	Percentage
Carbon	0.08
Manganese	2.00
Phosphorus	0.045
Sulphur	0.030
Silicon	0.75
Chromium	16-18
Nickel	10–14
Molybdenum	2–3
Nitrogen	0.10
Iron	Balance

so it is (*S/N* ratio) to be maximized. Taguchi technique tries to attenuate the noise as a result of the elimination of noise issue is not recommended. Taguchi technique offers rich compact variance for the experiment with optimum setting of technique management parameters. That is why Taguchi ways that square measure uses modish of experiment with constant improvisation processes to induce the required results.

3.3 Design Using Minitab

MINITAB can give every static and dynamic response tests during very static response tests; the quality characteristic of interest incorporates a mounted limit. During very dynamic response tests, the quality characteristic operates over a range of values, and so the goal is to optimize the quotient between associate degree sign and associate degree of an output response. MINITAB calculates response tables. A Taguchi design associate degree orthogonal array is that the methodology inside that they use different types, two, three, four, five, and mixed level of designs choices area unit shown throughout this Table 2.

First of all it is been chosen for what number factors area unit there for the experiment. After that, during this experiment three factors applied: voltage (V), feed rate (F) and concentration of electrolyte (C) were taken into consideration.

3.4 Experimental Procedure

3.4.1 Electrolyte Flow Maintaining

The electrolyte plays a vital role in the machining operation. The removal of material is due to the current flow. So the tool as well as the work piece has to be dipped in the electrolyte. If there is an obstruction in dipping of tool and work piece, there will be machining variation which leads to less efficiency. For maintaining the dipping of tool and work piece, the electrolyte level in the machining tank is to be maintained with the same level. The constant maintaining of the electrolyte depends upon the flow in the inlet as well as outlet. Thus, maintaining a
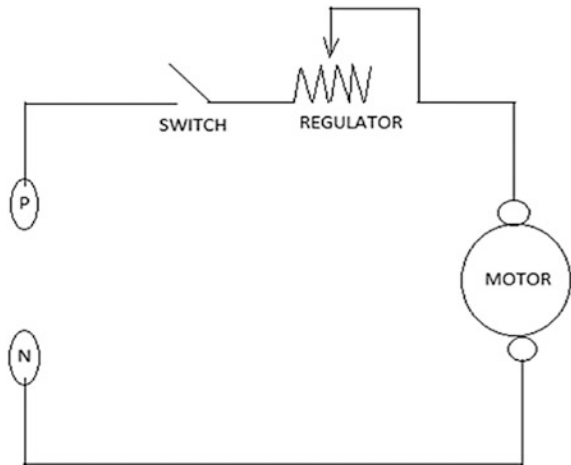
Table 2 Process parameters and their levels

Machining parameter	Unit	Level		
		Level-1	Level-2	Level-3
Applied voltage	V	10	15	20
Electrolyte concentration	g/L	0.1	0.3	0.5
Micro-tool feed rate	μm/s	10	15	20

Fig. 1 Circuit before
regulating flow
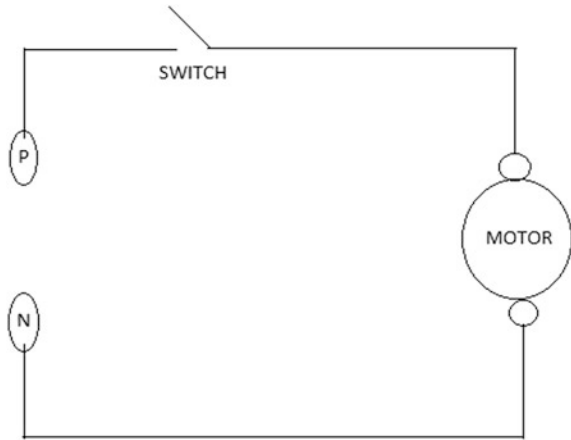
Fig. 2 Circuit after
regulating flow

constant flow rate in both inlet and outlet requires measuring of flow rates in both
the areas. A sensor set-up can be used to maintain the electrolyte level in the
machining tank. If we considered the flow rate as a parameter of machining, it will
be worth in using sensors. Also, sensors will cost high. Thus, different method of
setting up regulator overcomes the problem of maintaining constant electrolyte
level in the machining tank. An experiment was done by setting a regulator set-up
in the current set-up which is shown in Figs. 1 and 2.

3.4.2 EMM Measurement

The starting work piece weight has to be taken for measuring the MRR value. The work piece is then placed in horizontal manner, and the copper tool (diameter = 486 µm) is placed in vertical manner. The electrolyte is made to flow through the tool. The machining is then carried out by varying the input parameters. The time required for measuring each sample was noted down. During machining, care should be taken that the tool does not come in closeness with the work piece. After machining is completed, the final weight of the sample is measured. The MRR and overcut values were measured using Talysurf (Taylor Hobson) and video measuring system, respectively (Table 3).

4 Results and Discussion

4.1 Effects of Material Removal Rate

From the responses obtained from the experiment, it is ascertained that the machinability of electronic countermeasures primarily depends on the small tool voltage, feed rate and solution concentration. The MRR slightly will increase with raise in small to tool feed rate at that time feed rate have predominant will increase with rise in voltage within the vary of eight to ten and so decrease, however the result is a smaller amount than the feed rate on MRR. However MRR is cutto tiny extent with will increase in concentration then preponderantly will increase with rise in concentration (Fig. 3).

Table 3 Experimental Observations

| Sample no	Voltage (V)	Electrolyte concentration (g/L)	Micro-tool feed rate (µm/s)	MRR (mg/min)	Overcut (µm)	Machining time (min)
1	10	0.1	10	0.3101	614.605	5.15
2	15	0.3	15	0.8337	667.123	4.34
3	20	0.5	20	1.345	346.912	4.05
4	10	0.1	10	0.5632	576.07	4.48
5	15	0.3	15	0.5255	384.84	4.05
6	20	0.5	20	0.9565	584.66	5.15
7	10	0.1	10	1.0762	429.775	4.05
8	15	0.3	15	0.9897	618.725	5.15
9	20	0.5	20	0.6540	525.83	4.40

Main Effects Plot for MRR (mg/min)
Data Means
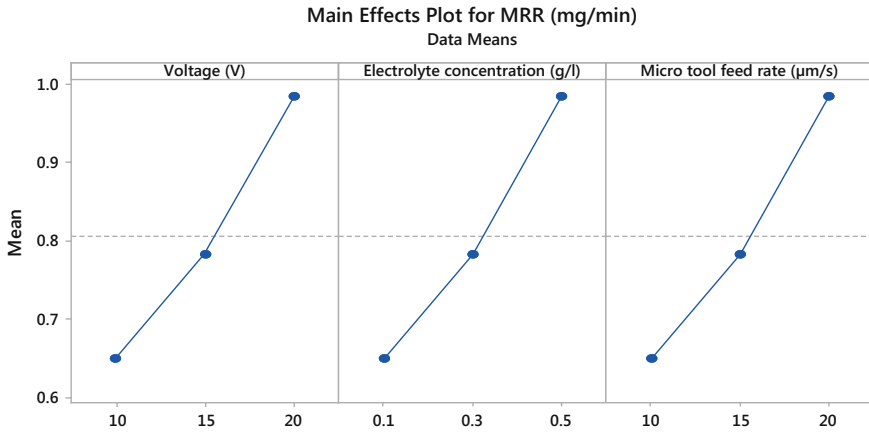
Fig. 3 Main effect plot for material removal rate

4.2 Effects on Overcut

The overcut value rises with an increase in the micro-tool feed rate up to a particular value and then decreases. The same way the overcut rises with an increase in electrolyte concentration until a particular value and then decreases. On the other hand, the overcut decreases with increase in the voltage. The best-overcut value is obtained for the input parameter having voltage at 9 V, micro-tool feed rate 0.9 µm/min and concentration of electrolyte 20 g/L. The overcut value is bad for the input parameters having voltage 9 V, electrolyte concentration 25 g/L and micro-tool feed rate 1 µm/s (Figs. 4, 5 and 6).

Main Effects Plot for Over cut (µm)
Data Means
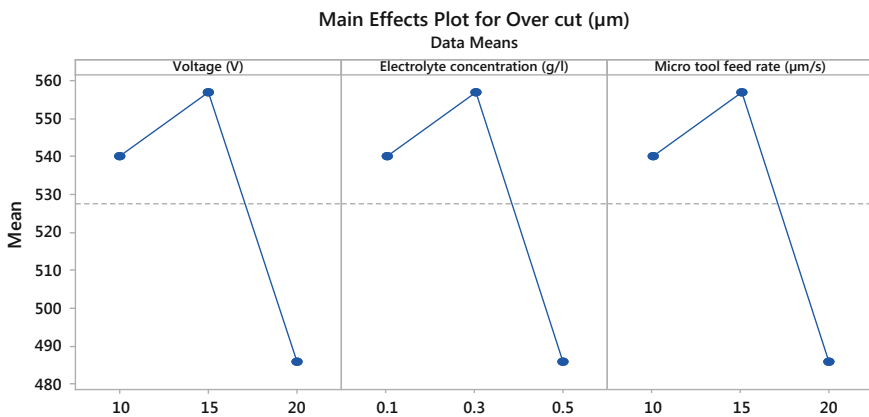
Fig. 4 Main effect plot for overcut

Fig. 5 Overcut for best parameter
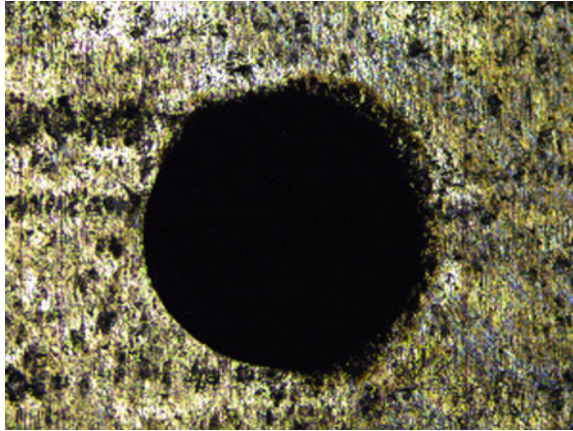
Fig. 6 Overcut for worst parameter
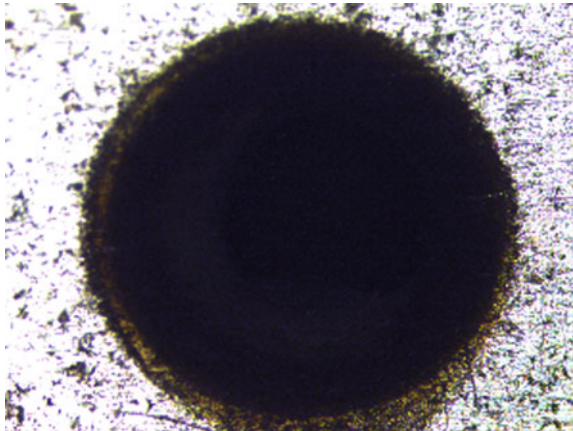
5 Conclusions

In the present project, three input parameters, namely voltage, micro-tool feed rate and electrolyte concentration, are considered. With tungsten carbide as the work piece, copper being the tool is used and NaCl as the electrolyte and the EMM process was carried out nine experiments that were conducted by varying the input parameters and the output parameters, like MRR, and overcut was measured for all the nine experiments. The following conclusions were arrived

- Among the three input parameters, the micro-tool feed rate has the greater significance and electrolyte concentration has lower significance.
- From the Taguchi's optimization technique, it is inferred that voltage at 10 V, micro-tool feed rate 15 μm/min and electrolyte concentration 0.3 g/L are the optimum parameters for machining tungsten carbide by EMM process.

References

1. Munda, J., Bhattacharyya, B.: Investigation into electrochemical micromachining (EMM) through response surface methodology based approach. Int. J. Adv. Manuf. Technol. **35**, 821–832 (2008)
2. Munda, J., Malapati, M., Bhattacharyya, B.: Control of micro-spark and stray-current effect during EMM process. J. Mater. Process. Technol. **194**, 151–158 (2007)
3. Rajurkar, K.P., Zhu, D., McGeough, J.A., Kozak, J., De Silva, A.: New Developments in Electro-Chemical Machining. National science foundation
4. Rajurkar, K.P., Zhu, D., We, B.: Minimization of machining allowance in electrochemical machining. J. Mater. Process. Technol. **86**, 200–207 (1999)
5. Bhattacharyya*, B., Sorkhel, S.K.: Investigation for controlled electrochemical machining through response surface methodology-based approach. J. Mater. Process. Technol. **86**, 200–207 (1999)
6. Bhattacharyya*, B., Doloi, B.N., Sorkhel, S.K.: Experimental investigations into electrochemical discharge machining (ECDM) of non-conductive ceramic materials. J. Mater. Process. Technol. 95, 145–154 (1999)
7. Bhattacharyya, B., Malapati, M., Munda, J., Sarkar, A.: Influence of tool vibration on machining performance in electrochemical micro-machining of copper. Int. J. Mach. Tools Manuf. **47**, 335–342 (2007)
8. Malapatiand, M., Bhattacharyya, B.: Investigation into electrochemical micromachining process during micro-channel generation. Mater. Manuf. Process. **26**, 1019–1027 (2011)

Optimization of Machining Parameters on Laser Beam Machining of Titanium Alloy (Ti 3Al-2.5V) Using Taguchi Method

R. Manoj Samson, T. Geethapriyan, S. Senkathir, Ashwin Ashok and Aditya Rajesh

Abstract As titanium alloy (Ti 3Al-2.5V) has high strength and stiffness with excellent corrosion resistance, it finds its application in aerospace and industrial application. Ti grade 9 is hard, and we have adopted CO_2 laser beam techniques to machine Ti grade 9. We have chosen oxygen and nitrogen gases as assisted gases. Of the various laser beam energy techniques, carbon dioxide laser beam is found to be one of the emerging trends in machining complicated and circuitous parts with maximum accuracy and in less time. Design of experiment is represented by Taguchi's L9 orthogonal array. Two sets of experiments were conducted with oxygen and nitrogen as assisted gases. Material removal rate and surface roughness were calculated and optimized using group Taguchi relational analysis. It is found that surface finish and material removal rate are improved by using nitrogen gas for machining titanium alloy (Ti 3Al-2.5V) using CO_2 laser.

Keywords Taguchi method · Titanium alloy · CO_2 laser

1 Introduction

Compared to the conventional type of machining technique, non-conventional type provides us with one of the non-contact-type machining tools to machine hard metal like titanium alloy. In this paper work involves the cutting of titanium alloy grade 9 sheet using CO_2 laser beam. Literature says that laser beam has the potential to machine the surface of hard material up to 3 mm and of various process parameters such as laser power, cutting speed, pressure and density, where laser power and cutting speed produce cut quality surface finish. This laser beam works on the

R. M. Samson (✉) · T. Geethapriyan · S. Senkathir · A. Ashok · A. Rajesh
Department of Mechanical Engineering, SRM University, Kattankulathur,
Chennai 603203, India
e-mail: manoj.sam6@gmail.com

principle of population inversion of electrons, that is majority of the electrons are excited to higher energy unstable state from lower energy stable state due to absorption of energy from the external source. This titanium alloy grade 9 sheet is cut at varying gas pressure, cutting speed, laser power and focal point. Different focal point is obtained using different lenses like plano-convex lens and meniscus lens. Meniscus lens provides sharp small spot with high power density which is a mandatory parameter for cutting hard metal. This lens is generally made from zinc selenide, gallium arsenide and germanium with high transmissivity to provide small spot size with high power density. Plano-convex lens is used in application where relatively large focal length is required. The gas used is fixed either oxygen or nitrogen, keeping this constant other parameters like cutting speed, gas pressure, laser power and focal point are varied and this is done for both the gases. Based on the results, suitable design is suggested material removal rate and surface roughness for both nitrogen and oxygen. After obtaining the optimized material removal rate and surface roughness, verification of the integrity of the results obtained is carried out. This optimization of the machining parameters is done by Grey-Taguchi approach, and it was confirmed by conducting a confirmation test. The graph which was generated using Minitab 17 software clearly represents of each input parameter over the response parameter. Keeping 95% as the confidence limit, error obtained for each of the response parameter for both material removal rate and surface roughness is calculated.

2 Experimental Set-up

2.1 Laser-Cutting System

Metal cutting is performed by using the state-of-the-art CO_2 laser-cutting method. High-power laser Rofin-Sinar CO_2 is used for metal cutting. Schematic diagram for laser-cutting layout is described below.

2.2 Beam Delivery

The most important component in the CO_2 laser beam is the quality of beam it produces, which includes the laser power, work area and the correct time of beam delivery. A beam delivery mechanism comprises of one mirror telescope, beam bending mirrors and a phase changer.

2.3 Lenses

2.3.1 Meniscus Lens

These are the lenses made from high transmissivity ratio especially made from zinc selenide, gallium arsenide and germanium. These types of lenses are used to obtain shot spot size with high power density. Focal length, diameter, shape and coating are all the design variables, which will directly interfere with the working of CO_2 laser. Principle states that the more shorter the focal length, the more laser power it will produce with short focal depth and small focused spot size. These lenses have one-side surface concave and the other-side convex as shown in the Fig. 3.3, and this arrangement creates a lesser beam diameter, thus truncating the spherical abbreviation beam waste.

2.3.2 Plano-Convex Lens

It has one surface convex and the other surface is simply plain; this is the most simplest combination of all possible lenses. These lenses generally find an application, where obtaining a small focal length is not relatively important. The lenses are placed in such a manner that flat surface should face towards the work piece, while the convex surface always faces towards the laser source.

2.4 Nozzle

A nozzle is typically used to increase the flow rate of gases. From theory of gas dynamics, each types of nozzle is unique in properties. In this experiment, a supersonic minimal length nozzle gives the best design for shock-free flow, ease of manufacturing and minimum nozzle length. Supersonic nozzle has a contracting part followed by an expansion part as per the desired gas properties and Mach number [1]. For commercial laser-cutting operation, sonic nozzles are preferred. They are generally not preferred for thin material since assist inlet gas pressure should be higher to get good quality and better surface finish [2].

2.5 Talysurf Coherence Correlation Interferometer (CCI)

Surface roughness of the machined surface of the work piece is measured using non-contact-type "Talysurf CCI LITE". The average roughness value for each sample is measured as shown in Fig. 3.6. It is simply a 3D surface roughness profiler used for measuring microroughness and step height measurement with 1 angstrom resolution. It has a magnification of 5×, 10×, 20×, 25× and 50×.

2.6 Scanning Electron Microscope

This type of microscope focuses electron beam to produce image of the specimen. The interaction of the electron with the atom in the sample produces various electrical signals that brief about sample's surface topology and its composition. The heat-affected zone of the work piece is captured during the analysis, and results are obtained accurately. Magnification obtained is from $30\times$ to $800000\times$. Image resolution of about 3 nm can be obtained.

2.7 Selection of Materials

Titanium and its alloys showcase a unique combination of mechanical and physical properties. Moreover, corrosion resistance, which have made them desirable for critical applications in aircrafts, industrial influence, chemical and energy industry service [3], shows excellent elevated temperature properties up to 600 °C and high melting point. Titanium alloys are found to exhibit excellent fatigue strength, resistance to fracture, long life, non-toxic, non-allergenic and fully biocompatible. The most important property is its non-magnetic property.

2.8 Selection of Process Parameter

All the input and output parameters are classified into different types under each category as follows.

2.8.1 Variable Parameters for N_2

Keeping N_2 gas, nozzle diameter—1 mm, stand-off distance 0.7 mm, gating frequency—10,000 Hz all these parameters as fixed, the experiment is carried out at three different levels as shown in Table 1. Gas pressure for N_2 is kept to be almost double as compared to O_2 in order to obtain the optimum results, and this is purely done on trial-and-error basis.

2.8.2 Variable Parameters for O_2

Keeping N_2 gas, nozzle diameter—1 mm, stand-off distance 1 mm, gating frequency-10,000 Hz all these parameters as fixed, the experiment is carried out at three different levels as shown in Table 2.

Table 1 Variable parameters for N_2

Factors	Laser power	Gas pressure	Cutting speed	Focal point
Units	W	Bar	m/min	mm
Level 1	3000	8	1900	0
Level 2	3500	9	2000	−1
Level 3	4000	10	2100	1

Table 2 Variable parameters for O_2

Factors	Laser power	Gas pressure	Cutting speed	Focal point
Units	W	Bar	m/min	mm
Level 1	1200	1.0	2.5	0
Level 2	1300	0.6	2.7	−1
Level 3	1400	0.8	2.9	1

2.9 Design of the Experiment (DOE)

DOE is one of the most important tools that could be used in various experimental analyses. It not only allows various input factors to be analysed, determining their corresponding effect on the output, but also helps to identify any missed out important interaction, which would have been overlooked while taking input parameters at the same time [4].

2.10 DOE Procedure

DOE can be performed in multiple ways. One of the most economical approaches, which satisfies the ultimate need of the problem solving and process design optimization project, would be Taguchi approach. The work piece used here is alloy material titanium alloy (Ti 3Al-2.5V) dimensions of the product 400×500. In machining, we use two different gasses, oxygen and nitrogen [5]. Two sets of L9 orthogonal array for machining are given in the table for two different gasses. The machining has both constant and variable parameters, according to orthogonal array to find the output parameters of MRR and SR. After the experiment is done, calculate the MRR and find the SR by surface roughness tester. Calculate the *S/N* ratio, normalized *S/N* ratio and grey-relational grade by the formula. Give the rank to the grey-relational grade and get optimized value from the rank the highest value is optimized value. The input parameter/dependent parameter and output/ independent parameter are to be optimized using nine different experiments [6], which are been carried out as shown in the Table 3. This parameter is taken by using oxygen as an inert gas. However, we have four variables and three levels. Table 3 shows the table for oxygen.

Table 3 Table for O_2

Experiment number	Laser power (W)	Gas pressure (bar)	Cutting speed (m/min)	Focal position (mm)
1	1200	1.0	2.5	0
2	1200	0.6	2.7	−1
3	1200	0.8	2.9	1
4	1300	1.0	2.7	1
5	1300	0.6	2.9	0
6	1300	0.8	2.5	−1
7	1400	1.0	2.9	−1
8	1400	0.6	2.5	1
9	1400	0.8	2.7	0

Table 4 Table for N_2

Experiment number	Laser power (W)	Gas pressure (bar)	Cutting speed (m/min)	Focal position (mm)
1.	3000	8	1900	0
2.	3000	9	2000	−1
3.	3000	10	2100	1
4.	3500	8	2000	1
5.	3500	9	2100	0
6.	3500	10	1900	−1
7.	4000	8	2100	−1
8.	4000	9	1900	1
9.	4000	10	2000	0

The input parameter/dependent parameter and output/independent parameter are to be optimized using nine different experiments, which have been carried out as shown in Table 4. This parameter is taken by using nitrogen as an inert gas. However, we have four variables and three levels. Table 4 shows the table for nitrogen.

Based on Taguchi, we had conducted nine experiments with four input parameters like gas pressure, cutting speed, laser power and focal point. Tables 3 and 4 show the design of experiments for nitrogen and oxygen, respectively. We had calculated material removal rate and surface roughness. Surface roughness is found using non-contact-type Talysurf. The calculated material removal rate and surface roughness on titanium alloy (Ti 3Al-2.5V) using oxygen and nitrogen gases are shown in Table 5. With these response parameters like surface roughness and material removal rate, the optimal setting of predominant process parameter is found by using Grey-Taguchi analysis (Fig. 1).

Table 5 Table for MRR and SR

Experiment no	Material removal rate (m³/min)		Surface roughness (µm)	
	Oxygen	Nitrogen	Oxygen	Nitrogen
1.	208.2	310.1	7.78	6.83
2.	210.4	321.56	7.27	4.36
3.	148.39	257.16	2.43	1.32
4.	213.37	324.6	6.71	4.81
5.	229.68	347.35	2.78	1.14
6.	269.19	398.44	4.83	2.05
7.	269.41	399.1	6.87	3.43
8.	287.49	414.18	6.17	2.65
9.	188.09	287.97	11.6	8.06

Fig. 1 Work piece specimen

3 Results and Discussion

3.1 Taguchi Optimization

Dr. Taguchi from Japan has introduced a method based on orthogonal array, which gives us much lesser variation to obtain optimum setting of the control parameter that is given as a design in Taguchi method.

3.2 Grey Relation Analysis

It works on using a specific concept of information similar to that of binary algebra. If the information is present and it is perfect, then it is regarded as white. Similarly, if no information is present, then it is portrayed as black. However, perfectly black or white is regarded as an idealized case, and in reality, it always lies between black and white.

Main Effects Plot for MRR(m3/min)

Data Means
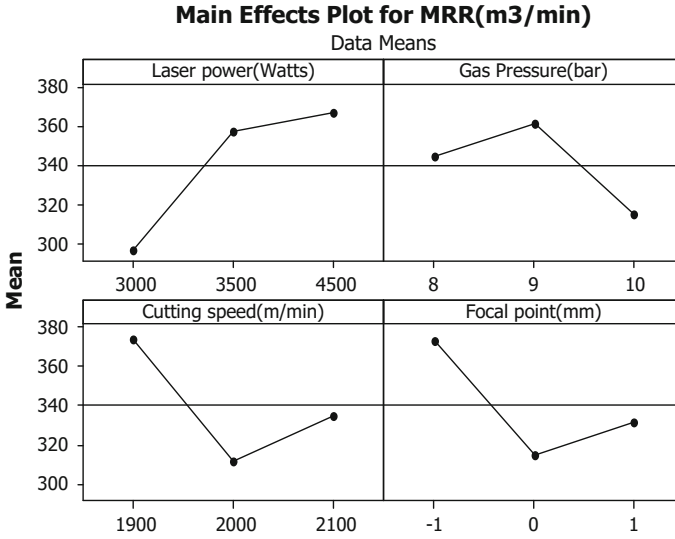
Fig. 2 Main effect plots for MRR of N_2

3.3 Steps Involved in Grey-Relational Analysis

Step-1 Transform the given information into S/N curve, otherwise called as shear strength vs number of cycles into Y_{nj} using suitable equation depending upon quality characteristics.

Step-2 After obtaining the *S/N* ratio, next task is to normalize the given date evenly and scale it to acceptable range for further analysis.

Step-3 Final step is to calculate the grey coefficient for the given normalized *S/N* ratios.

3.4 Grey-Relational Optimization

Grey relation method is the technique used for solving interrelationships among the multiple responses. This analysis follows the following steps:

Step-1 After transferring the responses into *S/N* ratio Y_{nj} using the suitable equations depending upon the quality characteristics (Table 6)

$$S/N \ \text{RATIO OF MRR} = -10 * \log(1/X) \sum \left(1/Y_{nj}^2\right)$$

$$S/N \ \text{RATIO OF SR} = -10 * \log(1/x) \sum Y_{nj}^2$$

Table 6 Values of *S/N* ratio to normalized *S/N* ratio

Ex No.	Material removal rate (mm³/min)				Surface roughness (µm)			
	S/N ratio of O_2	*S/N* ratio of N	Normalized *S/N* ratio of O_2	Normalized *S/N* ratio of N	*S/N* ratio of O_2	*S/N* ratio of N	Normalized *S/N* ratio of O_2	Normalized *S/N* ratio of N
1.	46.36	49.83	0.51	0.42	−17.81	−16.68	0.71	0.90
2.	46.46	50.14	0.52	0.50	−17.23	−12.78	0.67	0.66
3.	43.42	48.20	0	0	−7.71	−2.41	0	0
4.	6.58	50.22	0.54	0.52	−16.53	−13.64	0.62	0.71
5.	47.22	50.81	0.66	0.68	−8.88	−3.40	0.08	0.06
6.	48.60	52.02	0.90	0.99	−13.67	−6.23	0.42	0.24
7.	48.60	52.03	0.90	1	−16.73	−10.70	0.63	0.52
8.	49.17	52.34	1	1	−10.02	−8.46	0.16	0.38
9.	45.48	49.18	0.35	0.28	−21.28	−18.12	0.27	1

Table 7 Values of grey relation rank and grade

Ex. no	Grey-relational coefficient				Grey-relational grade		Rank	
	MRR		SR					
	O_2	N_2	O_2	N_2	O_2	N_2	O_2	N_2
1.	0.48	0.60	0.33	0.51	0.59	0.5	5	2
2.	1	0.33	1	0.33	0.33	0.33	6	4
3.	0.46	0.56	0.38	0.52	0.63	0.51	4	3
4.	0.34	0.35	0.91	0.56	0.34	0.60	7	1
5.	0.1	0.46	0.58	0.83	0.39	0.98	8	5
6.	0.1	0.57	0.37	0.83	0.51	1	2	6
7.	0	0.37	0.84	1	0.44	1	3	8
8.	0.65	0.40	0.73	0.43	1	0.28	1	9
9.	0.1	0.50	0.53	0.82	0.40	0.50	9	7

Step-2   To normalize the *S/N* ratio to the acceptable range and to distribute the data evenly using the following equation

$$\text{NORMALIZED } S/N \text{ OF MRR } Z_n = \left(Y_{nj} - \min Y_{nj}\right)/\left(\max Y_{nj} - \min Y_{nj}\right)$$
$$\text{NORMALIZED } S/N \text{ OF SR } Z_{nj} = \left(\max Y_{nj} - Y_{nj}\right)/\left(\max Y_{nj} - \min Y_{nj}\right)$$

where Z_{nj} is the normalized value of nth trial for nth dependent response.

Step-3   To calculate the grey coefficient (GC) for the normalized *S/N* ratio values as per the following equation.

$$GC_{nj} = \left(\Psi \min + \delta \Psi \max\right)/\left(\Psi_{nj} + \delta \Psi \max\right),$$

where GC is the grey coefficient for the *n*th trial of the dependent response, *d* is called the quality loss, and Ψ is the distinctive coefficient which has a range from 0 to 1 (Table 7).

The highest max–min value in the Tables 8 and 9 shows that high stand-off distance as the most influencing parameter on determining the response characteristics.

3.5   Effects of Process Parameters on MRR

The effect of gas pressure on MRR was tested in range from 0.6 to 1.0 bar. In this range, it was found that when the gas pressure increased, the MRR was almost of a fixed value. The tests were repeated at two different gases. Therefore, it is concluded that gas pressure has no effect on MRR in the test range. The test result of the effect of jet pressure on the MRR at different gasses. A number of experiments

Table 8 Average grey-relational grade for each input parameter of O_2

Control factor	Average grey-relational grade			Max–min
	Level 1	Level 2	Level 3	
Laser power (w)	0.486	0.548	0.611	0.123
Gas pressure (bar)	0.6038	0.564	0.477	0.126
Cutting speed (m/min)	0.6308	0.517	0.498	0.132
Focal point (mm)	0.4784	0.551	0.523	0.072

Table 9 Average grey-relational grade for each input parameter of N_2

Control factor	Average grey-relational grade			Max–min
	Level 1	Level 2	Level 3	
Laser power (W)	0.486	0.548	0.599	0.11
Gas pressure (bar)	0.6038	0.564	0.403	0.200
Cutting speed (m/min)	0.6306	0.5033	0.498	0.1326

were carried out to find the relations between the laser power and MRR [7]. During these tests, the laser power is varied from 1200 to 4000 W and the tests were repeated for cutting speed of 2.5–2.9 m/mm. It shows that MRR decreases with the increase of laser power. A number of experiments were carried to find the relations between the cutting speed and MRR. During these tests, the cutting speed varies from 2.5 to 2.9 m/mm. It shows that MRR increases with the increase of cutting speed. Main effect plots for MRR of oxygen are shown in Fig. 3. The MRR values were tested at four different focal points. The tests were repeated at three different laser powers. The tests show that the MRR values are nearly constant at different focal point. Therefore, it is concluded that the focal point distance has no effect on MRR value (Fig. 2).

3.6 Effect of Process Parameter on SR

The effect of gas pressure on surface roughness Ra parameter was tested under ranges of pressure 0.6–1 bar. In this range, it was found that when the gas pressure increased, the roughness Ra parameter was almost of a fixed value. The test was repeated using two inert gasses. Therefore, it is concluded that gas pressure had no effect on surface roughness Ra parameter in the test range. The effect of gas pressure on the surface roughness Ra parameter at different gasses. The surface roughness Ra parameter values were measured at different cutting speed that range from 2.1 to 2.5 m/min and the two different gasses [8]. As the cutting speed increases, the surface roughness decreases. The relation trend is of power function with medium regression ratio. Main effect plots for SR of nitrogen gas are as shown

Main Effects Plot for MRR(m3/min)

Data Means

Fig. 3 Main effect plots for MRR of O_2

Main Effects Plot for SR(μm)

Data Means
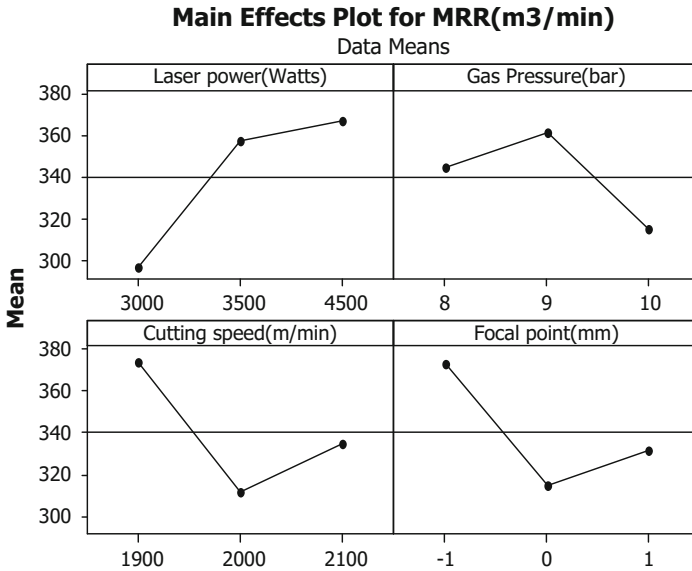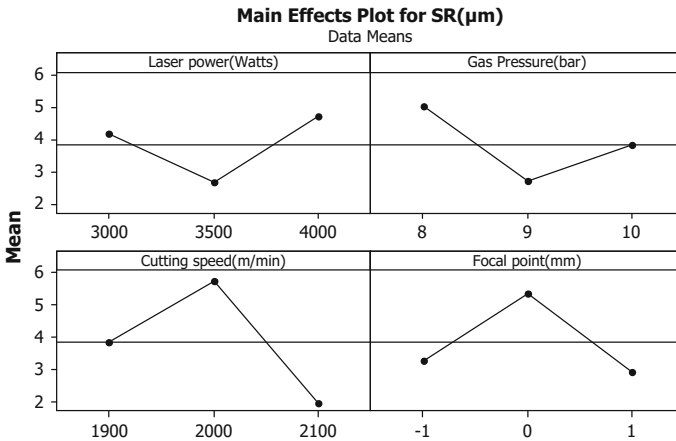
Fig. 4 Main effect plot for SR of N_2

in Fig. 4. The surface roughness Ra parameter values were tested at a range of laser power from 1200 to 4000 W [9]. The tests were repeated at two different cutting speeds. The surface roughness Ra values are nearly constant at different gasses. The higher the cutting speed yields, the lower the surface roughness. Main effect plot for SR of oxygen is shown in Fig. 5 [10].

Main Effects Plot for SR(µm)
Data Means
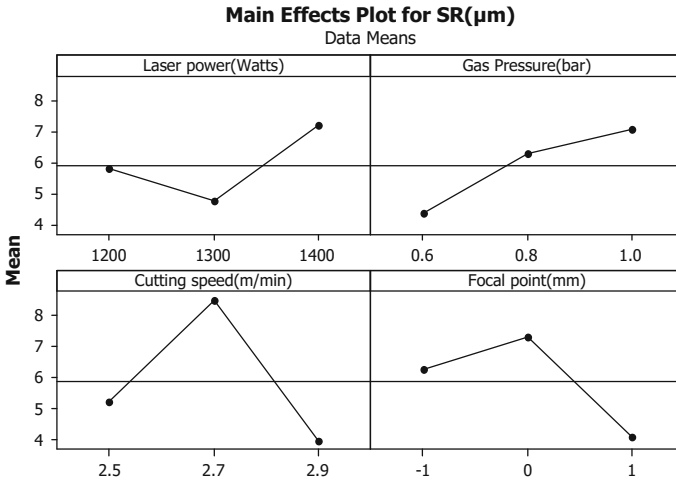
Fig. 5 Main effect plot for SR of O_2

1. Gas pressure—10 bar, cutting speed—1.9 m/min, laser power—4000 W, focal point—1 mm.

The better surface roughness of nitrogen gas because of low laser power and high focal point and the Ra value for better surface roughness for nitrogen is 4.2 µm. The parameters are shown in Fig. 6 [11].

2. Gas pressure—10 bar, cutting Speed—2.1 m/min, laser power—3000 W, focal point—1 mm.

The poor surface finishes value of oxygen gas because of gas pressure, cutting speed, laser power and focal point. The Ra value for poor surface roughness for nitrogen is 8.4 µm. Graphs are shown in Fig. 7.

3. Gas pressure—10 bar, cutting speed—2.1 m/min, laser power—1400 watts, focal point—1 mm.
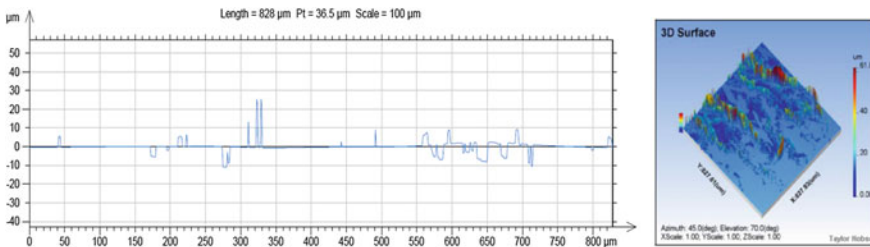
Fig. 6 2D and 3D graphs for better surface roughness for N_2
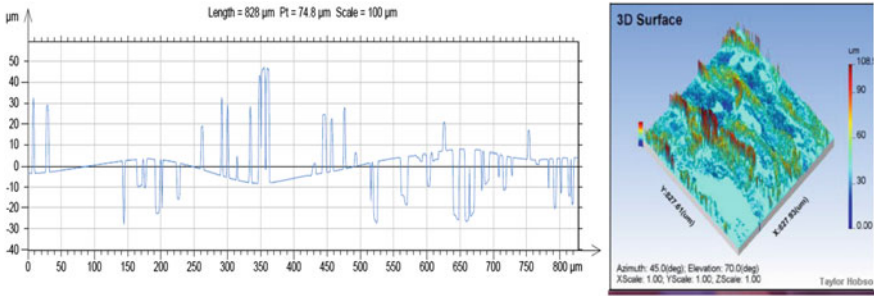
Fig. 7 2D and 3D graphs for poor surface roughness for N_2
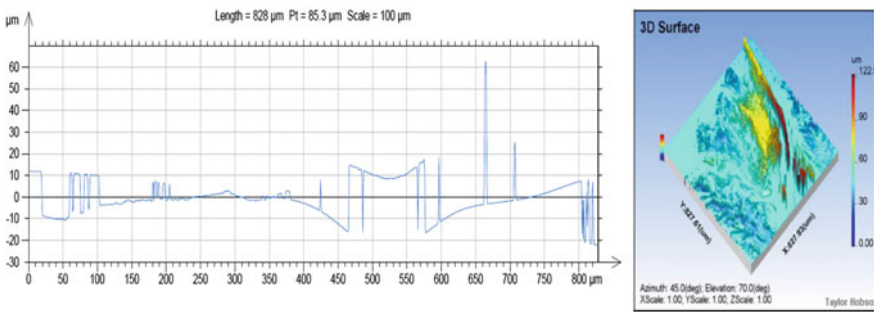
Fig. 8 2D and 3D graphs for better surface roughness for O_2

The better surface roughness of Oxygen gas because of low Laser power and High focal point. The Ra value for better surface roughness for oxygen is 7.2 µm. Graphs are shown in Fig. 8.

4. Gas pressure—10 bar, cutting speed—2.1 m/min, laser power—1200 W and focal point—1 mm.

The poor surface roughness of Oxygen gas because of low Laser power and High focal point [12]. The Ra value for poor surface roughness for oxygen is 11.5 µm. Graphs are shown in Fig. 9. The optimized graph of both oxygen and nitrogen is shown in 2D and 3D in Fig. 9 [13].

5. Gas pressure—10 bar, cutting speed—1.9 m/min, laser power—1400 W, focal point—1 mm.

The comparison of oxygen and nitrogen gasses give influence of low surface roughness. Graphs are shown in Figs. 10, 11 and 12.
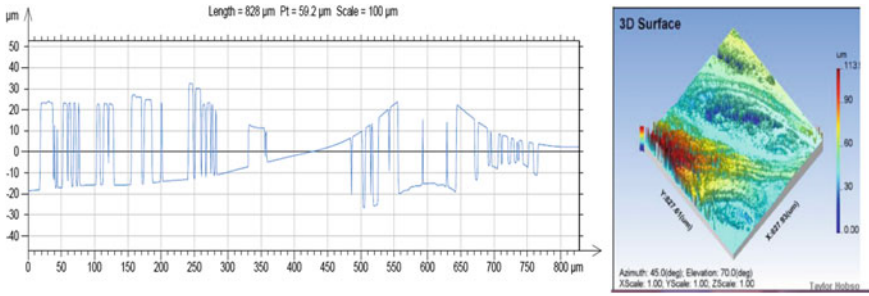
Fig. 9 2D and 3D graphs for poor surface roughness for O_2
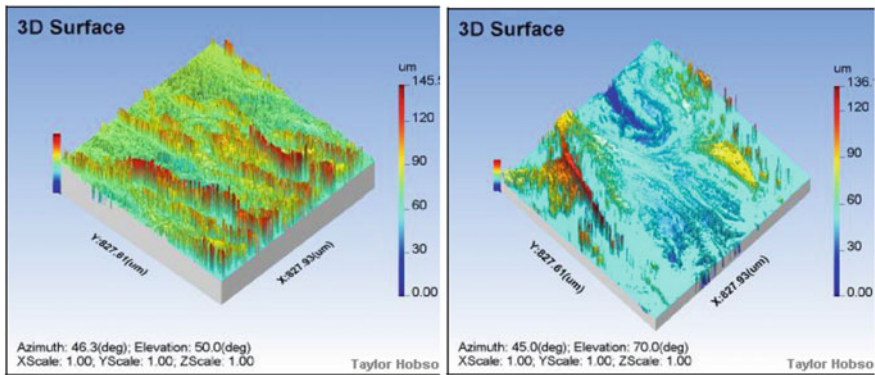
Fig. 10 3D graph for optimized value of O_2 and N_2

Fig. 11 Structure for N_2
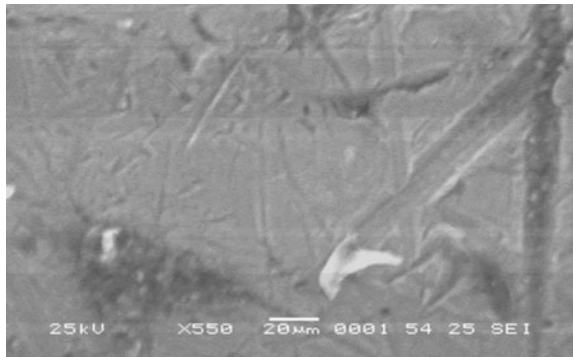
Fig. 12 Structure for O_2

3.7 SEM Analysis

Under scanning electron microscope (SEM), the specimen of the work piece is viewed and the image is obtained as shown below. The parameters are selected for the following parameters, gas pressure—10 bar, laser power 4000 W, type of cut—rough cut and cutting speed—2.1 m/min, magnification ratio of 100 μm. The below Fig. 13 shows a structure for nitrogen, and the Fig. 14 shows a structure for oxygen [14].

The below shown figure shows scanning electron microscope (SEM) image for poor and better work piece for heat-affected zone. The parameters are selected for the following parameters for better: gas pressure—10 bar, cutting speed—2.1 m/mm, laser power—4000 W, type of cut—rough cut, magnification ratio of 150 μm. The below Fig. 13 shows a better image for nitrogen, and the Fig. 14 shows s poor image for oxygen.

Fig. 13 Better image for N_2
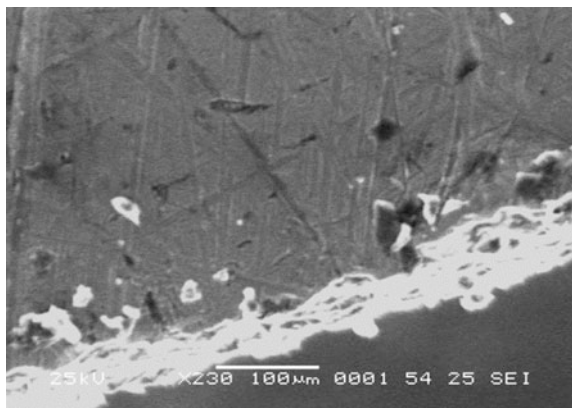
Fig. 14 Better image for O_2
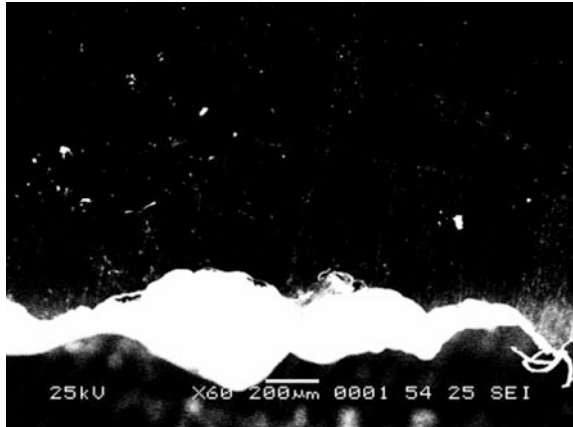
Fig. 15 Machined surface of N_2
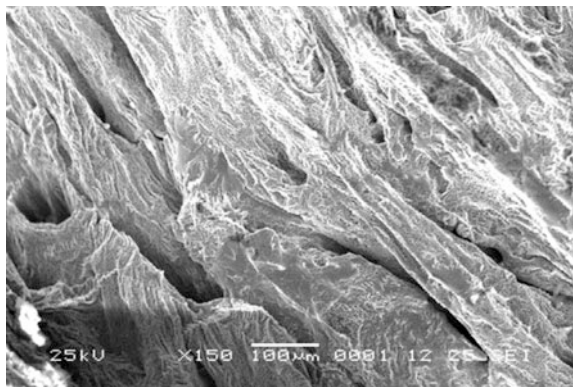
The below shown figure shows scanning electron microscope (SEM) for poor and better work piece for machined surface. These parameters are selected for the following parameters for better: gas pressure—10 bar, cutting speed—2.1 m/min, laser power—3000 W, type of cut—rough cut, magnifications ratio of 150 µm. The optimized values are obtained the experiment in which the grey-relational grade is ranked 1 of 9 experiments. The optimized values for various machining parameters are Material removal rate [15] is 45.6(g/min) and Surface roughness is 5.6 (µm). The above Fig. 15 shows a machined surface of nitrogen, and the Fig. 16 shows a machined surface of oxygen.

3.8 Confirmation Test

After obtaining the optimized values for material removal rate (MRR), surface roughness test had been carried out to verify the integrity of the results obtained.

Fig. 16 Machined
surface of O_2
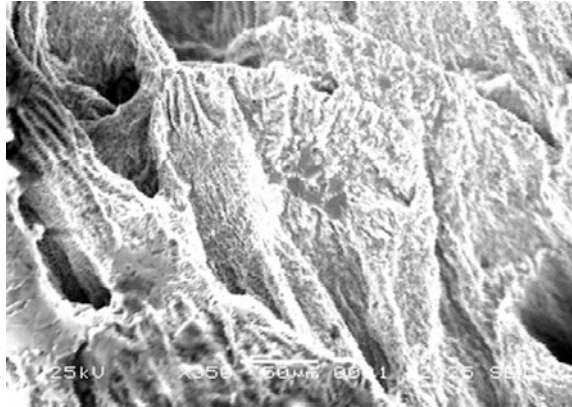
Finally, the satisfactory values are: MRR is 45.6 (g/min) and surface roughness is 5.6 (μm). As per 95% of confidence limit, the errors obtained for each of the response parameters are MRR: 4% error and surface roughness: 3.5% error. In this paper, titanium alloy (TiA3lV) was machined using one of the non-traditional machining processes called CO_2 laser beam machining. This alloy was chosen based on its prime application as a washer used in high-pressure turbine. The input parameters—laser power, gas pressure, cutting speed and focal point—were suitable varied to get the optimum values of response parameters like metal removal rate, surface roughness and heat-affected zone. The machining parameters were optimized using Grey-Taguchi approach, and it was confirmed by conducting a confirmation test. The graph which was generated using Minitab 17 software clearly represents of each input parameters over the response parameter. As per 95% of confidence limit, the error obtained for each of the response parameters are material removal rate is 4.67% error and Surface roughness is 3.25%. Through this experiment, we have learnt that Grey-Taguchi methodology can be effectively used to produce the optimum levels of machining parameters involved in CO_2 laser beam machining process.

4 Conclusion

In this present work, titanium alloy (Ti3Al2.5V) is machined using CO_2 laser beam machining. Titanium alloy is selected based on its applications in aerospace industries and high-pressure turbines, etc. The predominant input parameters like laser power, gas pressure, cutting speed and focal point were suitably varied to get optimum values of response parameters like material removal rate, surface roughness. These machining parameters are optimized using Taguchi-Grey analysis. The most suitable and optimal combination of the process parameter for getting better response parameter is found. The optimized satisfactory value of material removal

rate is 45.56 m^3/min and surface roughness is 3.5 μm under the condition of 4000 bar gas pressure, 2100 m/min cutting speed, type of rough cut and 1 mm of focal point. The most influencing factors for getting better material removal rate are cutting speed and pressure. The most influencing factors for getting better surface roughness are focal point and type of cut. It is found that SR and MRR are increased by 35 and 42%, respectively, while using nitrogen in place of oxygen in CO_2 laser beam machine. The confirmation test is carried out to check the integrity of the result obtained, and error percentage is found to be 4.67 and 3.25% for material removal rate and surface roughness, respectively.

References

1. Chen, K., Yaoh, Y.L., Modi, V.: Gas dynamic effects on laser cutting quality. J. Manuf. Process. **3**(No1), 38–49 (2001)
2. Chen, S.L.: analysis and modeling of reactive three-dimensional high-power CO2 laser cutting. Proc. I MECH E Part B J. Eng. Manuf. **212**(2), 113–128 (1998)
3. Asano, H., Suzuki, J., Kawakami, E.: Selection of parameters on laser cutting mild steel plates taking account of some manufacturing purposes. In: Fourth International symposium on laser precision microfabrication. Proceedings of SPIE, vol. 5063, pp. 418–425 (2003)
4. Di Pietro, P., Yaoh, Y.L.: An investigation into characterizing and optimizing laser cutting quality—a review. Int. J. Mach. Tools Manuf. **34**(2), 225–243 (1994)
5. Espinal, D., Kat, A.: Thermochemical modeling of oxygen-assisted laser cutting. J. Laser Appl. **12**(1), 16–22 (2000)
6. Mas,C., Fabbro, R.: Steady-state laser cutting modeling. J. Laser Appl. **15**(3), 145–152 (2003)
7. Chen, K., Lawrence Yaoh, Y., Modi, Vijay: Numerical simulation of oxidation effects in the laser cutting process. Int. J. Adv. Manuf. Technol. **15**(11), 835–842 (2004)
8. Lu, C.: Study on prediction of surface quality in machining process. J. Mater. Process. Technol. **205**(1–3), 439–450 (2008)
9. Chen, K., Yao, Y.L., Modi, V.: Gas jet-workpiece interactions in laser machining. J. Manuf. Sci. Eng. **122**, 429–438 (2000)
10. Jimin, C., Jianhua, Y., Shuai, Z., Tiechuan, Z., Dixin, G.: Int. J. Adv. Manuf. Technol. **33**(5–6), 469–473 (2007)
11. Ermolaev, G.V., et al.: Mathematical modelling of striation formation in oxygen laser cutting of mild steel. J. Phys. D Appl. Phys. **39**, 4236–4244 (2006)
12. Chen, S.-L.: Thermal modelling of cutting front edge dynamic behaviour in high-power reactive CO2 laser cutting. Proc. I MECH E Part B J. Eng. Manuf. **212**(7), 555–570 (1998)
13. Farooq, K., Kar, A.: Removal of laser-melted material with an assist gas. J. Appl. Phys. **83**(12), 7467–7473 (1998)
14. Gabzdyl, J.T., Morgan, D.A.: Assist gases for laser cutting of steels. In: ICALEO, pp. 443–447 (1992)
15. Yousef, B., Knopf, G.K., Bordatchev, E.V., Nikumb, S.K.: Neural network modeling and analysis of material removal process during laser machining. Int. J. Adv. Manuf. Technol. **22**(1–2) (2003)

Parametric Optimization of Abrasive Water Jet Machining of Beryllium Copper Using Taguchi Grey Relational Analysis

R. Manoj Samson, T. Geethapriyan, A. C. Arun Raj, Ashwin Ashok and Aditya Rajesh

Abstract Abrasive water jet machining is a non-conventional machining process to machine complicated intricate shapes, abrasive water jet machine is most suited as it can cut both conducting and nonconductive material with better finish. Beryllium copper grade C25 is used as a material for machining considering its applications in petroleum nozzle washer used in petroleum products and also in marine, aerospace industries. In this work, the predominant process parameters like pressure, abrasive flow, and standoff distance are varied to obtain optimum values of response parameters like (MRR) material removal rate and surface roughness. Since the multi-response optimisation cannot be performed by conventional Taguchi method, Grey-Taguchi methodology is used. Abrasive flow rate and standoff distance are the most influenced process parameters to obtain higher MRR and also for better surface-roughness. After obtaining the optimised values for machining parameters using Grey-Taguchi Methodology. A confirmatory test is performed to test the integrity of the obtained results.

Keywords Taguchi method · Abrasive flow · Standoff distance
MRR

1 Introduction

Abrasive water jet cutting or machining is same as (LBM) laser beam machining process and (EBM) electron beam machining and its similarity is in terms of concentration of a given amount of energy into a small point to cause material removal. AWJM uses a powerful fine water jet which travels at a very high velocity, to which abrasive materials are mixed for cutting work pieces like titanium (Ti) and granite. This would make a kerf which is a fine cut into the material.

R. M. Samson (✉) · T. Geethapriyan · A. C. Arun Raj · A. Ashok · A. Rajesh
Department of Mechanical Engineering, SRM University, Kattankulathur,
Chennai 603203, India
e-mail: manoj.sam6@gmail.com

1.1 Problem Identification

The essential requirements are problems identified, setting up objective, sorting out methodology, generation of prototype, creation of mathematical model, conducting experiments and testing. The problems identified are that the abrasive jet can cut through anything includes itself, the mixing tube is expensive and wears only in use for few hundred hours, and would result in a higher cost of operation. Plugging is caused by dirt on large particles in the abrasive, and this becomes a big problem with abrasive water jet nozzle being made better with fine tune mixing tube design.

1.2 Objective

To analyse the effect of grain sizes on machining performance or machining such as MRR, Surface roughness parameters in AWJM.

To optimize the process parameters like Pressure, abrasive, Abrasive mass flow rate on MRR and Surface Roughness.

And also to determine the optimum input process parameter to achieve the better and response using taguchi-grey relational analysis.

Principle

Being a non-traditional machining process it uses conventional mechanical energy to cut and also to machine materials which are soft and non-metallic in nature. It also uses water jet of high velocity to cut a soft work piece. In water jet machining water at high velocity jet is allowed to strike the work piece provided. During the process the K.E of the water jet is converted to PE (pressure energy). This induces a stress on the work piece which is high enough to remove unwanted particles of the work piece.

Process parameters of AWJM

Water Pressure, diameter of abrasive grains size, transverse speed, (SOD), abrasive mass flow rate, abrasive materials, orifice diameter, nozzle diameter, material removal rate, kerf taper angle, surface roughness, depth of cut.

2 Experimental Details

2.1 Material Selection

Copper beryllium alloys can be used for applications like good electrical and thermal conductivity and high strength. Copper beryllium alloys have two groups, high conductivity alloys and high strength alloys. Most commonly used Grades are

Table 1 Composition of Beryllium copper C25

Composition	Be Cu (%)
Zinc	0.01
Tin	0.06
Iron	0.12
Beryllium	2.36
Copper	96.82

C17000, C17200, C17500, C25, and C17510. For this application, C25 is our material of interest due to the vast applications.

Beryllium copper Grade C25 composition as obtained from laboratory after determining composition (Table 1).

Cast beryllium coppers are commonly used in plastic injection moulds. Having high conductivity along with high fluidity and reproducibility master patterns makes them suitable for high production speeds, while maintaining oxidation resistance and oxidation resistance.

Applications of Be Cu (C25)

They are used in applications such as electrical equipment such as switches and relays blade, Petroleum nozzle washers, cases for magnetic devices, high speed plastic moulds.

This application is mainly based on the use of beryllium copper (C25) in making of Petroleum pump washer (Fig. 1).

Usually the Beryllium copper washers in Petroleum nozzles are machined using Stamping process. But these processes have the following disadvantages.

Fig. 1 Beryllium copper washer

Disadvantages of Stamping include, low material removal rate, rough surface finish, heat affected zone and high power consumption. Thus, we prefer Abrasive water jet machining AWJM for overcoming such problems. Following are its advantages,

High material removal rate
Better surface finish
No heat affected zone.

2.2 Abrasive Selection

2.2.1 Garnet 80 Mesh

Garnet abrasive is made of natural Almandine garnet fine grains which are known for natural hardness, durability and their abrasive characteristics. Garnet abrasive is used in all water jet cutting machines globally. Garnet 80 mesh is the most suitable abrasive for cutting purpose in AWJM. The use of garnet 80 mesh abrasive as compared to other abrasives i.e. tungsten carbide, aluminium oxide, in water jet machining process.

2.3 Tool Selection

2.3.1 Nozzle

The different nozzles used in the AWJM are Silicon carbide. Boron carbide Sapphire, Tungsten Carbide the tool which is selected for carrying out the machining process is Tungsten Carbide. These are the following advantages.

More thermal conductivity—400 W/m K
Better machinability
Easily available

Intricate shapes can be made at low cost.

2.3.2 Orifice

The centre of abrasive water jet nozzle is an orifice which creates a water jet stream. These are generally made from a synthetic jewel like sapphire, ruby, and diamond. The effective diameter of water jet stream is smaller than the orifice itself because of fluid flow through a hole under pressure due to cross section variation.

3 Experimental Methods

3.1 Experimental Setup

The AWJM setup consists of machining chamber, high pressure pump along with an articulated cutting head and also an abrasive water jet nozzle with a catcher tank and abrasive hopper, Pc based controller *X-Y* transverse system, filtration unit, pump and a reservoir. The work piece provided is fixed on the fixture inside the machining chamber and tool is attached on the articulated cutting head. The whole setup of AWJM is integrated by a personal computer. The input parameters factors like Pressure (Bar), Flow rate of abrasives (g/min) and SOD in (mm) are also varied using the software OMAX.

Initial trial experiments are conducted to find out the range of each input parameters like Pressure, flow rate of abrasives in (g/min) and SOD in (mm) that can be used as a pre-set value before starting the actual experiments. After determining the range, the actual experiments (L_9) are conducted by suitably varying the input parameters. Each type of experiment takes different time durations depending upon the parameters and the capability of the machine. After the completing each experiment, the work piece is carefully removed from the machining chamber and cleaned thoroughly to check for the washer which has been made by the machine.

Catcher tank

Water gets filled in the catcher tank and the energy is made to dissipate after it has cut the material under machining.

Abrasive Water jet Nozzle

Pressurized water is made to pass through mini diametrical orifice and will form a jet of water. It then passes through a mini venturi section where trace amounts of abrasives are pulled into the stream of water. The most commonly used nozzle is tungsten carbide with its diameter is 0.6 mm.

Experiments are conducted on the AWJM equipment. The work piece (Be Cu rectangular sheet of ($200 \times 250 \times 2.5$ mm) is fixed on the fixture inside the machining chamber and the tool (Nozzle at diameter of 6 mm) is attached on the articulated cutting head. The whole setup of AWJM is integrated by a personal computer. The input parameters (factors) like Pressure (*P*), flow rate of abrasives (g/min) and SOD (mm) are varied using the software OMAX. The Purified R.O Water is pumped through a motor from the reservoir.

3.2 Design of Experiment

Due to the simplicity, Taguchi method is opted for optimization procedures using variables which will provide the desired data's from less no: of trials of various levels.

$$DOF = (P-1)(F) + (P-1)(P-1)(Q) + 1$$

where (DOF) is the degree of freedom, and F is the no. of independent variables, P is their corresponding levels and Q is the number of interactions. In our experiment number of levels, $P = 3$, number of independent variables, $F = 3$ and number of interactions, $Q = 0$. Therefore degree of freedom (DOF) = 7. But as per Taguchi design of experiments we choose L_9 orthogonal table (Table 2).

3.3 Process Parameters

Process parameters are classified to two different categories namely input parameters also known as (independent parameters) and output parameters also known as (dependent parameters) (Table 3).

The input parameters (factors) used are Pressure (Bar), flow rate of abrasive (g/min) and SOD (mm). These factors are selected based on the fact that less number of research works has been done with this combination.

Water pressure

The water pressure range required for AWJM is from (1400–1800 bar). With increase in water pressure, the depth of cut increases and beyond this critical

Table 2 Design of experiments

Experiment	Pressure in (bar)	Type	Abrasive flow rate in (g/min)	Standoff distance in (mm)
1	1400	Rough	190	2
2	1400	Standard	310	3
3	1400	Super fine	433	4
4	1600	Super fine	190	3
5	1600	Rough	310	4
6	1600	Standard	433	2
7	1800	Standard	190	4
8	1800	Rough	310	3
9	1800	Super fine	433	2

Table 3 Average grey relational grade for each input parameter

Factors	First level	Second level	Third level
Pressure in (bar)	1400	1600	1800
Abrasive flow rate in (g/min)	190	310	433
Stand-off distance in (mm)	2	3	4
Type of cut	Rough	Standard	Super fine

pressure point the depth of cut will increase linearly with increase in the water pressure for a particular set of values.

Standoff distance

An increase in the standoff distance causes a significant decrease in the depth as the jet power reaching the work piece decreases with increase in standoff distance, and if the standoff distance is less then it causes damage. The optimum standoff distance value which is equal to 2 mm is determined.

Abrasive mass flow rate

The depth of cut and the abrasive mass flow rate have linear relation initially up to a particular value after which there is inverse relationship with depth of cut.

3.4 Response Measurement

After the machining process, the measurements of response parameters like MRR (g/min), surface roughness (µm) and radial overcut (µm) are to be measured as per their formulas for carrying out the optimization part of the project.

3.4.1 Material Removal Rate

MRR is calculated based on weight measured before machining and after machining of the work piece. The weight measurement of the work piece was done by the equipment called, Electronic weighing machine with the accuracy up to 4 decimal places.

The formula for the Material Removal Rate is given by,

$$\text{MRR} = (\text{IW} - \text{FW})/t \ (\text{g/min})$$

where,

IW   Weight before machining in (g) of the work piece
FW   Weight after machining in (g)
t Time for Machining in (min)

3.4.2 Surface Roughness

Surface roughness of the Machined Surfaces of the work pieces are measured using non-contact type, "Talysurf CCI LITE". The average roughness (value for each sample is measured) as shown in the below figure. The measured and calculated values for MRR (g/min), surface roughness (μm) are tabulated and in that best and worst image are obtained for surface roughness (μm) and radial overcut (μm) are also highlighted.

3.4.3 SEM Analysis

Scanning Electron Microscope is an electron microscope using focused electron beams to synthesize images. The electrons are made to interact with other atoms from within same sample, and producing different types of signals that contains details about the surface composition and topology. Heat affected zone of the work piece is captured in the SEM.

4 Result and Discussion

4.1 Taguchi Optimization

Dr. Taguchi from Japan has introduced a method on orthogonal array, which gives us a much lesser variation to obtain optimum setting of the control parameter is given by design in Taguchi method (Table 4).

4.2 Grey Relational Analysis

Taguchi method only deals with optimization of only single response. It gives different optimization combinations for various responses. So, it is very much required to introduce multiresponse optimization methods for these processes.

GRA is coupled along with Taguchi method and is employed for multi response optimization. In this method, they can be converted into normalized single response.

The GRA procedure is as follows,

- Convert the responses into signal to noise ratio using higher the better or lower the better criterion.
- Normalize the signal to noise ratio.
- Compute GR coefficient for normalized signal to noise ratio.
- Compute GR grade.
- Rank the GR grade (Table 5).

Table 4 Process parameters and its response

Experiment number	Pressure (bar)	Type	Rate of flow of abrasive (g/min)	Standoff-distance in (mm)	Abrasive orifice diameter in (mm)	MRR in (g/min)	Surface roughness (Ra) μm
1	1400	Rough	190	2	6	40.45	2.84
2	1400	Standard	310	3	7	23.706	1.78
3	1400	Super fine	433	4	8	15.462	1.69
4	1600	Super fine	190	3	6	16.125	2.94
5	1600	Rough	310	4	7	30.752	3.14
6	1600	Standard	433	2	8	24.178	2.15
7	1800	Standard	190	4	6	27.8	2.57
8	1800	Rough	310	3	7	31.333	1.38
9	1800	Super fine	433	2	8	17.951	1.77

Table 5 Signal to noise (S/N) ratio with normalized values of response parameters

Sample No.	MRR in (g/min)		Surface roughness (µm)	
	S/N ratio	Normalized S/N ratio	S/N ratio	Normalized S/N ratio
1	29.919	0.7346	−9.06	0.877
2	27.497	0.4445	−5.008	0.3102
3	23.785	0	−4.557	0.2472
4	24.149	0.0435	−9.336	0.9199
5	29.757	0.7152	−9.938	1
6	27.668	0.465	−6.648	0.5397
7	28.88	0.6107	−8.198	0.7565
8	32.138	1	−2.79	0
9	25.081	0.1552	−4.959	0.303

4.3 Quality Characteristics

The responses obtained from each trial is to be converted into S/N ratio in order to find the quality characteristics. When MRR is maximized, it is taken as superior **23**. Since the S/N ratio for the response is tabulated from these equations. S/N ratio for larger the better case (MRR):

$$\text{S/N ratio} = -10 * \log(1/x)\Sigma(1/Y2nj)$$

Radial overcut and surface roughness are smaller the better type and their S/N ratio are computed from these equations.

S/N ratio for smaller the better case (SR and ROC):

$$\text{S/N ratio} = -10 * \log(1/x)\Sigma(Y2nj)$$

where,

x is the number of experimental replication
Ynj is the response of nth trail of jth dependent level

A graph is plotted for Material removal rate versus Pressure (Bar), rate of flow of abrasive (g/min) and Standoff-distance (mm) to find out the influence of each input parameter over MRR. This graph is generated in the Minitab 17 software.

4.4 Grey Relational Optimisation

This optimization process is used for solving interlinked relationships among the multiple responses. The analysis consists of the following rules.

Step 1: Convert the responses to the S/N ratio Ynj using the required equations.

Step 2: Normalize S/N ratio and distribute evenly the data and also scale to acceptable range using these equations.

$Znj1/4(Ynj\_min\, Ynj)/(\max Ynj\_min\, Ynj)$

(for larger better case)

$Znj1/4(\max Ynj\_Ynj) = (\max Ynj\_min\, Ynj)1/2$

(for smaller better case)

where Znj is the normalized value of nth trial for jth dependent responses.

Step 3: Calculate the (GC) grey co-efficient for normalized S/N ratio values as per these equations

$GCnj = (\Psi\min + \delta\Psi\max)/(\Psi nj + \delta\Psi\max)$

d is the quality loss and W is the distinctive coefficient which varies from 0 to 1.

Step 4: $Gn = (1/Q)\Sigma GCnj$
where,

Q is number of responses = 3
$GCnj$ is the grey co-efficient for nth trail for jth dependent response

Step 5: Use the response graph method to choose optimal levels of input factors based on the maximum average Gn value (Table 6).

From the above table it can be inferred that the values of response parameters for 9th experiment are optimized value since it is ranked 1. Mean grey relational for each input parameter for 80 grain size the below table is lists the control parameters (Table 7).

Table 6 Grey relational coefficient

Experiment	Grey relational coefficient		GR grade	Rank
	MRR	SR		
1	0.653	0.82	0.7275	2
2	0.473	0.417	0.445	7
3	0.333	0.399	0.366	9
4	0.343	0.8619	0.62	5
5	0.639	1	0.8195	1
6	0.483	0.5206	0.5018	6
7	0.562	0.689	0.6255	4
8	1	0.333	0.6665	3
9	0.3718	0.4177	0.3947	8

Table 7 Average grey relational grade for each input parameters

Control factors	Average grey relational grade			Max-min
	Level 1	Level 2	Level 3	
Pressure	0.5128	0.6411	0.5617	0.1283
Stand-off distance	0.5413	0.5706	0.6035	0.0625
Abrasive mass flow rate	0.6516	0.6431	0.4209	0.2308
Type of cut	0.7373	0.5241	0.4542	0.2831

4.5 Effect of Process Parameters on MRR

Figure 2 shows the significant influence of stand-off distance and abrasive flow rate on MRR in (g/min).

Higher the stand-off distance lower will be the MRR up to a limit and then starts to increase the MRR level.

The effect of jet pressure on MRR was tested in range of pressures from 1400 to 1800 bar. In this range it was found that when the jet pressure increased the MRR was almost of a fixed value. The tests were repeated at two abrasive flow rates. Therefore, it is concluded that jet pressure has no effect on MRR in the test range. The test results of the effect of jet pressure on the MRR at standoff distances. A number of experiments were carried out to find the relation between the abrasive flow rate and MRR. During these tests the abrasive flow rate varied from 190 to 433 g/min. It shows that MRR increases with the increase of abrasive flow rate. The trend is of a polynomial function with high regression ratio $R2$.

The MRR values were tested at three different stand-off distances. The tests were repeated at three different type of cut. The tests show that the MRR values are
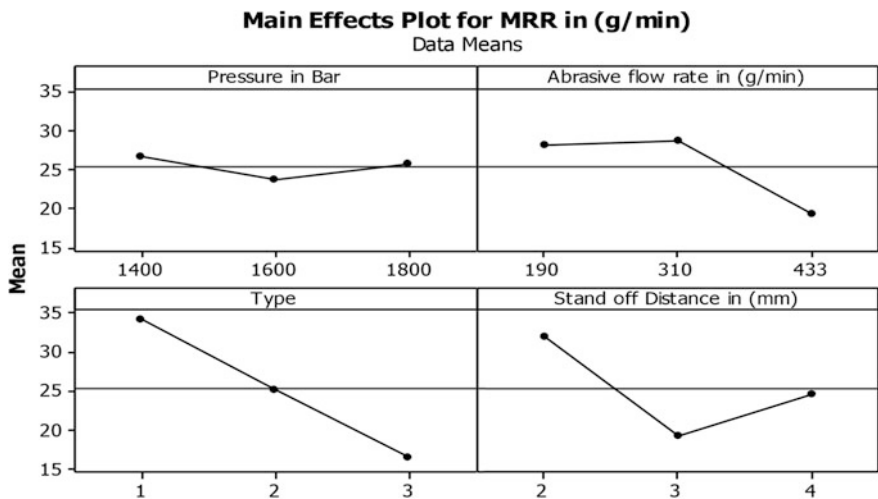
Fig. 2 Main effect's plots for MRR

nearly constant at different stand-off distances. Therefore, it is concluded that the Type of cut (Rough) has more effect on MRR value.

The regression equation is

$$\text{MRR in (g/min)} = 52.2 - 0.00211 \text{ Pressure in Bar}$$
$$- 0.0150 \text{ Abrasive flow rate in (g/min)}$$
$$- 7.87 \text{ Type} - 1.03 \text{ Standoff Distance in (mm)}$$

4.6 Effect of Process Parameters on SR

The effect of jet pressure on surface roughness Ra parameter was tested under ranges of pressures from 1400 to 1800 bar. In this range it was found that when the jet pressure increased the surface roughness Ra parameter was almost of a fixed value. The tests were repeated at one abrasive flow rates. Therefore, it is concluded that jet pressure has no effect on surface roughness Ra parameter in the test range. The effect of jet pressure on the surface roughness Ra parameter at different abrasive flow rates.

Effect of process parameters on surface roughness

Figure 3 shows the influence of process parameters on Surface roughness in micron level. It is clearly understood that pressure and stand-off distance has a positive impact on the values surface roughness. The highest value of surface
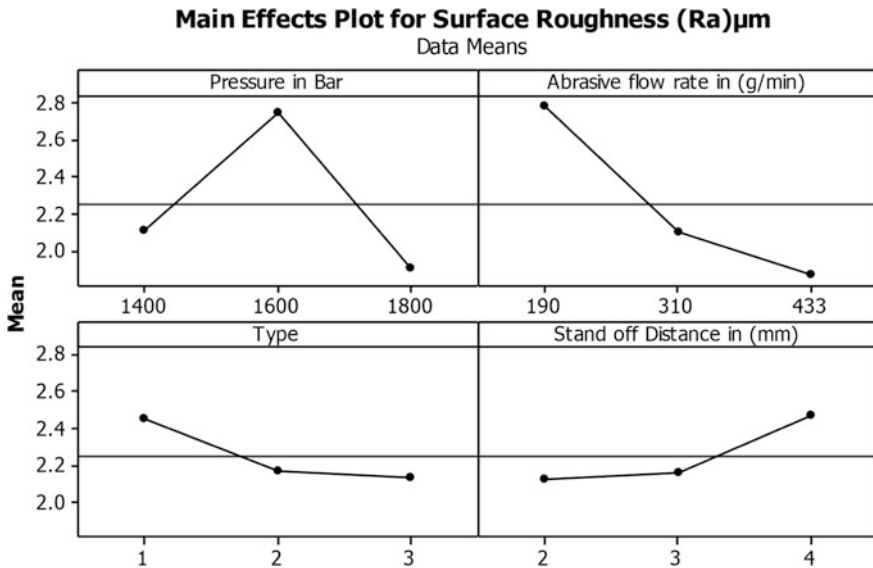
Fig. 3 Main effect's plots for surface roughness

roughness is obtained by varying the pressure of the abrasive jet, however a saturation limit is obtained with increase in the pressure of the abrasive jet. Whereas abrasive flow rate has a negative impact on the surface roughness value, as more the abrasive flow rate, less will be the surface roughness value.

The surface roughness Ra parameter values were tested at a range of abrasive flow rate from 190 to 433 g/min. The tests were repeated at different traverse speeds. The surface roughness Ra values are nearly constant at different abrasive flow rates. The higher the traverse speed yields that the surface roughness is decreasing by increasing the abrasive flow rate.

The effect of stand-off distance on the surface roughness was tested. The test was conducted at three different stand-off distances and repeated at two traverse speeds. The surface roughness parameter Ra values changes barely with the increase of the stand-off distance. Therefore, it is concluded that the Abrasive flow rate and Pressure has effect on depth of cut in the range.

The regression equation is

$$
\begin{aligned}
\text{Surface Roughness } (Ra) \text{ μm} =\ & 3.70 - 0.00049 \text{ Pressure in Bar} \\
& - 0.00352 \text{ Abrasive flow rate in(g/min)} \\
& - 0.082 \text{ Type} + 0.199 \text{ Standoff Distance in(mm)}
\end{aligned}
$$

4.6.1 Influence of Abrasive on SR

The poor Surface roughness of 80 grain size and there parameters are shown in Fig. 4. In this figure, indicates the higher surface roughness was achieved because the lower Stand-off distance has produced more peak and valley surface from the workpiece, due to that high pressure and rough cut is achieved.

Pressure—1400 bar, Mass flow rate—190 g/min, Type of cut—Rough cut, Standoff distance—2 mm.

The better Surface roughness of 80 grain size and there parameters are shown in Fig. 5.
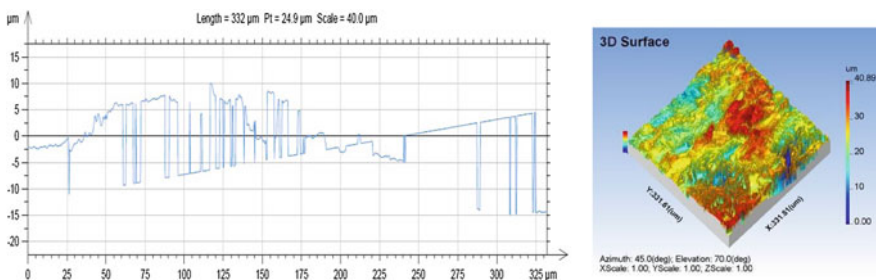
Fig. 4 2D and 3D graphs for poor surface roughness
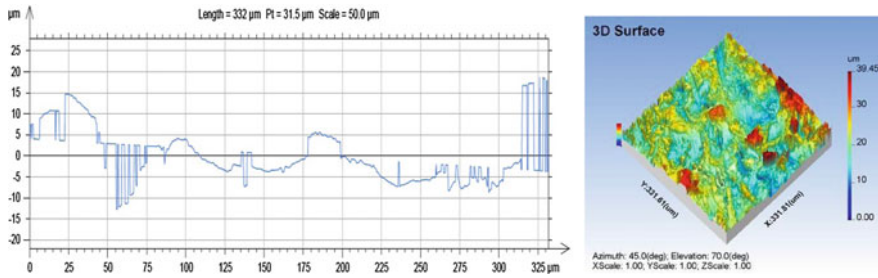
Fig. 5 2D and 3D graphs for better surface roughness
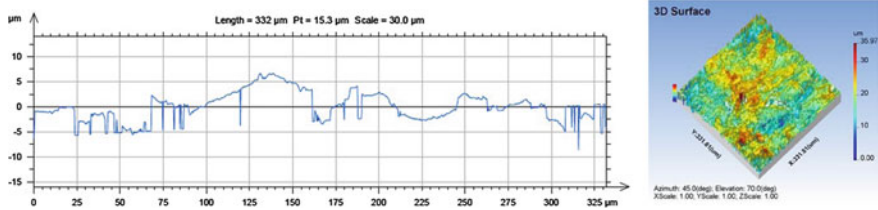
Fig. 6 2D and 3D graphs for moderate surface roughness

Pressure—1800 bar, Mass flow rate—190 g/min, Type of cut—Rough, Standoff distance—3 mm.

The optimized Graph of 80 mesh grain size shown in 3D graph. This Fig. 5 indicates better surface roughness was achieved due to higher value of stand-off distance and pressure (Fig. 6)

Pressure—1800 bar, Mass flow rate—433 g/min, Type of cut—Supper fine, Stand-off distance—2 mm. This figure indicates moderate surface roughness due to higher pressure values and comparatively lower stand-off distance.

4.7 SEM Analysis

Figures 7, 8 and 9 shows Scanning electron microscope (SEM) for poor work piece these parameters are selected for the following parameters, Pressure—1400 bar, Standoff distance—2 mm, Type of cut—Rough cut and Abrasive mass flow rate of 190 g/min. Magnification ratio of 100 μm.

Figures 10 and 11 shows Scanning electron microscope (SEM) for poor work piece these parameters are selected for the following parameters, Pressure—1800 bar, Standoff distance—3 mm, Type of cut—Rough cut and Abrasive mass flow rate of 310 g/min. Magnification ratio of 100–500 μm.

Fig. 7 Structure
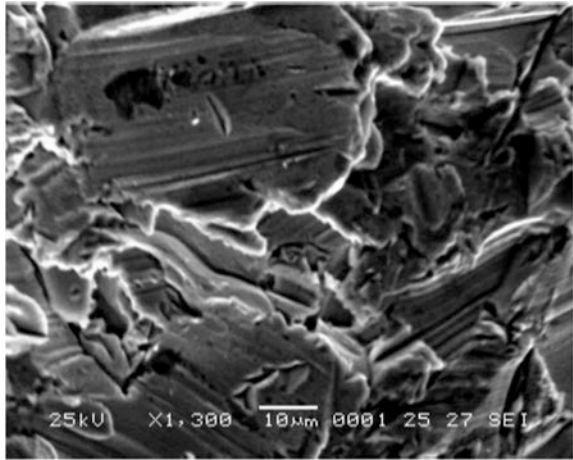
Fig. 8 Poor solidification area
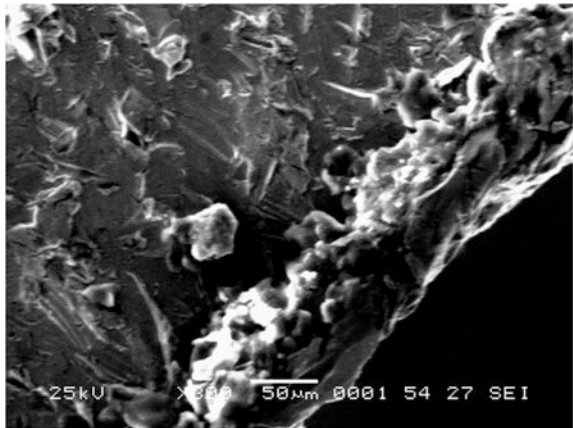
Fig. 9 Poor heat affected zone
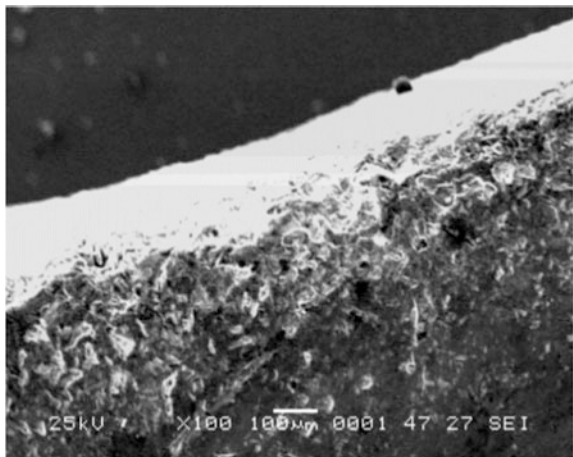
Fig. 10 Better solidification area
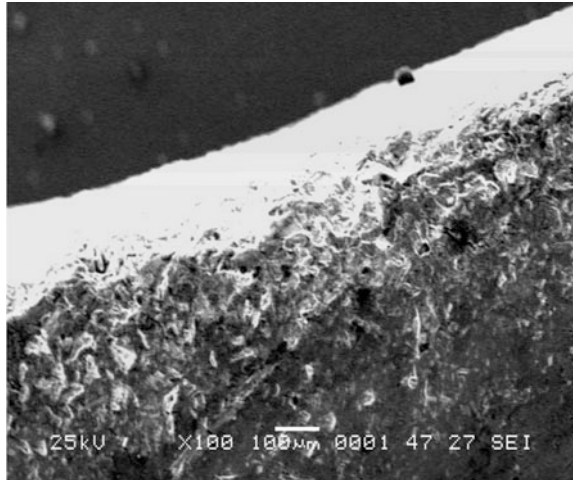
Fig. 11 Better heat affected zone
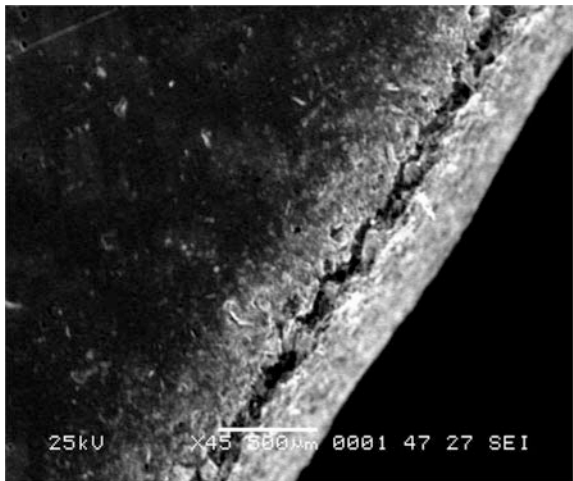
High heat affected zones are the main places for crack generation and low heat affected zones are the places where crack initiation does not take place and is strong compared to heat affected zone.

Figures 12 and 13 shows Scanning electron microscope (SEM) for poor work piece these parameters are selected for the following parameters, Pressure—1600 bar, Standoff distance—4 mm, Type of cut—Super fine and Abrasive mass flow rate of 310 g/min. Magnification ratio of 500 μm. The optimized values are obtained from the experiment in which the grey relational grade is ranked 1 out of 9 experiments. The optimized values for various machining parameters are

Fig. 12 Optimized
solidification
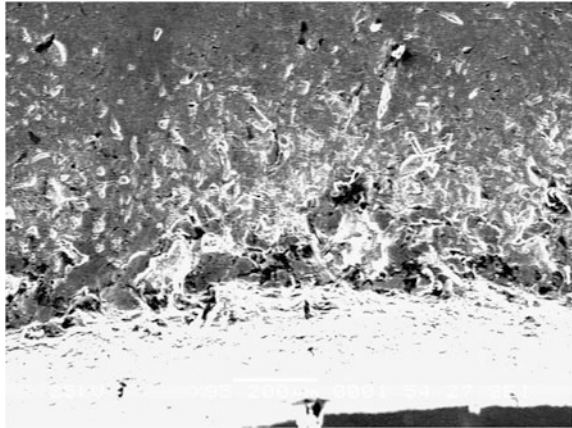
Fig. 13 Optimized heat
affected area zone
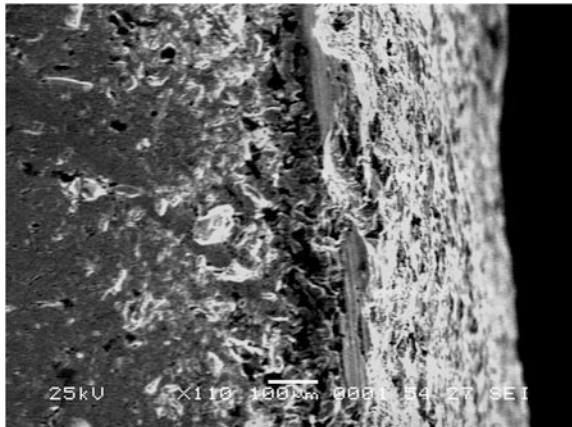
Material removal rate is 30.752 (g/min).
Surface roughness is 3.14 (μm).

4.8 Confirmation Test

After obtaining the optimized values for Material removal rate (MRR), Surface
Roughness, a confirmatory test was carried out in order to verify the integrity of the
results obtained.

Finally, the satisfactory values are,

Material removal rate is 30.752 (g/min) with Surface roughness of 3.14 (μm).

As per 95% of confidence limit, the error obtained for each of the response
parameters are:

Material removal rate: 3.31% error, Surface roughness: 3.98% error.

Beryllium copper Grade C25 was machined using AWJM. This alloy was chosen Based on its prime application in fuel injector nozzle used in diesel engine. The input Parameters like Pressure and abrasive flow rate and stand-off distance were suitably varied to get the optimum values of response parameters like metal removal Rate, surface roughness.

The machining parameters were optimized using Grey-Taguchi approach and it was confirmed by conducting a confirmation test. The graph which was generated using

Minitab 17 software clearly represents the influence of each input parameter. Over the response parameter.

As per 95% of confidence limit, the error obtained for each of the response Parameters are:

Material removal rate: 3.31% error
Surface roughness: 3.98% error

Through these experiments we have learnt that Grey-Taguchi methodology can be effectively used to find the optimum levels of machining parameters involved in Abrasive water jet Machining process.

5 Conclusion

Beryllium copper grade C25 is machined using abrasives in WJM and the predominant input parameters like Pressure in (bar), Standoff distance (mm), abrasive flow rate (g/min) and type of cut, where suitably varied to get the optimum values of response parameter's like Material removal rate, Surface roughness. These machining parameters are optimized using Taguchi-Grey relational analysis.

The optimal process parameters for obtaining better response is found. The optimized satisfactory value of material removal rate is 30.752 g/min and surface roughness 3.14 μm under the condition of pressure 1600 bar, standoff distance 4 mm, type of cut rough, mass flow rate of abrasive 310 g/min.

The most influencing factors for getting better material removal rate is standoff distance and pressure. The most influencing factor for getting better surface roughness is abrasive mass flow rate and type of cut. The confirmation test was carried out and error percentage is found to be Material removal rate 3.31%, Surface roughness is found to be 3.98% respectively.

References

1. Korat, M.M., Acharya, G.D.: A review on current research and development in abrasive waterjet machining. Int. J. Eng. Res. Appl. **4**(1) (Version 2) (2014)
2. Liu, H., Wang, J., Kelson, N., Browna, R.J.: A study of abrasive waterjet characteristics by CFD simulation. J. Mater. Process. Technol. **153–154**, 488–493 (2004)
3. Akkurt, A., Kulekci, M.K., Seker, U., Ercan, F.: Effect of feed rate on surface roughness in abrasive waterjet cutting applications. J. Mater. Process. Technol. **147**, 389–396 (2004)
4. Chithirai Pon Selvan, M., Mohana Sundara Raju, N: Analysis of surface roughness on abrasive water jet cutting on cast iron. Int. J. Sci. Environ. Technol. **1**(3), 174–182 (2012)
5. Azmir, M.A., Ahsan, A.K., Rahman, A., Noor, M.M., Aziz, A.A.: Optimization of Abrasive of waterjet machining process parameters using orthogonal arrays with grey relational analysis. In: Regional Conference on Engineering Mathematics, Mechanics, Manufacturing & Architecture (EM 3 ARC). Computational & Experimental Mechanics Research Group (2007)
6. Nagdeve L, Chaturvedi V, Vimal J.: Parametric optimization of abrasive waterjet machining using Taguchi methodology. IJREAS 2(6) (2012)

Investigation of Surface Damages in Hole Making on Luffa/Jute/Glass Reinforced Plastics

R. Vinayagamoorthy, Ankur Sharma, Vignesh Iyer and G. Navneeth

Abstract This research has been performed to investigate the surface damages induced during the drilling process on hybrid plastic composite. Plastic composite has been manufactured by adding three reinforcements, namely luffa fruit fiber, jute mat, and glass mat in polyester matrix. A set of holes are made at different points by altering the operating parameters. Central composite design methodology has been used for designing the experiment, for analysing the data, and for optimizing the output parameters. The operating factors considered are spindle revolution rate, tool traverse rate, and tool point angle. The surface damage of each hole in its profile and on its inner walls is noted as the output parameters. A thorough investigation on the effect of each operating factors on the output responses has been done. A desirability-based optimum condition has been taken by setting the goals as minimizing the output responses and repetitive confirmatory runs are made. Comparison between the optimum situation and confirmatory experiments showed very minimal difference. Hence, the optimization is highly consummate for the hybrid composite.

Keywords Plastic drilling · Damage factor · Wall roughness · Optimization
Hybrid composite

R. Vinayagamoorthy (✉) · A. Sharma · V. Iyer · G. Navneeth
Department of Mechanical Engineering, Sri Chandrasekharendra
Saraswathi Viswa Mahavidyalaya, Kancheepuram 631561,
Tamil Nadu, India
e-mail: vin802002@gmail.com

A. Sharma
e-mail: sharmaankur2121@gmail.com

V. Iyer
e-mail: vigneshraman911@gmail.com

G. Navneeth
e-mail: ganesan.navneeth@gmail.com

1 Introduction

Polymer matrix composites are one among the several composites which are utilized as structural parts for machineries and supporting structures in almost all industries [1]. Polymeric composites are prepared by reinforcing a fiber in a polymeric matrix. At the inception, polymeric composites are manufactured by using synthetic reinforcements like carbon, aramid, and glass. Later, because of the competent properties natural fibers have been utilized as reinforcements in polymeric composites [2–5]. Once a composite is manufactured, its characteristics must be tested to know its capacity against different loading conditions. A bio-fiber needs some chemical treatment and heat treatment to improve its surface properties, and consequently, it helps to improve the mechanical strength of the laminate [6–8]. Machining of polymeric composites is majorly done to produce holes which will help during assembly of components and as a finishing operation for removal of burrs, blunting the corners, and for surface polishing [9, 10]. Among the different machining operations, hole making is a vital operation and assessing the machinability of a new polymeric composite is also important. Holes are made in polymeric composites by the drilling process and occasionally by milling. In general, the main input factors considered are the spindle revolution rate, spindle feed or tool traverse rate, drill point angle, drill size, flutes. Similarly, the main output parameters to be considered are the damage of the thrust force and torque induced, surface roughness, cutting temperature, etc.

During hole making, by drilling thrust force along the axis of the tool is induced in the machining region and the inner surface of the hole get affected during hole drilling. The tool traverse rate and drill size have more influence over the thrust force, whereas tool traverse rate and spindle revolution rate dominantly affect the roughness [11]. Another study recorded that the roughness is majorly influenced by the spindle revolution rate and the nature of work used [12]. Hole making ability also depends upon the selection of matrix and reinforcement materials. The forces induced at the time of drilling a thermoplastic composite material will be smaller than induced at the time of drilling a thermoset composite material [13]. In the same way, a thermoplastic composite develops continuous chips whereas a thermoset composite develops discontinuous chips during hole drilling [14]. Apart from the machining parameters, the constituents of work material also have an influence on the machinability. As compared to a synthetic fiber, the presence of a natural fiber in composite alleviates the axial force and turning moment during hole drilling [15]. During hole making, the area near the hole is prone to damage. The damage is otherwise called as delamination or deface. Among the various drilling parameters, the tool angle and tool traverse rate have a main role in concluding the hole damages [16]. An experiment has been conducted to analyze the damages induced during hole drilling on wooden composites and recorded that tool traverse rate and size of the drill are mainly affecting the delamination [17]. Although there are few investigations made in the past, machinability of bio-fiber reinforced plastics is yet to be studied in detail. In particular, research on the machinability of hybrid

bio-fiber composites is meager. The authors [18] in one of the research made four different composites by altering the proportions of luffa, jute mat, and glass mat in polyester matrix and studied their characteristics. It has been reported that the composite with equal composition of luffa, jute, and glass produced the maximum strengths. This composite is taken for the present machining study. Holes have been drilled in the composite, and the damages induced are investigated by the help of design of experiments.

2   Material Processing, Machining, and Measurement

Luffa is a natural fiber derived from the *luffa cylindrica* plant. The structure of luffa is woven by nature in three dimensions such that they form a strong layered fiber than any other natural fiber. Luffa is used as bathing brushes and available in plenty. The fiber has been supplied by a local dealer and cleaned by thoroughly washing in water. Then, the fibers are immersed in 5% NaOH solution for 2 h. The fiber is then washed in water to remove the excess NaOH present in the fiber. After this treatment, the fiber is dried in a furnace at 70 °C. These pretreatments help to remove useless celluloses and enhance its surface bonding capacity with the resin [19]. The composite sample has been prepared by wet layup technique in the size of 300 mm length, 300 mm width, and 8 mm thick plate. A polyester resin proportion of 70%, luffa proportion of 10%, jute proportion of 10%, and glass proportion of 10% has been maintained during the composite preparation. The characteristics of the fabricated composite, namely tensile, flexural, compression, and impact strengths, have been evaluated by ASTM standard testing procedures, namely D638, D790, D695, and D256. The characteristics of the composite are shown in Table 1. The surface morphology of fabricated composite indicates uniform spread of reinforcements in the matrix as shown in Fig. 1.

Machining operations are carried out on a computer controlled vertical machining center of make Bharat Fritz Werner. The center has an upper limit spindle revolution rate of 6000 rpm. The spindle may traverse up to 510, 410, and 46 mm along *x*-, *y*-, and *z*-axes. The composite sample has been sized to 100 mm length and 50 mm width to hold it easily in the machine vice as shown in Fig. 2. Three HSS drill tools of size 8 mm have been procured, and their point angles are ground to 90°, 120°, and 150°. The input or operating factors considered are spindle revolution rate or speed, tool traverse rate, and tool angle of the drill tool. Based on

Table 1 Characteristics of the composite

S. No.	Characteristics	Value
1.	Tensile strength (MPa)	28.11
2.	Compressive strength (MPa)	49.46
3.	Flexural strength (MPa)	116.49
4.	Impact energy (J)	42
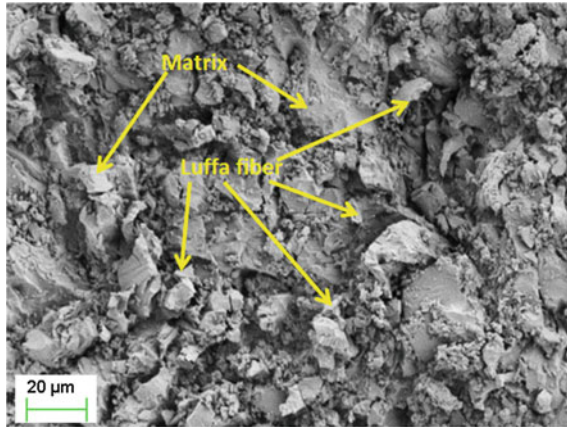
Fig. 1 Morphology of fabricated composite
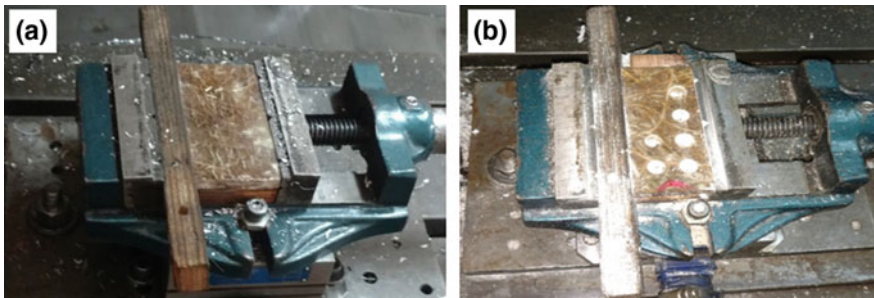
Fig. 2 a Sample before drilling. **b** Sample after drilling

Table 2 Operating factors assignment	S. No.	Input factor	Value
	1.	Speed	2000, 2500, 3000 rpm
	2.	Feed	0.1, 0.2, 0.3 mm/rev
	3.	Point angle	90°, 120°, 150°

the previously undergone studies on machining of hybrid composites, the process parameters and their limits have been adopted [10, 13–15].

The assignment of values to different factors is shown in Table 2. The responses considered are the damage factor and wall surface roughness. The damage or deface factor has been evaluated by noting the largest portion of the damaged hole in a toolmakers microscope. The ratio of diameter of drilled hole to the tool diameter gives the deface factor as expressed in Eq. 1 [20, 21]. The roughness is tested by using a roughness analyser. During this measurement, the roughness of the inner

wall is noted at three points and the average of three is considered as the wall roughness of the hole.

$$\text{Deface factor} = \frac{d_{\max}}{d} \tag{1}$$

where $d_{\max}$ is the largest hole diameter and d is the tool diameter

3 Statistical Modeling Procedure

Among the several statistical modeling, response surface analysis (RSA) is an easiest method to analyze and predicts the output parameters. The three-dimensional charts in response analysis help to analyze the influence of different operating factors on the responses. This method also helps to optimize a given problem, and using that, the workable conditions are easily identified [22]. Response surface analysis also gives regression equations through which an output parameter may be predicted for any operation factor. The RSA may be performed by using either central composite design or Box-Behnken design, and they certainly help to decrease the experimental trials performed during experimentation. This study utilizes CCD technique for modeling and optimization. Among the CCD types, the present study uses face-centered CCD in which the star points are positioned at the center of faces of the factorial space and hence $\alpha = \pm 1$. The design table containing different trial runs and observed responses are shown in Table 3.

4 Discussions

Table 4 shows the analysis of variance (ANOVA) for output parameters. The model value F value in comparison to the lack of fit F value shows that the model is significant and the lack of fit is insignificant for both the output parameters. R^2 and adjusted R^2 are very close in both the output parameters. This shows that the developed model is adequate for predicting the damage factor and wall roughness. Adequate precision (AP) is also an important factor which studies the closeness of predicted value with predicted error. The AP values of 26.84 and 38.033 for damage factor and wall roughness are well above 4, so the model is highly adequate for prediction. The significance of each input factor on the responses is analyzed by studying the p value. A value less than 0.05 indicates that the factor has predominant influence on the output [15]. It has been found that all the three factors, namely spindle revolution rate, tool traverse rate, and tool angle are predominant for damage factor. Among the two factor interaction, the speed-feed combination has a predominant influence on the wall roughness. Considering the wall roughness, all input factors are significant and among the interactions, none of the interactions are significant.

Table 3 Experimental trials

Trial No.	Speed (rpm)	Feed (mm/rev)	Point angle (degree)	Deface factor (no unit)	Wall roughness (μm)
1	2000	0.1	90	1.22	5.21
2	3000	0.1	90	1.05	2.5
3	2000	0.3	90	1.34	6.32
4	3000	0.3	90	1.04	3.52
5	2000	0.1	150	1.28	5.75
6	3000	0.1	150	1.03	2.62
7	2000	0.3	150	1.39	6.79
8	3000	0.3	150	1.05	3.95
9	2000	0.2	120	1.3	5.92
10	3000	0.2	120	1.03	2.81
11	2500	0.1	120	1.08	3.9
12	2500	0.3	120	1.16	4.6
13	2500	0.2	90	1.1	4.22
14	2500	0.2	150	1.18	4.67
15	2500	0.2	120	1.16	4.53
16	2500	0.2	120	1.16	4.53
17	2500	0.2	120	1.16	4.53
18	2500	0.2	120	1.16	4.53
19	2500	0.2	120	1.16	4.53
20	2500	0.2	120	1.16	4.53

The response plot for deface factor is shown in Fig. 3. As the speed goes up, the deface goes down rapidly and a minimum deface is noted at a maximum speed. This happens because a low spindle speed elevates the torque induced at the interface of tool and work and this causes more force to act along the work around the drill zone and thus enhances the damage of the hole. Thus, a minimum speed of 3000 rpm must be maintained during drilling of hybrid composites to alleviate the damage. Elevation in the spindle feed directly elevates the deface tremendously. Elevation in the tool traverse rate represents the hike in the rate at which the tool entering the job. As the penetration rate is elevated, thrust force would be hiked and thus increases the damage of the profile [23]. As the point angle goes up, the deface factor also goes up notably. This happens because, as the point angle raises, the contact area tool and work go up. Hence, during the tool rotation it tries to remove more material and elevates the torque induced and subsequently the hole deface. The response model in quadratic form for deface factor is presented in Eq. 1.

Table 4 Analysis of variance

Factor/source	Sum of squares	Degrees of freedom	Mean square	F value	p value	% Contribution
Deface factor						
Model	0.2	9	0.022	60.36	<0.0001	Significant
Speed	0.18	1	0.18	475.74	<0.0001	85.71
Feed	0.01	1	0.01	27.54	0.004	4.76
Point angle	0.00324	1	0.00324	8.71	0.0145	1.54
Speed * feed	0.00605	1	0.00605	16.27	0.0024	2.88
Speed * point angle	0.0018	1	0.0018	4.84	0.0524	0.86
Feed * point angle	0.00005	1	0.00005	0.13	0.7215	0.023
Residual	0.00372	10	0.00037	–	–	–
Lack of fit	0.00372	5	0.00074	–	–	Not significant
Pure error	0	5	0	–	–	–
Total	0.21	19	–	–	–	–
$R^2 = 0.982$, Adj $R^2 = 0.966$, $AP = 26.84$						
Wall roughness						
Model	24.51	9	2.72	103.62	<0.0001	Significant
Speed	21.29	1	21.29	809.87	<0.0001	85.92
Feed	2.7	1	2.7	102.88	<0.0001	10.89
Point angle	0.4	1	0.4	15.37	0.0029	1.61
Speed * feed	0.005	1	0.005	0.19	0.672	0.02
Speed * point angle	0.026	1	0.026	1.01	0.3394	0.1
Feed * point angle	0.0072	1	0.0072	0.27	0.6121	0.03
Residual	0.26	10	0.026	–	–	–
Lack of fit	0.26	5	0.053	–	–	Not significant
Pure error	0	5	0	–	–	–
Total	24.78	19	–	–	–	–
$R^2 = 0.989$, Adj $R^2 = 0.979$, $AP = 38.033$						

$$
\begin{aligned}
\text{Deface factor} = {} & 1.91 - 6.54 \times 10^{-4}\,\text{Speed} + 2.18\,\text{feed} \\
& + 1.48 \times 10^{-3}\,\text{Point angle} - 5.5 \times 10^{-5}\,\text{Speed} \times \text{feed} \\
& - 1 \times 10^{-6}\,\text{Speed} \times \text{Point angle} + 8.33 \times 10^{-4}\,\text{feed} \\
& \times \text{Point angle} + 1.22 \times 10^{-7}\,\text{Speed}^2 - 1.45\,\text{feed}^2 \\
& + 6.06 \times 10^{-6}\,\text{Point angle}^2
\end{aligned} \tag{2}
$$
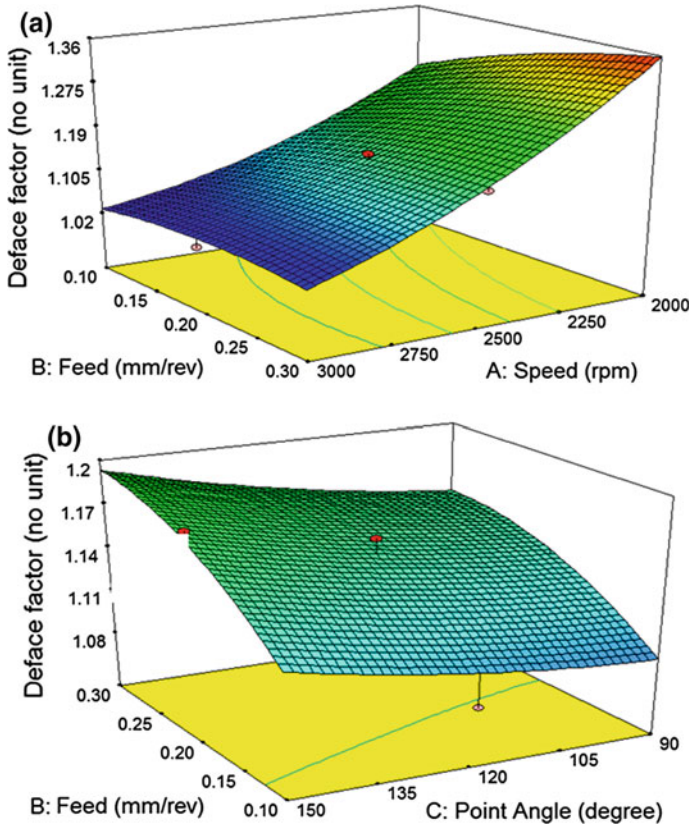
Fig. 3 **a** Speed-feed versus deface factor. **b** Feed-point angle versus deface factor

Response graph for roughness is shown in Fig. 4. An elevation in the spindle revolution rate alleviates the roughness, and this happens without any variation from the beginning to the end. This type of trend happens because at an elevated speed, the cutting points in the tool perform a cleaning action inside the hole surface. This phenomenon is similar to polishing and, hence, alleviates the roughness of the surface [10]. As the tool traverse rate is elevated, the roughness goes up tremendously. This takes place because at an elevated tool traverse rate, the thrust force will be hiked and subsequently the damage on the wall is enhanced. As the damage is elevated, the roughness also goes up. Elevation in the point angle slightly enhances the roughness. At an elevated point angle, the closeness of the drill and work goes up and prevents the polishing action thereby elevating the roughness. The response model for wall surface roughness is given in Eq. 2. The surface morphology of hole walls has been taken at three different conditions as shown in Fig. 5. It has been clearly identified that the surface seems to be more rough at a low speed, and at an elevated feed and point angle whereas as the speed is elevated, the surface gets polished and seems more smooth.
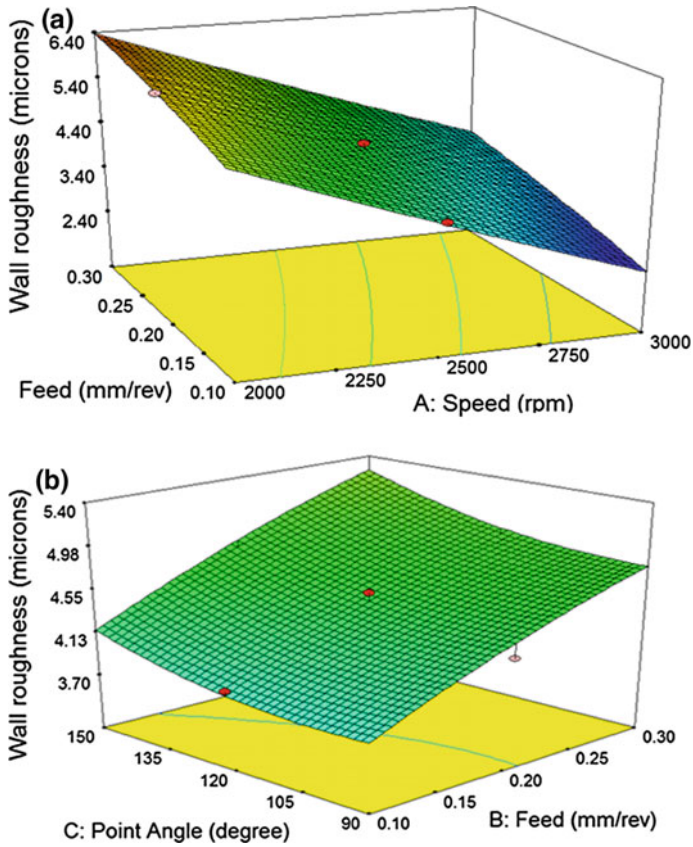
Fig. 4 **a** Speed-feed versus wall roughness. **b** Feed-point angle versus wall roughness
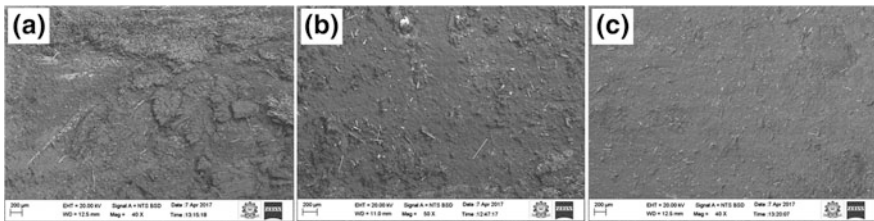
Fig. 5 Morphology of hole wall at **a** speed = 2000 rpm, feed = 0.3 mm/rev, point angle = 150°. **b** Speed = 2500 rpm, feed = 0.2 mm/rev, point angle = 120°. **c** speed = 3000 rpm, feed = 0.1 mm/rev, point angle = 90°

Table 5 Confirmation and comparison

S. No.	Input factors			Central composite design		Confirmatory	
	Speed	Feed	Point angle	Deface factor	Wall roughness	Deface factor	Wall roughness
1	3000	0.1	100	1.03	2.5	1.05	2.53
2						1.03	2.4
3						1.04	2.44
4						1.03	2.5
5						1.02	2.46

Error between CCD and confirmatory: deface factor = −0.39%, wall roughness = 1.36%

$$\begin{aligned}
\text{Wall roughness} = {} & 12.16 - 3.49 \times 10^{-3}\ \text{Speed} + 5.48\ \text{feed} \\
& - 0.019\ \text{Point angle} + 5 \times 10^{-4} \text{Speed} \times \text{feed} \\
& - 3.83 \times 10^{-6}\ \text{Speed} \times \text{Point angle} + 0.01\ \text{feed} \qquad (3) \\
& \times \text{Point angle} + 1.87 \times 10^{-7}\ \text{Speed}^2 - 6.82\ \text{feed}^2 \\
& + 1.41 \times 10^{-4}\ \text{Point angle}^2
\end{aligned}$$

5 Optimization and Confirmation

During the optimization process, the input factors are set within the range and the responses are set to be minimized. The optimum conditions are obtained on the maximum desirability approach in which a desirability nearer to 1 is selected. It has been noted that a highest speed of 3000 rpm, a lowest feed of 0.1 mm/rev, and a nearly lowest point angle of 100° are the optimum conditions for hole drilling. The optimized responses are found as 1.03 and 2.5 µm for deface factor and roughness, respectively. Confirmation runs are conducted repeatedly for five times. The responses are noted each time and the average of five readings is calculated for validation. The mean error between the CCD and confirmatory is calculated [24, 25] and are −0.39 and 1.36%, respectively, for the deface factor and roughness. The error values are minor, and hence, optimization is satisfied (Table 5).

6 Conclusions

This research is conducted to investigate the machinability of bio-fiber reinforced hybrid composites. Three input factors, namely the spindle revolution rate, feed of spindle, and tool angle. Two output parameters, namely the deface factor and wall surface roughness, have been studied. The major conclusions obtained from the investigations are presented below:

- All the input factors are majorly influencing both the output parameters. Speed and feed interaction mainly affects the deface factor, whereas the interactions do not affect the roughness.
- The feed rate and tool angle show a direct effect on both the deface factor and wall roughness. It is noted that a minimum spindle revolution rate of 3000 rpm is to be maintained for hole drilling on luffa reinforced hybrid composites.
- Optimum conditions are obtained and they are a highest spindle speed, lowest feed rate, and a nearly lowest point angle for hole drilling.
- Confirmatory experiments are conducted and a comparison is made between the CCD and confirmatory. The comparison showed only a minor difference, and therefore the modeling, analysis, and optimization are highly satisfied.

References

1. Vinayagamoorthy, R., Rajeswari, N., Vijayshankar, S., Vivekanandan, M., Sri Rama Murthy, B., Venkata Subramanian, M.: Surface and sub-surface analysis of hybrid polymeric composites during machining operations. Procedia Mater. Sci. **5**, 2075–2083 (2014)
2. Rajesh, G., Ratna Prasad, A.V., Gupta, A.V.S.S.K.S.: Mechanical and degradation properties of successive alkali treated completely biodegradable sisal fiber reinforced poly lactic acid composites. J. Reinf. Plast. Compos. **34**, 951–961 (2015)
3. Sathish, S., Kumaresan, K., Prabhu, L., Vigneshkumar, N.: Experimental investigation on volume fraction of mechanical and physical properties of flax and bamboo fibers reinforced hybrid epoxy composites. Polym. Polym. Compos. **25**, 229–236 (2017)
4. Vinayagamoorthy, R., Rajeswari, N.: Mechanical performance studies on *Vetiveria zizanioides*/jute/glass fiber reinforced hybrid polymeric composites. J. Reinf. Plast. Compos. **33**, 81–92 (2014)
5. Vinayagamoorthy, R.: A review on the polymeric laminates reinforced with natural fibers. J. Reinf. Plast. Compos. **36**, 1577–1589 (2017)
6. Shanmugam, D., Thiruchitrambalam, M.: Influence of alkali treatment and layering pattern on the tensile and flexural properties of palm leaf stalk fiber (PPLSF)/jute fiber polyester hybrid composites. Compos. Interfaces. **21**, 3–12 (2014)
7. Vinayagamoorthy, R., Saswath Kaundinya, S.L., Mani Teja, G.L.S.N., Adithya, K.: A study on the properties of natural sandwich laminates. Indian J. Sci. Technol. **9**, 1–6 (2016)
8. Vinayagamoorthy, R.: Influence of fiber surface modifications on the mechanical behavior of *Vetiveria zizanioides* reinforced polymer composites. J. Nat. Fibers. (2017). https://doi.org/10.1080/15440478.2017.1410513
9. Azmi, A.I., Lin, R.J.T., Bhattacharya, D.: Experimental study of machinability of GFRP composites by end milling. Mater. Manuf. Process. **27**, 1045–1050 (2012)
10. Vinayagamoorthy, R.: Parametric optimization studies on drilling of sandwich composites using the Box-Behnken design. Mater. Manuf. Process. **32**, 645–653 (2017)
11. Tsao, C.C., Hocheng, H.: Evaluation of thrust force and surface roughness in drilling composite material using Taguchi analysis and neural network. J. Mater. Process. Technol. **203**, 342–348 (2008)
12. Vinayagamoorthy, R., Rajeswari, N., Karthikeyan, S.: Investigations of damages during drilling of natural sandwich composites. Appl. Mech. Mater. **766–767**, 812–817 (2015)
13. Varatharajan, R., Malhotra, S.K., Vijayaraghavan, L., Krishnamurthy, R.: Mechanical and machining characteristics of GF/PP and GF/polyester composites. Mater. Sci. Eng. Part-B. **132**, 134–137 (2006)

14. Debnath, K., Singh, I., Dvivedi, A.: Drilling characteristics of sisal fiber-reinforced epoxy and polypropylene composites. Mater. Manuf. Process. **29**, 1401–1409 (2014)
15. Vinayagamoorthy, R., Rajeswari, N., Balasubramanian, K.: Optimization studies on thrust force and torque during drilling of natural fiber reinforced sandwich composites. Jordan. J. Mech. Ind. Eng. **8**, 385–392 (2014)
16. Vinayagamoorthy, R., Rajeswari, N., Vijayshankar, S., Balasubramaniam, K.: Drilling performance investigations on hybrid composites by using D-optimal design. Int. Rev. Mech. Eng. **8**, 952–961 (2014)
17. Valarmathi, T.N., Palanikumar, K., Sekar, S.: Parametric analysis on delamination in drilling of wood composite panels. Indian J. Sci. Technol. **6**, 4347–4356 (2013)
18. Vinayagamoorthy, R., Sivanarasimha, S., Vinay Kumar, K.R., Padmanabhan, Vijay: Characteristic investigations on loofah, jute and glass fiber reinforced sandwich polymeric composites. Appl. Mech. Mater. **813–814**, 14–18 (2015)
19. Vinayagamoorthy, R., Sivanarasimha, S., Padmanabhan, Vijay, Ganesh, V., Karthikeyan, S.: Experimenal studies on water absorption and thermal degradation of natural composites. Int. J. Appl. Eng. Res. **10**, 663–668 (2015)
20. Tan, C.L., Azmi, A.I., Muhammad, N.: Delamination and surface roughness analyses in drilling hybrid carbon/glass composite. Mater. Manuf. Process. **31**, 1366–1376 (2016)
21. Vinayagamoorthy, R.: A review on the machining of fiber-reinforced polymeric laminates. J. Reinf. Plast. Compos. **37**, 49–59 (2017)
22. Kannan, P., Balasubramanian, K., Vinayagamoorthy, R.: Defect reduction in ring blank casting through design of experiments. Int. Rev. Mech. Eng. **9**, 536–541 (2015)
23. Gaitonde, V.N., Karnik, S.R., Campos Rubio, J., Esteves Correia, A., Abrao, A.M., Paulo Davim, J.: Analysis of Parametric influence on delamination in high-speed drilling of carbon fiber reinforced plastic composites. J. Mater. Process. Technol. **203**, 431–438 (2008)
24. Vinayagamoorthy, R., Subramanyam, K.G., Kumar, T.N., Reddy, Y.H.: Modeling and analysis of drilling induced damages on hybrid composites. Indian. J. Sci. Technol. **9**, 1–10 (2016)
25. Vinayagamoorthy, R., Manoj, I. V., Narendra Kumar, G., Sai Chand, I., Sai Charan Kumar, G. V., Suneel Kumar, K.: A central composite design based fuzzy logic for optimization of drilling parameters on natural fiber reinforced composite. J. Mech. Sci. Technol. **32**, 2011–2020 (2018)

Defect Rectification in Forging Operation and Optimizing the Process Parameters

M. D. Vijaya Kumar and U. Vignesh Kumar

Abstract The increased adoption of forging technology for producing a wider range of components has accelerated the need to produce forged products with zero defects. The defects arising during forging process has to be addressed to achieve the industrial quality standards and to meet the customer requirements. The present study has major focus on developing a suitable scientific methodology to eliminate the forging failures. The research includes identifying the various types of defects arising during forging operation, analysing the possible causes of failures and studying the methodology adopted in industries to rectify the defects. Detailed study has been conducted on multiple dimensions like material testing, optimization of design, quality standards analysis. Further, spectrometry and scanning electron microscope test is used to study the nature of failure and to analyse the microstructural defects. Results show that with the adoption of suggested methodologies, the forging defects have been eliminated.

Keywords Forging defects · Optimization of design · Spectrometry test
Scanning electron microscope test · Microstructural defects

1 Introduction

Forging is the manufacturing process of forming the metals using compressive force. The forging operation is often employed for mass production of components. Thus, the defects formed during forging are of serious concern. The formation of internal cracks has been the major cause for rejection and failure of forged components [1]. It is difficult to identify the internal cracks formed during forging

M. D. Vijaya Kumar · U. Vignesh Kumar (✉)
Department of Mechanical Engineering, Chennai Institute of Technology,
Chennai, India
e-mail: vigneshkumartkm@gmail.com

M. D. Vijaya Kumar
e-mail: vijayakumar.md@gmail.com

(a) Component A   (b) Component B
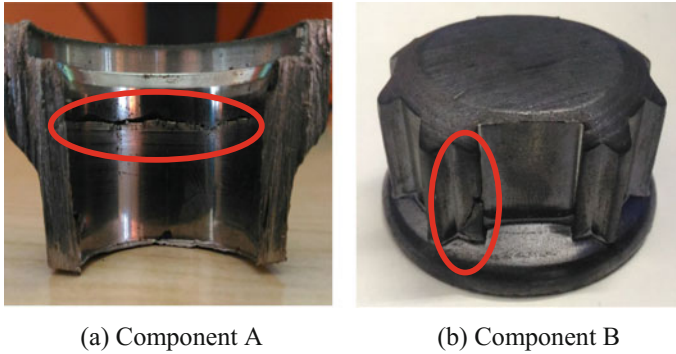
Fig. 1 Defects in different forged components A and B. **a** Cross-sectional view of a cylindrical component A depicting the crack inside it. **b** Propagation of crack on the outer surface of forged component B

operation through inspection methods as forging is performed at various stages and material deformation occurs correspondingly. Figure 1 shows the defects produced in various forged components. The failure may occur with poor design consideration also. Researches have been made regarding the failures during the forging operations and adequate methodology has been evolved to eliminate cracks on surface [2].

The present research on forging is carried out at a leading forging industry in Chennai, where the cold forged components have reported frequent undue cracks on the edges. Primary study has revealed that similar defects have been recurrent in different type of forged components. In order to study the issue in detail, the entire manufacturing processes have been analysed. Material testing has been performed on the component to study the nature of failure in detail.

2   Approach Methodology

Initially, the manufacturing process of the component has been studied and quality analysis is made. Further, spectrometry test is performed on the component to understand the material composition variance which may produce defect. Then, SEM test is performed to study the material flow and grain structure. The quality control tools are also utilized to study the failure in detail. The forging force and related calculations have been done to check the forging load and other process parameters [3].

2.1 Spectrometry Test

Spectrometry test is performed on the component to check the variation in chemical composition of the metal. Initially, the normal defect-free component is taken and its material composition is studied. Then, defected component is taken and its material properties are studied. Finally, the obtained results are compared relative to the standard grade equivalent.

2.2 Scanning Electron Microscope Test

Scanning electron microscope test is performed on the component defective surfaces to understand the grain structure along the cracked part and also to characterize the defect on the forged component. The grain structures are studied in selective locations on the defected part. Figure 4a shows the points of SEM imaging at which the grain structures are studied.

2.3 Quality Tools

Quality tools like production analysis, fishbone diagram, why-why analysis, quality analysis have been performed to study the quality variation in the components. About 2% of the total components produced is found to be defective.

2.4 Tool Design Evaluation

Design of the die and punch was studied and compared with customer requirement. The forging process has been virtually simulated using CAE and the areas of excessive stress concentration have been found out.

3 Defect Identification

The material investigation by spectrometry test, scanning electron microscope test and quality tools has revealed the causes of failure of the component.

3.1 Non-metallic Inclusion

With the analysis of material composition of normal and defective component by spectrometry test, the non-metals like manganese, silicon, sulphur have found to be higher than the standard range in the defective component. Non-metallic impurities like manganese may percolate and cause failure at localized points [4]. Excessive presence of manganese in the form of MnS, which precludes hot cracking, caused by grain-boundary melting of MnS films. Figures 2 and 3 show that the material composition is not uniform in the defective and non-defective components.
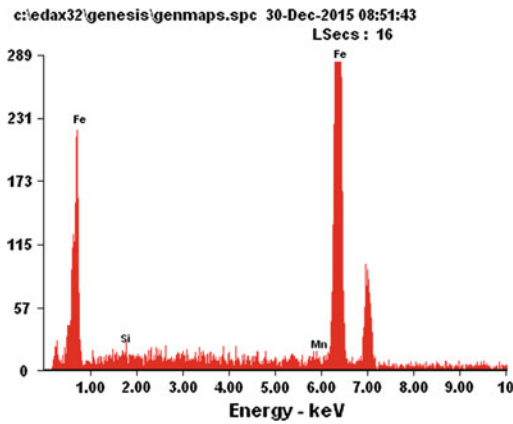
Element	Wt%	At%
SiK	01.49	02.92
MnK	01.46	01.47
FeK	97.04	95.61
Matrix	Correction	ZAF

Fig. 2 SEM test result of non-defective specimen
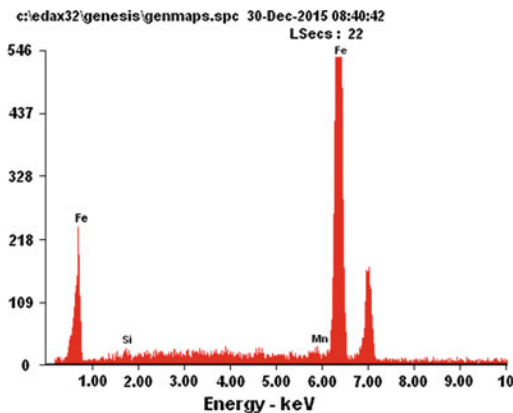
Element	Wt%	At%
SiK	01.02	02.02
MnK	01.28	01.29
FeK	97.69	96.69
Matrix	Correction	ZAF

Fig. 3 SEM test result of defective specimen
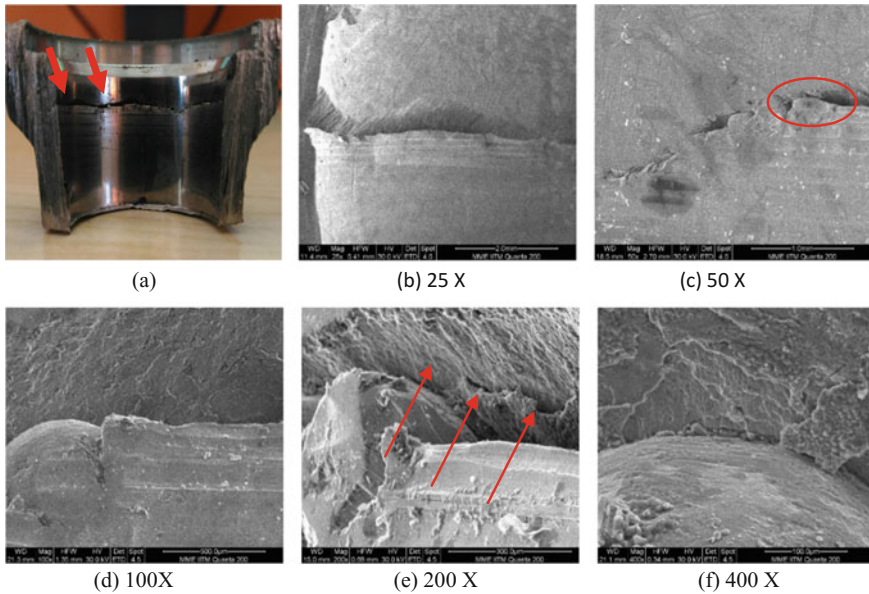
Fig. 4 SEM results of defective component. **a** Point at which SEM test is done. **b–f** Magnification of crack

3.2 Improper Heat Treatment

Improper heat treatment may result in excessive grain growth, burning along grain boundaries, brittle nature of material, inadequate carburization and formation of cracks on surface. The improper heat treatment has led to failure during forging. Figure 4 reveals that the grain flow is not laminar along the crack boundaries leading to failure of component (as marked by arrow). Figure 4a is the cross-sectional specimen which is used for SEM test. Figure 4b shows the propagation of crack with magnification 25×. The profile of the crack could be studied through the SEM image as in Fig. 4c with 50× magnification. Figure 4d gives the material flow characteristics inside the crack. Figure 4e shows the non-metallic films formed around the crack. Figure 4f gives detail on the grain structure inside the crack area. It is found that the material grain concentration is higher along the fractured area that leads to failure of the component as depicted in SEM image.

3.3 Poor Lubrication and Inadequate Design

Insufficient lubrication of the dies and punches may lead to poor material flow along the surface of the dies. Poor die polishing also leads to failure during forging. The

die design is found to be inadequate with respect to material flow condition [5–7]. The excess stress concentration in the outer edges is found to be the major cause of poor material distribution. Stress accumulation along the corners leads to formation of cracks on the components.

4 Defect Rectification Suggestions

4.1 Design Optimization

In order to enhance the material flow and to reduce the stress concentration along the corners, the fillet radius of the dies have been increased by 1 mm. Computational analysis has shown that the material flow is uniform under the new fillet radius, and the stress concentration has been greatly reduced in the previously failed area. The filler radius has been optimized considering the customers' specification of the part and also without affecting the workability of the component.

4.2 Coating of Forge Tools

Failure of forge tools also contributes to formation of cracks on the forged parts. In order to improve the life of forge tools, it is suggested to coat the dies and punches using aluminium, chromium, nitrate. The coating has high wear resistant even working at higher temperature. Other coatings have also been analysed but aluminium, chromium, nitrate have optimal performance under the field test conditions.

4.3 Ensuring Standard Material Composition

The material composition of the raw material has to be maintained as per the standard values. This would reduce the failure due to non-metallic inclusion and due to excessive hardness. The material vendor has been instructed to supply raw material under the given material composition rate. A new material inspection methodology has been adopted to eliminate material of sub-standard quality.

Fig. 5 Optimized forging tools

Fig. 6 Inspection of the component

5 Implementation and Results

After the implementation of suggested measures by coordination with various departments of the industry, feasible outcomes have been achieved with improved quality of product. Figure 5 shows optimized forging tools which are manufactured by CNC machining instead of manual machining process. Figure 6 depicts the inspection of the component. Inspection methods have been revised to ensure quality of products. Figures 7 and 8 show the installation of die in the hydraulic forging press. Various trials have been conducted post the implementation of the proposals. Components up to 35 lots have been continuously monitored and reviewed. Defects arising in the forged component have been reduced in a sequential manner. Focus has been given for quality as well as productivity of the

Fig. 7 Hydraulic press
forging

Fig. 8 Installation of
optimized die
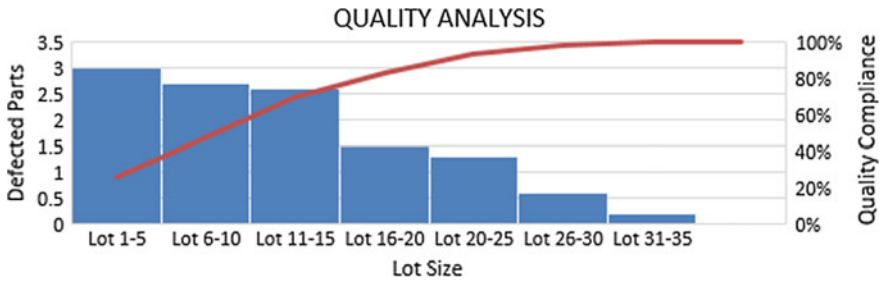
Fig. 9 Quality analysis post-implementation

component. Testing of multiple lots has shown that the defect on forged component has been eliminated. Figure 9 shows the quality analysis chart.

6 Conclusions

With the effective implementation of recommended measures, the crack issue has been eliminated from the forged component. Similar methodology and procedure have been employed in other forging components that have shown progressive results. The following inferences are made from the research work,

1. Effective design optimization with focus on stress distribution is essential to eliminate defects in forging and to improve material grain flow during forging.
2. AlCrN coating of forge tools has enhanced the life of dies and punches. Further, the defects due to surface irregularity in die have been minimized.
3. Material composition and hardness valued of raw material must meet nominal standards to eliminate defects due to non-metallic inclusions and due to excessive hardness.

References

1. Statharas, D., Sideris, J., Medrea, C., Chicinas, I.: Microscopic examination of the fracture surfaces of a cold working die due to premature failure. Eng. Fail. Anal. **18**, 759–765 (2011)
2. Tekkaya, A.E., Khalifa, N.B., Hering, O., Meya, R., Myslicki, S., Walther, F.: Forming-induced damage and its effects on product properties. CIRP Ann. Manuf. Technol. (2017). https://doi.org/10.1016/j.cirp.2017.04.113

3. Hawryluk, M., Jakubik, J.: Analysis of forging defects for selected industrial die forging processes. Eng. Fail. Anal. (2015). https://doi.org/10.1016/j.engfailanal.2015.11.008
4. Kim, D.K., Kang, S.Y., Lee, S., Lee, K.J.: Analysis and prevention of cracking phenomenon occurring during cold forging of two AISI 1010 steel pulleys. Metall. Mater. Trans. A. **30a** (1999)
5. Chen, C., Wang, Y., Ou, H., He, Y., Tang, X.: A review on remanufacture of dies and moulds. J. Clean. Prod. **64**, 13–23 (2014). https://doi.org/10.1016/j.jclepro.2013.09.014
6. Arentoft, M., Wanheim, T.: The basis for a design support system to prevent defects in forging. J. Mater. Process. Technol. **69**, 227–232 (1997)
7. Gariety, M., Ngaile, G., Altan, T.: Evaluation of new cold forging lubricants without zinc phosphate precoat. Int. J. Mach. Tools Manuf **47**, 673–681 (2007)

Wire Electrical Discharge Machining Integrity Studies on the Aluminium Nanocomposite

K. Rajkumar, L. Poovazhagan, G. Selvakumar and B. Muthukumar

Abstract Nanoparticles such as SiC and B_4C are popularly used as reinforcement in the AMMCs. Nanoparticles are majorly hindering the implementation of conventional machining. In addition, the profile and contour machining on the harder material is difficult in conventional machining process. Hence, non-conventional machining processes were used to shape the composite. Wire electrical discharge machining is normally proposed to cut the intricate shape with good surface finish on aluminium metal matrix composite. This present study investigates the effect of process parameters on the response parameter of WEDM on the aluminium metal matrix composite. Experiments were done by using a Taguchi's L18 orthogonal array. The interaction of machining parameter (T_{on}, T_{off}, servo voltage, current) on the response parameter (kerf, MRR, surface roughness) was determined using analysis of variance (ANOVA). Analysing signal to noise ratio, the optimum machining parameter was determined. Regression analysis was used to find the relationship between predicted and actual value. The result shows that voltage and pulse on time were the most significant factor for kerf width increment.

Keywords Surface integrity · Wire EDM · Metal composite · Nanoparticles

K. Rajkumar (✉) · L. Poovazhagan · G. Selvakumar · B. Muthukumar
Department of Mechanical Engineering, SSN College of Engineering,
Kalavakkam, Chennai, India
e-mail: rajkumark@ssn.edu.in

L. Poovazhagan
e-mail: poovazhaganl@ssn.edu.in

G. Selvakumar
e-mail: selvakumarg@ssn.edu.in

B. Muthukumar
e-mail: 066muthukumar@gmail.com

1 Introduction

Metal matrix composite (MMC) is widely accepted as an alternate engineering material for many applications require high strength and wear resistance at elevated temperature. The ceramic particles, namely silicon carbide (SiC) and boron carbide (B_4C), are familiar reinforcement [1, 2]. The strength of Al6061 enhanced with reinforcement of B_4C [3]. This positive factor of ceramic particles in another way affects machining of metal matrix composites by multiplying the cutting tool wear and brittleness of the matrix material [4].

On the other hand, there is an alternative machining process such as laser beam machining (LBM), abrasive water jet (AWJ) and electrical discharge machining (EDM) which are being exploited to reach a good quality cut. The laser beam machining (LBM) is a thermal energy as source to remove material by passing a narrow beam of light over the surface of the material. Owing to the high-intensity beam of light, heat generation on the surface is intensively as high so resulting in re-solidification layer. This makes the surface patch marks which ultimately produced a poor surface finish. The surface smoothness is the main requirement for the cut surface, so the secondary operation like etching, grinding, etc., are used [5]. In AWJ, mechanical energy is employed to remove material from the work. The main drawback is an uneven kerf width resulting in a poor-quality surface.

Another popular method like electrical discharge machining (EDM) facilitates a good-quality cut. But operating mechanism in this machining is a melting and vaporisation of material. As compared to other non-conventional machining processes, EDM method produced an exceptional surface finish in spite of high thermal resistance by reinforcement [6, 7]. Moreover, wire electrical discharge machining is controlled by computer numerical control (CNC) which provides a greater flexibility. The material removal occurs in the following phases: The first phase is ignition phase; that is, the delay time applied across the working gap until the fairly low discharge voltage. The second phase instantaneously occurs right after the first one when the current rapidly increases to peak current resulting in the formation of a plasma channel. In discharge phase, high-energy and high-pressure plasma channels are generated in between the work piece and tool, sustained for a period of time (T_{on}) causing melting and evaporation of a small amount of material in both electrodes. The fourth phase is followed by the collapsing of plasma channel when an electric energy turned off (T_{off}). Then immediately part of molten material is flushed away and the rest is resolidified on the machined surface [8].

The cutting performance indicators of WEDM are material removal rate, kerf width, surface integrity and surface roughness. These are controlled by servo voltage, wire tension, wire feed, spark gap, pulse duration, and dielectric flushing pressure. Due to high cost involved in machining trial, the trial and error method was not advised to set the operating parameter, so to determine optimum condition, robust model like Taguchi was used [9].

Ekici et al. [10] investigated effects of machining parameters on the MRR and surface roughness of Al/B4C metal matrix composite. Experimentation was conducted by varying wire tension, reinforcement percentage, wire speed, pulse on time and pulse off time. Taguchi L18 orthogonal array was used for designing the experiment. It revealed that pulse on time is the most significant factor for surface roughness, and wire speed is the significant parameter for material removal rate. They also found that Ra value increases with increase in B_4C.

Tosun et al. [11] investigated the effect of machining parameters on kerf and MRR. Experiments were carried out by varying pulse duration, open circuit voltage, wire speed and dielectric flushing pressure. They revealed that open circuit voltage affects the MRR and kerf more than the remaining parameters. It is reported that the optimum machining conditions depend on the weight of the minimum kerf and the maximum MRR. This present study explores the machining of aluminium/ SiC/B_4C hybrid composite by the WEDM process. The process parameters such as gap voltage, pulse on time, pulse of time, current intensity were varied, and the corresponding performance measures such as the material removal rate, surface roughness, cutting width (kerf) were evaluated based on the Taguchi L18 orthogonal array, and the influence of each input parameters was identified.

2 Experimental Work

2.1 Composite Fabrication

An ultrasonic cavitation's assisted casting process was used to fabricate aluminium 6061—hybrid nanocomposite. The alloy melt was stirred mechanically to homogeneous the mixture of nano-SiC (1.5 wt%) and nano-B_4C (0.5 wt%). After stirring, a 30-mm-height titanium transducer probe (Ti6Al4V) was dipped into the melt with power of 2 kW and 20 kHz frequency. The ultrasonically processed melt was poured into permanent steel mould of size 150 * 100 * 15 mm.

2.2 Machining Experiment

Specimen of size 25 mm * 10 mm * 10 mm was used as a work for this present experimentation which is shown in Fig. 1. Brass wire with 0.25 mm was used as tool, and demineralized water is used as dielectric medium. The experiments were performed on SC-100 model WEDM machine. During experiment, 7 mm length cut with 10 mm depth was made along the width axis. Table 1 shows parameters involved in this experiment.

Fig. 1 Binary image of specimen

Table 1 Parameters for experiment

Machining parameters	Symbol	Level 1	Level 2	Level 3	Constant parameter	
Voltage (V)	A	10	20	–	Wire off-set (mm)	0.1
Current (A)	B	180	210	230	Flushing pressure (kg/cm^2)	1
T_{on} (µs)	C	126	128	130	Wire feed (mm/min)	10
T_{off} (µs)	D	48	52	56	Wire tension (N)	0.1

2.3 Measurements

Kerf width was measured through an optical microscope. Figure 2 shows the machined specimen. The material removal rate was calculated by using the following formula:
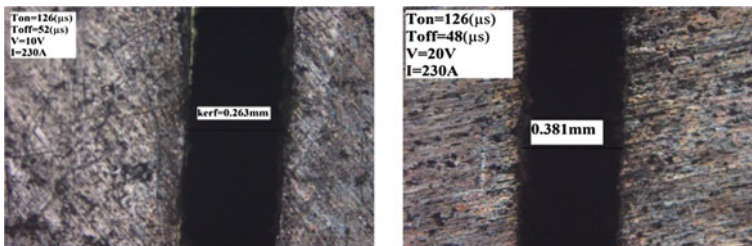
(a) Minimum kerf   (b) Maximum kerf

Fig. 2 Optical images of kerf at various processes parameters

$$\text{Material removal rate (MRR)} = V_c \times K \times t$$

where V_c—cutting speed (mm/min), K—kerf (mm), t—thickness of work piece (mm).

Mitutoyo surface roughness tester and SJ-210 series were used to measure the surface roughness. The average of three values was reported.

2.4 Taguchi Analysis

In our study, Taguchi L18 orthogonal array was used. The orthogonal array provides set of well-balanced experiment. The relative important machining parameter by relative to output response was determined using ANOVA. Contour plots were used to determine the relative importance between process variables. Table 2 shows the experimental results of the kerf, MRR, surface roughness and is affected by

Table 2 Experimental data of kerf, MRR and surface roughness

S. No.	Voltage (V)	Current (A)	T_{on} (μs)	T_{off} (μs)	Kerf (mm)	MRR (mm³/min)	Surface roughness (μm)
1	10	180	126	48	0.286	14.521	3.35
2	10	180	128	52	0.314	13.295	3.31
3	10	180	130	56	0.289	14.453	3.33
4	10	210	126	48	0.291	14.744	3.41
5	10	210	128	52	0.327	14.711	3.33
6	10	210	130	56	0.289	14.721	3.36
7	10	230	126	52	0.263	15.444	3.49
8	10	230	128	56	0.315	15.467	3.42
9	10	230	130	48	0.342	15.535	3.55
10	20	180	126	56	0.310	15.469	3.59
11	20	180	128	48	0.319	15.663	3.47
12	20	180	130	52	0.335	16.070	3.50
13	20	210	126	52	0.350	16.749	3.71
14	20	210	128	56	0.337	17.465	3.67
15	20	210	130	48	0.368	18.290	3.77
16	20	230	126	56	0.369	18.253	3.87
17	20	230	128	48	0.381	18.734	3.85
18	20	230	130	52	0.375	18.229	3.83

various process parameters such as voltage, current, pulse on and pulse off.

3   Results and Discussion

The effect of response parameters was analysed, and analysis of variance (ANOVA) and the results were presented as below.

3.1   Effect of Process Parameter on Kerf

Kerf is one of the cutting responses of work. The experiment result shows a minimum kerf (0.263 mm) at the parameter setting of T_{on} = 126 (µs), T_{off} = 52 (µs), V = 10 V, I = 230 A. Optical images of kerf width at different cutting condition are shown in Fig. 2. Table 3 shows ANOVA analyses for kerf. ANOVA table shows a voltage as an important parameter affecting kerf width which contributes 50.46% and another parameter, pulse on contributes 15.32%. From the table, voltage was a main influencing important parameter to kerf width. The generated spark is more at a high voltage which results in increased melting and evaporation of material produced a larger kerf width. Another important parameter T_{on} also increases the melting and evaporation of the material. This in turn increases the kerf width.

3.2   Effect of Process Parameter on Surface Roughness

Surface roughness determines the smoothness of the material. The experiment result Table 2 shows that the minimum surface roughness (3.31 µm) was obtained at parameter setting of voltage at 10 V, current 180 A, T_{on} 128 (µs), T_{off} 52 (µs). Table 4 shows the ANOVA analysis of input parameter on surface roughness. It shows a voltage has the major parameter for surface roughness that contributes 64.03% followed by T_{on} with 26.97%. Table 5 indicates that the voltage was the most important parameter for surface roughness. The increase in voltage increased current between the electrodes that help in the formation of high intense sparks.

Table 3   ANOVA analysis on kerf

Source	DF	SS	MS	F	P	% Contribution
Voltage	1	0.0101	0.0101	16.29	0.001	50.46
Current	2	0.0017	0.0008	0.73	0.01	8.82
T_{on}	2	0.0030	0.0015	0.287	0.008	15.32
T_{off}	2	0.0005	0.0002	0.2	0.015	2.68
Error	10	0.0045	0.0007			22.72
Total	17	0.0201				100.00

Table 4 ANOVA analysis of surface roughness

Source	DF	SS	MS	F	P	% Contribution
Voltage	1	0.412	0.412	28.49	0	64.03
Current	2	0.004	0.002	0.06	0.055	0.76
T_{on}	2	0.173	0.087	2.77	0.031	26.97
T_{off}	2	0.013	0.006	0.16	0.045	2.03
Error	10	0.04	0.103			6.20
Total	17	0.644				100.00

This resulted in molten metal formation at narrow gap; hence, the molten metal was not able to eject completely and a portion of the metal was redeposited on the surface. It deteriorates the surface quality. Higher peak current increases the discharge heat energy, and it leads to poor surface roughness. During high heat energy, the gas bubbles were formed and simultaneously it was entrapped in a dielectric flushing. Thus, crater forms on the surface of the work material. The size of the gas bubble was reduced with decrease in pulse on time and easily collapsed forming smaller pockmarks on the surface.

3.3 Effect of Process Parameter on MRR

The MRR is the important parameter for any machining process; in order to increase the production rate, MRR should be as much as high. In this experiment, the results show that the optimum MRR was achieved at voltage 20 V, current 230 A, pulse on time 128 µs and pulse off time 48 µs. Table 5 shows that the voltage was the major contribution on the MRR with 62.05% followed by pulse on time with 28.81%. It is observed that an increase in voltage increases the MRR. When current flow increased the heat generation was more at high points which result in significant melting and evaporation of material. Pulse on time increases the heat on surface for long time and thus results in the formation of molten metal. If T_{off} is sufficiently low, there is no build up phase hence no material removal.

3.4 Contour Plots

Contour plots are the graphical representation of potential variables influencing the processes.

Table 5 ANOVA analysis for on MRR

Source	DF	SS	MS	F	P	% Contribution
Voltage	1	26.96	26.96	26.17	0	62.05
Current	2	0.46	0.23	0.08	0.05	1.06
T_{on}	2	12.52	6.26	3.04	0.004	28.81
T_{off}	2	0.75	0.37	0.13	0.021	1.73
Error	10	2.76				6.35
Total	17	43.45				100.00

3.4.1 Contour Plots for Kerf

To increase the quality of cut, the kerf should be also minimum to obtain the required shape. Figure 3 shows the voltage less than 13 V and T_{on} less than 127 μs produced a minimum kerf width. The contour plots of the kerf clearly indicate the effect of process parameter. Figure 3a shows the relationship between T_{on} and voltage to kerf. The kerf widening occurred with T_{on} and voltage increase; hence, the optimisation region was divergent with both parameters. As seen in Fig. 3b, T_{off} shows a little effect on the kerf width due to material removal is practically nil. Figure 3c revealed that the current and voltage mostly affected the kerf width due to cumulative effect by these variables on the material removal leading to widening of kerf.
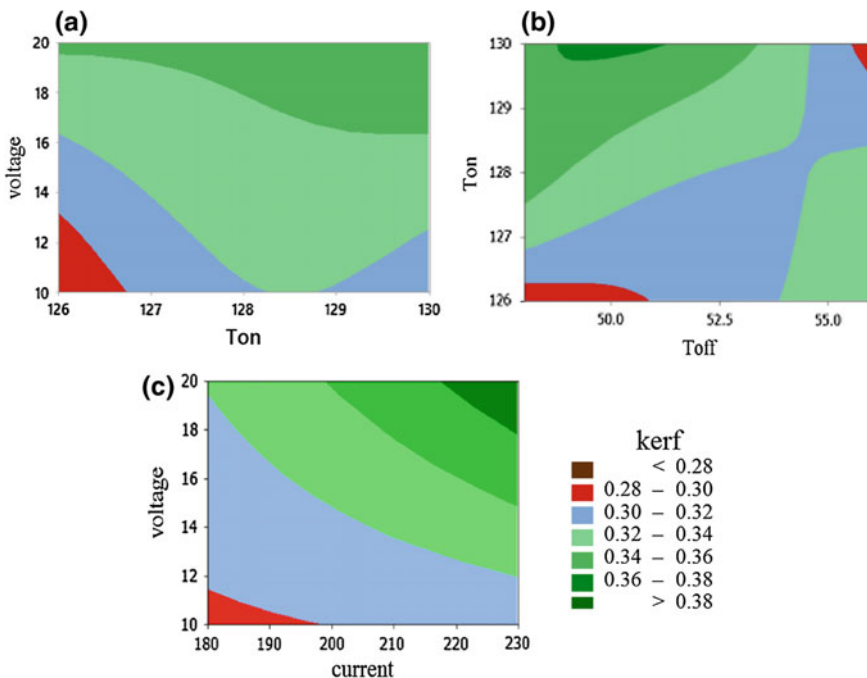
Fig. 3 Contour plots for kerf

3.4.2 Contour Plot for Surface Roughness

To improve the quality of the cut, the surface roughness is always minimum. From Fig. 4, when voltage <14 V and current <220 A, the optimum surface quality <3.4 µm was recorded. The current and voltage influenced the surface roughness of cut surface, as shown in Fig. 4a. The trend shows that the surface roughness was increased with increasing current and voltage. High intense sparks removed the material in the vicinity with uncontrolled manner. As seen in Fig. 4b the surface finish is significantly improved with an increase in pulse off time due to easy flushing of debris and reduced resolidified layer. Figure 4c shows the surface roughness initially increasing with voltage after that exceeds Ton 128 µs, then starts to decrease with voltage. This notably increased the current in interelectrode gap (IEG); hence, the spark strength was expected to be in higher order by the T_{on} time. Thus, the surface roughness was influenced by the current considering process variables.
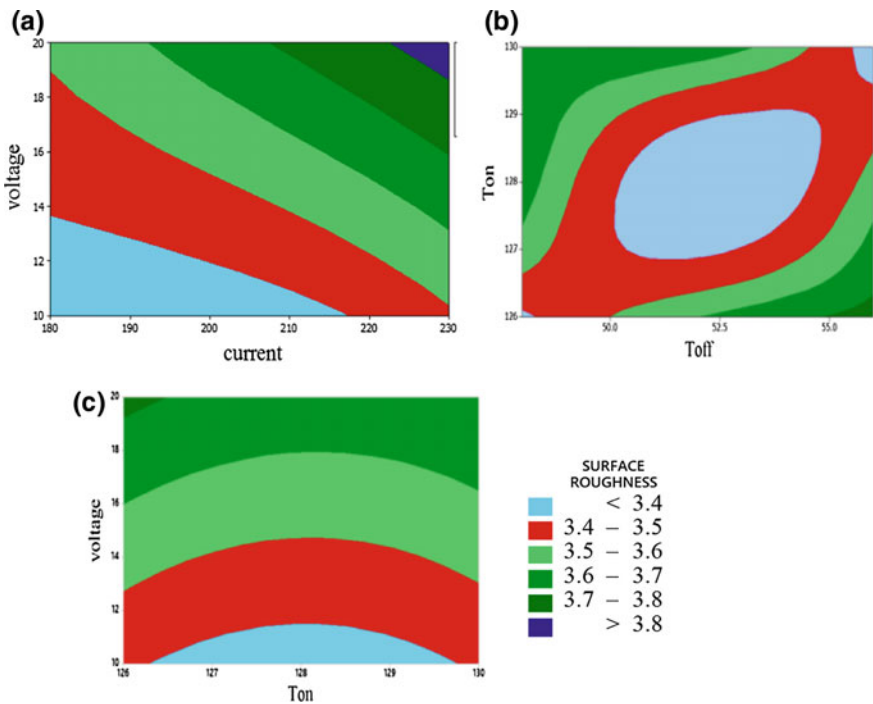
Fig. 4 Contour plot for surface roughness

3.4.3 Contour Plot for MRR

Higher production rate is an ultimate aim of the each process. To achieve this, MRR should be maximum. From Fig. 5, voltage >20 V and current >230 A produced an optimum MRR >18 mm^3/min. MRR increase with increasing current as result of high-intensity plasma evaporates more material from machining surface, as seen in Fig. 5a. Similarly, T_{on} increases the MRR due to high-energy spark which was sustained for a long duration, as shown in Fig. 5b. It can be seen that the MRR was very higher at low T_{off}. T_{off} allows a dielectric fluid to regain its original dielectric strength, as shown in Fig. 5c. Short duration disallowed the regain of dielectric fluid, and long duration reduced the high energy spark repetition.

4 Confirmation Test

The lower width i.e. 0.263 mm was obtained at a voltage of 10 V, a current 180 A, pulse on time of 126 μs and pulse of time of 56 μs. Similarly, for a higher MRR, the optimum values resulted in 18.652 mm^3/min with at voltage of 20 V (Level 2),
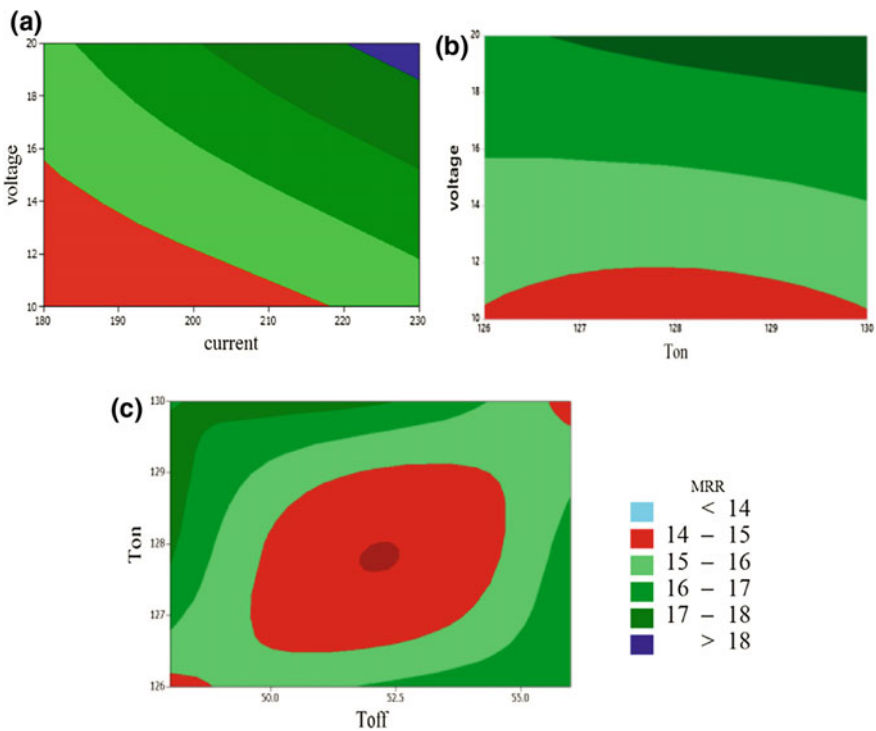
Fig. 5 Contour plots for MRR

(a) Kerf=0.263mm (b) Ra=3.22µm
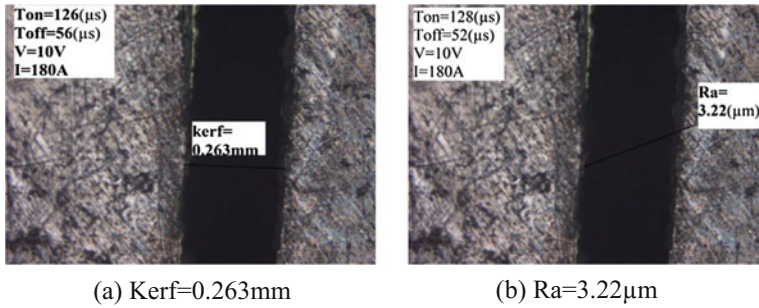
Fig. 6 Optical images of specimen after conformation test

current 230 A (Level 3), pulse on time of 130 µs (Level 3) and pulse of time of 48 µs (Level 1). On the other hand, for lower surface roughness, a value of 3.22 µm was recorded as optimum value, as evident of Fig. 6a, b.

5 Conclusions

In this research, an attempt has been made to investigate the effect of process parameters on wire electric discharge machining process while machining an aluminium hybrid nanocomposite. Experimentation was designed based on Taguchi's parameter by considering the following process parameters such as voltage, current, pulse on time and pulse off time, and the corresponding responses were kerf width, material removal rate and surface roughness. The following conclusions were drawn from the investigation:

1. All the factors investigated in the study were statistically significant for their impact on the kerf width with major contributions from voltage with 50.46% followed by T_{on} with 15.32%.
2. Voltage with 62.05% and T_{on} with 28.81%, the MRR was more affected than other parameters.
3. The counter plots for surface roughness revealed that voltage <14 V and current<220 A produced surface roughness <3.4 µm and were in optimisation domain. For MRR voltage >20 V and current >230 A, the optimum MRR >18 mm^3/min was achieved, and for kerf voltage <13 V and T_{on} <127 µs, the minimum kerf was achieved.
4. Confirmation experiments were conducted with optimised values, and results were obtained as 0.263 mm for kerf width, MRR for 18.652 mm^3/min and 3.22 µm for surface roughness.
5. The nanolevel reinforcement particles did not affected the cutting process. The melting and evaporating were the major mechanism of material removal. Voltage and T_{on} parameter significantly increased MRR, but negatively affected the kerf width and surface roughness.

References

1. Su, H., Gao, W., Feng, Z., Lu, Z.: Processing microstructure and tensile properties of nano-sized Al_2O_3 particle reinforced aluminum matrix composites. Mater. Des. **36**, 590–596 (2012)
2. Raj Kumar, K., Santosh, S., Javed Syed Ibrahim, S., Gnanavelbabu, A.: Effect of electrical discharge machining parameters on microwave heat treated aluminium, boron carbide, graphite composites. Procedia Eng. **97**, 1543–1550 (2014)
3. Rajkumar, K., Rajan, P.: Effect of boron carbide and graphite on machining characteristics of aluminium boron carbide composite. www.scientific.net/AMM.592-594.181 (2014)
4. Muthazhagan, C., Gnanavel babu, A., Bhaskar, G.B., Raj Kumar, K.: Influence of graphite reinforcement on mechanical properties of aluminium, boron carbide composites. www.scientific.net/AMR.845.398 (2013)
5. Mandal, A., Dixit, A.R., Chattopadhyaya, S., Paramanik, A., Hloch, S., Królczyk, G.: Improvement of surface integrity of Nimonic C 263 super alloy produced by WEDM through various post-processing techniques. Int. J. Adv. Manuf. Technol. https://doi.org/10.1007/s00170-017-9993-x (2017)
6. Muller, F., Monaghan, J.: Non-conventional machining of particle reinforced metal matrix composite. Int. J. Mach. Tools Manuf. **40**, 1351–1366 (2000)
7. Pramanik, A.: Developments in the non-traditional machining of particle reinforced metal matrix composites. Int. J. Mach. Tools Manuf. **86**, 44–61 (2014)
8. Braz, J.: The behaviour of graphite and copper electrodes on the finish die-sinking electrical discharge machining (EDM) of AISI P20 tool steel. Soc. Mech. Sci. Eng. **29**. https://doi.org/10.1590/s1678-58782007000400004 (2000)
9. Hewidy, M.S., El-Taweel, T.A., Safty, M.F.: Modelling the machining parameters of wire electrical discharge machining of Inconel 601 using RSM. J. Mater. Process. Technol. **169**, 328–336 (2005)
10. Ekici, E., Motorcu, A.R., Kuş, A.: Evaluation of surface roughness and material removal rate in the wire electrical discharge machining of Al/B4C composites via the Taguchi method. https://doi.org/10.1177/0021998315609788 (2015)
11. Tosun, N., Cogun, C., Tosun, G.: A study on kerf and material removal rate in wire electrical discharge machining based on Taguchi method. J. Mater. Process. Technol. **152**, 316–322 (2004)

Influence of Multi-hole Technique on Fabrication of Surface Nanocomposite by Friction Stir Processing

Parumandla Naresh and Adepu Kumar

Abstract In the present investigation, the multi-hole technique has been used to increase the composite surface region in the processed region. A double parallel hole technique is introduced to increase the composite surface region from pin contacting region to the entire processing region. For this, AA 6061-T6 aluminum alloy is taken as the base material and nanosized Al_2O_3 particles taken as reinforcement for fabrication of Al/Al_2O_3 surface composite by friction stir processing. All the surface composites were fabricated at a constant tool rotational speed of 1150 rpm and tool traverse speed of 15 mm/min. The dispersion of the reinforcement particles into the matrix material was examined by optical microscope, scanning electron microscope, and EDS analysis. From the results, it is observed that the composite region is increased from pin region to processed region without any defect and it is found that uniform distribution of the reinforced particles took place with an addition of 4.5 vol.% of reinforcement particles. From the mechanical test, it is observed that the microhardness and wear resistance properties increased.

Keywords Friction stir processing · Surface nanocomposite
Multi-hole technique · Microhardness · Wear

P. Naresh (✉)
Department of Mechanical Engineering, Madanapalle
Institute of Technology & Science, Madanapalle, India
e-mail: askar86@yahoo.com

A. Kumar
Department of Mechanical Engineering, National Institute
of Technology - Warangal, Warangal, India
e-mail: adepu_kumar7@yahoo.co.in

1   Introduction

In recent times, ceramic-reinforced metal matrix composites have attained popularity as materials used in the automotive, aerospace, and rail industries because of their highly improved strength and greater wear resistance [1]. Still, the poor weldability of metal matrix composites (MMCs) by fusion welding methods prevents their extensive use in industries. Downsides of the fusion welding processes include weak bonding between filler and parent materials, eutectic formation, and occurrence of porosity in welding zone [2]. Friction stir welding (FSW) is a new technique to join the materials under solid state by applying frictional force. This method was invented by Wayne Thomas in 1991 at TWI, UK. Friction stir processing (FSP) is considered a promising technique for fabrication of reinforced metal matrix composites while avoiding the drawbacks of conventional fusion welding processes [3]. A novel technique called friction stir processing (FSP) was adopted from FSW for surface modification of composites. It was reported that FSP could successfully refine the microstructure of reinforced surface composites such as 5052 Al/Al_2O_3, Cu/SiC, $SiC/Al_2O_3/Al$, and $AA6360/(TiC + B_4C)$ [4–6]. FSP is a versatile method with a comprehensive function for the processing, synthesis, and fabrication of materials. Moreover, FSP technique has been extensively deployed for fabrication of surface composites using different sizes of reinforcements [7]. Several investigators have studied the effect of process parameters, tool geometry, multiple passes, varying reinforcement particle size on mechanical and microstructural properties of composites [8–10]. However, limited attention has been paid to the incorporation methods of reinforcement into the matrix material. In the direct FSP technique, the reinforcements are firstly placed on the surface or into the holes or groove of a plate and processed with FSP. So far, many researchers have focused their attention mainly on groove technique to prepare surface metal matrix composites by applying single- and multi-pass FSP (Fig. 1).

In this research work, Al/Al_2O_3 surface nanocomposites were fabricated by FSP. A new method called 'multi-hole' technique was used to fabricate the surface composites. By varying the depth and position of the holes, surface nanocomposites were fabricated. Therefore, the effects of multi-hole technique on mechanical and microstructural properties of fabricated Al/Al_2O_3 surface nanocomposites were investigated.

2   Experimental Work

Initially, 4-mm-thick aluminum 6061-T6 alloy plate with dimensions of 80×120 mm was taken as base material/matrix material. Nano (40–50 nm) Al_2O_3 particles were used as reinforcement for fabrication of surface nanocomposites. The chemical composition of base material (AA 6061-T6) is shown in Table 1. A particularly designed (concave shoulder with taper threaded cylindrical tool)
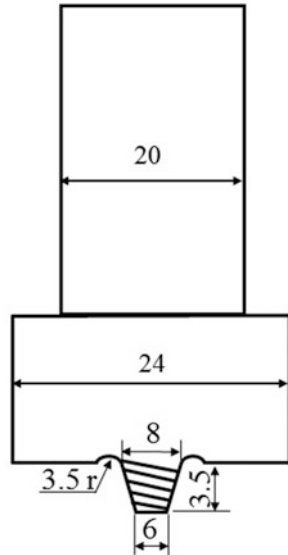
All Dimensions are in mm

Fig. 1 Tool geometry of the FSP tool

Table 1 Chemical composition of AA 6061-T6 aluminum alloy

Element	Mg	Si	Cu	Zn	Ti	Mn	Cr	Al
wt.%	0.85	0.68	0.22	0.07	0.05	0.32	0.06	Bal.

H13 tool steel was used as an FSP tool. At first, parallel double holes were made on the advancing side (AS) of the plate (pin contact region as well as shoulder contact region). The diameter of the hole, 1.5 mm, was kept constant for both pin and shoulder contact regions. The depth of the hole is varied at the pin contact region and which ranged between 1- and 3.5-mm distance was maintained at the shoulder contact region. Uniform pitch was maintained between the holes. The schematic diagram of the plates with multi-hole is shown in Fig. 2. Initially, all the holes were packed with nano Al_2O_3 powder and to avoid the escapement of reinforcement particles from the holes; the plate was processed with a plane shoulder tool (no probe) along the processed direction. The processed conditions of the FSP are chosen based on the previous work [11] and are given in Table 2.

The schematic diagram of FSP and plate having holes before process are shown in Figs. 3 and 4, respectively. The detailed experimental conditions are presented in Table 3. All the experiments were conducted on friction stir welding (FSW-3T) machine (Fig. 5). Before processing, all the plates were cleaned using ethanol. One-pass FSP was used to fabricate the surface nanocomposites. All the fabricate samples were machined by employing wire-cut EDM as per ASTM stands for
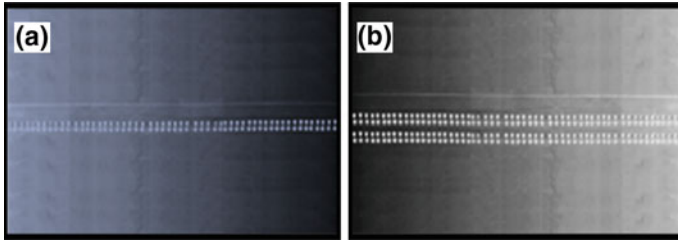
Fig. 2 Plates with multi-hole technique: **a** holes made in pin contact region; **b** holes made on both pin and shoulder contact region

Table 2 Process parameters and their values

Tool rotational speed (rpm)	1150
Tool traverse speed (mm/min)	15
Axial force (KN)	5
Tilt angle	2.5°
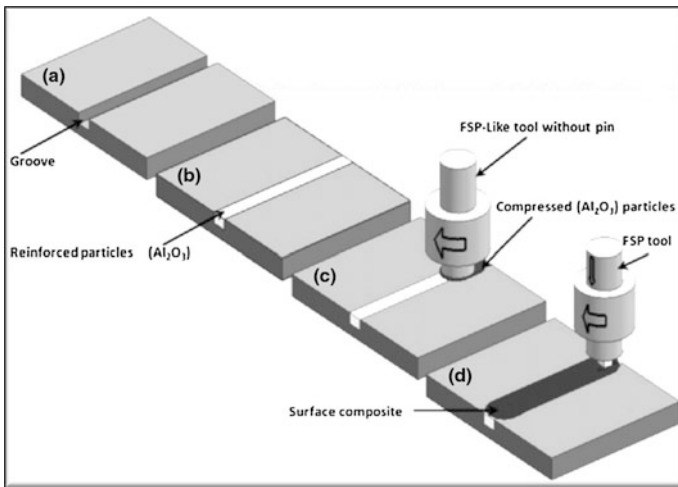
Fig. 3 Schematic operational diagram of FSP

conducting various tests. Keller's (20 ml HNO_3, 3 ml HCL, 2 ml HF, and 175 ml H_2O) reagent was used for the microstructural studies. Optical and scanning electron microscopes were used to study the microstructural behavior of the fabricated surface composites. By using Vickers' microhardness tester with 25 g load and 10 s dwell time, microhardness tests were conducted. The universal testing machine was used to conduct the tensile test for samples at room temperature. Wear test was performed by using a pin on disk machine with a constant load of 20 N, and
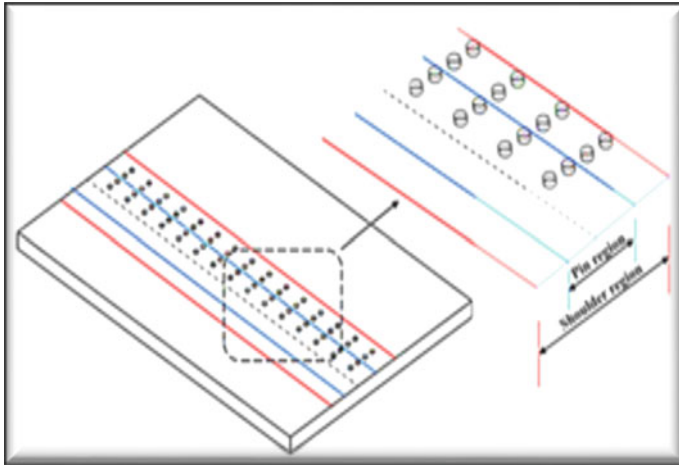
Fig. 4 Schematic diagram of multi-hole technique

Table 3 Detailed experimental sequence of multi-hole technique

Sample ID	Composite	Location of the holes	Dimensions of the holes (mm)		No. of holes	
			Pin region	Shoulder region	Pin region	Shoulder region
A1	Al + Al$_2$O$_3$	P	$D = 1.5, d = 1$	–	32	–
A2	Al + Al$_2$O$_3$	P	$D = 1.5, d = 2$	–	32	–
A3	Al + Al$_2$O$_3$	P	$D = 1.5, d = 3$	–	32	–
A4	Al + Al$_2$O$_3$	P	$D = 1.5, d = 3.5$	–	32	–
B1	Al + Al$_2$O$_3$	P + S	$D = 1.5, d = 1$	$D = 1.5, d = 1$	32	32
B2	Al + Al$_2$O$_3$	P + S	$D = 1.5, d = 2$	$D = 1.5, d = 1$	32	32
B3	Al + Al$_2$O$_3$	P + S	$D = 1.5, d = 3$	$D = 1.5, d = 1$	32	32
B4	Al + Al$_2$O$_3$	P + S	$D = 1.5, d = 3.5$	$D = 1.5, d = 1$	32	32

P pin contact region; *P + S* pin with shoulder contact region; *D* diameter of the hole; *d* depth of the hole

readings of weight loss had been noted at an even interval of 150 m traveling distance for a total of 1200 m.

3 Results and Discussion

3.1 *Macrostructure Analysis*

All the Al/Al$_2$O$_3$ surface nanocomposites were successfully fabricated without any surface defects like scalloping, cracks, surface galling. Smooth finished surfaces

Fig. 5 Friction stir welding machine
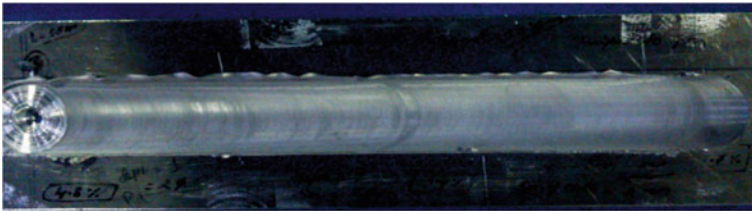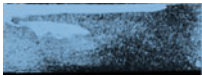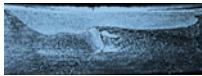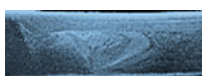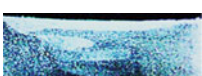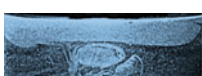
Fig. 6 Macrostructure of Al/Al$_2$O$_3$ fabricated surface nanocomposite

were observed on all fabricated surface nanocomposites. Some common semicircular patterns were observed throughout the processed region of surface composite due to tool rotational and traverse speed, and the exit hole occurred at the end of the process as shown in Fig. 6.

3.2 Microstructural Analysis

After visual examination, all the samples were cross-sectioned, polished, and etched with Keller's reagent for microstructural observations. From Table 4, it is observed that the dispersion of the reinforcement particles into the matrix material was uneven in A1–A4 experimental conditions, but where B1–B4 was concerned, more uniform dispersion of the reinforcement took place throughout the processed region. From Table 4, it is observed that the dispersion of the reinforcement into the SZ increased from the samples A1–A4. This is due to increase in depth of the hole in the pin region (1–3.5 mm). Similarly, the same nature of particle distribution was observed in sample B1–B4 and the dispersion of the particles occupied the entire processed region due to the location of the holes (pin with shoulder region). From the samples, A1–A4 and B1–B4, the amount of volume percentage of reinforcement increased with an increase in depth of the hole as well as area (shoulder region). A clear view of the increase in the composite area throughout the processed region can be seen in fabricated samples from B1 to B4. The dispersion of the reinforcement particles into the SZ as well as processed region (tool contact region) was increased continuously with an increase in the depth of the hole. A rich amount of reinforcement particles into the matrix was increased on the hole depth. When the depth of the hole was increased from 1 to 3.5 mm, more uniform dispersion of the reinforcement particles occurred into the matrix material. Microscopic examinations unveil that the process variables have a significant impact on the formation

Table 4 Macrograph of fabricated surface nanocomposite

Sample ID	Multi-hole technique (pin region)	Volume percentage (%)	Sample ID	Multi-hole technique (pin + shoulder region)	Volume percentage (%)
A1		1	B1		2
A2		2	B2		3
A3		3	B3		4
A4		3.5	B4		4.5

of surface nanocomposites. The nanoreinforcement particles were spread more usually and unvaryingly in the stir zone (SZ) in all fabricated surface nanocomposites. The mixture (reinforcement and matrix material) of plasticized material yields from the advancing side (AS) and travels toward retreating side (RS). At the advancing of the tool, the material becomes plasticized and forges toward the bottom of the pin. The dynamic stirring action of a tool directs the packed reinforcement toward the mix, with the plasticized matrix material forming the composite. A good mixture of the reinforcement particles with the matrix was observed in the fabricated surface nanocomposite.

Figure 7 shows the microstructure of the fabricated samples of B1–B4. From Fig. 7, it is observed that the richness of reinforcement particles into the SZ increased with an increase in the depth of the hole. From Fig. 7a, the reinforcement particles are distributed uniformly in the SZ at $d = 1$ mm. Very light white and dark bands can be seen from the composite fabricated at $d = 1$ mm. The amount of reinforcement particles was incorporated by increasing the depth of the hole from 1 to 2 mm as shown in Fig. 7b. An increase in volume percentage of reinforcement enhanced the richness of reinforcement particles into the SZ and formed more dark and white bands. Figure 7c, d shows that a rich amount of reinforcement particles accumulated with an increase in the depth of the hole from 3 to 3.5 mm. Figure 7d shows highly concentrated (dark region) Al_2O_3 particles into the SZ.
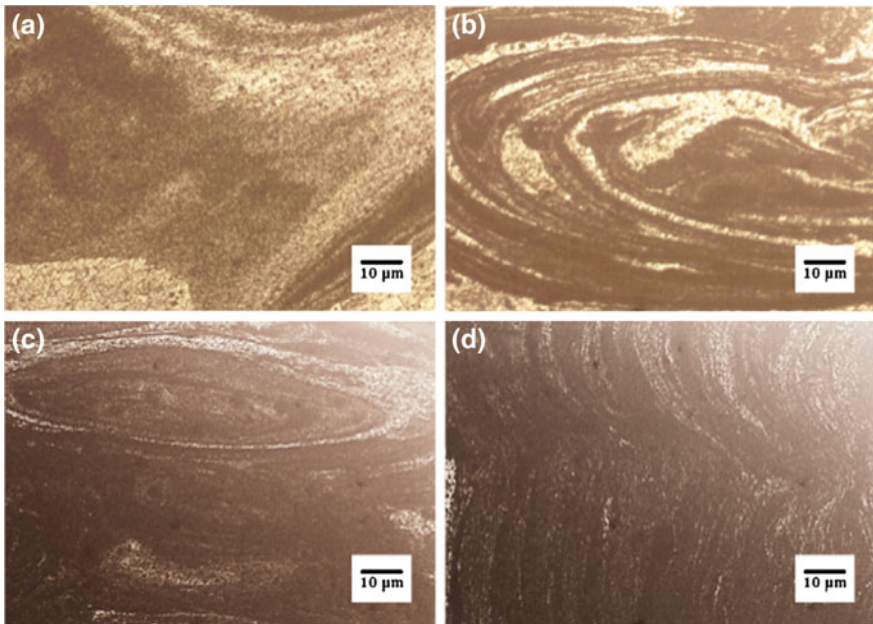
Fig. 7 Microstructures of fabricated surface nanocomposites with multi-hole technique at different depth of the holes; **a** $d = 1$ mm, **b** $d = 2$ mm, **c** $d = 3$ mm, **d** $d = 3.5$ mm

Figure 8 shows the microstructure of the processed region. During the process, the flow of the material varies from retreating side to advancing side. The flow patterns were explained clearly in Fig. 8. Different flow patterns can be observed in the composite fabricated with groove method and are shown in Fig. 8. From Fig. 8a, it is observed that the material on the retreating side is dragged from the bottom of the pin toward the upper surface on advancing side. The concave geometry of the tool and large downward forces help the material to flow into SZ easily. Transitional zones (stir zone (SZ), thermo-mechanical heat-affected zone (TMAZ), and heat-affected zone (HAZ)) are formed during the plasticization of material [12]. A non-uniform mixture of a surface composite layer can be observed from Fig. 8b. Tool rotational speed and transverse speed cause the material to form dark and white colored bands during the process. Figure 8c shows the interface region of the tool pin and shoulder. In this region, the plasticized material is dragged from the RS and pulled toward SZ on advancing side with the help of tool rotation. Figure 8d, e shows the HAZ regions formed during the process on advancing side and retreating side. Large sizes of grains were observed in the HAZ region. A similar way of grain growth took place on both sides of the processed
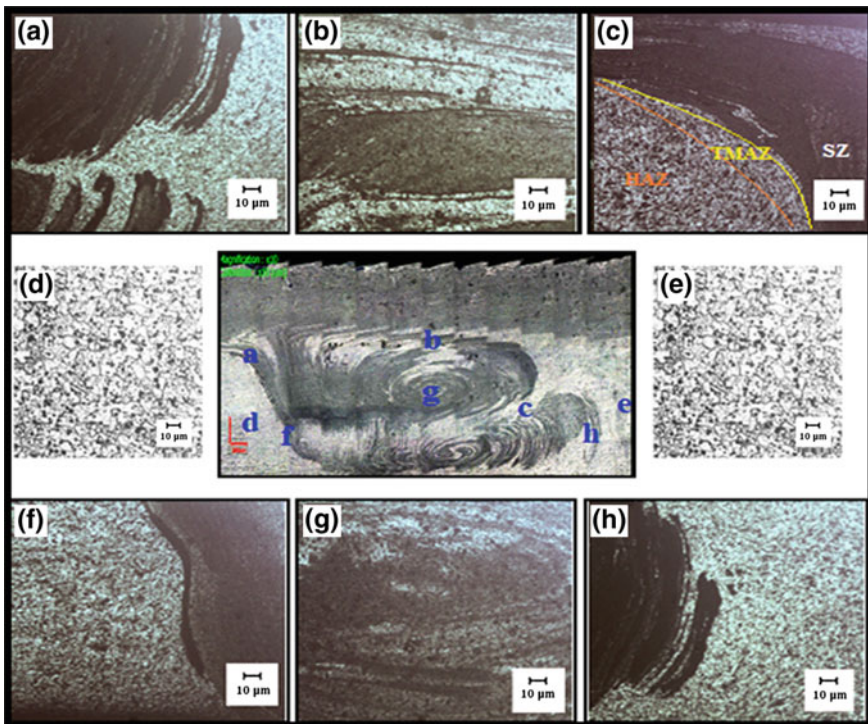
Fig. 8 Microstructures of fabricated composites: **a** Transitional zones, **b** Shoulder influenced region, **c** material flow taken short turn at RS, **d** HAZ region on AS, **e** HAZ on RS, **f** plasticized material flow forged by the shoulder of the tool, **g** Stir zone, **h** material flow at RS

region, and it was noticed that the size of the grain was increased and was large like the elongated grain while moving toward the base metal (BM) region. The geometry of the tool pin assumed great significance in plasticization of material flow. At this point, the geometry of tool pin is flexible to allow the rich mixture of reinforcement within the matrix at SZ which is shown in Fig. 8f. At the center of the SZ formation, an onion ringlike structure can be seen in Fig. 8g and it is observed that the flow of material is on retreating side. A quick return of material flow takes place during the process, which leads to the formation of onion ringlike structures. The number of onion rings is formed by high tool rotational speeds with low traverse speeds. Figure 8h shows the plasticized material drawn from beneath the pin toward retreating side. During the process, the reinforcement particles presented on the advancing side were continuously pushed toward retreating side because of tool rotation. A vortex flow on the advancing side creates a passage to reinforcement to spread over SZ.

3.3   EDS and XRD Analysis

The effect of adding reinforcement particles into the matrix is to increase the composite area and strength of the composite. It is very difficult to observe the distribution of nanoreinforcement particles into the matrix, and it can be detected by using energy dispersive spectroscopy (EDS). Figure 9 shows the EDS analysis of fabricated Al/Al_2O_3 surface composite. The result showed that Al_2O_3 particles were finely distributed into the matrix. A rich amount of nano Al_2O_3 particles has been circulated throughout the SZ, and the other elements like Mg, $CaCO_3$, SiO_2 were observed in the composite region.

Figure 10 shows SEM micrographs of fabricated surface nanocomposite by FSP. The white band region in Fig. 10a shows the agglomerated particles of Al_2O_3 nanoreinforcement which have been confirmed with the help of EDS. Figure 10b shows the distribution of reinforcement particles into the SZ center, and the dark region shows the matrix material.

Element	Weight%	Atomic%	Standard :
C K	5.33	11.10	C - CaCO3
O K	1.64	2.57	O - SiO2
Mg K	1.00	1.03	Mg - MgO
Al K	91.74	85.05	Al - Al2O3
Si K	0.28	0.25	Si - SiO2
Totals	100.00		

**Fig. 9** EDS analysis of Al/Al_2O_3 surface nanocomposite
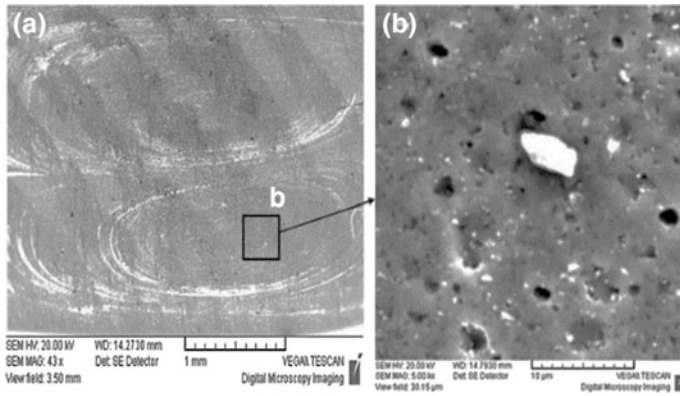
Fig. 10 SEM images of the Al/Al$_2$O$_3$ surface composite: **a** SZ of the surface composite; **b** enlarged region of the SZ center

X-ray diffraction (XRD) test was performed to find out the formation of any second phase elements between Al$_2$O$_3$ and matrix material during the composite fabrication. The phases of composites were examined through XRD. Figure 11 shows the XRD pattern of the fabricated surface composite. There were three major phases in the composites, these being Al$_2$O$_3$, Al$_4$Si, and Mg$_2$Si$_5$Al$_4$O$_{18}$. There were no peaks of other phases that formed in the composites. Similar results were observed in all fabricated surface composites (A1–A4 and B1–B4).

3.4 Microhardness

Microhardness test was performed to understand the uniform distribution of the reinforcement particles in the fabricated surface nanocomposites. Figure 12 shows that fabricated surface nanocomposites exhibit superior microhardness values than
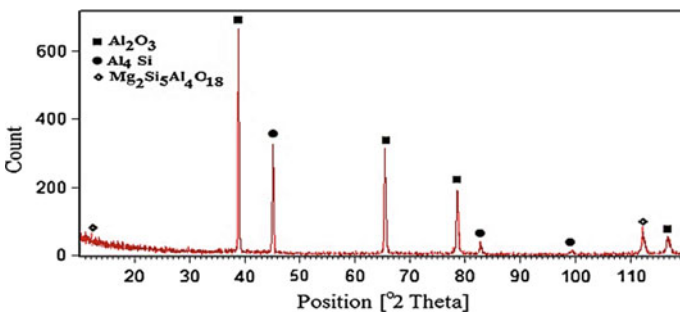
Fig. 11 XRD pattern of surface nanocomposite
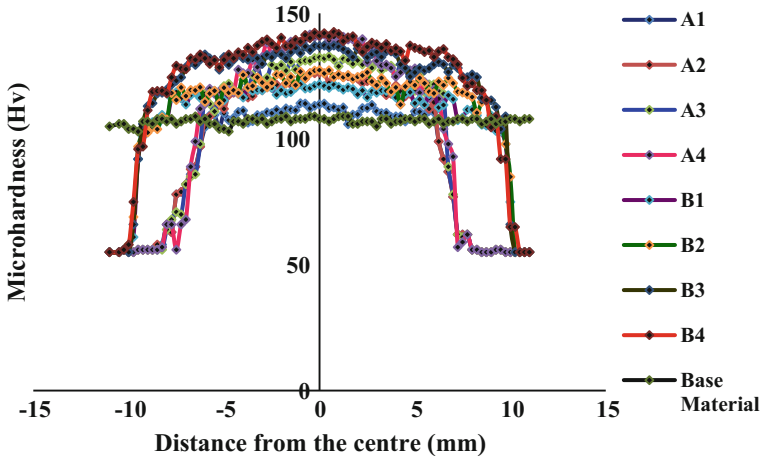
Fig. 12 Microhardness graphs of FSPed Al/Al$_2$O$_3$ composites

compared with the as-received base material. At the center of the SZ, the microhardness was much higher than the transitional zones (TMAZ and HAZ) due to the pinning effect of the tool. The increase in microhardness of MMCs depends on strengthening mechanisms [14].

(a) Hall–Petch relationship (grain and subgrain boundary strengthening), (b) Orowan theory (dislocation of reinforcement particles due to pinning effect), (c) coefficient of thermal expansion (CET) (the cause of dislocation induced between the reinforcement and the matrix material due to the change of CET), and (d) elastic strain in the interface of matrix and reinforcement have a say in determining the increase in microhardness. In A1–A4 composites, microhardness increased in SZ and the B1–B4 composites showed an increase in microhardness all over the processed region. Sample A4 shows higher microhardness value (140.8 Hv) than B1–B3 on the SZ because of higher volume percentage of the nanoreinforcement presented at the SZ due to increasing depth of hole ($d = 3.5$ mm), but the dispersion of the reinforcement is restricted to SZ only. From the entire fabricated surface nanocomposites, sample B4 shows not only higher microhardness properties (141.5 Hv) and also increase in composite region up to processed region (tool contact region).

3.5 Tensile Test and Fractography

Tensile properties of various surface nanocomposites are shown in Table 5. An average of three test results was shown in Table 5. The tensile properties of composites exhibited lower values than as-received base material due to the addition of Al$_2$O$_3$ reinforcement particles, increasing the brittle nature of the composite.

Table 5 Tensile properties of surface nano composites fabricated by multi hole technique

Sample ID	Ultimate Tensile Strength (UTS, MPa)*	Yield Strength (YS, MPa)*	Percentage of Elongation (%EL)*
A1	145.9	108.5	6.14
A2	158.5	122.8	5.72
A3	164.6	126.8	5.82
A4	176.7	146.4	4.93
B1	181.2	133.5	6.02
B2	179.3	128.7	5.36
B3	192.5	146.4	5.56
B4	194.1	159.7	5.48
BM	295	271	12

*Average values of 3 testing results

All the samples were notched like cup and cone shape, and the fracture surfaces were inspected with scanning electron microscopy.

From the results, it is observed that the failure occurred at the ductility end, such as micro-void coalescence which took place in the notched region as shown in Fig. 13. Dimple-like structures were seen in the failure region, which may be due to the presence of reinforcement particles in the matrix as shown in Fig. 13a, b. From the SEM micrographs of the fractured surface, it is observed that the presence of impurities and hard reinforcement particles could be the cause of lower elongation. The addition of nano Al_2O_3 particles into the matrix resulted in a decrease in tensile properties than as-received base material. The increase of reinforcement volume percentage into the matrix was caused by an increase in tensile properties from
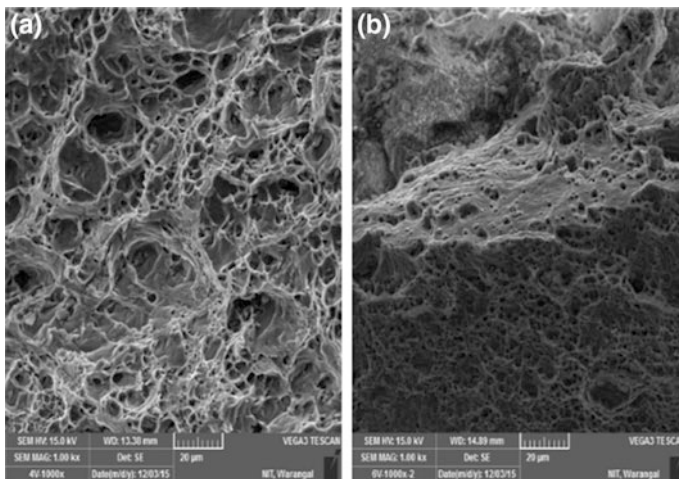
Fig. 13 Fractography of surface composites: **a** larger dimples; **b** smaller dimple

145.9 to 194.1 MPa (UTS), but the brittle nature in Al/Al$_2$O$_3$ composite led to primary failure in the composites. Similarly, the percentage of elongation decreased from 12 to 5.48% El.

3.6 Wear

The wear rate of surface nanocomposites is shown in Fig. 14. The wear rate of Al/ Al$_2$O$_3$ surface nanocomposites reduced as compared with as-received aluminum alloy. The addition of Al$_2$O$_3$ into the matrix and dynamic recrystallization leads to an increase in wear resistance. Figure 14 shows the coefficient of friction graph of surface nanocomposite and base material (as-received) concerning the sliding distance. The coefficient of friction of surface composite (i.e., 0.43) is lower when compared with the base material (0.6). Low coefficient of friction indicates that the nature of wear mechanism is abrasive. From Fig. 14, it was observed that the coefficient of friction of base material (as-received Al alloy) gradually increased and was much higher at initial stages of the process due to the joining of the worn debris to Al surface. This leads in turn to abrasive wear mechanism, and in later stages, it becomes adhesive wear mechanism. The microstructural modification occurred
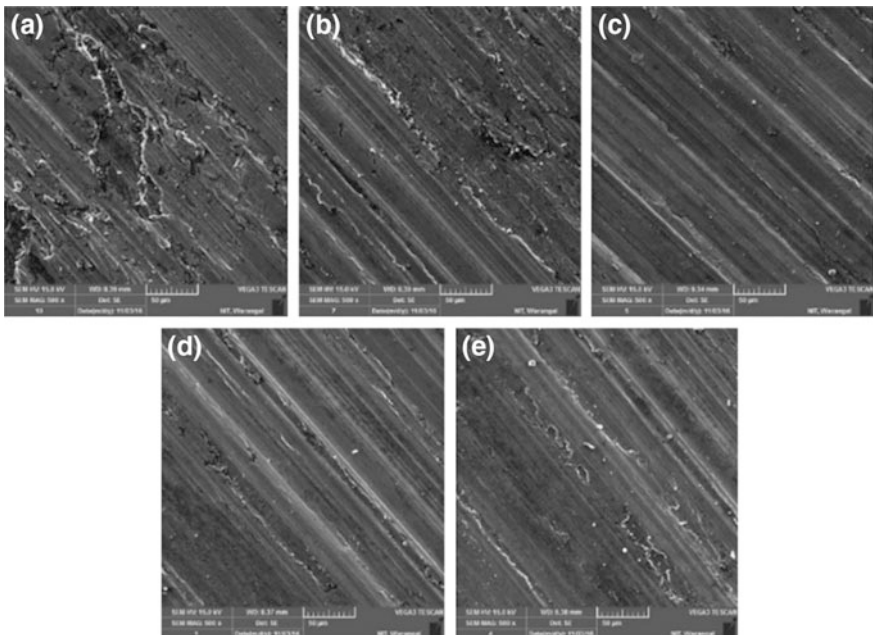
Fig. 14 SEM micrograph of worn surfaces of **a** base material, **b** sample B1, **c** sample B2, **d** sample B3, **e** sample B4
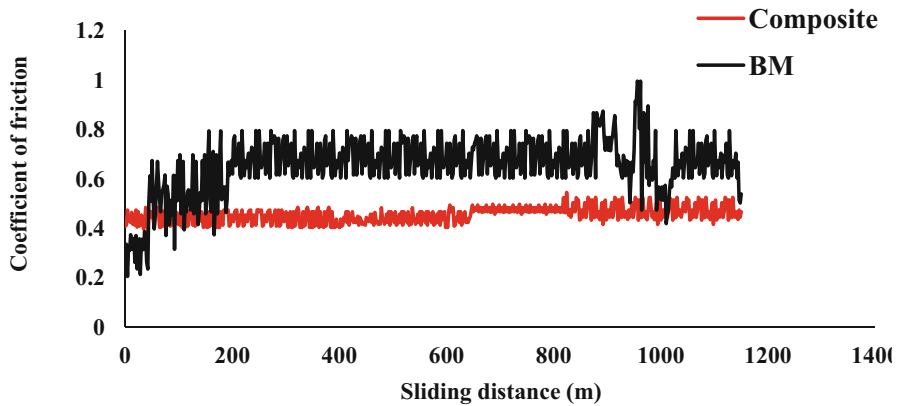
Fig. 15 Variation in the coefficient of friction with sliding distance for as-received Al alloy and surface nanocomposite of Al/Al$_2$O$_3$

with the addition of reinforcement particles, resulting in the strengthening of the matrix. The major contributions toward increasing wear resistance of surface composites by FSP are (a) Orowan strengthening mechanism due to uniform distribution of Al$_2$O$_3$ particles into the matrix and (b) the fine grain refinement of the matrix. Many researchers observed similar result with an addition of reinforcement particles into the matrix [14–16]. It is also shown in Fig. 15e that it was the least wear rate compared with other combinations of composites as shown in Fig. 15a–d. During the test, reinforcement particles pulled out from the matrix and formed a thin oxide film which acts as a solid lubricant; this improved the wear resistance by reducing the coefficient of friction [17, 18]. This solid lubricant reduces the friction between the disk and composite surface and leads to reducing the removal of material from the surface of the composite. The worn surfaces of Al/Al$_2$O$_3$ composites are shown in Fig. 15. From Fig. 15a, it is seen that the material is lost at a high rate from the surface of base material compared with other micrographs of composite surfaces. The increase of reinforcement particles into the matrix causes minimal weight loss from the composites shown in Fig. 15b–e. The results were observed in all combination of composites.

Figure 16 shows the rate of wear took place at a constant load of 20 N with varying sliding distances. The addition of Al$_2$O$_3$ reinforcement to the matrix was used in the reduction of weight loss and showed superior wear resistance than as-received base material. From Fig. 16, it is observed that the added Al$_2$O$_3$ particles acted as load-bearing components, as explained by many researchers [17, 18]. The hardness of Al$_2$O$_3$ reduces the removal material from the surface of composites. Lower wear rate occurred at B4 composite because of greater volume percentage (4.5%) of nanoparticles present in the matrix.
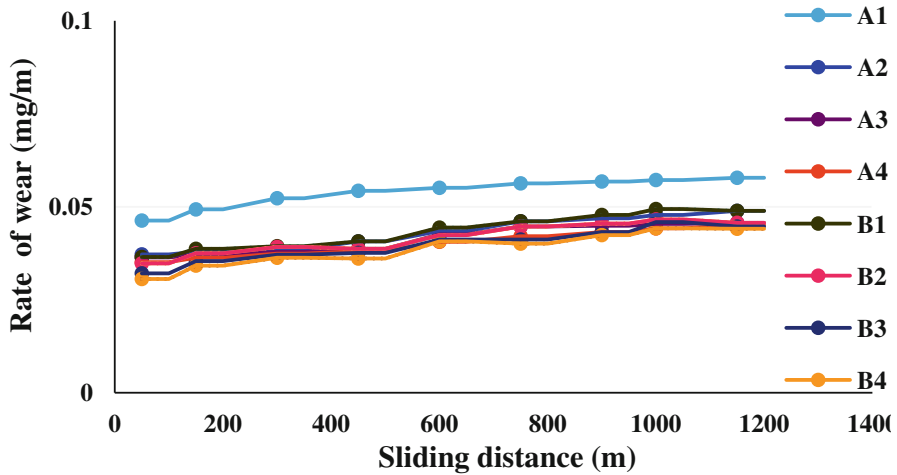
Fig. 16 Effect of Al$_2$O$_3$ reinforcements on rate of wear

4   Conclusions

In the present investigation, the multi-hole (pin contact region and pin with shoulder contact region) technique was successfully used for producing Al/Al$_2$O$_3$ surface nanocomposites on a large area without agglomeration. From the experiments and investigations, the following conclusions can be drawn:

- The microstructural examination of Al/Al$_2$O$_3$ surface nanocomposites fabricated by FSP showed that nano Al$_2$O$_3$ particles were well dispersed in the Al matrix.
- The composites made with multi-hole technique (pin with shoulder contact region) exhibited excellent dispersion of reinforcement particles throughout the processed region having no defects.
- The composites with Al$_2$O$_3$ particles apparently increased the microhardness of surface composites as compared with as-received base material from 108 to 141.5 Hv.
- The tensile properties of fabricated composites, shown to be 194.1 MPa, are very low than compared with the base material.
- The better wear resistance properties of Al/Al$_2$O$_3$ surface nanocomposite can be attributed to the presence of nano Al$_2$O$_3$ reinforcement, which contributes significantly to an increase in strength of the composite.

References

1. Tjong, S.C., Ma, Z.Y.: Microstructural and mechanical characteristics of in situ metal matrix composites. Mater. Sci. Eng. R **29**, 49–113 (2000)
2. Storjohann, D., Barabash, O.M., Babu, S.S., David, S.A., Sklad, P.S., Bloom, E.E.: Fusion and friction stir welding of aluminum-metal–matrix composites. Metall. Mater. Trans. **36**, 3237–47 (2005)
3. Mishra, R.S., Ma, Z.Y.: Friction stir welding and processing. Mater. Sci. Eng. R **50**, 1–78 (2005)
4. Sharifitabar, M., Sarani, A., Khorshahian, S., ShafieeAfarani, M.: Fabrication of 5052Al/ Al_2O_3 nanoceramic particle reinforced composite via friction stir processing route. Mater. Des. **32**, 4164–4172 (2011)
5. Barmouz, M., Givi, M.K.B., Seyfi, J.: On the role of processing parameters in producing Cu/ SiC metal matrix composites via friction stir processing: investigating microstructure, microhardness, wear and tensile behavior. Mater. Charact. **62**, 108–117 (2011)
6. Rejil, C.M., Dinaharan, I., Vijay, S.J., Murugan, N.: Microstructure and sliding wear behavior of AA6360/(TiC + B4C) hybrid surface composite layer synthesized by friction stir processing on aluminum substrate. Mater. Sci. Eng. A **552**, 336–344 (2012)
7. Barmouz, M., Asadi, P., Givi MKB, Taherishargh, M.: Investigation of mechanical properties of Cu/SiC composite fabricated by FSP: effect of SiC particles' size and volume fraction. Mater. Sci. Eng. A **528**, 1740–1749 (2011)
8. Dehghani, M., Amadeh, A., Mousavi, S.A.A.A.: Investigations on the effects of friction stir welding parameters on intermetallic and defect formation in joining aluminum alloy to mild steel. Mater. Des. **49**, 433–441 (2013)
9. Kumar, K., Kailas, S.V., Srivatsan, T.S.: Influence of tool geometry in friction stir welding. Mater. Manuf. Process. **23**(2), 188–194 (2008)
10. Ma, Z.Y., Liu, F.C., Mishra, R.S.: Superplastic deformation mechanism of an ultrafine-grained aluminum alloy produced by friction stir processing. Acta Mater. **58**, 4693–4704 (2010)
11. Naresh, P., Kumar, A.: Effect of nano reinforcement on fabrication of Al/Al_2O_3 surface composite by friction stir processing. Mater. Sci. Forum **830–831**, 467–471 (2015)
12. Sharifitabar, M., Sarani, A., Khorshahian, S., ShafieeAfarani, M.: Fabrication of 5052 Al/ Al_2O_3 nanoceramic particle reinforced composite via friction stir processing route. Mat. Des. **32**, 4164–4172 (2011)
13. Lloyd, D.J.: Particle reinforced aluminum and magnesium matrix composites. Int. Mater. Rev. **39**, 1–24 (1994)
14. Mahmoud, E.R.I., Takahashi, M., Shibayanagib, T., Ikeuchi, K.: Wear characteristics of surface-hybrid-MMCs layer fabricated on aluminum plate by friction stir processing. Wear **268**, 1111–1121 (2010)
15. Alidokht, S.A., Zadeh, A.A., Soleymani, S., Assadi, H.: Microstructure and tribological performance of an aluminium alloy based hybrid composite produced by friction stir processing. Mater. Des. **32**, 2727–2733 (2011)
16. Soleymani, S., Zadeh, A.A., Alidokht, S.A.: Microstructural and Tribological Properties of Al5083 based Surface Hybrid Composite Produced by Friction Stir Processing. Wear **278– 279**, 41–47 (2012)
17. Gui, M., Kang, S.B.: Aluminum hybrid composite coatings containing SiC and graphite particles by plasma spraying. Mater. Lett. **51**, 396–401 (2001)
18. Tjong, S.C., Lau, K.C., Wu, S.Q.: Wear of Al-based hybrid composites containing BN and SiC particulates. Metall. Mater. Trans. A **30A**, 2551–2555 (1999)

Accelerated Testing Model Prediction of Fatigue Life of AA5083-H111— AA6061-T6 Friction Stir Weldment

K. Rajkumar, A. Gnanavelbabu and K. M. Nambiraj

Abstract The heat treatable and non-treatable aluminium alloys are extensively used in ship hull and commercial automobiles where required to join the dissimilar materials. These dissimilar materials can be joined by solid-state friction stir welding process. This welding process will enhance joint properties like grain refinement in stir zone which results in increased yield strength and hardness. The above mentioned applications, there will be induced mechanical dynamic force influenced life of joints or fatigue life. Hence, the evaluation of welded joint properties is not only important but also fatigue life prediction is paramount. The present investigation is focused on the joining of dissimilar materials such as AA5083-H111—AA6061-T6 by friction stir welding process with function of traverse speed, rotational speed and axial force. The optimization of welding process parameters was done for tensile strength of the joint. The fatigue life of the joint was predicted with accelerated life model testing (ALT). Anderson–Darling (AD) test was conducted to find the suitable model for distribution of fatigue life data which yield that lognormal was best fit. The relationship between the tensile strength factors to the fatigue behaviour was established through the ALT inverse power law model (IPL). The parameters for the IPL-lognormal distribution were calculated by using maximum likelihood function. The S–N curve for this dissimilar joined material was effectively constructed with various percentages of maximum tensile stress and constant compressive stress.

Keywords Fatigue · FSW · Tensile · ALT · Anderson–Darling method

K. Rajkumar (✉)
Department of Mechanical Engineering, SSN College of Engineering, Chennai, India
e-mail: rajkumark@ssn.edu.in

A. Gnanavelbabu
Department of Industrial Engineering, Anna Universiy, Chennai, India
e-mail: dr.agbabu@gmail.com

K. M. Nambiraj
Department of Mechanical Engineering, Jeppiaar SRR Engineering College, Chennai, India
e-mail: nambiraj14@gmail.com

1   Introduction

Dissimilar joined aluminium alloys were provided tailored properties to the automobile and aerospace applications because of its high specific strength and stiffness. Enormous focuses have been paid for establishing fatigue failure behaviour aluminium alloys. However, fatigue-related studies on the dissimilar friction weld aluminium material have been the recent attraction to the researchers due to large-scale applications in many industrial products.

Friction stir welding (FSW) process is more effective for refining the microstructure of metals and metal alloys. Pressure exerted by the weld tool with generated heat concurrently forces plasticized material into back of the weld tool pin, and then, advent of tool makes the deformed materials get cooling. This results in perfect joining of materials [1, 2]. Al alloy is known for high thermal conductivity material which is difficult to join by traditional methods, even though established method like TIG results in defects such as like porosity and cracks. Hence, FSW is being increasingly used for joining of similar and dissimilar aluminium alloys. Some researchers donated that the welding speed, rotational speed and axial force were significant effects on tensile strength of joint [3, 4].

The experimental strain-life prediction of materials is a time-consuming and expensive method. Several authors analysed fatigue analysis of welded joints which are made from aluminium alloy. Notably, strain-controlled fatigue tests were conducted on 0.25 mm depth crack specimen. This study reveals the crack initiation of joints was at moderate loads. In this study strain-life prediction by considering only base material properties and not taken into account of heat affected zone properties [5].

The fatigue testing produces the time to failure of materials under the stated strain or loading conditions. It is well known that the failure of materials occurred at higher stress or strain. Accelerated life testing conditions where higher stress or load is given materials to failure faster rate. The computed stress to life at higher stress is extrapolated to normal working stress using an inverse powerlaw model [6]. The evaluated accelerated life was around 85–95% of the actual test life with 95% reliability level and $\pm15\%$ standard deviation. Therefore, it is expected that the accelerated life prediction will provide a suitable method for determining the criterion for fatigue design and for predicting a specific target life [7–9].

The present investigation is to identify the optimum process parameter of dissimilar aluminium alloy weld joining Al–Mg alloy AA5083-H111 and Al–Mg–Si alloy AA6061-T6 using friction stir welding. The relationship between strength factors was analysed using *S/N* ratio. The mechanical and microstructural behaviour were investigated, and the life of weld material was identified and analysed with accelerated life testing (ALT) method.

Table 1 FSW parameters

Parameters	Code	Unit	Level 1	Level 2	Level 3
Rotational speed	W	rpm	1000	1150	1300
Traverse speed	V	mm/min	35	52	69
Axial force	F	kN	3	4.5	5

2 Experimental Work

Aluminium AA6061 alloy has medium strength and good corrosion resistance. Heat treatment was carried out on AA6061 at a temperature 520 °C and then quenched in oil. Aluminium 5083 alloys show an exceptional performance in seawater and industrial chemical environments. Post-welded 5083 alloy retains excellent strength and ductility. The non-heat treatable alloys depend primarily on cold work to increase strength. Annealing was carried out in the range of 410 °C on the AA5083 alloy for 3 h.

Employed FSW tool was H13 tool steel with straight cylindrical threaded (SCT) pin profile. The pin specifications were diameter of 6 mm, shoulder diameter of 18 mm and length of 5.3 mm and inclination of 0°. The heat treated tool was used and its hardness was 55 HRC. Taguchi design L9 orthogonal array was used to optimize the FSW parameters values. The friction welding process is carried out on AA5083 H111—AA6061 T6 materials to make nine different samples by varying FSW parameters. The parameters used in the FSW are rotational speed, traverse speed and axial force and their levels as shown in Table 1.

3 Results and Discussion

3.1 Mechanical Properties

The hardness and yield strength of nine samples varying with FSW parameters are shown in Table 2, and mean effect is plotted in Fig. 1. From the obtained value, it is clear that initially at lower rotational speed the tensile strength will be high and slowly decreases with increase in rotational speed and then increases. In case of both welding/traverse speed, initially the tensile strength increases and at once it reaches a peak of 154 MPa and it slowly decreases with increase in traverse speed. When considering the axial force, it was bit different with other parameter. Because at first it was near mean tensile strength, later it slows down its strength and at a particular moment the tensile strength increases with increase in axial force. Table 2 shows the yield strength of FSW welded specimens. The experimental results show that 118 and 186 MPa are the lowest and highest tensile strength.

Table 2 Mechanical properties of FSW samples

Sample number	W (rpm)	V (mm/min)	Axial force (kN)	Hardness (BHN)	Yield strength				S/N ratio
					R1	R2	R3	Avg.	
1	1000	35	3.0	97.31	155	145	144	148	43.42
2	1000	52	4.5	98.33	148	149	153	150	43.55
3	1000	69	6.0	95	191	185	182	186	45.40
4	1150	35	6.0	85.33	162	155	169	162	44.19
5	1150	52	3.0	82.66	161	165	148	158	44.02
6	1150	69	4.5	92.33	107	125	122	118	41.50
7	1300	35	4.5	84.33	135	139	137	137	42.79
8	1300	52	6.0	97.66	149	151	151	153	43.73
9	1300	69	3.0	97.33	155	149	131	145	43.24
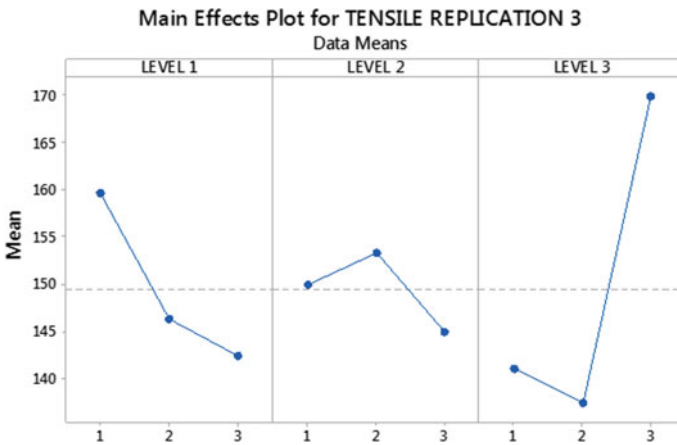
Fig. 1 Parameters with response graph for yield strength

3.2 Inverse Power Law—Lognormal Distribution

The inverse power law (IPL) model is important in the analysis of life data. The model has been widely used in reliability engineering for non-thermal accelerated stresses such as load or stress and is given by

$$L(w) = \frac{1}{KW^n} \tag{1}$$

The type of data used for the analysis is called the right censored data. Censoring is a condition in which the value of the measurement of observation is only partially known. During modelling of the time-to-failure data of the components, there is an

Table 3 S–N curve data for 10, 30, 50 and 80%, respectively

Stress (MPa)	10%	30%	50%	80%
+	48,971,867	1,813,773	391,775	95,648
Base	63,920,012	2,367,408	511,360	124,844
−	109,512,419	4,056,016	876,099	213,891

obvious reason for censoring; i.e., we do not have to necessarily wait for all subjects to fail. Thus, for right censored data, the data point (time to death) is larger than a certain value (the censoring time).

The weld specimen is chosen based on the optimal condition i.e higher S/N ratio. The fatigue test conducted by setting a stress value of 10,30,50 and 80% of max tensile strength (186 MPa)with stress variation $\pm 5\%$ and stress ratio is $R = 0$. This testing condition followed the high cycle fatigue and ASTM standard. The following formulae used for calculating the accelerated factor (af) show the level of accelerating testing stress and cycle to failure (Nf).

$$\text{af} = \left(\frac{1}{\pi}\right)\left(\frac{kc}{\sigma_{max}\alpha}\right)^2 \tag{2}$$

$$\text{Nf} = \frac{\left(\text{af}^{-\left(\frac{m}{2}+1\right)}\right) - \left(a_i^{\left(-\frac{m}{2}+1\right)}\right)}{\left(-\frac{m}{2}+1\right)\alpha^m A\sigma_r^{\left(m\right)\pi^{\left(\frac{m}{2}\right)}}} \tag{3}$$

where $\sigma_{max} = 186.5$ MPa, $\sigma_{min} = 0$, $\sigma_0 = 500$ MPa, $\sigma_u = 314$ MPa, $\sigma_r = 186 - 0 = 186$ MPa, Kc $= 100$ MPa, $a_i = 0.5$ mm, $\alpha = 1.12$, $m = 2.1$ and $A = 6.9 \times 10^{-12}$ MPa$^{1/2}$

Values are substituted and calculated based on the stress amplitude percentile like 10, 30, 50 and 80%, respectively, which are shown in Table 3. The reason behind this percentage is to find the relationship between stress amplitude and acceleration factor.

3.3 Anderson–Darling (A-D) Test

The fatigue data are analysed through the either the A-D test or statistical P value. The A-D test statistically determines magnitude of lognormal cumulative distribution function. This value is determined by finding square of the distance between the straight line and the plotted point. The choice of a proper distribution for the obtained data is determined by conducting A-D statistical test. Using MINITAB software, we can able to calculate the A-D value by analysing goodness of fit distribution. Table 4 shows A-D statistical value for the fatigue life data which are

obtained through friction stir welding. Selection of distribution is based on least A-D statistical value among the three distribution models being considered for the data distribution. Comparing the Weibull, normal and lognormal values, lognormal has the lowest value. Hence, it follows the lognormal probability distribute function.

Acceleration testing provides a prediction of normal condition data from the accelerated life data. The life data of accelerated conditions are lying parallel to each other in probability sheet confirms ALT programme. Figure 2 shows that lognormal distribution of fatigue failure data is parallel as result of identical failure mechanism.

The acceleration factor is one of the important life characteristics as shown in Fig. 3. AF is referred to relative stress between user stress levels to higher (accelerated) test stress level. This figure shows the stress was steadily increased to test at accelerated level.

Failure rate plots are very useful since they indicate the failure pattern of the system. The failure rate versus time plot in Fig. 4 shows the behaviour of the failure rate at the normal usage stress level. The Y-axis is the value of the failure rate at the normal usage stress level means less than yield strength. The failure rate increases at an increasing rate as T increases initially and gradually reduces over a period.

From the lognormal plot, it is proved that failure mechanism for the all stress amplitude was same. Hence, obtained failure data at accelerated condition was extrapolated to the below yield strength of fabricated joint which are given. Figure 5 shows the behaviour of the lifetime–load relationship characteristics

Table 4 A-D value data set

Welded joints	Three-way probability		
	Anderson–Darling value		
Distribution	Weibull	Normal	Lognormal
Optimal	1.532	1.488	1.484
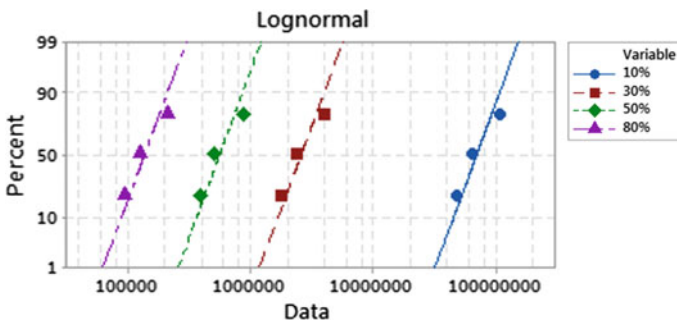
Fig. 2 Lognormal plot of lifetime
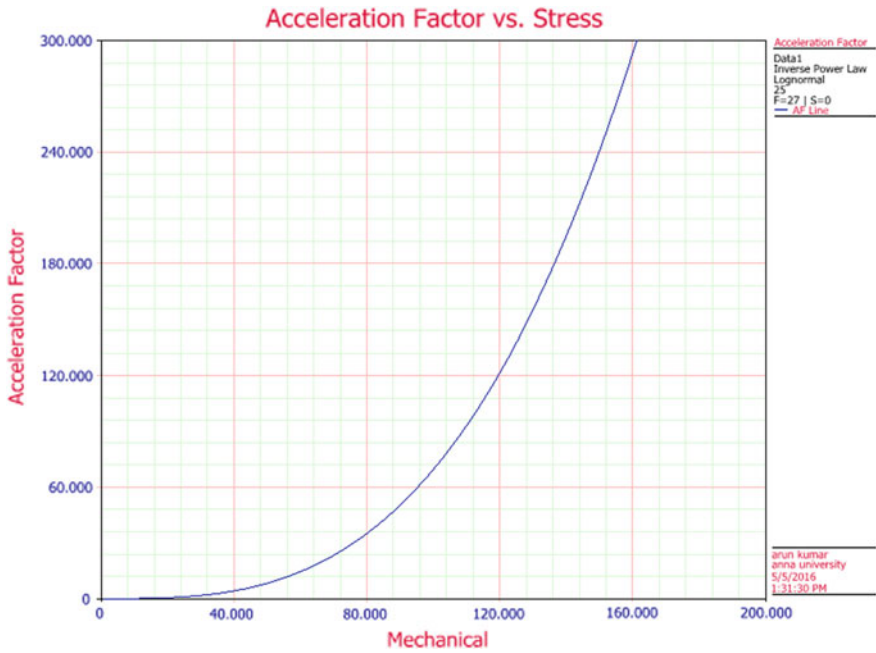
Fig. 3 Variation of acceleration factor versus stress
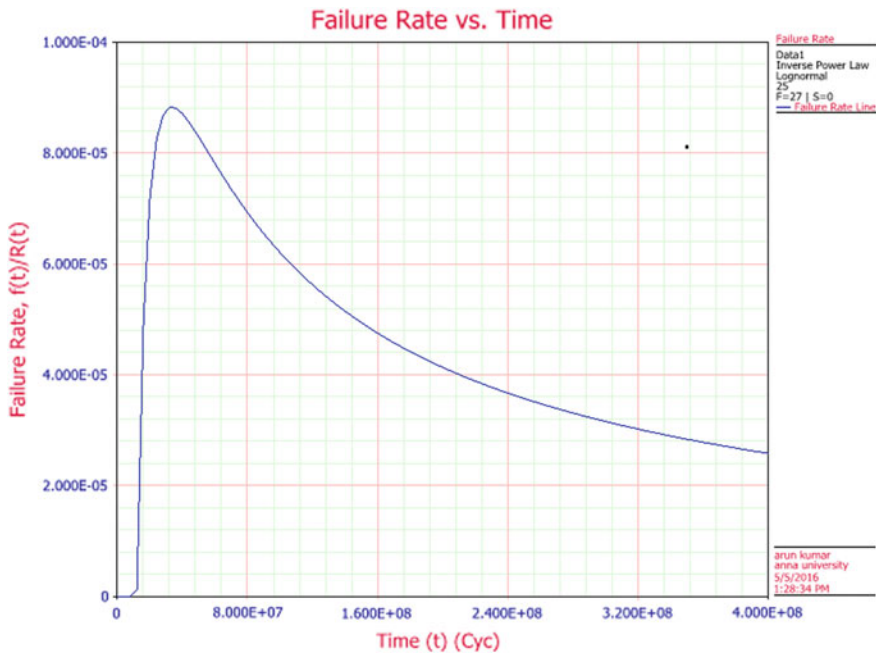
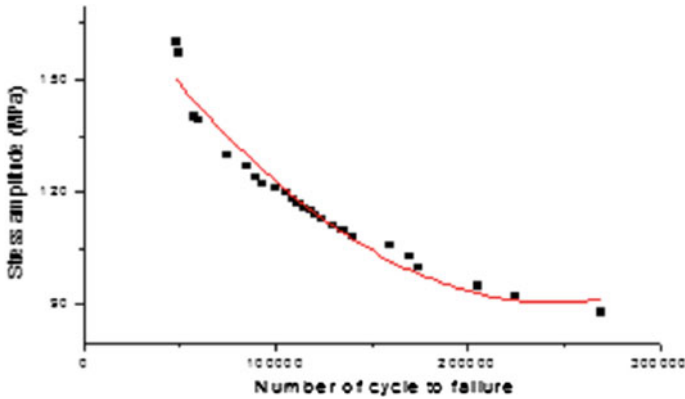**Fig. 4** Variation of failure rate of aluminium welds with time

Fig. 5 *S–N* curve

of dissimilar aluminium weldment AA6061-T6 and AA5083-H111 plates. The number of cycles versus load plot shows the failure of welded joint to the fatigue cycle. The obtained life at normal usage condition is extrapolated from accelerated condition. It indicates that the predicted life of the AA6061-T6 and AA5083-H111 plates is quite longer. Therefore, it is more economical to use this accelerated life testing method.

4 Conclusions

Dissimilar friction stir welding of AA6061-T6 and AA5083-H11 was carried out, and then, process parameters were optimized to further conduct the accelerated life testing. Friction stir welding can produce satisfactory butt welds between AA6061-T6 and AA5083-H11. The maximum yield strength of joint was 186 MPa. ALT has been designed to predict the fatigue failure of the fabricated joints with various accelerated stress conditions in terms of higher than the yield strength. Anderson–Darling statistical test has been conducted for the obtained data, and it recommended that a lognormal distribution is suitable for best fitting of data. The lognormal fatigue failure data at various accelerated conditions show that linear and parallel to eachother which confirms that fatigue failure mechanism is the same. Accelerated stress fatigue test data were extrapolated through the lognormal inverse power law to the different stresses which are below the yield strength of weld joint. ALT provides an economical way to construct the *S–N* curve for dissimilar aluminium alloys FSW joints.

References

1. Murr, L.E.: A review of FSW research on dissimilar metal and alloy systems. J. Mater. Eng. Perform. **19**, 1071–1089 (2010)
2. Threadgill, P.L., Leonard, A.J., Shercliff, H.R.: Friction stir welding of aluminium alloys. Int. Mater. Rev. **54**, 49–93 (2009)
3. Lakshminarayanan, A.K., Balasubramanian, V.: Process parameters optimization for friction stir welding of RDE-40 aluminium alloy using Taguchi technique. Trans. Nonferrous Met. Soc. **18**, 548–554 (2008)
4. Bayazid, S.M., Farhangi, H., Ghahramani, A.: Investigation of friction stir welding parameters of 6063-7075 aluminum alloys by Taguchi method. Procedia Mater. Sci. **11**, 6–11 (2015)
5. Moreira, P.M.G.P., de Jesus, A.M.P., Ribeiro, A.S., de Castro, P.M.S.T.: Fatigue crack growth in friction stir welds of 6082-T6 and 6061-T6 aluminium alloys: a comparison. Theor. Appl. Fract. Mech. **50**, 81–91 (2008)
6. Agrawal, R., Uddanwadiker, R., Padole, P.: Low cycle fatigue life prediction. Int. J. Emerg. Eng. Res. Technol. **2**(4), 5–15 (2014)
7. Baek, S.Y., Bae, D.H.: Accelerated life prediction of fillet-type, gas-welded joints. Int. J. Automot. Technol. **11**(3), 375–380 (2010)
8. Rajkumar, K., Kundu, K., Aravindan, S., Kulkarni, M.S.: Accelerated wear testing for evaluating the life characteristics of copper-graphite tribological composite. Mater. Des. **32**, 3029–3035 (2011)
9. Rajkumar, K., Aravindan, S., Kulkarni, M.S.: Wear and life characteristics of microwave sintered copper-graphite composites. J. Mater. Eng. Perform. **21**, 2389–2397 (2012)

Development of Mathematical Models and Evaluation of the Optimal Process Parameters for Laser Surface Hardening of Low Alloy Steel Using Elitist Non-dominated Sorting Genetic Algorithm

S. Vignesh, G. Muthukumaran, P. Dinesh Babu, K. P. Arulshri, R. Sivabalakrishnan and G. Surya

Abstract The process parameters of the laser hardened zone play a vital role in determining the surface hardness of the material after the hardening process. The most influencing input parameters such as laser power and traveling speed are considered in conducting the experimental work. The ultimate aim is to obtain maximum hardness, minimum width, and maximum depth after the laser surface hardening (LSH). The desired output responses are obtained by optimizing the process parameters and suggesting it for future research to eliminate the unnecessary trials. Trial and error procedures of finding out the optimal conditions incur more time and effort. Thus, the optimization was carried out using the non-conventional technique, elitist non-dominated sorting genetic algorithm (NSGA-II). The laser surface hardening was carried out on the low alloy steel using fiber laser source. The experimental trials were designed using response surface methodology (RSM), and the mathematical equations were developed using

S. Vignesh (✉) · K. P. Arulshri · R. Sivabalakrishnan · G. Surya
Department of Mechatronics, Bannari Amman Institute of Technology,
Sathyamangalam 638401, India
e-mail: vignesh@bitsathy.ac.in

K. P. Arulshri
e-mail: arulshri@bitsathy.ac.in

R. Sivabalakrishnan
e-mail: sivabalakrishnan@bitsathy.ac.in

G. Surya
e-mail: surya.mc15@bitsathy.ac.in

G. Muthukumaran · P. Dinesh Babu
School of Mechanical Engineering, SASTRA University, Thanjavur 613401, India
e-mail: muthukumaran.g@mech.sastra.edu

P. Dinesh Babu
e-mail: dineshbabu@mech.sastra.edu

regression analysis. The mathematical models are utilized by the NSGA-II algorithm by conducting 'n' iterations for 'm' population levels to find out the optimized zone for performing the hardening process.

Keywords Low alloy steel · Laser surface hardening · Elitist non-dominated sorting genetic algorithm · Surface hardness · Response surface methodology

1 Introduction

The research on surface engineering is mainly carried out to eliminate the flaws that occur in the surface region of mechanical assemblies or components [1]. Laser surface hardening is a novel approach in the field of surface engineering [2]. A finely controlled heating of considerable heat power density is obtained when the laser source is used for hardening [3]. Laser surface hardening (LSH) is the most preferred way of improving the mechanical and metallurgical properties of the material. Though there are many laser systems such as Nd-YAG and others are available, the fiber lasers are considered for this research due to their simplicity and high reliability [4, 5]. The fiber laser source is said to exhibit a higher hardness than the base material hardness at a power less than the other laser sources. They carried out an evolutionary algorithm based investigation for the tolerance allocation of the mechanical components and assemblies. They conducted sensitivity analysis study on the mechanical units and concluded that an improved optimized model can be developed when we use evolutionary-based algorithms. Vignesh et al. [6] investigated the optimal process parameters using statistical and evolutionary techniques based on the experimental analysis carried out on double-sided friction stir welded aluminum alloy joints. They have compared the solutions obtained through two different techniques and suggested the better one. The mathematical models have been developed, and the optimal solutions on the laser welded process parameters are discussed in the research carried out by Vignesh et al. [7]. The non-dominated sorting genetic algorithm (NSGA-II) methodology is mainly preferred as it can be employed for intricate mechanical assemblies [8].

2 Methodology

The optimization is carried out using the evolutionary technique, with the intention to attain a superior optimized result than the statistical approach. The elitist non-dominated sorting genetic algorithm is considered in current research work.

Fig. 1 Process stream of NSGA-II algorithm
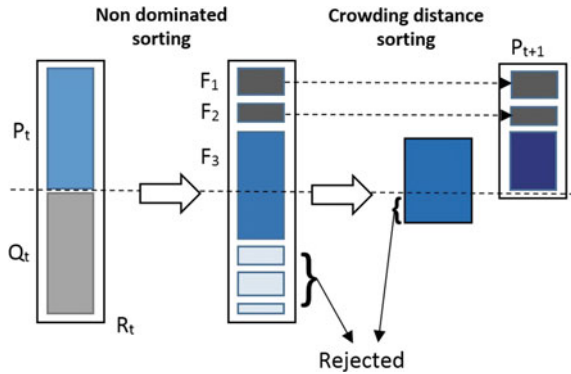
2.1 Elitist Non-dominated Sorting Genetic Algorithm

This algorithm introduced by Deb et al. [9] is a well-known methodology for optimizing the process parameters in achieving the desired output responses. It uses an elite preserving mechanism for retaining the previously obtained good solutions. It also utilizes a quick non-dominated sorting method. An arbitrary parent population P_o is formed and sorted based on the non-domination. The computational complexity is reduced by adopting a special book-keeping procedure. The child population Q_o with the size of N is created using the recombination and mutation operators. Then, the NSGA-II algorithm shown in Fig. 1 is followed.

2.2 Steps Involved in the Optimization

The procedure followed in optimization is shown in the Fig. 2. The experimental data is utilized by response surface, methodology and the mathematical models are developed for the output responses. The developed models are used in NSGA-II technique. The parameters required in the NSGA-II optimization are entered as required.

2.3 Considerations Involved in the Work

The various parameters utilized for the laser hardening process and the optimization using genetic algorithm are discussed in this topic. The mathematical models developed using response surface methodology which are utilized in the NSGA-II algorithm are shown in the Eqs. (1)–(3).
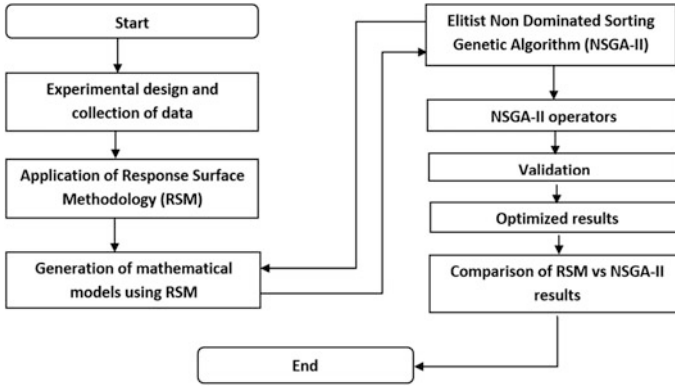
Fig. 2 Steps involved in the process

3 Results and Discussion

3.1 Development of Mathematical Models

The mathematical models for the output responses for maximizing the surface hardness, minimizing the width, and maximizing the depth of the laser surface hardened zone are given below.

$$
\begin{aligned}
\text{Hardness} = &+ 663.88889 + 0.23000 \times \text{Power} - 0.022917 \times \text{Travel Speed} \\
&- 2.50000 \times 10^{-5} \times \text{Power} \times \text{Travel Speed} \\
&- 9.33333 \times 10^{-5} \times \text{Power}^2 + 1.15741 \times 10^{-5} \times \text{Travel Speed}^2
\end{aligned}
\tag{1}
$$

$$
\begin{aligned}
\text{Width} = &+ 0.84333 - 9.73333 \times 10^{-4} \times \text{Power} - 3.47222 \times 10^{-5} \times \text{Travel Speed} \\
&- 8.33333 \times 10^{-8} \times \text{Power} \times \text{Travel Speed} \\
&+ 1.12000 \times 10^{-6} \times \text{Power}^2 + 3.11450 \times 10^{-22} \times \text{Travel Speed}^2
\end{aligned}
\tag{2}
$$

$$
\begin{aligned}
\text{Depth} = &+ 0.19222 + 6.80000 \times 10^{-4} \times \text{Power} - 1.35417 \times 10^{-4} \times \text{Travel Speed} \\
&- 1.25000 \times 10^{-7} \times \text{Power} \times \text{Travel Speed} \\
&- 5.33333 \times 10^{-8} \times \text{Power}^2 + 2.89352 \times 10^{-8} \times \text{Travel Speed}^2
\end{aligned}
\tag{3}
$$

3.2 Influence of Process Factors and Levels for Each Input Parameter

The input parameters considered in the study are laser power (W) and traveling speed (mm/min). The fiber laser system was used for the hardening of the material in the range of 500–1000 W and 720–1200 mm/min. The parameters with three different levels are shown in Table 1.

3.3 GA Parameters

The input provided for the parameters required during the optimization process is shown below in Table 2.

Table 1 Process parameters and their levels

Parameters involved	Units	Levels		
		1	2	3
Laser power	W	500	750	1000
Traveling speed	mm/min	720	960	1200

Table 2 Parameters considered in the GA algorithm

Sl. No.	Parameter	Input provided
1	Population size	100
2	No. of generations	100
3	No. of functions	2
4	No. of real-coded variables	0
5	Selection strategy	Tournament
6	Real-coded variable no.	0
7	Lower limits on 0th variable	500
8	Upper limits on 0th variable	1000
9	Variable bounds	Rigid
10	Real-coded variable no.	1
11	Lower limits on 1st variable	720
12	Upper limits on 1st variable	1200
13	Variable bounds	Rigid
14	Crossover parameter	10
15	Crossover probability	0.8
16	Mutation probability	0.3
17	Random seed	0.9986

Table 3 Objective functions considered

Factor	Goal
Hardness	Maximize
Width	Minimize
Depth	Maximize

3.4 Objective of the Research Work

The ultimate aim of the work is to obtain the process parameters at which the preferred level of output responses is obtained. The desired output response in this work is to improve the surface hardness of the material after laser hardening through a fiber laser system. The objective functions are shown in Table 3.

3.5 Execution of the Genetic Algorithm (GA)

The models developed by RSM were used in the optimization for running the genetic algorithm program code in the Visual Studio 6.0 software. The required number of generations was performed in achieving the desired output responses. The objective of the NSGA-II program is to find out the input parameters that would maximize the surface hardness, minimize the width, and maximize the depth of the laser hardened material. The optimized solutions were observed as a separate output file showing the results for all the 'n' iterations with 'm' population levels.

After the execution of the GA program, the optimized parameters are shown at the 100th iteration in the output file. It was found that the optimized solutions obtained through elitist non-dominated sorting genetic algorithm tend to produce better output results than the statistical method of optimization. This way of evolutionary optimization is much faster and simple in obtaining optimum solutions. The results obtained through NSGA-II are shown in Table 4.

The plot in Fig. 3 shows how the output responses vary for each iteration level. The number of iterations and the output responses such as hardness, width, and depth are plotted. It is clear that as the number of iteration increases, the hardness and depth will increase and the width will decrease. As the objective of the optimization is to maximize the hardness and depth and minimize the width, the graph plots shown are valid.

Table 4 Optimized solution

Methodology	Laser power (W)	Traveling speed (mm/min)	Surface hardness (HV)	Width (mm)	Depth (mm)
NSGA-II	1000	720	772	2.77	0.64
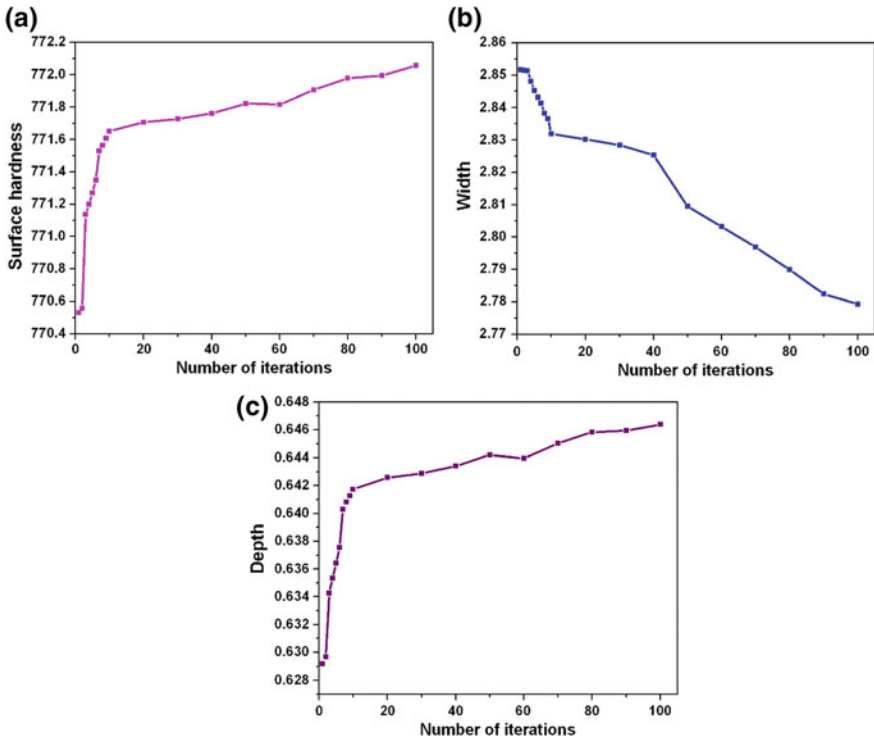
Fig. 3 Plots showing the no. of iterations or generations versus output responses **a** hardness, **b** width, **c** depth

4   Conclusions

- It is clear from the GA parameters and results that the low alloy steel can be laser hardened with fiber laser source to improve surface hardness better than the statistical way of optimization.
- The optimum values of the process parameters are defined with the help of NSGA-II algorithm. The laser power of 1000 W and traveling speed of 720 mm/min were suggested by the non-dominated sorting algorithm. These optimized results were found to produce the desired output responses.
- The maximum hardness of 772 HV, minimum width of 2.77 mm, and maximum depth of 0.64 mm are obtained for the optimized process parameters.
- The surface hardness on the laser hardened zone was found to be higher than the actual hardness of the base material, low alloy steel (360–380 HV).
- Thus, the optimized results can be used for obtaining the maximum hardness and depth and minimum width. This reduces the unnecessary trials for identifying the optimal parameters.

References

1. Cotell, C.M., Sprague, J.A., Smidt, F.A.: Handbook ASM Surface Engineering, vol. 5. ASM International USA (1994)
2. Sandven, O.A.: Laser surface hardening. In: Metal Handbook, Heat Treating, vol. 4, pp. 286–296. ASM International, Materials Park (1997)
3. Pan, Q.Y., Huang, W.D., Song, R.G., Zhou, Y.H., Zhang, G.L.: The improvement of localized corrosion resistance in sensitized stainless steel by laser surface remelting. Surf. Coat. Technol. **102**, 245–255 (1998)
4. Canning, J.: Fiber lasers and related technologies. Opt. Lasers Eng. **44**, 647–676 (2006)
5. Aouici, H., Yallese, M.A., Fnides, B., Mabrouki, T.: Machinability investigation in hard turning of AISI H11 hot work steel with CBN tool. Mechanika **6**, 71–77 (2010)
6. Vignesh, S., Dinesh Babu, P., Balamurugan, C., Martin Vinoth, S.: Comparison of the optimized process parameters of double-sided friction stir welded aluminium alloy joints using statistical and evolutionary techniques. Appl. Mech. Matr. **852**, 317–323 (2016)
7. Vignesh, S., Dineshbabu, P., Muthukumaran, G., Martin Vinoth, S., Sureshbabu, K.: Development of mathematical models and optimization of the laser welding process parameters using response surface methodology. ARPN J. Eng. Appl. Sci. **11**, 7978–7983 (2016)
8. Sivakumar, K., Balamurugan, C., Ramabalan, S.: Evolutionary sensitivity-based conceptual design and tolerance allocation for mechanical assemblies. Int. J. Adv. Manuf. Technol. **48**, 307–324 (2010)
9. Deb, K., Pratap, A., Agarwal, S., Meyarivan, T.: A fast and elitist multiobjective genetic algorithm NSGA-II. IEEE Trans. Evol. Comput. **6**, 182–197 (2002)

Effectiveness of Cryogenic Cooling in Turning of Inconel 625 Alloy

M. Dhananchezian

Abstract The present study is to investigate the role of cryogenic cooling using liquid nitrogen as coolant on the tool wear and surface roughness in turning of Inconel 625 with PVD-TiAlN-coated carbide inserts. The machining parameters of the experimental works were cutting conditions (dry and cryogenic cooling), cutting speeds (43, 71, 118 m/min), feed rate (0.1 mm/rev), and cutting depth (1 mm). The surface roughness (R_a) was significantly improved to a maximum of 50.52% by cryogenic cooling with the current cutting parameters. The scanning electron microscope (SEM) investigation of the used cutting inserts revealed the substantial reduction in tool wear under cryogenic cooling compared to dry turning in all the machining trails undertaken.

Keywords Inconel 625 alloy · Turning · Cryogenic cooling · Liquid nitrogen
Surface roughness (R_a) · Tool wear

1 Introduction

Inconel 625 is widely employed in aerospace, nuclear, marine. and chemical processing industries due to its high strength, strong corrosion resistance, excellent thermal fatigue properties, and resistance to aqueous corrosion at ambient to slightly elevated temperature. In general, various types of machining operation, turning in particular, are being used in order to generate the desired shape of mechanical components. But turning of superalloy always faced with some difficulties in which rapid tool wear is the main one. High cutting temperature is one of the main reasons for rapid tool wear and hence exhibits poor machinability while machining nickel-based superalloys. To overcome this problem, a proper effective cooling system of the metal cutting process could be helpful.

M. Dhananchezian (✉)
Department of Mechanical Engineering, Sri Sivasubramaniya Nadar College of Engineering,
Kalavakkam, Chennai 603110, India
e-mail: dhananchezianm@ssn.edu.in

2 Literature Review

Maurotto et al. [1] studied and compared the machinability of Ti-15-3-3-3 and Ni-625 alloys in ultrasonically assisted turning over conventional machining. It observed that improvement in surface quality, lower cutting force and increase in material removal rate under ultrasonically assisted turning when compared to conventional turning. Ramanujam et al. [2] optimized the machining parameters based on minimum surface roughness, power consumption, and maximum material removal rate by using fuzzy-based principal component function coupled with Taguchi's design of experiment during dry turning operation of Inconel 625. Finally, it reported the optimal cutting conditions (cutting speed of 70 m/min, feed rate of 0.103 mm/rev, and depth of cut of 0.4 mm) for the better machinability properties.

Altin [3] comparatively studied the effects of cutting tool coating material and cutting speed on cutting forces and surface roughness by turning Hastelloy X and Inconel 625 using Taguchi method. It reported that the cutting tool and cutting speed have a higher effect on cutting force and surface roughness in Inconel 625. Jain et al. [4] investigated the optimal setting of process parameters in turning Inconel 625 for maximizing the material removal rate of the manufactured component. It found that optimal combination of machining parameters in order to improve the performance of the machining process.

Lotfi et al. [5] predicted the tool wear of PVD-TiAlN-coated carbide and ceramic inserts using Usui's wear rate model when turning Inconel 625. It found that the predicted values were in good agreement with experimental values. It also concluded that low depth of cut and cutting speed with middle level of feed rate were the appropriate cutting conditions for PVD-TiAlN-coated carbide insert, while ceramic insert should be applied under condition of low depth of cut, middle level of speed rate, and high cutting speed.

As it was reviewed regarding the turning of Inconel 625 alloy, only few works were available and also may be no work is made in the cryogenic turning of Inconel 625. Therefore, this work intends to study the effect of cutting speeds and cryogenic turning using liquid nitrogen on tool wear and surface roughness when turning Inconel 625 with PVD-TiAlN-coated carbide tool inserts.

3 Experimental Procedure

The work material used in the machining experiments is Inconel 625, in bar form with the diameter of 30 mm and 200 mm length. The PVD-TiAlN nano-multilayer-coated carbide inserts (CNMG 120408 FF–WS25PT) and tool holder (PCLNR 1616 H12) manufactured by WIDIA were used. The turning operations were performed on UNITECH (MTT 636) with a variable speed between 70 and 2000 rpm. Three different cutting speeds, i.e., 43, 71, and 118 m/
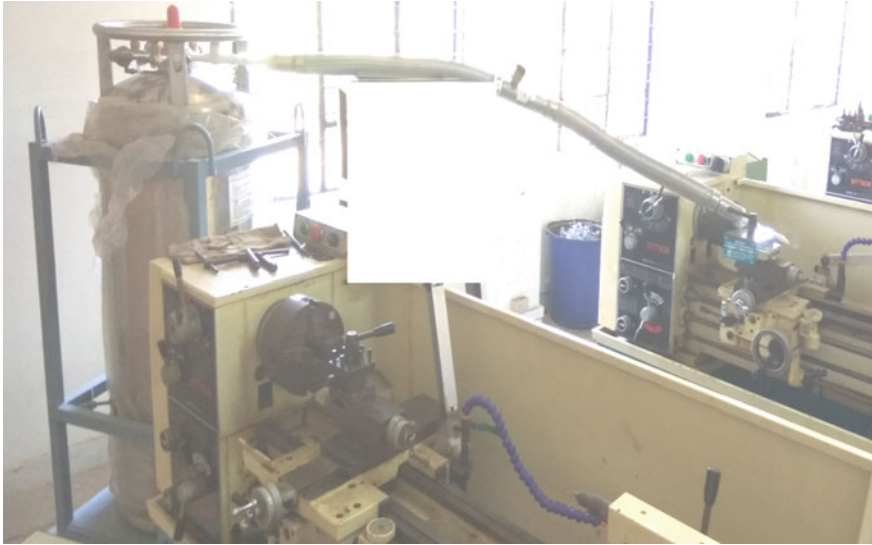
Fig. 1 Photograph view of the experimental setup for turning Inconel 625 alloy with liquid nitrogen as a coolant

min, along with a constant feed rate (f) of 0.1 mm/rev and depth of cut (t) of 1 mm were selected during turning under dry and cryogenic environments. The cutting length for turning trials was 40 mm for measuring surface finish and 100 mm for studying the tool wear. Figure 1 shows the machine tool used in the research work. In cryogenic environments, from the self-pressurized cylinder (DURA-CYL 160 HP, CHART, MVE model), liquid nitrogen was focussed at the cutting point under 20 bar pressure through SNT make "Anaconda" series super insulated vacuum jacketed flexible hose pipe and by stainless steel nozzle of a diameter 2 mm. The mean surface roughness (R_a) of the machined workpiece after each test was measured using surface roughness tester. The worn cutting inserts were examined using scanning electron microscope.

4 Result and Discussion

4.1 Surface Roughness

The surface roughness (R_a) of the machined surface when turning of Inconel 625 with PVD-TiAlN-coated carbide inserts with varying cutting speeds under dry cutting and cryogenic cooling is shown in Fig. 2. The turning process was subjected to cryogenic cooling; the R_a values of the work surface after being machined by PVD-TiAlN-coated carbide inserts with a cutting length of 40 mm were 1.002, 0.607, and 0.378 µm for the corresponding cutting speeds of 43, 71, and 118 m/min,

Fig. 2 Mean surface roughness value (R_a) with cutting speed while turning Inconel 625
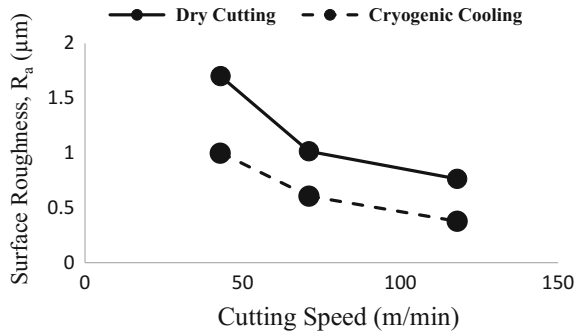
respectively. However, when the turning process was conducted under dry conditions, for the same cutting parameters, the R_a values of the machined surface were 1.701, 1.016, and 0.764 µm. From this experimental work, it was observed that low surface roughness values were obtained in cryogenic cooling when compared to dry turning process and provided the improvement by maximum of 50.52%. The difference in surface roughness value was due to variation in tool wear for both the cutting environments.

4.2 Tool Wear

Figures 3, 4, and 5 show the SEM photograph views (rake, major, and minor flank surfaces) of worn-out tips for turning Inconel 625 with PVD-TiAlN-coated carbide inserts after a machining length of 100 mm with varying cutting speeds (43, 71, and 118 m/min) under dry and cryogenic cutting conditions. It was observed from the SEM views of Figs. 3, 4, and 5 that both rake and flank surface wears (crater wear, main and auxiliary flank wears) increased with the increase in cutting speeds under dry and cryogenic turning. At low cutting speed of 43 m/min, the major flank as well as the rake face underwent substantial wear in dry turning. There is loss of material below the main cutting edge surface; i.e., main flank surface and also some peel off material were observed under dry machining. The flaking of material on the rake surface near the main cutting edge and small amount of chip adherent was observed in rake face. As the cutting speed was increased to 71 m/min under dry turning, flaking was observed on the face of tool near the cutting point of the tool. There is substantial wear in the major and auxiliary flank surfaces. Nose of the tool underwent wear and adherent deposits of chip material was observed on rake surface in dry turning. At higher cutting speed of 118 m/min, the higher worn out at the nose and auxiliary flank surface was observed under dry turning. High flaking in the auxiliary surface and peel off in the rake surface near the corner as well as major and minor cutting edge surfaces were observed under dry turning. The SEM photographs in Figs. 3, 4, and 5 clearly show that the tool wear is substantially

Rake Surface	Major Flank Surface	Minor Flank Surface
(a) Dry Turning		
(b) Cryogenic Turning		
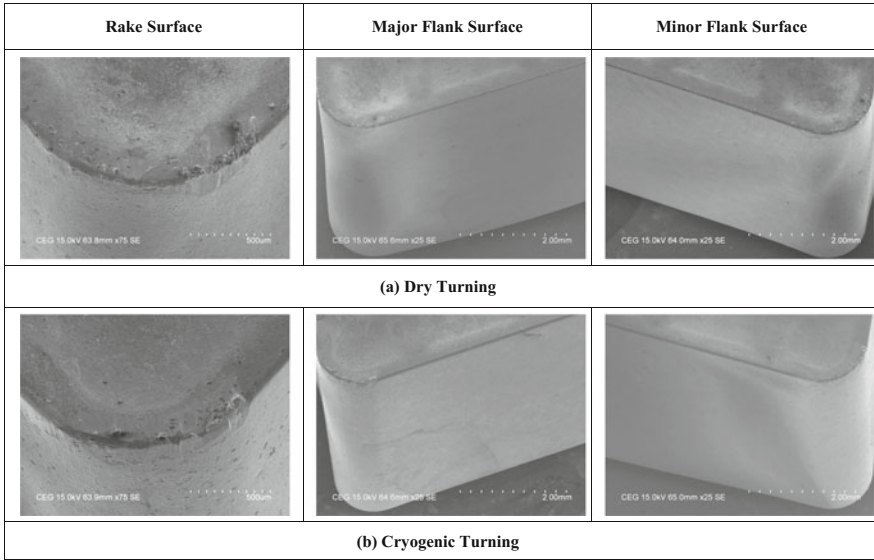
Fig. 3 SEM views of worn-out tip while turning Inconel at $V_c = 43$ m/min under dry and cryogenic cutting environments

Rake Surface	Major Flank Surface	Minor Flank Surface
(a) Dry Turning		
(b) Cryogenic Turning		
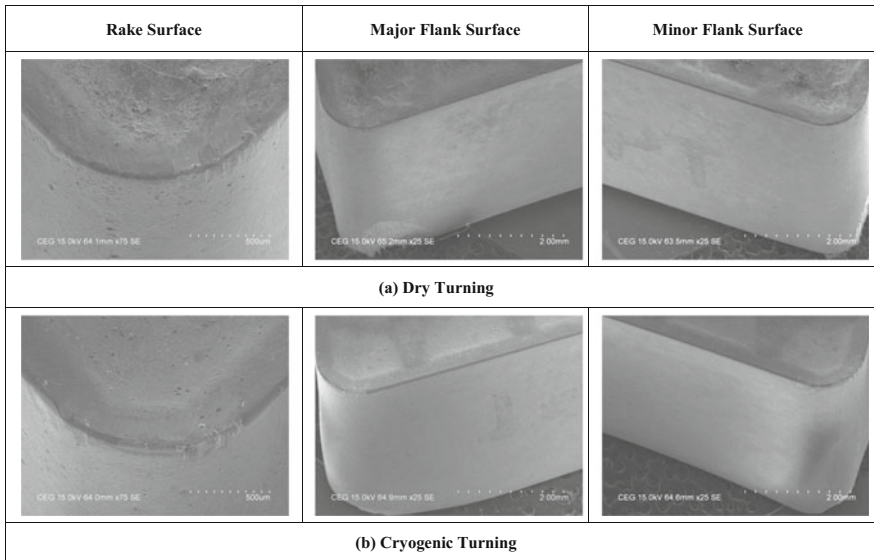
Fig. 4 SEM views of worn-out tip while turning Inconel at $V_c = 71$ m/min under dry and cryogenic cutting environments

Rake Surface	Major Flank Surface	Minor Flank Surface
(a) Dry Turning		
(b) Cryogenic Turning		
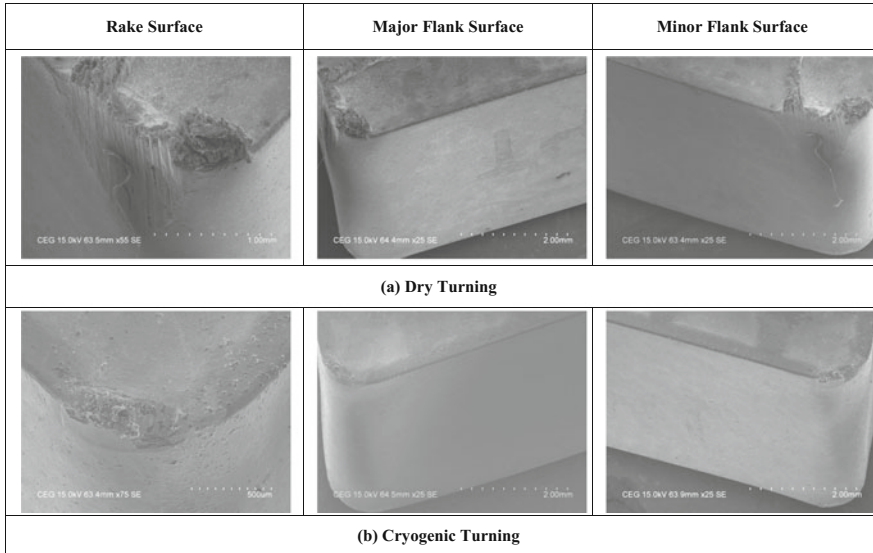
Fig. 5 SEM views of worn-out tip while turning Inconel at V_c = 118 m/min under dry and cryogenic cutting environments

reduced in the respect of rake, major, and minor flank surfaces by the application liquid nitrogen as coolant in the turning of Inconel 625 alloy with PVD-TiAlN-coated carbide inserts. The liquid nitrogen as coolant was applied at the cutting point, which cools the cutting edges and provides lubrication at the sliding and interacting surfaces and thereby reduced the tool wears.

5   Conclusion

The study results indicated that compared with dry turning, liquid nitrogen cooling provided maximum of 50.52% improvement in surface roughness. The cryogenic turning using liquid nitrogen enabled the reduction of temperature-dependent tool wear mechanism which in turn controls the edge depression and nose of the cutting insert. Thus, the experimental results proved that liquid nitrogen as coolant significantly improved the surface finish and reduced the tool wear while turning Inconel 625 with PVD-TiAlN-coated carbide inserts when compared to dry turning.

References

1. Maurotto, A., Muhammad, R., Roy, A., Babitsky, V.I., Silberschmidt, V.V.: Comparing machinability of Ti-15-3-3-3 and Ni-625 alloys in UAT. Procedia CIRP **1**, 330–335 (2012)
2. Ramanujam, R., Venkatesan, K., Saxena, V., Pandey, R., Harsha, T., Kumar, G.: Optimization of machining parameters using fuzzy based principal component analysis during dry turning operation of Inconel 625—a hybrid approach. Procedia Eng. **97**, 668–676 (2014)
3. Altin, A.: A comparative study on optimization of machining parameters by turning nickel based super alloys according to Taguchi method. In: 3rd International Conference and Exhibition on Mechanical & Aerospace Engineering, San Francisco, USA, 05–07 Oct 2015
4. Jain, H., Tripathi, J., Bharilya, R., Jain, S., Kumar, A.: Optimisation and evaluation of machining parameters for turning operation of Inconel-625. Mater. Today Proc. **2**(4–5), 2306–2313 (2015)
5. Lotfi, M., Jahanbakhsh, M., Akhavan Farid, A.: Wear estimation of ceramic and coated carbide tools in turning of Inconel 625: 3D FE analysis. Tribol. Int. **99**, 107–116 (2016)

Crashworthiness Analysis of a Novel Aluminum Bi-tubular Corrugated Tube—Experimental Study

Arameh Eyvazian, Sara Najafian, Hozhabr Mozafari and A. Praveen Kumar

Abstract Crashworthiness is the ability of a structure to protect its occupant during an impact. Metallic tubes are deemed as one of the most popular structures to dissipate crushing energy during collision. Easy manufacturing, low cost of assembly, and high energy absorption capacity can be counted as the main merits of these structures. Introducing corrugations along the length of circular tubes is a well-known method to improve crashworthiness. It was found that the uniformity of the load–displacement behavior of crushed corrugated tubes improved, compared with that one for tubes without corrugation. In this paper, a novel bi-tubular corrugated tube is designed, and experimental compression tests were conducted to evaluate the crashworthiness characteristics under lateral loading conditions. Critical crashworthiness parameters such as the total absorbed energy were extracted, and the efficacy of the structure was compared with its conventional corrugated counterpart. It was found that the novel corrugated tube can interestingly improve the crashworthiness of the energy absorber device. Moreover, it was observed that the bi-tubular tube's efficacy improves by adding more corrugations along the tube. To wrap it up, a novel bi-tubular tube with continuous corrugation

A. Eyvazian (✉)
Mechanical and Industrial Engineering Department, College of Engineering,
Qatar University, Doha, Qatar
e-mail: eyvazian@qu.edu.qa

S. Najafian
Department of Mechanical Engineering, University of Massachusetts Lowell,
Lowell, MA, USA
e-mail: Sara_Najafian@student.uml.edu

H. Mozafari
Department of Mechanical and Material Engineering, University of Nebraska-Lincoln,
Lincoln, NE, USA
e-mail: Hmozafari2@unl.edu

A. Praveen Kumar
Department of Mechanical Engineering, SSN College of Engineering,
Chennai 603110, India
e-mail: praveenphd15@gmail.com

along the tube can strengthen the crashworthiness of the conventional corrugated tubes by large.

1 Introduction

Crashworthiness is the ability of a structure to protect its occupants during an impact. This protection can be achieved through absorbing kinetic energy and dissipating in an irreversible way [1]. With this regard, many crashworthy components have been proposed by considering higher energy absorption capacity as the key factor of design [2–6]. Metallic tubes are deemed as one of the most popular structures so as to dissipate crushing energy during collision. Easy manufacturing, low cost of assembly, and high energy absorption capacity can be counted as the main merits of these structures. Therefore, there are many researches about crashworthiness of these structures in recent decades. The mechanism of energy absorption of metallic structures can be addressed to the plastic deformation in a number of ways such as inversion, flattening, and folding. Deformation can take place in axial or lateral direction. However, oblique crushing might occur in some cases [7–9]. Understanding the behavior of energy absorber devices has been studied by many researchers. Moreover, employing novel materials to enhance the crashworthiness properties of metallic energy absorbers has attracted a huge attention [10–12]. Geometry of energy absorbers is another critical parameter in determining the efficiency of the crashworthy components [13–17]. Honeycomb sections [18–21], frusta [22–25], square [26, 27], and circular tubes [28–30] were investigated as common configurations of thin-walled energy absorbers. Investigation about crashworthiness of circular tubes has a long history. These studies were mainly based on empirical and analytical methods as well as experimental techniques. Recently, aggregation of finite element method with previous techniques is very useful for researches to perform parametric studies.

Lateral compression of circular tubes was studied [31] in which an analytical prediction was derived to obtain yield initiation. This research study also indicated the contribution of material properties and geometrical factors to collapse mode of circular tubes. Gupta et al. [32] presented a detailed experimental and computational investigation of circular aluminum and mild steel tubes subjected to laterally quasi-static loading. Then, basic mechanism of deformation and the effects of process parameters on deformation behavior of the tubes were discussed. Reddy et al. [33] studied the effect of external constraints, and they experimentally showed that the absorbed energy by the tubes with side constraints is three times more than that by the tubes without side constraints. Morris et al. [34] conducted experimental and numerical investigations into the static lateral compression of circular tubes, with different diameters aligned axially inside each other, energy absorbers with the

aid of rigid flat platens. Singace et al. [35] experimentally studied the advantage of introducing corrugation on circular tubes. It was found out that the uniformity of the load–displacement behavior of crushed corrugated tubes improved compared with that one for tubes without corrugation.

Eyvazian et al. [36–39] studied corrugated tubes under axial and lateral loading. Their results showed that corrugated tubes have gained a significant improvement in the crashworthiness properties when crushed in lateral direction to four times, also, and the number and direction of the corrugation affect the crashworthiness. It was observed that crashworthiness depends on the aspect ratio of corrugation geometries, and it has been proved that the highest absorption occurred when the ratio of inner corrugation is equal to one. In the present paper, a new bi-tubular corrugated tube is developed. Two simple designs proposed in the previous study [21] have been chosen to analyze the bi-tubular effects.

The principal aim is to improve crashworthiness properties of conventional corrugated tubes. Therefore, the novel bi-tubular tubes were experimentally created, and then, lateral quasi-static compression tests were performed. The details of tube and experimental tests as well as the obtained results are provided in the following sections.

2 Experimental Work

2.1 Specification and Test Specimen

To investigate the effects of using bi-tubular corrugated tube instead of a single corrugated counterpart, specimens are subjected to quasi-static lateral compression tests. Six specimens have been tested under compressive loading as shown in Fig. 1. Seamless aluminum alloy tubes (AA6060, no heat treatment), due to low density and high energy absorption, are selected for this study. Tube wall thickness is 1.4 mm for the specimens with outer corrugations and 1.5 mm for the specimens with inner corrugations. Corrugation depth and length are 5.5 mm and 7.5 mm, respectively. To determine the influence of increasing number of corrugations on bi-tubular corrugated tube, two specimens made with one corrugation and two of them are with two lateral corrugations but with the same geometries. The bi-tubular tubes have been developed by combining a tube with inner corrugations and outer corrugations (Fig. 1e, f). The details of the geometries of the designed tube are given in Table 1. The specimens are named in accordance with their corrugation shape. For example, CID1 is a corrugated tube with one inner corrugation, and COD1 stands for a corrugated tube with one outer corrugation. The letter of D in here means that all the tubes have the same diameter. BTC1 means a bi-tubular corrugated tube with one corrugation. Similar pattern of labeling exists for the other tubes.
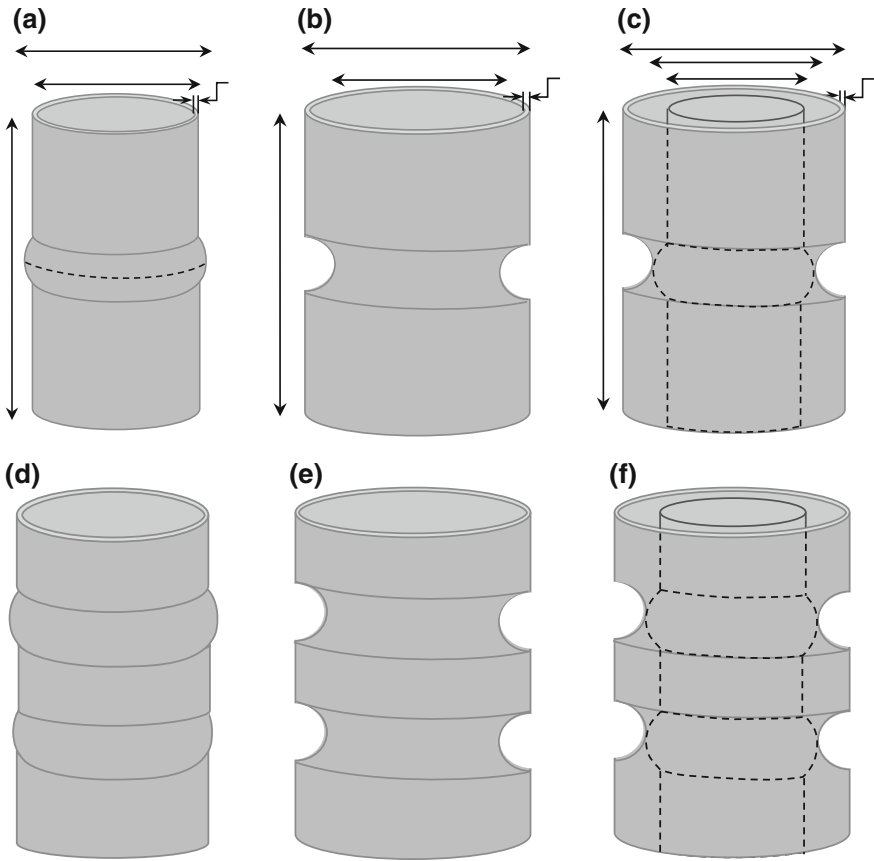
Fig. 1 Schematic of designed specimens for the test **a** COD1, **b** CID1, **c** BTC1, **d** COD2, **e** CID2, and **f** BTC2

Table 1 Designed specimen dimensions

Type	Wall thickness (mm)	Tube diameter (mm)	Length (mm)
COD1	1.4	78.5, 82.6	90
CID1	1.5	96.7, 85.6	90
BTC1	1.4 + 1.5	96.7, 85.6, 78.5, 82.6	90
COD2	1.4	78.5, 82.6	90
CID2	1.5	96.7, 85.6	90
BTC2	1.4 + 1.5	96.7, 85.6, 78.5, 82.6	90

2.2 Quasi-Static Compression Test

In order to study the efficacy of bi-tubular tubes on the lateral compression response, the specimens underwent quasi-static lateral loading. The experimental test's setup is depicted in Fig. 2, and the specimen is placed between two dies which fixed the two sides of the tubes after initiation of contact. All the specimens were cut from one continuous tube made up of aluminum alloy A6060.

Instron digital testing machine with a full-scale load of 500 kN was used. The loading rate of compression was 5 mm/min to ensure that no dynamic effect was induced. Loads and displacements were captured by an automatic data acquisition system. It is worthy to mention that these devices generally are used in higher impact velocities, i.e., dynamic loading conditions; nevertheless, quasi-static loading condition should be initially considered to determine the predominant geometrical deformation shapes which are directly related to the response of the tube under dynamic loading conditions. To stimulate quasi-static conditions and in order to ensure that no dynamic effect was present, all the tubes were compressed at a rate of 5 mm/min until limited crush, which implies complete compaction of the tested tube with a sharp increase in the recorded load. Although these devices are usually exposed to much higher velocities, it is common to analyze the quasi-static response first, since the same predominant geometrical effects will also occur under dynamic loading conditions. In general, quasi-static tests are representative for dynamic tests. It is to mean that if specimens with corrugation have better energy absorption characteristic under quasi-static loading, the same fact applies to impact loading, and most of the publications in this field are based on quasi-static loading.

3 Results and Discussion

Different crushing steps were recorded and depicted in Fig. 3. It can be seen that during the compression there are four plastic hinges formed at vertical and horizontal corners which is common for corrugated tubes. One interesting difference is for the deformation of inner tubes with respect to the outer tube where the outer
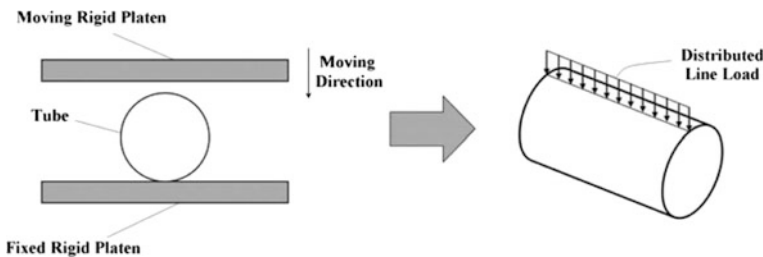
Fig. 2 Schematic of loading procedure (at the starting moment)
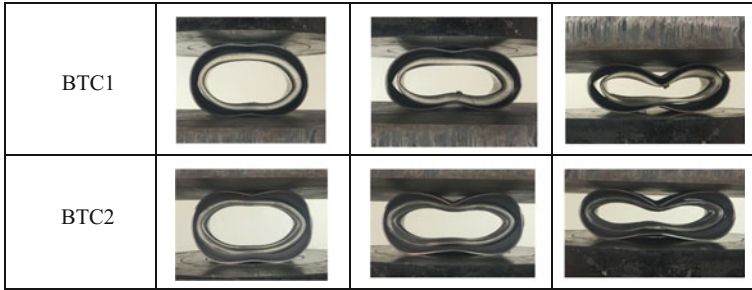
Fig. 3 Deformation frames of BTC1 and BTC2 tubes under lateral loading conditions
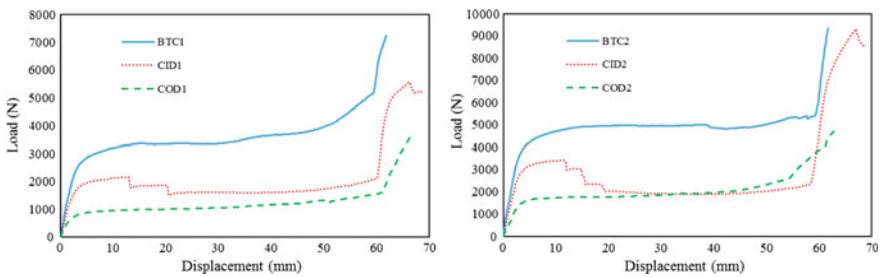

Fig. 4 Load–displacement diagrams for the studied specimens

tube experiences more severe plastic deformation because of the induced reaction forces at the locations of contact with the inner tube.

Moreover, the uniformity of deformation for BTC2 is relatively higher from which more attached inner–outer corrugation is introduced. It was proved before that more corrugation per unit of length can improve the crashworthiness of corrugated tubes under lateral loading circumstances. Figure 4 shows the load–displacement diagrams for all specimens. It is clear that the load–displacement of the COD specimens is smoother than that of CIO tubes. Moreover, it is obvious that the load taken by BTC tubes is significantly higher than each of their components. A large plateau region is observed for all the tubes which is proportional to their corrugated geometry. Furthermore, for all the tubes the load increases sharply at the beginning, although there is not any sharp peak of load which is a significant benefit of these structures compared with straight tubes. After this point, the tubes are crushed with a nearly constant force which continues up to the densification point in which the value of load increases tremendously.

In order to have a better understanding of the crashworthiness efficacy of the BTC tubes, the total absorbed energy for each specimen was extracted in Fig. 4. It can be seen that total absorbed energy of bi-tubular corrugated tubes is higher than the summation of the absorbed energy for CID and COD tubes. For the tube with one corrugation at the middle, the total energy absorption of BTC1 is 134 and 172%

Fig. 5 Total absorbed energy
for the studied specimens
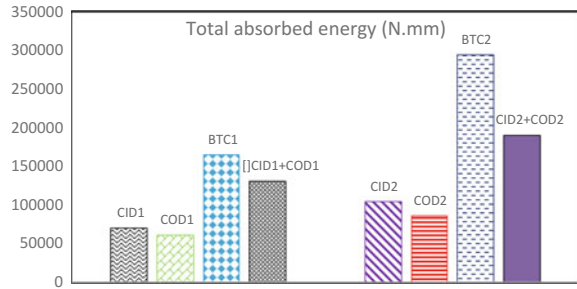
higher than CID1 and COD1, respectively. Besides, the energy absorption of BTC1 tube is 25% higher than that for summation of CID1 and COD1. The reason is the interaction of the corrugated section in BTC1 which can enhance the capability of the corrugated tube in terms of crashworthiness. We achieved the same idea for the tube with two corrugations. It can be seen that the absorbed energy of BTC2 tube is significantly higher than that of CID2 and COD2 tubes, even 54% higher than total absorbed energy of both CID2 and COD2. The later observation illustrates the influence of corrugation number in crashworthiness of BTC tubes (Fig. 5).

4 Conclusions

In this research, we proposed a novel design for corrugated tubes under lateral loading. The idea was to interact the inner corrugation and outer corrugation to magnify the plastic dissipated energy. Our results revealed that the new design interestingly improved the crashworthiness of the structure. Although manufacturing of these tubes was done by employing special technique to exactly match the corrugation tips to each other. It is well known that when the corrugation patterns are introduced into a straight metallic circular tube, the corrugated tube undergoes inelastic deformation and takes folding in accordance with the predesigned corrugation patterns. However, interaction of different corrugations has not been studied preceding this research. Our achievements can shed some lights to draw the attention of designers so as to tackle in this area and come with new designs with improved crashworthiness response. Finally, it was found that the effect of bi-tubular is directly related to the number of corrugations along the tube. Therefore, having a fully corrugated bi-tubular tube is promising to relieve the drawbacks of conventional corrugated tubes.

References

1. Li, Y., et al.: Use of high strength steel sheet for lightweight and crashworthy car body. Mater. Des. **24**(3), 177–182 (2003)
2. Alghamdi, A.: Collapsible impact energy absorbers: an overview. Thin Wall. Struct. **39**(2), 189–213 (2001)
3. Bisagni, C.: Crashworthiness of helicopter subfloor structures. Int. J. Impact Eng. **27**(10), 1067–1082 (2002)
4. Marsolek, J., Reimerdes, H.-G.: Energy absorption of metallic cylindrical shells with induced non-axisymmetric folding patterns. Int. J. Impact Eng. **30**(8), 1209–1223 (2004)
5. Olabi, A.-G., Morris, E., Hashmi, M.: Metallic tube type energy absorbers: a synopsis. Thin Wall. Struct. **45**(7), 706–726 (2007)
6. Nalla Mohamed, M., Praveen Kumar, A.: New insight to improve energy absorption characteristics of long circular tubes with stiffeners as controllable energy dissipating devices. Procedia Eng. **173**, 1399–1406 (2017)
7. Pirmohammad, S., Marzdashti, S.E.: Crushing behavior of new designed multi-cell members subjected to axial and oblique quasi-static loads. Thin Wall. Struct. **108**, 291–304 (2016)
8. Reyes, A., Langseth, M., Hopperstad, O.: Square aluminum tubes subjected to oblique loading. Int. J. Impact Eng. **28**(10), 1077–1106 (2003)
9. Tarlochan, F., et al.: Design of thin wall structures for energy absorption applications: enhancement of crashworthiness due to axial and oblique impact forces. Thin Wall. Struct. **71**, 7–17 (2013)
10. Praveen Kumar, A., Nalla Mohamed, M.: Crush performance analysis of combined geometry tubes under axial compressive loading. Procedia Eng. **173**, 1415–1422 (2017)
11. Tarlochan, F., Ramesh, S., Harpreet, S.: Advanced composite sandwich structure design for energy absorption applications: blast protection and crashworthiness. Compos. B Eng. **43**(5), 2198–2208 (2012)
12. Mahdi, E., Sebaey, T.: Crushing behavior of hybrid hexagonal/octagonal cellular composite system: aramid/carbon hybrid composite. Mater. Des. **63**, 6–13 (2014)
13. Azimi, M.B., Asgari, M.: A new bi-tubular conical–circular structure for improving crushing behavior under axial and oblique impacts. Int. J. Mech. Sci. **105**, 253–265 (2016)
14. Niknejad, A., Moeinifard, M.: Theoretical and experimental studies of the external inversion process in the circular metal tubes. Mater. Des. **40**, 324–330 (2012)
15. Kılıcaslan, C.: Numerical crushing analysis of aluminum foam-filled corrugated single-and double-circular tubes subjected to axial impact loading. Thin Wall. Struct. **96**, 82–94 (2015)
16. Xiao, Y., et al.: Crashworthiness design of horsetail-bionic thin-walled structures under axial dynamic loading. Int. J. Mech. Mater. Des. **12**(4), 563–576 (2016)
17. Praveen Kumar, A., Nalla Mohamed, M., Jusuf, A., Dirgantara, T., Gunawan, L.: Axial crash performance of press-formed open and end-capped cylindrical tubes—a comparative analysis. Thin Wall. Struct. **124**, 468–488 (2018)
18. Mozafari, H., et al.: In plane compressive response and crushing of foam filled aluminum honeycombs. J. Compos. Mater. **49**(26), 3215–3228 (2015)
19. Mahmoudabadi, M.Z., Sadighi, M., Eyvazian, A.: Theoretical and experimental crushing analysis of metal square honeycombs under quasi-static loading. In: ASME 2010 10th Biennial Conference on Engineering Systems Design and Analysis, American Society of Mechanical Engineers (2010)
20. Yin, H., Wen, G.: Theoretical prediction and numerical simulation of honeycomb structures with various cell specifications under axial loading. Int. J. Mech. Mater. Des. **7**(4), 253 (2011)
21. Crupi, V., et al.: Computed tomography-based reconstruction and finite element modelling of honeycomb sandwiches under low-velocity impacts. J. Sandwich Struct. Mater. **16**(4), 377–397 (2014)
22. Meguid, S., Yang, F., Hou, P.: Crush behaviour of foam-filled thin-walled conical frusta: analytical, numerical and experimental studies. Acta Mech. **227**(12), 3391–3406 (2016)

23. Azimi, M.B., Asgari, M.: Energy absorption characteristics and a meta-model of miniature frusta under axial impact. Int. J. Crashworthiness **21**(3), 222–230 (2016)
24. Alkhatib, S.E., et al.: Collapse behavior of thin-walled corrugated tapered tubes under oblique impact. Thin Wall. Struct. **122**(Supplement C), 510–528 (2018)
25. Alkhatib, S.E., Tarlochan, F., Eyvazian, A.: Collapse behavior of thin-walled corrugated tapered tubes. Eng. Struct. **150**(Supplement C), 674–692 (2017)
26. Langseth, M., Hopperstad, O.: Static and dynamic axial crushing of square thin-walled aluminium extrusions. Int. J. Impact Eng. **18**(7–8), 949–968 (1996)
27. Zhang, X., Cheng, G., Zhang, H.: Theoretical prediction and numerical simulation of multi-cell square thin-walled structures. Thin Wall. Struct. **44**(11), 1185–1191 (2006)
28. Nalla Mohamed, M., Praveen Kumar, A.: Numerical and experimental study of the effect of orientation and stacking sequence on petalling of composite cylindrical tubes under axial compression. Procedia Eng. **173**, 1407–1414 (2017)
29. Guillow, S., Lu, G., Grzebieta, R.: Quasi-static axial compression of thin-walled circular aluminium tubes. Int. J. Mech. Sci. **43**(9), 2103–2123 (2001)
30. Abramowicz, W., Jones, N.: Dynamic axial crushing of circular tubes. Int. J. Impact Eng. **2**(3), 263–281 (1984)
31. DeRuntz, J.A., Hodge, P.G.: Crushing of a tube between rigid plates. J. Appl. Mech. **30**(3), 391–395 (1963)
32. Gupta, N., Sekhon, G., Gupta, P.: Study of lateral compression of round metallic tubes. Thin Wall. Struct. **43**(6), 895–922 (2005)
33. Reddy, T.Y., Reid, S.: Lateral compression of tubes and tube-systems with side constraints. Int. J. Mech. Sci. **21**(3), 187–199 (1979)
34. Morris, E., Olabi, A., Hashmi, S.: Experimental and numerical analysis of the static lateral compression of tube type energy absorbers with different indenters. Eng. J. **59**(8), 505–510 (2005)
35. Singace, A.A., El-Sobky, H.: Behaviour of axially crushed corrugated tubes. Int. J. Mech. Sci. **39**(3), 249263267–261265268 (1997)
36. Eyvazian, A., et al.: Axial crushing behavior and energy absorption efficiency of corrugated tubes. Mater. Des. (1980–2015) **54**, 1028–1038 (2014)
37. Mozafari, H., Eyvazian, A., Hamouda, A.M.: The effect of number of corrugation on crashworthiness of aluminum corrugated tube under lateral loading. Procedia Eng. **173**, 1275–1282 (2017)
38. Eyvazian, A., Mozafari, H., Hamouda, A.M.: Experimental study of corrugated metal-composite tubes under axial loading. Procedia Eng. **173**, 1314–1321 (2017)
39. Eyvazian, A., Akbarzadeh, I., Shakeri, M.: Experimental study of corrugated tubes under lateral loading. Proc. Inst. Mech. Eng. L J. Mater. Des. Appl. **226**(2), 109–118 (2012)

Design Analysis and Optimization of Electric Solenoid Shroud for Starter Motor Used in Mild Hybrid Passenger Car

Varatharaj Neelakandan, Thulasirajan Ganesan and Praveen Chakrapani Rao

Abstract Starter motor is used to start the engine by cranking the flywheel by means of pinion and ring gear engagement through electrical solenoid linear activations. Solenoid linear movement has to be activated in few milliseconds for starter and engine ring gear engagement which is very crucial design in it. The parts involved in solenoid for linear activations are very sensitive in environmental conditions. This is causing high durability impact, warranty cost and less reliability. The paper discusses the solenoid shroud redesign for the better performance and higher durability with suitable silicone polymer material to withstand the temperature and nonlinear characteristic for the solenoid linear activation of starter motor start stop application. The shroud design talks about the packaging of the shroud to meet the overall starter sizing and sealing capability of the shroud and its deformation characteristics which talks about the geometry nonlinearity and design for interference and with starter housing. The comparison between natural rubber and specially selected silicone polymer for the shroud application is detailed. Hence the results of the paper discussed on the methodology of the shroud design and analysis procedure and material selections. The finite element analysis of the shroud considering its environmental factors has been explained. The effect of material for the smooth solenoid operation has been explained which impacts the application of shroud in solenoid used starter motor for the start stop mild hybrid passenger car application.

Keywords Starter motor · Electric solenoid dynamics · Polymer material FEA nonlinear · Durability · Shroud optimisation

V. Neelakandan (✉) · T. Ganesan · P. C. Rao
Comstar Automotive Technologies Pvt. Ltd, Chengalpattu, Tamil Nadu 603204, India
e-mail: nvaratha@comstarauto.com

T. Ganesan
e-mail: gthulasi@comstarauto.com

P. C. Rao
e-mail: cpraveen@comstarauto.com

1   Introduction

The starter motor is an electromechanical product which is used to start the auto-motive engine for moving the vehicle. The starter motor consists of solenoid, motor, planetary gears, drive and pinion system. The solenoid is mounted on the housing by means of screws and connected to the drive assembly through the shift lever for the back and forward movement to the ring gear engagement which is on the engine flywheel. The typical starter motor is shown in Fig. 1.

The starter motor is mounted on the engine housing block, and it is outside exposed to the severe more extreme environmental conditions like hot, cold, muddy, rainy The starter has to work on the multiple operating conditions and environment without failure. The solenoid is the electromechanical subsystem in the starter motor which is assisting to engage and disengage the pinion gear to the ring gear. The solenoid is electrified by the battery power, and the plunger moves towards the terminals then the contact get connected and motor gets power to rotate the pinion gear through the armature and planetary gear systems.

The shrouds' one end of the outer circumference is fitted on the solenoid frame and housing, and another end of the shrouds' inner circumference is fitted on the plunger ring as shown in Fig. 2. When the plunger moves towards the electrical terminals, it pulls the shroud inside the solenoid frame which may give severe stress to the shroud life. The starter motor durability life for the mild hybrid application
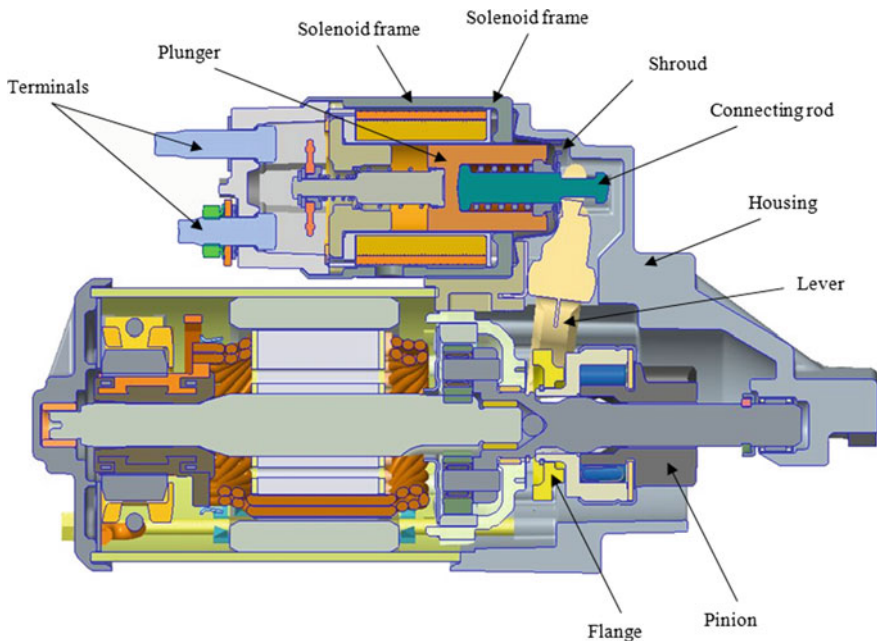
Fig. 1 Starter motor cross section
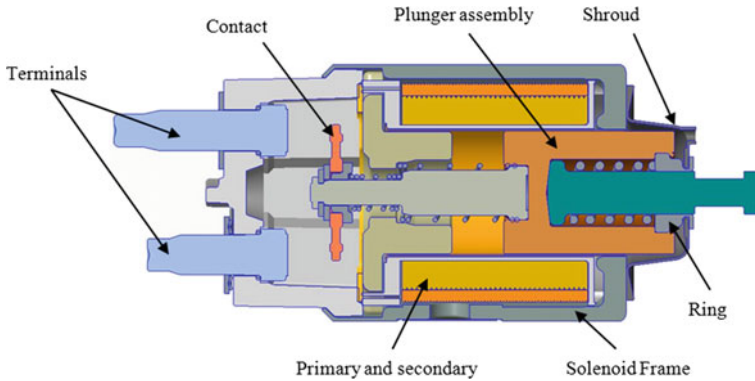
Fig. 2 Solenoid cross section

increased to 500 thousands cycles which is very high compared to the conventional starter application has only 150 thousands cycles. Each time of solenoid activations by battery switch on, the plunger moves to and fro for performing its function.

2 Design Analysis and Optimization Method of Shroud

2.1 Design Loads

Shroud is mounted inside the housing and comes along with solenoid assembly. The shroud displacement is linear along the axis of the solenoid assembly. The required total displacement is fixed based on the pinion engagement distance and shift lever ratio. Design loads of the shroud depend on many factors as shown in Fig. 3.

While designing the shroud, the environmental factor is most important as it contains hot temperature, cold temperature, mud, dust water ingress during rain. Durability cycle is based on the vehicle requirements and type of engine application. If the engine is used for mild hybrid, then the durability of the starter is more, and hence, the shroud duty cycle requirements are more. Shroud has to properly sit in the housing and perform its function without any wear and tear. Material for the shroud has been chosen as rubber, and the shroud is functioning under the large deformations. The existing and new shroud is shown in Fig. 4.

Fig. 3 Design loads

Fig. 4 Shroud designs

| (a) Existing shroud | (b) New shroud |
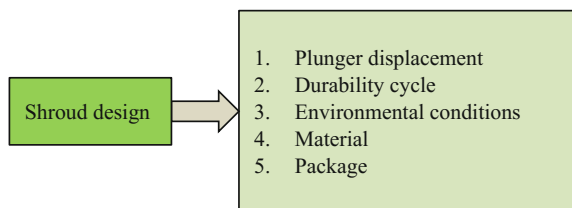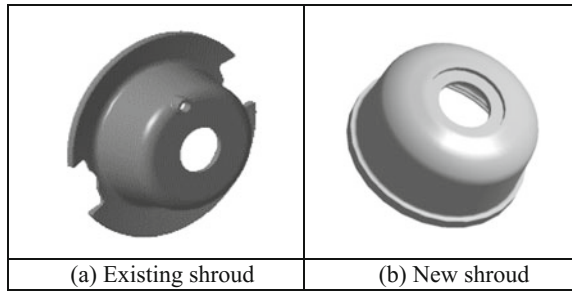
2.2 Material

Shroud is to be more flexible for the large displacement under the tension as well as compression for its function to perform. The rubber is the flexible material chosen as the base material and designed for the existing design which was used for the conventional starter motor, and solenoid shroud had 150 thousands cycle of durability. The silicone material has been taken as the shroud material for the mild hybrid application. The properties [1] of both the material are shown in Fig. 5.

The neoprene and silicone is the rubber medium, and these are the hyperelastic material behaviour which is highly nonlinear contact and nonlinear material [2, 3]. The Mooney Revlin material model as the material properties for the shroud finite element analysis. The stress and strain characteristics have been studied based on the tested data for various methods and that was taken to the analysis for predicting the Mooney–Rivlin parameters. There are uniaxial, biaxial and shear strain curves which have been plotted for the nonlinear shroud—hyperelastic material as shown in Fig. 5.

Shroud Matrial Name	Neoprene	Silicone
Chemical Name	Polychloroprene Rubber	Polysiloxane
Nomenclature	CR	Si
Mechanical Properties		
Hardness Range	45 ShoreA	45 Shore A
Posion ratio	0.4999	0.4999
Tensile strength	20 MPa	27MPa
Heat Resistance (°c)		
Maximum Intermittent	125°c	300°c
Low Temperature Resistance	-40°c	-60°c

(a) Properties
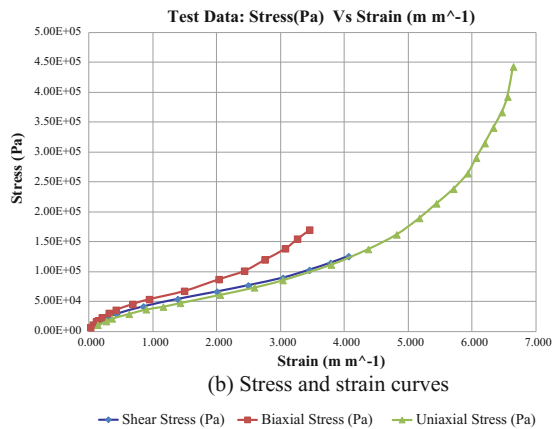
(b) Stress and strain curves

Fig. 5 Properties, stress and strain curves

2.3 Mooney–Rivlin Material Model

In continuum mechanics, Mooney–Rivlin (MR) [4] solid is a hyperelastic material model where the strain energy density function W is a linear combination of two invariants of the left Cauchy–Green deformation tensor. The model was proposed by Melvin Mooney in 1940 and expressed in terms of invariants by Ronald Rivlin in 1948. There are so many hyperelastic material models which exist in commercial FEA softwares. Mooney–Rivlin material model is one of the few famous material models. It has very good advantage when behaviour of hyperelastic material is unknown. There are four different variations present. Each model is differentiated by its use of the number of the independent constants. The Mooney–Rivlin model is a special case of the generalized Rivlin model which has the form [4, 5].

$$W = \sum_{i+j=1}^{N} C_{ij}(\vec{I}_1 - 3)^i(\vec{I}_2 - 3)^j + \sum_{k=1}^{N} \frac{1}{d_k}J_{el} - 1)^{2k} \tag{1}$$

where are material constants related to the distortional response and material constants related to the volumetric response. Assumption of the incompressibility makes the last term volumetric response zero. For different formulation are with incompressibility as follows,

Two-term Mooney–Rivlin model is as follows:

$$W = C_{10}(I_1 - 3) + C_{01}(I_2 - 3) \tag{2}$$

Three-term Mooney–Rivlin model is as follows:

$$W = C_{10}(I_1 - 3) + C_{01}(I_2 - 3) + C_{11}(I_1 - 3)(I_2 - 3) \tag{3}$$

Five-term Mooney–Rivlin model is as follows:

$$W = C_{10}(I_1 - 3) + C_{01}(I_2 - 3) + C_{20}(I_1 - 3)^2 + C_{11}(I_1 - 3)(I_2 - 3) + \ldots + D_1(J - 1)^2 \tag{4}$$

As a result, the incompressible polynomial model is expressed in terms of the first and second strain invariant only. The volume is subject to the uniaxial tensile stress σ. Axes 1, 2 and 3 denote coordinate axes, which are parallel to the principal axes of the cube. The three principal stretches with regard to the coordinate axes are λ_1, λ_2 and λ_3. If λ is the stretch parallel to the tensile stress σ, deformations in 2 and 3 are equal [6]. The corresponding mathematical expressions are $\lambda_1 = \lambda$ and $\lambda_2 = \lambda_3$. Since the material is considered incompressible, $\lambda_2 = \lambda_3 = \lambda^{1/2}$. Resulting from this, the two strain invariants for an incompressible material in tension or compression are $I_1 = \lambda^2 + 2\lambda^{-2}$ and $I_2 = \lambda^{-2} + 2\lambda$.

The actual relation between engineering stress and stretch for an incompressible material under tension/compression is

Table 1 MR material constants

Constant	Value	Unit
Material constant C10	10,067	Pa
Material constant C01	2287.6	Pa
Material constant C20	116.17	Pa
Material constant C11	−130.18	Pa
Material constant C01	6.7045	Pa
Incompressibility parameter D1	1.44 E−07	Pa^{-1}

$$\sigma_e = 2 * \left(\lambda - \lambda^{-2}\right) * \left(\frac{dW}{dI_1} + \frac{1}{\lambda} * \frac{dW}{dI_2}\right) \tag{5}$$

where

σ_e: engineering stress; λ: stretch, parallel to σ_e

W: strain energy; I_1, I_2: strain invariants

By using the above equation, the stress values for different materials are evaluated. The strain energy density function for different material is considered from equation. Based on the Moony–Rivlin modelling concept, material constant has been calculated by the curve fitting method using the simulation software [7, 8]. Those constants are provided in Table 1.

2.4 Analysis Results for Existing Shroud Design

The existing shroud which is made up of neoprene material and its displacement has been calculated is 13 mm based on the solenoid plunger axial movement. The same displacement 13 mm is applied at shroud end face in the simulation setup, and the shroud behaviour is predicted. The displacement results have been extracted at every instance of 3.1, 6.1, 9.25 and 13 mm as shown in Fig. 6. In the first two instances, the shroud movements are smooth and no abnormality in the compression of the neoprene shroud material. But in the next two instances of displacement, the shroud is getting squeezed and compressed abnormally which affects the performance and durability life of the solenoid and starter motor. The shear elastic strain level of the existing shroud at 13 mm displacement condition is 31.7% as shown in Fig. 7 which is causing the tearing of the shroud design.

2.5 Analysis Result for New Shroud Design

The new shroud is designed for addressing the increased durability $\left(C_f\right)$, increased temperature $\left(T_f\right)$ environment and shroud compression issues. The shroud material $\left(M_f\right)$ is chosen as silicone rubber material, and its displacement $\left(D_f\right)$ has been calculated which is 10.50 mm based on the solenoid plunger axial movement.

(a) Displacement @ 3.1mm	(b) Displacement @ 6.1mm	(c) Displacement @ 9.25mm	(d) Displacement@ 13mm
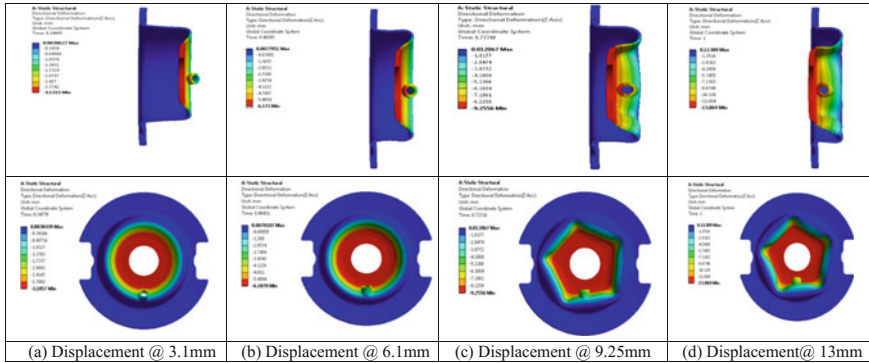
Fig. 6 Existing shroud displacement characteristics

(a) Shear strain convergence   (b) Shear strain plot
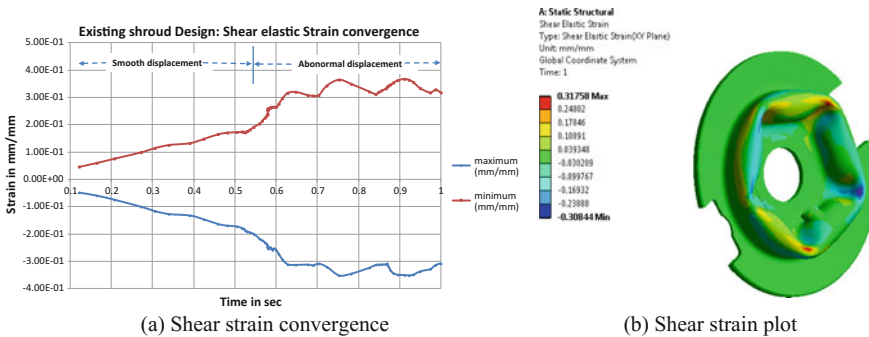
Fig. 7 Existing shroud shear elastic strain characteristics

The same displacement of 10.5 mm is applied at the shroud end face in the simulation setup and predicted the shroud behaviour. The displacement results have been extracted at every instance of 3.1, 5.27, 7.5 and 10.5 mm as shown in Fig. 8. In all the displacement instances, the shroud movement is smooth and no abnormality is in the compression of the new geometry shroud with silicone material. This affects positively to increase the performance and durability life of the solenoid and starter motor. The shear elastic strain level of the new geometry (G_f) shroud at 10.5 mm displacement condition is 21.7% as shown in Fig. 9 which is lesser than the existing shroud design.

The new geometry shroud has been checked for the plunger ring and solenoid mounting sealing (S_f) capability as shown in Fig. 10. This will ensure that the shroud will not come out from plunger mounting and solenoid-housing mounting. The new shroud design also ensures that the there is enough space available inside the housing (H_f) for the compression and expansion. This has been checked by finite element analysis by more iterations with modified shroud geometries. The surface finishing of the housing is also maintained for the better wear rate and

| (a) Displacement @ 3.1mm | (b) Displacement @ 5.27mm | (c) Displacement @ 7.5mm | (d) Displacement@ 10.4mm |
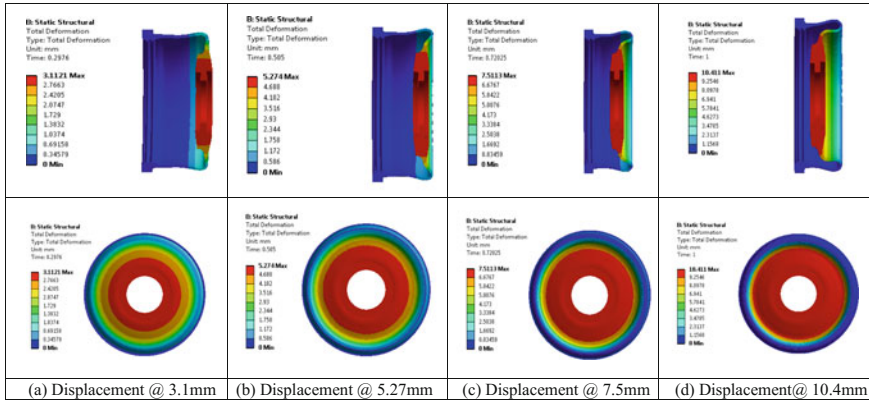
Fig. 8 New shroud displacement characteristics

(a) Shear strain convergence   (b) Shear strain plot
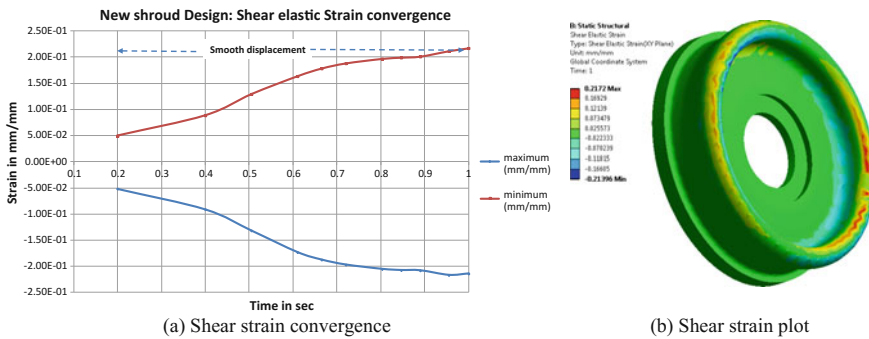
Fig. 9 New shroud shear elastic strain characteristics

| (a) Shroud with Plunger ring | (b) shroud with Housing |
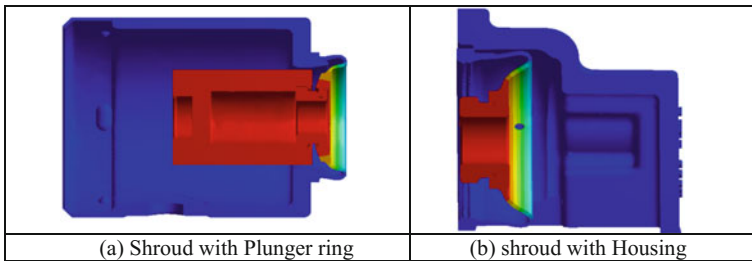
Fig. 10 New shroud design interface and fit check

compression set property while the shroud is fitted with solenoid and housing as shown in Fig. 10. The new geometry shroud is studied for the mouldability (U_f) for quick and better manufacturing quality.

3   Conclusion

This paper discussed existing shroud design and its characteristics on displacement through finite element analysis method. The existing shroud geometry is inadequate for the smooth compression and expansion function to meet the solenoid and starter durability life. The new geometry is arrived and optimized for better shroud design, and it has been analysed with finite analysis method for identifying its functional characteristics. The above analysis brought the shroud design influencing factor as below

$$\text{Shroud design factors } (D_{sf}) = f\big(D_f, M_f, G_f, S_f, H_f, X_f, T_f, C_f, U_f\big) \tag{6}$$

where

D_f	Plunger displacement
M_f	Shroud material
G_f	Shroud geometry
S_f	Sealing compatibility
H_f	Space available inside the housing
X_f	Housing surface finish
T_f	Starter motor working temperature
C_f	Durability cycle
U_f	Shroud material mould compatibility

Hence, the methodology of the shroud design and analysis procedure and material selections is discussed. The finite element analysis of the shroud considering its environmental factors has been explained. The effect of geometry of the shroud for the smooth solenoid operation has been explained which impacts the application of shroud in the electrical solenoid used in the starter motor for start stop mild hybrid passenger car application.

References

1. Shietsu Silicone: Characteristics properties of silicone rubber compounds. https://www.shinetsusilicone-global.com/catalog/pdf/rubber_e.pdf
2. Jadhav, A.N., Bahulikar, S.R., Sapate, N.H.: Comparative study of variation of Mooney–Rivlin hyperelastic material models under uniaxial tensile loading. IJARIIE-ISSN(O)-2395-439 **2**(4) (2016)
3. Kumar, N., Venkateswara Rao, V.: Hyperelastic Mooney–Rivlin model: determination and physical interpretation of material constants. MIT Int. J. Mech. Eng. **6**(1), 43–46 (2016). ISSN: 2230-7680 © MIT Publications

4. Shahzad, M., Kamran, A., Siddiqui, M.Z., Farhan, M.: Mechanical characterization and FE modelling of a hyperelastic material. Mater. Res. **18**(5), 918–924 (2015)
5. Rivlin, R.S.: Large elastic deformations of isotropic materials I: fundamental concepts. Philos. Trans. R. Soc. Lond. A. **240**(822), 459–490 (1948)
6. Treloar, L.R.G.: Stress-strain data for vulcanised rubber under various types of deformation. Trans. Faraday Soc. (1944). https://doi.org/10.1039/TF9444000059
7. Dadkhah, F., Zahiri, A.: Finite element analysis of silicone rubber spacers used in automotive engine control modules. http://www.ansys.com/-/media/ansys/corporate/resourcelibrary/conference-paper/2004-int-ansys-conf-73.pdf
8. Pachpande, D.J., Tembhare, G.U., Wagle, S.M.: Stress analysis of thick wall bellows using finite element method. Int J. Eng. Res. Technol. **4**(7) (2015). ISSN: 2278-0181

Shock and Vibration Prevention Using Angular Mounts with Different Types of Oil-Based Elastomers

Sudheer Kumar Battula, P. Rama Murthy Raju and Ch Ratnam

Abstract In this article, S&V ('shock and vibration') angular mounts are utilized to condense transmitted sound vibration of different machinery and safeguard the equipment against submerged explosion. Getting the purpose of having a noiseless ship is workable, if the machines fitted on these ships are also noiseless and their vibrations are isolated. This can be accomplished through legitimate condition-monitoring of suitable vibration isolation mounts. For this, numerous mounts are used in diesel engines on board ships. To get the better durability of engines' life and other running machines, both elastic and viscous (damping) elastomers are distinctive material that makes it useful for preparing vibration mounts. Here different types of oil-based elastomers are used as a vibration-absorbing part in mounts as it can be designated to get better dynamic properties. Utilizing the tentatively assessed estimations of the elastomeric damping and mount stiffness, the tested spring-mass model of the dynamic reaction utilizing an elastomeric angular mount as the versatile component can be precisely recreated. In this distinction, it is found that the single DOF of perfect spring-mass model utilizing steady damping and stiffness values be able to anticipate the response reaction of the system exactly at resonance except not at non-resonance frequencies. The method proposed is compared and validated by its experimental results.

Keywords Shock · Vibration · Engine isolated angular mount
Viscoelastic material · Condition-monitoring

S. K. Battula (✉)
Department of Mechanical Engineering, LBR College of Engineering
JNTUK, Mylavaram, Krishna District, Vijayawada, India
e-mail: sudheerbattula1984@gmail.com

P. R. M. Raju
Department of Mechanical Engineering, SRKR Engineering College AU,
Bhimavaram, W.G. District, India

S. K. Battula · C. Ratnam
Department of Mechanical Engineering, Andhra University College of Engineering,
Visakhapatnam, India

1   Introduction

The terms S&V (shock and vibration) are by and large used to refer to the dynamic mechanical excitation that may cause a dynamic reaction of a physical structure, as a rule a mechanical structure that is presented to that excitation. To be more particular, a shock is a dynamic excitation with a generally brief term, and a vibration is a dynamic excitation with a moderately long length when contrasted with the time required for a physical structure presented to that excitation to completely react. Both S&V excitations can seem either as an information motion or power at the mounting focuses or as a pressure field over the outside surface of the physical arrangement of intrigue. In either case, the essential portrayal of a shock or vibration is given by the momentary size of the excitation as a component of time, which is known as a period history. Shock and vibration excitations can be comprehensively delegated being either deterministic or arbitrary. The idea of using vibration isolation mount was proposed by Nashif et al. [1] that gives a thorough review of different mounting systems. The terms shock and vibration acquire both theoretical and experimental data significantly. A method is implemented to get the optimum shape of an elastomeric engine mount using parameter (thickness) optimization by Kim and Kim [2]. In an engine mount, the lower noise and vibration reduction are acquired. In order to obtain effective noise and vibration isolation, the frequency must be close to the operating frequency. A original design through mathematical modelling and simulation for semi-active hydraulic mounts by Vahdati and Ahmadian [3]. Recent researches focused and developed efforts on improving isolation mount equipment to attain improved vibration isolation, noise reduction with good compression and ageing properties [4]. Material development is a major contribution to improve isolation mounts. Different types of elastomers that permit specification of the amount damping have been developed. By the assistance of processing techniques, formulation and elastomers must give dynamic properties exactly and improve the consistency of such properties with respect to the varying engine ambience. However, the solely elastomeric mount cannot handle the sophisticated combination of stiffness and damping required in the modern engine, which are important dynamic behaviours to represent the performance of an engine isolated mount system [5]. Therefore, the angular mount called sandwiched mount, which is a combination of a new and modern elastomeric mount and a viscous damper, was developed with new materials such as PU, CR, NR, blend systems, iso-octane, toluene, styrene and divinylbenzene and their novel structures and creative isolate mechanism are developed following the development of the vehicle, are introduced.

2   Materials

Here we utilized two materials; M.S is the most renowned type of material because it is usually less in cost and gives material properties with satisfactory results for some applications. It neither brittle nor ductile. For the making of polyurethane, natural and neoprene rubbers are mainly used. There are three steps. Satisfactory blending is important to acquire and exacerbate that procedure legitimately, cures adequately, the essential properties for utilization. A Banbury interior blender is generally utilized to blend the composite mixings. It consists of two winding-moulded rollers that work totally in an encased chamber. A two-step process is usually used to ensure that premature vulcanization does not occur. The vast majority of the fixings are blended at around 120 °C of initial step and the included vulcanizing agents at lower temperature in the second step. Here we blend the elastomeric compound up to 10 min. Transfer, compression and moulding procedures are utilized to shape the last step. Once it was shaped, the elastic compound is vulcanized at different temperatures by running from 100 to 200 °C. Apply agent to the elastic for quite a while. From that point onward, we need to indentify if any volumetric swelling happens or not. Here we use the fluid agent to place the elastomers in these agents for three different stages of temperatures with three different times, i.e. 70% iso-octane + 30% toluene and 70% styrene + 30% divinylbenzene.

2.1   Fabrication

In this experimentation, a homogenous beam of M.S ('Mild steel') with following measurement 300*10*10 mm was utilized to approve the Young's modulus estimation system, of the base layer material ('mild steel'). For instance of a sandwiched beam, the integrated elastomeric material was the centre material and 'mild steel' was taken as the base pillar material. It comprises of both upper angular die and lower angular die, where upper angular die and the lower angular die are fixed by utilizing screws. On the upper part of the angular die, we apply weight of 24 tones up to 20 min. We get a temperature of 155 °C at the intersection of elastic and steel plates. Along these, at that temperature elastomer is adhered to the upper and lower angular steel plates (Fig. 1).

3   Experimental Work

A new technique, dynamic mechanical analysis (DMA), is used to characterize the materials study, and it is very useful for viscoelastic study behaviour of polymeric materials [6]. Alternative testing method for determining dynamic modulus and
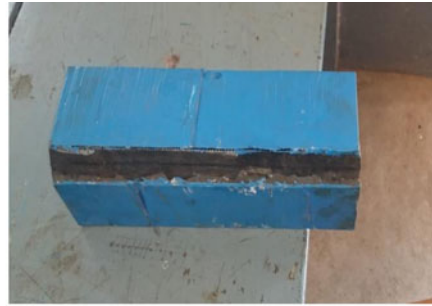
(a) PU Elastomer-angular mount   (b) NR Elastomer-angular mount

(a) Neoprene Elastomer-angular mount

Fig. 1 a PU elastomer-angular mount, **b** NR elastomer-angular mount, **c** neoprene elastomer-angular mount

damping loss factor of the elastomeric damping materials has been fabricated [8, 9]. The experimental techniques for getting the dynamic properties of viscoelastic materials were reviewed. Different methods using the vibration isolation response of work piece under static and dynamic conditions are available to determine the damping loss factor, and a comparison of different test methods for measuring vibration damping properties of materials has been reported [10]. In forced vibration, a sandwiched angular beam mount is prepared using elastomers as a core material, and the angular mount beam is tested through universal compression testing machine. The technique utilizes the elastomeric material to be tested in combination with vibration angular mount beam either in shear or extension. In this experiment, the elastomers are sandwiched between two angular metal plates, the test samples were about 30 × 10 × 5 mm shear modulus, and shear loss factors are obtained from forced vibration response method. The experimental loss factor data are compared with the loss factor obtained for these elastomers from the dynamic mechanical analysis. There is no reported work on oil-based angular elastomeric mounts on a blend of polymers according to the literature [2, 4, 7] engine mount, hydraulic engine mounts with elastomers has been done but oil-based angular mounts has not been done so far. In this article, a type of isotopic angular mount

oil-based elastomers is fabricated by curing methods. The influences of preparation conditions and relationship between elastomeric properties and effects of for this type of angular mounts are also discussed in detail.

$$E^* = E^{\mathrm{I}} + i E^{\mathrm{II}} \tag{1}$$

$$|E^*| = \frac{\sigma_A}{\varepsilon_A} \tag{2}$$

$$|E^*| = \sqrt{[E^{\mathrm{I}}(\omega)]^2 + [E^{\mathrm{II}}(\omega)]^2} \tag{3}$$

$$E^{\mathrm{I}}(\omega) = |E^*|. \cos \delta \tag{4}$$

$$E^{\mathrm{II}}(\omega) = |E^*|. \sin \delta \tag{5}$$

$$\tan \delta = \frac{E^{\mathrm{II}}(\omega)}{E^{\mathrm{I}}(\omega)} \tag{6}$$

E^{II} and E^{I} are the loss modulus and storage modulus, respectively. The storage modulus and loss modulus of temperature were obtained as a function of temperature at six different frequencies.

4 Vibration Theory

Vibration and sound control issues can be illuminated with different elastomeric items that require understanding essential product design concepts and vibration theory. Vibration is here and there characterized as intermittent, non-periodic or transient oscillatory development of a dissident dynamic structure. It happens in basically all mechanical systems, produces sound, undesirable wear that debase the execution and unwavering quality of structures and machines, and even disastrous failure. On the opposite side for different systems, vibration is fundamental for the correct functioning of those structures. In this manner, analysis and control of vibration are essential issues of a mechanical design. Vibrating models can be partitioned into two categories: direct system model, whose motion is depicted by bilinear differential conditions and nonlinear system model, whose motion is represented by nonlinear differential equations.

Considering the simplest case where there is no damping, the motion of the spring-mass system for linear differential equation is described by:

$$mx(t) + kx(t) = ft \tag{7}$$

Here assume the case where there is no force useful to the system 3, $f(t) = 0$. Consequently, the free-vibration response of the undamped system is obtained by solving the linear second-order differential equation, in the form of:

$$x\,t = Ce^{st} \tag{8}$$

$$ms^2 + k = 0 \tag{9}$$

$$s = \pm\sqrt{k/m} = \pm i\omega n \tag{10}$$

The constant ωn is the so-called natural frequency of the system.

$$x(t) = A \cos \omega n\,t + B \sin \omega n\,t \tag{11}$$

'a' and 'b' constants can be resoluted considering the primary conditions $x(0) = x0$ and $\dot{x}(0) = \dot{x}0$. If $\dot{x}0 = 0$, Eq. (6) becomes: $x(t) = x_0 \cos (\omega nt)$.

That is, the mass has an oscillating movement of frequency $\omega n = \sqrt{k/m}$.

Considering the case where damping exists, the equation of movement, for the free-vibration case, is

$$m x(t) + c x(t) + k x(t) = ft \tag{12}$$

$$ms^2 + cs + k = 0 \tag{13}$$

$$S1, 2 = \frac{1}{2m}(-c \pm \sqrt{c^2 - 4mk}) \tag{14}$$

From the analysis and defining a parameter $\xi = \frac{c}{2\sqrt{mk}}$ called damping factor, one may see that, depending on the value of ξ, one may have three different cases: Critically damped system—$\xi = \mathbf{1}$:

$$x(t) = (A + Bt)e^{-\omega nt} \tag{15}$$

The limit of periodic motion represents critical damping; hence, the displaced body is restored to symmetry in the direct probable time and without oscillation. Over damped system—$\xi > \mathbf{1}$:

$$x\,t = X1^{es1t} + X2^{es2t} \tag{16}$$

Under damped system—$\xi > \mathbf{1}$:

$$x(t) = e^{-\xi\omega nt}\left[X_1 e^{i\omega n\sqrt{1-\xi^2 t}} + X_2 e^{-i\omega n\sqrt{1-\xi^2 t}}\right] \tag{17}$$

Therefore, an exponentially motion of the body is decaying harmonic oscillation with frequency $\omega_d = \omega_n\sqrt{1 - \xi^2}$. The free undamped vibration of a multi-degree

of freedom (MDOF) system is described by [M] {x (*t*)} + [K] {x (*t*)} = {0}, where [M] and [K] are $m \times m$ matrices with *n* being the DOF of the system.

5 Results and Discussion

5.1 Dynamic Mechanical Analysis

5.1.1 Frequency Sweep Estimations

The variation of tan δ with frequency for precise mounts and similar examples is plotted in Fig. 2b. Generally, tan δ expanded with expanding recurrence with tan δ esteems for pu, nr, cr angular mounts observed to be lower than for the other at most frequencies albeit generally larger increments in tan δ up to 100 Hz contrasted with different examples happened to such an extent that at higher frequencies investigated tan δ esteems for pu, nr, cr were at the upper end of these obtained. It can be watched that damping factor for pu elastomer was low as contrasted and different elastomers.

5.1.2 Temperature Sweep Estimations

Figure 2c speaks to the variation of tan δ versus temperature for pu, nr, cr angular mounts and near examples. The tan δ crest is related with the glass transition
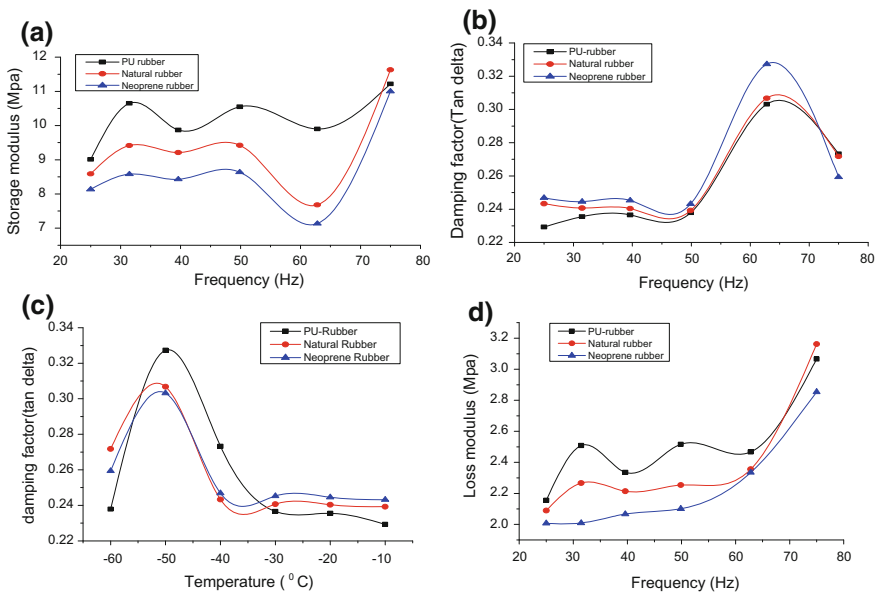
Fig. 2 **a** Storage modulus, **b** frequency versus tan δ, **c** temperature versus tan δ, **d** loss modulus
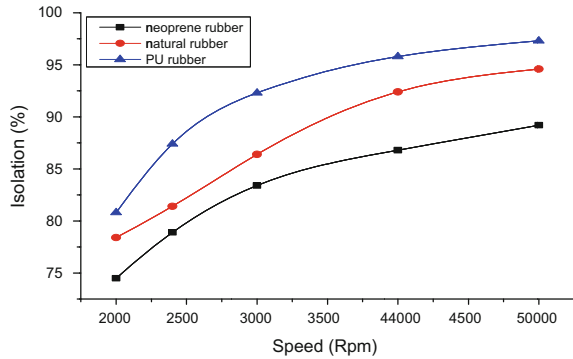
temperature of the materials. The elastomeric dynamic properties are controlled by the glass change temperature Tg. Elastomers having least Tg will have the most minimal tan δ (highest strength) polyurethane which has a genuinely low Tg (-60 ° C) and accordingly has a low tan δ natural elastic has a low Tg (-60 °C), yet the progress locale stretches out above encompassing temperature. It is thus has a high tan δ and is likewise utilized as a part of vibration damping (Fig. 3, Tables 1 and 2).

6   Finite Element Model Formulation

The finite element method is a numerical tool originally developed for the analysis of complex structures and to address modelling, which are applied to engineering applications in a wide variety including acoustics, fluid dynamics, heat transfer and others. Dynamic tests are performed over the model with different thickness variations created in ANSYS, and deflections obtained in static and dynamic are compared (Fig. 4, Table 3).

7   Conclusion

In this study, different types oil-based elastomeric angular mounts were designed and manufactured, and experiments were carried out and analysed. It was found that energy absorption for comparative, vibration isolation angular mounts with different elastomers was generally found higher in polyurethane elastomeric angular mount on over the remaining natural and neoprene angular mount and comparable results of elastomers during curing on tan δ over wide frequency and temperature. The elastomeric dynamic properties are determined by its glass transition temperature Tg.

Table 1 Dynamic mechanical analysis: for PU, natural and neoprene rubber

S. no.	Freq. (Hz)	PU rubber				Natural rubber				Neoprene rubber			
		E^l	E^{ll}	E^*	Tan δ	E^l	E^{ll}	E^*	Tan δ	E^l	E^{ll}	E^*	Tan δ
1	25.00	9.012	2.156	9.266	0.2293	8.589	2.090	8.840	0.2433	8.134	2.008	8.378	0.2469
2	31.47	10.65	2.509	10.94	0.2355	9.418	2.267	9.687	0.2407	8.578	2.009	8.831	0.2446
3	39.62	9.871	2.336	10.14	0.2366	9.211	2.214	9.474	0.2404	8.429	2.067	8.679	0.2453
4	49.88	10.55	2.516	10.87	0.2379	9.422	2.254	9.688	0.2393	8.636	2.101	8.888	0.2432
5	62.80	9.899	2.467	10.20	0.3032	7.680	2.356	8.033	0.3068	7.134	2.335	7.506	0.3273
6	75.00	11.22	3.066	11.63	0.2733	11.63	3.162	12.06	0.2718	11.00	2.854	11.37	0.2594

E^l, E^{ll}, E^* and Tan δ are storage modulus, loss modulus, complex modulus and damping factor

Table 2 Percentage of isolation for elastomeric angular mount at different engine rpm

S. no.	RPM	PU mount-isolation (%)	NR mount-isolation (%)	CR mount-isolation (%)
1	2000	80.8	78.5	73.4
2	2400	87.4	82.7	76.2
3	3000	92.3	87.5	79.8
4	4000	95.8	91.2	84.6
5	5000	97.3	93.8	87.9
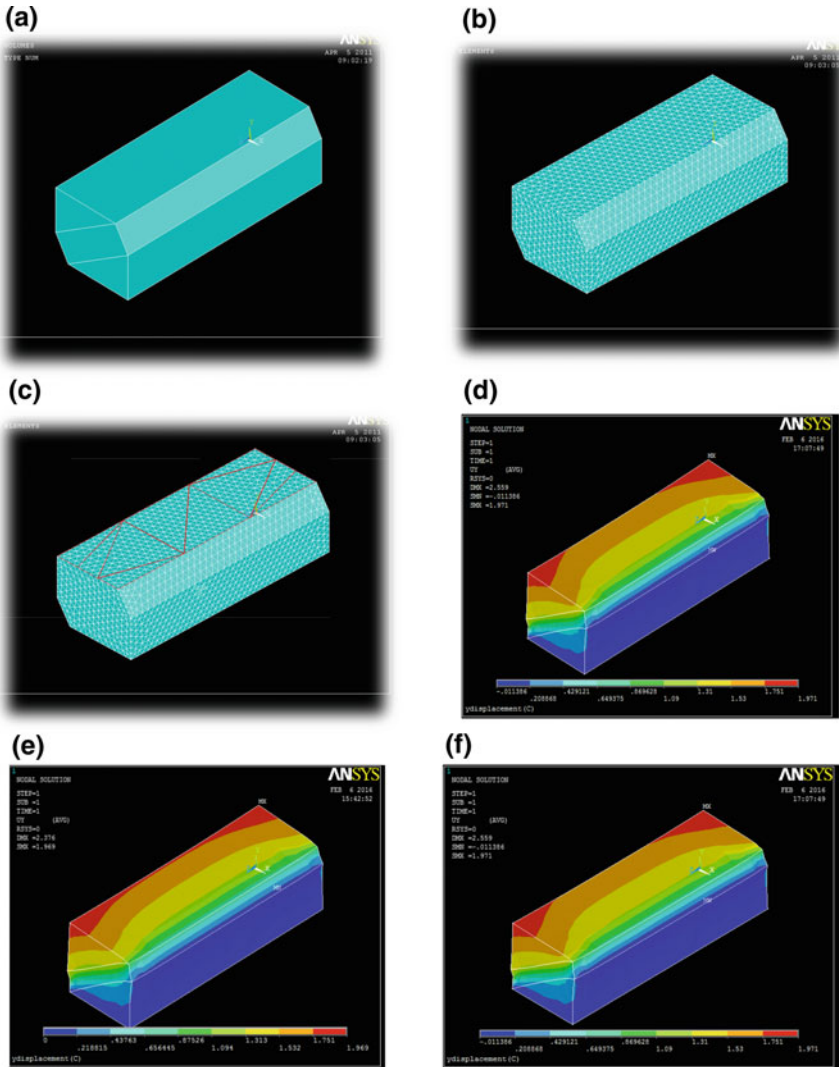
Fig. 4 **a**, **b**, **c**, **d**, **e**, **f** Finite element model, finite mesh model, finite loaded model, deflection figure of angular mounts with polyurethane, natural and neoprene elastomer

Table 3 Comparison of deflection results for different elastomers

	Theoretical	Before ageing	Before ageing	After ageing	After ageing
Type of rubber	Deflection (mm)	Static test (practical) Deflection (mm)	Dynamic test (ANSYS) Deflection (mm)	Static test (practical) Deflection (mm)	Dynamic test (ANSYS) Deflection (mm)
Polyurethane rubber	1.34	1.5	1.36	1.2	1.1
Natural rubber	1.42	1.33	1.56	1.41	1.095
Neoprene rubber	1.50	1.45	1.61	1.76	1.91

Elastomers having lowest Tg will have the lowest tan δ polyurethane which has a fairly low Tg (-60 °C) and thus has a low tan δ compared to remaining elastomers and finally, defection resulted values proved that polyurethane angular mounts achieved better results after ageing when compared to that of the before ageing.

References

1. Nashif, A.D, Jones, D.I.G., Henderson, J.P.: Vibration Damping. Wiley, New York (1985)
2. Kim, J.J., Kim, H.Y.: Shape design of an engine mount by a method of parameter optimization. Comput. Struct. **65**(5), 725–731 (1997)
3. Vahdati, N., Ahmadian, M.: Single pumper semi-active fluid mounts. In: Proceedings of IMECE 2003, Washington, DC, 16–21 Nov 2003
4. Rashid, A.A., Yahiya, S.R.: Mechanical and ageing properties of hybrid carbon black filled natural rubber composites for engine mount application. In: 6th Asian-Australasian Conference on Composite Materials: Progress of Composites 2008 in Asia and Australasia, ACCM 2008, pp. 300–303, Sept 2008
5. Vahdati, N., Saunders, L.K.L.: High frequency testing of rubber mounts. ISA Trans. **41**, 145–154 (2002)
6. Gomes, M.J.M., Pouzada, A.S.: Dynamic behavior of rubber compounds for engine mounts. Key Eng. Mater. **230–232**, 303–306 (2002)
7. Menard, K.P.: Dynamic Mechanical Analysis: A Practical Introduction. CRC Press (2008)
8. Nielsen, L.E.: Mechanical Properties of Polymers and Composites. Dekker, New York, NY, USA (1974)
9. Pereira, R., Arenas, J.P., Zumelzu, E.: Comparison of four test methods to measure damping properties of materials by using piezoelectric transducers. Mater. Des. **32**(4), 2423–2428 (2011)
10. Ghosh, P., Stocek, R., Gehde, M., Mukhopadhyay, R., Krishnakumar, R.: Investigation of fatigue crack growth characteristics of NR/BR blend based tire tread compounds. Int. J. Fract. **188**, 9–21 (2014)

Retrofitting of RC Beams Using Polymer Ferrocement Laminates—Laboratory Model Study and Finite Element Analysis

R. Manoharan, R. Rajkumar, B. Gokula Krishnan and R. Aravindh

Abstract The present study is an attempt for strengthening the reinforced concrete beam damaged due to overloading using polymer ferrocement laminates which were directly glued into the cracked tension face of the beam by epoxy adhesives. Beams of size 3200 mm length, 125 mm width and 250 mm depth were casted and tested under two-point loading condition. The beams were subjected to overloading by applying 70% ultimate load for four beams and 80% ultimate load for two beams. The beams subjected to collapse condition were strengthened by polymer ferrocement laminates with two different volume fractions of 4.94 and 7.41%. The theoretical and experimental moment–curvature behaviour observed in the case of control specimens were compared with polymer ferrocement laminate beams, and the results were validated using ANSYS software.

Keywords Concrete · Rehabilitation · Adhesives · Ferrocement laminates Mortar

R. Manoharan
Corporation of Chennai, Chennai, India
e-mail: manogis@gmail.com

R. Manoharan
Sathyabama University, Chennai, India

R. Rajkumar (✉) · B. Gokula Krishnan · R. Aravindh
Department of Civil Engineering, SSN College of Engineering,
Kalavakkam, Chennai, India
e-mail: rajkumarr@ssn.edu.in

B. Gokula Krishnan
e-mail: krish2445@hotmail.com

R. Aravindh
e-mail: aravindhraj97@gmail.com

1   Introduction

Concrete construction is generally expected to be serviceable throughout its intended design life. However, these expectations are not sometimes fulfilled due to structural deficiency. Physical damage can arise from fire, exploration as well as from restoration to meet its functional requirements by appropriate repair techniques. The excess of load applied beyond the design loads on structural members overload the structure, and it causes basic symptoms of cracking, spalling and disintegration, in which overloading leads to the following types of failures:

- Excessive flexural crack
- Shear and diagonal tension crack
- Shear bond failure leading to side split
- Cracking in slabs
- Excessive compression failure
- Surface spalling due to excessive compression and bulging
- Large deflection
- Settlement of foundation.

1.1   Characteristics of Ferrocement

- Ferrocement is a thin material.
- Ferrocement mesh is distributed throughout its thickness.
- Ferrocement is reinforced in two directions (transverse and longitudinal).
- Ferrocement is a matrix made of fine mortar or paste instead of concrete which contains large size aggregate.

1.2   Advantages of Ferrocement

- Simplicity of its construction
- Lesser dead weight of the elements due to smaller thickness and easy repairability
- High tensile strength
- Corrosion of reinforcement is less
- Easier mouldability to any required shape.

2 Literature Review

Massod et al. [4] in his investigation concluded that the addition of polymer to cement mortar and concrete improves short- and long-term properties. Limaye et al. [3] in his experimental investigation concluded that addition of latex and epoxy polymer to cement mortar made it more workable and the strength increases quite significantly. Colville et al. [1] in his studies inferred that improving the bond strength of masonry mortar using polymer additives also increases the tensile strength, improves water retention and reduces permeability. Gao et al. [2] reported that the flexural and compressive strength of cement mortar improved due to addition of silica fume (SF). Nassif and Najm [5] conducted a series of experiments, and the results showed that the proposed composite beams have good ductility, cracking strength and ultimate capacity.

3 Scope and Objectives

- To study the characteristics of polymer modified mortar as a retrofitting material.
- To study extent of damage due to overloading in RC Beams.
- To study the bonding effect of polymer ferrocement laminates.
- To study the overall performance of the beams with respect to conventional beams.
- To assess the flexural behaviour of retrofitted beams.
- To study the behaviour using finite element programme, ANSYS.

4 Methodology

- To study the characteristics of cement mortar with polymer by conducting compressive strength test, split tensile strength test.
- To study the characteristics of polymer ferrocement composite by conducting flexure test.
- Casting and testing of under-reinforced beam specimens subjected to overloading.
- Comparing the flexure strength of control beam with respect to the beams rehabilitated with polymer ferrocement laminates.
- Analyse and report the results with reference to the behaviour of control beams.

Table 1 Properties of mesh

Type of mesh as fabricated	Woven mesh	Welded mesh
Shape of mesh	Square	Square
Gauge size of mesh	1/2 no 20	1/2 no 15
Spacing of wires (mm)	4.23	15
Diameter of mesh (mm)	0.86	1.44

5 Materials

Fine aggregate	As per IS 383-1970 confirms code II
Water	Fresh, clean and potable
Mix proportion	Cement:Sand = 1:2
w/c ratio	0.4 (for control)
w/c ratio	0.3 (for AR Polymer)
Workability	Slump not exceeding 50 mm
Admixtures	To improve tensile strength and flexural strength, Nitobond AR from FOSROC chemicals, *W/C* reduced from 0.4 to 0.3
Ferrocement	Square woven mesh, square weld mesh (properties are given in Table 1)

6 Experimental Setup

The experimental set up is shown in Fig. 1. The details of the specimen cast for testing are as follows:

Fig. 1 Testing of beams under flexure

- Size of beams—125 mm × 250 mm
- Effective span of beam—3000 mm
- Grade of concrete—M20
- Type of cement—Portland pozzolana cement(PPC)
- Main reinforcement—2 numbers of 12 mm diameter bars
- Compression reinforcement—2 numbers of 8 mm diameter bars
- Shear reinforcement—6 mm diameter stirrups
- Type of load—Static load
- Type of test—Two-point loading

The deflections are measured at mid-span and at 1/3rd points of the beams. The internal and external strains could be measured using electrical strain gauges and DEMEC gauge.

The following observations are made from the static load conducted on the beam specimens.

- Cracking load
- Ultimate load
- Deflections
- Crack width
- Strain measurements using DEMEC gauge
- Strain measurement using electrical strain gauge.

6.1 Retrofitting of Beams Using Ferrocement Laminates

The beams are retrofitted with different volume fractions of ferrocement laminates to improve the strength. The beams were arranged with its soffit facing upwards for surface preparation and for ferrocement laminates bonding work. The concrete substrates of service load damaged beams and ferrocement laminates were prepared well as shown in Fig. 2.

Prior to bonding of the laminates, the tension face of the beam bonding ferrocement laminates was grained to remove the laitance surface as shown in Fig. 3. After surface preparation, the longitudinal cracks caused by service load were scaled by using filler material (corocretin IHL-18).
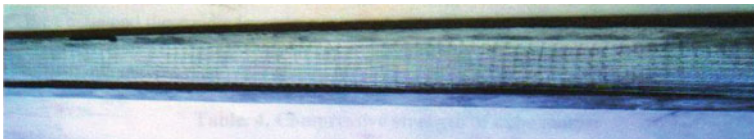
Fig. 2 Casting polymer ferrocement laminate

Fig. 3 Grinding the tension face of beam

7 Experimental Results

The compressive strength of cubes after twenty-eight days of curing is shown in Table 2. The results of split tensile strength and the flexural strength of the specimens are shown in Tables 3 and 4, respectively.

The crack patterns witnessed during the tests for the control beam and the retrofitted beam are as shown in Figs. 4 and 5, respectively. The load versus deflection characteristics observed for the control specimens and the retrofitted

Table 2 Compressive strength of cube

S. No.	Curing days	*W/C* ratio	Designation	Average compressive strength, N\mm^2
1	28	0.40	Plain mortar	35.5
2	28	0.30	Plain mortar + AR (10%)	40.1

Table 3 Split tensile strength of cylinder

S. No,	Curing days	*W/C* ratio	Designation	Average split tensile strength, N\mm^2
1	28	0.40	Plain mortar	28.21
2	28	0.30	Plain mortar + AR (10%)	37.42

Table 4 Flexural strength of beam

S. No.	Curing days	*W/C* ratio	Designation	Average flexural strength, N\mm^2
1	28	0.40	Plain mortar	3.89
2	28	0.30	Plain mortar + AR (10%)	4.2

Fig. 4 Crack patterns in control beam
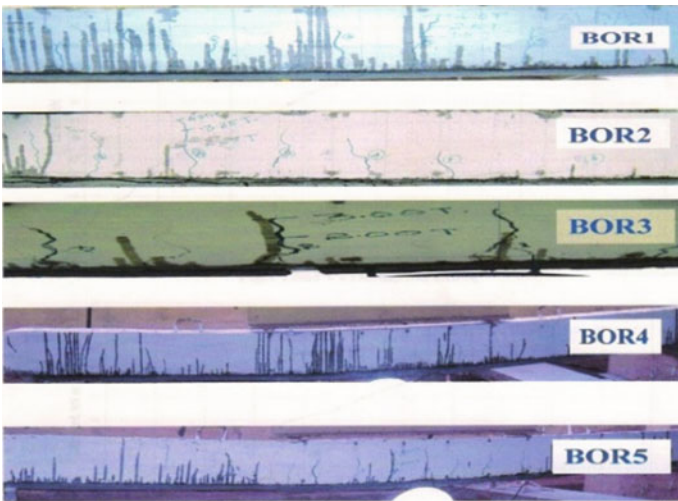
Fig. 5 Crack patterns in retrofitted beam

specimens are shown in Figs. 6, 7, 8 and Figs. 9, 10, 11, respectively. The load-deflection curve clearly indicates the increase in the load carrying capacity of the beams retrofitted with ferrocement laminates.

Perfect Beam – BP₁
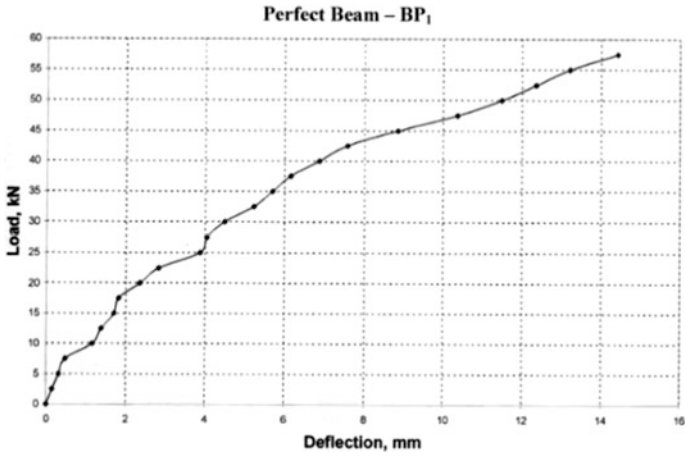
Fig. 6 Load versus deflection characteristics in control beam 1

Perfect Beam – BP₂
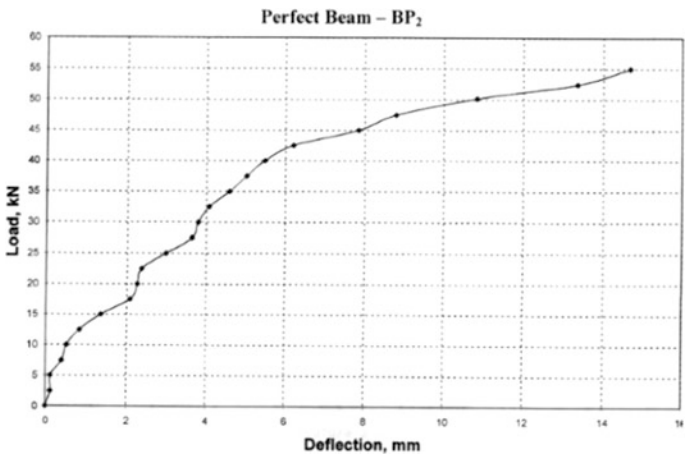
Fig. 7 Load versus deflection characteristics in control beam 2

8 Numerical Analysis

8.1 Theoretical Moment–Curvature Relationship

The load-deformation characteristics of flexural member at yield and at ultimate moment are mainly dependent on the moment–curvature characteristics of sections, since most of the deformations of members of normal proportion arise from strain associated with flexure. The curvature will vary along the length of the member

Perfect Beam – BP3

Fig. 8 Load versus deflection characteristics in control beam 3

Rehabilitated Beam – BOR₁
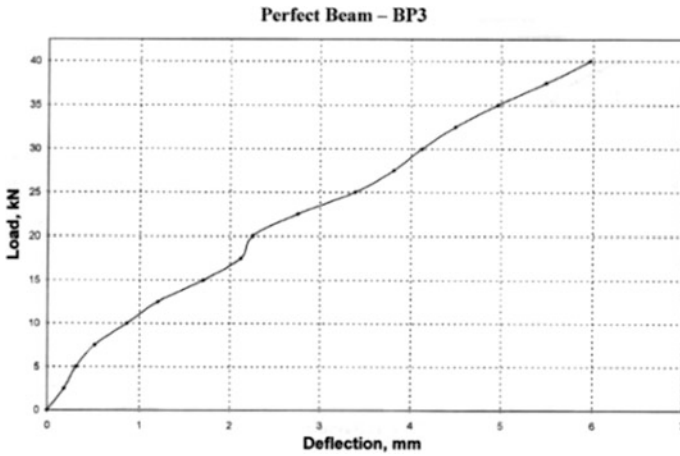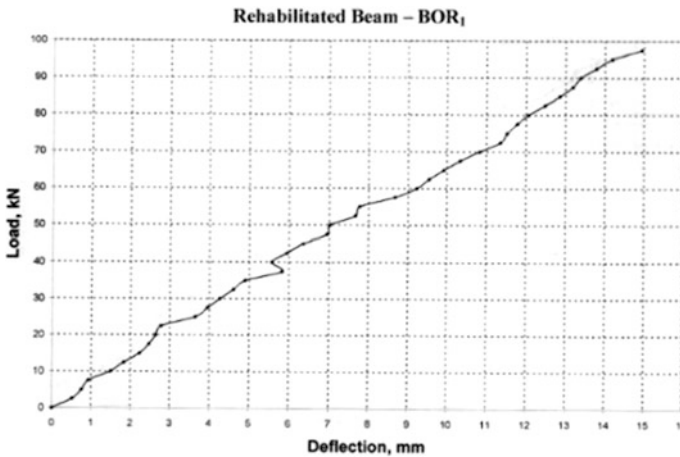
Fig. 9 Load versus deflection characteristics in retrofitted beam 1

because of the fluctuation of the neutral axis depth and the strain between the cracks. With increase in moment, cracking of the concrete reduces the flexural rigidity of the sections in the lesser reinforced section than for the over reinforced section. The moment–curvature relationship for a practical beam, in which the tension steel yields, can be idealized to the trilinear relationship. The first stage is cracking, the second is the yield of the tension steel, and the third is the limit of useful strain in concrete. Theoretical moment–curvature curves for reinforced concrete sections with flexure and axial load can be derived based on assumption
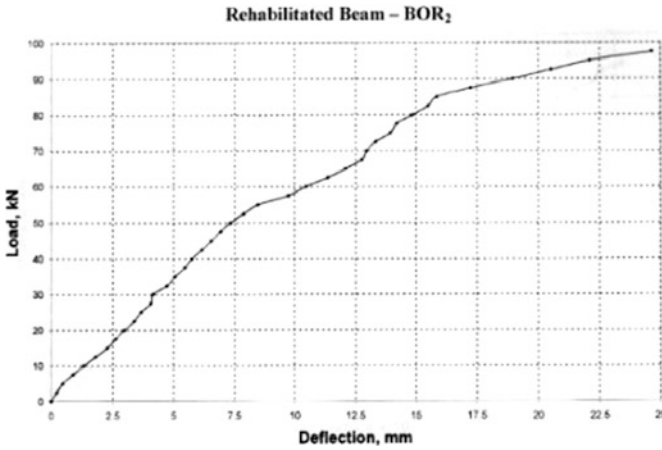
Fig. 10 Load versus deflection characteristics in retrofitted beam 2
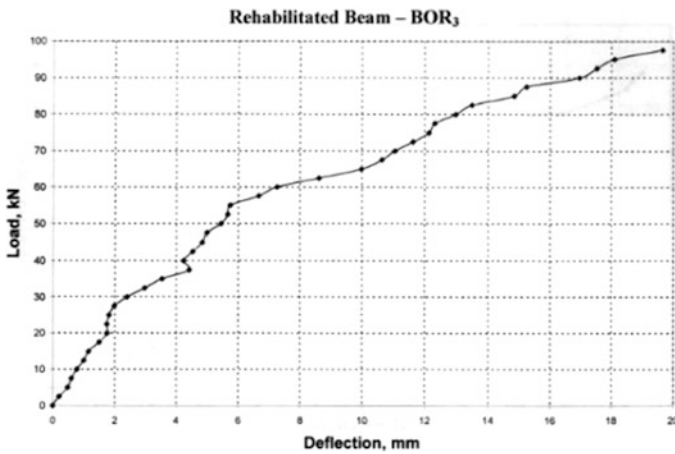
Fig. 11 Load versus deflection characteristics in retrofitted beam 3

like those used for the determination of the flexure strength. It is assumed that plane sections before bending remain plane after bending and that the stress–strain curves for concrete and steel are known. The curvature associated with a range of bending moments and axial loads can be determined using these assumptions and from the requirements of strain compatibility and equilibrium of forces.

8.2 ANSYS

In this study, the finite element software, **ANSYS,** is used to model the specimen. The description and properties of the modelling elements are as follows:

8.3 Solids 65 (3-D Reinforced Concrete Solid)

SOLID 65 are used for the three-dimensional modelling of solids with or without reinforced bars (rebar). The solid is capable of cracking in tension and crushing in compression. The element is defined by eight nodes having three degrees of freedom at each node: translation in the nodal x, y and z directions. Up to three different rebar specifications may be defined. The control specimen and the retrofitted beam modelled using ANSYS software are shown in Figs. 12 and 13, respectively. The reinforcement details in the beam are modelled using Link 83 as shown in Fig. 14, and the deformed shape of the control beam is presented in Fig. 15. The stress patterns shown in Figs. 16 and 17 for the control beam and the beam with ferrocement laminates, respectively, clearly depict that the beam retrofitted with ferrocement laminates has greater load carrying capacity when compared to the stress contour of the control beam.

Fig. 12 ANSYS modelling —control beam
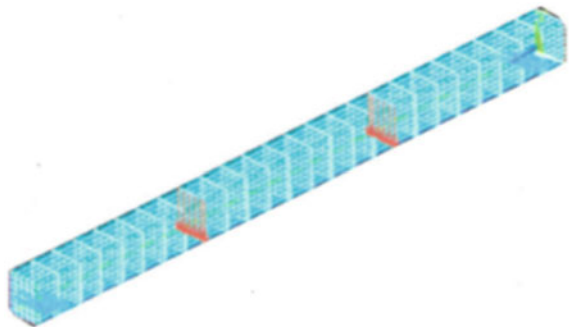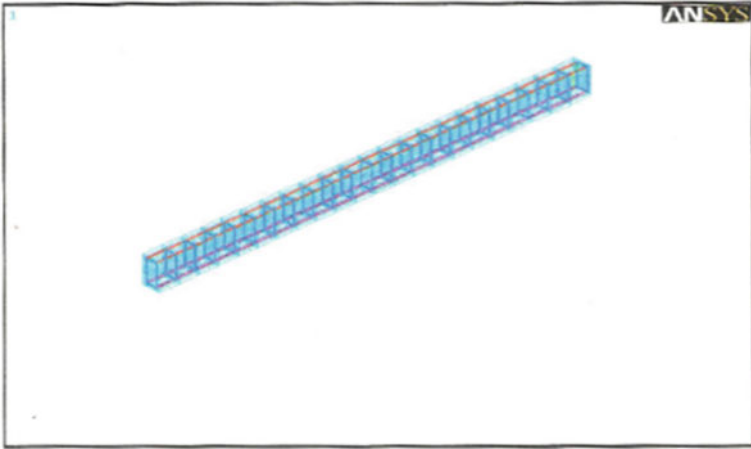
Fig. 13 ANSYS modelling—retrofitted beam
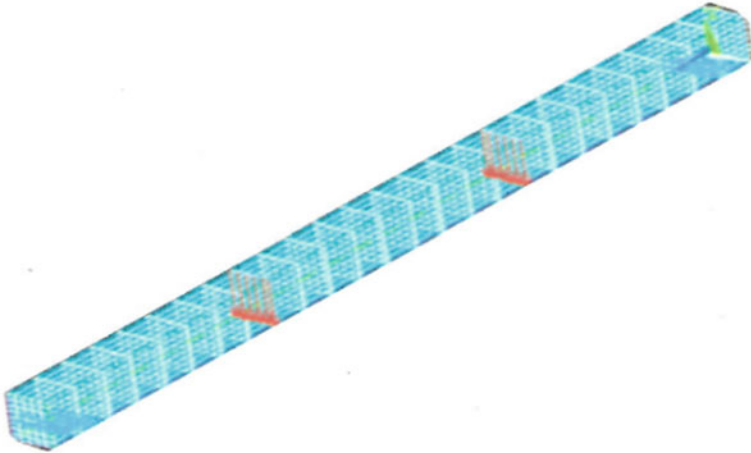
Fig. 14 ANSYS modelling—reinforcement
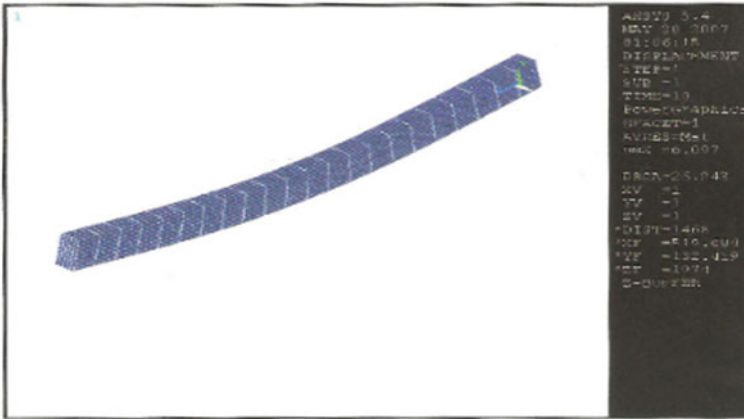
Fig. 15 Deformed shape of control beam
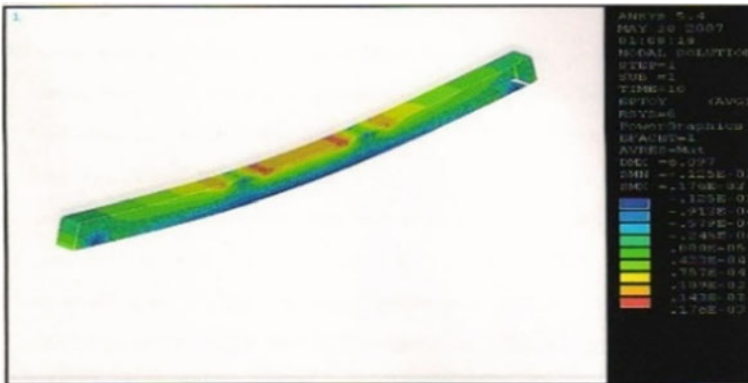
Fig. 16 Strain contour at *Y* direction of control beam
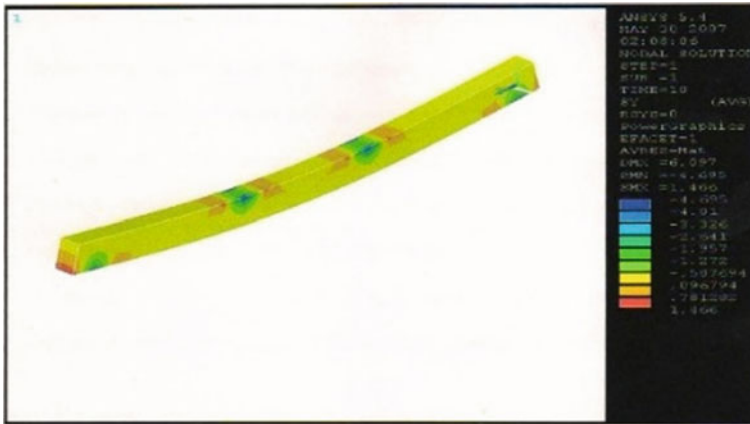
Fig. 17 Stress contour at *Y* direction of ferrocement beam

9   Conclusions

The following conclusions are drawn from the study.

- The NITOBOND AR polymer used in the present study gained a better strength with high cohesivity, better workability which is free from problems of stiffing, coagulation, bleeding and segregation.
- The appearance at the first crack was delayed by the presence of polymer ferrocement laminate. The improvements are dependent on the volume fraction of the reinforcements in the ferrocement laminates.
- Square mesh being an effective reinforcement for polymer modified ferrocement laminate achieved good ductility and load carrying capacity with volume fraction of 7.41% with decrease in average crack spacing and width.
- The enhancement in load carrying capacity of rehabilitated beam achieved 79% higher strength when compared with the conventional beam.
- The experimental result showed good agreement with the analytical results.
- Considering the economic aspects of rehabilitation, this method proves to be a cost-effective solution and can be used for retrofitting and strengthening method for a wide range of applications.
- The method is simple to understand and apply and therefore may be utilized for common rural engineering works with desired results.

References

1. Colville, J., Miltenherger, A.M.: Tensile bond strength of polymer modification mortar. J. Mater. Civ. Eng., pp. 1–5 (1999)
2. Gao, J.M., Qian, C.X., Wang, B., Murino, K.: Experimental study on properties of polymer modified cement mortar with silica fume. Cem. Concr. Res. **32**, 41–45 (2002)
3. Limaye, R.G., Kamt, M.K.: Experimental studies on polymer modification of cement mortar. Indian Concr. J., pp. 153–158 (1992)
4. Massod, A., Arif, M., Akhtar, S., Haquie, M.: Rehabilitation of RC and FRP beams by ferrocement an experimental investigation. J. Struct. Eng., pp. 321–326 (2005)
5. Nassif, H.H., Najm, H.: Experimental and analytical investigation of ferrocement-concrete composite beams. Cement and Concrete Composites. Elsevier Science. **26** (7), 787–796 (2004) https://doi.org/10.1016/j.cemconcomp.2003.08.003

Comparative Evaluation TIG and FS Welding of Cast Al–Mg–Sc Alloy

K. Subbaiah

Abstract Cast aluminum–magnesium–scandium (Al–Mg–Sc) alloy is used in this study to carryout the possibilities of various welding techniques. In this study, Bead-on-plate welds were made on cast Al–Mg–Sc alloy using both tungsten inert gas (TIG) and friction stir (FS) welding processes. Microstructural characterization revealed that FS-weld microstructure consisted of fine and fragmented recrystallized grains compared to TIG welding. Mechanical properties of FS-welded joints were better than TIG-welded joints. Evaporation of magnesium was more in TIG welding than FS welding. It is concluded that FS welding process resulted in significantly stronger joints and is more suitable to join cast Al–Mg–Sc alloy.

Keywords TIG welding · FS welding · Scandium · Tensile properties
Microstructure · Vaporization

1 Introduction

Small addition of transition elements has large influence on the properties of Al alloys. The addition of scandium is first proposed by Wiley in 1971 [1] with aluminum alloys. To date, it has been reported that a small amount of scandium largely improves properties of Al alloys such as microstructure, strength, recrystallization temperature, weldability. [2–7]. Most of these favorable effects are mainly due to the fine dispersion of the Ll_2–Al_3Sc precipitate, which is stable, spherical, and coherent with the matrix [4]. The increase in strength results from both the precipitation of ordered Al_3Sc particles and the preservation of a fine grain structure [6].

Tack [8] has patented the effect of TIG welding on tensile properties of wrought Al–Mg–Sc alloys. Extensive work on C557 alloy (wrought Al–Mg–Sc alloy) FS

K. Subbaiah (✉)
Department of Mechanical Engineering, SSN College of Engineering, Chennai 603110,
Tamil Nadu, India
e-mail: subbaiahk@ssn.edu.in

welding was done and reported the advantage of the welded joints [9, 10]. Comparative investigations on the microstructure and mechanical properties of FS and TIG welded joints for wrought Al–Mg–Sc alloy have been reported in the literature [11–13].

Though research work of comparative study of FS welding with other welding techniques has been reported for wrought alloys, it appears that systematic study and detailed comparison between FS and TIG welding for Cast Al–Mg–Sc aluminum alloy have not been reported yet.

2   Experimental Work

In this work, a study of the microstructure and mechanical properties of TIG and FS bead-on plate welding was carried out. Microstructural studies, tensile tests, microhardness measurements, and chemical compositional analysis of the welded joints and cast base metal were performed in order to determine the influence of each welding process on the mechanical properties.

The joints under each condition were examined by optical microscopy and scanning electron microscopy (SEM) with X-ray energy-dispersive spectroscopy (EDS). The tensile test specimens perpendicular to the weld interface were machined from the joints by wire-cut EDM. The Vickers hardness measurements were made every 1 mm across the weld using 1 N load and a dwell time of 15 s.

3   Results and Discussions

3.1   Microstructure

The microstructure of the cast Al–Mg–Sc base metal is shown in Fig. 1a. The image shows the base metal zone with Al_3Sc particles heterogeneously precipitated and dispersed in the matrix. The matrix also shows fine dark particles of undissolved $Al_6(Fe,Mn)$, Al_3Mg_2, and Mg_2Si in Al solid solution. Some casting voids were also observed and shown in Fig. 1b. During solidification of aluminum, there is a 6% reduction in the volume of the melt. This causes the casting voids in the cast Al–Mg–Sc alloy.

The weld microstructure of the TIG weld is shown in Fig. 1c. It naturally contains cast grains due to fusion welding process. On the other hand, the weld nugget microstructure of the FS welding shown in Fig. 1d is very fine and fragmented compared to the cast base metal microstructure shown in Fig. 1a and TIG weld microstructure shown in Fig. 1c.

(a) Cast Al-Mg-Sc alloy **(b)** Shrinkage cavity in cast base metal
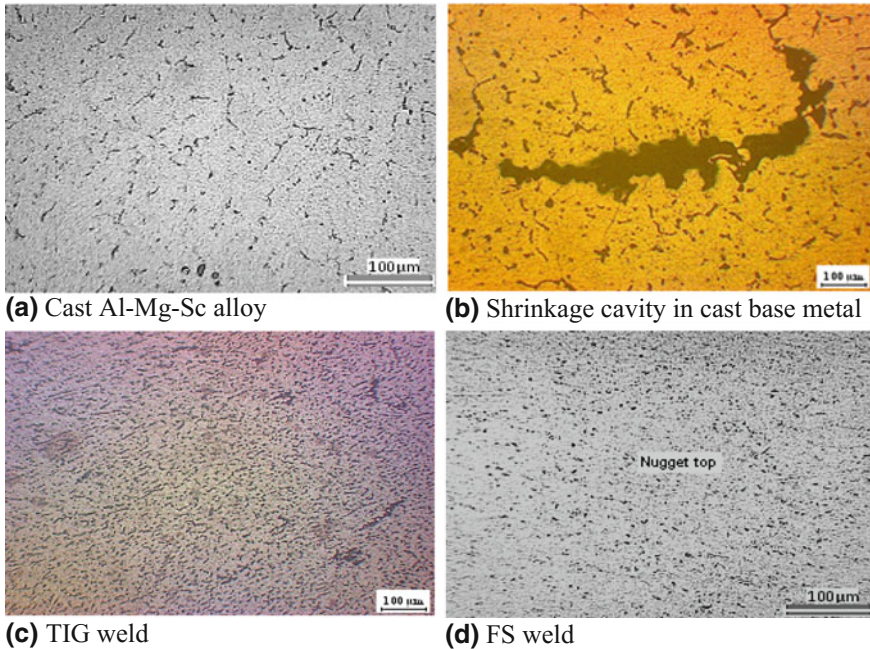
(c) TIG weld **(d)** FS weld

Fig. 1 **a** Cast Al–Mg–Sc alloy, **b** shrinkage cavity in cast base metal, **c** TIG weld, **d** FS weld

3.2 Hardness

The hardness values across the transverse cross sections of the TIG and FS welded samples were plotted in Fig. 2. The hardness values of TIG welded cast Al–Mg–Sc alloy are nearly symmetrical with respect to the weld. There has been a drop of 18% in the hardness at the weld zone in the case of TIG welding. The hardness values of FS welding are not symmetrical with respect to the weld nugget. The drop in hardness in the entire FS welding process is well within 8% than that of cast Al–Mg–Sc alloy.

3.3 Tensile Properties

The tensile properties of the TIG- and FS-welded samples were shown in Table 1. The TIG-welded samples' tensile properties are slightly greater than the properties of the base metal. And the tensile properties of FS-welded samples were far better than the base metal properties. The percentage elongation of FS-welded samples is better than that of the TIG-welded joints and the base metal. Formation of columnar grains at HAZ of the TIG-welded joint was mainly responsible for less increase in ductility.
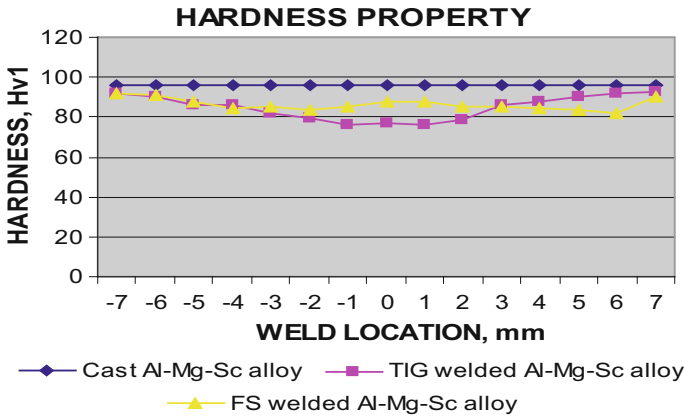
Fig. 2 Hardness of cast Al–Mg–Sc base metal and TIG- and FS-welded joints

Table 1 Tensile properties of cast Al–Mg–Sc base metal, TIG- and FS-welded joints

Type of weld	Yield stress, MPa	Tensile strength, MPa	% Elongation
Base metal	217	228	6.8
TIG welded joint	225	241	8
FS-welded joint	271	316	22.7

3.4 Chemical Compositional Analysis

The magnesium, manganese, and zinc present in the base metal were subjected to evaporation during fusion welding processes of aluminum alloys [14]. In our study, we have got a loss of 35% magnesium and 10% scandium in the fusion zone of the TIG weld bead of cast Al–Mg–Sc alloy plates. There was a heavy loss of iron also observed in the TIG welding process. The minimum variation of volatile elements in the FS welding was observed. The magnesium and scandium reduction reduces the solid solution strengthening of the alloy. The reduction of iron has automatically reduced the number density of the intermetallic compound Al_6(Fe, Mn) in the TIG-welded joints. The reduction of scandium causes the dissolution of the precipitate Al_3Sc in the TIG-welded joints (Table 2).

Table 2 Chemical composition of cast Al–Mg–Sc base metal, TIG and FS welds

	Mg	Mn	Fe	Sc	Ti
Base metal	3.954	0.647	0.356	0.293	0.023
TIG welding	2.567	0.656	0.032	0.263	0.009
FS welding	4.45	0.645	0.366	0.287	0.005

3.5 Discussion

The TIG weld contains pores of size less than 40 μm in the HAZ, whose presence will introduce stress concentration in the cross section, which will reduce the strength of the joint. Being a fusion welding process, in TIG welding process, the microstructure of the weld contains cast coarse grains. But presence of the dispersoid Al_3Sc overcomes all the drawbacks of TIG welding process and produces better tensile properties compared to the cast base metal properties. The FS weld contains fine, dynamically recrystallized grains compared to the microstructure of the cast base metal. The recrystallized grains retain most of the base metal properties. The Al_3Sc dispersoid also subjected to fragmentation due to forging and extrusion operation occurring in the FS welding process, which enhances the tensile properties of the FS-welded joint compared to both TIG welding process and cast base metal properties.

The distribution of hardness is symmetrical with respect to the weld centerline in the case of TIG welding. The distribution of hardness is not symmetrical in the case of FS welding. The reason for unsymmetrical distribution is that the advancing side and retreating side of FS welding subjected to variable pressures. As the welding direction and the tool rotation direction coinciding on the advancing side, the distribution of precipitates and strain rate application is more. The drop in hardness in the weld zone is more in the case of TIG welding compared to FS welding.

The chemical compositional study on both TIG and FS welding reveals that there is vaporization of volatile elements such as magnesium, manganese, iron, titanium, and scandium from the weld beads. In TIG welding, the reduction in magnesium was observed to be equivalent to 35% of that of the base metal. The Al–Mg alloys are solid-solution-strengthened alloys and derive their strength mainly from the addition of magnesium and manganese. Hence, 35% reduction of magnesium in the weldzone reduces the tensile properties as well as hardness distribution of TIG welded joints. The presence of magnesium in the weld bead of the FS-welded joint is more compared to the cast base metal, because of the fragmentation of the precipitates in the weld nugget. This increase in the magnesium percentage also helps to improve the tensile properties of the FS-welded joints [10].

4 Conclusions

The cast Al–Mg–Sc alloy plates were bead-on-plate welded by both TIG and FS welded.

The microstructural studies of FS-welded cast Al–Mg–Sc alloys revealed that the microstructure of the weld is fine, fragmented, and pore-free compared to the weld microstructure of TIG welding.

The tensile properties and ductility of FS-welded joints are better than that of TIG-welded joints and the cast base metal.

TIG-welded samples' hardness distributions were symmetrical with respect to the weld, whereas the hardness values of FS-welded samples were not symmetrical. Hardness drop was less in FS-welded joints.

Magnesium evaporation of 35% is mainly responsible for reduced mechanical properties in the case of TIG welding of cast Al–Mg–Sc alloys.

References

1. Willey, L.A.: United States Patent No. 3,619,181 (1971)
2. Roder, O., Schauerte, O., Lutjering, G., Gysler, A.: Correlation between microstructure and mechanical properties of Al-Mg alloys without and with scandium. Mater. Sci. Forum. 217–222, 1835–1840 (1996)
3. Aiura, T., Sugawara, N., Miura, Y.: The effect of scandium on the as-homogenized microstructure of 5083 alloy for extrusion. Mater. Sci. Eng. A **280**,139–45 (2000)
4. Davydov, V.G., Rostova, T.D., Zakharov, V.V., Filatov, YuA, Yelagin, V.I.: Scientific principles of making an alloying addition of scandium to aluminum alloys. Mater. Sci. Eng., A **280**, 30–36 (2000)
5. Filatov, Y.A., Yelagin, V.I., Zakharov, V.V.: New Al-Mg-Sc alloys. Mater. Sci. Eng., A **280**, 97–101 (2000)
6. Lathabai, S., Lioyd, P.G.: The effect of scandium on the microstructure, mechanical properties and weldability of a cast Al–Mg alloy. Acta Mater. **50**, 4275–4292 (2002)
7. Ahmad, Z., Jabbar, A.A.B., Abdullahi, K., Abbas, M.: Effect of scandium doping on the corrosion resistance and mechanical behavior of Al-3Mg alloy in neutral chloride solutions. Mater. Sci. Appl. **2**, 244–258 (2011)
8. Tack., US Patent 6 139 653
9. Lapasset, G., Girard, Y., Campagnac, M.H., Bolvin, D.: Investigation of the microstructure and properties of a Friction stir welded Al-Mg-Sc alloy. Mater. Sci. Forum. 426–432, 2987–2992 (2003)
10. Subbaiah, K., Geetha, M., Govindaraju, M., Koteswara Rao, S.R.: Mechanical properties of friction stir welded cast Al-Mg-Sc alloys. Trans. Indian Inst. Metals. **65**(2), 155–158 (2012)
11. Cabello Munoz, A., Ruckert, G., Huneau, B., Sauvage, X., Marya, S.: Comparison of TIG welded and Friction Stir welded Al-4.5Mg-0.26Sc alloy. J. Mater. Process. Technol. **197**, 337–43 (2008)
12. Zhao, J., Jiang, F., Jian, H., Wen, K., Jiang, L., Chen, X.: Comparative investigations of tungsten inert gas and friction stir welding characteristics of Al-Mg-Sc alloy plates. J. Mater. Des. **31**, 306–311 (2010)
13. He, Z, Peng, Y., Yin, Z., Lei, X.: Comparison of FSW and TIG welded joints in Al-Mg-Mn-Sc-Zr alloy plates. Trans. Nonferrous Met. Soc. China. **21**, 1685–1691 (2011)
14. Cieslak, M.J., Fuerschbach, P.W.: On the weldability, composition, and hardness of pulsed and continuous Nd:YAG laser welds in aluminum alloys 6061,5456, and 5086. Metall. Mater. Trans. B **19**, 319–329 (1988)

Effect of Continuous and Pulsed Current Tungsten Inert Gas Welding of Cast Al–Mg–Sc Alloy

D. Arunkumar and K. Subbaiah

Abstract The vacuum induction melted cast aluminum–magnesium–scandium (Al–Mg–Sc) alloy was subjected to continuous and pulsed current tungsten inert gas welding. The comparative study between the two joining methods was done using mechanical and metallurgical characterization techniques. The microstructure of TIG welding was coarser than that of the P-TIG welding process. The tensile failures were observed at the weld in the case of P-TIG welding and at the base metal for TIG welding. The TIG welded joints were stronger than the P-TIG welded joints as well as the cast base metal. The loss of hardness was more in P-TIG welding than the TIG welding process compared to the base metal hardness values. The evaporative losses of magnesium are more or less the same in both the welding processes. TIG welding of Cast Al–Mg–Sc alloy plate is more reliable than P-TIG welding.

Keywords Cast alloy · Transition metals and alloys · Mechanical properties
TIG welding

1 Introduction

The 5000 series aluminum alloys are widely used in transportation industries such as construction of fast boat hulls, fast trains and railway wagons, due to their lightweight and resistance to corrosion. Magnesium and manganese are the major alloying elements with aluminum, and this combination has been classified as non-heat treatable alloys [1]. Upto 6% of magnesium is added to get the required properties and addition of more than that leads to unwanted problems.

Madhusudhan Reddy et al. [2] have performed welding trials with P-TIG welding, which was developed in the 1950s. P-TIG welding process is performed by altering the welding current at a selected regular frequency [2]. Peak and base

D. Arunkumar · K. Subbaiah (✉)
Department of Mechanical Engineering, SSN College of Engineering,
Chennai 603110, Tamil Nadu, India
e-mail: subbaiahk@ssn.edu.in

current, pulse frequency and the pulse on-time are the important parameters, which will affect the performance of any welded joint [3].

Willey in 1971 [4] patented the effect of scandium addition with aluminum. Addition of scandium with aluminum produces Al_3Sc particles, which enhances the yield strength of the new alloy. Grain refinement, reduction in dendritic arm spacing and susceptibility to crack formation reduces sharply are the important characteristics of addition of scandium. An increase in the mechanical properties was also reported in the literature [1, 5].

In this study, pulsed-TIG and TIG welding trials were conducted on cast Al–Mg–Sc alloys. The relative merits and demerits of both TIG and P-TIG welding process were compared with cast base metal.

2 Experimental Work

An AC TIG welding machine with 2% Th Tungsten electrode was used to weld (bead on-plate) the 5-mm-thick VIM Cast Al–Mg–Sc plates. The argon shielding gas flow rate was 40 l/min. The welding speed was kept at 150 mm/min. The constant current used in the TIG welding process was 140 A, whereas, the peak and base currents used in P-TIG were 200 A and 80 A, respectively. 6 Hz pulse frequency and 50% of cycle time as pulse on-time was fixed in the experiment. Both weldings were done at 16 V.

3 Results and Discussion

3.1 Microstructural Study

[A] Optical Microstructure of Cast Al–Mg–Sc Base Metal

The optical microstructure of the VIM cast alloy is shown in Fig. 1. As the cast alloy was prepared by mixing Al-4.2%, Mg-0.7%, Mn alloy and Al-2% Sc master alloy in a vacuum induction melting furnace, it contained Al_3Sc precipitates from the scandium master alloy and precipitates such as Al_3Mg_2, Mg_2Si and intermetallic compounds like $Al_6(Fe,Mn)$ in it [6, 7]. When aluminum is cooled from liquid state to solid state; there is a reduction in volume of 6% observed [8]. The shrinkage cavity shown in Fig. 2 is due to the above phenomena.

[B] Optical microstructure of TIG welded joints of cast Al–Mg–Sc alloy

The intersection of the HAZ and the base metal is shown in Fig. 3. In the HAZ, the microstructure shows re-crystallization of Al_3Sc, this became finer and fragmented and also contains no voids. Both Al_3Mg_2 and Mg_2Si re-precipitated to finer particles which could be resolved at higher magnification. Small gas pores which
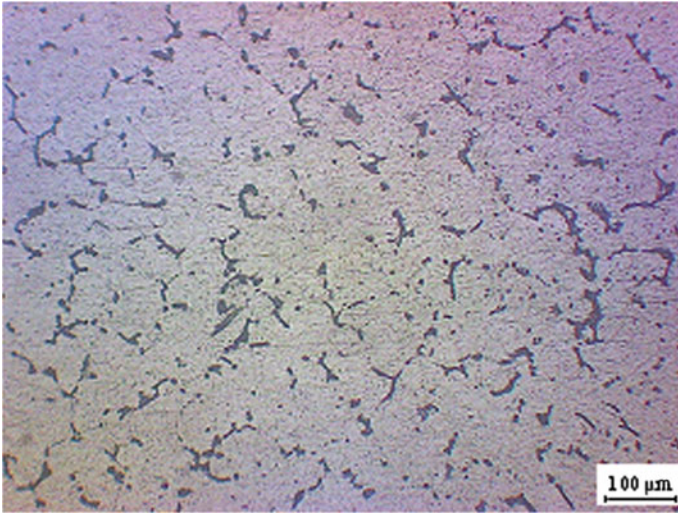
**Fig. 1** Cast Al–Mg–Sc alloy microstructure
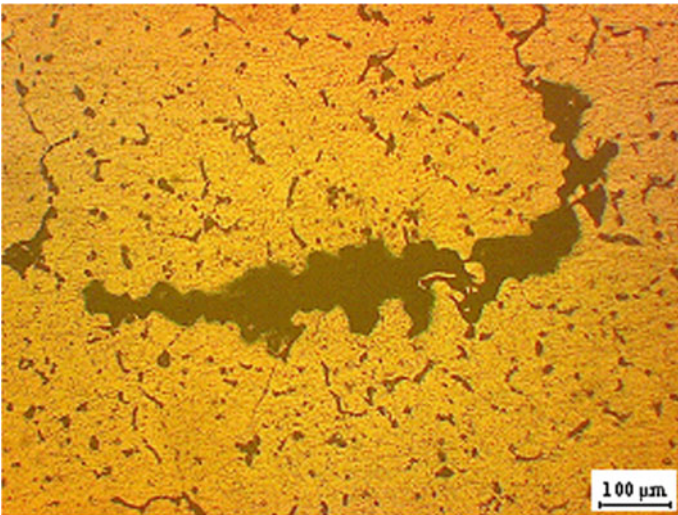
Fig. 2 Casting voids in cast base metal

are formed during the TIG welding process due to melting and solidification are shown in Fig. 3. Small pores of size less than 50 μm have been observed in the HAZ are shown by Fig. 3.

The microstructure of the weldzone of the TIG welded joint is shown in Fig. 4. The weldzone matrix with fine homogeneously distributed dispersion of Al_3Sc, which recrystallized due to solutionizing and subsequent precipitation. The total
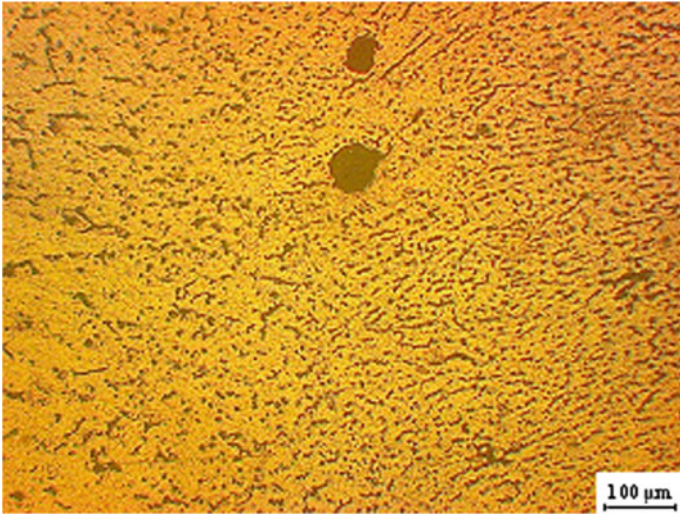
Fig. 3 Microstructure of BM and HAZ
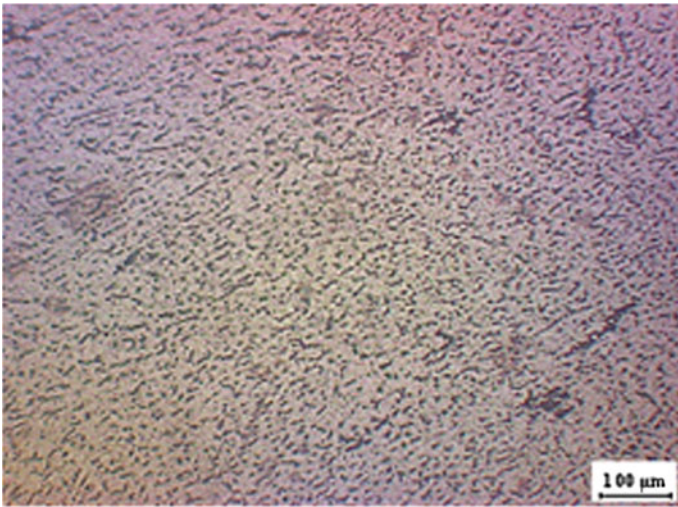
Fig. 4 Microstructure of TIG weld

elimination of casting voids was also observed in the weldzone. The size of the dispersiod Al_3Sc has been reduced to still smaller size compared to the cast base metal.

[C]　**Optical microstructure of P-TIG welded joints of cast Al–Mg–Sc alloy**

The intersection of HAZ and base metal is shown in Fig. 5. The microstructure shows recrystallization of Al_3Sc and other precipitates. It has been observed that the shrinkage voids formed in the cast base metal is totally eliminated. Formation of pores is also not observed either in the HAZ or in the weldzone. The microstructure of P-TIG welded joint, weld is shown in Fig. 6. The weldzone contains coarse grains. Total elimination of casting voids and pores have been observed.

[D]　**SEM microstructure of TIG and P-TIG welded joints of cast Al–Mg–Sc alloy**

The SEM microstructure of the cast Al–Mg–Sc base metal is shown in Fig. 7. The SEM micrograph of both TIG and P-TIG welds are shown in Figs. 8 and 9. The TIG weldzone shown in Fig. 8 contains less dendrite, which is distributed in a random fashion. The P-TIG weldzone shown in Fig. 9 contains uniformly distributed coarse grains.

3.2　Tensile Properties

The tensile properties of the TIG and the P-TIG welded samples were found out and shown in Table 1. The tensile properties of the TIG welded joints, viz., yield, UTS, and ductility were 220 MPa, 237 MPa, and 8.1%, respectively, which are higher than the base metal values. There is an increase of 8% in the strength values of TIG welded samples compared to the base metal properties.
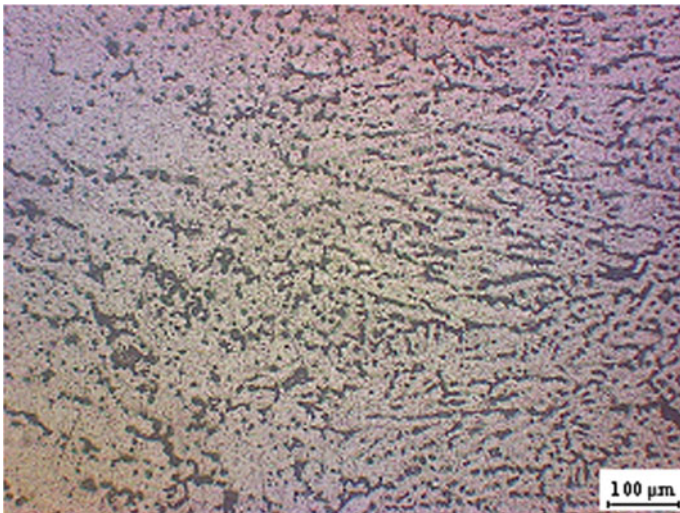
Fig. 5　Microstructure of BM and HAZ
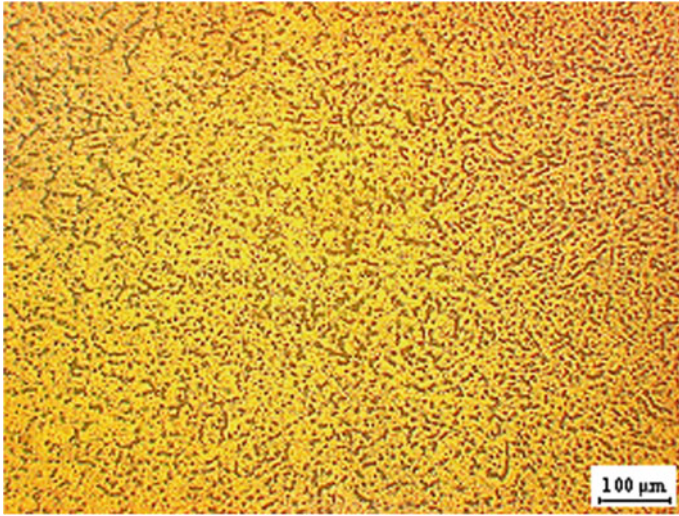
Fig. 6 Microstructure of P-TIG weld

Fig. 7 SEM of base metal
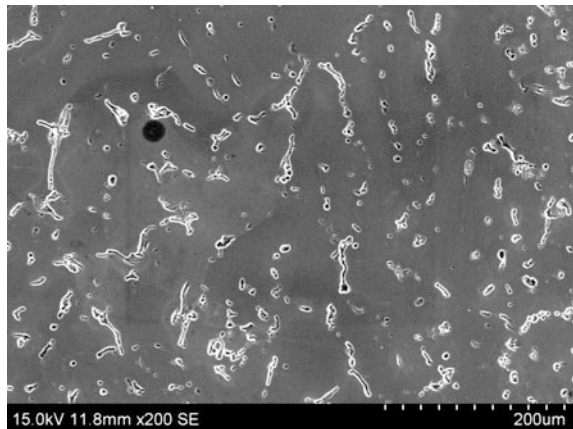
The tensile properties of the P-TIG welded joints, viz., yield, UTS, and ductility were 193 MPa, 207 MPa, and 7.5%, respectively, which are less than the base metal values. There is a decrease of 5.5% in the strength values of P-TIG welded samples compared to the base metal properties. We can conclude from Fig. 9 that the tensile properties of the P-TIG welds are the least compared to both TIG and the base metal tensile properties.

There is an increase of 15 and 7% in the ductility values of TIG and P-TIG welded samples compared to the base metal properties, respectively. We can conclude from Table 1 that the ductility property of both TIG and P-TIG welded samples were better than the base metal properties.
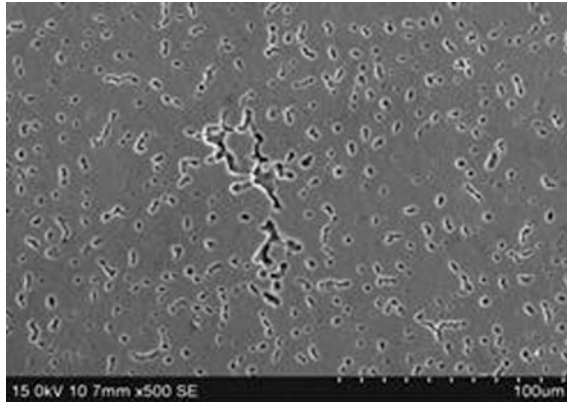
Fig. 8 SEM of TIG weld
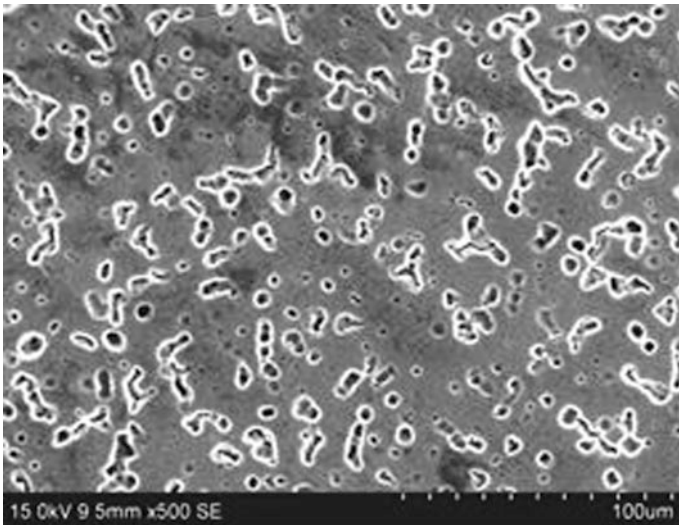
Fig. 9 SEM of P-TIG weld

Table 1 Tensile properties of TIG, P-TIG welded joints, and cast Al–Mg–Sc base metal

	Yield stress, MPa	Ultimate tensile strength, MPa	% Elongation
TIG welding	220	237	8.1
P-TIG welding	193	207	7.5
Cast base metal	203	214	7.0

3.3   Fracture Locations

The broken samples of the TIG and P-TIG welded cast Al–Mg–Sc alloys after the
tensile testing is shown in Figs. 10 and 11. The failures in the case of TIG welded
joints are mostly outside the weldzone, whereas the failures in the case of P-TIG
welded joints are on the junction of HAZ and the base metal. This indicates that the
TIG welds are stronger than the cast base metal and P-TIG welds.

3.4   Hardness

The hardness values have been measured across the transverse cross sections of the
welds. The hardness values of both TIG and P-TIG welds were less than the
hardness value of the base metal, i.e., 96 Hv1. We can conclude from Fig. 12 that
the hardness values of TIG welded samples were better than the hardness values of
P-TIG welded samples.

3.5   Chemical Composition

The magnesium, manganese, and zinc present in the base metal were subjected to
evaporation during fusion welding processes of aluminum alloys [9]. The chemical
compositions of the two weld beads and the base metal were listed out in Table 2.
The loss of magnesium in both TIG and P-TIG welds are around 35%, when
compared to the base metal. The presence of Mn and Zn has increased slightly in
both types of welds compared to the base metal. The loss of scandium in both the
TIG and P-TIG welds are nearly equal to 12.3%.
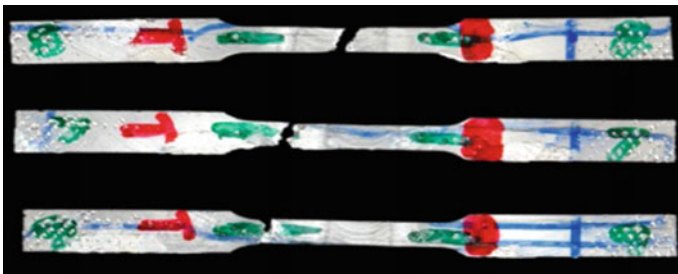
Fig. 10 Tensile specimens after testing
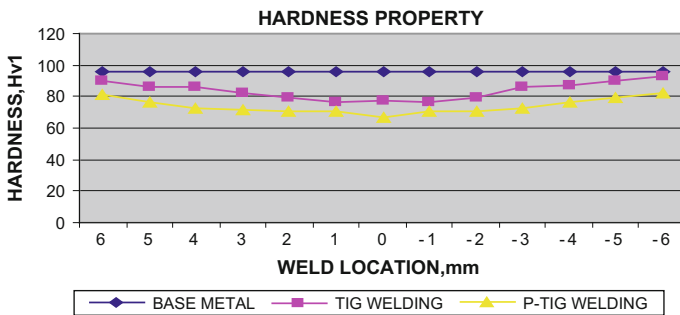
Fig. 11 Broken samples after testing

Fig. 12 Hardness properties of TIG, P-TIG welded joints, and cast base metal

Table 2 Chemical composition of the TIG, P-TIG welded joints, and the cast base metal

	Mg	Mn	Fe	Si	Zn	Cu	Cr	Sc	Ti
Base metal	3.954	0.647	0.356	0.133	0.00	0.016	0.023	0.293	0.023
TIG	2.567	0.656	0.032	0.208	0.066	0.032	0.008	0.263	0.009
P-TIG	2.559	0.654	0.033	0.206	0.065	0.035	<0.005	0.265	0.008

4 Conclusions

The effect of constant and pulsed current TIG welding processes on the microstructural characterization and mechanical properties of the cast aluminum–magnesium–scandium alloy was investigated.

- The microstructural evaluation of the P-TIG weld contains fine grains compared to the TIG weld region and the base metal.
- The tensile properties of both TIG and P-TIG welded samples revealed some interesting phenomena. The tensile properties of TIG welded samples are better than the tensile properties of the cast base metal and P-TIG welding. On the

other hand, the tensile properties of P-TIG welded samples are less than the tensile properties of the cast base metal and TIG welding.

- The hardness and tensile properties of the TIG welded samples are better than the cast base metal and P-TIG welds. The hardness and tensile properties of the P-TIG welded samples were inferior to both TIG welding samples and the cast base metal samples.
- The evaporation of magnesium in both TIG and P-TIG welds were found to be more or less the same amount. Further, studies are required to confirm the mechanisms of grain refinement.

References

1. Filatov, Y.A., Yelagin, V.I., Zakharov, V.V.: New Al-Mg-Sc alloys. Mater. Sci. Eng., A **280**, 97–101 (2000)
2. Madhusudhan Reddy, G., Gokhale, A.A., Prasad Rao, K.: Mater. Sci Technol. **14**, 61 (1993)
3. Balasubramanian, M., Jayabalan, V., Balasubramanian, V.: J. Mater. Sci. Technol. **22**(6), 821 (2006)
4. Willey, L.A.: US Patent No 3,619,181 (1971)
5. Davydov, V.G., Rostova, T.D., Zakharov, V.V., Filatov, Y.A., Yelagin, V.I.: Scientific principles of making an alloying addition of scandium to aluminum alloys. Mater. Sci. Eng. A **280**, 30–36 (2000)
6. Attallah, M.: Microstructure-property development in friction stir welds of aluminum-based alloys. Ph.D. Thesis, Metallurgy and Materials Department, School of Engineering, University of Birmingham, UK (2007)
7. Attallah, M.M., Davis, C.L., Strangwood, M.: Microstructure-hardness relationships in friction stir welded AA5251. J. Mater. Sci. **42**, 7299–7306 (2007)
8. Hatch, J.E.: Aluminum: Properties and Physical Metallurgy. ASM International, Materials Park, Ohio, U.S, p. 209 (1984)
9. Subbaiah, K., Geetha, M., Sridhar, N., Koteswara Rao, S.R.: Comparison of tungsten inert gas and friction stir welding of AA 5083-H321 aluminium alloy plates. Trends in welding research. Proceedings of the 9th International Conference, pp. 598–603. ASM International, June 4–8, Chicago, Illinois, USA (2012)

Tool Pin Profile Studies on Friction Stir Welded Joints of AA5052-H32 and AA6061-T6 Aluminum Alloys

S. Balamurugan and K. Subbaiah

Abstract Aluminum–Magnesium alloys are widely used in the construction of transportation industries bodies of structures in automobile, railways, and marine industries. The fusion welding techniques such as metal inert gas welding and tungsten inert gas welding are widely used in the fabrication sectors. During fusion welding, the important alloying elements, which have been added for improvement in strength, will be subjected to evaporation. The loss of alloying elements in the welded joints is compensated by adding suitable welding filler rods during the welding processes. Friction stir welding is a recently introduced solid-state welding technique, which eliminates most of the solidification defects found in fusion welding techniques. In friction stir welding process, the tool pin profile plays an important role in mixing the materials to be joined. Selection of suitable pin profile will reduce the defects to be formed in the welded joints and improve its welded joint efficiency. The friction stir welded joints of AA5052-H32 and AA6061-T6 were subjected to mechanical and metallurgical characterization, and the results were analyzed. In this research, an attempt has been made to study the feasibility of joining the dissimilar combination by using cylindrical pin profile.

Keywords Friction stir welding · Dissimilar joints · Cylindrical tool pin profile
Tensile properties

S. Balamurugan · K. Subbaiah (✉)
Department of Mechanical Engineering, SSN College
of Engineering, Chennai 603110, Tamil Nadu, India
e-mail: subbaiahk@ssn.edu.in

S. Balamurugan
e-mail: kirubalas@gmail.com

1 Introduction

The joining of dissimilar materials is becoming increasingly important in industrial applications [1]. Many engineering applications such as power generation, chemical, petrochemical, nuclear, aerospace, transportation, and offshore construction require the joining of dissimilar materials using different methods, especially friction welding and friction stir welding [2]. Due to the different chemical, mechanical, and thermal properties of materials, the joining of dissimilar materials presents more challenges than joining similar materials [3].

Although different works on FSW of dissimilar aluminum alloys have been conducted so far; however, additional studies seem to be of importance owing to the complex mechanical behavior and metallurgical events during and after FSW [4]. The aims of this research are to study the effects of rotational and linear speed of tools as well as to investigate the produced microstructures and precipitation distribution in dissimilar FSW of AA5000 and AA6000 aluminum alloys [4–13].

2 Experimental Work

The 5 mm plates have been FS welded using an indigenously designed and developed machine (30 KN; 300 rpm; 1.5 HP). The tool was made in high-speed steel, M2, quenched at 1020 °C, characterized by a 50–55 HRc. The shoulder diameter is 15 mm, and the cylindrical tool is having a diameter of 5 and 4.7 mm height. The friction stir welding parameters are given in Table 1. The experimental procedure used in this study is given elsewhere [14].

3 Results and Discussion

3.1 Microstructural Studies of the Welded Joints

The optical microstructures of the dissimilar friction stir welded joints of AA5052-H32 and AA6061-T6 with cylindrical pin profile are shown in Figs. 1, 2, 3, 4, 5, 6, 7, and 8. The AA6061-T6 aluminum alloy base metal microstructure is shown in Fig. 1. The grains are seen fully and in elongated position. The black particles are the strengthening precipitates in 6000 series aluminum alloys, viz. Mg_2Si. The heat-affected zone microstructure of the dissimilar welded joint on the

| Table 1 Friction stir welding parameters		
Rotational speed, RPM	800
Traverse speed, mm/min	80
Axial force, KN	10

Fig. 1 AA6061-T6 base metal
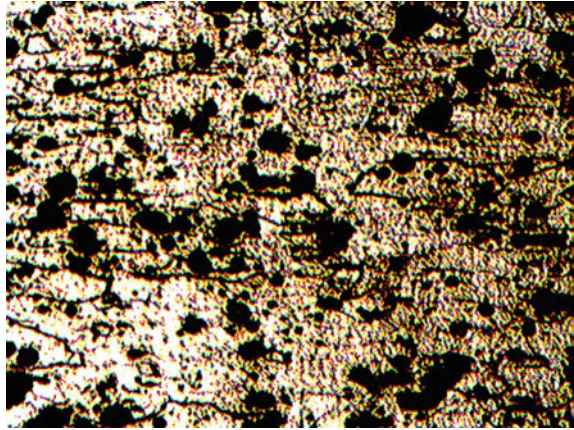
6061 side is shown in Fig. 2. This microstructure shows the dissolution of grain boundaries of 6061 aluminum alloy. The intersection of AA6061-T6 and AA5052-H32 aluminum alloys is shown in Figs. 3 and 4. The top side of the FS weld microstructure on the AA6061-T6 aluminum alloy is shown in Fig. 5. The heterogeneous microstructures of the FS welded joints are shown in Figs. 6 and 7. The tunnel defect formed during the friction stir welding process is shown in Fig. 8. The weld microstructure is shown in Fig. 9. The AA5052-H32 base metal microstructures are shown in Fig. 10.

3.2 Tensile Properties of the Welded Joints

The tensile properties of friction stir welded joints of AA5052-H32 and AA6061-T6 aluminum alloy plates with cylindrical pin profile are found out and listed in Table 2. Generally, the weld nugget tensile strength will be less than that of the base materials. This experiment also gave the similar results. Cylindrical pin showed the tensile strength of 162.18 MPa with a joint efficiency of 73.05% (based on the UTS of the weaker alloy, viz. AA5052-H32).

Similar results were obtained by Devaiah et al. [10] on DFSW of AA5083-H321 and AA6061-T6 aluminum alloys with square pin profile. Amit Goyal et al. [11] have performed DFSW of AA5086-H32 and AA6061-T6 aluminum alloys, and they concluded that out of the five tools pin profiles used in their experiment square pin produced the best weld with joint efficiency around 74%. In our study, the cylindrical pin profiled tool produced around 73% welded joint efficiency. By using better tool pin profile, viz. square and triangle, the welded joint efficiency enhancement can be obtained.
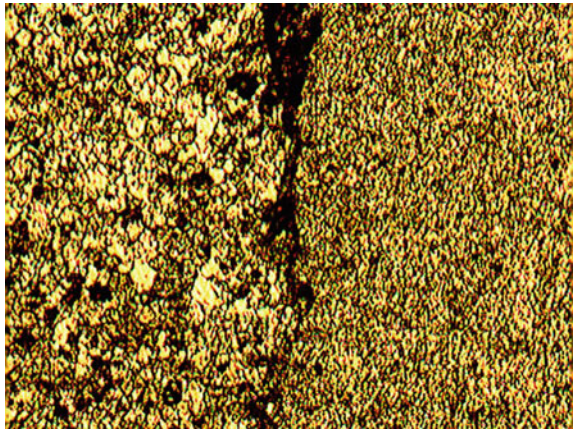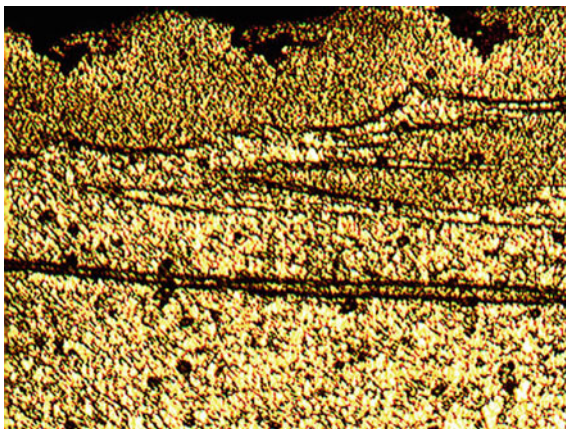
Fig. 2 HAZ on AA6061-T6
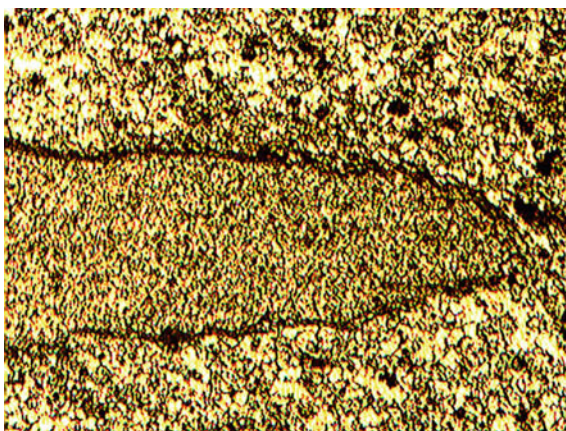side
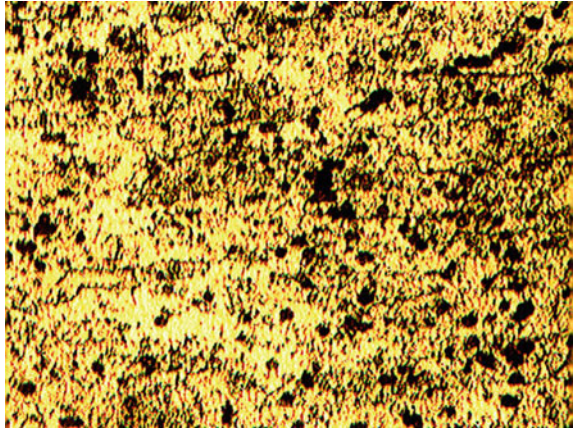
Fig. 3 AA6061-T6 and
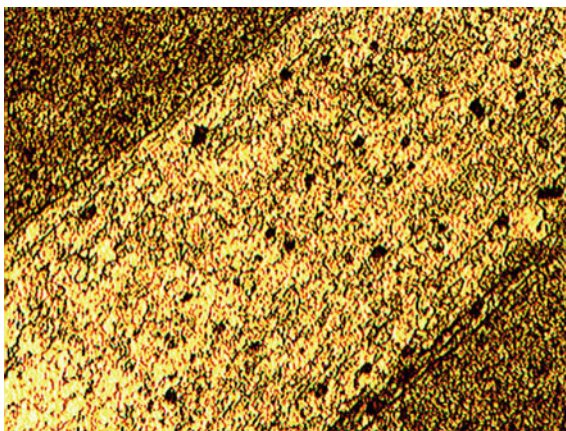AA5052-H32 side
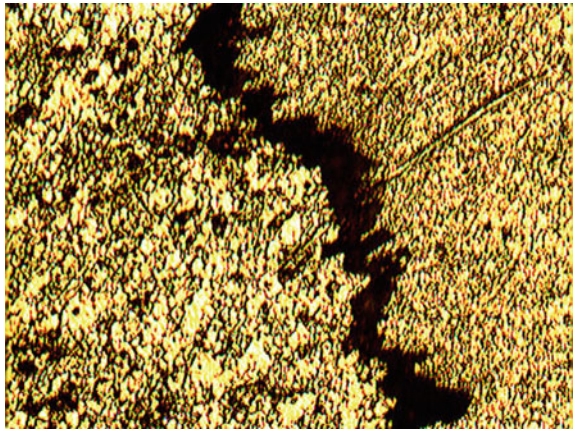
Fig. 4 AA6061-T6 and
AA5052-H32 side

Fig. 5 Weld top surface
AA6061-T6 side

Fig. 6 AA6061-T6 and
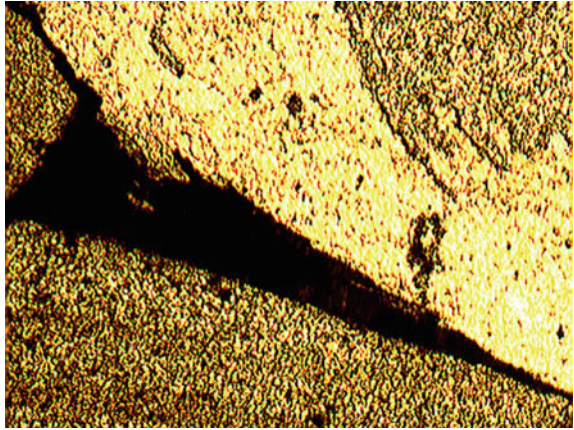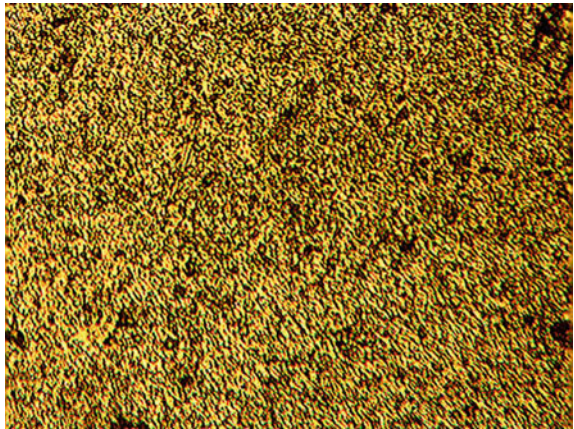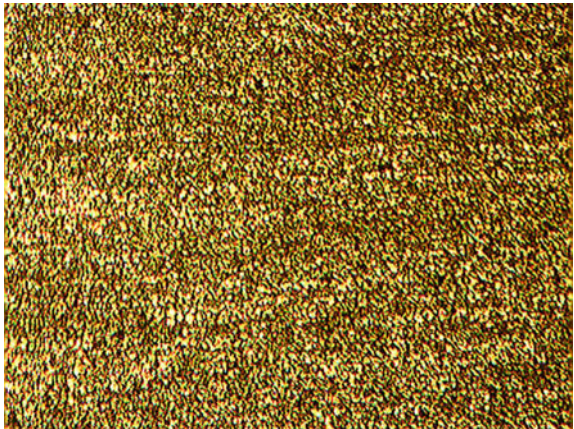AA5052-H32 × 100

Fig. 7 AA5052-H32 and
AA6061-T6 × 100

Fig. 8 AA6061-T6 and AA5052-H32 × 100
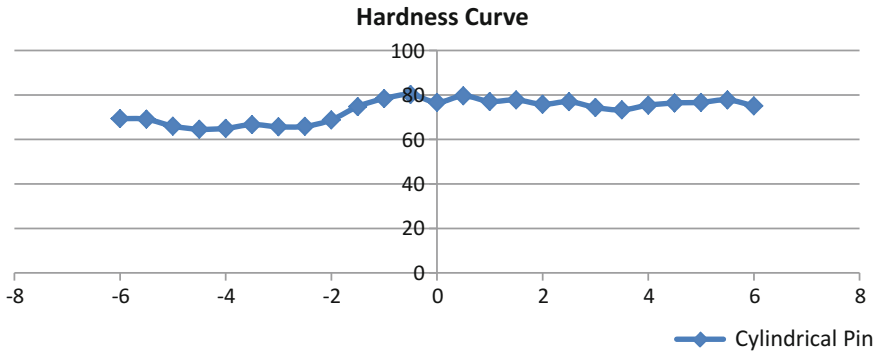

Fig. 9 Weld (AA5052-H32 and AA6061-T6)

Fig. 10 AA5052-H32 base metal

Table 2 Tensile properties of the base metals and welded joint

Material	Tensile strength, MPa	Elongation, %	Joint. efficiency, %
Base metal—AA5052-H32	222	12	–
Base metal—AA6061-T6	325.08	15.93	–
DFSW joint properties	162.18	7.857	73.05

Fig. 11 Hardness distribution of the dissimilar friction stir welded joints

3.3 Hardness Distribution of the Welded Joints

The hardness values along the transverse cross section of the dissimilar friction stir welding of AA5052-H32 and AA6061-T6 aluminum alloys have been shown in Fig. 11 for cylindrical pin. The AA5052-H32 alloy, which has been kept in the right side, is having the hardness values of the base metal around 65 HV1. The AA6061-T6 alloy, which has been kept in the left side, is having the hardness values of the base metal around 110HV1. As the amount of heat supplied is less than the required value, the hardness of the AA6061-T6 base metal is below 115HV1.

4 Conclusions

- The FS welded joint of AA5052-H32 and AA6061-T6 aluminum alloys are possible with cylindrical pin profile. The welded joint efficiency is around 73% of the weaker base metal (AA5052-H32). The dissimilar alloy combination of AA5052-H32 and AA6061-T6 will have to be friction stir welded using square and triangle pin-profiled tools.

References

1. Xue, P., Xiao, B.L., Ni, D.R., Ma, Z.Y.: Enhanced mechanical properties of friction stir welded dissimilar Al–Cu joint by intermetallic compounds. J. Mater. Sci. Eng. A **527**, 5723–5727 (2010)
2. Ouyang, J., Yarrapareddy, E., Kovacevic, R.: Microstructural evolution in the friction stir welded 6061 aluminum alloy (T6-temper condition) to Copper. J. Mater. Process. Technol. **172**, 110–122 (2010)
3. Al-Roubaiy, A.O., Nabat, S.M., Batako, A.D.L.: Experimental and theoretical analysis of friction stir welding of Al–Cu joints. Int. J. Adv. Manuf. Technol. **71**, 1631–1642 (2014)
4. Jamshidi Aval, H., Serajzadeh, S., Sakharova, N.A., Kokabi, A.H., Loureiro, A.: A study on microstructures and residual stress distributions in dissimilar friction-stir welding of AA5086-AA6061. J. Mater. Sci. **47**, 5428–5437 (2012)
5. Shigematsu, I., Kwon, Y.-J., Suzuki, K., Imai, T., Saito, N.: Joining of 5083 and 6061 aluminum alloys by friction stir welding. J. Mater. Sci. Lett. **22**, 353–356 (2003)
6. Palanivel, R., Mathews, P.K., Murugan, N.: Influence of tool pin profile on the mechanical and metallurgical properties of friction stir welding of dissimilar aluminum alloy. Inter. J. Eng Sci. Technol. **2**(6), 2109–2115 (2010)
7. Ilangovan, M., Boopathy, S.R., Balasubramanian, V.: Microstructure and tensile properties of friction stir welded dissimilar AA6061-AA5086 aluminum alloy joints. Trans. Nonferrous Met. Soc. China **25**, 1080–1090 (2015)
8. Cho, J.-H., Kim, M.-H., Choi, J.-W.: FSW Properties of Aluminum alloy 5000/6000 for small boat. J. Weld. Join. **32**(1), 34–39 (2014)
9. Jamshidi Aval, H., Serajzadeh, S., Kokabi, A.H., Loureio, A.: Effect of tool geometry on mechanical and microstructural behaviors in dissimilar friction welding of AA 5086-AA 6061. Sci. Technol. Weld. Join. **16**(7), 597–604 (2011)
10. Devaiah, D., Kishore, K., Lakshminarayana, P.: Effect of welding speed on mechanical properties of dissimilar friction stir welded AA5083-H321 and AA6061-T6 aluminum alloys. Int. J. Adv. Eng. Res. Sci. **4**(3), 22–28 (2017)
11. Goyal, A., Rohilla, P.K., Kaushik, A.K.: Effect of process parameters of friction stir welded dissimilar AA6061-T6 and AA5086-H32 aluminum alloy joints. Int. J. Theo. App. Mech. **12**(1), 21–32 (2017)
12. Kumbhar, N.T., Bhanumurthy, K.: Friction stir welding of Al 5052 with Al 6061 alloys. J. Metall. (2012)
13. Ramachandran, K.K., Murugan, N., Shashi Kumar, S.: Friction stir welding of aluminum alloy AA5052 and HSLA steel. Weld. J. **94**(9), 291s–300s (2015)
14. Subbaiah, K., Geetha, M., Govindaraju, M., Koteswara Rao, S.R.: Mechanical properties of friction stir welded cast Al–Mg–Sc alloys. Trans. Indian Inst. Metals. **65**(2), 155–158 (2012)

Retraction Note to: Interfacial Science in Metal–Ceramic Joining for Thermoelectric Module

S. Stalin, K. Kalaichelvan and T. Sujitha

Retraction Note to:
Chapter "Interfacial Science in Metal–Ceramic
Joining for Thermoelectric Module"
in: K. S. Vijay Sekar et al. (eds.),
Advances in Manufacturing Processes,
Lecture Notes in Mechanical Engineering,
https://doi.org/10.1007/978-981-13-1724-8_31

The authors have retracted this chapter [1] because they did not have permission to use the data in the study which belongs to Anna University International Advanced Research Centre for Powder Metallurgy and New Materials (ARCI). All authors agree to this retraction.

[1] Stalin S., Kalaichelvan K., Sujitha T. (2019) Interfacial Science in Metal–Ceramic Joining for Thermoelectric Module. In: Vijay Sekar K., Gupta M., Arockiarajan A. (eds) Advances in Manufacturing Processes. Lecture Notes in Mechanical Engineering. Springer, Singapore.

The retracted version of this chapter can be found at
https://doi.org/10.1007/978-981-13-1724-8_31